frontiers | Research Topics

Personalized radiation therapy: Guided with imaging technologies

Edited by
Yingli Yang, Davide Cusumano and Jing Cai

Published in
Frontiers in Oncology

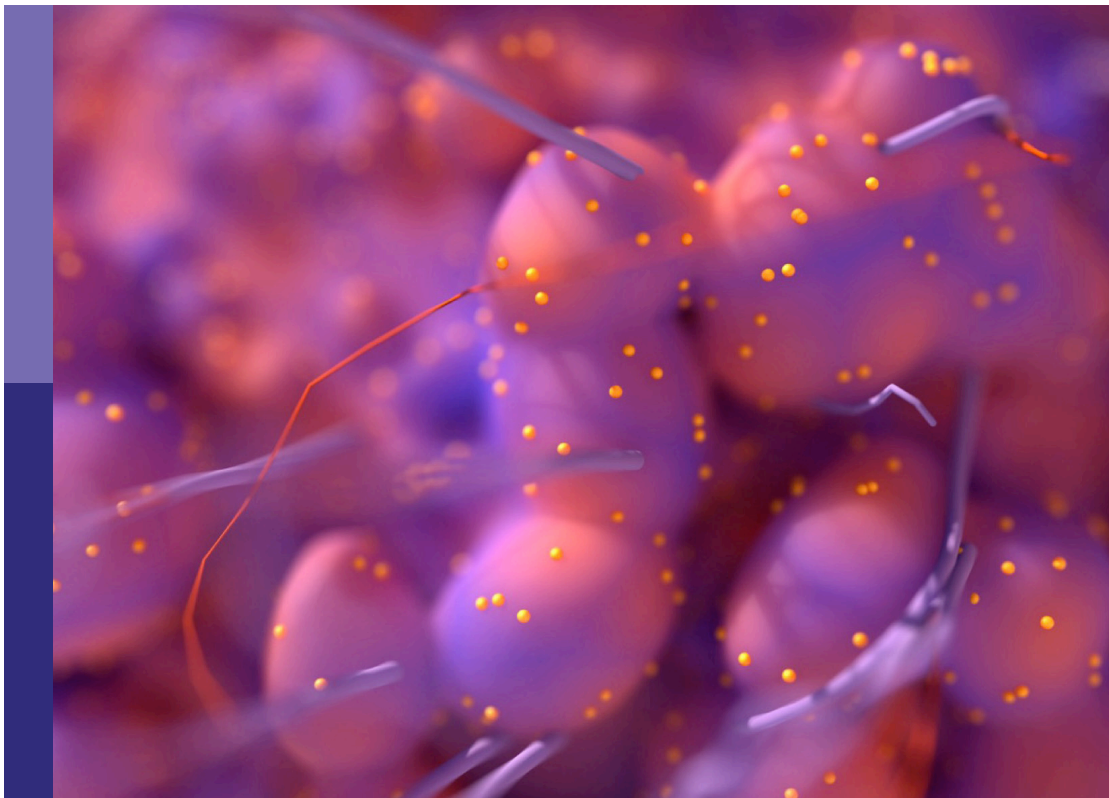

ISSN 1664-8714
ISBN 978-2-83251-109-1
DOI 10.3389/978-2-83251-109-1

About Frontiers

Frontiers is more than just an open access publisher of scholarly articles: it is a pioneering approach to the world of academia, radically improving the way scholarly research is managed. The grand vision of Frontiers is a world where all people have an equal opportunity to seek, share and generate knowledge. Frontiers provides immediate and permanent online open access to all its publications, but this alone is not enough to realize our grand goals.

Frontiers journal series

The Frontiers journal series is a multi-tier and interdisciplinary set of open-access, online journals, promising a paradigm shift from the current review, selection and dissemination processes in academic publishing. All Frontiers journals are driven by researchers for researchers; therefore, they constitute a service to the scholarly community. At the same time, the *Frontiers journal series* operates on a revolutionary invention, the tiered publishing system, initially addressing specific communities of scholars, and gradually climbing up to broader public understanding, thus serving the interests of the lay society, too.

Dedication to quality

Each Frontiers article is a landmark of the highest quality, thanks to genuinely collaborative interactions between authors and review editors, who include some of the world's best academicians. Research must be certified by peers before entering a stream of knowledge that may eventually reach the public - and shape society; therefore, Frontiers only applies the most rigorous and unbiased reviews. Frontiers revolutionizes research publishing by freely delivering the most outstanding research, evaluated with no bias from both the academic and social point of view. By applying the most advanced information technologies, Frontiers is catapulting scholarly publishing into a new generation.

What are Frontiers Research Topics?

Frontiers Research Topics are very popular trademarks of the *Frontiers journals series*: they are collections of at least ten articles, all centered on a particular subject. With their unique mix of varied contributions from Original Research to Review Articles, Frontiers Research Topics unify the most influential researchers, the latest key findings and historical advances in a hot research area.

Find out more on how to host your own Frontiers Research Topic or contribute to one as an author by contacting the Frontiers editorial office: frontiersin.org/about/contact

Personalized radiation therapy: Guided with imaging technologies

Topic editors

Yingli Yang — Department of Radiation Oncology, UCLA Health System, United States

Davide Cusumano — Agostino Gemelli University Polyclinic (IRCCS), Italy

Jing Cai — Hong Kong Polytechnic University, Hong Kong, SAR China

Citation

Yang, Y., Cusumano, D., Cai, J., eds. (2023). *Personalized radiation therapy: Guided with imaging technologies*. Lausanne: Frontiers Media SA.

doi: 10.3389/978-2-83251-109-1

Table of contents

frontiers | Frontiers in Oncology

TYPE Editorial
PUBLISHED 06 December 2022
DOI 10.3389/fonc.2022.1078265

OPEN ACCESS

EDITED AND REVIEWED BY
Timothy James Kinsella,
Brown University, United States

*CORRESPONDENCE
Yingli Yang
yyl12920@rjh.com.cn

SPECIALTY SECTION
This article was submitted to Radiation Oncology, a section of the journal Frontiers in Oncology

RECEIVED 24 October 2022
ACCEPTED 09 November 2022
PUBLISHED 06 December 2022

CITATION
Yang Y, Cai J and Cusumano D (2022) Editorial: Personalized radiation therapy: Guided with imaging technologies.
Front. Oncol. 12:1078265.
doi: 10.3389/fonc.2022.1078265

Editorial: Personalized radiation therapy: Guided with imaging technologies

Yingli Yang[1,2]*, Jing Cai[3] and Davide Cusumano[4,5]

[1]Department of Radiology, Ruijin Hospital, Shanghai Jiaotong Univeristy School of Medicine, Shanghai, China, [2]SJTU-Ruijing_UIH Institute For Medical Imaging Technology, Shanghai, China, [3]Department of Health Technology and Informatics, The Hong Kong Polytechnic University, Hung Hom, Hong Kong, Hong Kong SAR, China, [4]Mater Olbia Hospital, Olbia, Italy, [5]Fondazione Policlinico Universitario Agostino Gemelli IRCCS, Rome, Italy

KEYWORDS

personalized radiotherapy, MR guided RT (MRgRT), biology guided radiotherapy (BgRT), functional imaging, image guidance

Editorial on the Research Topic
Personalized radiation therapy: Guided with imaging technologies

Over the years, with developments in technology and radiobiology, radiation therapy has evolved into a primary treatment method for many cancer patients with certain disease sites. However, in current radiotherapy (RT) practices, we are still treating each patient within a specific tumor type and stage with a common dose, ignoring the wide per-patient and per-tumor-sub-volume dose-response variations and missing the opportunity to dynamically modify the dose distribution based on tumor response (1). Radiation therapy (RT) efficacy is crippled by this lack of patient-specific treatment strategy. More and more studies have shown the value of personalized cancer treatments. Vendors and research institutes are also working on new treatment technologies with achieving personalized radiation therapy as one of the goals (2–5) Among all the newly introduced technologies, majority of them involves novel integration of imaging technologies. Such as, MR guided radiation therapy (MRgRT), biology-guided radiotherapy (BgRT) with onboard PET, CT guided RT, CBCT-guided RT with modern platform based on artificial intelligence (AI), and dedicated MR simulator for RT. In combination with the introduction of AI and radiomics into RT, online adaptive treatments and treatment response prediction are becoming practical to be included into clinical RT practice (6). The current issue highlights recent works in advancing personalized radiation therapy, specifically with the help of imaging guidance.

Among a number of proposals submitted, 19 of which were accepted for publication in the special issue. The accepted papers can be grouped in to the following three main

directions: (1) importance of personalized radiation therapy; (2) image based treatment response prediction; (3) exploration of personalized treatment.

Importance of personalized radiation therapy

Iezzi et al. presented a study on evaluating the dosimetric importance of on-line adaptive for breast IMRT treatment. A strategy is also proposed to make automatic prediction based on daily CBCT if on-line adaptive is necessary for that specific fraction. Also targeting on breast cancer, Wang et al. introduced their study on the incidental irradiation to internal mammary node (IMN) for patients underwent different type of surgery, radical mastectomy vs. breast-conserving surgery, and different radiotherapy regimens. Their study came to the conclusion that surgery type was the influencing factor of dose to IMN with conventional radiotherapy strategy. This opens up a question: is it possible to achieve more optimal dose to IMN regardless of the surgery type patients received with personalized RT? Zhang et al. used a "Sphere-mask" optical positioning system (S-M_OPS) retrospectively analyzed the setup errors for a large group of patients with different disease sites. In addition to introducing the efficiency and setup accuracy of S-M_OPS, the study also highlighted the residual setup errors with different mainstream setup tools, which can be further accounted for by on-line personalized RT.

Image based treatment response prediction

Luo et al. introduced their model that is based on CT radiomics, clinical and dosimetric parameters to predict 1-year local control for lung cancer patients treated with SBRT. On the platform of low field MRgRT, Chiloiro et al. performed a study evaluating a "delta radiomics" approach to predict 2-year disease-free-survival (2yDFS) for rectal cancer patient undergoing neoadjuvant chemoradiotherapy (nCRT). For the same type of patients, Shi et al. investigated the usage of combined information of pretreatment blood biomarkers and MRI based morphological information to predict nCRT treatment response. Besides anatomical information, different medical imaging modalities can also provide functional information. Currently, anatomical change is still the main clinical criteria for treatment response evaluation. However, functional change, such as metabolism, cellular density, and vasculature, usually happens earlier than morphological changes (7–11) This is a highly desirable feature for treatment response prediction so that it can be used to improve treatment efficacy with early intervention. Zhou et al. performed a comprehensive review on the applications of functional imaging in liver-sparing RT. Kooreman et al. introduced an interesting study investigating longitudinal treatment response monitoring, using perfusion MRI techniques on a cohort of prostate patients. They evaluated two different perfusion MRI techniques, Intravoxel Incoherent Motion (IVIM) and Dynamic Contrast-Enhanced (DCE) MRI, finding significant correlations. This study highlighted the possibility of using IVIM as a non-contrast alternative perfusion MRI for longitudinal acquisition to achieve early treatment response prediction. For a cohort of head and neck patients, Chen et al. performed pre-treatment and weekly mid-treatment FDG-PET/CT acquisition during standard chemoradiotherapy. Tumor voxel dose-response matrix (DRM) constructed based on the serial FDG-PET/CT was proven to be a predictive tool for treatment response. Also with FDG-PET, Ji et al. developed a convolutional neural network (CNN) taking pre-treatment FDG-PET and spatial dose distribution as input to predict RT treatment outcome as a synthetic post-treatment FDG-PET, which can be used for adaptive RT decision making or on-line planning.

Exploration of personalized treatment

Personalized treatment is a broad definition, and the personalized portion can happen at different steps of the entire RT workflow. Hooshangnejad et al. introduced a novel patient-specific duodenal pacer simulator algorithm, which can serve as a decision support system to provide optimal spacer location for placement guidance. Ku et al. introduced a novel fiducial marker (FM) implantation procedure by adding a patient specific pre-implant planning and simulation step. For patients with invisible lung tumors treated on CyberKnife, this retrospective study proved that the additional step reduces the patient radiation exposure and increases the number of FMs inserted around tumors. Zhang et al. explored an augmented reality (AR) – assisted RT positioning system using HoloLens 2. This is an interesting and novel patient specific positioning study and concluded that the proposed AR-assisted RT positioning method is highly feasible with several advantages. Using image guidance to personalize RT during treatment planning or treatment fractions is gaining a lot of research interests in the past several years. Zhu et al. used multiparametric MRI including 3D ASL to differentiate high and low blood perfusion areas within GTV for a group of adult non-enhancing low-grade gliomas (NE-LGGs). This generated information can be used to guide personalized RT boost for

treatment efficacy improvements. Also for tumor segmentation purpose, Lau et al. explored a gradient-based method using 18F-PSMA-1007 PET/CT for prostate cancer lesion contouring and quantification. Nie and Li proposed predictive strategy to project tumor volume onto 2D MR cine from 4D MRI libraries for personalized MRgRT. By accurately predict respiratory motion during 2D cine imaging and projecting tumor volume contour on 2D cine, real-time assessment of beam-to-tumor conformality was proven to be feasible and promising for personalized MRgRT. Last but not the least, biology-guided radiation therapy (BgRT), represented by RefleXion X1™, the first FDA cleared BgRT system, is another novel and promising technology that can potentially bring meaningful personalized RT into routine clinical practice. Seyedin et al. described a planning comparison study on RefleXion X1™ and proved its potential as a powerful tool to reduce the radiation dose to nearby structures by using real-time positron emission imaging.

We have presented here some snapshots of different research activities in our field related personalized radiotherapy. We are hoping this can serve as a handy reference resource for students and researchers who are interested in this area and inspire more and more studies to further advance personalized RT with the ultimate goal of maximizing RT efficacy for every patient.

Author contributions

YY, JC and DC contributed to conception and writing of the editorial. All authors contributed to the article and approved the submitted version.

Conflict of interest

The authors declare that the research was conducted in the absence of any commercial or financial relationships that could be construed as a potential conflict of interest.

Publisher's note

References

1. Hall EJ, Giaccia AJ. Radiobiology for the Radiologist, LWW; 8th edition. (2018), ISBN-10: 1496335418.

2. Sasa Mutic JF. Dempsey, "The ViewRay system: Magnetic resonance-guided and controlled radiotherapy". *Semin Radiat Oncol* (2014) 7:196–9. doi: 10.1016/j.semradonc.2014.02.008

3. Kerkhof EM, Raaymakers BW, van Vulpen M, Zonnenberg BA, Ruud Bosch JLH, vanMoorselaar RJA, et al. A new concept for non-invasive renal tumour ablation using real-time MRI-guided radiation therapy. *BJU Int* (2011) 1:63–8. doi: 10.1111/j.1464-410X.2010.09458.x

4. Shirvani SM, Huntzinger CJ, Melcher T, Olcott PD, Voronenko Y, Bartlett-Roberto J, et al. Biology-guided radiotherapy: Redefining the role of radiotherapy in metastatic cancer. *Br J Radiol* (2021) 94:1117. doi: 10.1259/bjr.20200873

5. Jonsson J, Nyholm T, Soderkvist K. The rationale for MR-only treatment planning for external radiotherapy. *Clin Trans Radiat Oncol* (2019) 18:60–5. doi: 10.1016/j.ctro.2019.03.005

6. Gao Y, Ghodrati V, Kalbasi A, Fu J, Ruan D, Cao M, et al. Prediction of soft tissue sarcoma response to radiotherapy using longitudinal diffusion MRI and a deep neural network with generative adversarial network-based data augmentation. *Med Phys* (2021) 48:3262–372. doi: 10.1002/mp.14897

7. Bhatnagar P, Subesinghe M, Patel C, Prestwich R, Scarsbrook AF. Functional imaging for radiation treatment planning, response assessment, and adaptive therapy in head and neck cancer. *Radiographics* (2013) 33(7):1909–29. doi: 10.1148/rg.337125163

8. Tsien C, Cao Y, Chenevert T. Clinical applications for diffusion magnetic resonance imaging in radiotherapy. *Semin Radiat Oncol* (2014) 24:218–26. doi: 10.1016/j.semradonc.2014.02.004

9. Teo QQ, Thng CH, Koh TS, Ng QS. Dynamic contrast-enhanced magnetic resonance imaging: Applications in oncology. *Clin Oncol* (2014) 26:e9–20. doi: 10.1016/j.clon.2014.05.014

10. Dijkhoff RAP, Beets-Tan RGH, Lambregts DMJ, Beets GL, Maas M. Value of DCE-MRI for staging and response evaluation in rectal cancer: A systematic review. *Eur J Radiol* (2017) 95:155–68. doi: 10.1016/j.ejrad.2017.08.009

11. Knopp MV, von Tengg-kobligk H, Choyke PL. Functional magnetic resonance imaging in oncology for diagnosis and therapy monitoring. *Mol Cancer Ther* (2003) 2:419–26.

frontiers in Oncology

ORIGINAL RESEARCH
published: 31 January 2022
doi: 10.3389/fonc.2021.819047

A Combined Model to Improve the Prediction of Local Control for Lung Cancer Patients Undergoing Stereotactic Body Radiotherapy Based on Radiomic Signature Plus Clinical and Dosimetric Parameters

Li-Mei Luo[1,2†], Bao-Tian Huang[2†], Chuang-Zhen Chen[2], Ying Wang[1,2], Chuang-Huang Su[3], Guo-Bo Peng[4], Cheng-Bing Zeng[2], Yan-Xuan Wu[2], Ruo-Heng Wang[1,2], Kang Huang[1,2] and Zi-Han Qiu[5]*

[1] Department of Radiation Oncology, Shantou University Medical College, Shantou, China, [2] Department of Radiation Oncology, Cancer Hospital of Shantou University Medical College, Shantou, China, [3] Department of Radiation Oncology, Shantou Central Hospital, Shantou, China, [4] Department of Radiation Oncology, Meizhou People's Hospital (Huangtang Hospital), Meizhou Academy of Medical Sciences, Meizhou, China, [5] Department of Otolaryngology-Head and Neck Surgery, The First Affiliated Hospital of Shantou University Medical College, Shantou, China

Purpose: Stereotactic body radiotherapy (SBRT) is an important treatment modality for lung cancer patients, however, tumor local recurrence rate remains some challenge and there is no reliable prediction tool. This study aims to develop a prediction model of local control for lung cancer patients undergoing SBRT based on radiomics signature combining with clinical and dosimetric parameters.

Methods: The radiomics model, clinical model and combined model were developed by radiomics features, incorporating clinical and dosimetric parameters and radiomics signatures plus clinical and dosimetric parameters, respectively. Three models were established by logistic regression (LR), decision tree (DT) or support vector machine (SVM). The performance of models was assessed by receiver operating characteristic curve (ROC) and DeLong test. Furthermore, a nomogram was built and was assessed by calibration curve, Hosmer-Lemeshow and decision curve.

Results: The LR method was selected for model establishment. The radiomics model, clinical model and combined model showed favorite performance and calibration (Area under the ROC curve (AUC) 0.811, 0.845 and 0.911 in the training group, 0.702, 0.786 and 0.818 in the validation group, respectively). The performance of combined model was significantly superior than the other two models. In addition, Calibration curve and Hosmer-Lemeshow (training group: P = 0.898, validation group: P = 0.891) showed good calibration of combined nomogram and decision curve proved its clinical utility.

OPEN ACCESS

Edited by:
Yingli Yang,
UCLA Health System, United States

Reviewed by:
Weiwei Zong,
Henry Ford Health System, United States
Feng Liu,
Avera McKennan Hospital and University Health Center, United States

***Correspondence:**
Bao-Tian Huang
hbt830910@126.com

†These authors have contributed equally to this work and share first authorship

Specialty section:
This article was submitted to Radiation Oncology, a section of the journal Frontiers in Oncology

Received: *20 November 2021*
Accepted: *31 December 2021*
Published: *31 January 2022*

Citation:
Luo L-M, Huang B-T, Chen C-Z, Wang Y, Su C-H, Peng G-B, Zeng C-B, Wu Y-X, Wang R-H, Huang K and Qiu Z-H (2022) A Combined Model to Improve the Prediction of Local Control for Lung Cancer Patients Undergoing Stereotactic Body Radiotherapy Based on Radiomic Signature Plus Clinical and Dosimetric Parameters. Front. Oncol. 11:819047. doi: 10.3389/fonc.2021.819047

Conclusions: The combined model based on radiomics features plus clinical and dosimetric parameters can improve the prediction of 1-year local control for lung cancer patients undergoing SBRT.

Keywords: lung cancer, stereotactic body radiotherapy, local control, radiomics, clinical, dosimetric, prediction model

INTRODUCTION

Lung cancer is the second most common cancer and the main cause of cancer-related deaths, more than 2.21 million patients worldwide are affected every year (1). With the improvement of radiotherapy technology, stereotactic body radiation therapy (SBRT) is generally recognized as a standard option for early stage lung cancer patients who are not fit or healthy enough to be candidates for surgery or who refuse operation due to various complications (2). SBRT is also well established in the treatment of oligometastatic patients, e.g., with pulmonary metastases (3). This precise modality uses high doses to ablative cancer target with low doses to protect surrounding tissue. The local control rate in 5 years after SBRT is about 72% with a median follow-up of 4 years for early stage localized tumors (4). Furthermore, a variety of studies have reported local control is excellent after SBRT; however, there are still patients suffering from local recurrence (5). Therefore, a model for accurately and individually predicting the local control status for lung cancer patients after SBRT is highly desirable.

The maximum standardized uptake value (SUVmax) in PET-CT was used to predict local recurrence after SBRT, but the results varied from institutions to patient groups, suggesting that its prognostic value was uncertain (6, 7). Several studies reported some clinical and dosimetric factors were influential parameters for local control prediction (8–11) and dose-response model to calculate local control possibility for lung SBRT patients employed clinical and dosimetric parameters were established (12–15). However, their models did not accurately predict patients' outcome, while other tumor individual characteristics were not considered. A comprehensive and noninvasive approach based on individual heterogeneous to screen candidate patients with tumor local control status is necessary.

Radiomics is based on the extraction of tumor features from traditional medical images to predict treatment effectiveness and prognosis of different diseases, including lung cancer, esophageal cancer, and prostate cancer (16–19). Moreover, radiomics has prognostic value in predicting clinical outcomes of pulmonary SBRT (20, 21). However, few prediction models considering radiomic signature combined with clinical and dosimetric parameters has been proposed to evaluate the tumor local control for lung cancer patients undergoing SBRT.

Therefore, the aim of our study is to generate a robust combined model for predicting 1-year tumor local control in primary and secondary lung cancer patients treated with SBRT by integrating radiomic signature and clinical and dosimetric parameters.

MATERIALS AND METHODS

The workflow of the study is shown in **Figure 1**.

Patients' Population and Treatment

We firstly analyzed retrospectively registered data from July 27, 2011 to December 7, 2018 of patients diagnosed with primary and secondary lung cancer and treated with lung SBRT in Cancer Hospital of Shantou (N = 134). Next, some patients with irradiation sites including chest wall, mediastinum, and thoracic vertebra (N = 4), who were lost to follow-up (N = 18) and did not complete the treatment course (N = 1) were excluded from the analysis. Finally, 119 patients with 18 patients had repeat lesions and 129 tumors were available for next analysis. The study was conducted in accordance with the Declaration of Helsinki and approved by the ethical board; however, patient written informed consent was waived. Our patients were staged by using the seventh editions of the AJCC staging system. Tumors were simulated *via* four-dimensional computed tomography (4DCT) or three-dimensional computed tomography (3DCT). The internal target volume (ITV) with 4DCT was defined by combining gross tumor volumes (GTVs) contoured at 10 respiratory phases. In addition, some ITV with 3DCT was defined by two GTVs contoured at the peak-exhale and peak-inhale respiratory phases; other ITV with 3DCT was defined by observing the tumor motion amplitude obtained from fluoroscopy. The planning target volume (PTV) was delineated by adding 5 mm of ITV in all directions. Cone beam computed tomography (CBCT) was used for image guidance and tumor localization before each fraction with correction. All patients were randomly assigned to the training group and validation group in a ratio of 7:3.

Follow-Up

Patients were evaluated with CT scans repeated every 3 months after the treatment in the first year, and then every 6 months thereafter (4). Tumor local control is defined as the absence of local recurrence of the tumor at the treatment site. Local recurrence was defined by pathologic confirmation, mass progression of the primary tumor, and the involved lobe on two consecutive CT at least 6 months, or the discretion of oncologists based on clinical symptoms and signs of patients (14, 22).

Clinical and Dosimetric Parameters Data Collection

We collected patients' baseline clinical and dosimetric parameters and 1-year tumor local status after SBRT. All the

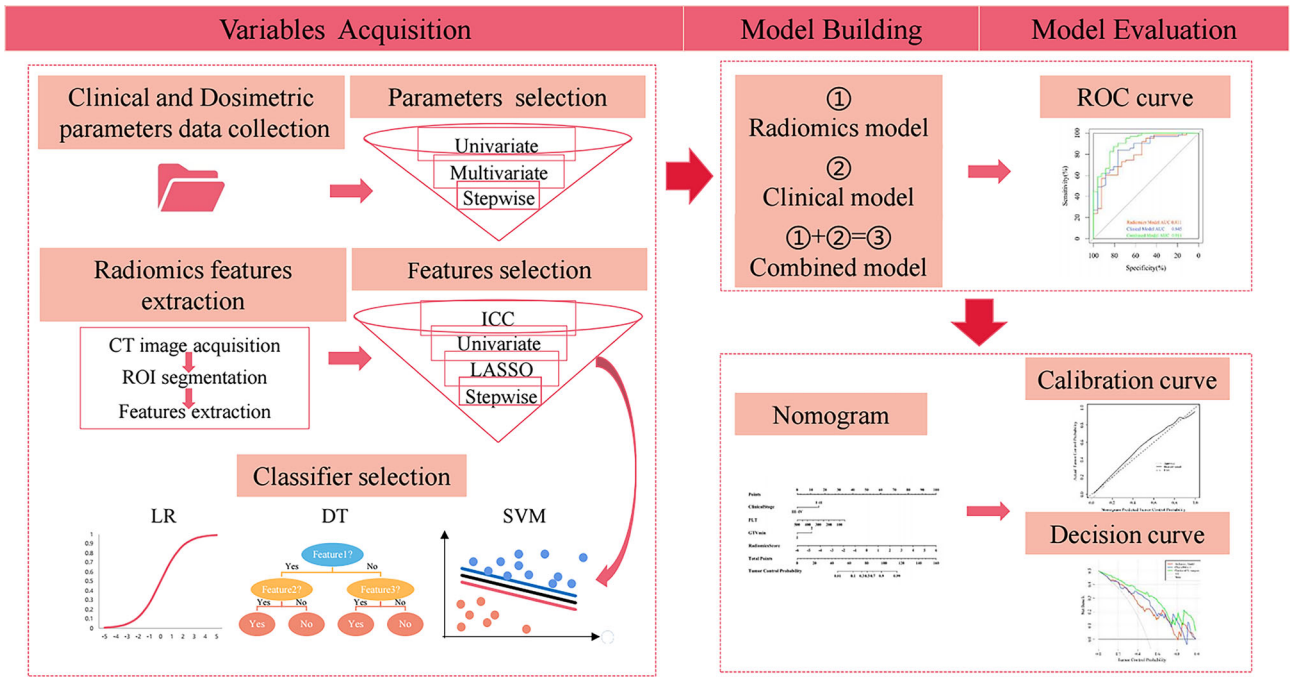

FIGURE 1 | Workflow of the study. ROI, region of interest; ICC, intraclass correlation coefficient; LASSO, least absolute shrinkage and selection operator; LR, logistic regression; DT, decision tree; SVM, support vector machine. ROC, receiver operating characteristic.

doses mentioned in this paper were biologically effective doses (BEDs), the linear-quadratic model with an α/β ratio of 10 Gy was adopted for calculating BEDs, BED = $n \times d \times [1 + d/(\alpha/\beta)]$, where n is the fraction number and d is the fractional dose (15). Clinical data included gender, age, smoking status, Karnofsky performance status (KPS), body mass index (BMI), clinical stage, location, histology, equivalent diameter, GTV, PTV, chemotherapy or not, lymphocyte, neutrophil, platelet (PLT), neutrophil-to-lymphocyte ratio (NLR), platelet-to-lymphocyte ratio (PLR), hemoglobin (Hb), tumor site, immobilization device, and 4DCT or not. Dosimetric data included the prescription dose that covers 95% of the target area expressed as BED (D_{95}) and the maximum dose in the whole plan (D_{max}); the minimum dose of PTV (PTV_{min}), mean dose of PTV (PTV_{mean}), and maximum dose of PTV (PTV_{max}) and dose inhomogeneity in PTV (PTV_{min}/PTV_{max}); and the minimum dose of GTV (GTV_{min}), mean dose of GTV (GTV_{mean}), and the maximum dose of GTV (GTV_{max}) and dose inhomogeneity in GTV (GTV_{min}/GTV_{max}).

Clinical and Dosimetric Parameter Selection

The univariate logistic regression (LR) analysis was applied to evaluate whether parameters were candidate predictors of 1-year tumor local control and a stepwise multivariate LR was used to determine the best variables of statistically significant parameters in univariate analysis.

CT Image Acquisition, Region of Interest Segmentation and Quantitative Radiomics Features Extraction

All patients underwent CT scanning prior to SBRT treatment using a Brilliance Big Bore CT (Philips Brilliance CT Big Bore Oncology Configuration, Cleveland, OH, USA). The detailed information of the CT scanners was as follows: tube voltage of 120 kVp, tube current of 350 mA, convolution kernel of standard, and construction matrix of 512 × 512. The scanning range was from the apex to the bottom of the lung. CT images were then transferred to an Eclipse treatment planning system (Version 10.0, Varian Medical System, Inc., Palo Alto, CA, USA) for the whole tumor delineation, also known as the region of interest (ROI) segmentation by one radiology doctor with more than 10 years of work experience (23).

Radiomics features were automatically extracted from each tumor segmentation using PyRadiomics (https://github.com/Radiomics/pyradiomics). The images which were used to extract the radiomics features could be either the original image or the derivative filtered images including Laplacian of Gaussian (LoG), Wavelet, Square, SquareRoot, Logarithm. Collectively, the feature types extracted from each image type include shape features provided the geometric volume of ROI, first-order features described the individual voxel value distribution in the intensity histogram of ROI, texture features reflected the organization and arrangement of the surface structure with slow change or periodic change, including gray-

level co-occurrence matrix (GLCM), gray-level dependence matrix (GLDM), gray-level run length matrix (GLRLM), gray-level size zone matrix (GLSZM), and neighborhood gray-tone difference matrix (NGTDM) (24). In order to ensure the repeatability of the results, the images and features were resampled and z-score normalized respectively.

Radiomics Feature Selection

A large number of radiomic features may result in overfitting of the model, reducing the predictive performance of the model. To overcome the dimensional disaster and reduce the bias caused by many radiomics features, we gradually use four methods of the intraclass correlation coefficient (ICC), univariant analysis, least absolute shrinkage and selection operator (LASSO), and stepwise regression to select the vital features from the training group. First, in order to minimize the differences between observers and enhance the robustness of features, two radiology doctors independently delineated 30 randomly chosen samples drawn from patients, and then the ICC was calculated from the extracted features of these 30 cases to assess intraobserver and interobserver reproducibility. The features with ICC >0.75 were considered stable for the further analysis. The ICC was conducted by using the "irr" package in R software (25). Subsequently, we evaluated remaining radiomics features using the independent samples *t*-test or the Mann-Whitney *U* test to collect statistically significant features with a *p*-value of <0.05. In addition, to deal with the high-dimensional data and enhance the prediction accuracy, the LASSO regression, as an effective dimensionality reduction method, was applied to select potentially important features by regularizing concurrently. The optimal area under curve and parameter log (λ) were determined through 10-fold cross-validation to control the complexity of the model and select the most robust and nonredundant radiomics features (26, 27). The LASSO logistic regression was conducted by using the "glmnet" package (28). Finally, stepwise regression is used to eliminate the redundant features to avoid the multicollinearity. Moreover, the importance of the most valuable features were analyzed and evaluated by correlation analysis.

Classifier Selection

We fed the final selected radiomics features into the classifiers to build the optimal radiomics model. In our study, LR, decision tree (DT), and support vector machine (SVM) were used to build and evaluate radiomics model, and the best classification method was selected for subsequent analysis (29–31). The DT model was performed using the "rpart" package (32), while the "e1071" package was employed to develop the SVM model (28), all of them are carried out by tuning the parameters. To complement the analyses, the radiomics signature (radiomics score) was calculated using the radiomics features. The best classifier was adopted for building clinical model and combined model.

Prediction Model Development

Accordingly, three different prediction models were described briefly as: the radiomics model composed of radiomics signature, the clinical model constructed from clinical and dosimetric parameters, and the combined model developed by combining radiomics signature and clinical and dosimetric parameters.

Model Performance Comparison

Based on receiver operating characteristic (ROC) curve, the prediction models were compared by calculating the area under the ROC curve (AUC) values, *p*-value, accuracy, sensitivity, specificity, and DeLong test. The ROC curves were plotted based on the "pROC" package (33).

Nomogram Construction and Validation

In order to visually and individually predict the tumor control probability (TCP) of lung cancer after SBRT, we created a nomogram which was developed by the prediction model with the best performance in the training group. The ability of the nomogram was conducted by the calibration curve and the Hosmer-Lemeshow test. The net benefits and the clinical usefulness of three models for prognosis was measured and compared by the decision curve analysis. The nomogram and the DCA were plotted using the "rms" package and the "dca.R." package, respectively (33).

Statistical Analysis

Statistical analyses were performed based on SPSS v.23.0 (SPSS Inc., Chicago, IL, USA) and R software v.4.0.2 (R Project for Statistical Computing, Vienna, Austria). The Student's *t*-test or Mann-Whitney *U* test was employed to compare continuous variables, and the Chi-square test or Fisher's exact test was applied for categorical variables. The optimal cutoff point was assessed by using the Youden's index on the ROC curve (34). An AUC comparison of the three prediction models with the best classifier methods was performed by DeLong test. The tests were two-sided, and *p*-values less than 0.05 were considered statistically significant.

RESULTS

Clinical and Dosimetric Parameters of Patients

Data for 129 tumors from 111 primary and secondary lung cancer patients treated with SBRT were available, of which 89 and 40 tumors were divided into the training and validation group, respectively. Baseline characteristics are presented on **Table S1**. Males constituted 93 (72.1%) of the sample. Mean age was 62 years. Most tumors (82.9%) were at a peripheral location compared with other location. A minority of tumors (18.6%) were treated with combined radiotherapy and concurrent chemotherapy. The median prescription dose was 48 Gy (range 18–70) delivered in a median of 4 fractions (range 1–12), and the median prescription dose in BED_{95} was 95.2 Gy (range 28.8–180). The distribution of fractionation schemes and BED_{95} used in our study was described in **Figure 2**; most used dose-fractionation scheme was 50 Gy in 4 fractions. One year after SBRT treatment, 91 tumors were local controlled and 38 local failures were observed. The optimal cutoff values of

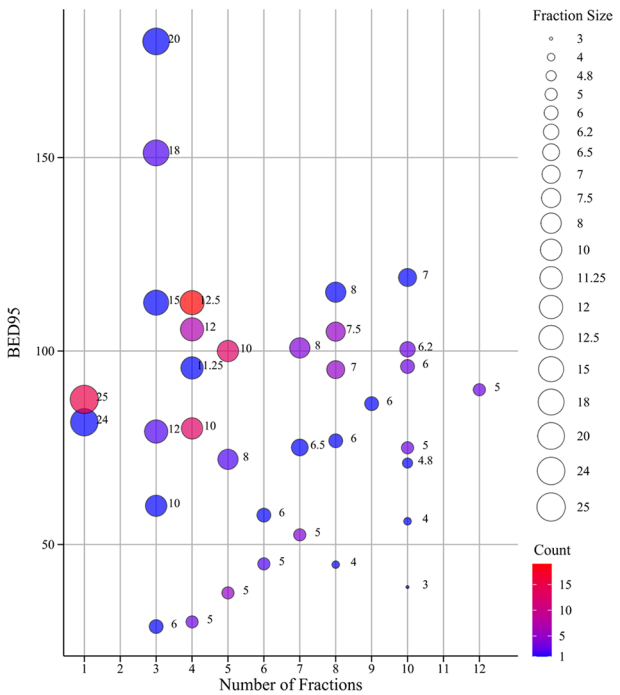

FIGURE 2 | The bubble chart of fractionation schemes and BED_{95}. The size of dots indicates the size of fraction; the different color of dots indicates different count ranges. BED_{95}, the prescription dose covers 95% of the target area expressed as BED.

dosimetric parameters based on ROC curve are shown in **Table 1**. No significant association was seen with baseline clinical and dosimetric characteristics in the training group and validation group of tumors. The balance of the two sets of data suggests that the patient grouping was reasonable.

Clinical and Dosimetric Parameter Selection

The relationship between clinical and dosimetric parameters and the 1-year tumor local status of primary and secondary lung cancer after SBRT for the training group is summarized in **Table 2**. In the univariate analysis, clinical stage status, history, PLT, PLR, Hb, D_{95}, D_{max}, PTV_{min}, PTV_{max}, PTV_{mean}, GTV_{min}, GTV_{max}, GTV_{mean}, and PTV_{min}/PTV_{max} were found to be significantly different between the 1-year local control status and the local failure status (all $p < 0.05$). Multivariate analysis indicated that clinical stage status, platelet (PLT), and the minimum dose of gross tumor volume ($BEDGTV_{min}$) were prognostic parameters for 1-year tumor local status.

Radiomics Feature Selection

Radiomics features were extracted and selected using the procedure shown in **Figure 3**. In total, 1,502 radiomics features were successfully extracted from each three-dimensional ROI, including 14 shape features, 288 first-order features, and 1,200 texture features. For intraobserver agreement, 1,090 features with ICC ≧0.75 between observers were included in further analyses. According to the univariate analysis, 46 radiomics features were collected, and then 10 potential radiomics features were calculated by the LASSO regression model with a penalty parameter $\lambda = 0.025$; we finally performed the stepwise regression analysis and obtained 4 important radiomics features, namely wavelet-LLL_glszm_SmallAreaEmphasis, wavelet-LHH_glcm_JointAverage, wavelet-LHH_ngtdm_Complexity, and squareroot_glcm_DifferenceEntropy. In the training group, the visible distributions of these radiomics features in local control group and local failure group and the correlation analysis of radiomics features are shown in **Figures 4**, **5**. It indicated that the larger the value of each radiomics features, the greater the possibility of 1-year tumor local control

TABLE 1 | The optimal cut-off values of dosimetric parameters.

Dosimetric parameters	BED_{95}	BED_{max}	$BEDPTV_{min}$	$BEDPTV_{max}$	$BEDPTV_{mean}$	$BEDGTV_{min}$	$BEDGTV_{max}$	$BEDGTV_{mean}$
Cutoff values	84.00	110.85	80.43	110.85	101.73	98.79	103.87	97.06

BED_{95}, the prescription dose covers 95% of the target area expressed as BED; BED_{max}, the maximum dose in the whole plan; $BEDPTV_{min}$, the minimum dose of PTV; $BEDPTV_{mean}$, mean dose of PTV; $BEDPTV_{max}$, the maximum dose of PTV; $BEDGTV_{min}$, the minimum dose of GTV; $BEDGTV_{mean}$, mean dose of GTV; $BEDGTV_{max}$, the maximum dose of GTV.

TABLE 2 | Univariate and multivariate analyses of clinical and dosimetric parameters.

Variable	Univariate analyses (logistic)		Multivariate analyses (logistic)		Multivariate analyses (stepwise)	
	p-value	*β*	*p*-value	*β*	*p*-value	*β*
Sex (man vs. woman)	0.299	−0.527				
Age (years)	0.615	−0.010				
Smoking status						
Current	Reference	Reference				
Former	0.990	−17.806				
Never	0.302	−0.506				
KPS (<80 vs. ≥80)	0.080	1.256				
BMI (kg/m^2)	0.914	0.008				
Clinical stage (I~II vs. III~IV)	0.001	−2.132	0.214	−1.284	0.034	−1.543
Location (central vs. peripheral)	0.252	−0.784				
Histology						
Adenocarcinoma	Reference	Reference	Reference	Reference		
Squamous cell carcinoma	0.405	−0.597	0.733	−0.425		
Unknown	0.020	−1.477	0.931	0.101		
Equivalent diameter (cm)	0.197	−0.177				
GTV (cm^2)	0.184	−0.005				
PTV (cm^2)	0.140	−0.004				
Chemotherapy (yes vs. no)	0.431	0.493				
Lymphocyte (10^9/L)	0.056	0.698				
Neutrophil (10^9/L)	0.176	−0.134				
PLT (10^9/L)	0.006	−0.010	0.115	−0.009	0.038	−0.009
NLR	0.128	−0.135				
PLR	0.011	−0.008	0.435	−0.004		
Hb (g/L)	0.031	0.037	0.376	0.021		
Immobilization device (vacuum bag vs. thermoplastic mask)	0.144	0.693				
4DCT (yes vs. no)	−0.851	0.109				
BED_{95} (<84.00 vs. ≥ 84.00) (Gy)	0.001	1.723	0.659	0.530		
BED_{max} (<110.85 vs. ≥110.85) (Gy)	<0.0001	2.431	0.992	14.790		
$BEDPTV_{min}$ (<80.43 vs. ≥80.43) (Gy)	0.004	1.484	0.396	1.386		
$BEDPTV_{max}$ (<110.85 vs. ≥110.85) (Gy)	<0.0001	2.351	0.992	−14.290		
$BEDPTV_{mean}$ (<101.73 vs. ≥101.73) (Gy)	<0.0001	2.128	0.727	0.616		
$BEDGTV_{min}$ (<98.79 vs. ≥98.79) (Gy)	<0.0001	2.258	0.510	0.848	0.009	1.699
$BEDGTV_{max}$ (<103.87 vs. ≥103.87) (Gy)	<0.0001	1.983	0.891	−0.266		
$BEDGTV_{mean}$ (<97.06 vs. ≥97.06) (Gy)	<0.0001	1.864	0.433	−1.752		
$BEDPTV_{min}/PTV_{max}$	0.004	−11.277	0.062	−13.31	0.071	−7.661
$BEDGTV_{min}/GTV_{max}$	0.075	−12.134				
Tumor site (primary vs. secondary)	0.398	−0.399				

KPS, Karnofsky performance status; BMI, body mass index; PTV, planning target volume; GTV, gross tumor volume; PLT, platelet; Hb, hemoglobin; NLR, neutrophil-to-lymphocyte ratio; PLR, platelet-to-lymphocyte ratio; 4DCT, four-dimensional computed tomography; BED_{95}, the prescription dose covers 95% of the target area expressed as BED; BED_{max}, the maximum dose in the whole plan; $BEDPTV_{min}$, the minimum dose of PTV; $BEDPTV_{mean}$, mean dose of PTV; $BEDPTV_{max}$, the maximum dose of PTV; $BEDPTV_{min}/PTV_{max}$, dose inhomogeneity in PTV; $BEDGTV_{min}$, the minimum dose of GTV; $BEDGTV_{mean}$, mean dose of GTV; $BEDGTV_{max}$, the maximum dose of GTV; $BEDGTV_{min}/GTV_{max}$, dose inhomogeneity in GTV.

and they were statistically supported. There was no significant correlation between the radiomics features with correlation coefficient <0.75.

Classifier Selection

The performance of model using difference classifiers are presented in **Table 3**. Our result reports that DT approach for classification were no more valuable than random classification with the AUC of the model below 0.5. We input these features into SVM classifier, which received the poor performance and the low specificity. Compared with the above methods, the LR was the optimum classifier with the best performance and accuracy.

Prediction Model Construction

On the basis of 4 radiomics factors, a radiomics model was created by the following formula:

$$\begin{aligned}\text{radiomics score} = &-27.645 + 14.393 \\ &\times \text{wavelet-LLL\_glszm\_SmallAreaEmphasis} \\ &+8.075 \times \text{wavelet-LHH\_glcm\_JointAverage} \\ &-3.386 \times \text{wavelet-LHH\_ngtdm\_Complexity} \\ &+9.196 \times \text{squareroot\_glcm\_DifferenceEntropy}\end{aligned}$$

The formula and these coefficients were calculated from the LR. To illustrate the validity of the radiomics score at the nomogram, the visible distributions of radiomics score for the 1-year tumor local control and local failure groups in the training group and validation group are shown in **Figure 4**. With the quantitative value of score increased, the tumor can be more possibly locally controlled in a year. The parameters of clinical stage status, PLT, and $BEDGTV_{min}$ were employed to build the clinical model. Furthermore, the parameters plus radiomics score were brought into building the combined model.

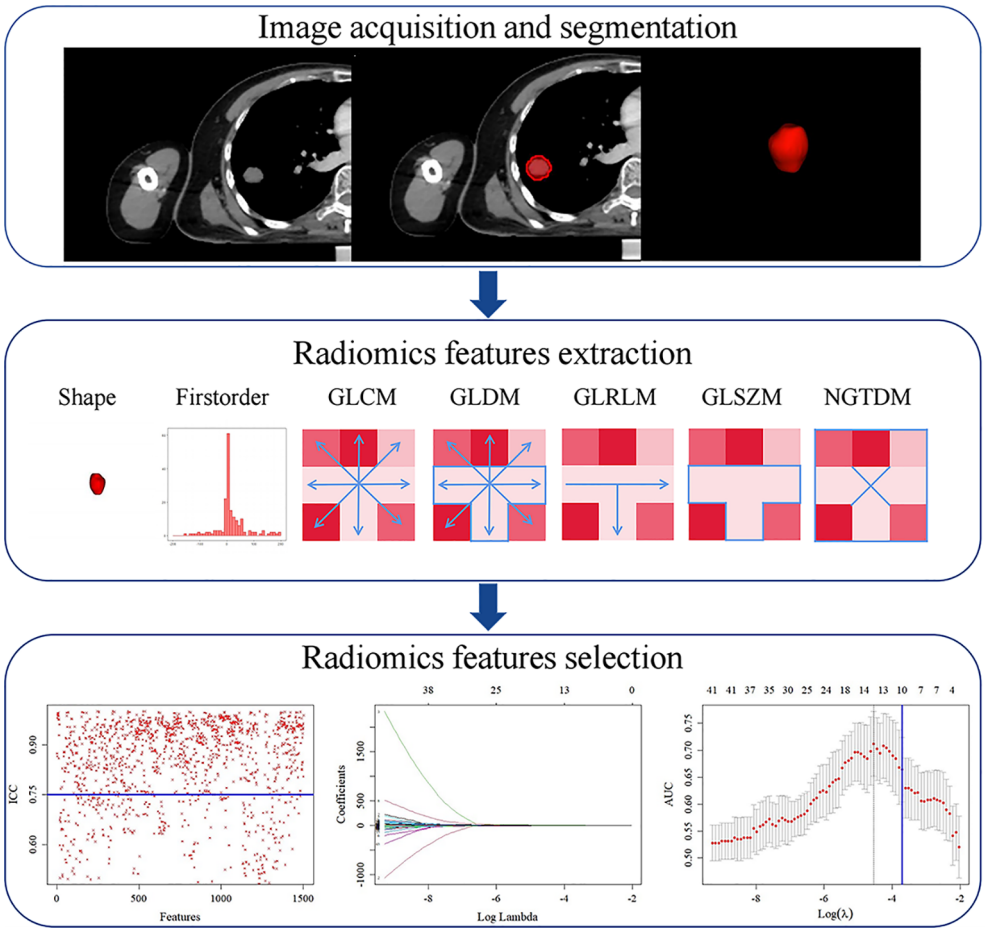

FIGURE 3 | Radiomics feature extraction and selection process. First, region of interest (ROI) segmentation was performed on CT image. Next, radiomics features were extracted from ROI. Finally, radiomics features dimension was reduced by intraclass correlation coefficient (ICC), least absolute shrinkage and selection operator (LASSO). GLCM, gray-level co-occurrence matrix; GLDM, gray-level dependence matrix; GLRLM, gray-level run length matrix; GLSZM, gray-level size zone matrix; NGTDM, neighborhood gray-tone difference matrix.

Prediction Model Performance Comparison

Figure 6 showed that the AUC with its 95% confidence interval (CI) of the radiomics model, clinical model, and combined model were 0.811 (95% CI: 0.713–0.910), 0.845 (95% CI: 0.757–0.934), and 0.911 (95% CI: 0.845–0.977) in the training group and 0.702 (95% CI: 0.507–0.898), 0.786 (95% CI: 0.638–0.933), and 0.818 (95% CI: 0.659–0.978) in the validation group, respectively. The accuracy values of the radiomics model, clinical model, and combined model were 67.4%, 82.0% and 85.4% in the training group and 92.9%, 77.5%, and 82.5% in the validation group, respectively. The combined model indicated a significant better performance than the radiomics model ($p = 0.025$) and the clinical model ($p = 0.033$) in the training group, while the radiomics model and clinical model displayed a similar performance ($p = 0.613$). We can also see the trend that the effect of the combined model is better than that of the single model in the validation group. Therefore, the optimal prediction model was based on a multivariable LR and conjoined the radiomics signature with clinical and dosimetric parameters. Moreover, the contribution of each selected feature in the combined model iss displayed in **Figure 7**.

Nomogram Establishment

A visualization-combined nomogram was constructed from integrating the radiomics score, clinical stage, PLT, and $BEDGTV_{min}$, as shown in **Figure 8A**. No significance was found in the Hosmer-Lemeshow test for the separated training sets ($p = 0.898$) and validation group ($p = 0.891$), indicating the proposed nomogram with good calibration was acceptable. The actual tumor control probability is that the patient population was divided into a few bins of increasing percentage of local control. The calibration curve of the combined nomogram confirmed that the probability of predicting 1-year tumor local control was consistent with the actual observation both in the training group (**Figure 8B**) and validation group (**Figure 8C**).

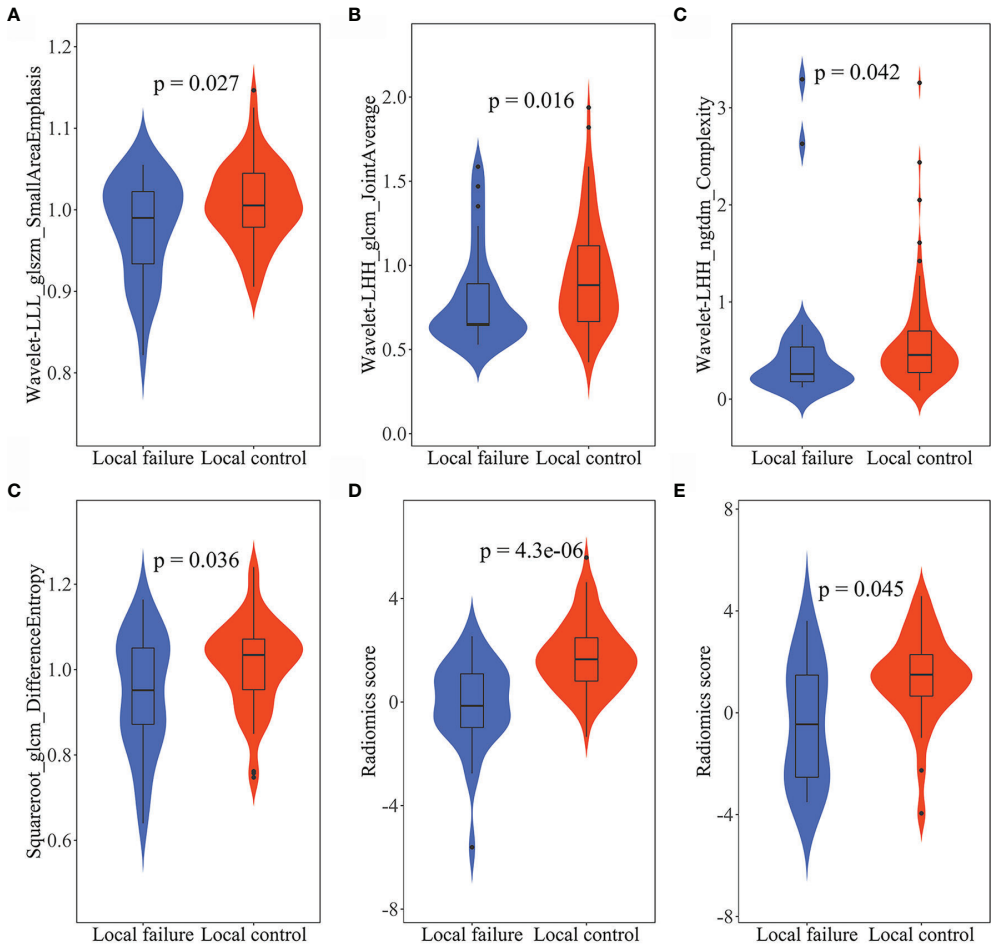

FIGURE 4 | The violin plots of radiomics features and radiomics score. The distribution of **(A)** wavelet-LLL_glszm_SmallAreaEmphasis, **(B)** wavelet-LHH_glcm_JointAverage, **(C)** wavelet-LHH_ngtdm_Complexity, and **(D)** squareroot_glcm_DifferenceEntropy in the training group. The distribution of radiomics score in the training group **(E)** and in the validation group **(F)**. The *p*-values were obtained by *t*-test or Wilcoxon rank sum test.

The decision curve revealed the radiomics model, the clinical model, and the combined nomogram were beneficial for predicting 1-year tumor local control probability. The area under the curve of the combined nomogram was larger than that of the other two models, indicating that the combined nomogram had the highest clinical feasibility and utility (**Figures 8D, E**).

DISCUSSION

In this study, a quantitative relationship between radiomics score, clinical and dosimetric features, and tumor local status was found. Moreover, we first established a new prediction model to correlate 1-year local control with radiomics score and clinical and dosimetric parameters for primary and secondary lung cancer patients undergoing SBRT. We also constructed and validated a combined nomogram with great discrimination to conveniently identify the tumor local status.

Improving the accuracy of local control prediction is of positive significance for medical and personal decision-making in many aspects (2). It is beneficial to find patients who are at high risk of locoregional failure and explore the treatment strategy of patients. Moreover, increasing systemic treatment and/or radiation dose to eradicate lesions and strengthening the follow-up management of patients can reduce local recurrence and improve the survival and prognosis. In clinical practice, some studies have proposed to overcome immune resistance mechanisms for lung cancer by using immunotherapy combined with SBRT; therefore, patients have more personalized treatment options (35, 36). Our nomogram model may provide important evidence to design future clinical trials, such as predicting whether these people would benefit from combination treatment to balance this positive strategic risk. More importantly, compared with the long-term outcome of overall survival, local control status avoids long-term follow-up and can early adjust treatment strategies. Therefore, our study provides a more effective tool to promptly achieve personalized treatment.

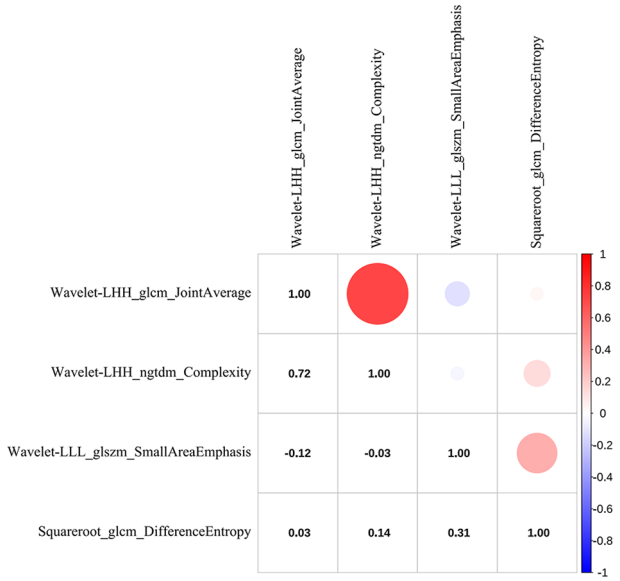

FIGURE 5 | The correlation heat map of radiomics features. Red indicates positive correlation, and blue indicates negative correlation; the darker the color, the stronger the relationship.

TABLE 3 | The performance of radiomics model using LR, DT, and SVM, clinical model and combined model.

Group	Methods	AUC (95% CI)	*p*-value	Accuracy (%)	Sensitivity (%)	Specificity (%)
Training	LR	0.811 (0.713–0.910)	0.000	67.4	57.1	92.3
	DT	0.832 (0.744–0.919)	1.000	90.9	79.4	80.8
	SVM	0.796 (0.691–0.901)	0.000	82.0	96.8	46.2
	Clinical	0.845 (0.757–0.934)	0.000	82.0	84.1	76.9
	Combined	0.911 (0.845–0.977)	0.000	85.4	87.3	80.8
Validation	LR	0.702 (0.507–0.898)	0.023	92.9	50.0	81.3
	DT	0.629 (0.429–0.830)	0.909	62.5	64.3	58.3
	SVM	0.714 (0.524–0.904)	0.018	75.0	85.7	50.0
	Clinical	0.786 (0.638–0.933)	0.002	77.5	78.6	75.0
	Combined	0.818 (0.659–0.978)	0.001	82.5	85.7	75.0

LR, logistic regression; DT, decision tree; SVM, support vector machine; AUC, area under the receiver operating characteristic curve (ROC); CI, confidence interval.

The correlation between radiomics features and SBRT outcomes has shown promising results. Lafata et al. investigated the relationship between pre-SBRT CT radiomics features and cancer recurrence for nonsmall cell lung cancer (NSCLC) and concluded that radiomics features may provide more predictive information in the identification of tumor local failures (37). Mattonen et al. compared the prognostic value of physician and radiomics data for local response of NSCLC treated with SBRT. Their findings similarly indicated that a radiomics score consisting of five appearance features can early and correctly predict local recurrence in a noninvasive way (18). Our results are consistent with these published studies (18, 20, 21, 37), as we found radiomics features were independent prognostic factors and radiomics score was significantly associated with tumor local status for primary and secondary lung cancer undergoing SBRT. These results may explain that radiomics has the ability to quantify tumor spatial and temporal heterogeneity by mathematically analyzing the spatial distribution and relationships of gray levels in CT images.

Many studies have focused on the effects of clinical and dosimetric parameters on local control (9, 10); however, no consensus has been reached so far and further investigation is needed. Ohri et al. developed a local TCP model with BED and tumor diameter for NSCLC patients after SBRT (14), while Ye et al. established a nomogram model with tumor size and SUVmax to predict 2-year locoregional recurrence and 2-year progression-free survival (7). However, their analysis lacked additional SBRT datasets for reliability verification and the SUVmax based on PET-CT is not easy to obtain. Our study avoided these limitations and showed that clinical stage, PLT value, and $BEDGTV_{min}$ were significantly correlated with the local control status. This finding is also in accordance with other studies (38–40). These results suggest that earlier clinical stage, lower PLT value and higher $BEDGTV_{min}$ contribute to tumor

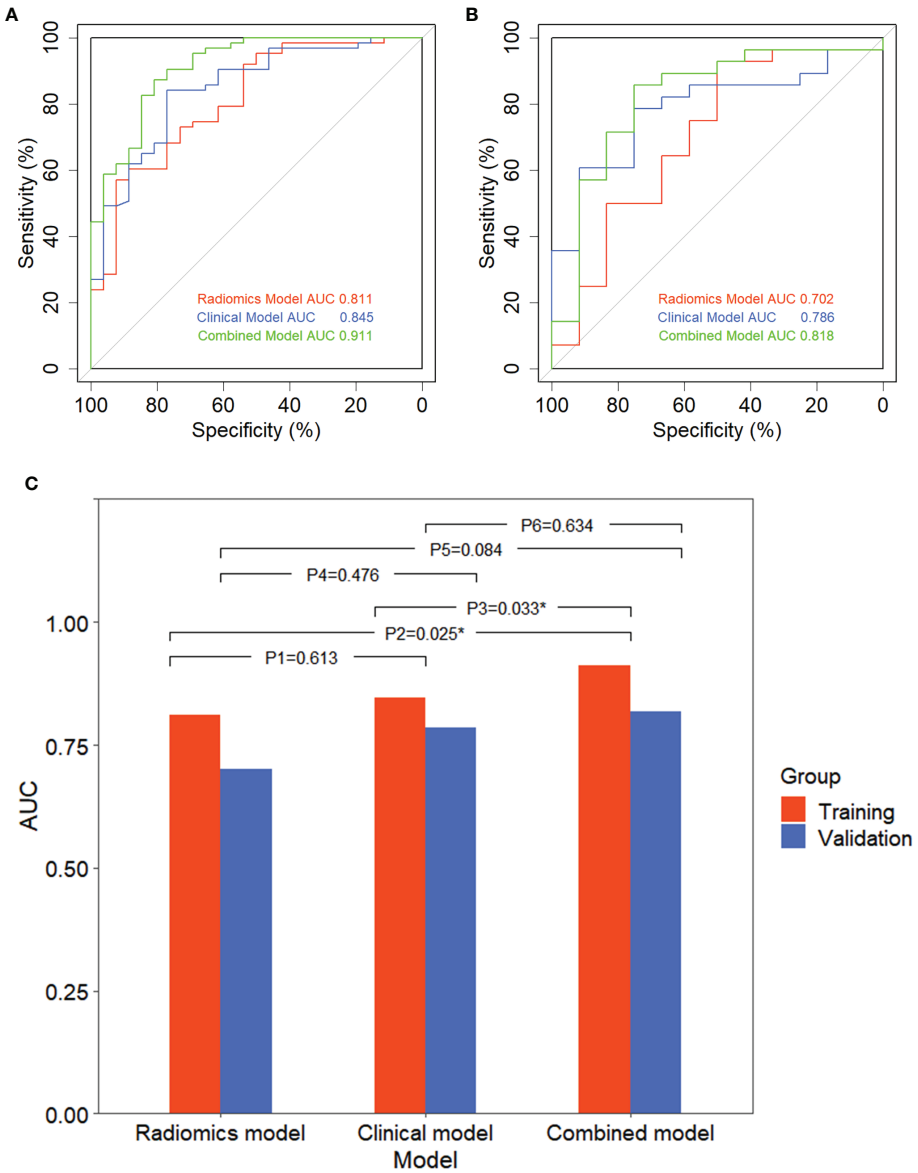

FIGURE 6 | Receiver operating characteristic (ROC) curve of three models and comparison of ROC curves. ROC curve of three models in the training group **(A)** and validation group **(B)**. **(C)** Comparison of ROC curves with DeLong test in the training group and validation group.P1, P2, and P3 are in the training group; P4, P5, and P6 are in the validation group; P1 and P4: radiomics model vs. clinical model; P2 and P4: radiomics model vs. combined model; P3 and P6: clinical model vs. combined model. *$p < 0.05$, expressive significance.

local control and should be considered when designing SBRT regimens.

However, these previous studies mainly focused on radiomics features (18, 20, 21, 37) or clinical and dosimetric parameters (7, 14, 15, 41). In our work, we combined radiomics features and the available clinical and dosimetric parameters to improve the prediction performance and accuracy for local control in lung SBRT. The combined model indicated outstanding performance in the training group and had good stability in the validation group. It failed to achieve statistical significance due to the small sample size, subtle differences in the data set or the mixed effect of other parameters. Similar results were obtained by Avanzo et al. who have demonstrated that combining BED features and image features in radiomics and deep learning improves the tumor response prediction of machine learning models for lung SBRT (42). This trend is in agreement with past studies, showing it is highly valuable to predict tumor local control in lung SBRT using multivariate factors (43). Meanwhile, the combined nomogram-integrated multiple features increases the value of personalized estimation and has great clinical application

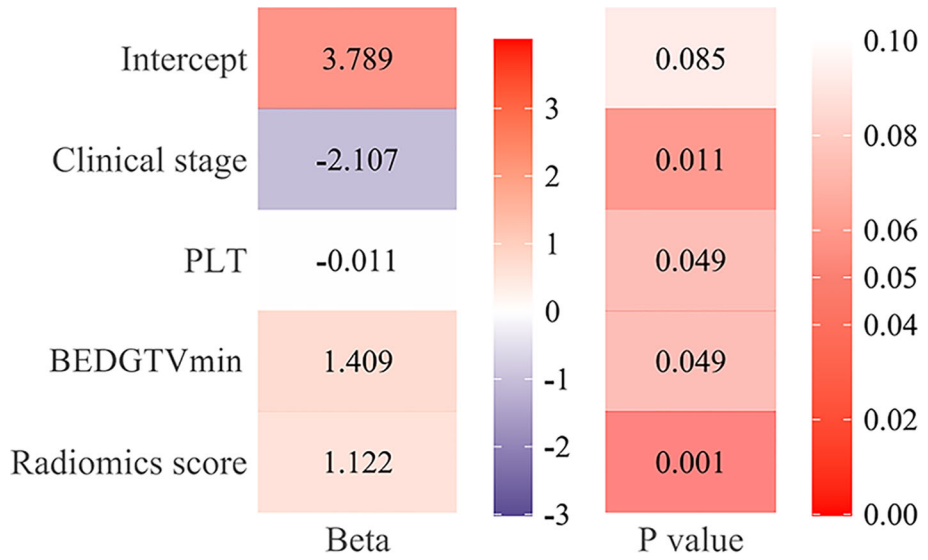

FIGURE 7 | The function of each feature in the combined model. The beta value and the *p*-value of radiomics score, clinical stage [III~IV], platelet (PLT), and $BEDGTV_{min}$ [≥98.79] in the combined model.

potential (19). More importantly, the variables involved in nomogram are derived from clinically available data without the need for additional expense, which will increase the clinical applicability.

It is worth noting that the incidence of local control in our study is lower than that reported previously. It might be due to the inconsistent design of treatment plans and the selection bias between different studies. According to our nomogram, the radiation dose should be increased for patients with a high risk of local recurrence. However, considering the patient's condition and nearby organs at risk, the BED_{95} used in our cohort, at a median of 95.2 Gy, was lower than the standard dose of 100 Gy (2). In addition, some metastatic lung cancer patients were treated with significantly lower radiation doses, such as 20~35 Gy in 4~7 fractions. This was probably the reason for the high local recurrence rate in our study. In our univariate analysis, BED_{95} was also a significant parameter. Due to the multicollinearity between dosimetric parameters, BED_{95} was removed from the final model by the stepwise regression methods. However, the last dosimetric parameters entering the model, namely $BEDGTV_{min}$, covered some prediction information of the BED_{95}. Also with more data, a continued work on verifying these results is imperative.

Finally, efforts have been made to reduce the risk of radiomics feature biases and improve the quality of the prediction models. A wide range of candidate radiomics features were extracted in our study, which provided the foundation for algorithms to select relevant radiomics features and obtained the valuable information to reflect the local control status of lung cancer lesions (24). In order to reduce the deviation of the interobservers and examine the feature stability, we calculated the ICC of radiomics features (44). In addition, we optimized feature selection by using univariate analysis, LASSO, and stepwise regression, thus ensuring the independence and robustness of each feature entering the final prediction model (26). Three popular classifiers were utilized to evaluate the performance of the radiomics model, and finally the classifier with the best accuracy and the highest prognostic performance was used to establish the prediction model (29, 30).

There are some limitations that should be considered in the study (1): Our study was a retrospective, single-center-based study and limited number of patients were involved in the study, and results from a prospective multicenter study with a greater number of population are needed (2). Local tumor failure was not pathologically confirmed by biopsy in the study, which added more uncertainty to our conclusions. However, data from the literature show that histological confirmation was not mandatory in NSCLC patients treated with SBRT (45). (3) Our study analyzed the tumor local control status from a mixture of primary and secondary lung tumor patients. However, it was found in the previous study that TCP models were not different between primary NSCLC and secondary NSCLC, because histological heterogeneity does not influence radiosensitivity of tumor in the SBRT (15). (4) Due to the limited sample size, our endpoint mainly focused on 1-year local control and further work is required to conduct a longer follow-up time and verify the practicability of the prediction model.

CONCLUSIONS

We found that there was a significant quantitative correlation between radiomics score and local control for patients

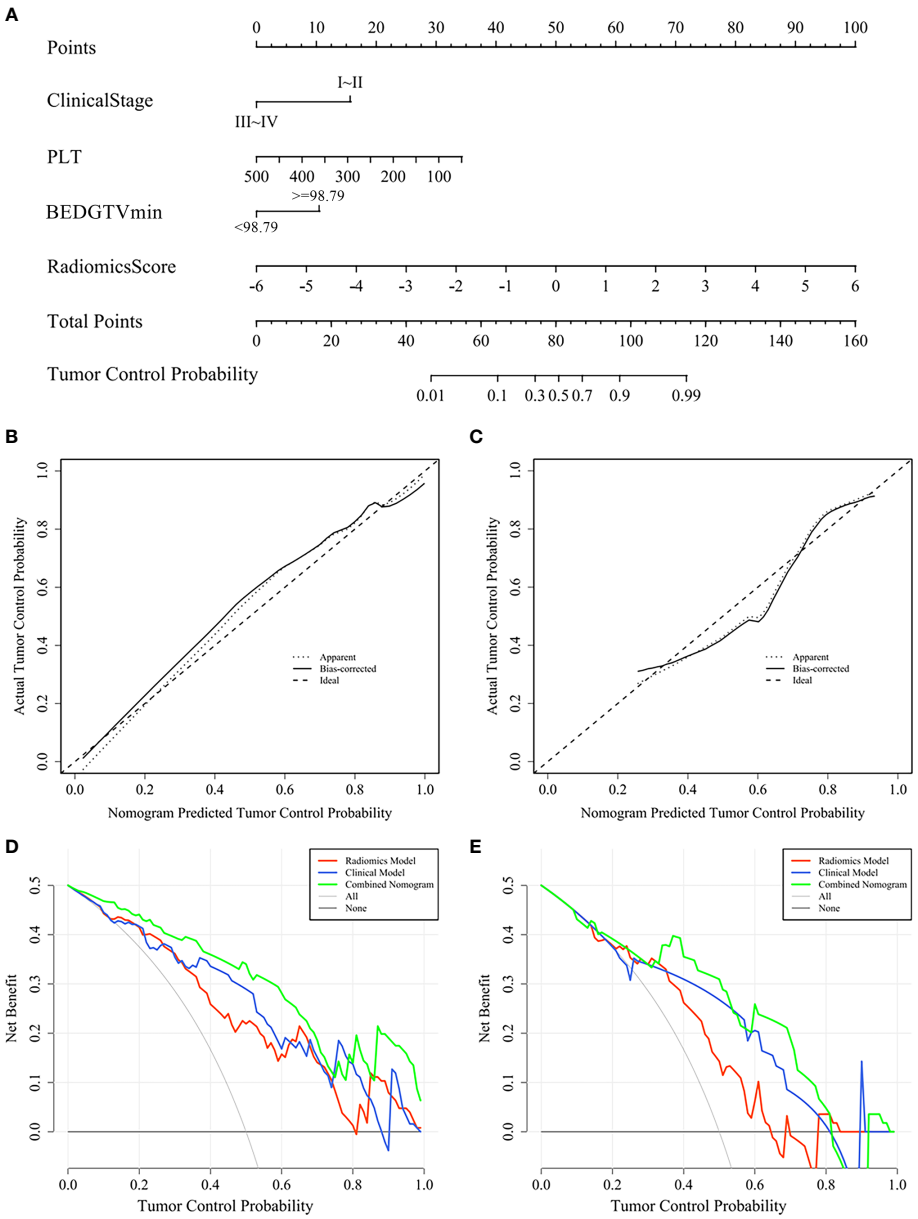

FIGURE 8 | Combined nomogram and evaluation of the nomogram in the training group and validation group. **(A)** A combined nomogram for prediction 1-year local control probability in lung cancer patients after SBRT. The calibration curve of the combined nomogram in the training group **(B)** and validation group **(C)**. The decision curve of each model in the training group **(D)** and validation group **(E)**.

undergoing SBRT, and we consider that it might be a promising and potential biomarker. According to the LR method, we developed a novel model using radiomics score plus clinical and dosimetric parameters to improve the prediction of local control. The nomogram we established have a potential to be a noninvasive, low-cost approach and could facilitate individualized treatment and follow-up, surveillance, and evaluation strategies for patients undergoing SBRT.

DATA AVAILABILITY STATEMENT

The raw data supporting the conclusions of this article will be made available by the authors, without undue reservation.

AUTHOR CONTRIBUTIONS

The author's responsibilities are as follows: B-TH, C-ZC, and L-ML conceived and designed the study. C-HS, L-ML, YW,

R-HW, KH, and Z-HQ contributed to data collection. L-ML, G-BP, C-BZ, and Y-XW analyzed data and interpreted THE data. L-ML and B-TH wrote the paper. B-TH had primary responsibility for final content. All authors contributed to the manuscript review and approved the final version.

FUNDING

This work was sponsored by THE National Natural Science Foundation of China (81602667), Medical Scientific Research Foundation of Guangdong Province (A2015534, B2016048), and the Creative and Facilitating Program of Shantou University.

ACKNOWLEDGMENTS

We thank all participants and staff for their endeavor and contribution in this study. We thank our hospital for their support of this research project.

SUPPLEMENTARY MATERIAL

The Supplementary Material for this article can be found online at: https://www.frontiersin.org/articles/10.3389/fonc.2021.819047/full#supplementary-material

REFERENCES

1. Sung H, Ferlay J, Siegel RL, Laversanne M, Soerjomataram I, Jemal A, et al. Global Cancer Statistics 2020: GLOBOCAN Estimates of Incidence and Mortality Worldwide for 36 Cancers in 185 Countries. *CA Cancer J Clin* (2021) 71(3):209–49. doi: 10.3322/caac.21660
2. Ettinger DS, Wood DE, Aisner DL, Akerley W, Bauman J, Chirieac LR, et al. Non-Small Cell Lung Cancer, Version 5.2017, NCCN Clinical Practice Guidelines in Oncology. *J Natl Compr Canc Netw* (2017) 15(4):504–35. doi: 10.6004/jnccn.2017.0050
3. Rusthoven KE, Kavanagh BD, Burri SH, Chen C, Cardenes H, Chidel MA, et al. Multi-Institutional Phase I/II Trial of Stereotactic Body Radiation Therapy for Lung Metastases. *J Clin Oncol* (2009) 27(10):1579–84. doi: 10.1200/jco.2008.19.6386
4. Schneider BJ, Daly ME, Kennedy EB, Antonoff MB, Broderick S, Feldman J, et al. Stereotactic Body Radiotherapy for Early-Stage Non-Small-Cell Lung Cancer: American Society of Clinical Oncology Endorsement of the American Society for Radiation Oncology Evidence-Based Guideline. *J Clin Oncol* (2018) 36(7):710–9. doi: 10.1200/jco.2017.74.9671
5. Timmerman R, Paulus R, Galvin J, Michalski J, Straube W, Bradley J, et al. Stereotactic Body Radiation Therapy for Inoperable Early Stage Lung Cancer. *JAMA* (2010) 303(11):1070–6. doi: 10.1001/jama.2010.261
6. Takeda A, Sanuki N, Fujii H, Yokosuka N, Nishimura S, Aoki Y, et al. Maximum Standardized Uptake Value on FDG-PET Is a Strong Predictor of Overall and Disease-Free Survival for Non-Small-Cell Lung Cancer Patients After Stereotactic Body Radiotherapy. *J Thorac Oncol* (2014) 9(1):65–73. doi: 10.1097/jto.0000000000000031
7. Ye L, Shi S, Zeng Z, Huang Y, Hu Y, He J. Nomograms for Predicting Disease Progression in Patients of Stage I Non-Small Cell Lung Cancer Treated With Stereotactic Body Radiotherapy. *Jpn J Clin Oncol* (2018) 48(2):160–6. doi: 10.1093/jjco/hyx179
8. Hörner-Rieber J, Bernhardt D, Dern J, König L, Adeberg S, Paul A, et al. Histology of Non-Small Cell Lung Cancer Predicts the Response to Stereotactic Body Radiotherapy. *Radiother Oncol* (2017) 125(2):317–24. doi: 10.1016/j.radonc.2017.08.029
9. Woody NM, Stephans KL, Andrews M, Zhuang T, Gopal P, Xia P, et al. A Histologic Basis for the Efficacy of SBRT to the Lung. *J Thorac Oncol* (2017) 12(3):510–9. doi: 10.1016/j.jtho.2016.11.002
10. Kestin L, Grills I, Guckenberger M, Belderbos J, Hope AJ, Werner-Wasik M, et al. Dose-Response Relationship With Clinical Outcome for Lung Stereotactic Body Radiotherapy (SBRT) Delivered *via* Online Image Guidance. *Radiother Oncol* (2014) 110(3):499–504. doi: 10.1016/j.radonc.2014.02.002
11. Diamant A, Chatterjee A, Faria S, Naqa IE, Bahig H, Filion E, et al. Can Dose Outside the PTV Influence the Risk of Distant Metastases in Stage I Lung Cancer Patients Treated With Stereotactic Body Radiotherapy (SBRT)? *Radiother Oncol* (2018) 128(3):513–9. doi: 10.1016/j.radonc.2018.05.012
12. Guckenberger M, Klement RJ, Allgäuer M, Appold S, Dieckmann K, Ernst I, et al. Applicability of the Linear-Quadratic Formalism for Modeling Local Tumor Control Probability in High Dose Per Fraction Stereotactic Body Radiotherapy for Early Stage Non-Small Cell Lung Cancer. *Radiother Oncol* (2013) 109(1):13–20. doi: 10.1016/j.radonc.2013.09.005
13. Mehta N, King CR, Agazaryan N, Steinberg M, Hua A, Lee P. Stereotactic Body Radiation Therapy and 3-Dimensional Conformal Radiotherapy for Stage I Non-Small Cell Lung Cancer: A Pooled Analysis of Biological Equivalent Dose and Local Control. *Pract Radiat Oncol* (2012) 2(4):288–95. doi: 10.1016/j.prro.2011.10.004
14. Ohri N, Werner-Wasik M, Grills IS, Belderbos J, Hope A, Yan D, et al. Modeling Local Control After Hypofractionated Stereotactic Body Radiation Therapy for Stage I Non-Small Cell Lung Cancer: A Report From the Elekta Collaborative Lung Research Group. *Int J Radiat Oncol Biol Phys* (2012) 84(3):e379–84. doi: 10.1016/j.ijrobp.2012.04.040
15. Guckenberger M, Klement RJ, Allgäuer M, Andratschke N, Blanck O, Boda-Heggemann J, et al. Local Tumor Control Probability Modeling of Primary and Secondary Lung Tumors in Stereotactic Body Radiotherapy. *Radiother Oncol* (2016) 118(3):485–91. doi: 10.1016/j.radonc.2015.09.008
16. Lambin P, Leijenaar RTH, Deist TM, Peerlings J, de Jong EEC, van Timmeren J, et al. Radiomics: The Bridge Between Medical Imaging and Personalized Medicine. *Nat Rev Clin Oncol* (2017) 14(12):749–62. doi: 10.1038/nrclinonc.2017.141
17. Aerts HJ, Velazquez ER, Leijenaar RT, Parmar C, Grossmann P, Carvalho S, et al. Decoding Tumour Phenotype by Noninvasive Imaging Using a Quantitative Radiomics Approach. *Nat Commun* (2014) 5:4006. doi: 10.1038/ncomms5006
18. Mattonen SA, Palma DA, Johnson C, Louie AV, Landis M, Rodrigues G, et al. Detection of Local Cancer Recurrence After Stereotactic Ablative Radiation Therapy for Lung Cancer: Physician Performance Versus Radiomic Assessment. *Int J Radiat Oncol Biol Phys* (2016) 94(5):1121–8. doi: 10.1016/j.ijrobp.2015.12.369
19. Huang Y, Liu Z, He L, Chen X, Pan D, Ma Z, et al. Radiomics Signature: A Potential Biomarker for the Prediction of Disease-Free Survival in Early-Stage (I or II) Non-Small Cell Lung Cancer. *Radiology* (2016) 281(3):947–57. doi: 10.1148/radiol.2016152234
20. Huynh E, Coroller TP, Narayan V, Agrawal V, Hou Y, Romano J, et al. CT-Based Radiomic Analysis of Stereotactic Body Radiation Therapy Patients With Lung Cancer. *Radiother Oncol* (2016) 120(2):258–66. doi: 10.1016/j.radonc.2016.05.024
21. Yu W, Tang C, Hobbs BP, Li X, Koay EJ, Wistuba II, et al. Development and Validation of a Predictive Radiomics Model for Clinical Outcomes in Stage I Non-Small Cell Lung Cancer. *Int J Radiat Oncol Biol Phys* (2018) 102(4):1090–7. doi: 10.1016/j.ijrobp.2017.10.046
22. Lenglet A, Campeau MP, Mathieu D, Bahig H, Lambert L, Vu T, et al. Risk-Adapted Stereotactic Ablative Radiotherapy for Central and Ultra-Central Lung Tumours. *Radiother Oncol* (2019) 134:178–84. doi: 10.1016/j.radonc.2019.01.035
23. Zhang L, Chen B, Liu X, Song J, Fang M, Hu C, et al. Quantitative Biomarkers for Prediction of Epidermal Growth Factor Receptor Mutation in Non-Small Cell Lung Cancer. *Transl Oncol* (2018) 11(1):94–101. doi: 10.1016/j.tranon.2017.10.012
24. Tao J, Lv R, Liang C, Fang J, Liu D, Lan X, et al. Development and Validation of a CT-Based Signature for the Prediction of Distant Metastasis Before

Treatment of Non-Small Cell Lung Cancer. *Acad Radiol* (2021) S1076-6332 (20):30700–5. doi: 10.1016/j.acra.2020.12.007
25. Kim SB, Heo YM, Hwang CM, Kim TG, Hong JY, Won YG, et al. Reliability of the EOS Imaging System for Assessment of the Spinal and Pelvic Alignment in the Sagittal Plane. *Clin Orthop Surg* (2018) 10(4):500–7. doi: 10.4055/cios.2018.10.4.500
26. Whittingham MJ, Stephens PA, Bradbury RB, Freckleton RP. Why Do We Still Use Stepwise Modelling in Ecology and Behaviour? *J Anim Ecol* (2006) 75 (5):1182–9. doi: 10.1111/j.1365-2656.2006.01141.x
27. Tibshirani R. Regression Shrinkage and Selection *via* the Lasso: A Retrospective. *J R Stat Soc B* (2011) 73(3):267–88. doi: 10.1111/j.1467-9868.2011.00771.x
28. Chen Y, Chen TW, Wu CQ, Lin Q, Hu R, Xie CL, et al. Radiomics Model of Contrast-Enhanced Computed Tomography for Predicting the Recurrence of Acute Pancreatitis. *Eur Radiol* (2019) 29(8):4408–17. doi: 10.1007/s00330-018-5824-1
29. Bektas CT, Kocak B, Yardimci AH, Turkcanoglu MH, Yucetas U, Koca SB, et al. Clear Cell Renal Cell Carcinoma: Machine Learning-Based Quantitative Computed Tomography Texture Analysis for Prediction of Fuhrman Nuclear Grade. *Eur Radiol* (2019) 29(3):1153–63. doi: 10.1007/s00330-018-5698-2
30. Zhou Y, Ma XL, Zhang T, Wang J, Zhang T, Tian R. Use of Radiomics Based on (18)F-FDG PET/CT and Machine Learning Methods to Aid Clinical Decision-Making in the Classification of Solitary Pulmonary Lesions: An Innovative Approach. *Eur J Nucl Med Mol Imaging* (2021) 48(9):2904–13. doi: 10.1007/s00259-021-05220-7
31. He B, Song Y, Wang L, Wang T, She Y, Hou L, et al. A Machine Learning-Based Prediction of the Micropapillary/Solid Growth Pattern in Invasive Lung Adenocarcinoma With Radiomics. *Transl Lung Cancer Res* (2021) 10(2):955–64. doi: 10.21037/tlcr-21-44
32. Rau CS, Wu SC, Chien PC, Kuo PJ, Chen YC, Hsieh HY, et al. Identification of Pancreatic Injury in Patients With Elevated Amylase or Lipase Level Using a Decision Tree Classifier: A Cross-Sectional Retrospective Analysis in a Level I Trauma Center. *Int J Environ Res Public Health* (2018) 15(2):277. doi: 10.3390/ijerph15020277
33. Chen H, Zeng M, Wang X, Su L, Xia Y, Yang Q, et al. A CT-Based Radiomics Nomogram for Predicting Prognosis of Coronavirus Disease 2019 (COVID-19) Radiomics Nomogram Predicting COVID-19. *Br J Radiol* (2021) 94 (1117):20200634. doi: 10.1259/bjr.20200634
34. Douma RA, le Gal G, Söhne M, Righini M, Kamphuisen PW, Perrier A, et al. Potential of an Age Adjusted D-Dimer Cut-Off Value to Improve the Exclusion of Pulmonary Embolism in Older Patients: A Retrospective Analysis of Three Large Cohorts. *Bmj* (2010) 340:c1475. doi: 10.1136/bmj.c1475
35. Theelen W, Chen D, Verma V, Hobbs BP, Peulen HMU, Aerts J, et al. Pembrolizumab With or Without Radiotherapy for Metastatic Non-Small-Cell Lung Cancer: A Pooled Analysis of Two Randomised Trials. *Lancet Respir Med* (2021) 9(5):467–75. doi: 10.1016/s2213-2600(20)30391-x
36. Tian S, Switchenko JM, Buchwald ZS, Patel PR, Shelton JW, Kahn SE, et al. Lung Stereotactic Body Radiation Therapy and Concurrent Immunotherapy: A Multicenter Safety and Toxicity Analysis. *Int J Radiat Oncol Biol Phys* (2020) 108(1):304–13. doi: 10.1016/j.ijrobp.2019.12.030
37. Lafata KJ, Hong JC, Geng R, Ackerson BG, Liu JG, Zhou Z, et al. Association of Pre-Treatment Radiomic Features With Lung Cancer Recurrence Following Stereotactic Body Radiation Therapy. *Phys Med Biol* (2019) 64 (2):025007. doi: 10.1088/1361-6560/aaf5a5
38. Ernani V, Appiah AK, Marr A, Zhang C, Zhen W, Smith LM, et al. Adjuvant Systemic Therapy in Patients With Early-Stage NSCLC Treated With Stereotactic Body Radiation Therapy. *J Thorac Oncol* (2019) 14(3):475–81. doi: 10.1016/j.jtho.2018.11.018
39. Dunlap NE, Larner JM, Read PW, Kozower BD, Lau CL, Sheng K, et al. Size Matters: A Comparison of T1 and T2 Peripheral Non-Small-Cell Lung Cancers Treated With Stereotactic Body Radiation Therapy (SBRT). *J Thorac Cardiovasc Surg* (2010) 140(3):583–9. doi: 10.1016/j.jtcvs.2010.01.046
40. Inoue H, Kosuga T, Kubota T, Konishi H, Shiozaki A, Okamoto K, et al. Significance of a Preoperative Systemic Immune-Inflammation Index as a Predictor of Postoperative Survival Outcomes in Gastric Cancer. *World J Surg Oncol* (2021) 19(1):173. doi: 10.1186/s12957-021-02286-3
41. Klement RJ, Allgäuer M, Andratschke N, Blanck O, Boda-Heggemann J, Dieckmann K, et al. Bayesian Cure Rate Modeling of Local Tumor Control: Evaluation in Stereotactic Body Radiation Therapy for Pulmonary Metastases. *Int J Radiat Oncol Biol Phys* (2016) 94(4):841–9. doi: 10.1016/j.ijrobp.2015.12.004
42. Avanzo M, Gagliardi V, Stancanello J, Blanck O, Pirrone G, El Naqa I, et al. Combining Computed Tomography and Biologically Effective Dose in Radiomics and Deep Learning Improves Prediction of Tumor Response to Robotic Lung Stereotactic Body Radiation Therapy. *Med Phys* (2021) 48 (10):6257–69. doi: 10.1002/mp.15178
43. Grossmann P, Stringfield O, El-Hachem N, Bui MM, Rios Velazquez E, Parmar C, et al. Defining the Biological Basis of Radiomic Phenotypes in Lung Cancer. *Elife* (2017) 6:23421. doi: 10.7554/eLife.23421
44. Wang L, Gao Z, Li C, Sun L, Li J, Yu J, et al. Computed Tomography-Based Delta-Radiomics Analysis for Discriminating Radiation Pneumonitis in Patients With Esophageal Cancer After Radiation Therapy. *Int J Radiat Oncol Biol Phys* (2021) 111(2):443–55. doi: 10.1016/j.ijrobp.2021.04.047
45. Videtic GMM, Donington J, Giuliani M, Heinzerling J, Karas TZ, Kelsey CR, et al. Stereotactic Body Radiation Therapy for Early-Stage Non-Small Cell Lung Cancer: Executive Summary of an ASTRO Evidence-Based Guideline. *Pract Radiat Oncol* (2017) 7(5):295–301. doi: 10.1016/j.prro.2017.04.014

Conflict of Interest: The authors declare that the research was conducted in the absence of any commercial or financial relationships that could be construed as a potential conflict of interest.

Publisher's Note: All claims expressed in this article are solely those of the authors and do not necessarily represent those of their affiliated organizations, or those of the publisher, the editors and the reviewers. Any product that may be evaluated in this article, or claim that may be made by its manufacturer, is not guaranteed or endorsed by the publisher.

GLOSSARY

SBRT	stereotactic body radiation therapy
CT	Computed tomography
SUVmax	maximum standardized uptake value
4DCT	four-dimensional computed tomography
3DCT	three-dimensional computed tomography
CBCT	Cone beam computed tomography
GTV	gross tumor volume
ITV	internal target volume
PTV	planning target volume
BED	biologically effective dose
KPS	Karnofsky performance status
BMI	body mass index
PLT	platelet
Hb	hemoglobin
NLR	neutrophil-to-lymphocyte ratio
PLR	platelet-to-lymphocyte ratio
BED_{95}	the prescription dose covers 95% of the target area expressed as BED
BED_{max}	the maximum dose in the whole plan
$BEDPTV_{min}$	the minimum dose of PTV
$BEDPTV_{mean}$	mean dose of PTV
$BEDPTV_{max}$	the maximum dose of PTV
$BEDPTV_{min}/PTV_{max}$	dose inhomogeneity in PTV
$BEDGTV_{min}$	the minimum dose of GTV
$BEDGTV_{mean}$	mean dose of GTV
$BEDGTV_{max}$	the maximum dose of GTV
$BEDGTV_{min}/GTV_{max}$	dose inhomogeneity in GTV
ROI	region of interest
GLCM	gray-level co-occurrence matrix
GLDM	gray-level dependence matrix
GLRLM	gray-level run length matrix
GLSZM	gray-level size zone matrix
NGTDM	neighborhood gray-tone difference matrix
ICC	intraclass correlation coefficient
LASSO	least absolute shrinkage and selection operator
LR	logistic regression
DT	decision tree
SVM	support vector machine
ROC	receiver operating characteristic
AUC	area under the ROC curve
CI	confidence interval
NSCLC	nonsmall cell lung cancer
TCP	tumor control probability
LVI	lymphovascular invasion
PET-CT	positron emission tomography-CT

frontiers in Oncology

ORIGINAL RESEARCH
published: 24 February 2022
doi: 10.3389/fonc.2022.831712

A Predictive Model of 2yDFS During MR-Guided RT Neoadjuvant Chemoradiotherapy in Locally Advanced Rectal Cancer Patients

Giuditta Chiloiro[1], Luca Boldrini[1], Francesco Preziosi[2], Davide Cusumano[1], Poonam Yadav[3], Angela Romano[1], Lorenzo Placidi[1], Jacopo Lenkowicz[1], Nicola Dinapoli[1], Michael F. Bassetti[3], Maria Antonietta Gambacorta[1] and Vincenzo Valentini[1]*

[1] Dipartimento Diagnostica per Immagini, Radioterapia Oncologica ed Ematologia Fondazione Policlinico Universitario Agostino Gemelli Istituto di Ricovero e Cura a Carattere Scientifico (IRCCS), Rome, Italy, [2] Dipartimento Universitario di Scienze Radiologiche ed Ematologiche, Università Cattolica del Sacro Cuore, Rome, Italy, [3] Department of Human Oncology, School of Medicine and Public Health, University of Wisconsin-Madison, Madison, WI, United States

OPEN ACCESS

Edited by:
John Varlotto, Marshall University, United States

Reviewed by:
Hong Zhu, Central South University, China
Ji Zhu, Fudan University, China

***Correspondence:**
Francesco Preziosi
preziosi.fra@gmail.com

Specialty section:
This article was submitted to Radiation Oncology, a section of the journal Frontiers in Oncology

Received: *08 December 2021*
Accepted: *31 January 2022*
Published: *24 February 2022*

Citation:
Chiloiro G, Boldrini L, Preziosi F, Cusumano D, Yadav P, Romano A, Placidi L, Lenkowicz J, Dinapoli N, Bassetti MF, Gambacorta MA and Valentini V (2022) A Predictive Model of 2yDFS During MR-Guided RT Neoadjuvant Chemoradiotherapy in Locally Advanced Rectal Cancer Patients. Front. Oncol. 12:831712. doi: 10.3389/fonc.2022.831712

Purpose: Distant metastasis is the main cause of treatment failure in locally advanced rectal cancer (LARC) patients, despite the recent improvement in treatment strategies. This study aims to evaluate the "delta radiomics" approach in patients undergoing neoadjuvant chemoradiotherapy (nCRT) treated with 0.35-T magnetic resonance-guided radiotherapy (MRgRT), developing a logistic regression model able to predict 2-year disease-free-survival (2yDFS).

Methods: Patients affected by LARC were enrolled in this multi-institutional study. A predictive model of 2yDFS was developed taking into account both clinical and radiomics variables. Gross tumour volume (GTV) was delineated on the magnetic resonance (MR) images acquired during MRgRT, and 1,067 radiomic features (RF) were extracted using the MODDICOM platform. The performance of RF in predicting 2yDFS was investigated in terms of the Wilcoxon–Mann–Whitney test and area under receiver operating characteristic (ROC) curve (AUC).

Results: 48 patients have been retrospectively enrolled, with 8 patients (16.7%) developing distant metastases at the 2-year follow-up. A total of 1,099 variables (1,067 RF and 32 clinical variables) were evaluated in two different models: radiomics and radiomics/clinical. The best-performing 2yDFS predictive model was a delta radiomics one, based on the variation in terms of area/surface ratio between biologically effective doses (BED) at 54 Gy and simulation (AUC of 0.92).

Conclusions: The results of this study suggest a promising role of delta radiomics analysis on 0.35-T MR images in predicting 2yDFS for LARC patients. Further analyses including larger cohorts of patients and an external validation are needed to confirm these preliminary results.

Keywords: delta radiomics, predictive model, rectal cancer, MRgRT, neoadjuvant chemoradiotherapy

INTRODUCTION

Colorectal cancer (CRC) is one of the most common tumors worldwide and the second most common cause of cancer death in the United States (1).

Rectal cancer represents one-third of all CRCs, with the second highest incidence and second leading cause of cancer death in Western society (2).

Neoadjuvant concurrent chemoradiotherapy (nCRT) or short-course radiotherapy followed by surgery with total mesorectal excision (TME) is considered the standard treatment for locally advanced rectal cancer (LARC) (3, 4).

This treatment approach has led to a significant reduction in local recurrence (LR) (5, 6), although a significant improvement in terms of disease-free survival (DFS) or overall survival (OS) was not demonstrated according to the results of several trials focused on this outcome (7–9).

Despite the improvements in treatment strategies achieved in recent years, distant metastases (DMs) are still the main cause of treatment failure and mortality in LARC patients (10, 11).

Disease-free survival has been used as primary endpoint in numerous trials and represents one of the most promising primary clinical endpoints for patient risk stratification (12).

While 3-year DFS (3yDFS) has been considered a surrogate endpoint for OS in resectable colon cancer, 2-year DFS (2yDFS) has been shown to be a stronger predictor of OS when compared to pathological complete response (pCR) in a pooled analysis of five randomised trials (8). A recent recommendation of outcome measures in rectal cancer suggests 2yDFS as an early predictor of OS and surrogate for good prognosis (12).

Predictive models including clinical data, genetic parameters, and radiomics features extracted from diagnostic images have been proposed for this purpose (13, 14).

More recently, tumor regression measured on magnetic resonance imaging (MRI) before and during nCRT has been applied to predict the pathological response (15, 16).

Fiorino et al. proposed the early regression index (ERI_{TCP}) for rectal cancer, a radiobiological parameter based on early regression volume that can predict pCR using 1.5-T staging MR images acquired before and during the neoadjuvant treatment, later confirmed also on 0.35-T hybrid magnetic resonance-guided radiotherapy (MRgRT) images (17, 18).

The introduction of MRgRT indeed opened a new era in radiation oncology, offering the possibility to deliver daily online adaptive treatments and to take benefit of images characterized by higher soft tissue contrast (19, 20).

Besides the blatant advantages related to image quality, the potential role of online MRI as predictors has been investigated in different frameworks (16, 18, 19, 21).

Radiomics and delta radiomics approaches, which study the variations of the radiomics parameters throughout the treatment, have been demonstrated to predict patient response (16, 19).

Furthermore, the change in image-based biomarkers in response to treatment may be used to predict the propensity of the tumour to metastasize, identifying early distant relapse, offering the possibility to fully tailor the follow-up protocols, according to the most innovative paradigms of translational personalized medicine (15, 17).

This multi-institutional retrospective study investigates the delta radiomics approach in patients undergoing nCRT treated with MRgRT, developing a predictive model able to evaluate the 2yDFS probability on hybrid 0.35-T images.

MATERIALS AND METHODS

Study Population

Patients were enrolled from two institutions equipped with 0.35-T MRgRT systems (MRIdian, ViewRay Inc., Cleveland, OH, USA): Fondazione Policlinico Universitario "Agostino Gemelli" IRCCS of Rome, Italy (FPG), and University of Wisconsin-Madison, USA (UW).

All patients were affected by histologically proven locally advanced rectal cancer (cT2–4, cN0–1, cM0), aged ≥18 years, and underwent nCRT on a hybrid 0.35-T MRgRT unit.

Prior to therapy, patients underwent digital rectal examination (DRE), pelvic diagnostic MRI to define T and N staging, contrast-enhanced total-body computed tomography (CT) for M staging, and multidisciplinary tumor board (MDTB) discussion.

Specific informed consent and MRI safety screening forms were administered to all the other patients prior to therapy start.

Patients showing clinical contraindications to MRI or denying specific consent to MRgRT were discarded.

Treatment Workflow and Treatment Outcome

The FPG patients underwent MRgRT with a simultaneous integrated boost (SIB) technique, delivering 55 Gy (2.2 Gy/fraction) to the gross tumor volume (GTV) and the corresponding mesorectum and 45 Gy (1.8 Gy/fraction) to the mesorectum *in toto* and lymphatic drainage stations, selected according to disease stage (22, 23).

The cohort from UW was treated delivering a sequential treatment, with 50.4 Gy in 28 fractions (1.8 Gy/fraction) to the GTV and corresponding mesorectum and 45 Gy in 25 fractions (1.8 Gy/fraction) to the mesorectum *in toto* and elective lymph node stations, according to institutional guidelines.

Concomitant chemotherapy schedules consisting of oral chronomodulate capecitabine (1,650 mg/mq)/5-fluorouracil (5-FU) 225 mg/mq in continuous infusion or an intensification schedule with capecitabine (1,300 mg/mq) plus oxaliplatin (60 mg/mq) were prescribed for all the Italian patients in relation to the clinical stage and general condition of individual patients.

All the patients treated in UW received concomitant capecitabine (825 mg/mq twice daily during MRgRT).

Clinical restaging was performed 6 to 8 weeks after the end of nCRT through diagnostic MR imaging, DRE, and endoscopic exam, when clinically indicated.

Clinical complete response (cCR) was defined as the absence of palpable masses at DRE and of any mucosal irregularity at endoscopic examination. As for MRI, the rectal wall should

appear normal or show only a thin hypointense thickening, with no suspicious lymph nodes visualized and low signal on b1000 images or low apparent diffusion coefficient (ADC) at the previous tumor site (24, 25).

Approximately 4 weeks after clinical restaging, patients underwent surgery that included lower anterior resection (AR), abdominal-perineal resection (APR), and transanal endoscopic microsurgery (TEM) or transanal minimally invasive surgery (TAMIS) in case of major or complete response.

Selected patients underwent a conservative approach in relation to a clinical complete response and MDTB decision (26, 27).

Pathological staging was carried out according to the pTNM classification (28), and the evaluation of the tumour response to neoadjuvant treatment was performed based on tumor regression grade (TRG) according to Mandard's classification (29, 30).

Adjuvant chemotherapy was administered in selected patients with clinical high-risk factors (cT4 and ypT3–4, ypN1–2, lymphovascular invasion of the tumor, or TRG = 4).

Clinical and imaging follow-up was carried out for all the patients included in the study, for at least 5 years from surgery.

2yDFS was defined as the absence of distant metastasis or local recurrence within 2 years from the end of nCRT.

MRI Protocol and Statistical Analysis

0.35-T 175-s 3D MR images were acquired using a true fast imaging with steady state precession (TrueFISP) sequence at the simulation phase and before each treatment fraction of the MRgRT treatment.

Images showed T2*/T1 image contrast, with 1.5 × 1.5 × 1.5-mm^3 spatial resolution and 1.5-mm slice thickness.

A total of five MR images were considered for each patient for the radiomics analysis.

In order to take into account the different fractionation schemes adopted in the two Institutions, the physical doses were converted into biologically effective doses (BED), considering an α/β ratio of 10 (18, 19).

The analyzed MR images were acquired at simulation and when the following biologically effective dose (BED) levels were reached: 13, 26, 40, 54, and 67 Gy.

MR images were then uploaded on a radiotherapy delineation console (Eclipse, Varian Medical System™, Palo Alto, CA, USA) for GTV segmentation, and GTV was contoured following the International Commission on Radiation Units Report 83 (ICRU 83) guidelines by an experienced radiation oncologist skilled in the treatment of lower gastrointestinal malignancies (31).

Contouring and revision of MRI images were blinded for all clinical data including information regarding the achieved pathologic response.

Figure 1 reports the example of a standard image dataset.

All the imported MR images were processed using signal normalization as described in similar experiences dealing with the same topic (21, 32).

After image preprocessing, radiomics features (RF) belonging to three families (morphological, statistical, textural) were extracted from each MRI considering the GTV as region of interest. Radiomics analysis was performed using MODDICOM, an image biomarker standardization initiative (IBSI) compliant in-house developed radiomics platform (33, 34).

In addition to the standard radiomics features, the variations of RF during treatment were quantified calculating the delta RF, which corresponds to the ratio between the values calculated at different BED levels and the corresponding one extracted at simulation.

A comprehensive database was then created combining the selected radiomics features (RF), general parameters related to diagnosis and treatment (sex, age, clinical TNM staging, radiotherapy dose, type of surgical procedure, and chemotherapy), clinical parameters related to blood analysis (hemoglobin, white blood cells, neutrophils, platelets, neutrophil–lymphocyte ratio), and outcome data (complete or not pathological response, DFS).

Statistical analysis was performed using R software (v 3.4.1, Wien, Austria) and dedicated packages.

The Wilcoxon–Mann–Whitney (WMW) test was performed to identify the ability of each RF in predicting 2yDFS at the univariate analysis.

Pearson correlation coefficient (PCC) was used to estimate the correlation among the delta radiomics features showing statistical significance ($p < 0.05$) at the univariate analysis.

Two logistic regression linear models were elaborated: the first one using the most significant delta RF, the second one combining two most significant delta RF showing the lowest mutual PCC. The significance performance of such model was evaluated in terms of the receiver operating characteristic curve (ROC) (35).

The area under the ROC curve was considered as the main performance metric, with the 95% confidence intervals calculated using the bootstrap method with 2,000 iterations (36).

The best cutoff threshold was identified maximizing the Youden index, and the values of sensitivity and specificity values at the best threshold were calculated (37).

RESULTS

A total of 48 consecutive patients were retrospectively enrolled for this analysis: 42 (87.5%) from FPG and 6 (12.5%) from UW.

Overall, the median age for FPG and UW patients was 62 (range 39–87) years and 54 (52–60), respectively. According to the TNM classification, 28 (58.3%) patients presented a cT3 (24 FPG, 4 UW), 13 a cT4 (11 FPG, 2 UW), and 7 a cT2 (7 FPG) disease.

Complete response, considering both patients with persistent cCR and pCR, was reached in 16 cases (33.3%).

Details of patient characteristics and clinical and treatment features are summarized in **Table 1**.

At a median follow-up of 31 months (range 4–47), 8 patients (16.7%) developed distant metastases, 5 patients at the lung, and 3 at the liver.

A total of 1,099 variables were calculated and evaluated at the univariate analysis, to quantify their ability in predicting the

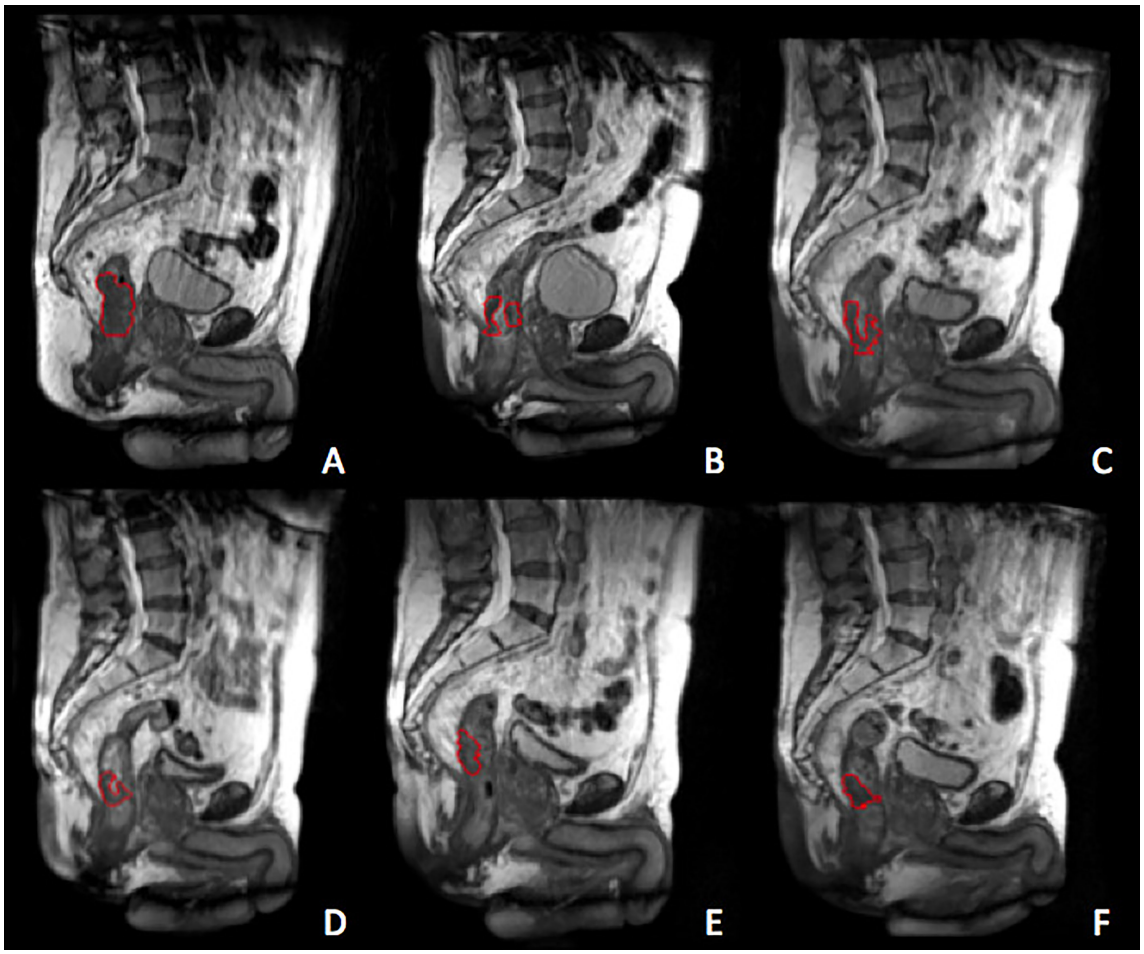

FIGURE 1 | Gross tumour volum (GTV) delineated at the treatment simulation **(A)** and at the different treatment fractions selected for the delta-radiomics analysis, corresponding to BED levels of 13 Gy **(B)**, 26 Gy **(C)**, 40 Gy **(D)**, 54 Gy **(E)** and 67 Gy **(F)**. The GTV is represented by the red contour.

2yDFS, more specifically, 1,067 RF (582 basal and 485 delta features) and 32 clinical variables.

The most significant RF in identifying 2yDFS was the variation in terms of the area/surface ratio, between BED at 54 Gy and simulation (AV(d4)), which showed an AUC of 0.92 (0.84–1 as 95% confidence interval).

As for clinical features, the type of concomitant and adjuvant chemotherapy showed statistical significance in predicting 2yDFS ($p = 0.04$).

When combining AV(d4) with the type of chemotherapy (Chemo+AV(d4)), an AUC value of 0.90 (0.81–0.99) was obtained, with a sensitivity of 1.00 and specificity of 0.875 at the best discriminative threshold.

The obtained ROC curves are shown in **Figure 2**, while **Table 2** reports values of sensitivity, specificity, and AUC for the two predictive models.

With regard to the ability of ERI_{TCP} in predicting 2yDFS, the best performance was obtained at a BED level of 40 Gy ($p = 0.04$), while only limited predictive ability was observed when a BED level of 26 Gy is reached ($p = 0.08$).

DISCUSSION

Accurate predictive models are very useful for treatment selection and risk stratification for LARC patients (14), and it is important to define the most appropriate endpoints in order to developed appropriately tailored treatments (12).

DFS is used as outcome in several studies about rectal cancer management (38–40). Basing on the previous work by Valentini et al., 2yDFS has been shown to be a reliable predictor of OS, even stronger than pCR achievement (8).

The feasibility of 2yDFS prediction using a delta radiomics approach was investigated in this retrospective multicentric study in LARC patients undergoing MRgRT.

TABLE 1 | Patient characteristics.

	Number of patients (%)
Median age (range)	62 (39–87)
Sex	
Male	33 (68.8%)
Female	15 (31.2%)
cT	
2	7 (14.6%)
3	28 (58.3%)
4	13 (27.1%)
cN	
0	13 (27.1%)
+	35 (72.9%)
Median radiotherapy dose [Gy] (range)	55 (50–59.4)
Median interval between end of nCRT and surgery [weeks] (range)	14.7 (6–31.4)
Surgical procedure	
APR	4 (8.3%)
AR	32 (66.7%)
TEM/LE	2 (4.2%)
No surgery	10 (20.8%)
ypT	
0	8 (21.1%)
1	2 (5.3%)
2	11 (28.9%)
3	17 (44.7%)
ypN	
0	29 (76.3%)
+	9 (23.7%)
pCR/cCR	
Yes	16 (33.3%)
No	32 (66.7%)
CT type	
With Oxa	17 (35.4%)
Without Oxa	2 (4.2%)
No	29 (60.4%)
2yDFS	
Yes	40 (83.3%)
No	8 (16.7%)

CT, chemotherapy; pCR, pathological complete response; cCR, clinical complete response; AR, anterior resection/low anterior resection; APR, abdominal-perineal resection; TEM, transanal endoscopic microsurgery; LE, local excision; 2yDFS, 2 year disease free survival.

Boldrini et al. (16) previously demonstrated that delta radiomics and image feature variation during MRgRT treatment may efficaciously describe LARC behavior in terms of post nCRT pCR prediction.

The results here obtained show a 2yDFS predictive ability with an AUC value of 0.92, using the delta AV at the fourth week of treatment.

Interestingly, the combination of delta RF with clinical features (i.e., chemotherapy administration) did not allow to achieve better predictive performances for 2yDFS in LARC patients.

This is in line with the recent studies that evaluated the correlation of delta radiomics features before and after chemoradiotherapy, demonstrating that delta radiomics signatures were independent predictors of treatment response (16, 41).

Besides the very limited delta radiomics experiences, few studies have shown that radiomics features can be extracted from MR scans and used to predict early distant recurrence of LARC patients (15, 42, 43).

A delta radiomics approach was used by Chiloiro et al. to predict the occurrence of DM (15), proposing a model with a balanced accuracy, accuracy, specificity, and sensitivity of 0.785, 0.809, 0.857, and 0.714, respectively. Li et al. (42) developed and validated a combined model that incorporated radiomics features and clinical factors, with an AUC of 0.842 and 0.802 for the training set and validation set, respectively, that may aid in individualized prediction of DM.

Moreover, Liu et al. (43) developed and validated an MRI-based radiomics signature for prediction of DM, by stratifying patients who might benefit from adjuvant chemotherapy.

Latest studies have demonstrated the validity of ERI_{TCP} to predict the pCR status and long-term distant metastasis-free survival (17, 18, 44). Fiorino et al. demonstrated that ERI_{TCP} showed high performances in predicting the pathological response (44) and predicts long-term DM-free survival after nCRT for rectal cancer (17).

Cusumano et al. (18) confirmed the validity of ERI_{TCP} as a pCR predictor in the context of low-tesla MRgRT and indicate 25 Gy as the best BED level to perform predictions.

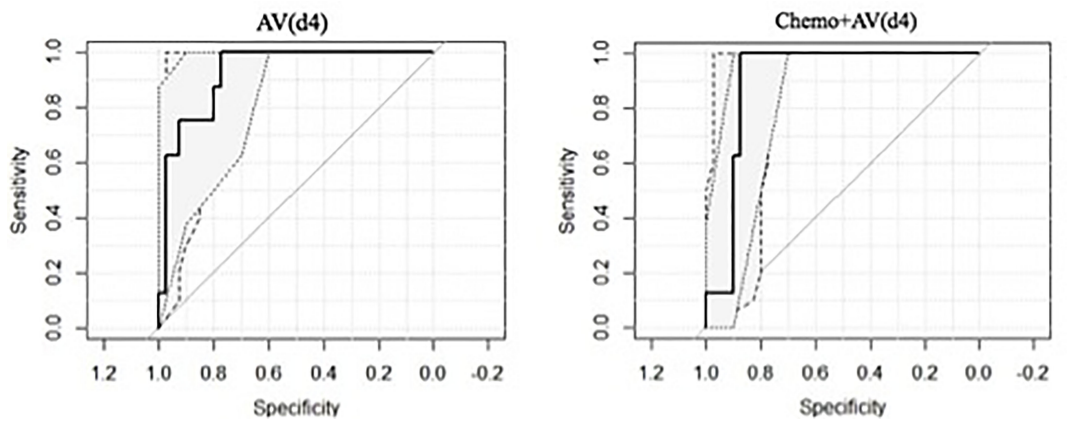

FIGURE 2 | ROC curves of the model elaborated.

TABLE 2 | Sensitivity, specificity, and AUC for the two predictive models.

	Sensitivity	Specificity	Threshold	J_index	AUC	AUC_Low	AUC_High
Chemo	0.75	0.700	0.117	-0.985	0.723	0.540	0.906
AV(d4)	1.00	0.775	0.138	-0.982	0.925	0.844	1.000
Chemo+AV(d4)	1.00	0.875	0.244	-0.981	0.903	0.814	0.991

In the current study, the best predictive performance of ERI_{TCP} was obtained when a BED level of nearly 40 Gy is reached ($p = 0.04$).

As far as the authors know, this study is the first to develop a predictive model of 2yDFS in rectal cancer using a delta radiomics approach with images acquired during the course of 0.35 T MRgRT.

The most significant radiomics features was AV(d4), which measures the variation of the GTV area/volume ratio between the fourth treatment week and the simulation, again indicating how the morphological variation of GTV during treatment can be predictable of 2yDFS, and not only of pCR, as already demonstrated in some studies (16, 18, 19).

Despite its novelty and methodological robustness, this study suffers some limitations.

First is the relatively small sample size based on retrospective analysis, reflecting the very low number of active MRgRT centers treating LARC patients with long-course radiotherapy.

Second is the limited number of other considered outcomes, which can be used to build a robust and accurate hybrid predictive model.

Last is the lack of a dataset containing a significant number of events to be considered as external validation set, which represents a mandatory step to demonstrate the applicability of the model in a cohort of patients from other institutions and moving toward the clinical application.

Despite these limitations, the results of this study support a promising role of delta radiomics analysis on low-field MR images in predicting 2yDFS for LARC patients.

Further analyses including larger cohorts of patients and a more robust external validation are needed to confirm these preliminary results.

One of the future directions of this work once reaching a significant number of patients will be that of carrying out a dedicated analysis on subpopulations treated with different adjuvant chemotherapy schemes, with the aim of obtaining indications on the optimal chemotherapy approach on the basis of radiomics information extracted from MRI, as already demonstrated on similar experiences carried out on 1.5-T MR images (45).

In the future, predictive models of 2yDFS should be designed in order to identify the subset of patients with a higher risk of DM for a specific adjuvant treatment definition and an effective therapy personalization, including the selection of patients that may benefit from intensified follow-up protocols aiming at the optimization of the available national health system resources.

DATA AVAILABILITY STATEMENT

The original contributions presented in the study are included in the article/supplementary material. Further inquiries can be directed to the corresponding author.

ETHICS STATEMENT

Ethical review and approval were not required for the study on human participants in accordance with the local legislation and institutional requirements. The patients/participants provided their written informed consent to participate in this study. Written informed consent was obtained from the individual(s) for the publication of any potentially identifiable images or data included in this article.

AUTHOR CONTRIBUTIONS

GC, LB, FP, DC, and AR participated in developing the concept of this manuscript, imaging segmentation, data analysis, researching and writing, manuscript preparation, and approval of the final manuscript draft. PY, LP, JL, ND, MFB, MAG, and VV participated in supervision. All authors contributed to the article and approved the submitted version.

REFERENCES

1. Siegel RL, Miller KD, Fuchs HE, Jemal A. Cancer Statistics, 2021. *CA: A Cancer J Clin* (2021) 71:7–33. doi: 10.3322/caac.21654
2. Ferlay J, Colombet M, Soerjomataram I, Dyba T, Randi G, Bettio M, et al. Cancer Incidence and Mortality Patterns in Europe: Estimates for 40 Countries and 25 Major Cancers in 2018. *Eur J Cancer* (2018) 103:356–87. doi: 10.1016/j.ejca.2018.07.005
3. Bosset J-F, Collette L, Calais G, Mineur L, Maingon P, Radosevic-Jelic L, et al. Chemotherapy With Preoperative Radiotherapy in Rectal Cancer. *N Engl J Med* (2006) 355:1114–23. doi: 10.1056/nejmoa060829
4. Sauer R, Becker H, Hohenberger W, Rödel C, Wittekind C, Fietkau R, et al. Preoperative Versus Postoperative Chemoradiotherapy for Rectal Cancer. *N Engl J Med* (2004) 351:1731–40. doi: 10.1056/nejmoa040694
5. Lutz MP, Zalcberg JR, Glynne-Jones R, Ruers T, Ducreux M, Arnold D, et al. Second St. Gallen European Organisation for Research and Treatment of Cancer Gastrointestinal Cancer Conference: Consensus Recommendations on Controversial Issues in the Primary Treatment of Rectal Cancer. *Eur J Cancer* (2016) 63:11–24. doi: 10.1016/j.ejca.2016.04.010
6. Sauer R, Liersch T, Merkel S, Fietkau R, Hohenberger W, Hess C, et al. Preoperative Versus Postoperative Chemoradiotherapy for Locally Advanced Rectal Cancer: Results of the German CAO/ARO/AIO-94 Randomized Phase

III Trial After a Median Follow-Up of 11 Years. *J Clin Oncol* (2012) 30:1926–33. doi: 10.1200/JCO.2011.40.1836
7. Valentini V, Gambacorta MA, Cellini F, Aristei C, Coco C, Barbaro B, et al. The INTERACT Trial: Long-Term Results of a Randomised Trial on Preoperative Capecitabine-Based Radiochemotherapy Intensified by Concomitant Boost or Oxaliplatin, for Ct2 (Distal)–Ct3 Rectal Cancer. *Radiother Oncol* (2019) 134:110–8. doi: 10.1016/j.radonc.2018.11.023
8. Valentini V, Van Stiphout RGPM, Lammering G, Gambacorta MA, Barba MC, Bebenek M, et al. Selection of Appropriate End-Points (pCR vs 2ydfs) for Tailoring Treatments With Prediction Models in Locally Advanced Rectal Cancer. *Radiother Oncol* (2015) 114:302–9. doi: 10.1016/j.radonc.2015.02.001
9. Van Gijn W, Marijnen CAM, Nagtegaal ID, Kranenbarg EMK, Putter H, Wiggers T, et al. Preoperative Radiotherapy Combined With Total Mesorectal Excision for Resectable Rectal Cancer: 12-Year Follow-Up of the Multicentre, Randomised Controlled TME Trial. *Lancet Oncol* (2011) 12:575–82. doi: 10.1016/S1470-2045(11)70097-3
10. Sun Y, Lin H, Lu X, Huang Y, Xu Z, Huang S, et al. A Nomogram to Predict Distant Metastasis After Neoadjuvant Chemoradiotherapy and Radical Surgery in Patients With Locally Advanced Rectal Cancer. *J Surg Oncol* (2017) 115:462–9. doi: 10.1002/jso.24522
11. Wang J, Li S, Liu Y, Zhang C, Li H, Lai B. Metastatic Patterns and Survival Outcomes in Patients With Stage IV Colon Cancer: A Population-Based Analysis. *Cancer Med* (2020) 9:361–73. doi: 10.1002/cam4.2673
12. Fokas E, Glynne-Jones R, Appelt A, Beets-Tan R, Beets G, Haustermans K, et al. Outcome Measures in Multimodal Rectal Cancer Trials. *Lancet Oncol* (2020) 21:e252–64. doi: 10.1016/S1470-2045(20)30024-3
13. Valentini V, Van Stiphout RGPM, Lammering G, Gambacorta MA, Barba MC, Bebenek M, et al. Nomograms for Predicting Local Recurrence, Distant Metastases, and Overall Survival for Patients With Locally Advanced Rectal Cancer on the Basis of European Randomized Clinical Trials. *J Clin Oncol* (2011) 29:3163–72. doi: 10.1200/JCO.2010.33.1595
14. Ryan JE, Warrier SK, Lynch AC, Ramsay RG, Phillips WA, Heriot AG. Predicting Pathological Complete Response to Neoadjuvant Chemoradiotherapy in Locally Advanced Rectal Cancer: A Systematic Review. *Colorectal Dis* (2016) 18:234–46. doi: 10.1111/codi.13207
15. Chiloiro G, Rodriguez-Carnero P, Lenkowicz J, Casà C, Masciocchi C, Boldrini L, et al. Delta Radiomics Can Predict Distant Metastasis in Locally Advanced Rectal Cancer: The Challenge to Personalize the Cure. *Front Oncol* (2020) 10:595012. doi: 10.3389/fonc.2020.595012
16. Boldrini L, Cusumano D, Chiloiro G, Casà C, Masciocchi C, Lenkowicz J, et al. Delta Radiomics for Rectal Cancer Response Prediction With Hybrid 0.35 T Magnetic Resonance-Guided Radiotherapy (MRgRT): A Hypothesis-Generating Study for an Innovative Personalized Medicine Approach. *Radiol Med* (2019) 124:145–53. doi: 10.1007/s11547-018-0951-y
17. Fiorino C, Passoni P, Palmisano A, Gumina C, Cattaneo GM, Broggi S, et al. Accurate Outcome Prediction After Neo-Adjuvant Radio-Chemotherapy for Rectal Cancer Based on a TCP-Based Early Regression Index. *Clin Trans Radiat Oncol* (2019) 19:12–6. doi: 10.1016/j.ctro.2019.07.001
18. Cusumano D, Boldrini L, Yadav P, Yu G, Musurunu B, Chiloiro G, et al. External Validation of Early Regression Index (ERITCP) as Predictor of Pathologic Complete Response in Rectal Cancer Using Magnetic Resonance-Guided Radiation Therapy. *Int J Radiat Oncol Biol Phys* (2020) 108:1347–56. doi: 10.1016/j.ijrobp.2020.07.2323
19. Cusumano D, Boldrini L, Yadav P, Yu G, Musurunu B, Chiloiro G, et al. Delta Radiomics for Rectal Cancer Response Prediction Using Low Field Magnetic Resonance Guided Radiotherapy: An External Validation. *Phys Med* (2021) 84:186–91. doi: 10.1016/j.ejmp.2021.03.038
20. Meng Y, Zhang Y, Dong D, Li C, Liang X, Zhang C, et al. Novel Radiomic Signature as a Prognostic Biomarker for Locally Advanced Rectal Cancer. *J Magn Reson Imaging* (2018) 48:605–14. doi: 10.1002/jmri.25968
21. Cusumano D, Boldrini L, Yadav P, Casà C, Lee SL, Romano A, et al. Delta Radiomics Analysis for Local Control Prediction in Pancreatic Cancer Patients Treated Using Magnetic Resonance Guided Radiotherapy. *Diagnostics* (2021) 11:72. doi: 10.3390/diagnostics11010072
22. Valentini V, Gambacorta MA, Barbaro B, Chiloiro G, Coco C, Das P, et al. International Consensus Guidelines on Clinical Target Volume Delineation in Rectal Cancer. *Radiother Oncol* (2016) 120:195–201. doi: 10.1016/j.radonc.2016.07.017
23. Chiloiro G, Boldrini L, Meldolesi E, Re A, Cellini F, Cusumano D, et al. MR-Guided Radiotherapy in Rectal Cancer: First Clinical Experience of an Innovative Technology. *Clin Trans Radiat Oncol* (2019) 18:80–6. doi: 10.1016/j.ctro.2019.04.006
24. Chiloiro G, Meldolesi E, Giraffa M, Capocchiano ND, Barbaro B, Coco C, et al. Could the Conservative Approach Be Considered Safe in the Treatment of Locally Advanced Rectal Cancer in Case of a Clinical Near-Complete or Complete Response? A Retrospective Analysis. *Clin Trans Radiat Oncol* (2021) 28:1–9. doi: 10.1016/j.ctro.2021.02.009
25. Beets-Tan RGH, Lambregts DMJ, Maas M, Bipat S, Barbaro B, Curvo-Semedo L, et al. Magnetic Resonance Imaging for Clinical Management of Rectal Cancer: Updated Recommendations From the 2016 European Society of Gastrointestinal and Abdominal Radiology (ESGAR) Consensus Meeting. *Eur Radiol* (2018) 28:1465–75. doi: 10.1007/s00330-017-5026-2
26. Maas M, Beets-Tan RGH, Lambregts DMJ, Lammering G, Nelemans PJ, Engelen SME, et al. Wait-And-See Policy for Clinical Complete Responders After Chemoradiation for Rectal Cancer. *J Clin Oncol* (2011) 29:4633–40. doi: 10.1200/JCO.2011.37.7176
27. Martin ST, Heneghan HM, Winter DC. Systematic Review and Meta-Analysis of Outcomes Following Pathological Complete Response to Neoadjuvant Chemoradiotherapy for Rectal Cancer. *Br J Surg* (2012) 99:918–928. doi: 10.1002/bjs.8702
28. Brierley JD, Gospodarowicz MK, Wittekind C. *TNM Classification of Malignant Tumours*. NJ: John Wiley & Sons (2017).
29. Mandard A-M, Dalibard F, Mandard J-C, Marnay J, Henry-Amar M, Petiot J-F, et al. Pathologic Assessment of Tumor Regression After Preoperative Chemoradiotherapy of Esophageal Carcinoma. Clinicopathologic Correlations. *Cancer* (1994) 73:2680–6. doi: 10.1002/1097-0142(19940601)73:11<2680::AID-CNCR2820731105>3.0.CO;2-C
30. Vecchio FM, Valentini V, Minsky BD, Padula GDA, Venkatraman ES, Balducci M, et al. The Relationship of Pathologic Tumor Regression Grade (TRG) and Outcomes After Preoperative Therapy in Rectal Cancer. *Int J Radiat Oncol Biol Phys* (2005) 62:752–60. doi: 10.1016/j.ijrobp.2004.11.017
31. Hodapp N. The ICRU Report No. 83: Prescribing, Recording and Reporting Photon-Beam Intensity-Modulated Radiation Therapy (IMRT). *Strahlenther Onkol* (2012) 188:97–9. doi: 10.1007/s00066-011-0015-x
32. Cusumano D, Meijer G, Lenkowicz J, Chiloiro G, Boldrini L, Masciocchi C, et al. A Field Strength Independent MR Radiomics Model to Predict Pathological Complete Response in Locally Advanced Rectal Cancer. *Radiol Med* (2021) 126:421–9. doi: 10.1007/s11547-020-01266-z
33. Dinapoli N, Alitto AR, Vallati M, Gatta R, Autorino R, Boldrini L, et al. Moddicom: A Complete and Easily Accessible Library for Prognostic Evaluations Relying on Image Features. *Proc Annu Int Conf IEEE Eng Med Biol Soc EMBS* (2015) 2015:771–4. doi: 10.1109/EMBC.2015.7318476
34. Zwanenburg A, Vallières M, Abdalah MA, Aerts HJWL, Andrearczyk V, Apte A, et al. The Image Biomarker Standardization Initiative: Standardized Quantitative Radiomics for High-Throughput Image-Based Phenotyping. *Radiology* (2020) 295:328–38. doi: 10.1148/radiol.2020191145
35. Yaparpalvi R, Hong L, Mah D, Shen J, Mutyala S, Spierer M, et al. ICRU Reference Dose in an Era of Intensity-Modulated Radiation Therapy Clinical Trials: Correlation With Planning Target Volume Mean Dose and Suitability for Intensity-Modulated Radiation Therapy Dose Prescription. *Radiother Oncol* (2008) 89:347–52. doi: 10.1093/jicru/ndn018
36. International Commissioning on Radiation Units and Measurements. Receiver Operating Characteristic (ROC) Analysis in Medical Imaging. *ICRU Rep* (2008) 8:1–62. doi: 10.1093/jicru/ndn008
37. Ruopp MD, Perkins NJ, Whitcomb BW, Schisterman EF. Youden Index and Optimal Cut-Point Estimated From Observations Affected by a Lower Limit of Detection. *Biom J* (2008) 50:419–30. doi: 10.1002/bimj.200710415
38. Sargent D, Shi Q, Yothers G, Van Cutsem E, Cassidy J, Saltz L, et al. Two or Three Year Disease-Free Survival (DFS) as a Primary End-Point in Stage III Adjuvant Colon Cancer Trials With Fluoropyrimidines With or Without Oxaliplatin or Irinotecan: Data From 12,676 Patients From MOSAIC, X-ACT, PETACC-3, C-06, C-07 and C89803. *Eur J Cancer* (2011) 47:990–6. doi: 10.1016/j.ejca.2010.12.015
39. Smith JJ, Chow OS, Gollub MJ, Nash GM, Temple LK, Weiser MR, et al. Organ Preservation in Rectal Adenocarcinoma: A Phase II Randomized Controlled Trial Evaluating 3-Year Disease-Free Survival in Patients With Locally Advanced Rectal Cancer Treated With Chemoradiation Plus

Induction or Consolidation Chemotherapy, and Total. *BMC Cancer* (2015) 15:767. doi: 10.1186/s12885-015-1632-z
40. Conroy T, Bosset JF, Etienne PL, Rio E, François É, Mesgouez-Nebout N, et al. Neoadjuvant Chemotherapy With FOLFIRINOX and Preoperative Chemoradiotherapy for Patients With Locally Advanced Rectal Cancer (UNICANCER-PRODIGE 23): A Multicentre, Randomised, Open-Label, Phase 3 Trial. *Lancet Oncol* (2021) 22:702–15. doi: 10.1016/S1470-2045(21)00079-6
41. Wan L, Peng W, Zou S, Ye F, Geng Y, Ouyang H, et al. MRI-Based Delta-Radiomics Are Predictive of Pathological Complete Response After Neoadjuvant Chemoradiotherapy in Locally Advanced Rectal Cancer. *Acad Radiol* (2020) 28 (Suppl 1):S95– 104. doi: 10.1016/j.acra.2020.10.026
42. Li M, Zhu YZ, Zhang YC, Yue YF, Yu HP, Song B. Radiomics of Rectal Cancer for Predicting Distant Metastasis and Overall Survival. *World J Gastroenterol* (2020) 26:5008–21. doi: 10.3748/wjg.v26.i33.5008
43. Liu Z, Meng X, Zhang H, Li Z, Liu J, Sun K, et al. Predicting Distant Metastasis and Chemotherapy Benefit in Locally Advanced Rectal Cancer. *Nat Commun* (2020) 11:4308. doi: 10.1038/s41467-020-18162-9
44. Fiorino C, Gumina C, Passoni P, Palmisano A, Broggi S, Cattaneo GM, et al. A TCP-Based Early Regression Index Predicts the Pathological Response in Neo-Adjuvant Radio-Chemotherapy of Rectal Cancer. *Radiother Oncol* (2018) 128:564–8. doi: 10.1016/j.radonc.2018.06.019
45. Di Dio C, Chiloiro G, Cusumano D, Catucci F, Boldrini L, Romano A, et al. Fractal-Based Radiomic Approach to Tailor the Chemotherapy Treatment in Rectal Cancer: A Generating Hypothesis Study. *Front Oncol* (2021) 11:774413. doi: 10.3389/fonc.2021.774413

Conflict of Interest: The authors declare that the research was conducted in the absence of any commercial or financial relationships that could be construed as a potential conflict of interest.

Publisher's Note: All claims expressed in this article are solely those of the authors and do not necessarily represent those of their affiliated organizations, or those of the publisher, the editors and the reviewers. Any product that may be evaluated in this article, or claim that may be made by its manufacturer, is not guaranteed or endorsed by the publisher.

frontiers in Oncology

ORIGINAL RESEARCH
published: 02 March 2022
doi: 10.3389/fonc.2022.839831

Dosimetric Evaluation of Incidental Irradiation to the Internal Mammary Chain After Surgery in Breast Cancer Patients

Wei Wang[1], Tao Sun[2], Yingtao Meng[1], Min Xu[1], Yingjie Zhang[1], Qian Shao[1], Yuanfang Song[3] and Jianbin Li[1]**

[1] Department of Radiation Oncology, Shandong Cancer Hospital and Institute, Shandong First Medical University and Shandong Academy of Medical Sciences, Jinan, China, [2] Department of Medical Physics, Shandong Cancer Hospital and Institute, Shandong First Medical University and Shandong Academy of Medical Sciences, Jinan, China, [3] Department of Radiation Oncology, Wei Hai Municipal Hospital, Cheeloo College of Medicine, Shandong University, Weihai, China

OPEN ACCESS

Edited by:
Jing Cai,
Hong Kong Polytechnic University, Hong Kong SAR, China

Reviewed by:
Christiane Matuschek, University Hospital of Düsseldorf, Germany
Vanessa Figlia, IRCCS Sacro Cuore Don Calabria, Italy

***Correspondence:**
Jianbin Li
lijianbin@msn.com
Yuanfang Song
1009593313@qq.com

Specialty section:
This article was submitted to Radiation Oncology, a section of the journal Frontiers in Oncology

Received: *20 December 2021*
Accepted: *21 January 2022*
Published: *02 March 2022*

Citation:
Wang W, Sun T, Meng Y, Xu M, Zhang Y, Shao Q, Song Y and Li J (2022) Dosimetric Evaluation of Incidental Irradiation to the Internal Mammary Chain After Surgery in Breast Cancer Patients. Front. Oncol. 12:839831. doi: 10.3389/fonc.2022.839831

Background and Purpose: The low rate of internal mammary node (IMN) recurrence was attributed to systemic therapy and internal mammary chain (IMC) coverage by the tangential fields of irradiation. This study aimed to evaluate the incidental irradiation dose to the IMC in breast cancer patients after surgery and to estimate the clinical predictive parameters affecting the magnitude of the IMC.

Materials and Methods: A total of 138 patients treated with postmastectomy radiotherapy and 210 patients undergoing radiotherapy after breast-conserving surgery (BCS) in our hospital were retrospectively analyzed. The mean dose (Dmean) to the IMC and the first to third intercostal spaces of IMC levels (ICS1–3) were evaluated. We evaluated the IMC coverage according to the type of surgery and whether the ipsilateral supraclavicular fossa (SCF) was included in the irradiation field.

Results: The incidental radiation dose to the IMC was 29.69 Gy, and the dose delivered to the IMC, ICS1, and ICS2 showed a greater coverage in the modified radical mastectomy (MRM) group when compared with the BCS group (32.85 vs. 27.1 Gy, 26.6 vs. 12.5 Gy, 34.63 vs. 30.42 Gy). The dose delivered to ICS3 showed no difference between the MRM and BCS groups (37.41 vs. 36.24 Gy). Furthermore, 131 patients (37.64%) received radiotherapy to the chest wall and ipsilateral SCF. In the univariate analysis, both surgery type and SCF irradiation were parameters affecting the Dmean of incidental radiation to the IMC (r = –0.179, P = 0.001; r = –0.175, P = 0.001). In the multivariate analysis, surgery type was the only correlative factor that affected incidental radiation dose to the IMC (r = –3.534, P = 0.000).

Conclusion: The real influencing factor of incidental dose to the IMC was the surgery form rather than the accession of SCF irradiation.

Keywords: breast cancer, radiotherapy, radical mastectomy, breast-conserving surgery, internal mammary chain incidental irradiation dose

INTRODUCTION

Adjuvant breast cancer radiotherapy reduces the risk of local/regional recurrence and improves overall survival (OS) of patients undergoing breast-conserving surgery (BCS) and mastectomy (1, 2). In 2016, the National Comprehensive Cancer Network published updated clinical practice guidelines, and the Royal College of Radiologists published a consensus statement that included internal mammary node (IMN) irradiation (IMNI) guidelines and practice changes (3, 4). IMNI was administered to patients with positive axillary lymph nodes (ALNs) and patients with medial or central breast cancers while ALN was negative.

When patients underwent three-dimensional (3D) treatment planning, the incidence and severity of radiation-induced lung injury and ischemic cardiac events were minimal and acceptable (5, 6). However, an ancillary result from the Korean Radiation Oncology Group 08-06 study has revealed that radiation pneumonitis (RP) increased in breast cancer patients (6.5% of patients who underwent IMNI vs. 3.3% of patients who did not undergo IMNI) with internal mammary chain (IMC) irradiation, and grade 2 RP was observed only in the IMNI group (5). In the Danish Breast Cancer Cooperative Group-IMN study, all patients with left-sided breast cancer were treated without IMNI (median follow-up period: 9.6 years), but a systematic review and meta-analysis proved that when IMNI was performed, patients with left-sided breast cancer were at a higher risk of cardiovascular (CV) death than those with right-sided breast cancer (6). This difference in CV mortality was more apparent after 15 years of follow-up (7). A 15-year analysis of the European Organization for Research and Treatment of Cancer (EORTC) 22922/10925 trial showed that IMC and supraclavicular fossa (SCF) lymph node chain irradiation significantly reduced breast cancer mortality and recurrence in patients with stage I–III breast cancer. However, this does not translate to improved OS, nor does it provide any indication of their late irradiation reactions (8).

The IMN metastasis rate for patients with positive ALN metastases was 28%–52%, whereas the metastasis rate for patients with IMN involvement of tumor with medial or central location was 32%–65% (9). Despite the high incidence of IMN involvement after primary breast cancer treatment, the overall recurrence rate in IMNs is <1.5% even when IMCs are not excised or irradiated (10–12). For patients with negative ALNs and one to three positive ALNs, the recurrence rate in IMN was <0.3% (9), and in the IMC irradiation group, the recurrence rate was 0.2% (10). The clinical outcomes of incidental radiation to regional lymph nodes in terms of locoregional control are gaining widespread attention (13–23). The exceptionally uncommon overall recurrence in the IMNs is associated with systemic treatment and incidental IMNI (10, 20).

We have proven that incidental irradiation dose to the IMC was not associated with radiotherapy technique, both for patients who underwent BCS and modified radical mastectomy (MRM) (21–23). Given the fact that the correlation identified between IMNI dose and surgical treatment is still unclear, our study evaluated the incidental irradiation of IMC drainage routes [first to third intercostal spaces (ICS1–3)] with no formal indication for irradiation of the IMC in a real-life cohort. First, the impact of the type of surgery on IMC coverage in breast cancer patients in China who did not receive IMC irradiation was investigated. Second, the impact of the addition of ipsilateral SCF irradiation on incidental IMNI dose was evaluated.

MATERIALS AND METHODS

Patient Population

Between April 2012 and May 2017, patients who had undergone MRM or BCS and ALN dissection were included in this retrospective study. Patients who had undergone a sentinel node biopsy followed by an axillary dissection in the case of a positive node were also included. All these patients were newly diagnosed with histologically confirmed invasive breast carcinoma.

All patients were confirmed to have no clinical or pathological evidence of IMN involvement at the time of diagnosis, and IMCs were not included in the clinical target volume (CTV). The Institutional Research Ethics Board of Shandong Cancer Hospital and Institute approved this study (SDTHEC201703014), and all methods were performed in accordance with relevant guidelines and regulations. The requirement for written informed consent from patients was waived due to the retrospective nature of the investigation (retrospective single-institution cohort study).

IMC Delineation

IMC CTV was defined by a radiation oncologist. IMC was delineated based on the Radiation Therapy Oncology Group (RTOG) breast cancer contouring atlas (online at: https://www.nrgoncology.org/Portals/0/Scientific%20Program/CIRO/BreastCancerAtlas_corr.pdf?ver=WoGzc4ixtKknUz1-6bVFCw%3d%3d), from ICS1–3 through the topography of the internal thoracic vessels. The planning target volume (PTV) of the IMC (PTV_{IMC}) was designed to include an expansion of 5 mm around the IMC CTV. The same contouring atlas was followed to minimize the interobserver variability in the IMC and achieve the most precise and objective comparison.

Treatment Planning

For patients undergoing MRM, the prescription dose to the PTV was 50 Gy in 25 fractions (2 Gy per fraction). For patients undergoing BCS, the prescription dose was 60.2 Gy in 28 fractions (2.15 Gy per fraction) to the PTV of the tumor bed and 50.4 Gy in 28 fractions (1.8 Gy per fraction) to the PTV of the breast. The enrolled patients were treated with one of the three irradiation techniques described below. All treatments were performed using 6-MV photon beams 5 days a week for 5–6 weeks.

Three-Dimensional Conformal Radiotherapy (3D-CRT)

The chest wall (breast) was treated with two opposite tangential fields, and the ipsilateral SCF was treated with a single anterior field. The criterion of the three-dimensional conformal radiotherapy (3D-CRT) plan was to ensure that at least 90% of the PTV received the prescription dose.

Field-in-Field Forward Intensity-Modulated Radiotherapy

The chest wall (breast) treatment plan involved the tangential field technique with static multileaf collimator segments and two parallel-opposed tangential fields. Two to five segmented fields were manipulated to maintain dose delivery to organs at risk, such as the ipsilateral lung and heart, within normally accepted tolerances and to reduce the volume of hot spots in the treatment field. Four to five fields were directed toward the SCF to guarantee dose uniformity. The criterion of the forward intensity-modulated radiotherapy (F-IMRT) plan was to ensure that at least 95% of the PTV received the prescription dose.

Inverse IMRT

The common isocenter was located at the center of the PTV. The tangential field technique was set to involve the entire PTV, and additional 0° and 40° MLC segments were constructed to involve the SCF. Additional subfields were set to reduce hot regions generated by the primary tangential fields and improve PTV dose uniformity to achieve dose homogeneity.

Statistical Methods

Statistical analysis was performed with the SPSS statistical analysis software package. Based on the normality of the distributions, the Mann–Whitney *U* test was used to assess the statistical significance of the differences between the covariates. The Spearman rank correlation test was used to assess the relationship between IMNI dose differences and the covariates. All tests were two-sided. The results were regarded as statistically significant when P was <0.05.

RESULTS

Between 2012 and 2017, a total of 348 breast cancer patients were enrolled in this retrospective study. Among these, 138 patients received adjuvant postmastectomy radiotherapy, and the remaining 210 underwent radiotherapy after BCS. A total of 335 patients were diagnosed with invasive ductal carcinoma, 3 with invasive lobular carcinoma, 1 with invasive papillary carcinoma, and 9 with ductal carcinoma *in situ*. **Table 1** outlines the patient and treatment characteristics. None of the patients received radiotherapy to the ipsilateral IMC.

The mean dose (Dmean) to the IMC was 29.69 Gy (range: 2.76–52.93 Gy) for all patients. According to the surgery employed, the Dmean to the IMC in patients undergoing MRM showed a greater coverage than in those undergoing BCS (32.85 vs. 27.10 Gy, P = 0.001). The incidental ICS1 dosimetry was also higher in the MRM group than in the BCS group. The differences in total IMC and ICS1–3 between the MRM and BCS surgical types while using different irradiation techniques are listed in **Table 2**.

Furthermore, 131 of the 348 patients (37.64%) received adjuvant postsurgical radiotherapy to the chest wall (breast) and ipsilateral SCF, and the remaining 217 (62.36%) received radiotherapy to the chest wall (breast) only. Except for patients who underwent F-IMRT, the average dose delivered to the IMC showed a greater coverage in the chest wall (breast) and ipsilateral SCF irradiation compared with only breast irradiation (**Table 3**). The dose delivered to the first two ICSs showed a greater coverage in patients with SCF irradiation than in those without SCF irradiation (**Figure 1**), whereas there was no significant difference for ICS3 (P = 0.296). Analysis of the patients who received 3D-CRT and inverse IMRT (I-IMRT) revealed that the Dmean of the IMC was also higher in patients with chest wall (breast) and ipsilateral SCF irradiation compared with only breast irradiation (P = 0.008, P = 0.016). However, there was no significant difference among patients who underwent F-IMRT (P = 0.407). For patients who underwent simultaneous integrated boost IMRT after BCS, the Dmean to the IMC in patients with inner-quadrant cancers showed a greater coverage of IMC than in patients with outer-quadrant cancers (**Table 4**). Similarly, the influence of the techniques was insignificant.

We evaluated the IMC coverage in patients treated after surgery, according to the type of surgery and whether the ipsilateral SCF was included in the irradiation field. In the univariate analysis, the incidental IMC dose was significantly higher in patients who underwent MRM and SCF irradiation. In the multivariate analysis, only the method of surgery was the correlative factor that affected incidental IMNI dose (**Table 5**).

TABLE 1 | Patient characteristics and treatment variables.

Characteristics	*n*	%
Age (years)		
Minimum	23	
Maximum	74	
Median	45	
Histology		
Invasive ductal carcinoma	335	96.26%
Invasive lobular carcinoma	3	0.86%
Invasive papillary carcinoma	1	0.29%
Ductal carcinoma *in situ*	9	2.59%
Tumor location		
Left-sided	154	44.25%
Right-sided	194	55.75%
Surgical		
MRM	138	39.66%
BCS	210	60.34%
Radiotherapy		
3D-CRT	118	33.90%
F-IMRT	119	34.20%
I-IMRT	111	31.90%
PTV		
Chest wall (breast)	217	62.36%
Chest wall + SCF	131	37.64%

DISCUSSION

During radiotherapy for breast cancer, the rates of major coronary events increased linearly with the mean heart dose (MHD) (24–26), and for every 1-Gy increase in MHD, the Dmean of the left anterior descending artery increased by

TABLE 2 | Comparison of the incidental IMC dose between the MRM and BCS groups.

All patients	IMC	ICS1	ICS2	ICS3
MRM	32.58 (2.76–50.93)	26.6 (4.83–48.18)	34.63 (4.06–51.71)	37.41 (3.46–54.7)
BCS	27.10 (4.09–52.93)	12.5 (1.69–54.29)	30.42 (3.65–63.13)	36.24 (4.79–57.91)
Z	–3.327	–6.922	–2.777	–1.103
P	0.001	0.000	0.005	0.270
3D-CRT				
MRM	33.8 (12.89–50.93)	27.78 (4.83–48.18)	36.42 (10.4–53.25)	38.43 (12.12–54.7)
BCS	26.84 (4.09–52.93)	11.4 (1.69–54.29)	30.82 (3.65–63.13)	34.5 (4.85–57.66)
Z	–2.328	–3.791	–1.978	–1.277
P	0.020	0.000	0.048	0.202
F-IMRT				
MRM	29.65 (2.76–46.64)	24.96 (6.85–50.27)	34.35 (4.06–51.7)	34.57 (4.79–57.91)
BCS	27.33 (4.12–51.40)	13.05 (1.77–50.68)	30.83 (3.72–61.18)	35.74 (4.79–57.91)
Z	–1.128	–3.537	–0.859	–0.005
P	0.259	0.000	0.391	0.996
I-IMRT				
MRM	32.95 (15.28–8.33)	26.49 (7.70–45.01)	34.65 (15.77–51.25)	39.21 (12.56–51.79)
BCS	26.5 (8.33–47.52)	12.68 (2.30–50.02)	30.04 (8.52–54.35)	38.13 (8.42–57.46)
Z	–2.407	–5.047	–1.833	–0.577
P	0.016	0.000	0.067	0.564

IMC, internal mammary chain; MRM, modified radical mastectomy; BCS, breast-conserving surgery.

3.4 Gy (27). The Breast Cancer Expert Panel of the German Society of Radiation Oncology (DEGRO) recommends an MHD <2.5 Gy for breast cancer radiation therapy (RT) treatment planning (28, 29). In patients with left-sided breast cancer who received IMC irradiation, the MHD was increased by nearly 3.5 Gy when compared with patients who did not receive IMC irradiation (8 vs. 5.6 Gy) (30). For left-sided breast cancer patients, the cumulative risk of cardiac deaths was 1.9% after 10 years, but it significantly increased to 6.4% after 20 years (29). The risk of breast cancer-specific mortality and a patient's cardiac risk factors must be individually weighed against the risk of radiation-induced cardiotoxicity. DeSelm et al. (31) mapped the anatomic pattern of isolated nodal recurrences (NRs) in breast cancer patients treated with suitable surgery with or without RT, and 153 eligible patients were enrolled. Among the 79 NRs in the IMN chain, 63.3% (50/79), 18% (14/79), and 13% (10/79) were located in the first, second, and third ICSs, respectively. According to the guidelines of the RTOG or European Society for Radiation therapy and Oncology (ESTRO), there were 97.5% (77/79) IMN recurrences in the CTV. After curative system treatment, the overall recurrence rate in the IMNs was <1.5% even when the IMC was not excised or irradiated (9–12). Therefore, studies on the contribution of incidental radiation doses to the IMC are still ongoing. The purpose of these studies is to combine the physical and technical parameters, as well as genomic and radiomic characteristics, to improve the forecast performance of IMN metastasis and to prevent low-risk patients from receiving unnecessary radiotherapy that necessitates tailored system treatment (surgery, chemotherapy, endocrinotherapy, or targeted therapy).

TABLE 3 | Comparison of the mean dose in IMC with SCF versus without SCF.

	SCF		No SCF		P
	N	IMC (Gy)	*N*	IMC (Gy)	
All	131	32.87	217	27.19	0.001
3D-CRT	45	34.10	73	26.44	0.008
F-IMRT	46	29.20	73	27.46	0.407
I-IMRT	40	32.95	71	26.45	0.016

IMC, internal mammary chain; SCF, supraclavicular fossa.

Regardless of the radiotherapy technique, incidental ICS1 dose is higher in patients who have undergone MRM than in those who have undergone BCS (**Table 2**). The result of the correlation analysis showed that surgical treatment could affect the incidental IMC dose. Sapienza et al. found that the dose delivered to the IMC showed no significant difference between MRM and MRM plus immediate reconstruction (16). Hence, for patients treated with semi-opposed tangential 3D-CRT or IMRT, the incidental dose delivered to the IMC was not associated with chest wall thickness after MRM. The presternal fat thickness was inversely correlated with IMC inclusion in the tangent fields (32), and further analysis of dosimetric parameters proved that the higher volume of the PTV_{IMC} receiving a radiation dose of 40 Gy (V_{40}) was correlated with a thin covering of presternal fat (33).

For patients treated with 3D-CRT after surgery, the Dmean to the IMC showed a greater coverage in patients who underwent MRM than in those who underwent BCS (20, 32, 34). Currently, IMRT has become the mainstream technology for treating breast cancer patients after surgery. A single–institute dosimetric study proved that the IMLN area receives higher incidental radiation dose for MRM than BCS in carcinoma breast patients treated with the F-IMRT technique (34). Patients with breast cancer who underwent postsurgery I-IMRT or F-IMRT were included in this study, and the calculated results have the same trend as the experimental results in patients who underwent 3D-CRT and I-IMRT. However, when patients underwent F-IMRT, the dose delivered to the IMC showed no significant difference between

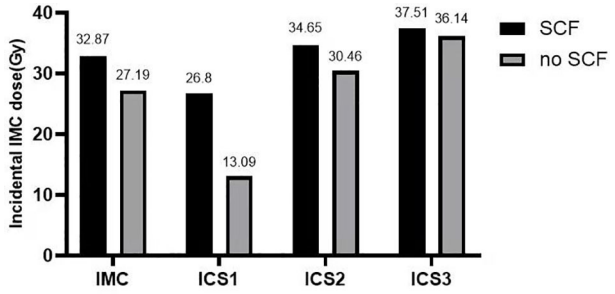

FIGURE 1 | Histogram: mean incidental dose to the IMC and the first to third intercostal spaces of the IMC. The dose delivered to the IMC and the first two ICSs showed greater coverage in patients with SCF irradiation (P = 0.001, 0.000, 0.011). IMC, internal mammary chain; SCF, supraclavicular fossa; ICS1, first intercostal space; ICS2, second intercostal space; ICS3, third intercostal space.

the MRM and BCS groups. To reduce OAR (e.g., ipsilateral lung, contralateral breast, heart) exposure, tomotherapy actively relocates isodoses from OAR areas toward areas usually with no restraint of the treatment plan optimization, such as the IMLN and ALN regions. Therefore, compared with 3D-CRT, the IMC incidental dose increased 106% during irradiation using the tomotherapy technique (13.5 vs. 27.8 Gy) (35). However, the tomotherapy technique has not become a routine radiotherapy option for breast cancer adjuvant radiotherapy.

With systematic and tailored therapy, an increasing number of breast cancer patients accept BCS directly or undergo BCS after neoadjuvant therapy (36, 37). Breast conservation versus mastectomy is associated with improved cosmetic outcomes and quality of life (38). Our previous study has found that a boost to the tumor bed in these patients did not increase the Dmean to the IMC, whether they underwent 3D-CRT, F-IMRT, or I-IMRT (21), which was consistent with the results of Sapienza et al. (the patient accepted CRT alone) (16). The location of the tumor bed is also a significant factor that influences IMC coverage. Regardless of the radiotherapy technique, a higher dose to the tumor bed increases the Dmean to the IMC in patients with inner-quadrant cancers.

TABLE 5 | Univariate and multivariate regression analyses of incidental IMC dose difference.

Characteristic	Univariate analysis		Multivariate analysis	
	r	*P*-value	Coefficient (SE)	*P*-value
Surgery method	−0.175	0.001	−3.534	0.000
Ipsilateral SCF irradiation	−0.179	0.001		

SCF, supraclavicular fossa; IMC, internal mammary chain.

According to the literature, SCF involvement is an insignificant predictor of IMC involvement dose (16, 23). In patients who received CRT, the incidental dose delivered to the IMC showed similar coverage in the SCF group compared with the non-SCF group (16). Therefore, it will be far more meaningful to study incidental IMC irradiation in a treatment plan that includes ipsilateral breast and supra/infraclavicular field. Our previous study found that when the influence of techniques was combined in patients with MRM, there was no significant increase in the Dmean to the IMC due to the addition of SCF (23). However, these two studies included a relatively small number of patients with SCF irradiation (nine and seven patients, respectively). The effect of regional lymphatic drainage area irradiation on the incidental IMC dose needs to be improved by increasing the sample size. A total of 131 patients with SCF irradiation were included in this study, and the dose delivered to the IMC showed a greater coverage of IMC in the SCF irradiation group compared with the non-SCF irradiation group (32.87 vs. 26.80 Gy). According to the correlation analysis, the irradiation field with or without SCF was not a parameter that affected the incidental Dmean of the IMC. The anatomic difference resulting from surgery type was the only parameter that affected IMC dose. According to our results, the addition of SCF irradiation increased the Dmean to the IMC in the 3D-CRT and I-IMRT groups, but not in the F-IMRT group (**Table 3**). Profound differences in the radiotherapy technique are most likely because for patients who underwent F-IMRT, SCF planning used half-beam irradiation (three to four fields), with the isocenter placed at the interface of the SCF field and chest wall/breast field. Furthermore, to reduce the apex pulmonis dose, the SCF field was irradiated with X-ray mixed with electron beams. Therefore, SCF plans were optimized

TABLE 4 | Impact of the location of the tumor bed on the incidental dose to the IMC.

	Location of the tumor (Gy)			*P*	
	Inner quadrants	Center quadrants	Outer quadrants		
3D-CRT	34.42 (6.29–52.93)	26.49 (8.92–46.42)	20.95 (4.09–49.39)	Inner vs. center	0.063
				Inner vs. outer	0.003
				Center vs. outer	0.315
F-IMRT	35.34 (6.35–51.4)	27.46 (8.72–47.17)	21.30 (4.12–47.24)	Inner vs. center	0.068
				Inner vs. outer	0.004
				Center vs. outer	0.366
I-IMRT	34.50 (8.38–44.68)	24.66 (13.91–40.83)	23.41 (8.33–47.52)	Inner vs. center	0.011
				Inner vs. outer	0.018
				Center vs. outer	0.920

IMC, internal mammary chain.

to deliver at least 90% of the PTV receiving the prescription dose, which was below the planning acceptance criteria of 3D-CRT and I-IMRT.

The Early Breast Cancer Trialists' Collaborative Group (EBCTCG) analyzed the long-term outcomes of neoadjuvant versus adjuvant chemotherapy in early breast cancer from 10 randomized trials and found that patients who received neoadjuvant chemotherapy (NACT) had a higher 15-year local recurrence after BCS than patients with the same dimensions who did not receive NACT (21.4% vs. 15.9%) (39). Thus, despite the increase in the feasibility of BCS for locally advanced breast cancer patients after NACT, to avoid underdosage in the IMC fields in patients who meet certain eligibility criteria (according to both preoperative clinical stage and postoperative pathological stage) and are indicated for elective IMNI, avoiding IMC irradiation using any of the above three techniques after BCS is not recommended.

CONCLUSIONS

IMC received inadequate incidental radiation dose coverage with all the three techniques (3D-CRT, F-IMRT, and I-IMRT), both in patients undergoing MRM and BCS. The incidental dose delivered to the IMC was significantly lower in patients undergoing BCS than in those undergoing MRM, especially for the first ICS. We concluded that the most important factor affecting the incidental IMC dose was not SCF irradiation but the operative approach.

DATA AVAILABILITY STATEMENT

Publicly available datasets were analyzed in this study. The datasets used and/or analyzed during the current study are available from the corresponding author on reasonable request: lijianbin@msn.com.

ETHICS STATEMENT

Approval was obtained from the Institutional Research Ethics Board of the Shandong Tumor Hospital Ethics Committee (SDTHEC201703014).

AUTHOR CONTRIBUTIONS

WW and JL participated in the study design, contributed to the data collection, and drafted the manuscript. TS, YZ, MX, and QS participated in the treatment planning. YM and YS made important contributions in collecting and analyzing the data and in revising the content. All authors read and approved the final manuscript.

FUNDING

This study received funding from the Natural Science Foundation of Shandong Province (No. ZR2020QH260), National Natural Science Foundation of China (No. 8217102734), Taishan Scholars Program of Shandong Province (No. ts 20190982), and Breast Disease Science Foundation of Shandong Province Medical Association (No. YXH2020ZX062).

ACKNOWLEDGMENTS

This manuscript was edited by Elsevier Language Editing Services.

REFERENCES

1. Early Breast Cancer Trialists' Collaborative Group. Effect of Radiotherapy After Breast-Conserving Surgery on 10-Year Recurrence and 15-Year Breast Cancer Death: Meta-Analysis of Individual Patient Data for 10801 Women in 17 Randomised Trials. *Lancet* (2011) 378:1707–16. doi: 10.1016/S0140-6736(11)61629-2
2. Early Breast Cancer Trialists' Collaborative Group. Effect of Radiotherapy After Mastectomy and Axillary Surgery on 10-Year Recurrence and 20-Year Breast Cancer Mortality: Meta-Analysis of Individual Patient Data for 8135 Patients in 22 Randomised Trials. *Lancet* (2014) 383:2127–35. doi: 10.1016/S0140-6736(14)60488-8
3. National Comprehensive Cancer Network. *Clinical Practice Guidelines in Oncology: Breast Cancer (Version 1.2016)* (2016). Available at: http://www.nccn.org.
4. Bloomfield DJCore Group facilitated by The Royal College of Radiologists. Development of Postoperative Radiotherapy for Breast Cancer: UK Consensus Statements – a Model of Patient, Clinical and Commissioner Engagement? *Clin Oncol (R Coll Radiol)* (2017) 29(10):639–41. doi: 10.1016/j.clon.2017.06.011
5. Choi J, Kim YB, Shin KH, Ahn SJ, Lee HS, Park W, et al. Radiation Pneumonitis in Association With Internal Mammary Node Irradiation in Breast Cancer Patients: An Ancillary Result From the KROG 08-06 Study. *J Breast Cancer* (2016) 19(3):275–82. doi: 10.4048/jbc.2016.19.3.275
6. Thorsen LB, Offersen BV, Dan H, Berg M, Jensen I, Pedersen AN, et al. DBCG-IMN: A Population-Based Cohort Study on the Effect of Internal Mammary Node Irradiation in Early Node-Positive Breast Cancer. *J Clin Oncol* (2016) 34(4):314–20. doi: 10.1200/JCO.2015.63.6456
7. Sardar P, Kundu A, Chatterjee S, Nohria A, Nairooz R, Bangalore S, et al. Long-Term Cardiovascular Mortality After Radiotherapy for Breast Cancer: A Systematic Review and Meta-Analysis. *Clin Cardiol* (2017) 40(2):73–81. doi: 10.1002/clc.22631
8. Poortmans PM, Weltens C, Fortpied C, Kirkove C, Peignaux-Casasnovas K, Budach V, et al. Internal Mammary and Medial Supraclavicular Lymph Node Chain Irradiation in Stage I-III Breast Cancer (EORTC 22922/10925): 15-Year Results of a Randomised, Phase 3 Trial. *Lancet Oncol* (2020) 21(12):1602–10. doi: 10.1016/S1470-2045(20)30472-1
9. Chen RC, Lin NU, Golshan M, Harris JR, Bellon JR. Internal Mammary Nodes in Breast Cancer: Diagnosis and Implications for Patient Management – a Systematic Review. *J Clin Oncol* (2008) 26(30):4981–9. doi: 10.1200/JCO.2008.17.4862
10. Poortmans PM, Collette S, Kirkove C, Van Limbergen E, Budach V, Struikmans H, et al. EORTC Radiation Oncology and Breast Cancer Groups. Internal Mammary and Medial Supraclavicular Irradiation in Breast Cancer. *N Engl J Med* (2015) 373(4):317–27. doi: 10.1056/NEJMoa1415369
11. Chen L, Gu Y, Leaw S, Wang Z, Wang P, Hu X, et al. Internal Mammary Lymph Node Recurrence: Rare But Characteristic Metastasis Site in Breast Cancer. *BMC Cancer* (2010) 10:479. doi: 10.1186/1471-2407-10-479

12. Galper S, Recht A, Silver B, Manola J, Gelman R, Schnitt SJ, et al. Factors Associated With Regional Nodal Failure in Patients With Early Stage Breast Cancer With 0-3 Positive Axillary Nodes Following Tangential Irradiation Alone. *Int J Radiat Oncol Biol Phys* (1999) 45:1157–66. doi: 10.1016/S0360-3016(99)00334-X
13. Kataria T, Bisht SS, Gupta D, Goyal S, Jassal K, Abhishek A, et al. Incidental Radiation to Axilla in Early Breast Cancer Treated With Intensity Modulated Tangents Andcomparison With Conventional and 3D Conformal Tangents. *Breast* (2013) 22(6):1125–9. doi: 10.1016/j.breast.2013.07.054
14. Belkacemi Y, Allab-Pan Q, Bigorie V, Khodari W, Beaussart P, Totobenazara JL, et al. The Standard Tangential Fields Used for Breast Irradiation do Not Allow Optimal Coverage and Dose Distribution in Axillary Levels I-II and the Sentinel Node Area. *Ann Oncol* (2013) 24(8):2023–8. doi: 10.1093/annonc/mdt151
15. Lee J, Kim SW, Son SH. Dosimetric Evaluation of Incidental Irradiation to the Axilla During Whole Breast Radiotherapy for Patients With Left-Sided Early Breast Cancer Radiotherapy for Patients With Left-Sidedearly Breast Cancer in the IMRT Era. *Med (Baltimore)* (2016) 95(26):e4036. doi: 10.1097/MD.0000000000004036
16. Sapienza LG, Chen MJ, Gomes MJ, Mansur DB. Unintended Irradiation of Internal Mammary Chain - Is That Enough? *Rep Pract Oncol Radiother* (2016) 21(1):25–30. doi: 10.1016/j.rpor.2015.07.006
17. Arora D, Frakes J, Scott J, Opp D, Johnson C, Song J, et al. Incidental Radiation to Uninvolved Internal Mammary Lymph Nodes in Breast Cancer. *Breast Cancer Res Treat* (2015) 151(2):365–72. doi: 10.1007/s10549-015-3400-9
18. Chung Y, Kim JW, Shin KH, Kim SS, Ahn SJ, Park W, et al. Dummy Run of Quality Assurance Program in a Phase 3 Randomized Trial Investigating the Role of Internal Mammary Lymph Node Irradiation in Breast Cancer Patients: Korean Radiation Oncology Group 08-06 Study. *Int J Radiat Oncol Biol Phys* (2015) 91(2):419–26. doi: 10.1016/j.ijrobp.2014.10.022
19. Leite ET, Ugino RT, Santana MA, Ferreira DV, Lopes MR, Pelosi EL, et al. Incidental Irradiation of Internal Mammary Lymph Nodes in Breast Cancer: Conventional Two-Dimensional Radiotherapy Versus Conformal Three-Dimensional Radiotherapy. *Radiol Bras* (2016) 49(3):170–5. doi: 10.1590/0100-3984.2015.0003
20. Kanyilmaz G, Aktan M, Koc M, Demir H, Demir LS. Unplanned Irradiation of Internal Mammary Lymph Nodes in Breast Cancer. *Radiol Med* (2017) 122(6):405–11. doi: 10.1007/s11547-017-0747-5
21. Song Y, Yu T, Wang W, Li J, Sun T, Qiu P, et al. Dosimetric Comparison of Incidental Radiation to the Internal Mammary Nodes After Breast-Conserving Surgery Using 3 Techniques-Inverse Intensity-Modulated Radiotherapy, Field-in-Field Intensity-Modulated Radiotherapy, and 3-Dimensional Conformal Radiotherapy: A Retrospective Clinical Study. *Med (Baltimore)* (2019) 98(41):e17549. doi: 10.1097/MD.0000000000017549
22. Wang W, Zhang Y, Xu M, Shao Q, Sun T, Yu T, et al. Postmastectomy Radiotherapy Using Three Different Techniques: A Retrospective Evaluation of the Incidental Dose Distribution in the Internal Mammary Nodes. *Cancer Manage Res* (2019) 11:1097–106. doi: 10.2147/CMAR.S191047
23. Wang W, Wang J, Qiu P, Sun T, Zhang Y, Shao Q, et al. Factors Influencing the Incidental Dose Distribution in Internal Mammary Nodes: A Comparative Study. *Front Oncol* (2020) 10:456. doi: 10.3389/fonc.2020.00456
24. Darby SC, Ewertz M, McGale P, Bennet AM, Blom-Goldman U, Bronnum D, et al. Risk of Ischemic Heart Disease in Women After Radiotherapy for Breast Cancer. *N Engl J Med* (2013) 368:987e98. doi: 10.1056/NEJMoa1209825
25. Taylor C, Correa C, Duane FK, Aznar MC, Anderson SJ, Bergh J, et al. Estimating the Risks of Breast Cancer Radiotherapy: Evidence From Modern Radiation Doses to the Lungs and Heart and From Previous Randomized Trials. *J Clin Oncol* (2017) 35(15):1641–9. doi: 10.1200/JCO.2016.72.0722
26. Taylor C, McGale P, Brønnum D, Correa C, Cutter D, Duane FK, et al. Cardiac Structure Injury After Radiotherapy for Breast Cancer: Cross-Sectional Study With Individual Patient Data. *J Clin Oncol* (2018) 36(22):2288–96. doi: 10.1200/JCO.2017.77.6351
27. Naimi Z, Moujahed R, Neji H, Yahyaoui J, Hamdoun A, Bohli M, et al. Cardiac Substructures Exposure in Left-Sided Breast Cancer Radiotherapy: Is the Mean Heart Dose a Reliable Predictor of Cardiac Toxicity? *Cancer Radiother* (2021) 25(3):229–36. doi: 10.1016/j.canrad.2020.09.003
28. Duma MN, Baumann R, Budach W, Dunst J, Feyer P, Fietkau R, et al. Heart-Sparing Radiotherapy Techniques in Breast Cancer Patients: A Recommendation of the Breast Cancer Expert Panel of the German Society of Radiation Oncology (DEGRO). *Strahlenther Onkol* (2019) 195(10):861–71. doi: 10.1007/s00066-019-01495-w
29. Piroth MD, Baumann R, Budach W, Dunst J, Feyer P, Fietkau R, et al. Heart Toxicity From Breast Cancer Radiotherapy : Current Findings, Assessment, and Prevention. *Strahlenther Onkol* (2019) 195(1):1–12. doi: 10.1007/s00066-018-1378-z
30. Taylor CW, Wang Z, Macaulay E, Jagsi R, Duane F, Darby SC. Exposure of the Heart in Breast Cancer Radiation Therapy: A Systematic Review of Heart Doses Published During 2003 to 2013. *Int J Radiat Oncol Biol Phys* (2015) 93(4):845–53. doi: 10.1016/j.ijrobp.2015.07.2292
31. DeSelm C, Yang TJ, Cahlon O, Tisnado J, Khan A, Gillespie E, et al. A 3-Dimensional Mapping Analysis of Regional Nodal Recurrences in Breast Cancer. *Int J Radiat Oncol Biol Phys* (2019) 103(3):583–91. doi: 10.1016/j.ijrobp.2018.10.021
32. Proulx GM, Lee RJ, Stomper PC. Internal Mammary Lymph Node Inclusion in Standard Tangent Breast Fields: Effects of Body Habitus. *Breast J* (2001) 7(2):111–6. doi: 10.1046/j.1524-4741.2001.007002111.x
33. Loganadane G, Kassick M, Kann BH, Young MR, Knowlton CA, Evans SB, et al. Standard Tangential Radiation Fields do Not Provide Incidental Coverage to the Internal Mammary Nodes. *Pract Radiat Oncol* (2020) 10(1):21–8. doi: 10.1016/j.prro.2019.07.014
34. Suryadevara A, Ahamed S, Alluri KR, Sresty MN. Incidental Radiation Dose to Internal Mammary Lymph Nodal Area in Carcinoma Breast Patients Treated With Forward Planning Intensity-Modulated Radiation Therapy Technique: A Single-Institute Dosimetric Study. *J Cancer Res Ther* (2020) 16(6):1350–3. doi: 10.4103/jcrt.JCRT_225_19
35. Mayinger M, Borm KB, Dreher C, Dapper H, Duma MN, Oechsner M, et al. Incidental Dose Distribution to Locoregional Lymph Nodes of Breast Cancer Patients Undergoing Adjuvant Radiotherapy With Tomotherapy - is it Time to Adjust Current Contouring Guidelines to the Radiation Technique? *Radiat Oncol* (2019) 14(1):135. doi: 10.1186/s13014-019-1328-7
36. Kim MK, Kim T, Moon HG, Jin US, Kim K, Kim J, et al. Effect of Cosmetic Outcome on Quality of Life After Breast Cancer Surgery. *Eur J Surg Oncol* (2015) 41(3):426–32. doi: 10.1016/j.ejso.2014.12.002
37. Jagsi R, Li Y, Morrow M, Witkamp A, Young-Afat DA, Braakenburg A, et al. Patient-Reported Quality of Life and Satisfaction With Cosmetic Outcomes After Breast Conservation and Mastectomy With and Without Reconstruction. *Ann Surg* (2015) 261(6):1198–206. doi: 10.1097/SLA.0000000000000908
38. Volders JH, Negenborn VL, Spronk PE, Krekel NMA, Schoonmade LJ, Meijer S, et al. Breast-Conserving Surgery Following Neoadjuvant Therapy-a Systematic Review on Surgical Outcomes. *Breast Cancer Res Treat* (2018) 168(1):1–12. doi: 10.1007/s10549-017-4598-5
39. Early Breast Cancer Trialists' Collaborative Group (EBCTCG). Long-Term Outcomes for Neoadjuvant Versus Adjuvant Chemotherapy in Early Breast Cancer: Meta-Analysis of Individual Patient Data From Ten Randomised Trials. *Lancet Oncol* (2018) 19(1):27–39. doi: 10.1016/S1470-2045(17)30777-5

Conflict of Interest: The authors declare that the research was conducted in the absence of any commercial or financial relationships that could be construed as a potential conflict of interest.

frontiers in Oncology

ORIGINAL RESEARCH
published: 24 March 2022
doi: 10.3389/fonc.2022.833231

Finite Element-Based Personalized Simulation of Duodenal Hydrogel Spacer: Spacer Location Dependent Duodenal Sparing and a Decision Support System for Spacer-Enabled Pancreatic Cancer Radiation Therapy

*Hamed Hooshangnejad[1,2], Sina Youssefian[1], Amol Narang[2], Eun Ji Shin[3], Avani Dholakia Rao[2], Sarah Han-Oh[2], Todd McNutt[2], Junghoon Lee[2], Chen Hu[4], John Wong[2] and Kai Ding[2]**

[1] Department of Biomedical Engineering, Johns Hopkins School of Medicine, Baltimore, MD, United States, [2] Department of Radiation Oncology and Molecular Radiation Sciences, Johns Hopkins School of Medicine, Baltimore, MD, United States, [3] Department of Gastroenterology, Johns Hopkins School of Medicine, Baltimore, MD, United States, [4] Division of Biostatistics and Bioinformatics, Sidney Kimmel Comprehensive Cancer Center, Johns Hopkins School of Medicine, Baltimore, MD, United States

OPEN ACCESS

Edited by:
Jing Cai,
Hong Kong Polytechnic University,
Hong Kong SAR, China

Reviewed by:
Tomer Charas,
Rambam Health Care Campus, Israel
Jinghao Sean Zhou,
University of Maryland, United States

***Correspondence:**
Kai Ding
kding1@jhmi.edu

Specialty section:
This article was submitted to Radiation Oncology, a section of the journal Frontiers in Oncology

Received: 10 December 2021
Accepted: 21 February 2022
Published: 24 March 2022

Citation:
Hooshangnejad H, Youssefian S, Narang A, Shin EJ, Rao AD, Han-Oh S, McNutt T, Lee J, Hu C, Wong J and Ding K (2022) Finite Element-Based Personalized Simulation of Duodenal Hydrogel Spacer: Spacer Location Dependent Duodenal Sparing and a Decision Support System for Spacer-Enabled Pancreatic Cancer Radiation Therapy. Front. Oncol. 12:833231. doi: 10.3389/fonc.2022.833231

Purpose: Pancreatic cancer is the fourth leading cause of cancer-related death, with a very low 5-year overall survival rate (OS). Radiation therapy (RT) together with dose escalation significantly increases the OS at 2 and 3 years. However, dose escalation is very limited due to the proximity of the duodenum. Hydrogel spacers are an effective way to reduce duodenal toxicity, but the complexity of the anatomy and the procedure makes the success and effectiveness of the spacer procedure highly uncertain. To provide a preoperative simulation of hydrogel spacers, we presented a patient-specific spacer simulator algorithm and used it to create a decision support system (DSS) to provide a preoperative optimal spacer location to maximize the spacer benefits.

Materials and Methods: Our study was divided into three phases. In the validation phase, we evaluated the patient-specific spacer simulator algorithm (FEMOSSA) for the duodenal spacer using the dice similarity coefficient (DSC), overlap volume histogram (OVH), and radial nearest neighbor distance (RNND). For the simulation phase, we simulated four virtual spacer scenarios based on the location of the spacer in para-duodenal space. Next, stereotactic body radiation therapy (SBRT) plans were designed and dosimetrically analyzed. Finally, in the prediction phase, using the result of the simulation phase, we created a Bayesian DSS to predict the optimal spacer location and biological effective dose (BED).

Results: A realistic simulation of the spacer was achieved, reflected in a statistically significant increase in average target and duodenal DSC for the simulated spacer. Moreover, the small difference in average mean and 5th-percentile RNNDs (0.5 and 2.1 mm) and OVH thresholds (average of less than 0.75 mm) showed that the simulation

attained similar separation as the real spacer. We found a spacer-location-independent decrease in duodenal V20Gy, a highly spacer-location-dependent change in V33Gy, and a strong correlation between L1cc and V33Gy. Finally, the Bayesian DSS predicted the change in BED with a root mean squared error of 3.6 Gys.

Conclusions: A duodenal spacer simulator platform was developed and used to systematically study the dosimetric effect of spacer location. Further, L1cc is an informative anatomical feedback to guide the DSS to indicate the spacer efficacy, optimum location, and expected improvement.

Keywords: FEMOSSA, Bayesian-based decision support system, finite element-based simulation, spacer-enabled pancreatic radiotherapy, personalized duodenal hydrogel spacer

1 INTRODUCTION

Pancreatic cancer is the fourth leading cause of cancer-related death and the 12th most common malignancy in the US, with nearly 60,000 cases each year and only less than 10% 5-year overall survival rate (1). More than one-third of the patients present with local and local/regional metastasis stage and are at great risk of distant progression (1–3). Therefore, local control (LC) is of great importance for these patients. Radiation therapy (RT), as a local-regional anticancer treatment, is an effective way to achieve LC, and using the dose escalation with intensity-modulated radiotherapy (IMRT) and stereotactic body radiation therapy (SBRT) can improve the RT outcome (4–7).

Recent studies have shown that RT together with dose escalation increases the OS at 2 years from 19% to 36%, and at 3 years from 9% to 31% (8, 9). Reaching the biologically effective dose (BED_{10}) of 70 Gy can considerably improve LC and overall survival rate (4, 10–15). However, the major concern with dose escalation is the toxicity of adjacent organs at risk (OARs), namely, stomach, bowel, and primarily duodenum, due to its proximity to the pancreas. MRI-guided RT is now used in some treatment units, in which high tumor doses can be delivered while still meeting the toxicity constraints of OAR (16, 17). However, a lack of compatibility with the current treatment system and time-consuming workflow limits its application. Achieving safe dose escalation for daily treatment using MRI information needs a new daily MRI image, which in turn triggers a new and longer and undesirable treatment plan (30 to 40 min longer). Unfortunately, even the detection of intra-fraction anatomic variation during the lengthy treatment would rarely lead to further intervention due to time constraints.

Another possible solution to deliver a high radiation dose while sparing the radiosensitive organs is the insertion of a spacer to increase the separation between the tumor and OARs. Duodenal hydrogel spacer implantation is shown to be an effective way to increase the separation between the tumor and duodenum to decrease the duodenal dose and toxicity (13, 18–26). The previous studies demonstrated that the injection of a rectal hydrogel spacer comes with many risks such as infection, inflammation, soft-tissue wall infiltration, and uncertainty in outcome of the procedure (27–29). Moreover, the misplaced hydrogel may decrease the efficacy and cause further discomfort for the patient (29). Similar risks are associated with the duodenal spacer for pancreatic cancer patients which makes the effectiveness of the spacer insertion procedure uncertain.

Additionally, the hard-to-reach location of the duodenum pancreas interface considerably increases the complexity of the procedure and chance of failure. Moreover, the duodenal hydrogel spacer system (TraceIT Tissue Marker; Boston Scientific, Marlborough, MA), at the current stage, is only designed to be used for separation of the head of the pancreas (HOP) and duodenum (**Figure 1**). However, stomach and bowel can also be major dose-limiting OARs for pancreatic RT. Thus, in such a case, the spacer may not have enough, or even, any benefits at all. Thus, the lack of a predictive model of spacer placement and dosimetric benefits may limit the optimal use of a duodenal spacer in practice.

The purpose of this study is to provide a preoperative decision support system by performing a systematic study of the different scenarios of spacer location in the duodenal loop. To do so, we took advantage of our in-house, anatomical-based and patient-specific hydrogel spacer simulation algorithm, FEMOSSA, to simulate the different scenarios of hydrogel spacer placement (30, 31). Next, we designed SBRT plans and used the result of dosimetric analysis of the RT plans to create a predictive decision support system (DSS) for the duodenal hydrogel injection procedure.

The DSS aims at helping the physician better decide whether the spacer procedure is beneficial, and FEMOSSA provides a preoperative simulation of spacer placement that can be used for a detailed examination of dose distribution and dosimetric analysis. If the spacer location is approved, the preoperative simulation guides the spacer insertion procedure. Hence, we hypothesize that the efficacy of the duodenal spacer highly depends on the duodenum-target geometry, and the DSS and FEMOSSA can personalize and optimize the hydrogel injection procedure and thus maximize the benefits and minimize the risks and uncertainties. As a result, we believe that this study is a realization of precision medicine in pancreatic cancer treatment (32).

2 MATERIALS AND METHODS

We divided our work into three phases: validation phase, simulation phase, and prediction phase. Due to the very limited number of clinical cases of the duodenal spacer, to

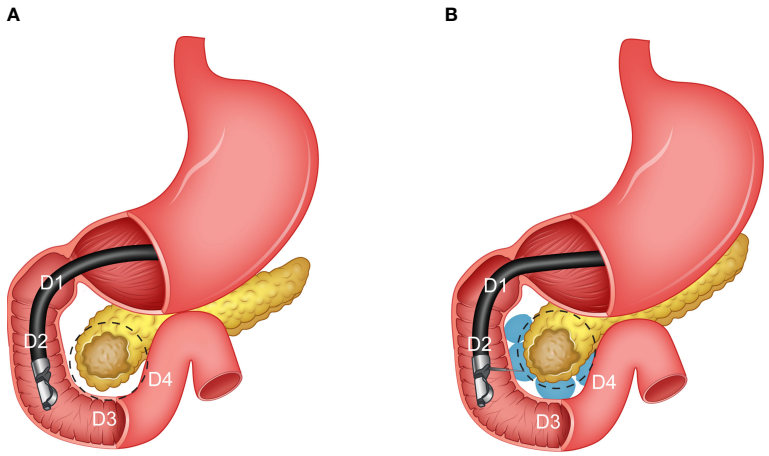

FIGURE 1 | An illustration of the pancreas and different sections of the duodenum (C loop). **(A)** Before the hydrogel injection (pre-injection), and **(B)** after the hydrogel injection (post-injection).

design and create a reliable predictive decision support system, we first extended the application of our hydrogel spacer simulation algorithm, FEMOSSA, to simulate different scenarios of spacer placement. Thus, as the first step, in the validation phase, we fine-tuned the FEMOSSA parameters to spacer insertion in the duodenum–pancreas interface problem and validated the simulation performance with the pair pre–post-injection data. FEMOSSA has already been validated for rectal spacer simulation and has shown strong performance in providing a patient-specific simulation of rectal hydrogel insertion compared to other studies (30, 33). Previously, our group also simulated the virtual spacer by shifting the structures (34), and more recently, another group used contour overriding (19). To the best of our knowledge, FEMOSSA is the first of its kind to provide an anatomical-based and patient-specific simulation of duodenal hydrogel spacers.

In the simulation phase, FEMOSSA was used to simulate four different spacer insertion scenarios to study the correlation between spacer location and benefits. Finally, in the prediction phase, SBRT plans were created for all scenarios and analyzed from the dosimetric point of view to create the DSS. For the validation phase, the spacer distribution was determined from a rigid registration of pre-and postinjection; however, for the simulation phase, by taking advantage of the FEMOSSA built-in user interface, we simulated the virtual spacer in various sections of the duodenal C-loop. **Table 1** shows an overview of the three phases of the study.

2.1 Data Collection and Preparation

Data from two cadavers and 20 patients, a total of 22 cases, were used for this study. Two cadavers and two patients with pre–postinjection scans available were used for the validation phase, and the pre-injection scans from the 20 patients (including the pre-injection scans from two patients used for validation) were included in the simulation and prediction phases of the study. Organ contours were delineated by clinicians using Varian Velocity (Varian Medical Systems, Palo Alto, CA). All scans were acquired with 2-mm slice thickness, 120 kVp, 200 mA, and 50 cm field of view.

2.2 Validation Phase

FEMOSSA parameters were, first, fine-tuned, and then the simulation result was validated on data from two cadavers and two patients that have been injected with duodenal hydrogel. Since, in this study, we used the same principles and only fine-tuned FEMOSSA for the duodenal spacer, for more detail on the different components of FEMOSSA we encourage the readers to refer to our previous study (Hamed 30). Similar figures of merit as our previous study were used to evaluate the duodenal spacer from different aspects: (1) dice similarity coefficient (DSC)

TABLE 1 | An overview of the three phases of the study.

	Validation phase	Simulation phase	Prediction phase
Purpose	Validating the virtual spacer platform	Studying the correlation of spacer location and benefits	Designing a decision support system for duodenal spacer
Data	4 cases with pre–post-injection pair scans	20 cases of pancreatic cancer patients	Dosimetric analysis from simulation phase
Method	Post-injection spacer distribution simulated in pre-injection	4 scenarios of virtual spacer were simulated, and RT plans designed	A Bayesian-based predictive model was created
Primary result	FEMOSSA was fine-tuned for virtual duodenal spacer	Spacer benefits highly depend on spacer location	The model predicts the optimal scenario and expected benefits of spacer

between the target and duodenum in postinjection (ground truth) and post-simulation scans, (2) radial definition of nearest neighbor distance (RNND), adapted to the C-loop-like anatomy of the duodenal loop, and (3) overlapped volume histogram (OVH) L_{1CC}, L_{3CC}, L_{5CC}, L_{10CC}, and L_{20CC} defined as the amount of uniform expansion of the target to have 1-, 3-, 5-, 10-, and 20-cc-volume overlaps with the duodenum (30).

2.2.1 Finite Element Model Generation

Here, we summarized the steps to create the FE model from the original contours. The generation of the FE model began by converting the 3D binary masks to triangular surface mesh. The surface mesh was smoothed using the volume-preserving Laplacian smoothing algorithm. A 3D four-node tetrahedral was used to create elements bounded to the triangular surface mesh and thus a volume mesh of the structures. To have an accurate representation of hollow organs, like the duodenum, we developed an algorithm that creates a volume 3D mesh bounded to two triangular surface meshes 2 to 3 mm away from each other. The thickness of 2 to 3 mm for the duodenum is chosen based on measurements from previous clinical studies (35–37). We turned this complex physical phenomenon into a more manageable and practically solvable problem by using an innovative, simplified, and yet realistic definition. We defined the spacer placement procedure as a translation of hydrogel distribution assembly from an initial position, tangent to the surface of ROIs, toward the final, desired spacer location that on its way pushes the proximal ROI surface and deforms them.

We ensure the well-posed definition of the FE problem by using boundary conditions inspired by the anatomy of the duodenum–pancreas interface. Comparing the pre-injection and postinjection scans revealed that the inferior surface of the horizontal part of the duodenum (D3) relatively stays in the same position. On the other hand, the descending and ascending parts of the duodenum (D2 and D4) move considerably. Due to the higher stiffness of the stomach and sphincter, the movement of the duodenum section immediately after the stomach (D1) is limited. Accordingly, the mesh nodes corresponding to the inferior wall of the D3 and the nodes on the duodenum mesh within 2-mm distance from the stomach were bound to mimic these restrictions. In the case of the target structure (HOP), no global movement, but rather a local deformation of the HOP–duodenum interface, was observed. Thus, we fixated the superior and inferior margins of HOP mesh, preventing global movements while allowing local deformation of the structure.

2.2.2 Finite Element Analysis

For the validation cases, the postinjection scans were used as the ground truth. To determine the spacer distribution in the pre-injection scan, we rigidly registered the postinjection scan to pre-injection. The distribution of the spacer in the rigidly registered scan was used for virtual spacer simulation in the pre-injection set. The FE model was, then, analyzed and solved for nodes' translation using the ABAQUS software package. The analysis was done on a Dell XPS 15, 7590, equipped with 2.4 GHz Intel Core i9, and 32 Gigabytes RAM. Finally, the results of FE analysis were interpreted as a deformation vector field that was applied to the pre-injection scan and structure set to create the post-simulation scan and structures.

2.2.3 Model Evaluation

Three figures of merit were used to evaluate the duodenal spacer from different aspects. First is the dice similarity coefficient (DSC) for target and duodenum postinjection (ground truth) and post-simulation masks. The DSC provides an insight into the general similarity of the 3D structures. However, the main goal of FEMOSSA is to simulate the separation of ROIs rather than producing the same exact contours, which is the purpose of the registration task. Thus, to evaluate the separation from a 3D point of view, we compared the OAR and target-overlapped volume histogram (OVH) between the post-simulation and postinjection. We chose five points on the OVH curve, L_{1CC}, L_{3CC}, L_{5CC}, L_{10CC}, and L_{20CC} -the uniform expansion of the target that overlaps with 1-, 3-, 5-, 10-, and 20-cc volume of OAR, respectively.

While OVH provides a volumetric 3D evaluation of the increase in separation, the radial nearest neighbor distance (RNND) gives a 2D evaluation of the separation. For any two given structures, RNND measures the closest distance from every point on one structure's margin to all the points on the margin of the other structure that fall in the same 3D spatial angle range (angle bin). Since the stomach and adjacent duodenum (D1) remain relatively in the same location compared to the surrounding structures, it was used as the origin for angle calculation. For every angle bin, a distribution of RNNDs was obtained, and the mean and 5th-percentile values were used as the representative values.

2.3 Simulation Phase

2.3.1 Virtual Spacer Simulation Scenarios

The pre-injection scan from 20 cases (Scenario Zero, S0) was augmented with three virtual spacer scenarios based on the involvement of the duodenum–target interface: between the target and D1–D2 (Scenario one, S1), D1–D2 and D3 (Scenario two, S2), and lastly, D1–D2, D3, and D4 (Scenario three, S3). Based on our experience in early trials, the injected hydrogel volume for each section was limited to less than 10 ml (20). SBRT plans were designed for the four scenarios and then analyzed to study the correlation between spacer location and benefits.

2.3.2 SBRT Planning

A total of 80 (20 cases and each case four scenarios) volumetric modulated arc therapy SBRT plans (33 Gy in 5 fractions) were designed according to the RT planning protocol in our institute. The gross target volume (GTV) was expanded by 3 mm to get mock GTV (GTV-multabc) from multiple CTs under active breath control. The GTV-multabc was further expanded by 2 mm to get the planning target volume (PTV). For further details, please refer to our previous study (14, 38).

The SBRT planning objectives and constraints were as follows: at least 90% of PTV volume receive 33 Gy, 100% of PTV volume receive 25 Gy, less than 1 cc of PTV volume receive ≥42.9 Gy, at least 95% of GTV-multabc volume receive 33 Gy,

100% of GTV volume receive 33, less than 25% of kidney volume receive ≥12 Gy, less than 50% of liver volume receive ≥12 Gy, less than 20 cc of duodenum, stomach, and bowel volume receive ≥20 Gy, less than 1 cc of duodenum, stomach, and bowel volume receive ≥33 Gy, and less than 1 cc of spinal cord volume receive ≥8 Gy. To avoid any planning bias, the planning parameters, namely, the number of beams, number of iterations, and objective functions, were identical for all the plans. Plans were optimized on the Pinnacle treatment planning system (Philips Radiation Oncology Systems, Milpitas, CA).

2.4 Prediction Phase

2.4.1 Predictive Decision Support System Design

A DSS was designed to determine (a) which OARs are the dose-limiting structures, (b) whether the patient will benefit from spacer insertion procedure, (c) how much separation is needed to achieve the desired BED, and (d) depending on patients' anatomy and dose-limiting OARs, predicted increase in *maxBED*, and thus the effectiveness of the spacer placement procedure. *maxBED* was defined as the BED value corresponding to the maximum achievable dose escalation by scaling the plan while no OAR constraints were violated. BED was calculated with α/β ratio of 10 for the tumor.

2.4.2 Decision Support System Implementation

As shown in **Figure 2**, the DSS is composed of three main components: (1) a neural network (NN) to predict the pre-injection *maxBED* using pre-injection $L1_{CC}$ anatomical information; (2) a linear regression model between desired-BED and minimum required $L1_{CC}$, and (3) a Bayesian regression model to predict the postinjection benefits of the spacer. For every new patient after the organs are delineated on the initial scan, OVH distances are extracted. The NN predicts the pre-injection *maxBED* using the $L1_{CC}$ for the three proximal OARs (duodenum, stomach, and bowel).

To decide whether the patient benefits from the spacer insertion, a desired BED value is needed as a reference value for making the decision. The corresponding $L1_{CC}$ ($L1_{CC_{TH}}$) to the desired BED is used to determine which OAR(s) and section of the duodenal loop are dose-limiting. In addition to the duodenum, stomach and bowel can potentially severely hinder achieving plan objectives due to their proximity to the target; however, unlike in the duodenum, spacer insertion in the pancreaticoduodenal space does not reduce the receiving dose to these ROIs.

For any given $L1_{CC_{TH}}$, there are three possible scenarios: (P1) only $L1_{CC_{duodenum}}$ is less than $L1_{CC_{TH}}$, (P2) $L1_{CC_{duodenum}}$ and one or both of $L1_{CC_{stomach}}$ and $L1_{CC_{bowel}}$ are less than $L1_{CC_{TH}}$, and (P3) none or only $L1_{CC_{stomach}}$ and/or $L1_{CC_{bowel}}$ are less than $L1_{CC_{TH}}$. The change in *maxBED* with spacer insertion (Δ*maxBED*) highly depends on the geometry of proximal OARs (P1–P3). P1 is the most beneficial case for spacer insertion, as the spacer insertion directly affects duodenal $L1_{CC}$ ($L1_{CC_{DUO}}$). On the other hand, there is less improvement for P2 as the duodenum is not the only limiting OAR. For the P3 scenario, however, spacer insertion is not beneficial, because *maxBED* is limited by the stomach and/or bowel, but the spacer can only spare the duodenum.

We created a Bayesian multiple linear regression model using MATLAB built-in function *bayeslm*. The input to the model is the spacer-induced change in duodenum separation ($\Delta L1_{CC_{DUO}}$). The output of the model is the spacer-induced change in *maxBED* for two possibilities P1 and P2 ($\Delta maxBED_{Px}$, $x = \{1, 2\}$). $\Delta maxBED_{P1}$ was defined as subtraction of pre-injection *maxBED* from post-simulation maximum achievable BED while only duodenum constraints are met. Similarly, $\Delta maxBED_{P2}$ was defined as subtraction of pre-injection *maxBED* from post-simulation maximum achievable BED while all constraints for the three proximal OARs are met.

We defined the Bayesian linear regression model as

$$\Delta maxBED_{Px} = \beta_0 + \beta_1 X + \beta_2 \Delta L1_{CC_{DUO}} + \beta_3 X \Delta L1_{CC_{DUO}} + \epsilon$$

where X is 0 for P1 and 1 for P2, and ϵ is the stochastic error term. The model creates an empirical distribution of prior probabilities for the model parameters using the Gibbs

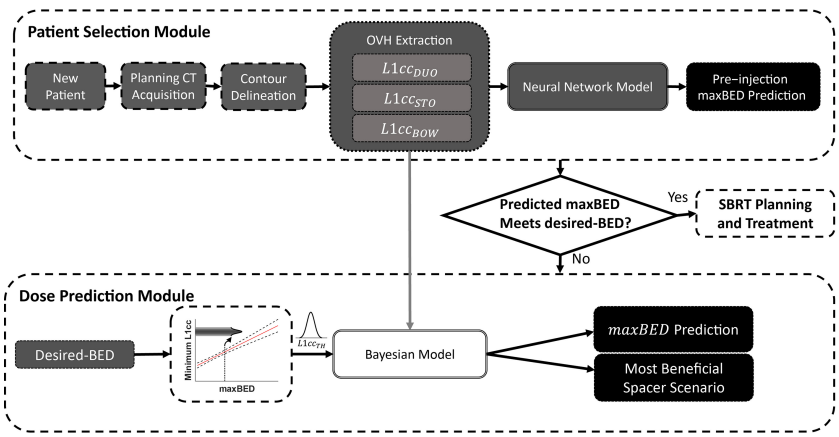

FIGURE 2 | The overview of the decision support system to predict the optimal location of the spacer and maximum achievable BED.

(Markov chain Monte Carlo algorithm) sampling method (10,000 draws). As a result, instead of point estimation, for each parameter an empirical posterior distribution was obtained and therefore incorporates the inherent high variability of the data.

To make a prediction using the model, DSS compares the $L1_{CC}$ of each proximal OAR with a minimum required distance $L1_{CC_{TH}}$ to find the limiting OARs. If the predicted pre-injection *maxBED* is less than desired-BED, depending on the patient-specific dose-limiting OARs, the Bayesian model predicts the change in *maxBED* after spacer placement. 10,000 samples from the posterior distribution of linear regression parameters, and the normal distribution of $L1_{CC_{TH}}$ (fitted to prediction mean and 95% confidence interval), were fed to the Bayesian regression model to generate a posterior probability of *maxBED*. For prediction, the input to the model is the amount separation needed, the subtraction of pre-injection $L1_{CC_{DUO}}$ from $L1_{CC_{TH}}$. The final output of the model is the maximum likelihood estimation of Δ*maxBED*.

2.5 Statistical Analysis

Using a pairwise permutation test (n = 1,000), we tested the relationship between pre-injection, post-simulation pair, and post-simulation, postinjection DSC values. Because of the small number of subjects in the validation phase, the normality assumption was circumvented by using a non-parametric permutation test.

3 RESULTS

3.1 Validation Results

The mean target DSC was 0.86 (range, 0.78 to 0.91) and 0.89 (range, 0.81 to 0.94) and duodenal DSC was 0.49 (range, 0.41 to 0.62) and 0.63 (range, 0.49 to 0.74) for pre–postinjection pair and post-simulation and post-injection pair, respectively. The statistically significant increase (p-value <0.01) in DSC values after simulation implies that the simulated ROIs are more similar in shape to postinjection ROIs. The low duodenal DSC is due to the highly variable shape of the duodenum.

The mean and 5th-percentile RNND profile for the pre-injection, postinjection, and post-simulation for a typical case is illustrated in **Figure 3**. The average difference between post-simulation and postinjection mean values and 5th-percentile values over all the cases were 0.5 and 2.1 mm, respectively. As seen in **Figure 3**, there was a visible increase in RNND values because of the spacer insertion. Although the post-simulation and postinjection profiles overlapped for the most part, they diverge on the right-hand side of the curve. This is the epitome of the natural variability of the duodenum. This portion of the curve corresponds to the D4 portion of the duodenum that was not injected with hydrogel in this case. As a result, the separation did not arise from the hydrogel and, therefore, was not captured by simulation.

The probability distribution of RNNDs, created by pooling data and normalizing the histogram of the RNNDs over all cases, showed similar probability distribution for both postinjection and post-simulation (**Figure 4**). The absolute mean difference of OVH L_{1cc}, L_{3cc}, L_{5cc}, L_{10cc}, and L_{20cc} between virtual and actual spacer were 0.04, 0.22,0.24, 0.34, and 0.75 mm, respectively.

3.2 Simulation and Planning Results

Due to the proximity of OARs, not all plans could achieve the 95% PTV coverage (clinical goal) while meeting all OAR constraints. To make the plans comparable, they were scaled to achieve 95% $<PTV_{V33Gy}$ <96%. **Figure 5** shows the duodenal V33Gy (**Figure 5A**) and V20Gy (**Figure 5B**) values broken down by the scenarios. As seen in **Figure 5B**, there was an improvement in duodenal low-dose volume (V20Gy) independent of spacer location; however, for high-dose volume, the optimum location of the spacer highly depended on the patient's anatomy, as no significant difference between scenarios was seen (**Figure 5A**). The S3 scenario has significantly lower V33Gy compared to all other scenarios since the full duodenal loop interface was separated from the target by the spacer. There was no significant difference between scenarios for

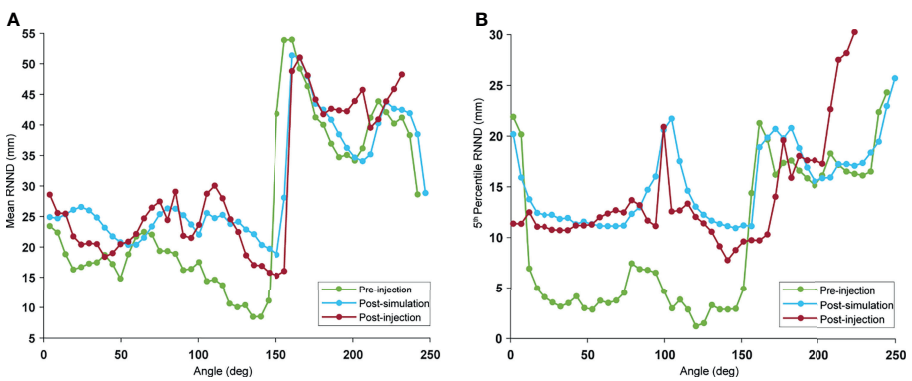

FIGURE 3 | Example of RNND profile: the RNND profile was calculated for every 5° angle bin, with 0° indicating the duodenum part adjacent to stomach (D1): pre-injection (green), post-simulation (blue), and post-injection (red). Every point on the curve shows **(A)** mean, and **(B)** 5th percentile of NND values of a single-angle bin.

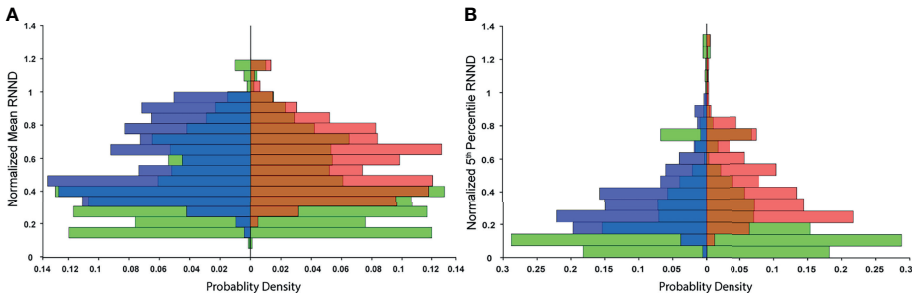

FIGURE 4 | Probability distribution of RNND values over all cases: to remove the effect of biological variability, RNND values for each case are first normalized to the maximum post-injection RNND of the same case. **(A)** shows three probability distributions of normalized mean RNND values for pre-injection (green), post-simulation (blue), and post-injection (red), and **(B)** shows the probability distribution of normalized 5th percentile NNDs.

stomach and bowel V33Gy and V20Gy, confirming the fact that duodenal spacer insertion does not increase the stomach and bowel sparing (**Figures 5C–F**).

A high correlation was found between duodenal L1cc and V33Gy (r^2 = 0.85). A Gaussian fit was used to capture both the volumetric (power) relationship and the non-negative nature of V33 Gy. Based on the fitted model, L1cc >7 mm achieved the clinical constraint of duodenal V33Gy <1 cc, and L1cc >14 mm, resulting in V33Gy = 0 (**Figure 6A**). V20Gy and L20cc were also highly correlated (Gaussian fit r^2 = 0.79), and L20cc >17 mm corresponds to V20Gy <20 cc (**Figure 6B**).

3.3 Decision Support System Prediction Results

The NN model root mean squared prediction error for the pre-injection *maxBED* was 2.7 and 3.1 Gy for the training and test data, respectively. Moreover, we found a high linear correlation between *maxBED* and the minimum of OARs L1cc ($minL1_{CC}$) shown in **Figure 7A** (r^2 = 0.74). The Bayesian predictive model root mean squared prediction error for Δ*maxBED* was 2.7 and 3.6 Gy, for the train and test data, respectively (**Figure 7B**). Finally, our model suggests that for 70 Gy BED an L1cc of 12.4 mm (95% confidence interval, 11.5 mm, 13.3 mm) is required.

4 DISCUSSION

In this study, we presented a new application for FEMOSSA as a physical-based, patient-specific spacer simulation algorithm for the duodenal hydrogel spacer. We have also used FEMOSSA for the simulation of the rectal spacer in our previous study (Hamed 30, 39). These studies prove the great potential and versatility of FEMOSSA as a patient-specific spacer simulation algorithm. Not only can it be applied to other anatomical locations like head and neck spacers (24), but also it can be of great interest to both physicists and physicians to gain better insight into the mechanics of soft-tissue and hydrogel interaction in plastic surgery (40), drug (41), and biomaterial (42) delivery.

Taking advantage of FEMOSSA allowed us to do a systematic study of the correlation between spacer location and spacer benefits that is infeasible in practice. The result was used to develop a DSS to help health professionals make the most informed clinical decision and potentially spare the patients from unnecessary trauma of an invasive endoscopic ultrasound (EUS)-guided procedure and reduce the cost and time of treatment.

We validated FEMOSSA by quantifying the separation between HOP and duodenum in the complex C-loop-like shape of the duodenal loop using newly defined RNND and OVH metrics. The RNND profile can further be used as informative, quantified feedback to guide the EUS-based spacer injection procedure as it provides a 2D radial measurement of separation similar to the radial EUS viewpoint. The OVH is a scalar, on-demand metric that quantifies the 3D relative geometry of ROIs. Previously, it has been shown to have a high correlation with plan dosimetric indices (34, 43) and used to predict objectives and constraints, for automatic or semiautomatic treatment planning (44–47).

Our result showed that OVH $L1_{CC}$ has a very high correlation with duodenal high-dose volume (V33Gy). Given that our analysis suggests V33Gy was the main limiting factor to achieve target objectives and is highly sensitive to spacer location, we believe that L1cc is an informative preoperative and intraoperative anatomical feedback to guide the spacer procedure. Moreover, it indicates that OVH L1cc can be a good factor for automatic treatment plan optimization. These results justify the use of L1cc as quantified feedback, sensitive to adjacent OARs anatomy and spacer location, to create the most informed DSS.

The DSS was designed based on an NN-based predictive model and a Bayesian regression model. The NN method is a fast, relatively simple method to model multivariable non-linear relationships. The advantage of the Bayesian model is that instead of a point estimation of parameters, a probability distribution is estimated and, therefore, incorporates high variability of data by resampling the parameters. More importantly, both the NN and Bayesian methods have transfer-learning advantage that gives the model the ability to get updated with the newly presented data.

Our study has a few limitations. First is the limited number of cases for the validation phase. The duodenal hydrogel spacer is a

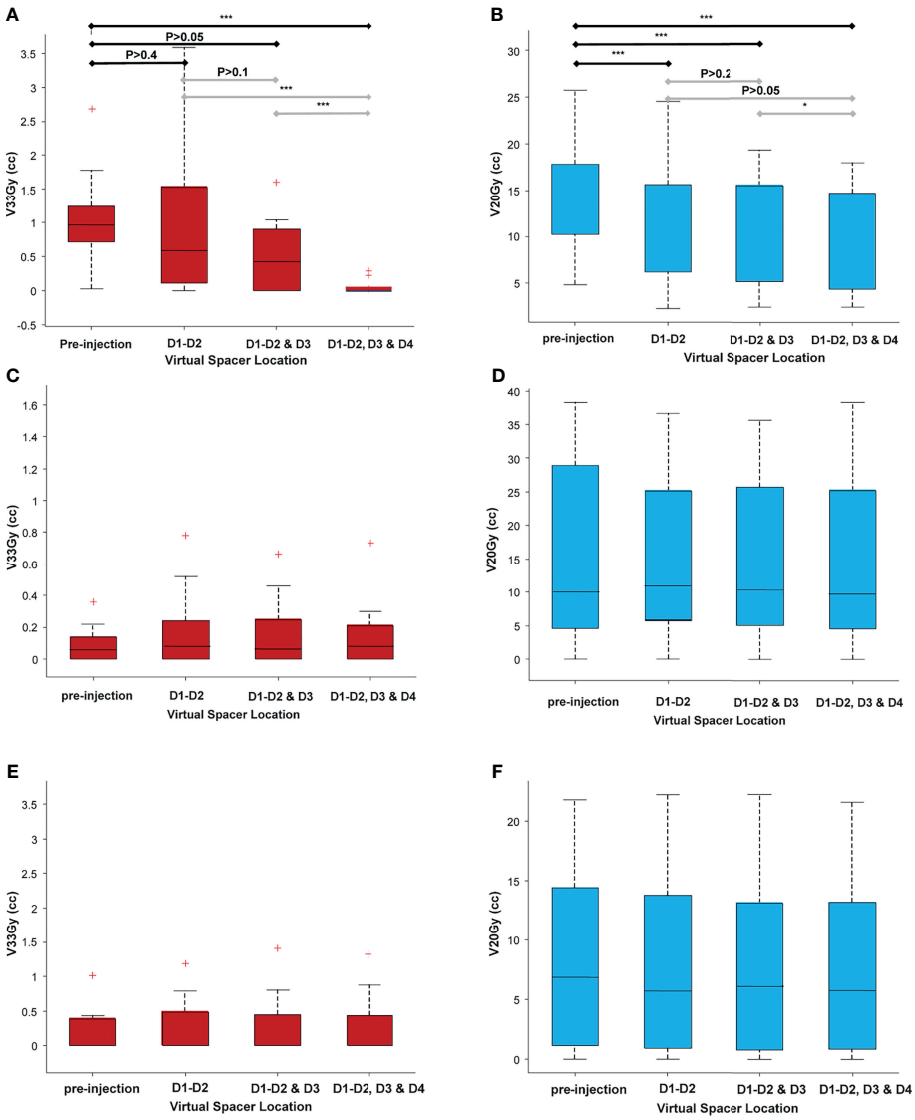

FIGURE 5 | A comparison of volume receiving high and low doses for all adjacent OARs (duodenum, stomach, and bowel), broken down for different scenarios. As seen, there is a statistically significant improvement in duodenal low-dose volume [20 Gy **(B)**] independent of scenario (spacer location), as opposed to the duodenal high-dose volume [33 Gy **(A)**] that highly depends on the location of the spacer. **(C–F)** The high-dose and low-dose volumes for bowel **(C, D)** and stomach **(E, F)**. There was no statistically significant difference between the volumes among the different scenarios, indicating that the duodenal spacer placement benefits have the most effect on duodenal sparing and minimal effect on sparing the bowel and stomach. *P ≤ 0.05, **P ≤ 0.01, ***P ≤ 0.001, red + indicates outlier defined as a value that is more than 1.5 times the interquartile range away from the bottom or top of the box. The double red pluses are just two outlier close to each other.

very novel procedure and not yet widely used in the clinic. Previous studies done by our group have used a small volume of hydrogel spacer (<5 cc) which only results in a small separation (<2 mm) (13; Avani Dholakia 23). In recent clinical trials, larger hydrogel volume (<10 cc) was injected to achieve more separation and thus better PTV coverage, but the number of clinical trials is very limited. To undermine the effect of this limitation, we evaluated the performance of our model rigorously with three figures of merit, namely, DSC, OVH, and RNND. Moreover, by using an advanced physical-based model, we further ensured that the simulation is based on anatomical properties and is realistic.

Another limitation of the study is the uncertainties of the spacer placement process that can be a possible source of error. Uncertainties such as day-to-day variations of organ shape (like change in abdominal filling), organ contours, and tumor volume change due to concurrent chemotherapy make predicting the exact shape and effect of hydrogel spacer nearly impossible. We addressed this issue by using the Bayesian model for the prediction model that allowed the use

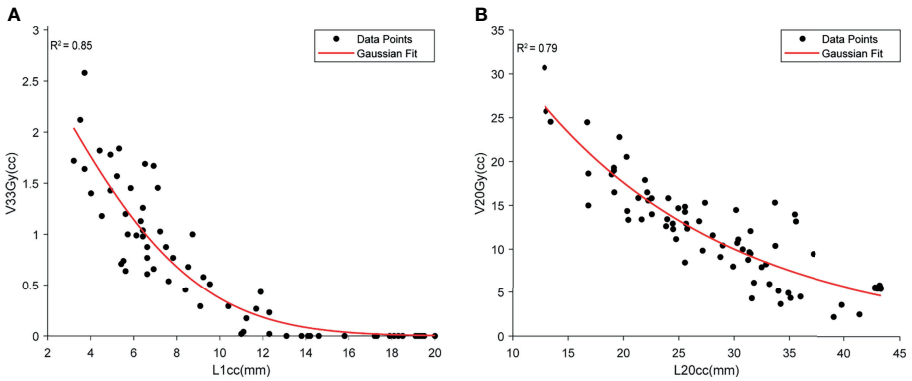

FIGURE 6 | The demonstration of the relationship between high-dose duodenal volume and L1cc **(A)** and low-dose duodenal volume and L20cc **(B)**. Both Gaussian models show a high correlation between the duodenal volume and OVH distances.

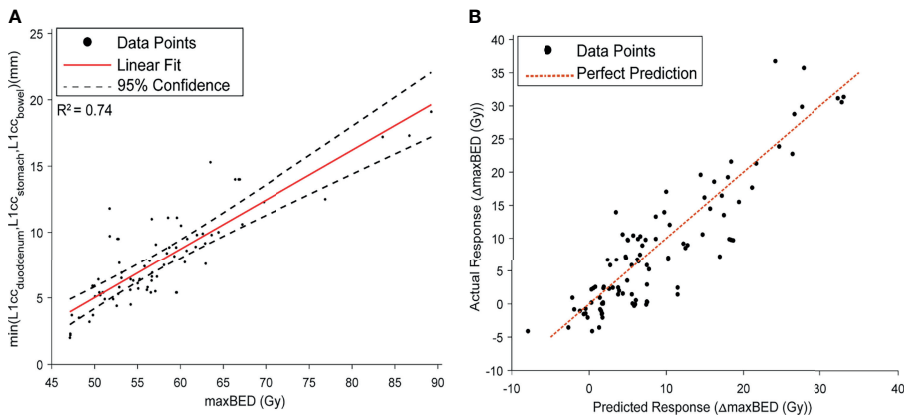

FIGURE 7 | **(A)** the Linear model fit between *maxBED* and $minL1_{CC}$. A high correlation was found between the two variables. **(B)** The prediction performance curve for the Bayesian model, predicting the *ΔmaxBED*.

of the Gibbs sampling method that in turn resulted in incorporating the uncertainty in our model and creating an empirical distribution of the data, and therefore a stochastic model. The Bayesian regression model generates an interval estimation of the parameters as opposed to point estimation, and therefore it allowed us to incorporate a higher level of uncertainty into the model's prediction.

Finally, another limitation of our study is that, although FEMOSSA can create a patient-specific and realistic simulation of the hydrogel spacer, using the finite element method results in a long computation time. Nevertheless, with recent optimizations of our algorithm, we reduced the time from 2 h to less than 30 min on a desktop computer. Moreover, here we showed the feasibility of using FEMOSSA-generated augmentation to create real-time models like the designed DSS and artificial-intelligence-based models that require a large number of training data but can provide instantaneous output. Using a real-time model will further reduce the uncertainties as it can be used intraoperatively and thus minimize the effect of anatomy change.

5 CONCLUSION

In this study, we extended the application of FEMOSSA to the duodenal spacer, and using the simulated augmented data, we developed a DSS to provide preoperative patient selection and thus guidance for optimal location of the spacer. We found that spacer benefit for a high-dose volume is highly dependent on the patient's anatomy and spacer location. Future work focuses on (1) improving the software and reliability of the model by incorporating a larger patient cohort, (2) adding more features to the DSS such as prediction of toxicity and cost-effectiveness, and (3) proposing a new workflow featuring preoperative simulation and intraoperative guidance to personalize and optimize the duodenal spacer procedure based on our studies on wavelet-based image guidance (25, 48).

DATA AVAILABILITY STATEMENT

The raw data supporting the conclusions of this article will be made available by the authors upon request.

ETHICS STATEMENT

The studies involving human participants were reviewed and approved by the Johns Hopkins Medicine Institutional Review Boards. The patients/participants provided their written informed consent to participate in this study.

AUTHOR CONTRIBUTIONS

The study was designed by all authors. HH and KD prepared the manuscript. HH, SY, and KD contributed to data analysis and interpretation. HH, KD, AN, and ES participated in collecting data. All authors contributed to the article and approved the submitted version.

FUNDING

Research reported in this publication was supported by the National Institutes of Health (award numbers R37CA229417). The content is solely the responsibility of the authors and does not necessarily represent the official views of the National Institutes of Health.

SUPPLEMENTARY MATERIAL

The Supplementary Material for this article can be found online at: https://www.frontiersin.org/articles/10.3389/fonc.2022.833231/full#supplementary-material

REFERENCES

1. Siegel RL, Miller KD, Fuchs HE, Jemal A. Cancer Statistic. *CA: A Cancer J Clin* (2021) 71(1):7–335. doi: 10.3322/caac.21654
2. Sener SF, Fremgen A, Menck HR, Winchester DP. Pancreatic Cancer: A Report of Treatment and Survival Trends for 100,313 Patients Diagnosed From 1985-1995, Using the National Cancer Database. *J Am Coll Surgeons* (1999) 189(1):1–7. doi: 10.1016/s1072-7515(99)00075-7
3. Shin SH, Kim HJ, Hwang DW, Lee JH, Song KB, Jun E, et al. The DPC4/SMAD4 Genetic Status Determines Recurrence Patterns and Treatment Outcomes in Resected Pancreatic Ductal Adenocarcinoma: A Prospective Cohort Study. *Oncotarget* (2017) 8(11):17945–59. doi: 10.18632/oncotarget.14901
4. Bruynzeel AME, Lagerwaard FJ. The Role of Biological Dose-Escalation for Pancreatic Cancer. *Clin Trans Radiat Oncol* (2019) 18:128–30. doi: 10.1016/j.ctro.2019.04.020
5. Ben-Josef E, Shields AF, Vaishampayan U, Vaitkevicius V, El-Rayes BF, McDermott P, et al. Intensity-Modulated Radiotherapy (IMRT) and Concurrent Capecitabine for Pancreatic Cancer. *Int J Radiat Oncol Biol Phys* (2004) 59(2):454–595. doi: 10.1016/j.ijrobp.2003.11.019
6. Li J, Ng J, Allendorf J, Saif MW. Locally Advanced Pancreatic Adenocarcinoma: Are We Making Progress? Highlights From The '2011 ASCO Annual Meeting'. Chicago, IL, USA; June 3-7, 2011. *JOP : J Pancreas* (2011) 12(4):347–505. doi: 10.6092/1590-8577/3078
7. Machtay M, Paulus R, Moughan J, Komaki R, Bradley JE, Choy H, et al. Defining Local-Regional Control and Its Importance in Locally Advanced Non-Small Cell Lung Carcinoma." *J Thorac Oncol : Off Publ Int Assoc Study Lung Cancer* (2012) 7(4):716–225. doi: 10.1097/JTO.0b013e3182429682
8. Krishnan S, Chadha AS, Suh Y, Chen H-C, Rao A, Das P, et al. "Focal Radiation Therapy Dose Escalation Improves Overall Survival in Locally Advanced Pancreatic Cancer Patients Receiving Induction Chemotherapy and Consolidative Chemoradiation." *Int J Radiat OncologyBiologyPhysics* (2016) 94(4):755–65. doi: 10.1016/j.ijrobp.2015.12.003
9. Berger AC, Garcia MJr., Hoffman JP, Regine WF, Abrams RA, Safran H, et al. Postresection CA 19-9 Predicts Overall Survival in Patients With Pancreatic Cancer Treated With Adjuvant Chemoradiation: A Prospective Validation by RTOG 9704. *J Clin Oncol : Off J Am Soc Clin Oncol* (2008) 26(36):5918–225. doi: 10.1200/JCO.2008.18.6288
10. Zaorsky NG, Lehrer EJ, Handorf E, Meyer JE. Dose Escalation in Stereotactic Body Radiation Therapy for Pancreatic Cancer: A Meta-Analysis. *Am J Clin Oncol* (2019) 42(1):46–55. doi: 10.1097/COC.0000000000000472
11. Zhu X, Cao Y, Su T, Zhu X, Ju X, Zhao X, et al. Failure Patterns and Outcomes of Dose Escalation of Stereotactic Body Radiotherapy for Locally Advanced Pancreatic Cancer: A Multicenter Cohort Study. *Ther Adv Med Oncol* (2020) 12:1–11.1758835920977155. doi: 10.1177/1758835920977155
12. Rudra S, Jiang N, Rosenberg SA, Olsen JR, Roach MC, Wan L, et al. Using Adaptive Magnetic Resonance Image-Guided Radiation Therapy for Treatment of Inoperable Pancreatic Cancer. *Cancer Med* (2019) 8(5):2123–32. doi: 10.1002/cam4.2100
13. Kerdsirichairat T, Narang AK, Thompson E, Kim S-H, Rao A, Ding K, et al. Feasibility of Using Hydrogel Spacers for Borderline-Resectable and Locally Advanced Pancreatic Tumors. *Gastroenterology* (2019) 157(4):933–355. doi: 10.1053/j.gastro.2019.07.012
14. Han-Oh S, Hill C, Wang KK-H, Ding K, Wright JL, Alcorn S, et al. Geometric Reproducibility of Fiducial Markers and Efficacy of a Patient-Specific Margin Design Using Deep Inspiration Breath Hold for Stereotactic Body Radiation Therapy for Pancreatic Cancer. *Adv Radiat Oncol* (2021) 6(2):1–9.1006555. doi: 10.1016/j.adro.2021.100655
15. Han-Oh S, Ding K, Song D, Narang A, Wong J, RongY, et al. Feasibility Study of Fiducial Marker Localization Using Microwave Radar. *Med Phys* (2021) 48:7271–82. doi: 10.1002/mp.15197
16. Hal WA, Straza MW, Chen X, Mickevicius N, Erickson B, Schultz C, et al. Initial Clinical Experience of Stereotactic Body Radiation Therapy (SBRT) for Liver Metastases, Primary Liver Malignancy, and Pancreatic Cancer With 4D-MRI Based Online Adaptation and Real-Time MRI Monitoring Using a 1.5 Tesla MR-Linac. *PloS One* (2020) 15(8):1-10.e02365705. doi: 10.1371/journal.pone.0236570
17. Hassanzadeh C, Rudra S, Bommireddy A, Hawkins WG, Wang-Gillam A, Fields RC, et al. Ablative Five-Fraction Stereotactic Body Radiation Therapy for Inoperable Pancreatic Cancer Using Online MR-Guided Adaptation. *Adv Radiat Oncol* (2021) 6(1):100506. doi: 10.1016/j.adro.2020.06.010
18. Lee D, Komatsu S, Terashima K, Toyama H, Matsuo Y, Takahashi D, et al. "Surgical Spacer Placement for Proton Radiotherapy in Locally Advanced Pancreatic Body and Tail Cancers: Initial Clinical Results." *Radiat Oncol* (2021) 16(1):1–11. doi: 10.1186/s13014-020-01731-z
19. Kawaguchi H, Demizu Y, Mukumoto N, Ishihara T, Miyawaki D, Komatsu S, et al. Efficacy of Spacers in Radiation Therapy for Locally Advanced Pancreatic Cancer: A Planning Study. *Anticancer Res* (2021) 41(1):503 LP – 508. doi: 10.21873/anticanres.14801
20. Rao AD, Feng Z, Shin EJ, He J, Waters KM, Coquia S, et al. A Novel Absorbable Radiopaque Hydrogel Spacer to Separate the Head of the Pancreas and Duodenum in Radiation Therapy for Pancreatic Cancer. *Int J Radiat Oncol Biol Phys* (2017) 99(5):1111–20. doi: 10.1016/j.ijrobp.2017.08.006
21. Han D, Hooshangnejad H, Chen C-C, Ding K. A Beam-Specific Optimization Target Volume for Stereotactic Proton Pencil Beam Scanning Therapy for Locally Advanced Pancreatic Cancer. *Adv Radiat Oncol* (2021) 6(6):1–9:100757. doi: 10.1016/j.adro.2021.100757

22. Kim S-H, Ding K, Rao A, He J, Bhutani MS, Herman JM, et al. EUS-Guided Hydrogel Microparticle Injection in a Cadaveric Model. *J Appl Clin Med Phys* (2021) 22(6):83–915. doi: 10.1002/acm2.13266
23. Rao AD, Shin EJ, Meyer J, Thompson EL, Fu W, Hu C, et al. Evaluation of a Novel Absorbable Radiopaque Hydrogel in Patients Undergoing Image Guided Radiation Therapy for Borderline Resectable and Locally Advanced Pancreatic Adenocarcinoma. *Pract Radiat Oncol* (2020) 10:508–13. doi: 10.1016/j.prro.2020.01.013
24. Rao AD, Coquia S, De Jong R, Gourin C, Page B, Latronico D, et al. Effects of Biodegradable Hydrogel Spacer Injection on Contralateral Submandibular Gland Sparing in Radiotherapy for Head and Neck Cancers. *Radiother Oncol* (2018) 126(1):96–9. doi: 10.1016/j.radonc.2017.09.017
25. Feng Z, Hooshangnejad H, Shin EJ, Narang A, Lediju Bell MA, Ding K. The Feasibility of Haar Feature-Based Endoscopic Ultrasound Probe Tracking for Implanting Hydrogel Spacer in Radiation Therapy for Pancreatic Cancer. *Front Oncol* (2021) 11:759811(November):759811. doi: 10.3389/fonc.2021.759811
26. Rao AD, Shin EJ, Beck SE, Garrett C, Kim S-H, Lee NJ, et al. Demonstration of Safety and Feasibility of Hydrogel Marking of the Pancreas-Duodenum Interface for Image Guided Radiation Therapy (IGRT) in a Porcine Model: Implications in IGRT for Pancreatic Cancer Patients. *Int J Radiat Oncol Biol Phys* (2018) 101(3):640–45. doi: 10.1016/j.ijrobp.2018.02.024
27. Müller A-C, Mischinger J, Klotz T, Gagel B, Habl G, Hatiboglu G, et al. Interdisciplinary Consensus Statement on Indication and Application of a Hydrogel Spacer for Prostate Radiotherapy Based on Experience in More Than 250 Patients. *Radiol Oncol* (2016) 50(3):329–65. doi: 10.1515/raon-2016-0036
28. Aminsharifi A, Kotamarti S, Silver D, Schulman A. Major Complications and Adverse Events Related to the Injection of the SpaceOAR Hydrogel System Before Radiotherapy for Prostate Cancer: Review of the Manufacturer and User Facility Device Experience Database. *J Endourology* (2019) 33(10):868–715. doi: 10.1089/end.2019.0431
29. Teh AYM, Ko H-T, Barr G, Woo HH. Rectal Ulcer Associated With SpaceOAR Hydrogel Insertion During Prostate Brachytherapy. *BMJ Case Rep* (2014) 10:08–513. doi: 10.1136/bcr-2014-206931
30. Hooshangnejad H, Youssefian S, Guest JK, Ding K. FEMOSSA: Patient-Specific Finite Element Simulation of the Prostate–Rectum Spacer Placement, a Predictive Model for Prostate Cancer Radiotherapy. *Med Phys* (2021) 48:3438–52. doi: 10.1002/mp.14990
31. Hooshangnejad H, Ding K. Predicting the Efficacy of Spacer Placement for Pancreatic Cancer Using a Novel Patient-Specific Virtual Spacer. In: *MEDICAL PHYSICS*, vol. 48. WILEY 111 RIVER ST, HOBOKEN 07030-5774, NJ USA (2021).
32. Chen RC, Gabriel PE, Kavanagh BD, McNutt TR. How Will Big Data Impact Clinical Decision Making and Precision Medicine in Radiation Therapy? *Int J Radiat Oncol Biol Phys* (2016) 95(3):880–45. doi: 10.1016/j.ijrobp.2015.10.052
33. Wijk Yv, Vanneste BGL, Walsh S, van der Meer S, Ramaekers B, van Elmpt W, et al. Development of a Virtual Spacer to Support the Decision for the Placement of an Implantable Rectum Spacer for Prostate Cancer Radiotherapy: Comparison of Dose, Toxicity and Cost-Effectiveness. *Radiother Oncol* (2017) 125(1):107–25. doi: 10.1016/j.radonc.2017.07.026
34. Feng Z, Rao AD, Cheng Z, Shin EJ, Moore J, Su L, et al. Dose Prediction Model for Duodenum Sparing With a Biodegradable Hydrogel Spacer for Pancreatic Cancer Radiation Therapy. *Int J Radiat Oncol Biol Phys* (2018) 102(3):651–59. doi: 10.1016/j.ijrobp.2018.07.184
35. Fanucci A, Cerro P, Fanucci E. Normal Small-Bowel Measurements by Enteroclysis. *Scand J Gastroenterol* (1988) 23(5):574–76. doi: 10.3109/00365528809093914
36. Fleischer AC, Muhletaler CA, James Jr AE. Sonographic assessment of the bowel wall. *Am J Roentgenol* (1981) 136(5):887–91.
37. Cronin CG, Delappe E, Lohan DG, Roche C, Murphy JM. Normal Small Bowel Wall Characteristics on MR Enterography. *Eur J Radiol* (2010) 75 (2):207–115. doi: 10.1016/j.ejrad.2009.04.066
38. Su L, Iordachita I, Zhang Y, Lee J, Ng SK, Jackson J, et al. Feasibility Study of Ultrasound Imaging for Stereotactic Body Radiation Therapy With Active Breathing Coordinator in Pancreatic Cancer. *J Appl Clin Med Phys* (2017) 18 (4):84–96. doi: 10.1002/acm2.12100
39. Hooshangnejad H, Youssefian S, Ding K. Virtual Spacer Implantation Platform Based on Finite Element Method for Simulation and Planning Patient-Specific Spacer Placement. *Int J Radiat Oncol Biol Phys* (2020) 108 (3):e302–3. doi: 10.1016/j.ijrobp.2020.07.723
40. Kalantar-Hormozi A, Mozafari N, Rasti M. Adverse Effects After Use of Polyacrylamide Gel as a Facial Soft Tissue Filler. *Aesthetic Surg J* (2008) 28 (2):139–425. doi: 10.1016/j.asj.2007.12.005
41. Li J, Mooney DJ. Designing Hydrogels for Controlled Drug Delivery. *Nat Rev Mater* (2016) 1(12):160715. doi: 10.1038/natrevmats.2016.71
42. Foster AA, Marquardt LM, Heilshorn SC. The Diverse Roles of Hydrogel Mechanics in Injectable Stem Cell Transplantation. *Curr Opin Chem Eng* (2017) 15:15–23. doi: 10.1016/j.coche.2016.11.003
43. Wall PDH, Carver RL, Fontenot JD. An Improved Distance-To-Dose Correlation for Predicting Bladder and Rectum Dose-Volumes in Knowledge-Based VMAT Planning for Prostate Cancer. *Phys Med Biol* (2018) 63(1):150355. doi: 10.1088/1361-6560/aa9a30
44. Yang Y, Ford EC, Wu B, Pinkawa M, van Triest B, Campbell P, et al. An Overlap-Volume-Histogram Based Method for Rectal Dose Prediction and Automated Treatment Planning in the External Beam Prostate Radiotherapy Following Hydrogel Injection. *Med Phys* (2013) 40(1):117095. doi: 10.1118/1.4769424
45. Wu B, Pang D, Lei S, Gatti J, Tong M, McNutt T, et al. Improved Robotic Stereotactic Body Radiation Therapy Plan Quality and Planning Efficacy for Organ-Confined Prostate Cancer Utilizing Overlap-Volume Histogram-Driven Planning Methodology. *Radiother Oncol : J Eur Soc Ther Radiol Oncol* (2014) 112(2):221–65. doi: 10.1016/j.radonc.2014.07.009
46. Wu B, Ricchetti F, Sanguineti G, Kazhdan M, Simari P, Jacques R, et al. Data-Driven Approach to Generating Achievable Dose-Volume Histogram Objectives in Intensity-Modulated Radiotherapy Planning. *Int J Radiat Oncol Biol Phys* (2011) 79(4):1241–475. doi: 10.1016/j.ijrobp.2010.05.026
47. Wu B, McNutt T, Zahurak M, Simari P, Pang D, Taylor R, et al. Fully Automated Simultaneous Integrated Boosted-Intensity Modulated Radiation Therapy Treatment Planning Is Feasible for Head-And-Neck Cancer: A Prospective Clinical Study. *Int J Radiat Oncol Biol Phys* (2012) 84(5):e647–535. doi: 10.1016/j.ijrobp.2012.06.047
48. Hooshangnejad H, Gharibzadeh S, Towhidkhah F. A Wavelet-Based Model for Foveal Detection of Spatial Contrast with Frequency Dependent Aperture Effect. *Adv Sci Technol Res J* (2016) 10(30):51–68. doi: 10.12913/22998624/62771

Conflict of Interest: The authors declare that the research was conducted in the absence of any commercial or financial relationships that could be construed as a potential conflict of interest.

frontiers | Frontiers in Oncology

ORIGINAL RESEARCH
published: 11 April 2022
doi: 10.3389/fonc.2022.838039

Dosimetric Impact of Inter-Fraction Variability in the Treatment of Breast Cancer: Towards New Criteria to Evaluate the Appropriateness of Online Adaptive Radiotherapy

Martina Iezzi[1], Davide Cusumano[2,3], Danila Piccari[2,3], Sebastiano Menna[2,3], Francesco Catucci[3], Andrea D'Aviero[3], Alessia Re[3], Carmela Di Dio[3], Flaviovincenzo Quaranta[3], Althea Boschetti[3], Marco Marras[3], Domenico Piro[3], Flavia Tomei[3], Claudio Votta[2,3], Vincenzo Valentini[2†] and Gian Carlo Mattiucci[2,3†]*

[1] Università Cattolica del Sacro Cuore, Rome, Italy, [2] Dipartimento Diagnostica per Immagini, Radioterapia Oncologica ed Ematologia, Fondazione Policlinico Universitario Agostino Gemelli IRCCS, Rome, Italy, [3] UOC Radioterapia Oncologica, Mater Olbia Hospital, Olbia, Italy

OPEN ACCESS

Edited by:
James Chow,
University of Toronto, Canada

Reviewed by:
Ping Xia,
Cleveland Clinic, United States
Mark Trombetta,
Allegheny Health Network,
United States

***Correspondence:**
Davide Cusumano
davide.cusumano@policlinicogemelli.it

†These authors have contributed equally to this work

Specialty section:
This article was submitted to Radiation Oncology, a section of the journal Frontiers in Oncology

Received: 17 December 2021
Accepted: 11 March 2022
Published: 11 April 2022

Citation:
Iezzi M, Cusumano D, Piccari D, Menna S, Catucci F, D'Aviero A, Re A, Di Dio C, Quaranta F, Boschetti A, Marras M, Piro D, Tomei F, Votta C, Valentini V and Mattiucci GC (2022) Dosimetric Impact of Inter-Fraction Variability in the Treatment of Breast Cancer: Towards New Criteria to Evaluate the Appropriateness of Online Adaptive Radiotherapy. Front. Oncol. 12:838039. doi: 10.3389/fonc.2022.838039

Purpose: As a discipline in its infancy, online adaptive RT (ART) needs new ontologies and *ad hoc* criteria to evaluate the appropriateness of its use in clinical practice. In this experience, we propose a predictive model able to quantify the dosimetric impact due to daily inter-fraction variability in a standard RT breast treatment, to identify in advance the treatment fractions where patients might benefit from an online ART approach.

Methods: The study was focused on right breast cancer patients treated using standard adjuvant RT on an artificial intelligence (AI)-based linear accelerator. Patients were treated with daily CBCT images and without online adaptation, prescribing 40.05 Gy in 15 fractions, with four IMRT tangential beams. ESTRO guidelines were followed for the delineation on planning CT (pCT) of organs at risk and targets. For each patient, all the CBCT images were rigidly aligned to pCT: CTV and PTV were manually re-contoured and the original treatment plan was recalculated. Various radiological parameters were measured on CBCT images, to quantify inter-fraction variability present in each RT fraction after the couch shifts compensation. The variation of these parameters was correlated with the variation of V95% of PTV (ΔV95%) using the Wilcoxon Mann–Whitney test. Fractions where ΔV95% > 2% were considered as adverse events. A logistic regression model was calculated considering the most significant parameter, and its performance was quantified with a receiver operating characteristic (ROC) curve.

Results: A total of 75 fractions on 5 patients were analyzed. The body variation between daily CBCT and pCT along the beam axis with the highest MU was identified as the best predictor (p = 0.002). The predictive model showed an area under ROC curve of 0.86 (95% CI, 0.82–0.99) with a sensitivity of 85.7% and a specificity of 83.8% at the best threshold, which was equal to 3 mm.

Conclusion: A novel strategy to identify treatment fractions that may benefit online ART was proposed. After image alignment, the measure of body difference between daily CBCT and pCT can be considered as an indirect estimator of V95% PTV variation: a difference larger than 3 mm will result in a V95% decrease larger than 2%. A larger number of observations is needed to confirm the results of this hypothesis-generating study.

Keywords: AI radiotherapy, predictive modeling, CBCT radiotherapy, inter-fraction dose variation, online adaptation

INTRODUCTION

In recent years, technological evolution and the advent of artificial intelligence (AI) have led to incredible improvements in the fight against cancer, opening treatment scenarios that were unthinkable just a few years ago (1).

In the field of radiation therapy (RT), the new cutting-edge technologies are able to modify online the RT treatment plan to effectively compensate for the patient anatomical variability, which is present during different treatment days, in a procedure known as online adaptive radiotherapy (ART) (2).

The modern technologies implementing online ART aim to integrate advanced AI-based systems to speed up the on-table adaptive procedure, to shorten the treatment slot time and avoid un-addressable organ variation that may occur during on-table ART procedure (3, 4).

To date, the RT systems licensed for online ART use the positioning images acquired through on-board MR scanners or Cone Beam Computed Tomography (CBCT) systems to elaborate the adapted treatment plans, with treatment slot times ranging from 15 to about 60 min, depending on the technology used and the case complexity (5–7).

Being a discipline in its infancy, there is an increasing need to define common ontologies and specific criteria to evaluate the appropriateness of online ART treatments. The benefits offered by such treatments are in fact a matter of study: although in some districts, such as the abdomen, the advantages offered by this approach are well demonstrated in the current literature, in others, the benefits are still under investigation, as they have to be balanced with the efforts required, in terms of both staff resources and patient stress (8–11).

Breast cancer is one of the anatomical sites in which the benefit of online ART is still under investigation: the adjuvant RT approach is in fact already very effective, as demonstrated by the results of several clinical trials present in literature with long-term outcome. In 2011, the Early Breast Cancer Trialists' Collaborative Group (EBCTCG) reported the results of a meta-analysis of 10,801 women treated with radiotherapy after breast conservative surgery, demonstrating that the use of adjuvant RT significantly reduced the risk of any first (locoregional or distant) recurrence and breast cancer mortality (12). A similar evidence was observed in patients treated with RT after mastectomy (13).

Recent experiences report percentages of local and regional recurrence after breast-conserving surgery followed by RT ranging from 7% to 13%, often associated to initial tumor size (14, 15).

However, despite the fact that local recurrences can be considered not common events, it is plausible to suppose that online ART treatments could contribute to further reduce such evidence, mainly in selected cases where the inter-fraction variability may lead to compromise the target coverage with respect to the prescribed dose, thus increasing the risk of local recurrence.

The aim of this study is to propose new evaluation criteria to identify which patients affected by right-side breast cancer could benefit in receiving online ART treatment, considering an RT treatment administered in intensity modulated radiation therapy (IMRT) modality.

Considering that the dose constraints related to nearby organs at risk (OARs) are widely met in the IMRT treatment of right breast, the main focus of attention is on the planning target volume (PTV) coverage with respect to the 95% of the prescribed dose, which has to be maintained higher than 95% as recommended by international guidelines (16, 17). For this purpose, it is necessary to quantify the dosimetric variation in the tumor coverage due to the daily inter-fraction variability; once compensated, the couch shifts, determined by the alignment of daily positioning images. Once such variability is quantified, a predictive model was also elaborated to correlate imaging parameters, related to patient positioning, to dosimetric effects on target coverage, with the idea of providing a valid tool to clinicians to know in advance the dosimetric impact of an inter-fraction variability effect.

MATERIALS AND METHODS

Patients and Treatment Characteristics

The present study has a retrospective nature and was based on the analysis of five patients affected by right breast tumor, with age higher than 18 years. Patients showed a diagnosis of Early Breast Cancer (EBC), were of legal age, and signed an informed consent for data collection and anonymized analyses.

An adjuvant RT treatment was administered to all of them, prescribing 40.05 Gy in 15 fractions (2.67 Gy/fraction) to the whole breast. A sequential boost consisting of 10 Gy in 5 fractions to the tumor bed was also prescribed in selected patients, according to the disease stage and clinical risk factors. Treatments were performed at Mater Olbia Hospital (Olbia, Italy) using Varian Ethos™ (Varian Medical System, Mountain View, California, US) between August and September 2021.

A simulation computed tomography (CT) image was acquired for all free breathing patients using the dedicated 16-

slice CT scanner (GE RT discovery, GE Healthcare, Chicago, Illinois) available in our department, keeping a slice thickness of 2.5 mm.

During CT simulation, the patient breathing motion was studied using a 4DCT acquisition in ten phases, and patients showing negligible sternum variation (less than 1 mm) in all the 4DCT phases were selected. Such selection was performed to limit the impact of breathing motion and ensure that the body variation object of the present study would be related to patient positioning.

Average CT image was reconstructed and used for therapy volume contouring and treatment planning. The clinical target volume (CTV) was outlined according to the ESTRO consensus guidelines and defined as the entire right mammary gland, while PTV was calculated as an anisotropic margin from CTV: 5 mm in the medio-lateral direction, 7 mm in the antero-posterior and cranio-caudal direction, with a crop margin of 5 mm from the body (18).

In case of the presence of prothesis, this was included in the CTV definition. Heart, esophagus, ipsilateral glenohumeral joint, spinal canal, spinal cord, thyroid gland, lungs, and contralateral breast were delineated and considered as OARs, subjected to the dose constraints reported in clinical experiences focused on breast cancer (19–22).

All the patients were treated following an intensity modulated RT (IMRT) technique consisting of four tangential beams, normalizing the treatment plan to the median target dose as recommended by ICRU Report 62 and 83 (16, 17). Treatments were administered without online adaptation.

During treatment therapy, all the CBCT acquisitions were performed using the longest acquisition time available for the thorax (30.8 s), to further reduce the impact of breathing motion on body variation.

For each patient, all the CBCT images acquired for patient positioning were rigidly aligned with the planning CT, excluding rotational shifts according to Ethos™ clinical workflow (23). Synthetic CT images were created transferring the Hounsfield Units (HU) from simulation CT to CBCT through a deformable registration.

The targets (CTV and PTV) and the nearby OARs (heart and lungs) were manually re-contoured on the daily images and treatment plan was recalculated considering the fluence of the original plan using Eclipse™ (Varian Medical System, Palo Alto, California) as treatment planning system (TPS), and Acuros™ XB (Varian Medical System, Palo Alto, California) version 15.6 as dose calculation algorithm (24).

Definition of Criteria for Adaptive Appropriateness

For each treatment fraction recalculated, the values of V95% and V105% of PTV were registered and considered as target metric values. The deviations of V95% and V105% parameters of PTV with respect to the values reported in the original plan were registered for each treatment fraction.

On the basis of the deviations observed and the value of the dose constraints, the treatment fractions were categorized as follows:

- ✓ *Optimal* when the treatment fraction showed a dose deviation from the original plan in V95%(PTV) < 2% and the dose objectives V95% (PTV) >95% and V105% (PTV) <5% remain preserved.
- ✓ *Not Optimal* when the treatment fraction showed a dose deviation from the original in V95% (PTV) ≥ 2%. In particular, a *not optimal* fraction can be considered:
  - ○ *Acceptable* if the dose objectives V95% (PTV) ≥95% and V105% (PTV) <5% remain preserved
  - ○ *Unacceptable* (to be adapted) in case the treatment fraction does not ensure the V95% (PTV) ≥95% and/or the V105% (PTV) results to be higher than 5%

The appropriateness of moving towards an adaptive approach was then evaluated based on the numbers of fractions categorized as "*not optimal*" observed during the standard treatment.

Predictive Model

Once the treatment fractions were classified into two categories, a predictive model was elaborated to quantify the probability of a treatment fraction categorized as *not optimal*, so that it could benefit from online adaptation.

Various radiological parameters were measured on CBCT images, with the aim of quantifying inter-fraction variability present in each RT fraction after the couch shifts compensation. The absolute difference in terms of body between daily CBCT and pCT was calculated along each beam axis, considering the isocenter plan as the reference plan. An example of the radiological parameters measured is reported in **Figure 1**.

The absolute body difference was also calculated considering the whole PTV as cranio-caudal (CC) extension and the maximum values observed were considered as additional parameters.

The variation of these parameters was correlated with the *not acceptable* fractions using the Wilcoxon Mann–Whitney test or the *t*-test, depending on the distribution of the variable with respect to the outcome, which was preliminarily evaluated using the Shapiro–Wilk test (25). The Benjamini–Hochberg method was adopted to correct for multiple comparisons (26, 27).

Not optimal fractions were considered as adverse events. A logistic regression model was calculated considering the radiological parameter showing higher significance at the univariate analysis, and its performance was quantified in terms of receiver operating characteristic (ROC) curve (28).

The area under the ROC curve (AUC) was used as target metric, and the 95% confidence interval (95% CI) was defined by means of a bootstrap approach with 2,000 iterations. The best cutoff threshold was determined maximizing the Youden Index, and the values of sensitivity and specificity at the best threshold were calculated accordingly, as reported in similar experiences (28–30).

RESULTS

The clinical characteristics of the patients included in the study and the corresponding dosimetric values of the considered

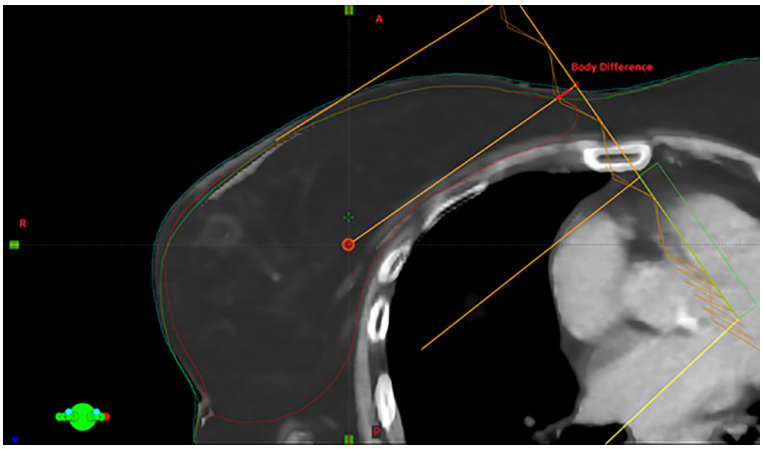

FIGURE 1 | Visual example of the body variation measurement: the difference between the body in CBCT and the corresponding one in simulation CT along the beam axis with higher MUs is highlighted in red.

treatment plans are reported in **Table 1**. All the patients had negative margins after breast surgery and they were characterized by a molecular profile "luminal A", which generally corresponds to low-grade tumors and a favorable prognosis (31). At the histological examination, all the patients received a diagnosis of ductal invasive carcinoma (non-special type).

A total of 75 fractions on 5 patients were analyzed: a general overview of the analysis of the treatment fractions is reported in **Figure 2**.

Out of a total of 75 fractions, 7 were found to be *not optimal*: specifically, three were not acceptable and four were acceptable. All the cases investigated showed the V105% of PTV always lower than 5%, so cases classified as *not optimal* are due to deviation related to V95% of PTV.

A patient with a larger initial CTV (Patient 5) was the case reporting the higher number of fractions that required online adaptation (5). As regards the results observed at the univariate analysis, the body variation along the beam axis with the highest MU was identified as the best predictor (p = 0.002).

The ROC curve of the model elaborated using such parameter is reported in **Figure 3**: it shows an AUC of 0.86 (95% CI, 0.82–0.99) with a sensitivity of 85.7% and a specificity of 83.8% at the best cutoff threshold, which was identified to be equal to 3 mm and to correspond to a Youden Index of 0.69.

Figure 4 reports the probability of obtaining a treatment fraction requiring online adaptation as a function of the body variation along the beam axis with the highest MU.

DISCUSSION

Patient selection is becoming a fundamental topic in the context of online ART treatments, and new criteria to identify patients who may effectively benefit from these technologies are needed (10, 32).

Compared to conventional RT, the online ART is in fact more time-consuming and requires a very experienced and committed staff, so its use has to be focused on selected cases (33–35).

TABLE 1 | Clinical and dosimetric characteristics of the patients analyzed.

		Patient 1	Patient 2	Patient 3	Patient 4	Patient 5
Clinical Characteristics	**Age**	53	51	63	58	69
	Grading	G1	G2	G2	G1	G1
	TNM Classification	pT1b pN1a	pT1b pN0	pT2m pN0	pT1b pN1mi	pT1b pN0
	Staging	IIA	IA	IIA	IB	IA
Dosimetric Characteristics	**Beam 1 (MU)**	409.7	364.2	253.7	405.3	317.8
	Beam 2 (MU)	224.8	240.9	307.6	323.5	290.5
	Beam 3 (MU)	251.1	190	231.1	254.7	296.2
	Beam 4 (MU)	248.3	176.7	251	194.9	319.6
	CTV volume (cc)	955.8	577	589.7	835.8	1225.8
	V95% PTV (%)	98.2	98.8	99.8	98	98.4
	V105% PTV (%)	0	0	0	0	0
	V20Gy Lung IPSI (%)	15.6	12.1	157	13.2	13.3
	Mean Dose Heart (Gy)	0.97	0.7	1.82	0.94	1.04
	Max Dose Spinal Canal (Gy)	0.54	0.52	0.53	0.7	0.69

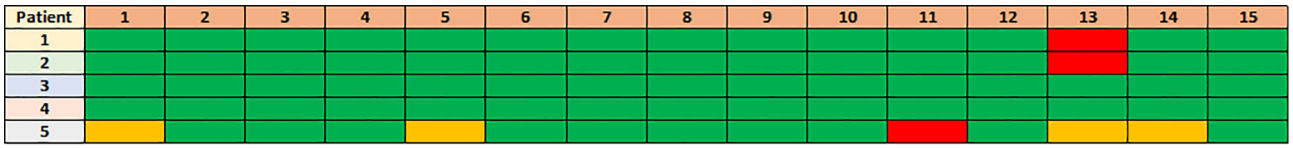

FIGURE 2 | Visual representation of the treatment fractions analyzed for each patient. The optimal fractions are in green, the non-optimal but acceptable fractions are in yellow, and the fractions requiring online adaptation are in red.

It is reasonable to assume that such selection criteria would be disease-specific and also that patients may take advantage of online ART in pathologies where standard RT treatments ensure high probability of care. In this perspective, it is necessary to define new metrics able to quantify the quality of each single RT treatment fraction, on the basis of the anatomical variations observed on the daily positioning imaging and their potential impact on dose distribution.

Classifying the quality of a treatment fraction is a very challenging aspect, as at this stage, the clinical impact that can have a non-optimal delivery of a treatment fraction is unknown. However, in the perspective of defining new correlations between the quality of treatment delivery and the clinical outcomes in the future, it is of utmost importance to immediately establish clear criteria to quantify the quality of a treatment fraction delivery.

In this methodological study, we proposed a new metric that quantifies the quality of the right breast treatments based on the value of PTV coverage and the related hot spot: such assumption can be considered reasonable in the right breast, as all the dose constraints related to OARs are widely met using IMRT modality (as reported in **Table 1**) and target coverage remains the only matter of concern.

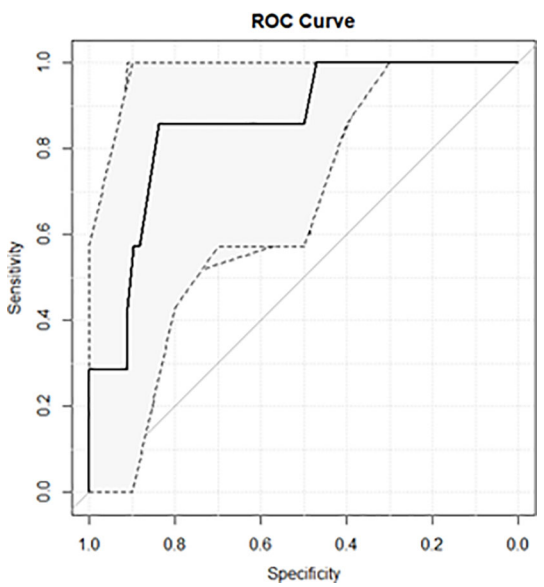

FIGURE 3 | ROC curve of the predictive model focused on identifying treatment fractions where a variation higher than −2% was observed in V95% of PTV.

Extending such metric to a larger cohort of patients with long follow-up could be interesting to investigate if local recurrence would be more present in patients with a higher number of suboptimal fractions.

On the basis of the metric defined in this study, we observed that patients with larger CTV are more prone to experiment target under-coverage due to inter-fraction variability: such type of patients could take advantage of online ART treatments. The study of V95% (PTV) variation has also led to the observation that the value of V95%(PTV)% >95% can be maintained for at least 90% of the treatment fractions if an initial objective goal of V95% (PTV) >98% is reached during the initial planning phase.

Once a metric that classifies the different treatment fractions is identified, it is important to identify predictors based on daily imaging that can alert radiation therapists on the possibility of delivering suboptimal fractions.

To be effective in clinical practice, such indicators should be easy and quick to calculate, to represent a reliable tool also in case of choosing to switch from a conventional treatment to an adaptive one.

In this experience, we observed that the variation of target coverage is correlated with the body variation along the beam axis containing the highest MU: in particular, the probability of observing a PTV under-coverage larger than 2% is equal to 2%, 12%, and 50% in the case of 1 mm, 3 mm, and 5 mm of body variation, respectively.

If confirmed on a larger cohort of patients, such correlation could become a reliable support to the RTTs, allowing the determination of clear thresholds easily identifiable in positioning imaging, beyond which clinician support is required before delivering the treatment fraction.

The main limitation of this study is obviously the reduced number of patients analyzed, mainly related to the recent clinical implementation of this new cutting-edge technology: it is important to remark that the only purpose of this study is to propose new methodological indications on how to approach and manage these novel technologies dedicated to daily ART. The preliminary results here reported require testing on larger cohorts of patients before being considered reliable for clinical use.

By increasing the number of patients enrolled, it will be possible in the near future to elaborate on a predictive model focused on the direct prediction of events considered unacceptable and requiring online adaptation: such a model will be feasible following the same methodology present in this experience once the number of adverse events are statistically sufficient.

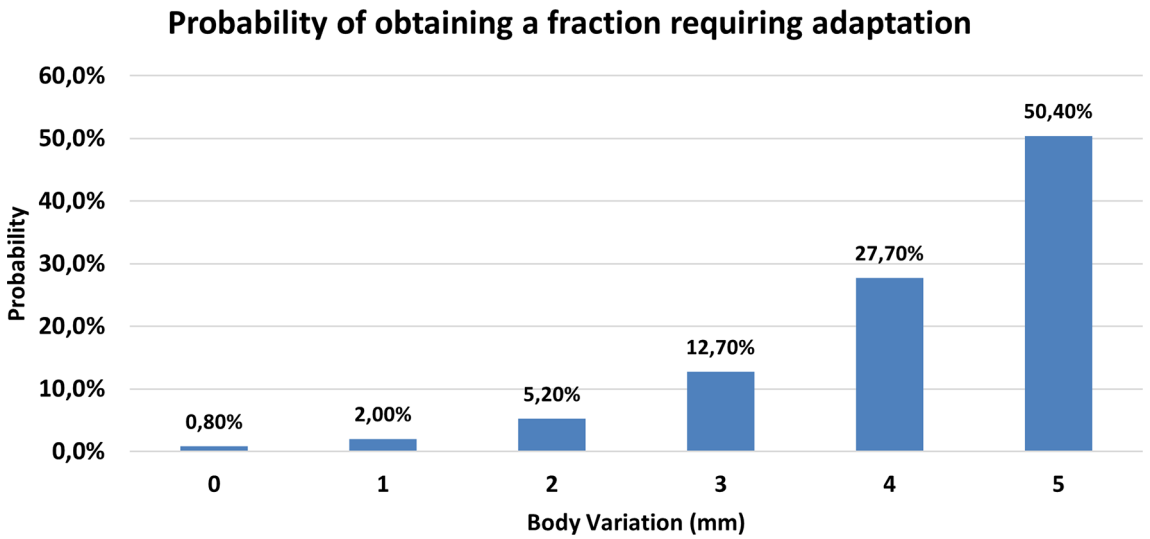

FIGURE 4 | Probability of obtaining a fraction requiring adaptation as a function of body variation measured along the beam axis with the highest MU.

Another source of potential uncertainty involves the impact of the breathing motion, which could lead to body variations not due to patient positioning, thus influencing the findings of the study. To limit such aspect, an accurate patient selection was carried out during CT simulation and long CBCT acquisition time was used during treatment, as detailed in the Materials and Methods section.

A last critical point that has to be noted is related to the arbitrary choice of 2% as the limit threshold to consider a fraction as not optimal: also, this value was chosen to propose a new methodology, allowing us to obtain a sufficient number of events in the minority class to make a feasible logistic regression model; a more precise cutoff value can be determined if a larger number of patients is considered. To the best of our knowledge, this represents the first experience that proposes the idea of correlating anatomical variations observed on daily imaging with dose variations in the treatment plan.

CONCLUSION

In this methodological study, a novel strategy to identify treatment fractions that may benefit online ART was proposed for patients affected by early right breast cancer. During the RT treatment, the measurement of body difference between daily CBCT and planning CT along the beam axis with the highest MU can be considered as an indirect estimator of V95% PTV variation: a difference larger than 3 mm will result in a V95% decrease of more than 2%. A larger number of observations are recommended before translating the findings of this study in clinical practice.

DATA AVAILABILITY STATEMENT

The raw data supporting the conclusions of this article will be made available by the authors, without undue reservation.

ETHICS STATEMENT

Ethical review and approval were not required for the study on human participants in accordance with the local legislation and institutional requirements. Written informed consent to participate in this study was provided by the participants' legal guardian/next of kin.

AUTHOR CONTRIBUTIONS

DC, MI, and FC conceptualized the work. GM and VV supervised the work. DaP, FQ, MM, and FT did the data collection. DoP, CV, and SM did the data analysis. DC, MI, AB, AR, AD'A, and CD wrote and revised the manuscript. All authors contributed to the article and approved the submitted version.

REFERENCES

1. Bi WL, Hosny A, Schabath MB, Giger ML, Birkbak NJ, Mehrtash A, et al. Artificial Intelligence in Cancer Imaging: Clinical Challenges and Applications. *CA Cancer J Clin* (2019) 69(2):127–57. doi: 10.3322/caac.21552
2. Francolini G, Desideri I, Stocchi G, Salvestrini V, Ciccone LP, Garlatti P, et al. Artificial Intelligence in Radiotherapy: State of the Art and Future Directions. *Med Oncol* (2020) 37:50. doi: 10.1007/s12032-020-01374-w
3. Cusumano D, Boldrini L, Dhont J, Fiorino C, Green O, Güngör G, et al. Artificial Intelligence in Magnetic Resonance Guided Radiotherapy: Medical

and Physical Considerations on State of Art and Future Perspectives. *Phys Med* (2021) 85:175–91. doi: 10.1016/j.ejmp.2021.05.010
4. Vandewinckele L, Claessens M, Dinkla A, Brouwer C, Crijns W, Verellen D, et al. Overview of Artificial Intelligence-Based Applications in Radiotherapy: Recommendations for Implementation and Quality Assurance. *Radiother Oncol* (2020) 153:55–66. doi: 10.1016/j.radonc.2020.09.008
5. Archambault L, Boylan C, Bullock D, Morgas T, Peltola J, Ruokokoski E, et al. Making On-Line Adaptive Radiotherapy Possible Using Artificial Intellgence and Machine Learning for Efficient Daily Replanning. *Med Phys Int J* (2020) 8:10.
6. Klüter S. Technical Design and Concept of a 0.35 T MR-Linac. *Clin Transl Radiat Oncol* (2019) 18:98–101. doi: 10.1016/j.ctro.2019.04.007
7. Winkel D, Bol GH, Kroon PS, van Asselen B, Hackett SS, Werensteijn-Honingh AM, et al. Adaptive Radiotherapy: The Elekta Unity MR-Linac Concept. *Clin Transl Radiat Oncol* (2019) 18:54–9. doi: 10.1016/j.ctro.2019.04.001
8. Mayinger M, Ludwig R, Christ SM, Dal Bello R, Ryu A, Weitkamp N, et al. Benefit of Replanning in MR-Guided Online Adaptive Radiation Therapy in the Treatment of Liver Metastasis. *Radiat Oncol* (2021) 16:84. doi: 10.1186/s13014-021-01813-6
9. Acharya S, Fischer-Valuck BW, Kashani R, Parikh P, Yang D, Zhao T, et al. Online Magnetic Resonance Image Guided Adaptive Radiation Therapy: First Clinical Applications. *Int J Radiat Oncol Biol Phys* (2016) 94:394–403. doi: 10.1016/j.ijrobp.2015.10.015
10. Lim-Reinders S, Keller BM, Al-Ward S, Sahgal A, Kim A. Online Adaptive Radiation Therapy. *Int J Radiat Oncol Biol Phys* (2017) 99:994–1003. doi: 10.1016/j.ijrobp.2017.04.023
11. Massaccesi M, Cusumano D, Boldrini L, Dinapoli N, Fionda B, Teodoli S, et al. A New Frontier of Image Guidance: Organs at Risk Avoidance With MRI-Guided Respiratory-Gated Intensity Modulated Radiotherapy: Technical Note and Report of a Case. *J Appl Clin Med Phys* (2019) 20:194–8. doi: 10.1002/acm2.12575
12. Early Breast Cancer Trialists' Collaborative Group (EBCTCG), Darby S, McGale P, Correa C, Taylor C, Arriagada R, et al. Effect of Radiotherapy After Breast-Conserving Surgery on 10-Year Recurrence and 15-Year Breast Cancer Death: Meta-Analysis of Individual Patient Data for 10,801 Women in 17 Randomised Trials. *Lancet* (2011) 378:1707–16. doi: 10.1016/S0140-6736(11)61629-2
13. EBCTCG (Early Breast Cancer Trialists' Collaborative Group),, McGale P, Taylor C, Correa C, Cutter D, Duane F, et al. Effect of Radiotherapy After Mastectomy and Axillary Surgery on 10-Year Recurrence and 20-Year Breast Cancer Mortality: Meta-Analysis of Individual Patient Data for 8135 Women in 22 Randomised Trials. *Lancet* (2014) 383:2127–35. doi: 10.1016/S0140-6736(14)60488-8
14. Botteri E, Bagnardi V, Rotmensz N, Gentilini O, Disalvatore D, Bazolli B, et al. Analysis of Local and Regional Recurrences in Breast Cancer After Conservative Surgery. *Ann Oncol* (2010) 21:723–8. doi: 10.1093/annonc/mdp386
15. Brewster AM, Hortobagyi GN, Broglio KR, Kau S-W, Santa-Maria CA, Arun B, et al. Residual Risk of Breast Cancer Recurrence 5 Years After Adjuvant Therapy. *J Natl Cancer Inst* (2008) 100:1179–83. doi: 10.1093/jnci/djn233
16. Hodapp N. [The ICRU Report 83: Prescribing, Recording and Reporting Photon-Beam Intensity-Modulated Radiation Therapy (IMRT)]. *Strahlenther Onkol* (2012) 188:97–9. doi: 10.1007/s00066-011-0015-x
17. Landberg T, Chavaudra J, Dobbs J, Gerard J-P, Hanks G, Horiot J-C, et al. Report 62. *J Int Commission Radiat Units Meas* (1999) os32:NP–P. doi: 10.1093/jicru/os32.1.Report62
18. Offersen BV, Boersma LJ, Kirkove C, Hol S, Aznar MC, Biete Sola A, et al. ESTRO Consensus Guideline on Target Volume Delineation for Elective Radiation Therapy of Early Stage Breast Cancer. *Radiother Oncol* (2015) 114:3–10. doi: 10.1016/j.radonc.2014.11.030
19. Bentzen SM, Constine LS, Deasy JO, Eisbruch A, Jackson A, Marks LB, et al. Quantitative Analyses of Normal Tissue Effects in the Clinic (QUANTEC): An Introduction to the Scientific Issues. *Int J Radiat Oncol Biol Phys* (2010) 76:S3–9. doi: 10.1016/j.ijrobp.2009.09.040
20. Nielsen MH, Berg M, Pedersen AN, Andersen K, Glavicic V, Jakobsen EH, et al. Delineation of Target Volumes and Organs at Risk in Adjuvant Radiotherapy of Early Breast Cancer: National Guidelines and Contouring Atlas by the Danish Breast Cancer Cooperative Group. *Acta Oncol* (2013) 52:703–10. doi: 10.3109/0284186X.2013.765064
21. Stovall M, Smith SA, Langholz BM, Boice JD, Shore RE, Andersson M, et al. Dose to the Contralateral Breast From Radiation Therapy and Risk of Second Primary Breast Cancer in the WECARE Study. *Int J Radiat Oncol Biol Phys* (2008) 72:1021–30. doi: 10.1016/j.ijrobp.2008.02.040
22. Sommat K, Ong WS, Hussain A, Soong YL, Tan T, Wee J, et al. Thyroid V40 Predicts Primary Hypothyroidism After Intensity Modulated Radiation Therapy for Nasopharyngeal Carcinoma. *Int J Radiat Oncol Biol Phys* (2017) 98:574–80. doi: 10.1016/j.ijrobp.2017.03.007
23. Yock AD, Ahmed M, Ayala-Peacock D, Chakravarthy AB, Price M. Initial Analysis of the Dosimetric Benefit and Clinical Resource Cost of CBCT-Based Online Adaptive Radiotherapy for Patients With Cancers of the Cervix or Rectum. *J Appl Clin Med Phys* (2021) 22:210–21. doi: 10.1002/acm2.13425
24. *EthosTM Therapy AI Technical Brief*. (2019). Available at: https://www.varian.com/sites/default/files/resource_attachments/EthosAITechnicalBrief_RAD10690_Sep19.pdf.
25. Taylor J. *Introduction to Error Analysis, the Study of Uncertainties in Physical Measurements. 2nd Edition* Vol. 1997). New York, NY: Published by University Science Books (1997). Available at: http://adsabs.harvard.edu/abs/1997ieas.book.....T.
26. McHugh ML. Multiple Comparison Analysis Testing in ANOVA. *Biochem Med (Zagreb)* (2011) 21:203–9.
27. Cusumano D, Meijer G, Lenkowicz J, Chiloiro G, Boldrini L, Masciocchi C, et al. A Field Strength Independent MR Radiomics Model to Predict Pathological Complete Response in Locally Advanced Rectal Cancer. *Radiol Med* (2020) 126(3):421–9. doi: 10.1007/s11547-020-01266-z
28. International Commissioning on Radiation Units and Measurements. *Receiver Operating Characteristic (ROC) Analysis in Medical Imaging*. Vol. 79. ICRU Report (2008).
29. Cusumano D, Boldrini L, Yadav P, Yu G, Musurunu B, Chiloiro G, et al. External Validation of Early Regression Index (ERITCP) as Predictor of Pathologic Complete Response in Rectal Cancer Using Magnetic Resonance-Guided Radiation Therapy. *Int J Radiat Oncol Biol Phys* (2020) 108:1347–56. doi: 10.1016/j.ijrobp.2020.07.2323
30. Cusumano D, Catucci F, Romano A, Boldrini L, Piras A, Broggi S, et al. Evaluation of an Early Regression Index (ERITCP) as Predictor of Pathological Complete Response in Cervical Cancer: A Pilot-Study. *Appl Sci* (2020) 10:8001. doi: 10.3390/app10228001
31. Gao JJ, Swain SM. Luminal A Breast Cancer and Molecular Assays: A Review. *Oncologist* (2018) 23:556–65. doi: 10.1634/theoncologist.2017-0535
32. Kerkmeijer LGW, Valentini V, Fuller CDD, Slotman BJ. Editorial: Online Adaptive MR-Guided Radiotherapy. *Front Oncol* (2021) 11:748685. doi: 10.3389/fonc.2021.748685
33. Güngör G, Serbez İ, Temur B, Gür G, Kayalılar N, Mustafayev TZ, et al. Time Analysis of Online Adaptive Magnetic Resonance–Guided Radiation Therapy Workflow According to Anatomical Sites. *Pract Radiat Oncol* (2020) 11(1): e11–e2. doi: 10.1016/j.prro.2020.07.003
34. Placidi L, Cusumano D, Boldrini L, Votta C, Pollutri V, Antonelli MV, et al. Quantitative Analysis of MRI-Guided Radiotherapy Treatment Process Time for Tumor Real-Time Gating Efficiency. *J Appl Clin Med Phys* (2020) 21:70–9. doi: 10.1002/acm2.13030
35. Byrne M, Archibald-Heeren B, Hu Y, Teh A, Beserminji R, Cai E, et al. Varian Ethos Online Adaptive Radiotherapy for Prostate Cancer: Early Results of Contouring Accuracy, Treatment Plan Quality, and Treatment Time. *J Appl Clin Med Phys* (2021) 23(1):e13479. doi: 10.1002/acm2.13479

Conflict of Interest: The authors declare that the research was conducted in the absence of any commercial or financial relationships that could be construed as a potential conflict of interest.

frontiers | Frontiers in Oncology

ORIGINAL RESEARCH
published: 13 May 2022
doi: 10.3389/fonc.2022.895544

Post-Radiotherapy PET Image Outcome Prediction by Deep Learning Under Biological Model Guidance: A Feasibility Study of Oropharyngeal Cancer Application

*Hangjie Ji[1], Kyle Lafata[2,3,4], Yvonne Mowery[2], David Brizel[2], Andrea L. Bertozzi[5,6], Fang-Fang Yin[2] and Chunhao Wang[2]**

[1] Department of Mathematics, North Carolina State University, Raleigh, NC, United States, [2] Department of Radiation Oncology, Duke University Medical Center, Durham, NC, United States, [3] Department of Radiology, Duke University Medical Center, Durham, NC, United States, [4] Department of Electrical and Computer Engineering, Duke University, Durham, NC, United States, [5] Mechanical and Aerospace Engineering Department, University of California, Los Angeles, Los Angeles, CA, United States, [6] Department of Mathematics, University of California, Los Angeles, Los Angeles, CA, United States

OPEN ACCESS

Edited by:
Jing Cai,
Hong Kong Polytechnic University,
Hong Kong SAR, China

Reviewed by:
Jianping Bi,
Hubei Cancer Hospital, China
Pei Yang,
Central South University, China
Sai Kit Lam,
Hong Kong Polytechnic University,
Hong Kong SAR, China

***Correspondence:**
Chunhao Wang
chunhao.wang@duke.edu

Specialty section:
This article was submitted to Radiation Oncology, a section of the journal Frontiers in Oncology

Received: 14 March 2022
Accepted: 11 April 2022
Published: 13 May 2022

Citation:
Ji H, Lafata K, Mowery Y, Brizel D, Bertozzi AL, Yin F-F and Wang C (2022) Post-Radiotherapy PET Image Outcome Prediction by Deep Learning Under Biological Model Guidance: A Feasibility Study of Oropharyngeal Cancer Application. Front. Oncol. 12:895544. doi: 10.3389/fonc.2022.895544

Purpose: To develop a method of biologically guided deep learning for post-radiation ^{18}FDG-PET image outcome prediction based on pre-radiation images and radiotherapy dose information.

Methods: Based on the classic reaction–diffusion mechanism, a novel biological model was proposed using a partial differential equation that incorporates spatial radiation dose distribution as a patient-specific treatment information variable. A 7-layer encoder–decoder-based convolutional neural network (CNN) was designed and trained to learn the proposed biological model. As such, the model could generate post-radiation ^{18}FDG-PET image outcome predictions with breakdown biological components for enhanced explainability. The proposed method was developed using 64 oropharyngeal patients with paired ^{18}FDG-PET studies before and after 20-Gy delivery (2 Gy/day fraction) by intensity-modulated radiotherapy (IMRT). In a two-branch deep learning execution, the proposed CNN learns specific terms in the biological model from paired ^{18}FDG-PET images and spatial dose distribution in one branch, and the biological model generates post-20-Gy ^{18}FDG-PET image prediction in the other branch. As in 2D execution, 718/233/230 axial slices from 38/13/13 patients were used for training/validation/independent test. The prediction image results in test cases were compared with the ground-truth results quantitatively.

Results: The proposed method successfully generated post-20-Gy ^{18}FDG-PET image outcome prediction with breakdown illustrations of biological model components. Standardized uptake value (SUV) mean values in ^{18}FDG high-uptake regions of predicted images (2.45 ± 0.25) were similar to ground-truth results (2.51 ± 0.33). In 2D-based Gamma analysis, the median/mean Gamma Index (<1) passing rate of test

images was 96.5%/92.8% using the 5%/5 mm criterion; such result was improved to 99.9%/99.6% when 10%/10 mm was adopted.

Conclusion: The developed biologically guided deep learning method achieved post-20-Gy ^{18}FDG-PET image outcome predictions in good agreement with ground-truth results. With the breakdown biological modeling components, the outcome image predictions could be used in adaptive radiotherapy decision-making to optimize personalized plans for the best outcome in the future.

Keywords: biological modeling, deep learning, image outcome prediction, radiotherapy, ^{18}FDG-PET

INTRODUCTION

Radiotherapy is a central component of the standard of care for many cancers. In the current era of image-guided radiotherapy (IGRT), medical imaging plays a critical role in radiotherapy practice regarding patient assessment, treatment volume definition, on-board patient positioning, and outcome assessment (1). In particular, imaging-based radiotherapy outcome assessment can capture early therapeutic responses for adaptive therapy to enhance radiotherapy efficacy (2). In addition, long-term therapeutic outcomes from image-based analysis provide useful information in treatment intervention of each patient towards optimized cancer care (3). Thus, medical imaging analysis for radiotherapy outcome assessment has become an irreplaceable component in precision medicine.

Technologies of medical imaging analysis have revolutionized image-based radiotherapy outcome reporting. Radiographic assessment of post-radiotherapy tumor morphological changes (i.e., Response Evaluation Criteria in Solid Tumors [RECIST]) was standardized to describe the response to therapy (4). Functional imaging modalities have now shifted outcome analysis from morphological description to physiological characterization. PET tracks the *in vivo* radioactive tracer distribution, for example, estimating glucose metabolism (^{18}F-FDG) or measuring tissue hypoxia (^{18}FMISO) (5). MR functional imaging, including dynamic contrast-enhanced MRI (DCE-MRI), diffusion-weighted MRI (DWI), and diffusion tensor MRI (DTI), can measure tissue properties such as blood volume/perfusion (6), cellular density (7), and cell movement direction (8). To non-invasively quantify *in vivo* physiology, functional imaging relies on mathematical models to extract quantitative parameters from phenotype image data. These mathematical models, which are often referred to as mechanism-based models, describe complex physiological processes using basic biological theories and fundamental laws in physical/chemical interactions (9, 10). The derived parameters of mechanism-based models can serve as surrogates of individual physiology functions to facilitate developing a personalized therapeutic approach.

Treatment response assessment using functional imaging is often reported as posttreatment changes relative to pretreatment baseline values. Image-based treatment outcome prediction, i.e., forecasting posttreatment image volumes before treatment initiation, has become an emerging topic in clinical oncology (11). The potential clinical application of image-based treatment outcome prediction in radiotherapy is conceptually promising: given an individual's pre-radiotherapy image, post-radiotherapy image predictions could be available at the treatment planning stage. Guided by these predictions, clinicians could simulate alternative treatment plans, such as target delineation revision and plan parameter tuning (beam angle, energy selection, etc.), for normal tissue sparing and could select a plan that predicts improved response to radiotherapy. This scenario can be applied to adaptive radiotherapy: the predicted intra-treatment images can be used to determine whether a revised radiotherapy plan would be advantageous. Additionally, when new intra-treatment image data are collected, the updated predictions can guide the adaptive planning strategy for optimal radiotherapy outcomes for individual patients (10). Driven by the rapid growth of computation power, deep learning techniques have recently become a practical approach for image-based treatment outcome prediction (12–14). However, few investigators have reported functional image outcome prediction in radiotherapy applications. Aside from the colossal computational workload due to image dimension requirement, the current mechanism-based models focus on spatial decoding of physiology within an image volume; for outcome prediction, a mechanism-based model must incorporate patient-specific treatment information to simulate spatiotemporal physiology evolution during a treatment course. Although pilot studies have reported the feasibility of post-radiotherapy functional image outcome prediction using treatment information (15), the adopted deep learning network ignored the biophysical modeling and generated its prediction *via* a "black box"; thus, the achieved prediction was reported at a fixed time point without any biological interpretation about how radiation dose affects the outcome. Radiotherapy outcome prediction with breakdowns from biological modeling is an unmet need.

In this work, we design a biologically guided deep learning framework for intra-treatment ^{18}FDG-PET image outcome prediction in response to oropharyngeal cancer intensity-modulated radiotherapy (IMRT). Based on the classic reaction–diffusion mechanism in disease progression, we propose a novel partial differential equation (PDE) as a biological model that incorporates spatial radiation dose distribution as a patient-specific treatment information variable. An encoder–decoder-based convolutional neural network (CNN) is designed and trained to learn the proposed

model, which governs the dynamics of tissue response to radiotherapy. Thus, with the explainability of the biological model, the developed deep learning model can generate post-radiotherapy ^{18}FDG-PET image outcome predictions with breakdown biological components.

MATERIALS AND METHODS

Biological Modeling

We hypothesize that the standardized uptake value (SUV) change in ^{18}FDG-PET in response to radiation can be described in a reaction–diffusion system, which represents a family of mathematical models widely used in describing pattern formations and evolving densities in physical, ecological, and biological systems (16). In the context of modeling tumor growth and therapeutic response dynamics, reaction–diffusion models have been applied to both preclinical and clinical works (9, 17, 18). Disease progression, in general, can be summarized by Eq. (1), which describes the malignancy proliferation (reaction) and spread (diffusion) (10):

$$U_t = \alpha \Delta U + \beta U \tag{1}$$

where U is the spatial distribution of disease (i.e., SUV intensity distribution in this work) and $U_t = \frac{\partial U}{\partial t}$ is the time derivative term describing the change of U in time. The term $\alpha \Delta U = \alpha(\frac{\partial^2 U}{\partial x^2} + \frac{\partial^2 U}{\partial y^2})$ describes the spreading of abnormal cell activities, where $\alpha > 0$ is the diffusion coefficient. The linear term βU represents the proliferation of localized malignancy. To incorporate tissue response to radiotherapy in the model in Eq. (2), we propose a new response term for the dose-induced changes of U,

$$U_t = \alpha \Delta U + \beta U + \mathcal{F}(DU) \tag{2}$$

where $\mathcal{F}(DU)$ is an $\mathcal{N}$ unknown operator that depicts U's local response to radiotherapy. Here we assume that the response term depends on the product of U and the radiotherapy plan's spatial dose distribution D. We also assume that the operator F depends on DU as the tissue response to cell killing from localized high radiation (10), and we will use a CNN to learn this operator. Thus, Eq. (2) is the core time-dependent PDE that models the post-radiotherapy biological response of abnormal tissue metabolism as SUV intensity (i.e., U) evolves in time.

Deep Learning Design

Formally, our problem is defined as follows: given a set of pre- and post-radiation ^{18}FDG-PET image pairs $\{(U_k^{pre}, U_k^{post})\}_{k=1,2,\ldots m}$ and the imposed radiation dose distribution images $\{D_k\}_{k=1,2,\ldots m}$ where m is the total number of image pairs, our goal is to learn the unknown response operator F and coefficients α, β in the model in Eq. (2) with the collected data of the form $\{(U_k^{pre}, U_k^{post}, D_k)\}_{k=1,2,\ldots m}$. Accordingly the learned model can predict a post-radiation ^{18}FDG-PET image U_k^{post} given the pre-radiation image U_k^{pre} and the associated spatial dose distribution D_k. In addition, since the learned model describes the evolution dynamics of U_k between the two states U_k^{pre} and U_k^{post} frames of U_k between U_k^{pre} and U_k^{post} can be simulated to study the intermediate stages of disease progression.

While a large body of work has focused on solving reaction–diffusion models like Eq. (2), i.e., finding U based on known coefficients and operators, little research has been devoted to the inverse problem of learning the model's coefficients and operators from observed U data. The numerical treatments of the inverse problem are typically complicated, as the observed data usually cannot provide sufficient information to determine a unique model, and regularizations are needed to produce meaningful model estimates. As such, we propose a deep neural network framework to learn the model in Eq. (2) from ^{18}FDG-PET images taken before and after radiation. Applying the forward Euler method on the PDE in Eq. (2), we obtain the discretized update rule:

$$U^{n+1} = U^n + h\alpha \Delta U^n + h\beta U^n + hF(DU^n) \tag{3}$$

where h is the time step, U^n is the approximate solution of the state U at the time $t_n = nh$, and the Lssssaplacian operator Δ can be approximated by a discrete operator D_{xy}^2 represented by a nine-point refined stencil (19):

$$D_{xy}^2 = \begin{pmatrix} 1/4 & 1/2 & 1/4 \\ 1/2 & -3 & 1/2 \\ 1/4 & 1/2 & 1/4 \end{pmatrix} \tag{4}$$

A deep neural network $N_{\mathcal{F}}$ is designed to approximate the response operator $\mathcal{F}$:

$$N_F : \psi \rightarrow N_F(\psi; \quad \theta) \tag{5}$$

where θ represents the free parameters. For simplicity, we assume that the operator F only depends on, $\psi = DU$, the product of the dose distribution D and the ^{18}FDG-PET image state variable U. A diffusion–proliferation operator G is used to combine both the diffusion and proliferation terms with undetermined coefficients α and βs

$$\mathcal{G}(U^n) = \alpha D_{xy}^2 U^n + \beta U^n \tag{6}$$

Given a group of three images consisting of the initial state ^{18}FDG-PET image $U_k^0 = U_k^{pre}$ at $t = 0$ prior to radiation, dose distribution map D_k, and the ground-truth final state ^{18}FDG-PET image U_k^{post} at $t = T$ (post-radiation), from Eqs. (3)–(6), we obtain the intermediate states U_k^{n+1} by

$$U_k^{n+1} = U_k^n + h\mathcal{G}(U_k^n) + hN_{\mathcal{F}}(D_k \circ U_k^n; \theta) \tag{7}$$

for $n = 0,1, \ldots, N_t - 1$. Here, $D_k \circ U_k^n$ represents the element-wise product of the dose distribution map D_k and the ^{18}FDG-PET image U_k^n at the time step t_n, N_t is the total number of steps, and the step size $h = T/N_t$. As a feasibility study, we consider the final time $T = 1$ and set the number of steps $N_t = 4$ in this work.

The similarity between the predicted post-radiation ^{18}FDG-PET image $U_k^{N_t}$ and the associated ground-truth image U_k^{post} is

defined based on the l_2 norm loss function:

$$\mathcal{L}(\theta) = \frac{1}{m}\sum_{k=1}^{m} \| U_k^{N_t} - U_k^{post} \|_2^2 \quad (8)$$

where m is the number of samples. By minimixing $\mathcal{L}(\theta)$, the deep neural network can learn the weights θ that characterize the response operator $\mathcal{F}$ and the undetermined coefficients α and β.

Figure 1 illustrates the designed deep neural network architecture. The network's input space is composed of pre-radiation ^{18}FDG-PET image U^{pre} and planned dose distribution map D as a set. The network is split into two branches: one that uses a CNN to learn the response operator $N_{\mathcal{F}}(DU^n)$ and the other one with only two trainable parameters to apply the diffusion–proliferation operator $\mathcal{G}$ [in Eq. (6)] on U^n. Specifically, the second branch of the network architecture mimics the traditional finite difference method and applies the discrete Laplacian operator and the linear operator on U^n with predicted α and β. Both branches are then merged by the rule in Eq. (7), which feeds the output U^{n+1} forward to the next cycle. This process is then repeated for N_t time steps to generate a predicted post-radiation ^{18}FDG-PET image, which will be compared against the ground-truth post-radiation ^{18}FDG-PET image.

The branch that learns the response operator $N_{\mathcal{F}}(DU^n)$ consist of a total of 7 convolutional layers and is built upon U-Net's encoder–decoder architecture (20). The architecture consists of a contracting path that extracts sufficient semantic context from $D \circ U^n$ and a symmetric expanding path that produces the up-sampled output. The contracting path starts with two applications of 3 × 3 convolutions, each followed by a batch normalization layer and a ReLU operation. Then a 2 × 2 max-pooling operation is performed for down-sampling where the number of feature channels is doubled. Then another two 3 × 3 convolutions operations are applied, each followed by batch normalization and a ReLU activation. The expanding path consists of an up-sampling of the feature map, followed by two 3 × 3 convolutional layers, again with batch normalization and ReLU operations. Finally, a 1 × 1 convolution is applied to map the 16-component feature to a single feature channel that reconstructs the transformed image corresponding to $N_{\mathcal{F}}(DU^n)$.

Patient Data and Network Training

In this work, 64 eligible oropharyngeal cancer patients who received curative-intent IMRT in our department were retrospectively studied under an institutional review board (IRB)-approved ^{18}FDG-PET imaging study (21). All patients were prescribed 70 Gy at 2 Gy/day fraction with concurrent chemotherapy. Prior to treatment initiation, each patient underwent an ^{18}FDG-PET/CT scan for target delineation. After 20-Gy delivery, each patient underwent a second ^{18}FDG-PET/CT scan as an intra-treatment evaluation for consideration for adaptive planning. These post-20-Gy ^{18}FDG-PET acquisitions were treated as the post-radiation scans in the modeling.

All ^{18}FDG-PET/CT exams were acquired by a PET/CT scanner (Siemens, Erlangen, Germany) in our department. PET acquisitions were performed using 400 × 400 matrix size

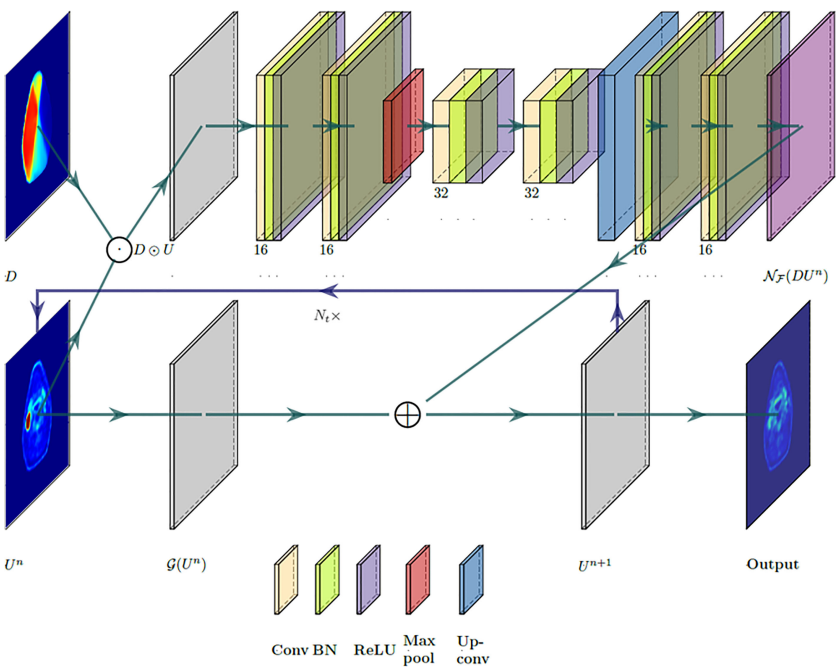

FIGURE 1 | A partial differential equation (PDE)-informed deep neural network design. Layers are color-coded by operations with associated feature numbers.

in a standard field of view (FOV) of 54 cm, and slice thickness was 2 mm. CT acquisitions were performed using 512 × 512 matrix size in an extended FOV of 65 cm (in-plane resolution = 1.27 mm), and slice thickness was 3 mm. PET images were reconstructed by the ordered subset expectation maximization (OSEM) algorithm with attenuation corrections using the CT acquisition information. The post-20-Gy ^{18}FDG-PET/CT images were registered to the corresponding pre-radiation images using Velocity^{TM} software (Varian Medical Systems, Palo Alto, CA, USA). Registrations started with rigid bony structure alignment, and a multi-pass deformable registration algorithm was adopted to improve soft tissue alignment near the anterior body surface. In the process of IMRT planning, all treatment plans were optimized and calculated using the Eclipse^{TM} treatment planning system (Varian Medical Systems, Palo Alto, CA, USA) with a 2.5-mm dose calculation grid size. All ^{18}FDG-PET images and spatial dose distribution maps of 20-Gy treatment were resampled to the CT simulation image grid size.

Of all 2D ^{18}FDG-PET axial images, those with sufficient ^{18}FDG uptake in the pre-radiation acquisition were selected by $SUV_{max} > 1.5$ excluding brain regions (22). Overall, 718 axial slices collected from 38 patients were used for neural network training, 233 axial slices from 13 patients were used for validation, and 230 axial slices from 13 patients were used for independent tests. During the neural network training, the loss function was defined as based on the l_2 norm in Eq. (8). Gradient updates were computed using batch sizes of 10 samples, and batch normalization was performed after each convolutional layer. The training utilized the Adam optimizer for up to 400 epochs, while an early stopping strategy on the loss function evaluated on the validation samples was adopted with a patience of 100 epochs. The overall training time was about 15 min in a TensorFlow environment using an NVIDIA TITAN^{TM} Xp graphic card.

Evaluation

The accuracy of post-20-Gy ^{18}FDG-PET image prediction was evaluated using 230 axial slices' results from 13 test patients. The prediction results were first visually inspected as qualitative evaluation. SUV mean values in high-uptake regions determined by Otsu's method (23) were quantitatively compared with the ground-truth results. Pixel-to-pixel SUV numerical differences were evaluated by Gamma tests within the body region (24). Multiple Gamma tests with different SUV difference tolerances and distance-to-agreement (DTA) tolerances were performed. While Gamma Index <1 was considered as acceptable pixel-wise results, Gamma Index passing rates, i.e., the percentage of pixels with Gamma Index <1, were reported as summarizing metrics.

RESULTS

Figure 2 shows an example case of post-20-Gy ^{18}FDG-PET image outcome prediction. As seen in the pre-radiation ^{18}FDG-PET image, SUV hotspots with clear edges were found on the patient's right side. After 20-Gy delivery shown by the bilateral side dose distribution in D, the ground-truth post-20-Gy^{18}FDG-PET image results demonstrated good therapy response with reduced hotspot sizes and decreased SUV intensities. The predicted ^{18}FDG-PET image captured the overall appearance in the ground-truth results without noticeable artifact marks. Two hotspots corresponding with the nodal disease were found in the prediction image at the same locations. The hotspots' sizes and SUV intensities were comparable, though the anterior hotspot intensity appeared to be lower than the ground-truth result. In the breakdown illustration of biological model terms in Eq. (3), the diffusion term demonstrated overall uniform intensity distribution around 0 except in hotspot regions; the core regions in hotspots had negative diffusion intensities, which suggested a spatial retraction of abnormal metabolism. The proliferation term had a similar appearance to the pre-radiation ^{18}FDG-PET image. The dose-response term indicated an elevated intensity region that corresponds to the anterior SUV hotspot; this suggests that the anterior SUV hotspot had a better response to 20-Gy than the posterior SUV hotspot, which had limited intensity in the dose-response map. The other areas within the body had close-to-zero dose-response intensity, while low intensities were found near the body surface. The Gamma Index map showed a good quantitative pixel-to-pixel SUV comparison between ground-truth and predicted post-20-Gy ^{18}FDG-PET images using the 5%/10 mm criterion.

In the test patient cohort, the SUV mean value of high-uptake regions in post-20-Gy predicted images was 2.45 ± 0.25, which was slightly lower than ground-truth results (2.51 ± 0.33, p = 0.015); the dice coefficient results of the segmented high-uptake regions were 0.89 ± 0.12. Gamma Index passing rate results of all testing axial slices are summarized in **Figure 3**. When the 5%/5 mm Gamma criterion was adopted, the median 2D Gamma passing rate was 96.5%. With the use of looser Gamma criteria, the passing rate results improved (5%/10 mm, median 99.2%, average 97.6%; 10%/5 mm, median 99.5%, average 98.6%). The highest median passing rate was 99.9% (average = 99.6%) when 10%/10 mm was used.

DISCUSSION

In this work, we successfully demonstrated the design of a biological model-guided deep learning framework for post-20-Gy ^{18}FDG-PET image outcome prediction in a unique cohort of patients undergoing IMRT for oropharyngeal cancer. For the first time, we demonstrated 3 breakdown biological components of oropharyngeal cancer response to radiation. One of the key innovations in this work is the biological model in Eq. (2), which was hypothesized as the mathematical equation that governs the post-radiation SUV change. The model was derived from the classic reaction–diffusion system, which has been utilized in many works of tumor growth and disease progression modeling (25–27). Although applying reaction–diffusion models to ^{18}FDG-PET image analysis (particularly to head and neck cancer) is less reported, some exploratory studies have demonstrated the validation of reaction–diffusion-type models

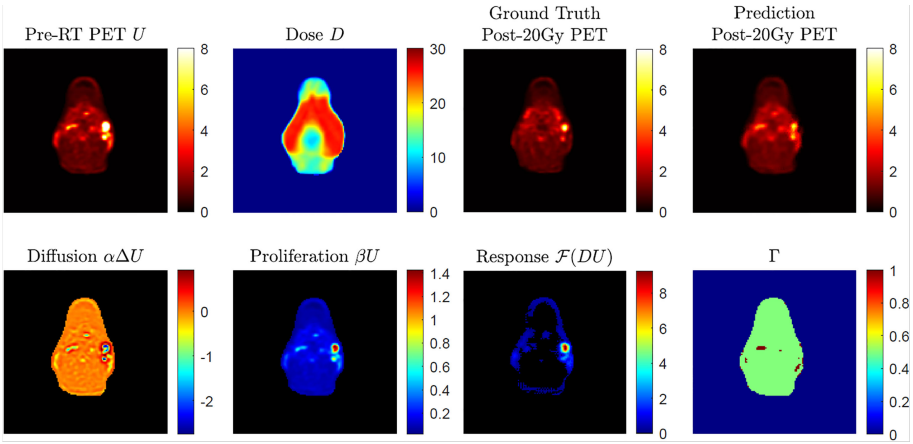

FIGURE 2 | An example of post-radiotherapy ^{18}FDG-PET image outcome with given pre-radiation ^{18}FDG-PET image and dose distribution map D, with a breakdown of predicted biological effects (diffusion, proliferation, and dose response in absolute value) in Eq. (2). The 2D Gamma (Γ) test result was obtained through acceptance criteria of 5%/10 mm.

in intracranial PET image modeling (28). Compared to the original reaction–diffusion models, the newly introduced dose-response term in Eq. (2) was hypothesized as a semantic component of dose-induced SUV image state changes. Adding additional terms in reaction–diffusion family models to account for therapeutic effect has been reported before in breast, lung, and pancreatic cancer studies (29–31); nevertheless, our approach of using spatial dose distribution in biological modeling is a novel design. Compared to the use of prescription dose levels for outcome assessment/prediction in many studies, the adoption of spatial dose distribution maintained heterogeneous radiation deposition information at the pixel level, which may be a more accurate approach for image-based outcome prediction with explainability from existing biology domain knowledge. Nevertheless, the designed deep learning model relies on the reaction–diffusion system hypothesis, which has yet to be widely acknowledged as general domain knowledge of tissue radiation response. In addition to the image result supports, the reaction–diffusion system hypothesis can be studied *via in vivo* functional imaging (such as diffusion-weighted MRI) and *in vitro* cell study to establish the benchmark evidence for oropharyngeal cancer applications.

As a deep learning approach, a CNN was designed to learn the proposed biological model. PDEs with known coefficients and operators can be solved by various numerical methods such as finite difference methods, finite element methods, and spectral methods. In the scientific computing field, solving differential

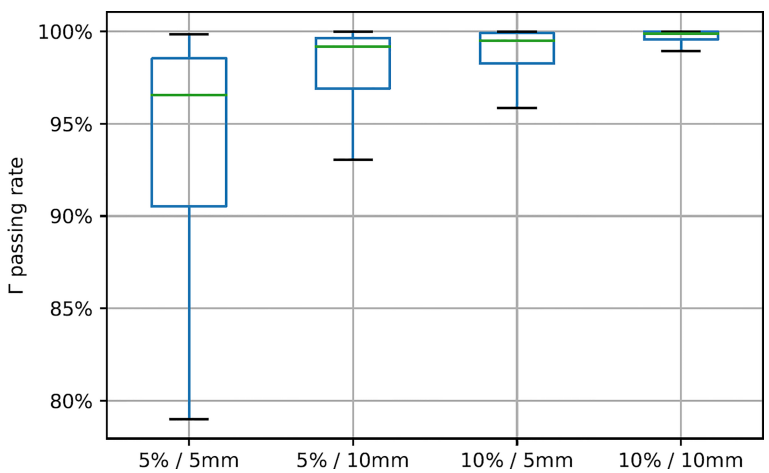

FIGURE 3 | Gamma Index passing rate summary with different gamma criteria. Green line positions represent median value, and box represents 25%/75% percentile with whiskers indicating 5%/95% percentile.

equations using CNN in complex systems has become popular for efficiency and accuracy (32). Additionally, differential equations specified by CNN can parameterize the continuous state transition with non-uniform sampling step sizes (33); that is, one may use images from different patients with different acquisition time points. The applied analysis of stochastic differential equations has demonstrated value for recent radiomic applications (34, 35); deep learning-based data assimilation may improve the performance of these techniques by providing a more accurate estimation of model hyper-parameters and coefficients. The use of CNN is necessary to learn the dose-response term $\mathcal{F}$ in Eq. (2), which is an unknown operator that is assumed to be related to the product of spatial dose distribution and ^{18}FDG-PET image variable (DU); without an analytical expression, it is difficult to approximate the operator $\mathcal{F}$ by classic numerical treatments of inverse problems. The proposed CNN in **Figure 1** revealed the dose-response term $\mathcal{F}(DU)$ as a whole, while the detailed mechanism of DU's contribution of ^{18}FDG-PET image prediction remains unclear. Inspired by the classic encoder–decoder U-net implementation, the CNN architecture in **Figure 1** was dedicated to the problem in Eqs. (3)–(7); with the loss function defined in Eq. (8), the training process had a fast convergence (**Supplementary Figure 1**). It would be of interest to further study the operator $\mathcal{F}$ for its analytical expression and possible biological explanations. Such works require more advanced mathematical theories supported by experimental data, preferably as *in vitro* implementations, to validate analytical designs as a biological model calibration process (10).

Based on the Gamma test results in **Figure 3**, the achieved ^{18}FDG-PET image predictions showed good agreement with ground-truth images. As a common quality assurance method in radiotherapy practice, Gamma analysis accounts for both intensity differences and systematic shifts in image prediction error. The Gamma test criteria need to consider multiple uncertainty sources in data processing and clinical preferences. For instance, the dose-response term results in **Figure 2** indicated very small but non-zero intensity values near the body surface, especially in anterior skin regions. While other normal tissues demonstrated very limited dose response, the observed skin regions' dose response may be noisy results related to deformable image registration uncertainties, which was mainly determined by patient weight loss during the radiotherapy course (36). Radiotherapy margin formulism that models treatment margin statistics should also be weighted in image prediction evaluation (37). In addition to these two potential factors, the adopted Gamma test criteria have incorporated many other factors, including SUV's intrinsic uncertainty, PET image acquisition resolution, PET-CT QA protocol, and SUV-based metabolic volume definition.

The current results demonstrated accurate image outcome prediction at the time point of post-20-Gy radiotherapy. The actual physiological change during the 20-Gy radiotherapy course is a continuous process, which is an inherent feature in the proposed model in Eq. (2); in other words, in addition to post-20-Gy ^{18}FDG-PET image outcomes at $t = 1$, our model can predict intermediate stage image outcomes between $t = 0$ and $t = 1$. To demonstrate this merit, **Figure 4** shows a simulation of intermediate stage ^{18}FDG-PET image outcome predictions as biological model solutions from the pre-radiation result at $t = 0$ to post-20-Gy prediction at $t = 1$. In general, the four predicted ^{18}FDG-PET images demonstrated a reasonable image state transition from $t = 0$ to $t = 1$ without abrupt changes. While the majority of normal tissue maintained steady SUV intensities during the presented time evolution, the SUV hotspot corresponding to the primary oropharyngeal tumor had shrinkage at its posterior boundary with slightly reduced intensity. Compared to the ground-truth post-20-Gy ^{18}FDG-PET image, the prediction image at $t = 1$ captured the SUV hotspot's morphological features, particularly at its posterior boundary. However, this simulation result cannot be validated by current clinical results because of the lack of longitudinal ^{18}FDG-PET scans during a radiotherapy course, which is mainly limited by ionizing radiation risk and potential high financial cost. On the other hand, longitudinal MRI exams are commonly utilized for cranial radiotherapy follow-up as standard care, and the image series can be used to validate the cranial model continuity in future works.

The current biological model was implemented in a 2D fashion on axial images. For each test patient, the post-radiation ^{18}FDG-PET image predictions were generated slice-by-slice to approximate volumetric rendering. In theory, the biological model in Eq. (2) and the demonstrated deep neural network could be implemented as 3D in the spatial domain; however, the computation workload for 3D implementation, especially for a generative task with complex nature, requires a large data sample size with curated data collection. In this work, 64 patients were collected with paired ^{18}FDG-PET exams in a clinical trial setup, and 1,181 high ^{18}FDG uptake axial slices were collected and were assigned to neural network training/validation/tests following a 60%/20%/20% ratio. Given the fact that 1) image slice thickness (3 mm) is larger than in-plane resolution (1.27 mm) and 2) paired image acquisitions were performed with a 2-week time interval, the model was confined for locoregional computation with a small 3×3 in-plane kernel size, and thus the information extraction was within an axial "slab" and did not involve information exchange in other slices. This underlying design made all 2D slices eligible as independent samples for deep learning training, and the current results from 2D implementation demonstrated good image prediction accuracy and established the technical feasibility of the proposed biological model-guided deep learning. 3D-based modeling would be ideal for brainstorming experiments, but this data cohort would be a very limited data sample size for generative deep learning tasks. Future studies using a larger patient cohort, potentially in a multi-institution collaboration, are planned to further investigate the proposed framework based on 3D implementation. Additionally, experiments using small animals are also planned for future developments of deep learning in image outcome prediction. Further investigation of the biological interpretation of the learned dose-response term may also lead to improved mathematical modeling for this problem.

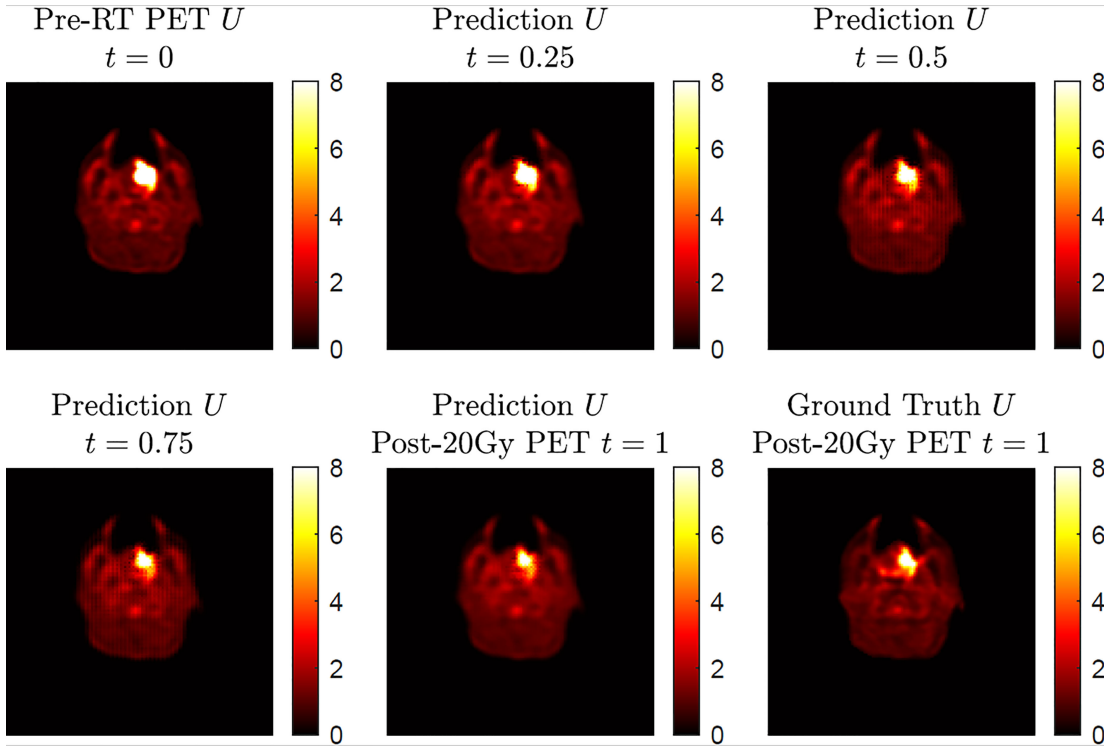

FIGURE 4 | A simulation of ^{18}FDG-PET image outcome transition based on a four-step execution with step size $h = 0.25$ showing the predicted transition from pre-radiation U at $t = 0$ to the predicted post-radiotherapy U at $t = 1$. The ground-truth post-20-Gy ^{18}FDG-PET image is included for comparison at $t = 1$.

As a feasibility study, the current results showed that the achieved post-20-Gy ^{18}FDG-PET image outcome prediction had good agreement with ground-truth results. Post-20-Gy ^{18}FDG-PET has been demonstrated as informing surrogates of recurrence-free survival and overall survival of human papillomavirus (HPV)-related oropharyngeal cancer (38). In a potential clinical application scenario, the current framework would allow a physician to determine if an ^{18}FDG-PET scan after 20-Gy radiation would facilitate improved adaptive radiotherapy clinical decision making. The impact of image prediction accuracy on clinical decision making was not rendered by the current results of technical development work; future works, preferably in a prospective fashion, are planned to investigate such clinical impacts from physicians' perspectives in clinical practice. Another crucial step toward this clinical application scenario is to verify the models' responses to different radiation therapy strategies. The current patient cohort from a clinical study received a uniform treatment regimen; thus, the developed model may not capture certain individual reactions after a drastically different radiotherapy approach. For deep learning developments, it would be ethically challenging to collect patient data with intentional treatment variations. Following the small animal experiments discussed above, with dedicated imaging platforms and radiotherapy machines, one can generate post-radiation samples with heterogeneous treatment strategies in multiple imaging sessions. Such experiments may provide valuable opportunities for studying biological models for improved deep learning intelligibility.

CONCLUSION

In this work, we developed a biological model-guided deep learning method for post-radiation ^{18}FDG-PET image outcome prediction. The proposed biological model incorporates spatial radiation dose distribution as a patient-specific variable, and a novel CNN architecture was implemented to predict post-radiotherapy ^{18}FDG-PET images from pre-radiation results. Current results demonstrate good agreements between post-20-Gy predictions and ground-truth results in a cohort of patients with oropharyngeal cancer. Future developments of the current methodology design will enhance the applicability of image outcome prediction in clinical practice.

DATA AVAILABILITY STATEMENT

The datasets studied for this study is collected from a clinical trial; due to PHI protection, the original image data cannot be published in the public domain. The studied deep learning design model will be available upon direct request to the corresponding author. Requests to access the datasets should be directed to chunhao.wang@duke.edu.

ETHICS STATEMENT

The studies involving human participants were reviewed and approved by Duke University. The patients/participants provided their written informed consent to participate in this study.

AUTHOR CONTRIBUTIONS

All authors participated in the study design. KL and CW collected image data. HJ completed computation works. All authors participated in writing and approved the final version.

FUNDING

HJ and AB were supported by the Simons Foundation Math+X investigator award number 510776 and the National Science Foundation under grant NSF DMS-1952339 during this work.

SUPPLEMENTARY MATERIAL

The Supplementary Material for this article can be found online at: https://www.frontiersin.org/articles/10.3389/fonc.2022.895544/full#supplementary-material

REFERENCES

1. Jaffray DA. Image-Guided Radiotherapy: From Current Concept to Future Perspectives. *Nat Rev Clin Oncol* (2012) 9(12):688. doi: 10.1038/nrclinonc.2012.194
2. Yan D. Adaptive Radiotherapy: Merging Principle Into Clinical Practice. *Semin Radiat Oncol* (2010) 20(2):79–83. doi: 10.1016/j.semradonc.2009.11.001
3. Chang Z, Wang C. Treatment Assessment of Radiotherapy Using MR Functional Quantitative Imaging. *World J Radiol* (2015) 7(1):1. doi: 10.4329/wjr.v7.i1.1
4. Therasse P, Arbuck SG, Eisenhauer EA, Wanders J, Kaplan RS, Rubinstein L, Verweij J, et al. New Guidelines to Evaluate the Response to Treatment in Solid Tumors. *J Natl Cancer Instit* (2000) 92(3):205–16. doi: 10.1093/jnci/92.3.205
5. Cherry SR, Sorenson JA, Phelps ME. *Physics in Nuclear Medicine E-Book*. Elsevier Health Sciences (2012).
6. d'Arcy JA, Collins DJ, Padhani AR, Walker-Samuel S, Suckling J, Leach MO. Magnetic Resonance Imaging Workbench: Analysis and Visualization of Dynamic Contrast-Enhanced MR Imaging Data. *Radiographics* (2006) 26 (2):621–32. doi: 10.1148/rg.262045187
7. Koh D-M, Collins DJ. Diffusion-Weighted MRI in the Body: Applications and Challenges in Oncology. *Am J Roentgenol* (2007) 188(6):1622–35. doi: 10.2214/AJR.06.1403
8. Le Bihan D, Mangin JF, Poupon C, Clark CA, Pappata S, Molko N, et al. Diffusion Tensor Imaging: Concepts and Applications. *J Magnet Res Imaging Off J Int Soc Magnet Res Med* (2001) 13(4):534–46. doi: 10.1002/jmri.1076
9. Hormuth DA, Jarrett AM, Yankeelov TE. Forecasting Tumor and Vasculature Response Dynamics to Radiation Therapy *Via* Image Based Mathematical Modeling. *Radiat Oncol* (2020) 15(1):4. doi: 10.1186/s13014-019-1446-2
10. Hormuth DA, Jarrett AM, Lima EA, McKenna MT, Fuentes DT, Yankeelov TE. Mechanism-Based Modeling of Tumor Growth and Treatment Response Constrained by Multiparametric Imaging Data. *JCO Clin Cancer Informat* (2019) 3:1–10. doi: 10.1200/CCI.18.00055
11. Yankeelov TE, Quaranta V, Evans KJ, Rericha EC. Toward a Science of Tumor Forecasting for Clinical Oncology. *Cancer Res* (2015) 75(6):918–23. doi: 10.1158/0008-5472.CAN-14-2233
12. Bychkov D, Turkki R, Haglund C, Linder N, Lundin J. Deep Learning for Tissue Microarray Image-Based Outcome Prediction in Patients with Colorectal Cancer. *Med Imaging Dig Pathol* (2016) 9791:298–303. doi: 10.1117/12.2217072
13. Chang Y, Lafata K, Liu C, Wang C., Cui Y., Ren L., et al. An Encoder-Decoder Based Convolutional Neural Network (ED-CNN) for PET Image Response Prediction Using Pre-RT Information: A Feasibility of Oropharynx Cancer IMRT. In. *Medical physics* vol. 46(6);pp. E283–E283: 111 RIVER ST, HOBOKEN 07030-5774, NJ USA: WILEY. (2019).
14. Hilbert A, Ramos LA, van Os HJA, Olabarriaga SD, Tolhuisen ML, Wermer MJH, et al. Data-Efficient Deep Learning of Radiological Image Data for Outcome Prediction After Endovascular Treatment of Patients With Acute Ischemic Stroke. *Comput Biol Med* (2019) 115:103516. doi: 10.1016/j.compbiomed.2019.103516
15. Wang C, Liu C, Chang Y, Lafata K, Cui Y, Zhang J, et al. Dose-Distribution-Driven PET Image-Based Outcome Prediction (DDD-PIOP): A Deep Learning Study for Oropharyngeal Cancer IMRT Application. *Front Oncol* (2020) 1592. doi: 10.3389/fonc.2020.01592
16. Britton NF. *Reaction-Diffusion Equations and Their Applications to Biology*. Cambridge, MA: Academic Press (1986).
17. Hormuth DA, Eldridge SL, Weis JA, Miga MI, Yankeelov TE. Mechanically Coupled Reaction-Diffusion Model to Predict Glioma Growth: Methodological Details. In: *Cancer Systems Biology*. Humana Press: New York, NY (2018). pp 225–41.
18. Jarrett AM, Hormuth DA, Barnes SL, Feng X, Huang W, Yankeelov TE. Incorporating Drug Delivery Into an Imaging-Driven, Mechanics-Coupled Reaction Diffusion Model for Predicting the Response of Breast Cancer to Neoadjuvant Chemotherapy: Theory and Preliminary Clinical Results. *Phys Med Biol* (2018) 63(10):105015. doi: 10.1088/1361-6560/aac040
19. Provatas N, Elder K. *Phase-Field Methods in Materials Science and Engineering*. Weinheim, Germany: John Wiley & Sons (2011).
20. Ronneberger O, Fischer P, Brox T. U-Net: Convolutional Networks for Biomedical Image Segmentation, in: *International Conference on Medical Image Computing and Computer-Assisted Intervention 2015*. Cham, Switzerland: Springer: (2015). pp. 234–41.
21. Mowery YM, Vergalasova I, Rushing CN, Choudhury KR, Niedzwiecki D, Wu Q, et al. Early 18F-FDG-PET Response During Radiation Therapy for HPV-Related Oropharyngeal Cancer May Predict Disease Recurrence. *Int J Radiat Oncol Biol Phys* (2020) 108(4):969–76. doi: 10.1016/j.ijrobp.2020.08.029
22. Simon E, Fox TH, Lee D, Waller AF, Pantalone P, Jani AB. PET Lesion Segmentation Using Automated Iso-Intensity Contouring in Head and Neck Cancer. *Technol Cancer Res Treat* (2009) 8(4):249–55. doi: 10.1177/153303460900800401
23. Otsu N. A Threshold Selection Method From Gray-Level Histograms. *IEEE Trans Syst Man Cybernet* (1979) 9(1):62–6. doi: 10.1109/TSMC.1979.4310076
24. Low DA, Mutic S, Dempsey JF, Gerber RL., Bosch WR., Perez CA., et al. Quantitative Dosimetric Verification of an IMRT Planning and Delivery System. *Radiother Oncol* (1998) 49(3):305–16. doi: 10.1016/S0167-8140(98)00125-X
25. Chen X, Summers RM, Yao J. Kidney Tumor Growth Prediction by Coupling Reaction–Diffusion and Biomechanical Model. *IEEE Trans Biomed Eng* (2012) 60(1):169–73.doi: 10.1109/TBME.2012.2222027
26. Hormuth DAII, Weis JA, Barnes SL, Miga MI, Quaranta V, Yankeelov TE. Biophysical Modeling of *In Vivo* Glioma Response After Whole-Brain Radiation Therapy in a Murine Model of Brain Cancer. *Int J Radiat Oncol Biol Phys* (2018) 100(5):1270–9. doi: 10.1016/j.ijrobp.2017.12.004
27. Swan A, Hillen T, Bowman JC, Murtha AD. A Patient-Specific Anisotropic Diffusion Model for Brain Tumour Spread. *Bull Math Biol* (2018) 80(5):1259–91. doi: 10.1007/s11538-017-0271-8
28. Rockne RC, Trister AD, Jacobs J, Hawkins-Daarud AJ, Neal ML, Hendrickson K, et al. A Patient-Specific Computational Model of Hypoxia-Modulated Radiation Resistance in Glioblastoma Using 18F-FMISO-PET. *J R Soc Interface.* (2015) 12(103):20141174. doi: 10.1098/rsif.2014.1174
29. Liu Y, Sadowski SM, Weisbrod AB, Kebebew E, Summers RM, Yao J. Patient Specific Tumor Growth Prediction Using Multimodal Images. *Med Imag Anal* (2014) 18(3):555–66. doi: 10.1016/j.media.2014.02.005
30. Mi H, Petitjean C, Dubray B, Vera P, Ruan S. Prediction of Lung Tumor Evolution During Radiotherapy in Individual Patients With PET. *IEEE Trans Med Imag* (2014) 33(4):995–1003. doi: 10.1109/TMI.2014.2301892

31. Weis JA, Miga MI, Yankeelov TE. Three-Dimensional Image-Based Mechanical Modeling for Predicting the Response of Breast Cancer to Neoadjuvant Therapy. *Comput Methods Appl Mechanic Eng* (2017) 314:494–512. doi: 10.1016/j.cma.2016.08.024
32. Li A, Chen R, Farimani AB, Zhang YJ. Reaction Diffusion System Prediction Based on Convolutional Neural Network. *Sci Rep* (2020) 10(1):1–9. doi: 10.1038/s41598-020-60853-2
33. Chen RT, Rubanova Y, Bettencourt J, Duvenaud D. Neural Ordinary Differential Equations. *ArXiv Preprint ArXiv* (2018) 1806.07366.
34. Lafata KJ, Corradetti MN, Gao J, Jacobs CD, Weng J, Chang Y, et al. Radiogenomic Analysis of Locally Advanced Lung Cancer Based on CT Imaging and Intratreatment Changes in Cell-Free Dna. *Radiol: Imaging Cancer* (2021) 3(4):e200157. doi: 10.1148/rycan.2021200157
35. Lafata K, Zhou Z, Liu J-G, Yin F-F. Data Clustering Based on Langevin Annealing With a Self-Consistent Potential. *Q Appl Math* (2019) 77(3):591–613. doi: 10.1090/qam/1521
36. Paganelli C, Meschini G, Molinelli S, Riboldi M, Baroni G. Patient-Specific Validation of Deformable Image Registration in Radiation Therapy: Overview and Caveats. *Med Phys* (2018) 45(10):e908–22. doi: 10.1002/mp.13162
37. Bortfeld T, van Herk M, Jiang SB. When Should Systematic Patient Positioning Errors in Radiotherapy Be Corrected? *Phys Med Biol* (2002) 47 (23):N297. doi: 10.1088/0031-9155/47/23/401
38. Lafata KJ, Chang Y, Wang C, Mowery YM, Vergalasova I, Niedzwiecki D, et al. Intrinsic Radiomic Expression Patterns After 20 Gy Demonstrate Early Metabolic Response of Oropharyngeal Cancers. *Med Phys* (2021) 48(7):3767–77. doi: 10.1002/mp.14926

Conflict of Interest: The authors declare that the research was conducted in the absence of any commercial or financial relationships that could be construed as a potential conflict of interest.

frontiers | Frontiers in Oncology

ORIGINAL RESEARCH
published: 07 June 2022
doi: 10.3389/fonc.2022.897130

Longitudinal Correlations Between Intravoxel Incoherent Motion (IVIM) and Dynamic Contrast-Enhanced (DCE) MRI During Radiotherapy in Prostate Cancer Patients

*Ernst S. Kooreman, Vivian van Pelt, Marlies E. Nowee, Floris Pos, Uulke A. van der Heide and Petra J. van Houdt**

Department of Radiation Oncology, The Netherlands Cancer Institute, Amsterdam, Netherlands

OPEN ACCESS

Edited by:
Davide Cusumano, Agostino Gemelli University Polyclinic (IRCCS), Italy

Reviewed by:
Kee Howe Wong, Royal Marsden NHS Foundation Trust, United Kingdom
Radka Stoyanova, University of Miami, United States

***Correspondence:**
Petra J. van Houdt
p.v.houdt@nki.nl

Specialty section:
This article was submitted to Radiation Oncology, a section of the journal Frontiers in Oncology

Received: *15 March 2022*
Accepted: *03 May 2022*
Published: *07 June 2022*

Citation:
Kooreman ES, van Pelt V, Nowee ME, Pos F, van der Heide UA and van Houdt PJ (2022) Longitudinal Correlations Between Intravoxel Incoherent Motion (IVIM) and Dynamic Contrast-Enhanced (DCE) MRI During Radiotherapy in Prostate Cancer Patients. Front. Oncol. 12:897130. doi: 10.3389/fonc.2022.897130

Purpose: Intravoxel incoherent motion (IVIM) is a promising technique that can acquire perfusion information without the use of contrast agent, contrary to the more established dynamic contrast-enhanced (DCE) technique. This is of interest for treatment response monitoring, where patients can be imaged on each treatment fraction. In this study, longitudinal correlations between IVIM- and DCE parameters were assessed in prostate cancer patients receiving radiation treatment.

Materials and Methods: 20 prostate cancer patients were treated on a 1.5 T MR-linac with 20 x 3 or 3.1 Gy. Weekly IVIM and DCE scans were acquired. Tumors, the peripheral zone (PZ), and the transition zone (TZ) were delineated on a T_2-weighted scan acquired on the first fraction. IVIM and DCE scans were registered to this scan and the delineations were propagated. Median values from these delineations were used for further analysis. The IVIM parameters D, f, D^* and the product fD^* were calculated. The Tofts model was used to calculate the DCE parameters K^{trans}, k_{ep} and v_e. Pearson correlations were calculated for the IVIM and DCE parameters on values from the first fraction for each region of interest (ROI). For longitudinal analysis, the repeated measures correlation coefficient was used to determine correlations between IVIM and DCE parameters in each ROI.

Results: When averaging over patients, an increase during treatment in all IVIM and DCE parameters was observed in all ROIs, except for D in the PZ and TZ. No significant Pearson correlations were found between any pair of IVIM and DCE parameters measured on the first fraction. Significant but low longitudinal correlations were found for some combinations of IVIM and DCE parameters in the PZ and TZ, while no significant longitudinal correlations were found in the tumor. Notably in the TZ, for both f and fD^*, significant longitudinal correlations with all DCE parameters were found.

Conclusions: The increase in IVIM- and DCE parameters when averaging over patients indicates a measurable response to radiation treatment with both techniques. Although low, significant longitudinal correlations were found which suggests that IVIM could potentially be used as an alternative to DCE for treatment response monitoring.

Keywords: DCE, IVIM, prostate cancer, treatment response, repeated measures, correlations, perfusion

1 INTRODUCTION

Non-invasive perfusion imaging is of interest in oncology, as low perfusion is related to hypoxia which holds prognostic value (1–3). A common way to measure perfusion is by using dynamic contrast enhanced (DCE-) MRI (2, 4, 5). In addition to prognosis, DCE has been shown to have value for mid-treatment response assessment in cervix (6), esophageal (7), and head-and-neck cancer (8–10).

Acquiring quantitative MRI (qMRI) images during radiation treatment for the purpose of treatment response monitoring has become feasible with the introduction of MR-guided radiotherapy. Using MR-linacs, which consist of a linear accelerator integrated with an MRI system, qMRI sequences can be acquired on each treatment fraction, without the increase of patient burden (11–16).

Although DCE-MRI is a candidate for treatment response monitoring, acquiring a DCE scan during each treatment fraction is undesirable due to the use of contrast agent. Alternative techniques that can provide perfusion information without the use of contrast agent are needed. One such alternative is intravoxel incoherent motion (IVIM), which is an extension to diffusion weighted imaging (DWI) (17). IVIM parameters provide information about diffusion and perfusion. It is based on the concept that inside a voxel, signal from water flowing in the capillaries can be separated from diffusing water (18). In addition to the diffusion coefficient (D), the perfusion parameters f (perfusion fraction), D* (pseudo-diffusion coefficient), and the product fD* can be determined.

Previous studies have investigated correlations between IVIM and DCE-MRI parameters in different tumor sites, with conflicting results (19). These studies usually determine the correlation between IVIM and DCE parameters on a single time point. For treatment response purposes however, correlations between changes in parameters, induced by radiation treatment, are more relevant. A study performed in 21 liver tumor-bearing rabbits assessed the correlations between IVIM and DCE parameters longitudinally, while the rabbits were treated with a vascular disrupting agent (20). Interestingly, the authors did not find any significant correlations between IVIM and DCE parameters when assessing the imaging time points separately, but did find a significant longitudinal correlation. This longitudinal correlation is of importance for treatment response monitoring purposes and indicates that IVIM could be a potential substitute for DCE-MRI for this purpose.

In the current study, longitudinal correlations between IVIM- and DCE parameters are assessed in a cohort of prostate cancer patients that were imaged weekly during radiation treatment. Each week a DCE and an IVIM scan were acquired to enable longitudinal assessment. The aim of this study is to determine whether IVIM and DCE parameters correlate when measured longitudinally and whether there is potential for IVIM to substitute DCE for treatment response monitoring.

2 MATERIALS AND METHODS

2.1 Patients

Twenty patients, with a median age of 70.5 (range 53 – 82) years with biopsy proven prostate cancer were included in this study. Only patients with an adequate renal function (glomerular filatration rate GFR > 60 ml/min/1.7m^2) were included. Thirteen patients were treated with 20 x 3 Gy and due to a change in clinical practice, seven patients were treated with 20 x 3.1 Gy. Treatment took place over the course of five weeks. Patient characteristics are presented in **Table 1**. The study was approved by the local ethics committee and each patient gave written informed consent.

2.2 Image Acquisition

All patients were treated on a 1.5 T MR-linac (Unity, Elekta AB, Stockholm, Sweden). This is a hybrid system, where a linear accelerator is integrated with an MRI scanner to enable concurrent patient irradiation and MRI acquisition. The MRI system of the MR-linac is based on a 1.5 T Ingenia system (Philips Healthcare, Best, The Netherlands), with split gradient coils to create a window for the radiotherapy beam (21). The system uses an 8-channel radio-translucent phased array receive coil (22).

TABLE 1 | Patient characteristics.

Patient characteristic	Median (range)
Age (years)	70.5 (53 – 82)
iPSA (ng/ml)	15 (8 – 38)
GFR (ml/min/1.7m^2)	
Pre-treatment	79 (67 – 107)
Post-treatment	82 (65 – 110)
ISUP	No. of patients
1	3
2	8
3	4
4	3
5	2

iPSA, initial prostate specific antigen; GFR, glomerular filtration rate; ISUP score, prostate cancer grading score.

A T_2-weighted anatomical scan, an IVIM scan and a DCE-MRI scan were acquired weekly over the course of five weeks, starting at the first day of treatment. Scan parameters can be found in **Table 2**. The IVIM sequence was optimized for the MR-linac system, which has lower gradient performance compared to diagnostic systems and lower SNR due to the simpler receive coil system (15, 23). To compensate this, the highest b-value was limited to 500 s/mm^2, and a relatively large isotropic acquisition voxel size of 4 mm^3 was used. To calculate contrast agent concentration values, the pre-contrast T_1 was measured using the variable flip angle (VFA) method with a similar sequence as the DCE scan, but with a TR/TE of 20/4 ms and flip angles of 3, 6, 10, 20, and 30 °. For the DCE scan, during the fifth dynamic, 15 mmol gadoteric acid (Dotarem, Geurbet, France) was injected at a rate of 3 mL/s using a power injector followed by a 30 ml saline flush. While a study by Wang et al. demonstrated no significant effect of radiation on the chemical composition of Gadolinium based contrast agents (24), DCE scans were acquired after the radiation treatment, without repositioning of the patient to avoid interactions of the contrast agent with radiation.

2.3 Image Registration

Tumor, peripheral zone (PZ), and transition zone (TZ) were delineated on the T_2-weighted scans of the first fraction. Of three patients, who received a trans-urethral resection of the prostate (TURP), the TURP cavity was delineated to be excluded from analysis. Tumors were delineated while consulting biopsy results and diagnostic images, following the PI-RADS V2.1 criteria (25).

The IVIM and DCE images were registered separately to the T_2-weighted scan of the first fraction which contained the delineations using rigid registration allowing rotations and translations. For IVIM, the b = 0 s/mm^2 image was used as this contains the most anatomical information. For DCE, the 100th dynamic was used as a scan with relatively high enhancement in the prostate signal. All registrations were checked visually and corrected manually when needed. After registration, the delineations were propagated to the IVIM and DCE scans, where only voxels that were fully inside the propagated delineation were included for further analysis.

IVIM scans were excluded when susceptibility artifacts were present inside any of the delineations, or when movement between b-values was present. DCE scans were excluded if patient movement occurred during the scan.

The volume of the structures was calculated by multiplying the number of voxels completely inside the delineation by the voxel size of the T_2-weighted scan they were delineated on.

2.4 Image Processing

2.4.1 IVIM

The bi-exponential IVIM model, $S_{(b)} / S_0 = fe^{-bD^*} + (1 - f)e^{-bD}$, was fitted using a segmented approach (26). Using the median signal intensity values from the delineations, the tissue diffusion coefficient (D) was determined first using the two highest b-values (150 and 500 s/mm^2). Next the perfusion fraction (f) was calculated using this D and the b = 0 s/mm^2 signal intensity. Both D and f were then used in combination with the signal intensities from the lowest two b-value images (0 and 30 s/mm^2) to calculate the pseudo-diffusion coefficient D*. The parameter fD* was calculated by multiplying f with D*.

2.4.2 DCE

To extract an arterial input function (AIF), external iliac artery was delineated on all DCE scans of all patients. Due to slight variations in the B_1 field (see **Supplementary Figure 1**), only the left external iliac artery was used. Signal intensities were converted to concentration time curves using the spoiled gradient echo equation following Schabel and Parker (27) assuming a T_1 value of 1429 ms for blood at 1.5 T (28) and a contrast agent relaxivity of 3.6 L mM^{-1} s^{-1} (29). Following Georgiou et al. the maximum relative change in concentration during the DCE scan was determined for all voxels inside this delineation (30). The voxels between the 50th and 95th percentile of this relative change were averaged to obtain an AIF for each treatment fraction. Per patient, the median AIF of all five measurements, based on peak height, was used for all tracer kinetic modeling for that patient. **Supplementary Figure 2** shows all AIFs of all patients.

TABLE 2 | MRI sequence parameters.

	T_2-weighted	IVIM	DCE
Sequence type	3D-TSE	ss-EPI	3D-FFE
Field of view (mm^3)	400 x 448 x 250	430 x 430 x 60	220 x 251 x 60
Acquired voxel size (mm^3)	1.2 x 1.2 x 1.2	3.98 x 3.98 x 4.00	2.62 x 2.62 x 7.00
Reconstructed voxel size (mm^3)	0.57 x 0.57 x 1.2	1.92 x 1.92 x 4.00	1.57 x 1.57 x 3.50
Flip angle (°)	90	90	35
TR/TE (ms)	1300/129	2960/82	4.0/1.9
Fat suppression	–	SPAIR	–
Parallel imaging (SENSE) factor	3.5	2.3	2
Acceleration factor	110	47	–
b-values (averages) (s/mm^2)	–	0 (8), 30 (8), 150 (8), 500 (16)	–
Phase encoding bandwidth (Hz/pixel)	–	32.9	–
Gradient timings Δ/δ (ms)	–	41.1/20.0	–
Dynamic scan time (s)	–	–	2.8
Number of dynamics	–	–	110
NSA	2	1	1
Acquisition time (m:ss)	5:48	5:11	5:04

A voxel-wise T_1-map was calculated from the VFA series using a linear implementation (31). The T_1 map was used to convert signal intensity to concentration values using the method of Schabel and Parker (27). The bolus arrival time was estimated for each voxel using an automated method (32). The volume transfer constant (K^{trans}) and the rate constant (k_{ep}) from the standard Tofts model (33) were calculated on a voxel-basis following the approach developed by Murase (34) using and median AIF as input. The extracellular extravascular space volume fraction (v_e) was then calculated on a voxel basis using (K^{trans}/k_{ep}).

2.5 Statistics

Baseline values from the IVIM and DCE parameters were taken from the scans of the first fraction. To check for differences in parameters between ROIs, a one-way analysis of variance (ANOVA) was performed for each parameter, with ROI as the independent variable. ANOVA results are presented with their *F*-statistic including within- and between group degrees of freedom, and *p*-value. Pearson correlation coefficients were calculated between IVIM and DCE parameters of the first fraction for each ROI.

To determine longitudinal correlations between the IVIM and DCE parameters, the *rmcorr* package in R was used (35). The rmcorr package provides a repeated measures correlation (r_{rm}), which takes into account the non-independence of repeated measures. To do so, the relationship between two continuous variables (in this case the IVIM and DCE parameters) is determined while controlling for between-patient variance. Specifically, separate parallel lines are fitted to the data of each patient using a common slope but allowing the intercept to vary per patient (35). The r_{rm} is then calculated from the sum of squares values for the measure and the error as follows:

$$r_{rm} = \sqrt{\frac{SS_{Measure}}{SS_{Measure} + SS_{Error}}}$$

The sign of r_{rm} is taken from the sign of the common slope. The degrees of freedom are calculated using N(k-1)-1, where k is the (average) number of repeated measures per participant and N is the total number of participants (35).

As IVIM and DCE measure different biological properties which are both related to perfusion, it is possible that their correlation depends on the particular tissue measured. Therefore, r_{rm} was calculated separately for each ROI. It can be interpreted as the intra-patient correlation between IVIM and DCE parameters during radiation treatment for a given ROI. Repeated measures correlation results are presented as r_{rm} (error degrees of freedom), *p*-value, and a 95% confidence interval calculated using bootstrapping with 10.000 resamples. Statistical significance was assumed for all tests when $p < 0.05$.

3 RESULTS

Imaging data was acquired on five fractions for 19/20 patients and one patient was imaged four times. This resulted in a total of 99 fractions with IVIM and DCE scans. Two DCE scans were excluded due to movement during acquisition, both from the same patient. Seven IVIM scans were excluded due to susceptibility artifacts causing deformations within the delineations and two IVIM scans were excluded because the patient moved between the acquisition of images with a different b-value, leaving 97 DCE acquisitions and 90 IVIM acquisitions for further analysis.

In two of the patients, no tumor was visible on the diagnostic scans and therefore not delineated. Of one patient with a TURP all remaining tissue was treated as tumor. The median (range) volume of the ROIs were 0.9 (0.1 – 14) cm^3 for the tumor, 8.9 (5.0 – 26) cm^3 for the PZ, and 20 (7.2 – 66) cm^3 for the TZ. An example of the delineations in two different patients is shown in **Figure 1**.

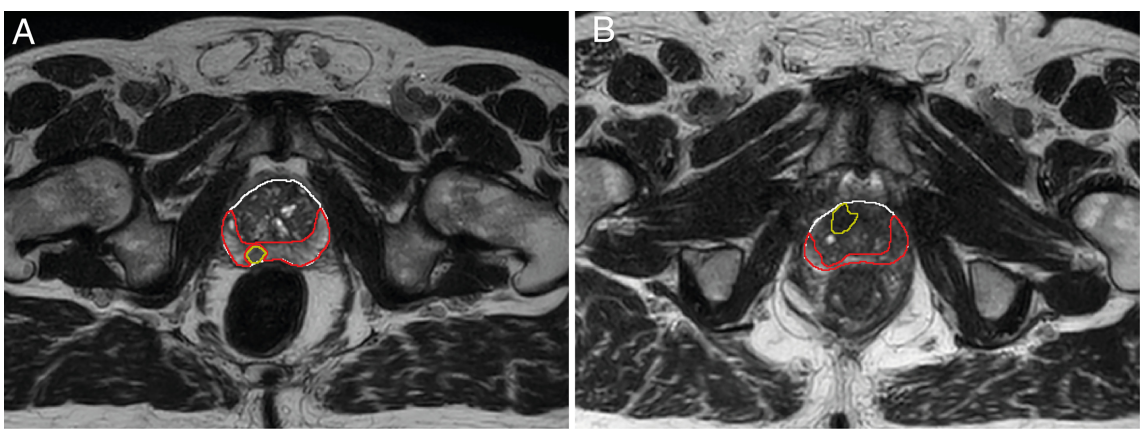

FIGURE 1 | Example of delineations of the different prostate zones of two different patients **(A, B)**. Delineations were made on T_2-weighted scans from the first treatment fraction. The entire prostate is shown in white, the peripheral zone (PZ) in red, and the tumor in yellow. The transition zone (TZ) was extracted in post processing by subtracting the PZ from the prostate delineation. Tumor voxels were excluded from all other zones during analysis.

Baseline mean values with the standard error of the mean (SEM) are presented in **Table 3**. These are based on the IVIM scans acquired before the patients received any radiation and the DCE scans acquired directly after a single dose of 3 or 3.1 Gy. One-way ANOVA revealed a statistically significant difference between the tumor, PZ, and TZ for D ($F_{2,44} = 15$, $p < 0.001$), K^{trans} ($F_{2,53} = 4.3$, $p = 0.02$) and v_e ($F_{2,53} = 3.9$, $p = 0.03$). No statistically significant correlations were found between IVIM and DCE parameters when using values from the first fraction only.

Figure 2 shows the average time trends over all patients of the IVIM and DCE parameters. All IVIM and DCE parameters increase in all ROIs over the weeks, except for

TABLE 3 | Pre-treatment values of the IVIM and DCE parameters.

	Tumor	PZ	TZ
D (10^{-3} s/mm^2)	1.12 ± 0.08	1.56 ± 0.07	1.45 ± 0.02
f	0.07 ± 0.02	0.09 ± 0.01	0.10 ± 0.01
D* (10^{-3} s/mm^2)	35 ± 12	28 ± 3	32 ± 2
fD* (10^{-3} s/mm^2)	3.9 ± 1.3	2.7 ± 0.4	3.2 ± 0.3
K^{trans} (min^{-1})	0.30 ± 0.04	0.14 ± 0.02	0.19 ± 0.02
k_{ep} (min^{-1})	0.58 ± 0.09	0.29 ± 0.07	0.38 ± 0.05
v_e	0.45 ± 0.08	0.25 ± 0.08	0.44 ± 0.05

The IVIM parameters were acquired before irradiation, the DCE parameters were acquired directly after receiving the first treatment fraction. Mean ± standard error of the mean (SEM) values of all patients are shown.

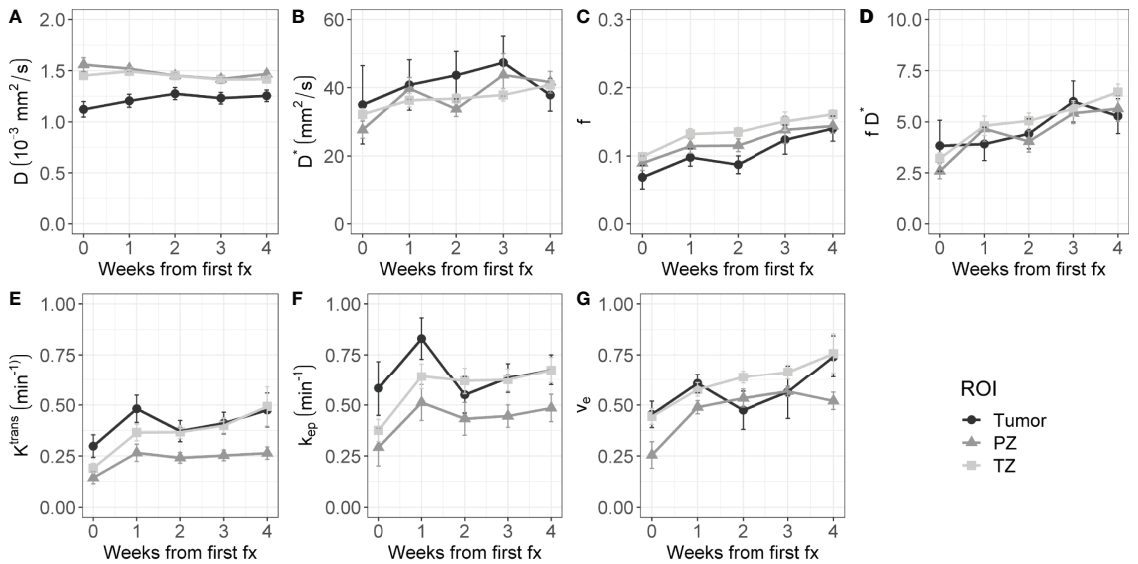

FIGURE 2 | Evolution of intravoxel incoherent motion (IVIM, **A–D**) and dynamic contrast-enhanced (DCE, **E–G**) parameters during radiation treatment. The average value of all patients is shown for the tumor, PZ, and TZ. Error bars indicate the standard error of the mean (SEM).

TABLE 4 | Repeated measures correlations between IVIM and DCE parameters, separately presented for each ROI.

		K^{trans}	k_{ep}	v_e
Tumor	D	$r_{(60)}$ = 0.04 [-0.13, 0.24], p = 0.74	$r_{(60)}$ = -0.08 [-0.33, 0.19], p = 0.55	$r_{(60)}$ = 0.19 [-0.05, 0.41], p = 0.15
	f	$r_{(60)}$ = 0.09 [-0.09, 0.32], p = 0.48	$r_{(60)}$ = 0.02 [-0.19, 0.27], p = 0.86	$r_{(60)}$ = -0.12 [-0.43, 0.24], p = 0.34
	D*	$r_{(54)}$ = -0.02 [-0.33, 0.25], p = 0.89	$r_{(54)}$ = -0.13 [-0.35, 0.13], p = 0.34	$r_{(54)}$ = 0.02 [-0.23, 0.27], p = 0.90
	fD*	$r_{(54)}$ = 0.03 [-0.24, 0.27], p = 0.82	$r_{(54)}$ = -0.09 [-0.33, 0.19], p = 0.53	$r_{(54)}$ = -0.08 [-0.35, 0.22], p = 0.58
PZ	D	$r_{(63)}$ = -0.21 [-0.39, -0.02], p = 0.09	$r_{(63)}$ = -0.06 [-0.27, 0.15], p = 0.64	**$r_{(63)}$ = -0.33 [-0.54, -0.11], p < 0.01**
	f	$r_{(63)}$ = 0.21 [0.01, 0.47], p = 0.10	$r_{(63)}$ = 0.07 [-0.15, 0.39], p = 0.56	**$r_{(63)}$ = 0.33 [0.14, 0.57], p < 0.01**
	D*	$r_{(63)}$ = 0.16 [-0.04, 0.36], p = 0.19	$r_{(63)}$ = 0.12 [-0.06, 0.32], p = 0.34	$r_{(63)}$ = 0.04 [-0.16, 0.27], p = 0.75
	fD*	$r_{(63)}$ = 0.23 [-0.03, 0.47], p = 0.07	$r_{(63)}$ = 0.13 [-0.12, 0.43], p = 0.29	$r_{(63)}$ = 0.20 [-0.01, 0.40], p = 0.11
TZ	D	$r_{(63)}$ = -0.01 [-0.17, 0.25], p = 0.94	$r_{(63)}$ = 0.16 [-0.01, 0.35], p = 0.21	$r_{(63)}$ = -0.13 [-0.29, 0.06], p = 0.29
	f	**$r_{(63)}$ = 0.38 [0.28, 0.64], p < 0.01**	**$r_{(63)}$ = 0.39 [0.19, 0.60], p < 0.01**	**$r_{(63)}$ = 0.37 [0.28, 0.62], p < 0.01**
	D*	$r_{(63)}$ = 0.21 [0.03, 0.52], p = 0.09	**$r_{(63)}$ = 0.35 [0.16, 0.54], p < 0.01**	$r_{(63)}$ = 0.19 [0.02, 0.53], p = 0.12
	fD*	**$r_{(63)}$ = 0.39 [0.26, 0.66], p < 0.01**	**$r_{(63)}$ = 0.48 [0.27, 0.66], p < 0.001**	**$r_{(63)}$ = 0.37 [0.24, 0.63], p < 0.01**

The degrees of freedom are shown between parentheses and the confidence interval of the repeated measures correlation is shown between brackets. Bold values show significant correlations ($p < 0.05$).

D in the PZ and TZ. The IVIM perfusion parameters increase steadily over the weeks. The DCE parameters steeply increase from the first to the second week and stabilize or slightly increase after that.

The r_{rm} calculated on the longitudinal data are presented in **Table 4**. No statistically significant correlations were found between any IVIM and DCE parameter in the tumor. In the PZ, statistically significant correlations were found only between D and v_e and between f and v_e. In the TZ, statistically significant correlations were found between f and K^{trans}, f and k_{ep}, and f and v_e. D* correlated significantly only with k_{ep}, while the product fD* did so with all DCE parameters. Graphs showing the common slope and the slope per patient of the significant within-subject longitudinal correlations are presented in **Figure 3** for D, **Figure 4** for f, **Figure 5** for D*, and **Figure 6** for fD*.

4 DISCUSSION

In this study, the longitudinal correlations between IVIM and DCE parameters in different ROIs of prostate cancer patients were assessed during radiation treatment. Weekly IVIM and DCE scans were performed and resulting correlations were tested taking into account the non-independence of repeated measurements on the same patients.

Baseline f and D* values of the IVIM parameters corresponded to values found in the literature, although the reported range is large. The baseline tumor D values found in this study ($1.12 \pm 0.08\ 10^{-3}$ mm^2/s) were higher than previously found (reported range: $0.13 - 1.06\ 10^{-3}$ mm^2/s) (36). Baseline K^{trans} and v_e values were consistent with those found in the literature, while the k_{ep} values were relatively low (37).

When averaging over patients, an increase in all perfusion parameters over the course of radiation treatment can be seen. In the DCE parameter values, this increase was the largest between week 0 and week 1, after which the values seemed to stabilize. This trend is also visible in the IVIM parameters D* and fD*. The similar behavior on the group level suggests that there is an overall biological response to radiation that can be measured similarly with both techniques. Previous results comparing DCE parameters before treatment to values acquired at a minimum of two years after treatment showed a decrease in K^{trans} and k_{ep} in the PZ and TZ (38). Taken together with the current results, this could indicate that perfusion is increased during treatment, followed by a decline longer after treatment. The discrepancy between short-term and long-term differences highlights the

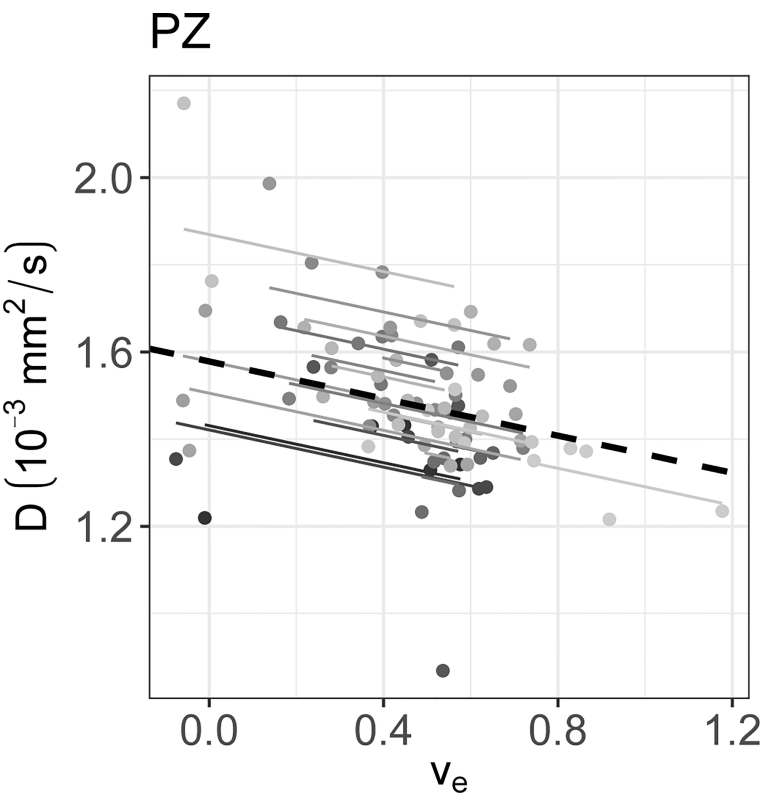

FIGURE 3 | The significant repeated measures correlation of D with the DCE parameters are shown. D only correlated significantly with v_e in the PZ. Each line shows the fit for a single patient and the dashed black line shows the overall common slope.

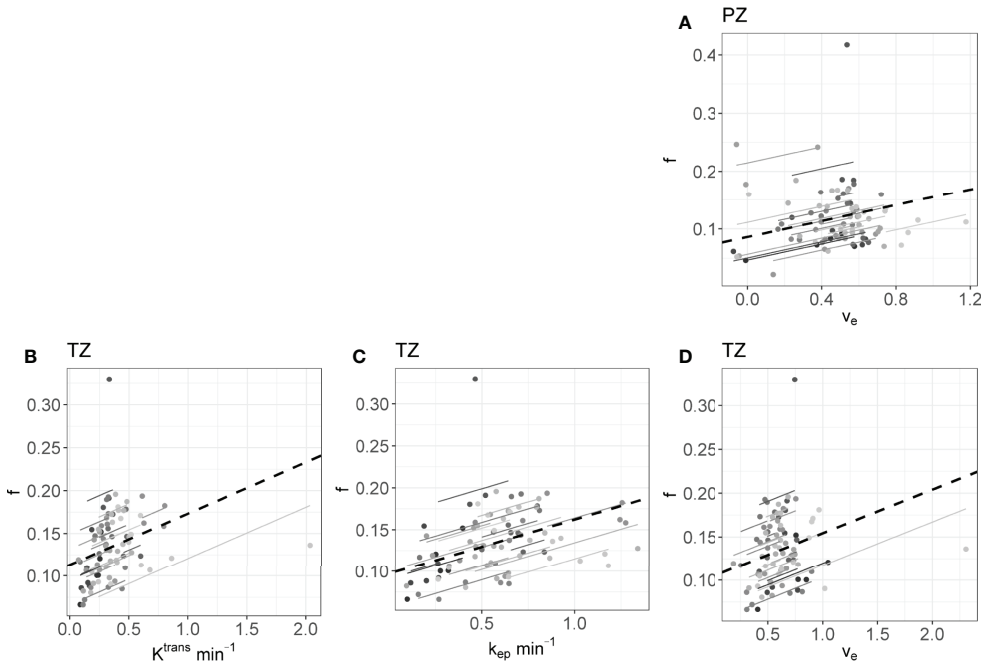

FIGURE 4 | The significant repeated measures correlations of f with the DCE parameters are shown. **(A)** is the correlation between f and v_e in the PZ, **(B–D)** are values from the TZ. Each line shows the fit for a single patient and the dashed black line shows the overall common slope.

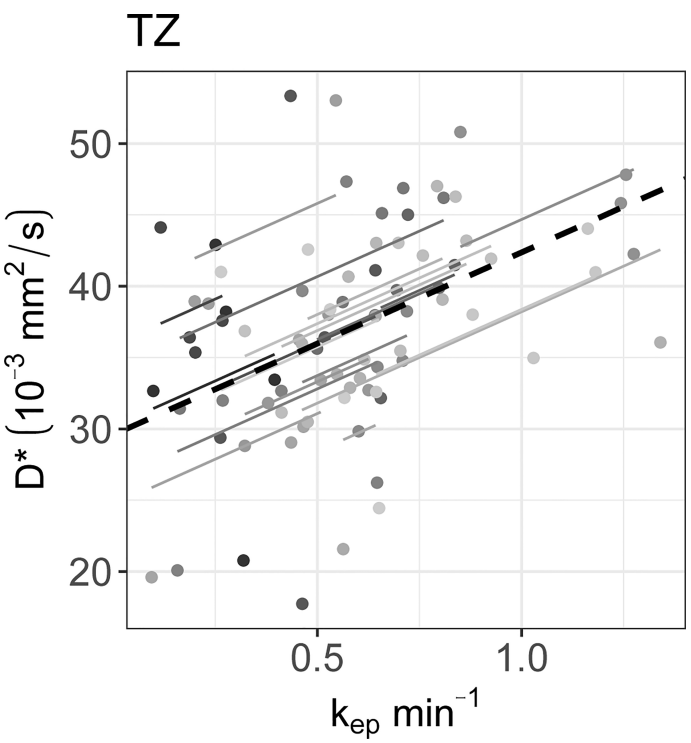

FIGURE 5 | The significant repeated measures correlations of D* with the DCE parameters are shown. D* only correlated significantly with k_{ep} in the TZ. Each line shows the fit for a single patient and the dashed black line shows the overall common slope.

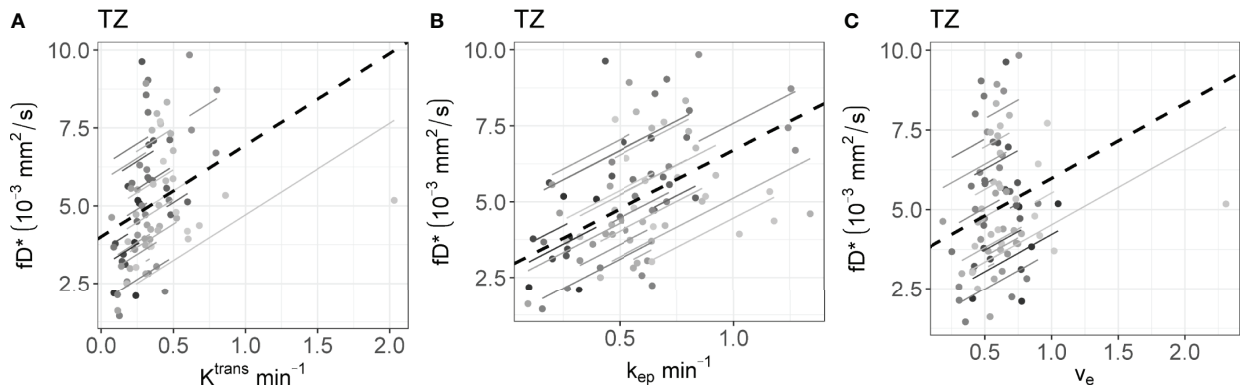

FIGURE 6 | The significant repeated measures correlation of fD* with the DCE parameters are shown. fD* only correlated significantly with DCE parameters in the **(A–C)** TZ. Each line shows the fit for a single patient and the dashed black line shows the overall common slope.

importance of determining the optimal measurement time for treatment response purposes.

A possible explanation for the early increase of the perfusion parameters in all prostate zones could be an inflammatory response to the radiation treatment in the entire prostate, similar to what was found previously in cervix patients (6). Such an overall response could limit the predictive value of early perfusion for treatment response in prostate cancer patients as it could obscure more subtle changes related to outcome. To investigate this, early changes in perfusion parameters should be related to clinical outcome data. However, these data were not available yet for the current study population.

Although comparison with histology has shown that IVIM parameters provide perfusion information, the specific interpretation of IVIM parameters and their relation to DCE parameters remains unclear (19, 39). Correlations between IVIM and DCE parameters should be carefully interpreted based on the context. When the goal is to assess the ability of both techniques to differentiate between tumor and benign tissue, as done in Pang et al. for prostate cancer (40), it is appropriate to use values from both ROIs combined to determine the correlation. In that case, the correlation reflects how differences between ROIs in IVIM parameters correlate with differences between ROIs in DCE parameters. A ROI effect is clearly visible in the scatterplots presented by Pang et al. (40). However, when investigating longitudinal data, we are interested in the correlation of changes within the ROIs over time. This within-ROI correlation could be different for different ROIs, and theoretically even have an opposite sign compared to the between-ROI correlation. This effect is known as Simpsons paradox (41).

In the current study, the focus is on treatment response monitoring. To measure the longitudinal correlations the r_{rm} was used on data from each ROI separately. The r_{rm} can in this case be interpreted for each ROI as the intra-patient correlation between IVIM and DCE parameters while measuring during treatment, indicating the degree to which both parameters reflect the same time trends induced by irradiation.

No significant correlations were found in the tumors. A reason for this could be a low precision of the IVIM and DCE parameters as acquired in the current study. Median values were calculated per ROI, and the variance of these median values scale with 1/n, where n is the number of voxels. As prostate tumors are relatively small, the variance of the median values is relatively high. We showed previously that the test-retest repeatability coefficient of IVIM parameters in prostate tumors is high for the current imaging sequence and analysis: 0.44 10^{-3} mm^2/s, 0.16 and 76.4 mm^2/s for D, f, and D* (15). Additionally, DCE parameters are known to have poor repeatability (42–44). Within-patient coefficients of variation reported previously in prostate tumors measured on a 1.5 T system were around 20% for K^{trans}, 15% for v_e and 30% for k_{ep} (45). Poor repeatability in both IVIM and DCE parameters can attenuate the correlation coefficients (46). In the TZ, which is the ROI with the largest volume, significant positive correlations were found, although all were low (< 0.5).

In order to test the correlations between IVIM and DCE parameters in different ROIs, 36 statistical tests were performed with a significance threshold of $\alpha = 0.05$. This means that the chance of finding at least one false positive result is 84%, because multiple testing inflates the type 1 error rate. However, since this is the first study to test the longitudinal correlation between IVIM and DCE parameters in humans undergoing radiation treatment, type I error rate is less of a concern. These correlations can be used as a direction for future studies.

In conclusion, when assessing changes in group averages over time, a clear increase in IVIM perfusion parameters was found. This increase was also present in all DCE parameters. Although low, it is encouraging that significant longitudinal correlations were found between IVIM- and DCE parameters, suggesting that IVIM could potentially be used as an alternative to DCE for treatment response monitoring purposes, in particular when repeated DCE-MRI is not feasible.

DATA AVAILABILITY STATEMENT

The raw data supporting the conclusions of this article will be made available by the authors, without undue reservation.

ETHICS STATEMENT

The studies involving human participants were reviewed and approved by the medical ethics committee of The Netherlands; Cancer Institute METC19.1644/N18BREL. The patients/participants provided their written informed consent to participate in this study.

AUTHOR CONTRIBUTIONS

EK, PH, MN, FP and UH contributed to the conception and design of the study. VP, MN, FP, and UH contributed to the acquisition of data for the study. EK, PH, and UH contributed to the analysis and interpretation of data for the study. EK wrote the first draft of the manuscript. All authors contributed to manuscript revision, read, and approved the submitted version.

FUNDING

This research was funded by ITEA3 project 16016 'STARLIT'. UH receives research support from Philips Healthcare and Elekta AB. The funder Elekta AB was not involved in the study design, collection, analysis, interpretation of data, the writing of this article or the decision to submit it for publication.

ACKNOWLEDGMENTS

The authors would like to thank Mutamba T. Kayembe, PhD for his input on the statistical analysis.

SUPPLEMENTARY MATERIAL

The Supplementary Material for this article can be found online at: https://www.frontiersin.org/articles/10.3389/fonc.2022.897130/full#supplementary-material

REFERENCES

1. Zahra MA, Hollingsworth KG, Sala E, Lomas DJ, Tan LT. Dynamic Contrast-Enhanced MRI as a Predictor of Tumour Response to Radiotherapy. *Lancet Oncol* (2007) 8:63–74. doi: 10.1016/S1470-2045(06)71012-9
2. García-Figueiras R, Baleato-González S, Padhani AR, Luna-Alcalá A, Vallejo-Casas JA, Sala E, et al. How Clinical Imaging Can Assess Cancer Biology. *Insights Into Imaging* (2019) 10:28. doi: 10.1186/s13244-019-0703-0
3. Hompland T, Hakon Hole K, Ragnum HB, Aarnes E-K, Vlatkovic L, Lie AK, et al. Combined MR Imaging of Oxygen Consumption and Supply Reveals Tumor Hypoxia and Aggressiveness in Prostate Cancer Patients. *Cancer Res* (2018) 78:4774–86. doi: 10.1158/0008-5472.CAN-17-3806
4. O'Connor JPB, Robinson SP, Waterton JC. Imaging Tumour Hypoxia With Oxygen-Enhanced MRI and BOLD MRI. *Br J Radiol* (2019) 92:20180642. doi: 10.1259/bjr.20180642
5. Cao Y. The Promise of Dynamic Contrast-Enhanced Imaging in Radiation Therapy. *Semin Radiat Oncol* (2011) 21:147–56. doi: 10.1016/j.semradonc.2010.11.001
6. Park JJ, Kim CK, Park SY, Simonetti AW, Kim EJ, Park BK, et al. Assessment of Early Response to Concurrent Chemoradiotherapy in Cervical Cancer: Value of Diffusion-Weighted and Dynamic Contrast-Enhanced MR Imaging. *Magn Reson Imaging* (2014) 32:993–1000. doi: 10.1016/j.mri.2014.05.009
7. Xie T, Ye Z, Pang P, Shao G. Quantitative Multiparametric MRI May Augment the Response to Radiotherapy in Mid-Treatment Assessment of Patients With Esophageal Carcinoma. *Oncol Res Treat* (2019) 42:326–33. doi: 10.1159/000499322
8. Wang P, Popovtzer A, Eisbruch A, Cao Y. An Approach to Identify, From DCE MRI, Significant Subvolumes of Tumors Related to Outcomes in Advanced Head-and-Neck Cancer. *Med Phys* (2012) 39:5277–85. doi: 10.1118/1.4737022
9. Baer AH, Hoff BA, Srinivasan A, Galbán CJ, Mukherji SK. Feasibility Analysis of the Parametric Response Map as an Early Predictor of Treatment Efficacy in Head and Neck Cancer. *Am J Neuroradiol* (2015) 36:757–62. doi: 10.3174/ajnr.A4296
10. Wong KH, Panek R, Dunlop A, Mcquaid D, Riddell A, Welsh LC, et al. Changes in Multimodality Functional Imaging Parameters Early During Chemoradiation Predict Treatment Response in Patients With Locally Advanced Head and Neck Cancer. *Eur J Nucl Med Mol Imaging* (2018) 45:759–67. doi: 10.1007/s00259-017-3890-2
11. van Houdt PJ, Yang Y, van der Heide UA. Quantitative Magnetic Resonance Imaging for Biological Image-Guided Adaptive Radiotherapy. *Front Oncol* (2021) 10:615643. doi: 10.3389/fonc.2020.615643
12. van Houdt PJ, Saeed H, Thorwarth D, Fuller CD, Hall WA, McDonald BA, et al. Integration of Quantitative Imaging Biomarkers in Clinical Trials for MR-Guided Radiotherapy: Conceptual Guidance for Multicentre Studies From the MR-Linac Consortium Imaging Biomarker Working Group. *Eur J Cancer* (2021) 153:64–71. doi: 10.1016/j.ejca.2021.04.041
13. Gurney-Champion OJ, Mahmood F, van Schie M, Julian R, George B, Philippens MEP, et al. Quantitative Imaging for Radiotherapy Purposes. *Radioth Oncol* (2020) 146:66–75. doi: 10.1016/j.radonc.2020.01.026
14. Yang Y, Cao M, Sheng K, Gao Y, Chen A, Kamrava M, et al. Longitudinal Diffusion MRI for Treatment Response Assessment: Preliminary Experience Using an MRI-Guided Tri-Cobalt 60 Radiotherapy System. *Med Phys* (2016) 43:1369–73. doi: 10.1118/1.4942381
15. Kooreman ES, van Houdt PJ, Keesman R, van Pelt VWJ, Nowee ME, Pos F, et al. Daily Intravoxel Incoherent Motion (IVIM) In Prostate Cancer Patients During MR-Guided Radiotherapy—A Multicenter Study. *Front Oncol* (2021) 11:705964. doi: 10.3389/fonc.2021.705964
16. Lawrence LSP, Chan RW, Chen H, Keller B, Stewart J, Ruschin M, et al. Accuracy and Precision of Apparent Diffusion Coefficient Measurements on a 1.5 T MR-Linac in Central Nervous System Tumour Patients. *Radioth Oncol* (2021) 164:155–62. doi: 10.1016/j.radonc.2021.09.020
17. Le Bihan D. What Can We See With IVIM MRI? *Neuroimage* (2019) 187:56–67. doi: 10.1016/j.neuroimage.2017.12.062
18. Le Bihan D, Breton E, Lallemand D, Aubin ML, Vignaud J, Laval-Jeantet M. Separation of Diffusion and Perfusion in Intravoxel Incoherent Motion MR Imaging. *Radiology* (1988) 168:497–505. doi: 10.1148/radiology.168.2.3393671
19. Federau C. Intravoxel Incoherent Motion MRI as a Means to Measure *In Vivo* Perfusion: A Review of the Evidence. *NMR BioMed* (2017) 30:1–15. doi: 10.1002/nbm.3780
20. Joo I, Lee JM, Grimm R, Han JK, Choi BI. Monitoring Vascular Disrupting Therapy in a Rabbit Liver Tumor Model: Relationship Between Tumor Perfusion Parameters at IVIM Diffusion-Weighted MR Imaging and Those at Dynamic Contrast-Enhanced MR Imaging1. *Radiology* (2016) 278:104–13. doi: 10.1148/radiol.2015141974
21. Raaymakers BW, Lagendijk JJW, Overweg J, Kok JGM, Raaijmakers AJE, Kerkhof EM, et al. Integrating a 1.5 T MRI Scanner With a 6 MV Accelerator: Proof of Concept. *Phys Med Biol* (2009) 54:N229–37. doi: 10.1088/0031-9155/54/12/N01

22. Hoogcarspel SJ, Zijlema SE, Tijssen RHN, Kerkmeijer LGW, Jürgenliemk-Schulz IM, Lagendijk JJW, et al. Characterization of the First RF Coil Dedicated to 1.5 T MR Guided Radiotherapy. *Phys Med Biol* (2018) 63:025014. doi: 10.1088/1361-6560/aaa303
23. Kooreman ES, van Houdt PJ, Keesman R, Pos FJ, van Pelt VWJ, Nowee ME, et al. ADC Measurements on the Unity MR-Linac – A Recommendation on Behalf of the Elekta Unity MR-Linac Consortium. *Radioth Oncol* (2020) 153:106–13. doi: 10.1016/j.radonc.2020.09.046
24. Wang J, Salzillo T, Jiang Y, Mackeyev Y, David Fuller C, Chung C, et al. Stability of MRI Contrast Agents in High-Energy Radiation of a 1.5T MR-Linac. *Radioth Oncol* (2021) 161:55–64. doi: 10.1016/j.radonc.2021.05.023
25. Turkbey B, Rosenkrantz AB, Haider MA, Padhani AR, Villeirs G, Macura KJ, et al. Prostate Imaging Reporting and Data System Version 2.1: 2019 Update of Prostate Imaging Reporting and Data System Version 2. *Eur Urol* (2019) 76:340–51. doi: 10.1016/j.eururo.2019.02.033
26. B Taouli ed. *Extra-Cranial Applications of Diffusion-Weighted MRI*. Cambridge: Cambridge University Press (2010). doi: 10.1017/CBO9780511778070
27. Schabel MC, Parker DL. Uncertainty and Bias in Contrast Concentration Measurements Using Spoiled Gradient Echo Pulse Sequences. *Phys Med Biol* (2008) 53:2345–73. doi: 10.1088/0031-9155/53/9/010
28. Zhang X, Petersen ET, Ghariq E, De Vis JB, Webb AG, Teeuwisse WM, et al. *In Vivo* Blood T1 Measurements at 1.5 T, 3 T, and 7 T. *Magn Reson Med* (2013) 70:1082–6. doi: 10.1002/mrm.24550
29. Rohrer M, Bauer H, Mintorovitch J, Requardt M, Weinmann H-J. Comparison of Magnetic Properties of MRI Contrast Media Solutions at Different Magnetic Field Strengths. *Invest Radiol* (2005) 40:715–24. doi: 10.1097/01.rli.0000184756.66360.d3
30. Georgiou L, Wilson DJ, Sharma N, Perren TJ, Buckley DL. A Functional Form for a Representative Individual Arterial Input Function Measured From a Population Using High Temporal Resolution DCE MRI. *Magn Reson Med* (2019) 81:1955–63. doi: 10.1002/mrm.27524
31. Chang LC, Cheng GK, Basser PJ, Pierpaoli C. Linear Least-Squares Method for Unbiased Estimation of T1 From SPGR Signals. *Magn Reson Med* (2008) 60:496–501. doi: 10.1002/mrm.21669
32. Cheong LH, Koh TS, Hou Z. An Automatic Approach for Estimating Bolus Arrival Time in Dynamic Contrast MRI Using Piecewise Continuous Regression Models. *Phys Med Biol* (2003) 48(5):N83–N88. doi: 10.1088/0031-9155/48/5/403
33. Tofts PS, Brix G, Buckley DL, Evelhoch JL, Henderson E, Knopp MV, et al. Estimating Kinetic Parameters From Dynamic Contrast-Enhanced T1-Weighted MRI of a Diffusable Tracer: Standardized Quantities and Symbols. *J Magn Reson Imag* (1999) 10:223–32. doi: 10.1002/(SICI)1522-2586(199909)10
34. Murase K. Efficient Method for Calculating Kinetic Parameters Using T1-Weighted Dynamic Contrast-Enhanced Magnetic Resonance Imaging. *Magn Reson Med* (2004) 51:858–62. doi: 10.1002/mrm.20022
35. Bakdash JZ, Marusich LR. Repeated Measures Correlation. *Front Psychol* (2017) 8:456. doi: 10.3389/fpsyg.2017.00456
36. He N, Li Z, Li X, Dai W, Peng C, Wu Y, et al. Intravoxel Incoherent Motion Diffusion-Weighted Imaging Used to Detect Prostate Cancer and Stratify Tumor Grade: A Meta-Analysis. *Front Oncol* (2020) 10:1623. doi: 10.3389/fonc.2020.01623
37. Gao P, Shi C, Zhao L, Zhou Q, Luo L. Differential Diagnosis of Prostate Cancer and Noncancerous Tissue in the Peripheral Zone and Central Gland Using the Quantitative Parameters of DCE-MRI. *Med (US)* (2016) 95(52): e5715. doi: 10.1097/MD.0000000000005715
38. Dinis Fernandes C, van Houdt PJ, Heijmink SWTPJ, Walraven I, Keesman R, Smolic M, et al. Quantitative 3T Multiparametric MRI of Benign and Malignant Prostatic Tissue in Patients With and Without Local Recurrent Prostate Cancer After External-Beam Radiation Therapy. *J Magn Reson Imaging* (2019) 50:269–78. doi: 10.1002/jmri.26581
39. Le Bihan D, Turner R. The Capillary Network: A Link Between IVIM and Classical Perfusion. *Magn Reson Med* (1992) 27:171–8. doi: 10.1002/mrm.1910270116
40. Pang Y, Turkbey B, Bernardo M, Kruecker J, Kadoury S, Merino MJ, et al. Intravoxel Incoherent Motion MR Imaging for Prostate Cancer: An Evaluation of Perfusion Fraction and Diffusion Coefficient Derived From Different B -Value Combinations. *Magn Reson Med* (2013) 69:553–62. doi: 10.1002/mrm.24277
41. Blyth CR. On Simpson's Paradox and the Sure-Thing Principle. *J Am Stat Assoc* (1972) 67:364–6. doi: 10.1080/01621459.1972.10482387
42. Shukla-Dave A, Obuchowski NA, Chenevert TL, Jambawalikar S, Schwartz LH, Malyarenko D, et al. Quantitative Imaging Biomarkers Alliance (QIBA) Recommendations for Improved Precision of DWI and DCE-MRI Derived Biomarkers in Multicenter Oncology Trials. *J Magn Reson Imaging* (2019) 49: e101–21. doi: 10.1002/jmri.26518
43. Klawer EME, van Houdt PJ, Simonis FFJ, van den Berg CAT, Pos FJ, Heijmink SWTPJ, et al. Improved Repeatability of Dynamic Contrast-Enhanced MRI Using the Complex MRI Signal to Derive Arterial Input Functions: A Test-Retest Study in Prostate Cancer Patients. *Magn Reson Med* (2019) 81:3358–69. doi: 10.1002/mrm.27646
44. Klawer EME, Houdt PJ, Simonis FFJ, den Berg CAT, Pos FJ, Heijmink SWTPJ, et al. Erratum to: Improved Repeatability of Dynamic Contrast-Enhanced MRI Using the Complex MRI Signal to Derive Arterial Input Functions: A Test-Retest Study in Prostate Cancer Patients (Magn Reson Med. 2019; 81: 3358–3369). *Magn Reson Med* (2021) 85:2334–6. doi: 10.1002/mrm.28606
45. Alonzi R, Taylor NJ, Stirling JJ, D'Arcy JA, Collins DJ, Saunders MI, et al. Reproducibility and Correlation Between Quantitative and Semiquantitative Dynamic and Intrinsic Susceptibility-Weighted MRI Parameters in the Benign and Malignant Human Prostate. *J Magn Reson Imaging* (2010) 32:155–64. doi: 10.1002/jmri.22215
46. Cohen J, Cohen P, West SG, Aiken LS. *Applied Multiple Regression/Correlation Analysis for the Behavioral Sciences. 3rd ed*. Lawrence Erlbaum Associates, Inc. 10 Industrial. New Jersey: Avenue Mahwah (2003).

Conflict of Interest: The Netherlands Cancer Institute is a member of the Elekta MR-linac consortium, which aims to coordinate international collaborative research relating to the Elekta Unity (MR-linac). Elekta and Philips are commercial partners within the consortium. Elekta financially supports consortium member institutions with research funding and travel costs for consortium meetings.

The authors declare that the research was conducted in the absence of any commercial or financial relationships that could be construed as a potential conflict of interest.

Publisher's Note: All claims expressed in this article are solely those of the authors and do not necessarily represent those of their affiliated organizations, or those of the publisher, the editors and the reviewers. Any product that may be evaluated in this article, or claim that may be made by its manufacturer, is not guaranteed or endorsed by the publisher.

frontiers | Frontiers in Oncology

ORIGINAL RESEARCH
published: 16 June 2022
doi: 10.3389/fonc.2022.860641

Clinical Evaluation of Fiducial Marker Pre-Planning for Virtual Bronchoscopic Navigation Implantation in Lung Tumour Patients Treated With CyberKnife

*Ki Man Ku[1,2], Bing Lam[3], Vincent W. C. Wu[1], Kwok Ting Chan[4], Chloe Y. Y. Chan[4], H. C. Cheng[5], Kamy M. Y. Yuen[2] and Jing Cai[1,6]**

[1] Department of Health Technology and Informatics, The Hong Kong Polytechnic University, Hong Kong, Hong Kong SAR, China, [2] Hong Kong Radiation Therapy Company Limited, Hong Kong, Hong Kong SAR, China, [3] Respiratory Medicine Centre, Hong Kong Sanatorium and Hospital, Hong Kong, Hong Kong SAR, China, [4] Department of Radiotherapy, Hong Kong Sanatorium and Hospital, Hong Kong, Hong Kong SAR, China, [5] Hong Kong Medical Physics Consulting Company Limited, Hong Kong, Hong Kong SAR, China, [6] Research Institute for Smart Aging, The Hong Kong Polytechnic University, Hong Kong, Hong Kong SAR, China

OPEN ACCESS

Edited by:
James Chow,
University of Toronto, Canada

Reviewed by:
Askin Gülsen,
University of Lübeck, Germany
Zetian Shen,
Fourth Affiliated Hospital of Nanjing Medical University, China

***Correspondence:**
Jing Cai
jing.cai@polyu.edu.hk

Specialty section:
This article was submitted to Radiation Oncology, a section of the journal Frontiers in Oncology

Received: 23 January 2022
Accepted: 13 May 2022
Published: 16 June 2022

Citation:
Ku KM, Lam B, Wu VWC, Chan KT, Chan CYY, Cheng HC, Yuen KMY and Cai J (2022) Clinical Evaluation of Fiducial Marker Pre-Planning for Virtual Bronchoscopic Navigation Implantation in Lung Tumour Patients Treated With CyberKnife. Front. Oncol. 12:860641. doi: 10.3389/fonc.2022.860641

Purpose: For the treatment of invisible lung tumours with CyberKnife (CK), fiducial markers (FMs) were implanted as an internal surrogate under virtual bronchoscopic navigation (VBN). This research aims to study the benefits of introducing an additional procedure in assigning the optimal FM positions using a pre-procedure planning system and performing virtual simulation before implantation. The objectives were 1) to reduce the duration of the FM implantation procedure, 2) to reduce the radiation exposure in dose area product (DAP) (dGy*cm^2) to patients, and 3) to increase the number of FMs implanted around the tumour.

Methods and Materials: This study is retrospective, single-centre, and observational in nature. A total of 32 patients were divided into two groups. In Group 1, 18 patients underwent conventional VBN FM implantation. In Group 2, 14 patients underwent additional pre-procedure planning and simulation. The steps of pre-procedure planning include 1) importing CT images into the treatment planning system (Eclipse, Varian Medical Systems, Inc.) and delineating five to six FMs in their ideal virtual positions and 2) copying the FM configuration into VBN planning software (LungPoint Bronchus Medical, Inc.) for verification and simulation. Finally, the verified FMs were deployed through VBN with the guidance of the LungPoint planning software.

Results: A total of 162 FMs were implanted among 35 lesions in 32 patients aged from 37 to 92 (median = 66; 16 men and 16 women). Results showed that 1) the average FM insertion time was shortened from 41 min (SD = 2.05) to 23 min (SD = 1.25), p = 0.00; 2) the average absorbed dose of patients in DAP was decreased from 67.4 cGy*cm^2 (SD = 14.48) to 25.3 cGy*cm^2 (SD = 3.82), p = 0.01 (1-tailed); and 3) the average number of FMs implanted around the tumour was increased from 4.7 (SD = 0.84) to 5.6 (SD = 0.76), p = 0.00 (1-tailed).

Conclusion: Pre-procedure planning reduces the FM implantation duration from 41.1 to 22.9 min, reduces the radiation exposure in DAP from 67.4 to 25.3 dGy*cm^2, and increases the number of FMs inserted around the tumour from 4.7 to 5.6.

Keywords: CyberKnife, fiducial marker, virtual bronchoscopic navigation, lung cancer, dose area product

INTRODUCTION

Lung stereotactic body radiation therapy (SBRT) is an advanced radiotherapy technique that delivers high and ablative doses of radiation to lung cancer patients as well as patients with metastatic lung tumours in an oligometastatic state, where the metastases are limited in number and location, with high precision (1–3). CyberKnife (CK) (Accuray, Inc., Sunnyvale, CA, USA) SBRT system uses a seamless integration of periodic X-ray imaging for internal target tracking integrated with Synchrony, which is an optical image guidance system for external respiratory motion tracking (4–6). Previous studies showed excellent local control at 1- and 2-year follow-ups for patients treated with CK SBRT (7–12).

Effective internal target tracking requires the implantation of metallic fiducial markers (FMs), which act as internal surrogates of the tumour's position and motion, before radiotherapy planning. The FM implantation procedure was performed under monitored anaesthesia care (MAC) in the Endoscopy Department by respiratory medicine specialists using either virtual bronchoscopic navigation (VBN) (13) or electromagnetic navigation bronchoscopy (ENB) (14). The VBN/ENB is designed as a Global Positioning System (GPS) to guide bronchoscopic tools to the predefined tumour location or until the tumour is visible. Efficiently placing an adequate number of FMs around the tumour can be challenging. When there were no strategies or standardized guidelines on VBN/ENB implantation, doctors have to navigate around the tumour through small bronchi and look for feasible locations under X-ray images or fluoroscopies by a C-arm machine. As a result, the overall procedure time for the FM implantation is prolonged, and the patient is exposed to a large amount of radiation from X-ray images or fluoroscopies. Furthermore, it is difficult for doctors to deploy an ideal amount of 5–6 FMs. Additionally, while searching the related literature, we found very limited references focusing on the standardized FM implantation procedure. Many studies investigated the FM implantation methods and their resulting complications, as well as the marker retention and migration rates (15–17). Some studies investigated the co-relationship between FMs and tumours to predict how well the FM configuration represents the tumour motion and to determine the desirable FM configuration (18, 19). However, few studies have described how to implant the FMs into desirable and appropriate positions and determined the FM configuration that best represents the tumour motion. In a more recent study, investigators showed that using an FM placement guidance system may increase the number of FMs being tracked (20).

To cope with the above difficulties, we introduced additional pre-procedure planning before the FM implantation in March 2019. Pre-procedure planning aims to predefine the proper positions and ideal configurations of the FMs. By doing this, we expected that the time of the FM implantation procedure could be reduced, which resulted in shorter MAC time and less radiation exposure to the patient and staff (20). We also expected that more FMs could be placed around the tumour to better represent the tumour motion (18, 19). This study aims to evaluate whether pre-procedure planning of optimal FM positions could improve the overall efficiency of FM implantation and increase the number of FMs implanted around the tumour. In particular, we try to answer the following questions in our investigation: 1) whether the proposed procedure can reduce the duration of the FM implantation procedure, 2) whether the proposed procedure can reduce the radiation exposure to the patient as well as staff during the FM implantation procedure, and 3) whether we can increase the number of FMs implanted around the tumour.

METHODS AND MATERIALS

Types of the Study and Patient Recruitment

This study is retrospective, single-centre, and observational in nature. The study proposal was submitted to and approved by the Research Ethics Committee of the Hong Kong Sanatorium and Hospital Group, and the Human Subjects Ethics Application Review System of the Hong Kong Polytechnic University. Patients with lung tumours and referred for CK treatment with fiducial tracking and those whose FMs will be implanted using VBN were included in this study. Patients who already had FMs in their lungs from previous CK treatment and those whose FMs will be used again for current CK treatment were excluded from this study. A total of 32 patients with lung tumours were referred for FM implantation using VBN before CK treatment had been selected. They were divided into two groups according to the methods of FM implantation. The first group of 18 patients were those who underwent VBN FM implantation and were treated with CK from June 2017 to August 2019. The second group of 14 patients were those who underwent additional pre-procedure planning before the VBN FM implantation from March 2019 to July 2020.

Pre-Procedure Planning Steps

Pre-procedure planning involves two steps. The first step is to predefine 5–6 optimal FM positions around the tumour on the patient's CT images in Eclipse (Eclipse, Varian Medical Systems, Inc., Palo Alto, CA, USA) radiotherapy treatment planning system (TPS). The second step is to import the CT image set together with the predefined FM positions into a VBN procedure

planning system (LungPoint Bronchus Medical, Inc., San Jose, CA, USA) for verification and simulation. FMs were then deployed through VBN implantation like previously, but this time with the guidance of a procedure planning system. For the second group of 14 patients who underwent pre-procedure planning, a set of low-dose CTs was performed and imported into the Eclipse RT planning system for an oncologist to delineate the preliminary target. After that, 5–6 predefined optimal FM positions were also contoured around the preliminary target. The procedures and guidelines of the FM contouring were as follows:

1. Delineate each of the FMs with a 0.5-cm-diameter sphere around the tumour and then label them as FM1 to FM5/6.

2. Keep the distance between each FM and the tumour between 1 and 3 cm. This can be performed by creating a pseudo-structure by expanding the tumour to 1 to 3 cm, depending on the size of the tumour and contouring the FMs on the circumference of the pseudo-structure. Although the co-relationship between the FMs and the tumour is better if the distance between them is shorter, the distance between any two individual FMs may be too short or less than the 18 mm, which is the minimum inter-FM distance required for CK tracking. Generally, for a tumour volume of 1 cc or less, a pseudo-structure should be created by expanding the tumour by 3 cm. For a tumour volume ranging from 1 to 3 cc, the pseudo-structure should be created by expanding the tumour by 2 cm. For a tumour volume of 3 cc or more, the pseudo-structure should be created by expanding the tumour by 1 cm.

3. Delineate the FMs as distal as possible in the small bronchi to increase the chance of fixation.

4. For tumours located in the middle of the lung with at least 2 cm of circumferential lung tissues, delineate 6 FMs and arrange the FMs, as follows (**Figure 1**):

a. Delineate two FMs to the most superior and inferior points of the pseudo-structure created from tumour expansion.
b. At a one-third longitudinal position from the superior point, delineate the other two FMs at either the left/right or anterior/posterior points of the pseudo-structure created from tumour expansion.
c. Delineate the last two FMs at the two-thirds longitudinal position from the superior point, in a perpendicular position opposing the previous pair and within the pseudo-structure created from tumour expansion.

5. For peripheral lung tumours with at least one side of the tumour not possible for FM implant, delineate 5 FMs and arrange the FMs, as follows (**Figure 2**):

a. Delineate two FMs to the most superior and inferior points if the blocked zone is at the circumferential tumour location or to either left/right or anterior/posterior if the blocked zone is located at the cranial–caudal directions, within the pseudo-structure created from the tumour expansion.
b. Evenly distribute the remaining 3 FMs at the most distal circumference of the pseudo-structure created from and at the opposite side of the blocked zone of the tumour.

6. Create a set-up plan with two 450° and 3150° oblique fields to simulate the two X-ray imaging views in CK, and review the FM configuration to obtain the following (**Figure 3**):

a. The minimum distance between each pair of FMs is larger than 18 mm in three-dimensional (3D) space.
b. The minimum angle between a triplet of fiducials should be at least 15°.

7. After the optimal FM positions in the Eclipse RT planning system are defined, import the low-dose CT again into another system, the LungPoint VBN procedure planning system (2018 version, Bronchus Medical, Inc., San Jose, CA, USA).

8. In the LungPoint system, generate the patient's bronchial tree automatically with the procedure planning system.

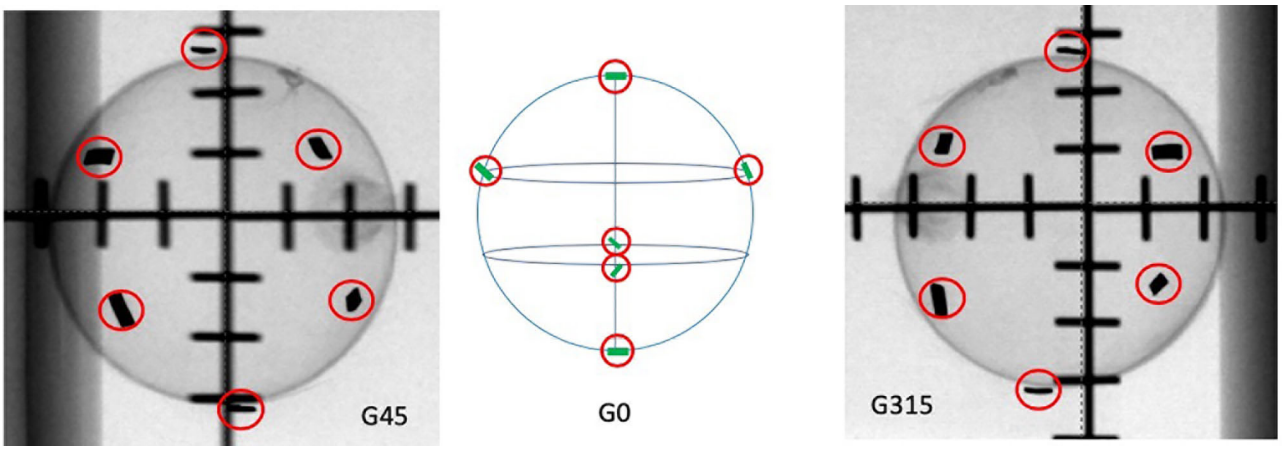

FIGURE 1 | The tested ideal FM configurations. G45 represents the 45° oblique view. G0 is the graphical illustration of how the FMs are ideally distributed on the surface of a sphere. G315 represents the 315° oblique view.

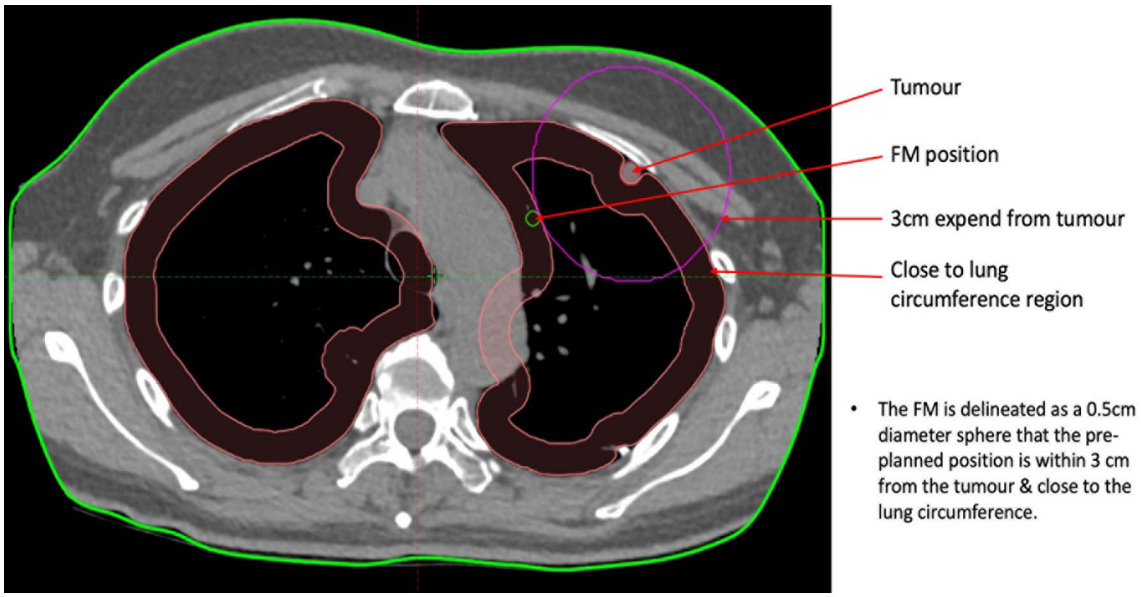

FIGURE 2 | Illustration of the guidelines for the pre-planned FM position.

9. Copy all the delineated FMs in the Eclipse RT planning system to the LungPoint procedure planning system manually.

10. Review the FMs' virtual positions to see if they are at or near the end of the most proximal small bronchi (**Figure 4**).

11. Press the play button. The system will then simulate the VBN process and guide the virtual bronchoscope to the target positions.

12. Assess and confirm that each of the pre-planned FM positions is reachable at the end of the simulation (**Figure 5**).

Fiducial Marker Implantation

All FMs, measured 0.8 × 5 mm (PointCoil MTCTXPC08) (**Figure 6**), were then implanted by a respiratory medicine specialist using VBN under the active guidance of the LungPoint procedure planning system.

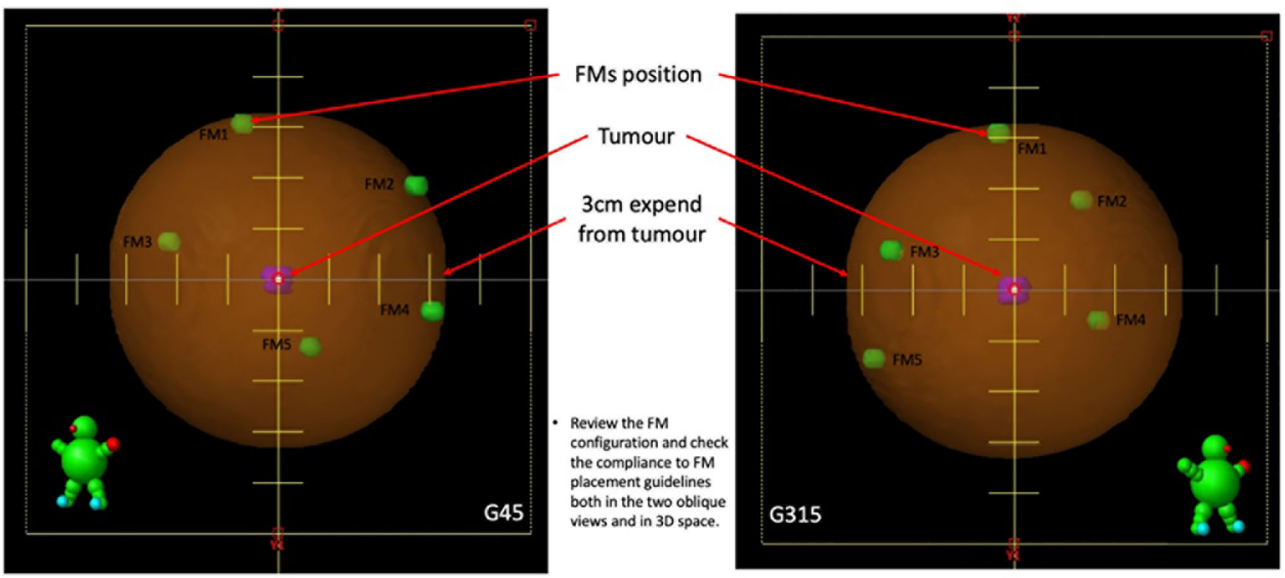

FIGURE 3 | Illustrations of the FM configuration review in the two oblique views.

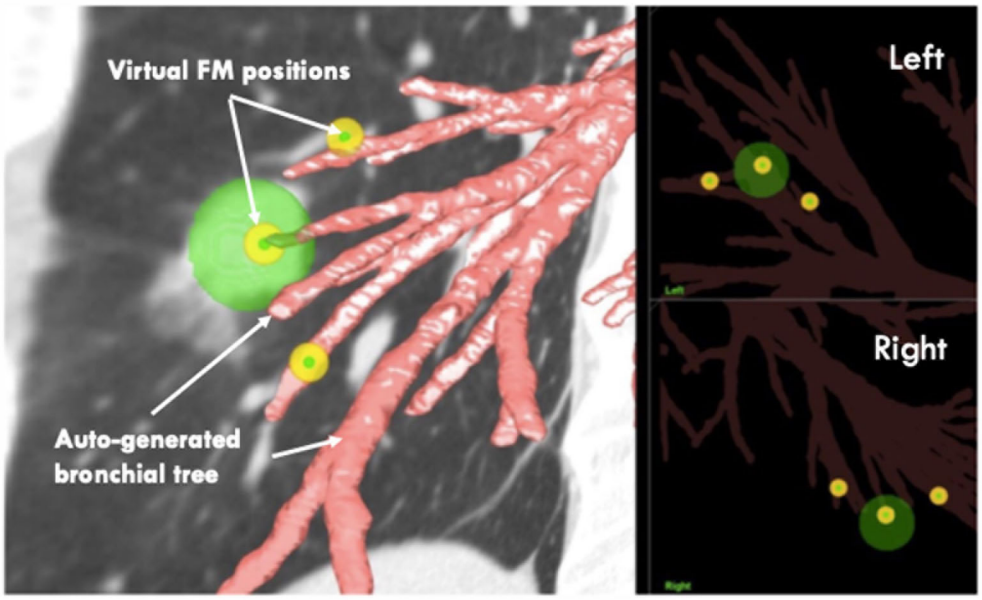

FIGURE 4 | Illustration of the autogenerated bronchial tree and the pre-planned FM positions.

Data Collection and Analysis

For the comparison of the FM implantation duration, the total time used for FM implantation with VBN for both groups was recorded. For the comparison of X-ray exposure to patients and staff, the dose area product (DAP) in $dGy*cm^2$, a quantity used in assessing the radiation risk from diagnostic X-ray examinations, was collected from the internal chamber of the manufacturer (Axiom Artis, Siemens, Munich, Germany) for each exposure for both groups. Furthermore, the total number of FMs implanted during the VBN session was collected and compared for each patient in both groups.

Data analysis was performed using Data Analyses, an add-in statistical tool of Microsoft Excel (Version 16.50, Microsoft 365 Subscription). A parametric, independent t-test was used to compare the means of the two groups of the patients. All p-values were two-sided. A p-value of less than 0.05 was statistically significant.

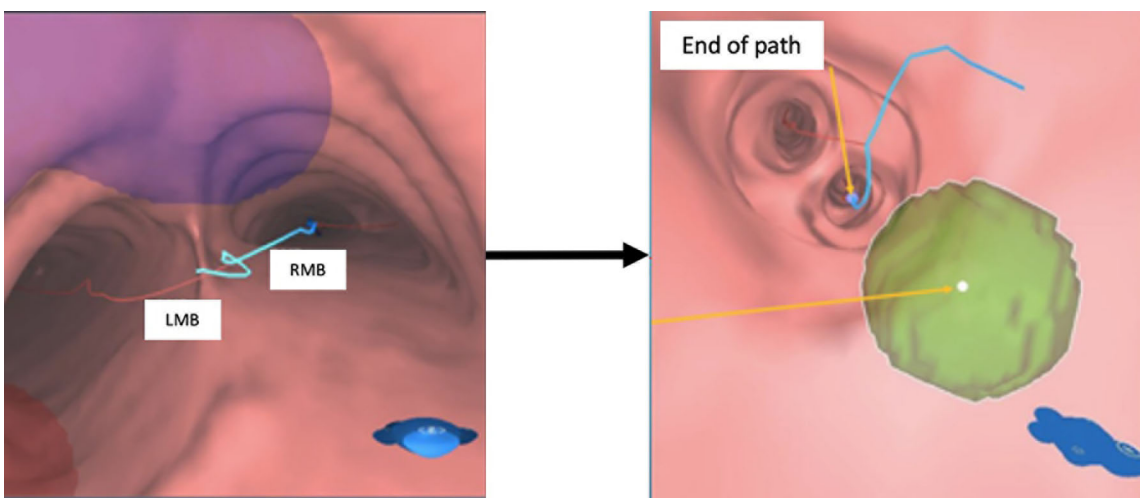

FIGURE 5 | VBN simulation in the pre-planning system. Left: animated simulation of the VBN guidance. Right: at the end of the route, virtual FM positions are reachable. VBN, virtual bronchoscopic navigation.

FIGURE 6 | PointCoil™ Marker is a 5-mm-long helical coil for IGRT. The design maximizes stability and minimizes artefacts. IGRT, image-guided radiotherapy.

RESULTS

A total of 32 patients (16 men and 16 women aged 37 to 92; median 59.5, SD = 16.58) were recruited for this study, and their demographics are summarized in **Table 1**. Twelve patients' lesions were centrally located, and 20 patients' lesions were peripherally located. There were 35 lesions in 32 patients, and a total of 162 FMs were inserted with no procedure-related complications noted.

For the insertion time comparison, the mean, minimum, maximum, and SD values of the procedure duration for both groups of patients are presented in **Table 2**. Results showed that the mean duration of FM implantation was reduced from 41.1 min (minimum 26.0 to maximum 56.0 min) for those without pre-procedure planning (Group 1) to 22.9 min (minimum 15.0 to maximum 30.0 min) for those with pre-procedure planning followed by VBN (Group 2). This difference was significant, p = 0.00 (1-tailed).

Figure 7 presents the duration frequencies of FM insertion for both groups of patients through a histogram. Results showed that for FM implantation without pre-procedure planning, most of the durations were from 35 to 55 min, while for FM

TABLE 1 | Patient demographic information.

Group	Gender	Age	Number of lesions	Side of lung	Location of tumour	Lobe of lung	FMs inserted
1	M	50	1	Rt	Central	RLL	4
1	M	82	1	Rt	Peripheral	RLL	3
1	F	53	1	Rt	Central	RLL	4
1	F	88	1	Rt	Central	RLL	5
1	M	53	1	Lt	Central	LUL	4
1	M	88	1	Lt	Peripheral	LLL	4
1	F	52	1	Lt	Peripheral	LLL	4
1	M	89	1	Rt	Central	RLL	4
1	M	88	1	Lt	Peripheral	LLL	5
1	F	53	1	Rt	Central	RUL	6
1	M	80	1	Rt	Central	RML	5
1	M	91	1	Lt	Peripheral	LUL	5
1	F	52	1	Rt	Peripheral	RML	6
1	M	84	1	Rt	Peripheral	RML	5
1	F	89	1	Lt	Central	LUL	5
1	F	48	1	Rt	Peripheral	RUL	6
1	M	65	1	Rt	Peripheral	RUL	4
1	M	65	1	Lt	Peripheral	LLL	5
2	F	54	2	Rt	Peripheral	RML	5
2	F	54	1	Lt	Peripheral	LLL	4
2	F	54	1	Lt	Peripheral	LLL	4
2	M	92	1	Rt	Peripheral	RLL	5
2	F	44	1	Rt	Peripheral	RUL	6
2	M	68	1	Rt	Peripheral	RLL	6
2	F	59	1	Lt	Peripheral	LLL	6
2	F	59	1	Lt	Peripheral	LUL	6
2	M	77	1	Lt	Central	LUL	6
2	M	52	2	Rt	Central	RUL	6
2	F	60	1	Lt	Peripheral	LUL	6
2	F	37	1	Lt	Peripheral	LLL	6
2	F	73	1	Rt	Central	RLL	6
2	M	52	2	Rt	Central	RUL	6

FMs, fiducial markers; RLL, right lower lobe; LUL, left upper lobe; LLL, left lower lobe; RUL, right upper lobe; RML, right middle lobe.

TABLE 2 | The procedure durations of both groups of patients (min).

	Group 1	Group 2
Mean	41.1	22.9
SD	8.7	4.7
Minimum	26.0	15.0
Maximum	56.0	30.0
Count	18.0	14.0

implantation with additional pre-procedure planning, all durations ranged from 15 to 30 min.

For the radiation exposure comparison, the mean, minimum, maximum, and SD values of the DAP (dGy*cm^2) are presented in **Table 3**. Results showed that the mean DAP of FM implantation was reduced from 67.4 (minimum 10.9 to maximum 217.6 dGy*cm^2) for those without pre-procedure planning (Group 1) to 25.3 (minimum 9.0 to maximum 47.2 dGy*cm^2) for those with pre-procedure planning followed by VBN (Group 2). This difference was significant, p = 0.01 (1-tailed).

Figure 8 presents the DAP frequency of FM insertion for both groups of patients through a histogram. Results showed that for FM implantation without pre-procedure planning, the DAPs were widely spread from 10 to 130 with 1 extreme case of more than 200 dGy*cm^2, while for FM implantation with additional pre-procedure planning, all DAPs were confined within 10 to 50 except one with 9.0 dGy*cm^2.

For the number of FMs implanted, the mean number of FMs inserted was increased from 4.7 for implantation without pre-procedure planning to 5.6 for implantation with additional pre-procedure planning. Meanwhile, the percentage of patients inserted with 5 to 6 ideal numbers of FMs was increased from 56% to 86%. This difference was significant, p = 0.00 (1-tailed).

Figure 9 presents the frequencies of FMs inserted for both groups of patients through a histogram. Results showed that for FM implantation without pre-procedure planning, the number of FMs inserted was widely spread from 3 to 6 and mostly 4 or 5, while for FM implantation with additional pre-procedure planning, most patients were inserted with the maximum amount of 6 FMs.

TABLE 3 | The DAP of both groups of patients (dGy*cm^2).

DAP (dGy*cm^2)	Group 1	Group 2
Mean	67.4	25.3
SD	56.1	13.8
Minimum	10.9	9.0
Maximum	217.6	47.2
Count	18.0	14.0

DAP, dose area product.

DISCUSSION

Respiratory motion is a major challenge for precision radiotherapy of lung cancer (21). Studies have shown that inaccurate tumour motion measurement and tracking can lead to errors in target volume determination and subsequently dose delivery (22, 23). FMs allow for reliable and accurate determination of the lung tumour's position and motion, and they have the potential to significantly improve treatment safety and outcome (24). In our centre, FM implantation is an essential procedure for all patients with invisible lung lesions and to be treated with CK. In this study, we aim to use an additional procedure before FM implantation to improve the overall efficiency by reducing the time for implantation and radiation exposure to the patient and staff, as well as the quality of the implantation by increasing the number of FMs deployed around the lesion, which means a higher chance of trackability more representative of the tumour motion (25).

Tolerability and Complication

FMs can be implanted into the lung using two methods, transthoracic/percutaneous and transbronchial through the patient's respiratory tract. Research showed that percutaneous or CT-guided transthoracic insertion of FMs is associated with a high risk of pneumothorax (16, 26–28). In contrast,

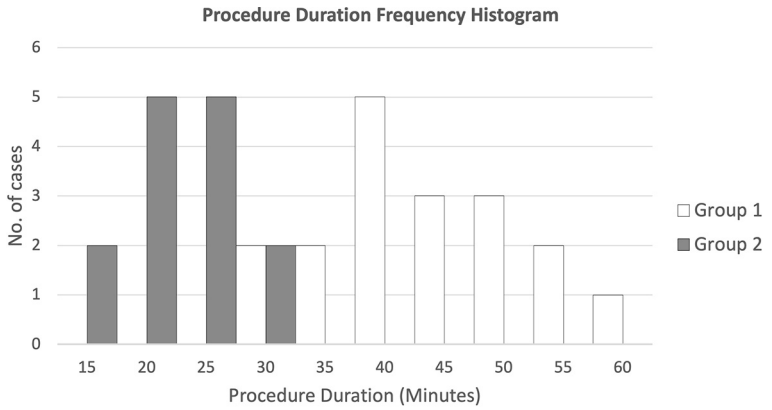

FIGURE 7 | Procedure duration frequency histogram for both groups of patients.

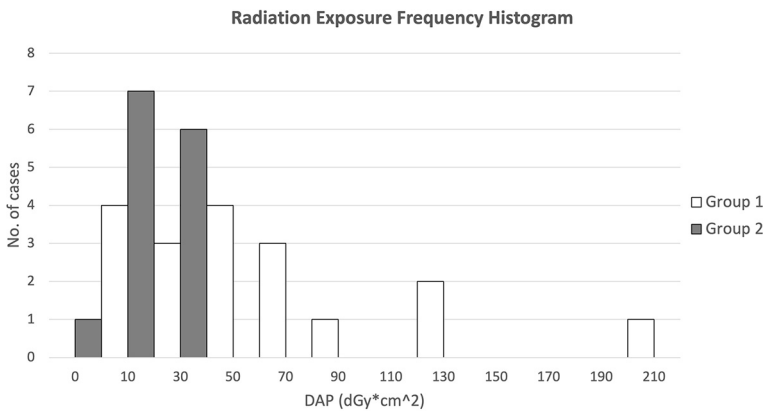

FIGURE 8 | The radiation exposure frequency histogram of both groups of patients (dGy*cm^2).

transbronchial FM implantation is much safer. A review of 5 studies using the transbronchial FM implantation method showed that 4 of them recorded 0% implantation-induced pneumothorax (14, 15, 29, 30), and the remaining one recorded 2.3% (31). Other recent studies showed that the rate of complication is usually associated with guided transbronchial biopsies (TBBs) performed before FM implantation (32, 33). In this study, there was neither bleeding nor pneumothorax in both groups of our patients after FM implantation with or without pre-procedure planning.

Improving the Fiducial Marker Insertion Efficiency

Previous FM insertions were complicated due to the absence of pre-procedure planning. The procedure is dependent on the experience and real-time decision making of a group of different health professionals, including an anaesthetist handling the patients' condition, a respiratory specialist manipulating the bronchoscope and navigating inside patients' bodies to look for a good position for the FM, a medical physicist, and a radiation therapist from the CK team staying in the control room, giving advice and confirming the location for FM deployment. With pre-procedure planning, we can decide where and how many FMs can be inserted and what will be the overall resulting configuration. We will also be aware of the possibility that one or more directions could not be feasible for FM deployment or that there are no small bronchi for FMs to be firmly anchored to. Thus, the FM insertion procedure becomes simpler.

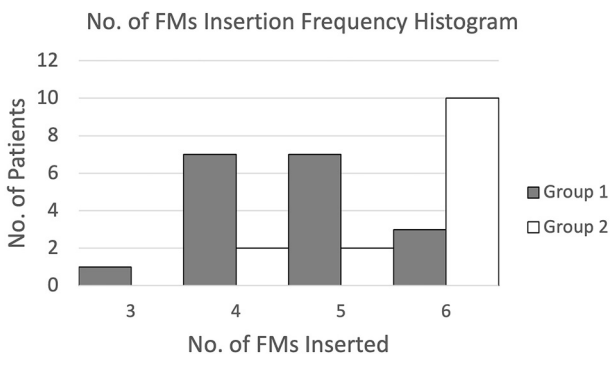

FIGURE 9 | Histogram of the number of FM insertion frequency.

The results of this study show that with pre-procedure planning, the average time of FM insertion can be reduced from 41.1 to 22.9 min or by 44% (median = 22.5 min). Furthermore, the overall procedure duration is more predictable, where 9 out of 14 patients' procedure times are within 20 to 25 min and the SD is reduced from 8.7 to 4.7 min. Improving efficiency brings several advantages. First, the time of patients under anaesthesia can be reduced. It is expected that the risk due to anaesthesia will also be reduced, and hopefully, this procedure can be tolerable by more patients. Second, utilization of the endoscopy room can be increased. With a shorter and more predictable duration, resource allocation will be more effective, and more patients can be arranged for endoscopy procedures. Furthermore, the cost of the procedure is expected to be reduced. The endoscopy room is one of the costliest components of a hospital, and a reduction in the procedure time is expected to be followed by a reduction in cost to patients, which results in a higher chance of continuing to enjoy organizational success.

In a more recently published study by Casutt et al. (2021) (33), the researchers evaluated FM implantation procedures using endobronchial insertion under fluoroscopy like ours but without pre-procedure planning. Their results showed that the median time of the procedure was 31.5 min (10-95 min). Our study showed a shorter duration (22.5 vs. 31 min) and a more consistent range of time (15–30 vs. 10–90 min). In addition, the average number of FMs implanted in Casutt's study was 3.0, while in our study, it was 5.6 with pre-procedure planning. The comparison reinforced that pre-procedure planning can improve FM implantation efficiency.

Reducing the Radiation Exposure

The main principle of radiation protection is to protect patients from unnecessary radiation and perform medical procedures with as low as reasonably achievable (ALARA) doses. In this study, we use the DAP measured during the examination as a quantitative tool to compare the radiation exposure of patients as well as staff during the FM insertion procedure.

The results of this study show that with pre-procedure planning, the average DAP is reduced from 67.4 to 25.3 $dGy*cm^2$ or by 62%. Furthermore, the overall radiation exposure to patient and staff become more consistent and predictable, which is shown by the reduced SD from 56.1 $dGy*cm^2$ in Group 1 patients to 13.8 $dGy*cm^2$ in Group 2 patients. This is largely due to the reduction in time of fluoroscopy. Because the location of FMs is predefined and the route to the designated location is guided by the VBN system, respiratory specialists can avoid frequent fluoroscopy during the procedure to locate the position of the endoscope and look for ways to the desired location. Furthermore, staff radiation exposure is expected to be reduced too, which also reduces the chance of staff overexposure resulting in manpower shortage.

Increasing the Number of Fiducial Markers Implanted

The lung tumour moves in all directions, and the amplitude can be up to 12 mm in the cranial–caudal direction (16). According to the CK guideline on FM placement, at least 3 FMs are required for 3D tumour tracking, while 4–6 are recommended for more secure and confident tumour motion tracking along with the CK treatment (34). Meanwhile, researchers also recommended implanting 4–6 FMs to improve marker reliability and tracking accuracy (35).

The results of this study show that the average number of FMs inserted only increased slightly from 4.7 to 5.6 with the application of pre-procedure planning. However, with the new workflow, 10 out of 14 patients can be inserted with 6 FMs, and no patient will be inserted with less than 4 FMs. This largely increases the reliability of the FMs in representing the true tumour motion and the confidence of continuous 3D tracking along with the treatment in considering the possibilities of FM migration.

The Effect on Target Trackability

Theoretically, we could expect better trackability based on the concept that with pre-procedure planning, the ideal locations of the FMs were preliminarily identified. The ideal locations could fulfil both the criteria that it should be at the distal end of small bronchi and located at a predefined distance away from the tumour, making a good overall configuration around the tumour, which means a higher chance of trackability. In reviewing this, we defined the trackability of the target or FMs by the number of FMs implanted to the number of FMs tracked when the CK treatment starts and compare the results of the two groups of patients.

Results showed that the trackability was increased from 41% (minimum 0% to maximum 75%) for patients without pre-procedure planning (Group 1) to 50% (minimum 33% to maximum 100%) for patients with pre-procedure planning (Group 2). However, the difference was insignificant, $p = 0.12$ (1-tailed). This could be explained by the patient-dependent nature of the probability of FM migration. For patients suffering from frequent coughing due to lung disease, migration or even loss of FMs is common.

The Values of This Study

FM tracking is the only choice for CK of non-small cell lung cancer (NSCLC) patients with small tumours that are invisible under the planar X-ray view. Real-time fiducial tracking together with Synchrony respiratory motion management results in excellent motion synchronized treatment with sub-millimetre margins to the targets (17). This study introduced a new set of implantation rules and guidelines that could become a helpful reference for other clinical centres using CK in SBRT. We expect that if the suggested pre-planned FM positions method is proved to be more effective, FM implantation procedures will be well-organized, and the results will be more predictable.

Assumptions and Limitations of the Study

There are some assumptions for this study. First, it is not possible to move all FMs in the same vectors and not cause differences in the FM centroid and displacement. Second, tumour shrinkage during the period of CK treatment is negligible. Although one previous study showed that the tumour will shrink during SBRT, the shrinkage rates were not necessarily uniform (18). In the present study, it is assumed that the size of the tumour remains unchanged. Therefore, all the FM displacements that will be measured after the CT images are fused are due to FM displacement.

This study also has some limitations. First, although an ideal FM configuration can be determined, it is nearly impossible to achieve. If the lung tumour is located near the lung circumference of the diaphragm, there will be a no-FM zone such as the chest wall and the diaphragm, which limits the all-around distribution of the FMs, resulting in an unevenly distributed FM arrangement and increasing the distance between the tumour and the FM centroid (**Figure 10**). Second, it is not well-known how close the VBN combined with ultrathin endoscopy-guided FM implantation can be to the pre-planned FM positions. It is assumed that the discrepancies between the two can be within 1 cm. Third, only small bronchi near the lung circumference are highly FM fixed. Therefore, only about one-third of the lung volumes are possible for FM implantation. Moreover, to some extent, the fixation of FMs was patient dependent. For example, coughing is one cause of FM migration. Patients with a coughing problem during the period of CK treatment may have a higher chance of FM migration and displacement. Finally, some patients have more than one tumour located close to each other. A set of FMs can be used to treat a combination of one or more tumours at the same time, but this will complicate the definition of the tumour centroid and the distance of the FM to the tumour.

Future Directions

The CK FM tracking system is complex. To achieve 6DOF FM tracking, criteria such as minimum distance between FM angles

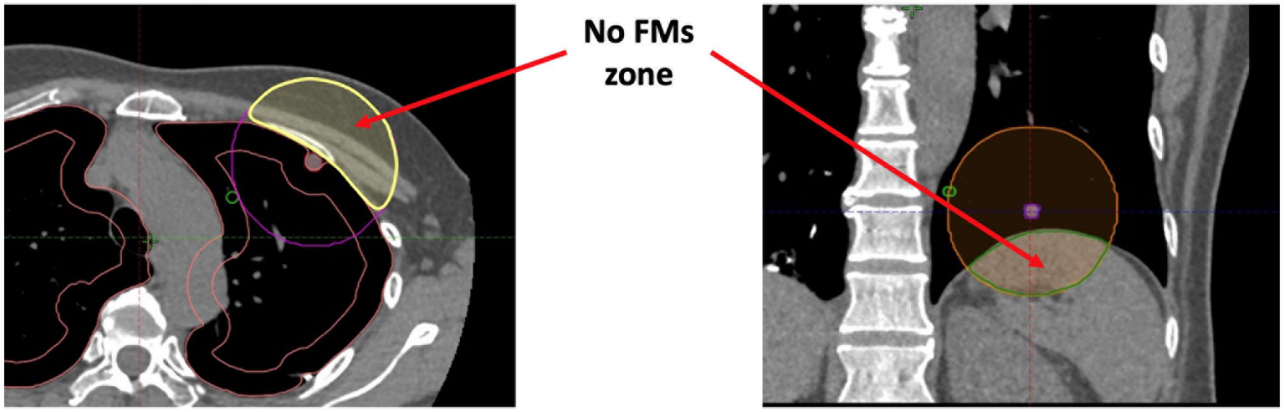

FIGURE 10 | The illustration of no-FM zone if the lung tumour is close to the lung circumference.

between FM configuration should all be fulfilled. However, there were no technical guidelines on how to implant FMs in fulfilling the CK tracking criteria. Furthermore, FMs cannot easily be fixed in the small bronchi after implantation. Future studies should focus on increasing FM stability and fixation by using different kinds of FMs and how to implant FMs into a designated position accurately. Moreover, future similar studies should consider increasing their sample size.

CONCLUSION

In this study, implementing additional pre-procedure planning before FM implantation improves the overall efficiency by reducing the duration from 41.1 to 22.9 min. Meanwhile, the new workflow reduces the radiation exposure by decreasing the DAP from 67.4 to 25.3 dGy*cm^2. Furthermore, the number of FMs inserted around the tumours is increased from 4.7 to 5.6, and the number of patients inserted with 5 or 6 FMs is increased from 56% to 86%.

DATA AVAILABILITY STATEMENT

The raw data supporting the conclusions of this article will be made available by the authors, without undue reservation.

ETHICS STATEMENT

The studies involving human participants were reviewed and approved by Hong Kong Sanatorium and Hospital Medical Group Research Ethics Committee, and Hong Kong Polytechnic University Ethics Committee. Written informed consent for participation was not required for this study in accordance with the national legislation and the institutional requirements.

AUTHOR CONTRIBUTIONS

KK proposed and developed the idea and wrote the manuscript. BL performed the procedure and helped obtain ethical approval. VW reviewed and commented on the proposal. KC and YC were responsible for data collection. HC and KY were responsible for data analysis. JC revised the manuscript and played a major role as a supervisor. All authors listed have made a substantial, direct, and intellectual contribution to the work and approved it for publication.

ACKNOWLEDGMENTS

We thank Dr. Bing Lam for the advice and assistance in obtaining ethical approval, and Mr. Dick Chan for his help in the project proposal application and follow-up. We also thank the nurses of the Endoscopy Centre, Dr. K. Y. Cheung and Mr. Tony Kong (medical physicists) of the Medical Physics and Research Department, and Ms. Miranda Poon and Ms. C. M. Wong (medical dosimetrists) of the Department of Radiotherapy of Hong Kong Sanatorium and Hospital for their invaluable input and evaluation and discussion of the results.

REFERENCES

1. Ashworth A, Rodrigues G, Boldt G, Palma D. Is There an Oligometastatic State in non-Small Cell Lung Cancer? A Systematic Review of the Literature. *Lung Cancer* (2013) 82(2):197–203. doi: 10.1016/j.lungcan.2013.07.026
2. Cai J, Malhotra HK, Orton CG. A 3D-Conformal Technique is Better Than IMRT or VMAT for Lung SBRT. *Med Phys (Lancaster)* (2014) 41(4):040601–n/a. doi: 10.1118/1.4856175
3. Macdermed DM, Weichselbaum RR, Salama JK. A Rationale for the Targeted Treatment of Oligometastases With Radiotherapy. *J Surg Oncol* (2008) 98:202–6. doi: 10.1002/jso.21102
4. Accuray Incorporation. Tracking Moving Targets and Introduction to Synchrony. (2015).
5. Chang Z, Liu T, Cai J, Chen Q, Wang Z, Yin FF. Evaluation of Integrated Respiratory Gating Systems on a Novalis Tx System. *J Appl Clin Med Phys* (2011) 12(3):71–9. doi: 10.1120/jacmp.v12i3.3495
6. Yang J, Lamond JP, Feng J, Wu X, Lanciano R, Brady LW. CyberKnife System. *Stereotactic Body Radiat Ther* (2012) 37–52. doi: 10.1007/174_2011_505
7. van der Voort van Zyp NC, Prévost J-B, Hoogeman MS, Praag J, van der Holt B, Levendag PC, et al. Stereotactic Radiotherapy With Real-Time Tumor Tracking for non-Small Cell Lung Cancer: Clinical Outcome. *Radiother Oncol* (2009) 91(3):296–300. doi: 10.1016/j.radonc.2009.02.011
8. Ng AW, Tung SY, Wong VY. Hypofractionated Stereotactic Radiotherapy for Medically Inoperable Stage I non-Small Cell Lung Cancer–Report on Clinical Outcome and Dose to Critical Organs. *Radiother Oncol* (2008) 87(1):24–8. doi: 10.1016/j.radonc.2008.02.015
9. Awano N, Ikushima S, Izumo T, Tone M, Fukuda K, Miyamoto S, et al. Efficacy and Safety of Stereotactic Body Radiotherapy Using CyberKnife in Stage I Primary Lung Tumor. *Jpn J Clin Oncol* (2017) 47(10):969–75. doi: 10.1093/jjco/hyx100
10. Janvary ZL, Jansen N, Baart V, Devillers M, Dechambre D, Lenaerts E, et al. Clinical Outcomes of 130 Patients With Primary and Secondary Lung Tumors Treated With Cyberknife Robotic Stereotactic Body Radiotherapy. *Radiol Oncol* (2017) 51(2):178–86. doi: 10.1515/raon-2017-0015
11. Khadige M, Salleron J, Marchesi V, Oldrini G, Peiffert D, Beckendorf V. Cyberknife ® Stereotactic Radiation Therapy for Stage I Lung Cancer and Pulmonary Metastases: Evaluation of Local Control at 24 Months. *J Thorac Dis* (2018) 10(8):4976–84. doi: 10.21037/jtd.2018.07.26
12. Virbel G, Le Fevre C, Noel G, Antoni D. Stereotactic Body Radiotherapy for Patients With Lung Oligometastatic Disease: A Five-Year Systematic Review. *Cancers* (2021) 13(14):3623. doi: 10.3390/cancers13143623
13. Asano F, Shinagawa N, Ishida T, Shindoh J, Anzai M, Tsuzuku A, et al. Virtual Bronchoscopic Navigation Combined With Ultrathin Bronchoscopy. A Randomized Clinical Trial. *Am J Respir Crit Care Med* (2013) 188(3):327. doi: 10.1164/rccm.201211-2104OC
14. Anantham D, Feller-Kopman D, Shanmugham LN, Berman SM, DeCamp MM, Gangadharan SP, et al. Electromagnetic Navigation Bronchoscopy-Guided Fiducial Placement for Robotic Stereotactic Radiosurgery of Lung Tumors: A Feasibility Study. *(Clinical report) Chest* (2007) 132(3):930. doi: 10.1378/chest.07-0522
15. Steinfort PD, Siva RS, Kron DT, Chee LR, Ruben BJ, Ball BD, et al. Multimodality Guidance for Accurate Bronchoscopic Insertion of Fiducial Markers. *J Thorac Oncol* (2015) 10(2):324–30. doi: 10.1097/JTO.0000000000000389
16. Bhagat N, Fidelman NE, Durack JC, Collins J, Gordon RL, LaBerge JM, et al. Complications Associated With the Percutaneous Insertion of Fiducial Markers in the Thorax. *Cardiovasc Interventional Radiol* (2010) 33(6):1186–1. doi: 10.1007/S00270-010-9949-0
17. Hoogeman M, Prevost JB, Nuyttens J, Poll J, Levendag P, Heijmen B. Clinical Accuracy of the Respiratory Tumour Tracking System of the Cyberknife: Assessment by Analysis of Log Files. *Int J Radiat Oncol Biol Phys* (2009) 74(1):297–303. doi: 10.1016/j.ijrobp.2008.12.041
18. Smith RL, Yang D, Lee A, Mayse ML, Low DA, Parikh PJ. The Correlation of Tissue Motion Within the Lung: Implications on Fiducial Based Treatments. *Med Phys* (2011) 38(11):5992–7. doi: 10.1118/1.3643028
19. Ueki N, Matsuo Y, Nakamura M, Mukumoto N, Iizuka Y, Miyabe Y, et al. Intra- and Interfractional Variations in Geometric Arrangement Between Lung Tumours and Implanted Markers. *Radiother Oncol* (2014) 110(3):523–8. doi: 10.1016/j.radonc.2014.01.014
20. Stowe H, Ogake S, Sharma S, Kelly S, McDonald M, Stanley K, et al. Improved Respiratory Motion Tracking Through a Novel Fiducial Marker Placement Guidance System During Electromagnetic Navigational Bronchoscopy (ENB). *Radiat Oncol* (2019) 14(1):124–4. doi: 10.1186/s13014-019-1306-0
21. Cai J, Read P, Larner JM, Jones DR, Benedict SH, Sheng K. Reproducibility of Interfraction Lung Motion Probability Distribution Function Using Dynamic MRI: Statistical Analysis. *Int J Radiat Oncol Biol Phys* (2008) 72(4):1228–35. doi: 10.1016/j.ijrobp.2008.07.028
22. Ge H, Cai J, Kelsey CR, Yin F-F. Quantification and Minimization of Uncertainties of Internal Target Volume for Stereotactic Body Radiation Therapy of Lung Cancer. *Int J Radiat Oncol Biol Phys* (2013) 85(2):438–43. doi: 10.1016/j.ijrobp.2012.04.032
23. Vergalasova I, Cai J. A Modern Review of the Uncertainties in Volumetric Imaging of Respiratory-Induced Target Motion in Lung Radiotherapy. *Med Phys* (2020) 47(10):e988–1008. doi: 10.1002/mp.14312
24. Chang JY, Shirvani SM, Loo BW, Lamond JP, Slotman BJ, Nagata Y. Primary Lung Cancer. *Stereotactic Body Radiat Ther* (2012), 137–62. doi: 10.1007/174_2012_550
25. Seppenwoolde Y, Shirato H, Kitamura K, Shimizu S, van Herk M, Lebesque JV, et al. Precise and Real-Time Measurement of 3D Tumor Motion in Lung Due to Breathing and Heartbeat, Measured During Radiotherapy. *Int J Radiat Oncol Biol Phys* (2002) 53(4):822–34. doi: 10.1016/S0360-3016(02)02803-1
26. Kupelian PA, Forbes A, Willoughby TR, Wallace K, Mañon RR, Meeks SL, et al. Implantation and Stability of Metallic Fiducials Within Pulmonary Lesions. *Int J Radiat OncolBiolPhysics* (2007) 69(3):777–85. doi: 10.1016/j.ijrobp.2007.03.040
27. Kord M, Kluge A, Kufeld M, Kalinauskaite G, Loebel F, Stromberger C, et al. Risks and Benefits of Fiducial Marker Placement in Tumor Lesions for Robotic Radiosurgery: Technical Outcomes of 357 Implantations. *Cancers* (2021) 13(19):4838. doi: 10.3390/cancers13194838
28. Scher N, Bollet M, Bouilhol G, Tannouri R, Khemiri I, Vouillaume A, et al. Safety and Efficacy of Fiducial Marker Implantation for Robotic Stereotactic Body Radiation Therapy With Fiducial Tracking. *Radiat Oncol* (2019) 14(1):167–7. doi: 10.1186/s13014-019-1373-2
29. Minnich DJ, Bryant AS, Wei B, Hinton BK, Popple RA, Cerfolio RJ, et al. Retention Rate of Electromagnetic Navigation Bronchoscopic Placed Fiducial Markers for Lung Radiosurgery. *Ann Thorac Surg* (2015) 100(4):1163–6. doi: 10.1016/j.athoracsur.2015.04.060
30. Weiss E. Long-Term Safety and Stability of Gold Coil Fiducial Markers in Non-Small-Cell Lung Cancer Image-Guided Radiotherapy. *Int J Radiol Radiat Ther* (2017) 3(1):172–6. doi: 10.15406/ijrrt.2017.03.00049
31. Harley DP, Krimsky WS, Sarkar S, Highfield D, Aygun C, Gurses B. Fiducial Marker Placement Using Endobronchial Ultrasound and Navigational Bronchoscopy for Stereotactic Radiosurgery: An Alternative Strategy. *Ann Thorac Surg* (2010) 89(2):368–74. doi: 10.1016/j.athoracsur.2009.09.048
32. Belanger AR, Burks AC, Chambers DM, Ghosh S, MacRosty CR, Conterato AJ, et al. Peripheral Lung Nodule Diagnosis and Fiducial Marker Placement Using a Novel Tip-Tracked Electromagnetic Navigation Bronchoscopy System. *J Bronchol Interv Pulmonol* (2019) 26(1):41–8. doi: 10.1097/LBR.0000000000000528
33. Casutt A, Noirez L, Bernasconi M, Koutsokera A, Beigelman-Aubry C, Kinj R, et al. Endobronchial Coil Spring Fiducial Markers for CyberKnife® Stereotactic Body Radiation Therapy. *Respirology* (2021) 26(5):469–76. doi: 10.1111/resp.14006
34. Fiducial Placement Guidelines. *In Fiducial Tracking. Accuray Inc*. USA: Accuray Incorporation Training Materials (2015).

35. Goldsmith C, Green MM, Middleton B, Cowley I, Robinson A, Plowman NP, et al. Evaluation of CyberKnife® Fiducial Tracking Limitations to Assist Targeting Accuracy: A Phantom Study With Fiducial Displacement. *Cureus* (2018) 10(10):e3523. doi: 10.7759/cureus.3523

Conflict of Interest: Authors KK and KY were employed by Hong Kong Radiation Therapy Company Limited. Author HC was employed by Hong Kong Medical Physics Consulting Company Limited.

The remaining authors declare that the research was conducted in the absence of any commercial or financial relationships that could be construed as a potential conflict of interest.

Publisher's Note: All claims expressed in this article are solely those of the authors and do not necessarily represent those of their affiliated organizations, or those of the publisher, the editors and the reviewers. Any product that may be evaluated in this article, or claim that may be made by its manufacturer, is not guaranteed or endorsed by the publisher.

frontiers | Frontiers in Oncology

SYSTEMATIC REVIEW
published: 17 June 2022
doi: 10.3389/fonc.2022.898435

Functional Liver Imaging in Radiotherapy for Liver Cancer: A Systematic Review and Meta-Analysis

*Pi-Xiao Zhou, Ying Zhang, Quan-Bin Zhang, Guo-Qian Zhang, Hui Yu and Shu-Xu Zhang**

Radiotherapy Center, Affiliated Cancer Hospital and Institute of Guangzhou Medical University, Guangzhou, China

OPEN ACCESS

Edited by:
Yingli Yang,
UCLA Health System, United States

Reviewed by:
Shirin Sioshansi,
UMass Memorial Medical Center, United States
Chi-Leung Chiang,
The University of Hong Kong, Hong Kong, SAR China

***Correspondence:**
Shu-Xu Zhang
gthzsx@gzhmu.edu.cn

Specialty section:
This article was submitted to Radiation Oncology, a section of the journal Frontiers in Oncology

Received: *17 March 2022*
Accepted: *19 May 2022*
Published: *17 June 2022*

Citation:
Zhou P-X, Zhang Y, Zhang Q-B, Zhang G-Q, Yu H and Zhang S-X (2022) Functional Liver Imaging in Radiotherapy for Liver Cancer: A Systematic Review and Meta-Analysis. Front. Oncol. 12:898435. doi: 10.3389/fonc.2022.898435

Backgrounds: Functional liver imaging can identify functional liver distribution heterogeneity and integrate it into radiotherapy planning. The feasibility and clinical benefit of functional liver-sparing radiotherapy planning are currently unknown.

Methods: A comprehensive search of several primary databases was performed to identify studies that met the inclusion criteria. The primary objective of this study was to evaluate the dosimetric and clinical benefits of functional liver-sparing planning radiotherapy. Secondary objectives were to assess the ability of functional imaging to predict the risk of radiation-induced liver toxicity (RILT), and the dose-response relationship after radiotherapy.

Results: A total of 20 publications were enrolled in descriptive tables and meta-analysis. The meta-analysis found that mean functional liver dose (f-MLD) was reduced by 1.0 Gy [95%CI: (-0.13, 2.13)], standard mean differences (SMD) of functional liver volume receiving ≥20 Gy (fV_{20}) decreased by 0.25 [95%CI: (-0.14, 0.65)] when planning was optimized to sparing functional liver ($P > 0.05$). Seven clinical prospective studies reported functional liver-sparing planning-guided radiotherapy leads to a low incidence of RILD, and the single rate meta-analysis showed that the RILD (defined as CTP score increase ≥2) incidence was 0.04 [95%CI: (0.00, 0.11), $P < 0.05$]. Four studies showed that functional liver imaging had a higher value to predict RILT than conventional anatomical CT. Four studies established dose-response relationships in functional liver imaging after radiotherapy.

Conclusion: Although functional imaging modalities and definitions are heterogeneous between studies, but incorporation into radiotherapy procedures for liver cancer patients may provide clinical benefits. Further validation in randomized clinical trials will be required in the future.

Keywords: liver neoplasms, functional liver imaging, radiotherapy, dose-response, radiation-induced liver toxicity (RILT)

INTRODUCTION

Hepatocellular carcinoma (HCC) is the fifth most common cancer and the third most common cause of cancer-related death globally, and its incidence is increasing year by year (1, 2). Moreover, the liver is the most common site of metastasis for other primary cancers (3). The liver was considered a contraindication to radiotherapy in the past because the radiation dose could not be safely delivered to the whole liver and could lead to acute radiation-induced liver toxicity (RILT) and even death (1, 4). Although, stereotactic body radiotherapy (SBRT) can provide a highly conformal dose of intense radiation to tumors while minimizing damage to organs at risk (OARs) and has become an effective treatment for liver tumors with excellent local control rates of 80% to 90% (5). However, RILT was a complex condition with a wide range of clinical symptoms ranging from an asymptomatic elevation of liver enzymes to liver failure and death, with an G3+ incidence of 5% to 36% in SBRT patients, limiting the implementation of high-dose radiotherapy (4–7). This risk was further increased by several pre-existing factors in the liver parenchyma, including hepatitis B virus and hepatitis C virus infection and cirrhosis (5). Until now, there was no specific treatment for RILT (4).

HCC patients have significant heterogeneity in liver function, which may be the result of organ structure, disease, or previous treatment injuries (8). The clinical liver function assessment was usually graded using Child-Turcotte-Pugh (CTP) tools, but it can be influenced easily by clinician's subjective and other confusing factors (9). The further problem was that the widely used dose-volume constraint of the normal liver relies on anatomical CT imaging (which provides morphological information) and fails to consider liver function inhomogeneities in planning (5, 9).

Currently, functional liver imaging modalities include dual-energy CT, Magnetic Resonance Imaging (MRI), Single-Photon Emission Computed Tomography (SPECT), and Positron Emission Tomography (PET), all of which can provide quantitative visualization of liver function distribution. Integrate liver function 3-dimensional distribution information into planning for optimization (such as changing beams direction) to safely deliver a higher dose and minimize the 'best functional' (i.e., functional liver) liver dose (8, 10). Functional liver imaging complements anatomical CT imaging and provides insight into RILT beyond the existing anatomy-based dose-volume predictive model. Though functional imaging studies have shown a higher value in predicting radiation-induced lung injury than anatomical CT planning parameters (e.g., functional lung mean dose greater than lung mean dose), but its value in predicting RILT was unknown (11). In addition, there was no clear consensus on functional liver imaging modalities, functional liver definition, and functional planning optimization. Therefore, this systematic review was focused on evaluating the potential utility value of functional liver imaging in liver cancer radiotherapy.

MATERIALS AND METHODS

The systematic review was performed using structured search terms following the PRISMA guidelines (12). Our research questions regarding patients, interventions, comparisons, outcomes, and study design (PICOS) methods are described in **Supplemental A (Table 1)**. This systematic review and meta-analysis had been pre-registered on the PROSPERO (CRD42021257779).

Search Strategy

We performed a systematic literature search in five electronic databases on April 10, 2021: PubMed, Embase, Cochrane, Sinomed, Chinese National Knowledge Infrastructure (CNKI). All eligible literature with a publication date between 1990 and search date was included. In PubMed and Embase databases, the search strategies of combining subject headings and free text words were adopted. The following subject headings searches were used: "Liver Neoplasms" AND "Radiotherapy". All the 'Entry Terms' of the subject headings were used as free text words. These were finally combined with key words "functional liver", "liver function", or "functioning liver". Searches in Embase database adopted a similar principle and were adjusted according to the database's thesaurus. While in the Cochrane database, subject headings combined with keywords were used. The keywords search strategy was used in two Chinese databases. A manual secondary search of the reference list uncovered an additional 18 studies. There were no restrictions on language. The complete search strategy for each database was available in **Supplemental B**.

Study Selection

The following study inclusion criteria were followed: (i) Functional liver imaging utilized in external radiotherapy for patients with liver cancer; (ii) Comparison of the differences in dose-volume parameters (DVP) between the functional liver sparing and the anatomical CT radiotherapy planning; or (iii) Investigate the ability or parameters of functional liver imaging to predict RILD (radiation-induced liver disease, defined as CTP score increase ≥2), and the dose-response relationship; or (iv) Exploring liver cancer patients' RILD rate after delivery of functional liver protection planning-guided radiotherapy.

Editorials, letters, reviews, and case reports were excluded. When several publications on the same topic existed simultaneously from the same research team, the article with the wealthiest data or the latest publication was chosen. The number of patients included in each study was not less than five. Mean ± standard deviation (SD) or median (range) of the planning parameters that cannot be obtained were excluded from the meta-analysis.

Data Collection

Data were extracted independently from each article by two reviewers and recorded in a prepared data collection form. Any differences between the extracted data from the two were resolved by negotiation or by a third reviewer.

Data collected included: first author, year of publication, study type, functional liver imaging modality, patient characteristics, number of patients, the definition of the functional liver, functional liver imaging technology parameters, information of radiotherapy planning, assessment of the dose-response relationship, the association between the

functional liver dosimetric and clinical outcomes (RILT, prognosis). The dosimetric (fV_{20}: functional liver volume receiving ≥20 Gy; f-MLD: mean functional liver dose) were collected from comparative studies of functional liver sparing and anatomical CT planning. Two reviewers evaluated literature (non-randomized controlled trials) quality using the Newcastle–Ottawa scale (NOS), and a score of seven or higher was considered a high-quality study. Differences were resolved through negotiation or by a third reviewer.

Meta-Analysis

Meta-analysis was performed for the differences in f-MLD and fV_{20} between conventional anatomical and functional planning. Not all studies provide mean ± SD, and if raw data are not available, but median values and confidence intervals are provided, then the method described can be used to calculate (13). Some studies only provided the mean value without SD or only the difference between anatomical and functional planning, so these studies were also excluded.

Meta-analysis and corresponding plots were performed using the statistical software - Review Manager (RevMan) Version 5.4 (The Cochrane Collaboration, 2020) or Stata 16.0. Heterogeneity was assessed using the I^2 statistic (I^2 >50%, showed significant heterogeneity). Random-effects models were more applicable to mitigate heterogeneity than fixed-effects models, so random-effect model was selected for meta-analysis. We evaluated publication bias using funnel plots and Egger's test checked (when the number of studies included in meta-analysis was ≥ 10, P value < 0.05 considered significant). Sensitivity analysis was performed by exclude studies one-by-one.

RESULTS

A total of 66 publications were enrolled in the full-text assessments. Forty-seven publications met the inclusion criteria for descriptive analysis (**Figure 1**). Twenty-seven of them were excluded because they were case reports, number of patients less than five, had no available information or had already included the latest or most informative publication of the same research team (14–40). Finally, the remaining twenty articles met the meta-analysis or descriptive tables (3, 5, 6, 9, 10, 41–55).

Nine functional liver imaging studies met inclusion criteria for comparison of functional liver and conventional anatomical planning dosimetric (3, 5, 41–44, 49, 50, 55) (**Table 1**). Almost all studies showed statistically significant decrease of functional liver dose in the functional liver-sparing planning compared to the conventional anatomical planning, without significant change in the target consistency index (CI), homogeneity index (HI), or OARs dose. Some studies reported that f-MLD and fV_{20} were associated with the collected data endpoints (RILD), and had sufficient published data available for meta-analysis. According to the NOS score, all studies were of high quality, and the evaluation details are shown in **Supplemental A (Table 2)**.

Eight publications were selected for f-MLD meta-analysis (3, 41–44, 49, 50, 56). Two articles used different thresholds to defined functional liver, and compared dose differences between functional liver-sparing and conventional anatomical planning (41, 50). Some studies were not included in the meta-analysis because they were incomplete (only mean value or percentage difference), and raw data were unavailable (44, 49, 53). When only one threshold was included from each study (the threshold which showed the maximum difference between conventional and functional liver-sparing planning), the f-MLD was decreased by: 1.0 Gy [95%CI: (-0.13, 2.13), I^2 = 0%] between functional liver-sparing and conventional anatomical planning (**Figure 2A**). Sensitivity analysis found the result was robust, and no significant publication bias was identified by visual observation from the funnel plot (**Supplemental A Figure 1**). Four papers were eligible for fV_{20} meta-analysis (3, 5, 42, 55). The SMD was used because the fV_{20} value in these four studies were expressed in different forms (cc, cm^3 and percentage). The fV_{20} SMD was decreased by: [0.25, 95%CI:(-0.14, 0.65), I^2 = 0%] between functional liver-sparing and conventional anatomical planning (**Figure 2B**). Currently, there were significant statistical difference in f-MLD and fV_{20} between functional liver-sparing and conventional anatomical planning (P >0.05).

Four of the studies showed that functional liver imaging was statistically significant in predicting the endpoint of RILT, while no correlation was found with anatomic planning (9, 44, 53, 54) (**Table 2**). Although the endpoints used to evaluate RILD were inconsistent across studies. Seven studies evaluated RILT after functional liver-sparing planning-guided radiotherapy, six of which were prospective and one retrospective (6, 44, 48, 51–53, 55) (**Table 2B**). A total of 180 patients were included, 111 had a baseline CTP score A, and the rest had score B or higher (55 patients), and one publication did not describe baseline liver function. Altogether, thirteen participants were described to have developed RILD. Logan et al. (48) showed that patients who developed RILD had poorer baseline liver function (both CTP B/C). The single rate meta-analysis of the incidence of RILD in the included studies showed an incidence of 0.04 [95%CI: (0.00, 0.11), I^2 = 58.5%, P <0.05] when functional liver-sparing planning-guided radiotherapy (after double-arcsine transformations) (**Figure 3**). And three studies described correlations between functional liver imaging and prognosis, two of which demonstrated the functional liver dose-volume parameters to predict prognosis (9, 47).

Four publications described the dose-response relationship between radiation dose received and liver function decline (6, 10, 45, 46) (**Table 3**). Three studies used linear models (6, 10, 46), and another study had a sigmoid-shaped dose-response curve. Changes in liver function with dose were similar across the four studies, despite differences in population heterogeneity, radiotherapy techniques, prescription dose, time points, and dose-response model parameters.

The most frequently utilized functional liver imaging technique in included literature was SPECT (tracer: ^{99m}Tc-Sc, ^{99m}Tc- HIDA or ^{99m}Tc-GSA) with 14 publications, followed by MRI (Gd-EOB-DTPA) with four papers, PET (^{18}F-FDG) with two studies, and dual-energy CT (Iodine) with one literature.

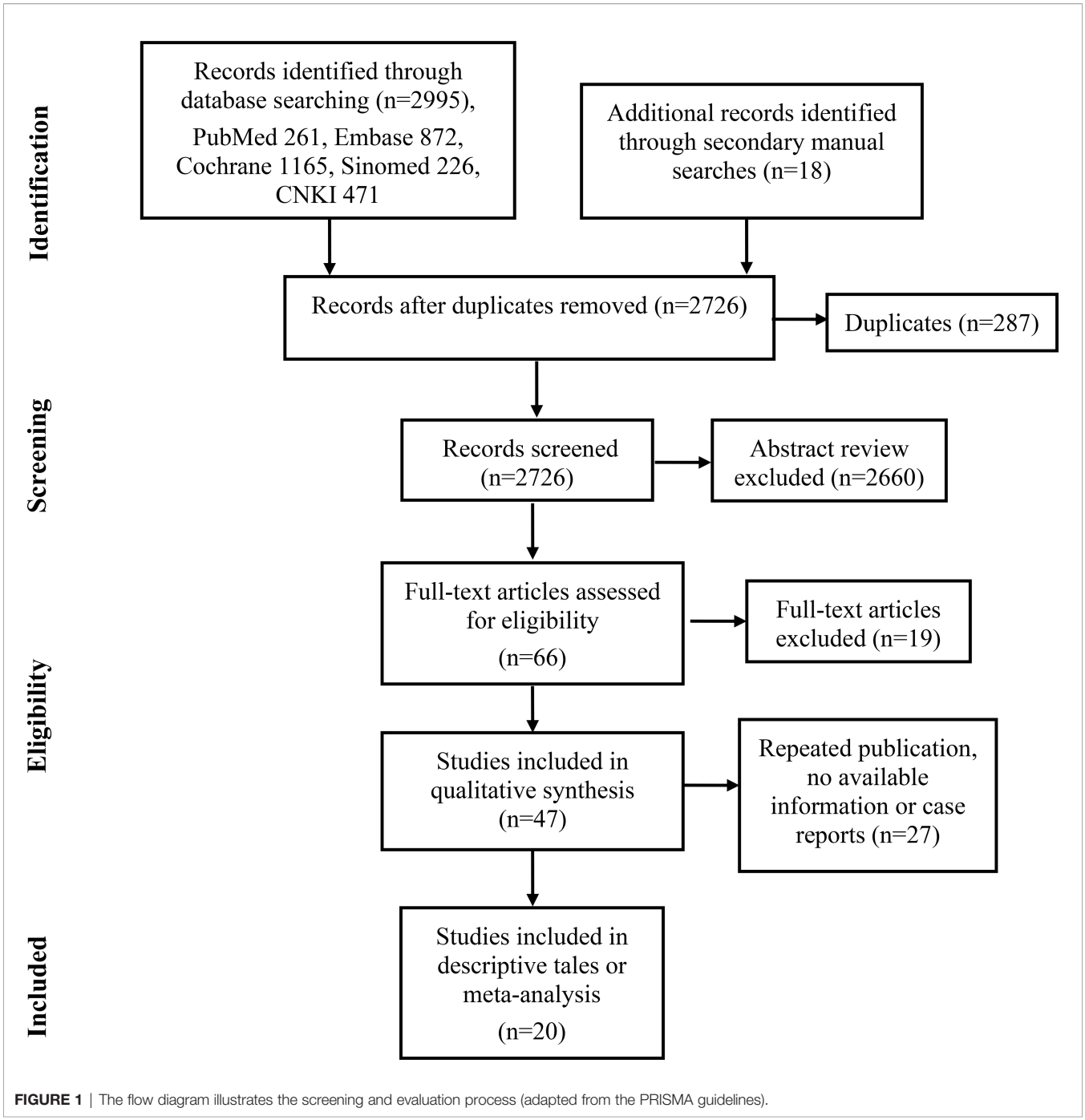

FIGURE 1 | The flow diagram illustrates the screening and evaluation process (adapted from the PRISMA guidelines).

Thirteen studies provided functional liver imaging scans parameters. Many studies used one or more methods to suppress the effect of breathing motion in both the accuracy of liver tumor volume measurements and image registration (e.g., end-exhale CT, four-dimensional CT, abdominal compression, breathing-hold, or Calypso-guide gating). Several registration systems or toolkits were mentioned in the literature. For instance, Smartadapt/MIM software, Velocity software, insight segmentation, and registration toolkit (**Supplemental A Table 3**).

DISCUSSION

The current evaluation of the liver radiotherapy planning was based on the assumption of uniform and consistent liver function. Although with the advancement of radiotherapy technology, the dose distribution in the target area has been improved, and radiation dose to surrounding OARs has been reduced. However, there are still a minority of liver cancer radiotherapy patients who will have a significant RILT, leading to treatment interruption or even death by acute liver failure.

TABLE 1 | Provides detailed descriptions of each study, including patients' information, functional imaging/planning technique utilized, functional liver definition and key findings.

Reference	Patients	ReferenceTypes	Characteristics	Technology,contrast agent,RT technique	Definition FL	Benefit of FL sparing (% difference between means)	Comparing planning quality
Ohira et al. (2020) (3)	10 (15)	Article	HCC 86% GTV: NS 36.8-65Gy	DECT (Iodine) VMAT (SBRT)	NID<0.46	*f-MLD ↓ 1.9 Gy *fV5 ↓ 58.7 cc, 53.8 cc, 27.2 cc, 13.3 cc	No SS change CI, SS HI ↑; No SS change to OARs
Toya et al. (2019) (5)	11	Article	HCC 100% PTV: 42.9 cm3 (M) 50Gy	SPECT/CT (99mTc-GSA) VMAT (SBRT)	60%-80% of max	*fV5-20 ↓ 1.5%, 2.1%, 1.4%, 0.7%	No SS difference CI, HI; No SS change to OARs
Furukawa et al. (2020) (41)	10	Article	HCC 100% GTV: NS 40-50Gy	SPECT (^{99m}Tc-HIDA) SBRT	25%-100% max; 50%-100% max	*f-MLD↓ 2Gy/3Gy; *$fV_{D<15Gy}$ ↓ 50%/41.9%	No SS difference CI; Dose to OARs NS
Tsegmed et al. (2017) (42)	20	Article	HCC 100% PTV: 16.2 cm3 48Gy	MRI (Gd-EOB) IMRT (SBRT)	HBP L/S ≥1.5	*f-MLD ↓ 0.5 Gy *fV5-20 ↓ 3%, 3%, 1.9%, 0.7%	SS CI ↑; No SS change to OARs
Bowen et al. (2015) (43)	10	Article	HCC 100% GTV: (M) 88 cm^3 37.5-60Gy	SPECT/CT (^{99m}Tc-Sc) VMAT/PBS	43%-90% of L/S max	*f-MLD ↓ 20%	Dose to PTV or OARs NS
Long et al. (2018) (44)	17	Article	HCC: 100% GTV: 29.5cc 27.5-50Gy	SPECT (^{99m}Tc-HIDA) SBRT	50%-100% of max	*f-MLD ↓ 1.18 Gy *$fV_{D<15Gy}$ ↑ 0.15%	No SS difference CI; Dose to OARs NS
Simeth et al. (2018) (49)	10	Conference	HCC 100% GTV: NS 55Gy	MRI (Gd-EOB) -	36% to max	*f-MLD ↓ 10.5%	Dose to PTV or OARs NS
Fode et al. (2017) (50)	7	Article	6 mCRC/1 IHC CTV: 25.1cc (M) 45-56.25Gy	PET/CT(^{18}F-FDG) VMAT (SBRT)	10%/20%/30% volume with the highest SUV	*f-MLD↓ 0.8/0.6/0.4 Gy; $fV_{D<15Gy}$ ↑ 6%/4%/3%	No SS difference CI; Dose to OARs NS
Lin et al. (2019) (55)	10	Article	HCC 100% PTV: 122.7 cm3 50-62Gy	MRI (Gd-EOB) IMRT	T1WI, high signal area in HBP (20min)	*f-MLD ↓ 0.54 Gy *fV5-20 ↓ 0.41cm^3,0.32cm^3, 0.22 cm^3, 0.14 cm^3	No SS difference CI and HI; No SS change to OARs

*Key: *, denotes statistically significant result; No., number; FL, functional liver; mCRC, metastatic colorectal cancer; IHC, intrahepatic cholangiocarcinoma; ^{18}F-FDG, 2-[18F] fluoro-2-deoxy-D-galactose; SUV, standard uptake values; f-MLD, functional liver volume mean dose; $fV_{D<15Gy}$, volume of functional liver receiving less than 15 Gy; SS, statistically significant; CI, conformity index; OARs, organs at risk; NS, non-specified; HCC, hepatocellular carcinoma; ^{99m}Tc-HIDA, technetium-99-mebrofenin (Tc99m) hepatobiliary iminodiacetic acid (HIDA); ^{99m}Tc-Sc, ^{99m}Tc-Sulphur colloid; PBS, proton pencil beam scanning; L/S, liver-to-spleen ratio; DECT, Dual-energy computed tomography; NID, normalized iodine density; fVx, functional liver volume receiving ≥x Gy; HI, homogeneity index; MU, monitor unit; SC, spinal cord; PTV, planning target volume; Gd-EOB-DTPA, Gadolinium ethoxybenzyl diethylenetriamine pentaacetic acid; HBP, hepatobiliary phase; T1WI, T1 weighted image. ↑, increase; ↓, decrease.*

However, previous studies have shown that functional liver imaging can identify the distribution of liver function and could be integrate it into radiotherapy planning to protect the higher-functioning liver volumes. That is the first systematic review and meta-analysis of functional liver imaging in radiotherapy for liver cancer. Meta-analysis indicated that functional liver preservation radiotherapy planning could potentially reduce f-MLD and fV_{20}, but no statistical significance. Because some studies were abandoned before meta-analysis due to incomplete data, so future functional liver-sparing comparative planning studies should clearly state the primary functional liver mean doses differences (± SD). Dose constraints regimens and parameters optimization settings also should be clearly provided for functional liver-sparing and conventional anatomical planning to guarantee consistency. However, the single rate meta-analysis of the incidence of RILD with functional liver-sparing planning-guided radiotherapy showed that the incidence of RILD was only 4%, which was lower than previously reported for the conventional anatomical planning radiotherapy.

The maximum clinical significance of functional liver imaging planning was to reduce the incidence of RILT without reducing overall survival. In the included literature, studies showed that functional liver dose-volume parameters (e.g., fV_{20}) helped predict the occurrence of RILT. In clinical, it was a challenge to improve the survival rate, and reduce the incidence of RILT of HCC patients with first portal vein tumor thrombus (PVTT). However, Shirai et al. (18) showed that no RILD occurred in

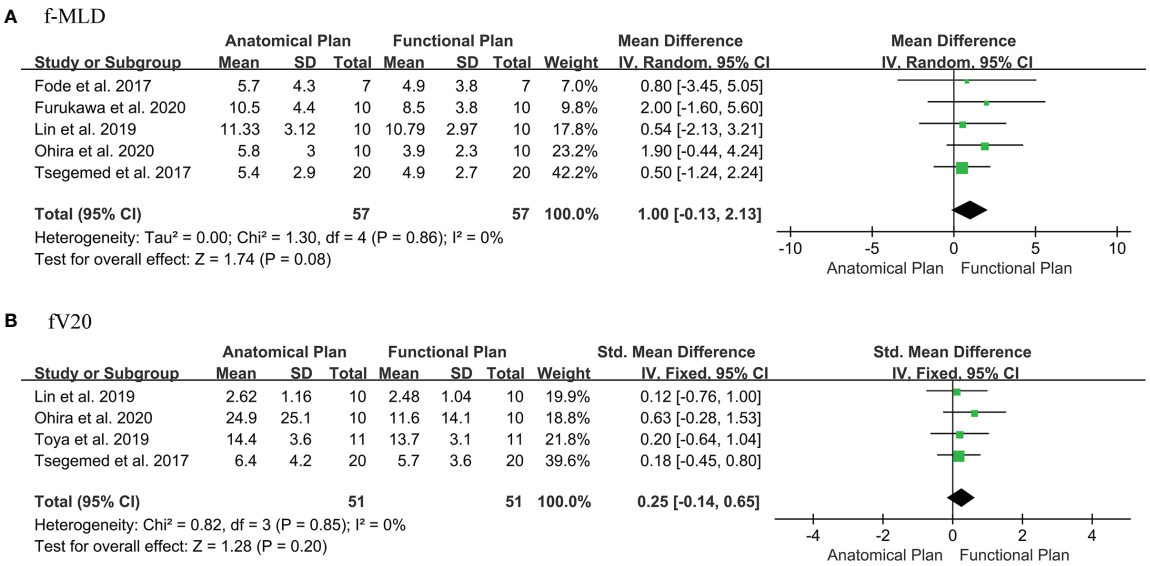

FIGURE 2 | Forest plot of the difference in dose-volume parameters of functional liver between the functional liver-sparing and conventional anatomical plans. **(A)** f-MLD (functional liver mean dose); **(B)** fV_{20} (functional liver volume receiving ≥ 20 Gy).

patients with large hepatocellular carcinoma (greater than 14 cm) or combined PVTT who received the functional liver-sparing planning-guided radiotherapy (38). In terms of prognosis, Shirai et al. (18) showed that median overall survival in HCC patients with PVTT treated with functional liver-sparing planning-guided radiotherapy was comparable to the previously reported PVTT radiotherapy combined with transcatheter arterial chemoembolization or surgical hepatectomy. At present, there is not enough data to establish a probability model of normal tissue complications. Future publications should provide sufficient information on the value of functional liver dosimetric and anatomical liver dosimetric to predict RILT, which can be used to guide the establishment of functional liver-based dose limitations.

A similar dose-response relationship was observed on the functional liver imaging after radiotherapy, which decreased with the increase of radiation dose. Most of the publications evaluated the time points for evaluation were about one month after RT treatment, and only one was evaluated at three months. The functional imaging modality used in all publications was nuclear medicine imaging. Currently, there was not enough data to assess the best functional liver imaging modalities.

The definition of the functional liver was inconsistent in included publications (e.g., for SPECT, functional liver was defined as the percentage of maximum liver radioactivity counts (ranging from 10%, 20%, 30%, 50% to 100% max), the ratio to heart or spleen radioactivity counts, etc.), and no clear clinical evidence to guide the optimal definition. Furukawa et al. (41) showed that functional liver defined as > 50% of max radioactive counts with f-MLD decreased beyond >25% of maximum in functional liver-sparing planning (in SPECT/CT). Theoretically speaking, it was best to avoid radiation doses to liver tissue other than the tumor, but this was impossible with current radiotherapy techniques. However, it was possible to establish non-overlapping functional liver regions by defining different thresholds so that the more functional liver tissue should give more weight to protection without sacrificing conformity of tumor target volume and other OARs.

In the systematic review, 20 studies utilized different functional imaging techniques and radioactive tracers (contrast agents), most of which used nuclear medicine imaging. SPECT provides three-dimensional imaging of indirect or direct liver function by injecting different radiotracers. SPECT combined with low-resolution CT can improve tissue contrast and the accuracy of local radioactivity uptake estimation (47). The radioactive tracer ^{99m}Tc-HIDA is transported to hepatocytes *via* albumin to be taken up by organic anion transport protein (OATP1 B1/B3) and excreted in the biliary system without bio-metabolic conversion (55, 56). To exclude individual metabolic differences, divided by body surface area (liver uptake rate %/min/m2), De Graaf et al. (56) suggested the functional liver defined as 30% of the maximum radioactivity count. ^{99m}Tc-GSA is binding specifically to the desialic acid glycoprotein receptor expressed on hepatocytes, and suggested defining voxels below 54% of the maximum radioactivity count as background (56). ^{99m}Tc-Sc is taken up by Kupffer cells of the hepatic reticuloendothelial system, and its activity is closely related to liver function (43). PET/CT functional imaging provides better spatial and temporal resolution than SPECT (57). ^{18}F-FDG is a radio-labeled galactose analogue that is metabolized by intrahepatic galactokinase and can be used to noninvasively quantify local hepatic metabolic function and visualize metabolic heterogeneity (50, 58). MRI-based functional imaging seamlessly connects to clinical examinations workflow, has a higher temporal and spatial resolution, and does not rely on

TABLE 2 | Description of functional liver imaging correlating with clinical liver function, radiation-induced liver disease and prognosis.

a) Conventional anatomical planning radiotherapy

Reference	Patients	ReferenceType	Characteristics	Imaging type, Plan technique, Definition FL	Morbidity or correlation with CTP (RILD) after RT	Prognosis
Schaub et al. (2018) (9)	47	–	HCC: 95.7% GTV: 33.43cm^3 (M) CTP: 29A 18B/C	SPECT/CT (99mTc-Sc) SBRT/PRT >30% of max	11 RILD (CTP +2) TLF and L/Smean (*CTP +2).	f-MLD/fV20 (*RILD-special survival, AUC 0.74/0.78, cutoff 23Gy/36%)
Bowen et al. (2016) (47)	30	–	HCC 100% GTV: 15 cm^3 (M) CTP 16A, 12B, 2C	SPECT/CT (^{99m}Tc-Sc) - 20%-70 % of max	–	TLF (cutoff >0.30) (*OS)
Nakamura et al. (2015) (54)	30	–	HCC 100% CTP 26A, 4B	MRI (Gd-EOB) SBRT	W-LSC (*CTP +2, AUC 0.83, cutoff 1.88)	–

b) Functional liver protection planning-guided radiotherapy

Reference	Patients	Reference Type	Characteristics	Imaging type, Plan technique, Definition FL	Morbidity or correlation with CTP (RILD) after RT	prognosis
Fode et al. (2017) (7)	14 (15)	PO	mCRC 100% -	PET/CT (^{18}F-FDG) IMRT (SBRT) 10%-30% volume with highest SUV	No G3+ acute morbidity (No RILD)	Last follow-up (M 16.6 mo), 10 survived
Long et al. (2018) (44)	17	PO	HCC: 100% GTV: 29.5cc CTP: 12A 5B	SPECT (^{99m}Tc-HIDA) SBRT 50%-100% max	3 RILD (CTP +2, 6 mo); 10 patients developed decompensation (*$fV_{D<15Gy}$, AUC 0.929, cutoff < 2.915%/min/m^2)	–
Logan et al. (2016) (48)	10	PO	HCC 100% - CTP: 5A, 5B	SPECT/CT (^{99m}Tc-Sc) IMRT/PRT 20% to 50% of max	2 RILD (both CTP B8-9)	OS (med) was 116 days; FLV (*OS, SPECT thresholds of 30%, 35%, 40%, 43%, and 45% of max)
Kudithipudi et al. (2017) (51)	22 (39)	PO	HCC 100% PTV: 293.0cm^3 (M) CTP: 14A, 8B	SPECT (^{99m}Tc-Sc) SBRT/FSRT Related body surface area	No RILD CTP score preservation rate 59% (1 year)	OS: 59% (2 years)
Hasan et al. (2016) (52)	32	PO	HCC 100% CTP: 32A	SPECT (^{99m}Tc-Sc) -	No RILD 73%/56% retained CTP A (1/2 years)	OS: 87%/63% (1/2 years)
Shirai et al. (2015) (53)	75	RO	HCC with PVTT GTV: 448.7cm^3 (M) CTP: 39A 36B/C	SPECT (^{99m}Tc-GSA) 3D-CRT Areas of uptake exceeds tumor	8 RILD (CTP +2) fV20 (*CTP +1 vs. +2, AUC 0.792, cutoff 26.4%)	1 year, 2 years, 5 years OS were 47.0%, 20.4%, 11.2%;
Lin et al. (2019) (55)	10	PO	HCC 100% PTV: 122.7 cm^3 (M) CTP: 9A 1B	MRI (Gd-EOB) IMRT T1, high signal area in HBP (20min)	No RILD	–

*Key, *, functional liver imaging more predictive risk of CTP +1/RILD (CTP +2) or prognosis; PO, prospective; RO, retrospective; FL(V), function liver (volume); M, mean; Med, median; mo, months; CTP, Child-Turcotte-Pugh; OS, overall survival; SS, statistically significantly; +2, score increase ≥2; G2+, grade ≥2+; HCC, hepatocellular carcinoma; GTV, gross target volume; AUC, area under the curve; NS, non-specified; mCRC, metastatic colorectal cancer; ^{18}F-FDG, 2-[18F] fluoro-2-deoxy-D-galactose; SUV, standard uptake values; ^{99m}Tc-Sc, ^{99m}Tc sulfur colloid; TLF, FLV×L/S_{mean}; L/S_{mean}, liver-to-spleen uptake ratio; LM, liver metastases; f-MLD, functional liver volume mean dose; BBT, broad biochemical toxicity (defined as a 50% increase in each of the 3 measured liver enzymes); PRT, proton radiotherapy; ^{99m}Tc-HIDA, technetium-99-mebrofenin (Tc99m) hepatobiliary iminodiacetic acid (HIDA); $fV_{D<15Gy}$, volume of functional liver receiving less than 15 Gy; fV20, functional liver volume receiving ≥20Gy; PVTT, portal vein tumor thrombus; ^{99m}Tc-GSA, Tc-99 m-galactosyl human serum albumin; Gd-EOB-DTPA, Gadolinium ethoxybenzyl diethylenetriamine pentaacetic acid; HBP, hepatobiliary phase; W-LSC, weighted liver-spleen ratio;*

ionizing radiation (59). Gd-EOB-DTPA, which is also selectively taken up by functional hepatocytes *via* OATP1 B1/B3, resulted in a significant shortening of T1 values in the functional liver. This leads to advancing the signal peak on T1WI to 20 min in the hepatobiliary phase in the functional liver (55, 60). DECT uses two different X-ray photon energies to quantitatively measure iodine density in tissues, which with high spatial resolution, high reproducibility, and low cost (3).

The modalities and acquisition parameters of functional liver images will affect the reconstruction and registration with anatomical CT images. Of the included publications, twelve described the image registration methods, most of which used

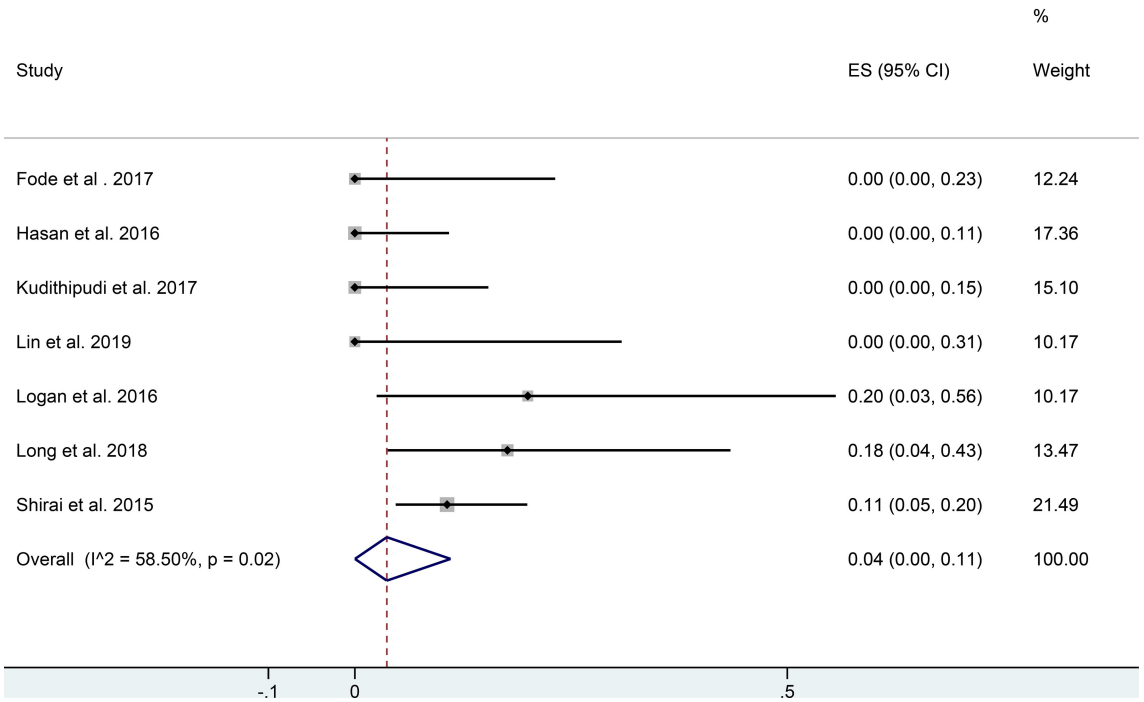

FIGURE 3 | Forest plot of single rate mete-analysis in incidence of RILD for functional liver protection planning guided radiotherapy. (RILD, radiation-induced liver disease).

MIM software, Smartadapt software, Velocity software, and insight segmentation and registration toolkit. The accuracy of image registration was critical in which the registration error between functional and anatomical CT images may lead to the spared inaccuracy of functional liver volume. Fukumitsu et al. (61) showed that for liver image registration, the performance of MIM and Velocity was generally similar. Insight segmentation and registration toolkit (ITK) was used to match image data, and the assessment results can be visualized and support different matching tasks in a clinical setting (62).

There were also some limitations in our study. First, published studies included in this review were in a small number of patients cohort and heterogeneous (patients characteristics, functional imaging modalities, radiotherapy techniques). It might be that functional liver imaging is still in the stage of clinical exploration and there are various treatment

TABLE 3 | Description of dose–response relationship after radiotherapy.

Reference	Study Type	No.	Characteristic	Planning technique	Imaging Type,contrast agent	Time points	Dose–response model and parameters
Fode et al. (2017) (6)	PO	14	Age: (M) 72 LM 100% -	IMRT (SBRT) 45-60Gy	PET/CT ^{18}F-FDG:100 (MBq)	1 month	**linear model** approximately -1.2% metabolic function per Gy, D_{50} of 22.9 Gy/3 F
Wang et al. (2013) (10)	PO	14	Age: 44-83 10 HCC, 3 CC, 1LM -	SBRT (8) 33Gy IMRT (3) 52Gy 3D-CRT 62Gy	SPECT ^{99m}Tc-HIDA (10 mCi)	1 month	**linear model** approximately -0.33% of HEF per Gy
Price et al. (2018) (45)	PO	15	- HCC 100%	SBRT/PRT NA	SPECT/CT ^{99m}Tc-Sc (-)	1 month	**Gompertz model** Maximum uptake median -0.11% per Gy, D_{50} 13Gy.
De Bari et al. (2018) (46)	PO	6	Age: (M) 69 3 LM and 3 HCC PTV: 130 cc	SBRT 30 Gy	SPECT/CT ^{99m}Tc-HIDA (200MBq)	3 months	**linear model** mean -0.78% of perfusion per Gy

Key, PO, prospective observational; M, mean; LM, liver metastases; HCC, hepatocellular carcinoma; ^{99m}Tc-HIDA, technetium-99-mebrofenin (Tc99m) hepatobiliary iminodiacetic acid (HIDA); CC, cholangiocarcinoma; HEF, hepatic extraction fraction (obtained from SPECT data); ^{18}F-FDG, 2-[18F] fluoro-2-deoxy-D-galactose. ^{99m}Tc-Sc, ^{99m}Tc-Sulphur colloid; PRT, proton radiotherapy.

options available for liver cancer (such as early stage mostly choosing surgical resection, and local advanced stage opting for systemic therapy combined with radiofrequency ablation or intervention, etc.). Second, f-MLD and fV_{20} meta-analysis showed that both exhibited no statistically significant differences between functional liver preservation and anatomical plans (although all studies indicated a significant reduction). However, there was no significant heterogeneity or publication of bias. It might be associated with the number of patients, functional liver definition, and the difference of optimization. Negative results do provide a stronger warning to later investigators, reminding them to include larger study samples, report data in detailed (mean ± SD) or provide raw data in the appendix for data extraction, and give greater priority (weight) to functional liver in functional liver-sparing planning design. Third, most of the publications reviewed comprehensively did not report sufficient information to be included in the meta-analysis (e.g., no SD). And different studies reported inconsistent dose-volume parameters in functional plans (e.g., fV_{15}, $fV_{<15Gy}$), and inconsistent parameter units (such as cm^3, cc, or percentage) compared with anatomical plans. Fourth, although the single rate meta-analysis of RILD incidence in the prospective observational studies of functional liver-sparing planning-guided radiotherapy indicated the potential to decrease RILD (but both SBRT and 3D-CRT were included, subgroup analysis was not performed). However, the reported endpoints of RILT were inconsistent (including CTP score increase 1 or 2 (RILD), or liver function decompensation), which may be a weakness of the current studies. In the future, sufficient randomized clinical intervention trials should be established to examine the differences in RILD incidence between functional liver-sparing and conventional anatomical planning. Probabilistic modeling of normal tissue complications should also be investigated to provide the optimal dose-limiting regimens for functional liver preservation planning-guided radiotherapy.

CONCLUSION

The 20 studies in this systematic review suggested that functional liver imaging provided information on functional dose-volume parameters that can more acuate predict the risk of RILT than anatomical CT (e.g., fV_{20}). We found a similar dose-response for functional liver imaging after radiotherapy, indicating the potential to integrate functional liver imaging into treatment planning to decrease functional dose metrics. The meta-analysis showed that there were insufficient data to confirm that functional liver-sparing planning significantly reduced f-MLD and fV_{20} compared with anatomical CT planning. Different studies have used a wide variety of functional liver thresholds, and no standard threshold has been established. Functional liver-sparing planning-guided radiotherapy could reduce the incidence of RILD, but has yet to be validated in prospective randomized clinical intervention trials.

DATA AVAILABILITY STATEMENT

The original contributions presented in the study are included in the article/**Supplementary Material**. Further inquiries can be directed to the corresponding author.

AUTHOR CONTRIBUTIONS

P-XZ performed the study concept and design, and wrote the manuscript. YZ and G-QZ performed literature collection, and data analysis. Q-BZ and HY conducted literature screen, data collection, and quality evaluation. S-XZ verified data and revised the manuscript. All authors contributed to the article and approved the submitted version.

ACKNOWLEDGMENTS

The authors thank all the people who had participated in this study.

SUPPLEMENTARY MATERIAL

The Supplementary Material for this article can be found online at: https://www.frontiersin.org/articles/10.3389/fonc.2022.898435/full#supplementary-material

REFERENCES

1. Donadon M, Solbiati L, Dawson L, Barry A, Sapisochin G, Greig PD, et al. Hepatocellular Carcinoma: The Role of Interventional Oncology. *Liver Cancer (Basel)* (2016) 6:34–43. doi: 10.1159/000449346
2. Yang JD, Hainaut P, GJ G, Amadou A, Plymoth A, Roberts LR. A Global View of Hepatocellular Carcinoma: Trends, Risk, Prevention and Management. *Nat Rev Gastroenterol Hepatol* (2019) 16:589–604. doi: 10.1038/s41575-019-0186-y
3. Ohira S, Kanayama N, Toratani M, Ueda Y, Koike Y, Karino T, et al. Stereotactic Body Radiation Therapy Planning for Liver Tumors Using Functional Images From Dual-Energy Computed Tomography. *Radiother Oncol* (2020) 145:56–62. doi: 10.1016/j.radonc.2019.12.002
4. Koay EJ, Owen D, Das P. Radiation-Induced Liver Disease and Modern Radiotherapy. *Semin Radiat Oncol* (2018) 28:321–31. doi: 10.1016/j.semradonc.2018.06.007
5. Toya R, Saito T, Kai Y, Shiraishi S, Matsuyama T, Watakabe T, et al. Impact of 99m Tc-GSA SPECT Image-Guided Inverse Planning on Dose–Function Histogram Parameters for Stereotactic Body Radiation Therapy Planning for Patients With Hepatocellular Carcinoma: A Dosimetric Comparison Study. *Dose-Response* (2019) 17:500665362. doi: 10.1177/1559325819832149
6. Fode MM, Bak-Fredslund K, JB P, Worm E, Sørensen M, Høyer M. A Phase I Study on Stereotactic Body Radiotherapy of Liver Metastases Based on Functional Treatment Planning Using Positron Emission Tomography With 2-[18F] Fluoro-2-Deoxy-D-Galactose. *Acta Oncol* (2017) 56:1614–20. doi: 10.1080/0284186X.2017.1366051

7. Kim J, Jung Y. Radiation-Induced Liver Disease: Current Understanding and Future Perspectives. *Exp Mol Med* (2017) 49:e359. doi: 10.1038/emm.2017.85
8. Partridge M, Yamamoto T, Grau C, Høyer M, Muren LP. Imaging of Normal Lung, Liver and Parotid Gland Function for Radiotherapy. *Acta Oncol* (2010) 49:997–1011. doi: 10.3109/0284186X.2010.504735
9. Schaub SK, Apisarnthanarax S, Price RG, Nyflot MJ, Chapman TR, Matesan M, et al. Functional Liver Imaging and Dosimetry to Predict Hepatotoxicity Risk in Cirrhotic Patients With Primary Liver Cancer. *Int J Radiat Oncol Biol Phys* (2018) 102:1339–48. doi: 10.1016/j.ijrobp.2018.08.029
10. Wang H, Feng M, Frey KA, Ten Haken RK, Lawrence TS, Cao Y. Predictive Models for Regional Hepatic Function Based on 99mtc-IDA SPECT and Local Radiation Dose for Physiologic Adaptive Radiation Therapy. *Int J Radiat Oncol Biol Phys* (2013) 86:1000–6. doi: 10.1016/j.ijrobp.2013.04.007
11. Bucknell NW, Hardcastle N, Bressel M, Hofman MS, Kron T, Ball D, et al. Functional Lung Imaging in Radiation Therapy for Lung Cancer: A Systematic Review and Meta-Analysis. *Radiother Oncol* (2018) 129:196–208. doi: 10.1016/j.radonc.2018.07.014
12. Page MJ, McKenzie JE, Bossuyt PM, Boutron I, Hoffmann TC, Mulrow CD, et al. The PRISMA 2020 Statement: An Updated Guideline for Reporting Systematic Reviews. *BMJ* (2021) 372:n71. doi: 10.1136/bmj.n71
13. Hozo SP, Djulbegovic B, Hozo I. Estimating the Mean and Variance From the Median, Range, and the Size of a Sample. *BMC Med Res Methodol* (2005) 5:13. doi: 10.1186/1471-2288-5-13
14. Kai Y, Toya R, Saito T, Matsuyama T, Fukugawa Y, Shiraishi S, et al. Stereotactic Body Radiotherapy Based on 99mtc-GSA SPECT Image-Guided Inverse Planning for Hepatocellular Carcinoma. *In Vivo* (2020) 34:3583–8. doi: 10.21873/invivo.12202
15. Shen S, Jacob R, Bender LW, Duan J, Spencer SA. A Technique Using 99mtc-Mebrofenin SPECT for Radiotherapy Treatment Planning for Liver Cancers or Metastases. *Med Dosim* (2014) 39:7–11. doi: 10.1016/j.meddos.2013.08.006
16. De Bari B, Jumeau R, Deantonio L, Adib S, Godin S, Zeverino M, et al. Role of Functional Imaging in Treatment Plan Optimization of Stereotactic Body Radiation Therapy for Liver Cancer. *Tumori J* (2016) 102:e21–4. doi: 10.5301/tj.5000523
17. Shirai S, Sato M, Suwa K, Kishi K, Shimono C, Sonomura T, et al. Feasibility and Efficacy of Single Photon Emission Computed Tomography-Based Three-Dimensional Conformal Radiotherapy for Hepatocellular Carcinoma 8 Cm or More With Portal Vein Tumor Thrombus in Combination With Transcatheter Arterial Chemoembolization. *Int J Radiat Oncol Biol Phys* (2010) 76:1037–44. doi: 10.1016/j.ijrobp.2009.03.023
18. Shirai S, Sato M, Suwa K, Kishi K, Shimono C, Kawai N, et al. Single Photon Emission Computed Tomography–Based Three-Dimensional Conformal Radiotherapy for Hepatocellular Carcinoma With Portal Vein Tumor Thrombus. *Int J Radiat Oncol Biol Phys* (2009) 73:824–31. doi: 10.1016/j.ijrobp.2008.04.055
19. Long D, Huang K, Tann M, Burney H, Kong FM, Rhome RM, et al. Changes in Liver Function After Functional Liver Image-Guided Hepatic Therapy (FLIGHT) as Assessed by Hepabobiliary Iminodiacetic Acid Scans. *Int J Radiat Oncol Biol Phys* (2019) 105:S59. doi: 10.1016/j.ijrobp.2019.06.497
20. Long DE, Huang C, Tann M, Dawson B, Bartlett G, Maluccio MA, et al. Prospective Trial of Functional Liver Image-Guided Hepatic Therapy (FLIGHT) With Hepatobiliary Iminodiacetic Acid (HIDA) Scans and Update of Institutional Experience. *J Clin Oncol* (2019) 37:Supplement 4. doi: 10.1200/JCO.2019.37.4_suppl.373
21. Schaub SK, Price RG, Nyflot M, Chapman TR, Matesan MC, Vesselle HJ, et al. Liver Toxicity Risk Stratification Based on Functional Imaging and Dosimetry for Hepatocellular Carcinoma. *Int J Radiat Oncol Biol Phys* (2017) 99:S144–5. doi: 10.1016/j.ijrobp.2017.06.335
22. Kudithipudi V, Day EE, Thai NV, Kirichenko AV. Hepatic Failure Progression is Not Hastened in Intermediate-Risk Hepatocellular Carcinoma After Stereotactic Radiation Therapy (SRT) With Functional Treatment Planning. *Int J Radiat Oncol Biol Phys* (2016) 96:E179–80. doi: 10.1016/j.ijrobp.2016.06.1041
23. Tsegmed U, Kimura T, Nakashima T, Nakamura Y, Higaki T, Imano N, et al. Gd-EOB-DTPA Enhanced MRI Guided Stereotactic Body Radiation Therapy Planning for Patients With Hepatocellular Carcinoma. *Int J Radiat Oncol Biol Phys* (2015) 93:E147–8. doi: 10.1016/j.ijrobp.2015.07.925
24. Kudithipudi V, Gayou O, Thai NL, Kirichenko AV. Liver Stereotactic Radiation Therapy (SRT) With Functional Treatment Planning for Patients With Intermediate-Stage Hepatocellular Carcinoma (HCC). *Int J Radiat Oncol Biol Phys* (2014) 90:S372. doi: 10.1016/j.ijrobp.2014.05.1199
25. Apisarnthanarax S, Chapman TR, Vesselle HJ, Miyaoka RS, Kinahan PE, Sandison GA, et al. Quantitative Imaging of Global Variability and Regional Heterogeneity in Liver Function With 99mtc-Sulfur Colloid SPECT/CT in Hepatocellular Carcinoma Patients. *Int J Radiat Oncol Biol Phys* (2014) 90:S372. doi: 10.1016/j.ijrobp.2014.05.1200
26. Tsegmed U, Kimura T, Nakashima T, Nakamura Y, Higaki T, Katsuta T, et al. Functional Image-Guided Stereotactic Body Radiation Therapy Planning Using the Intensity Modulated Radiation Therapy Technique for Patients With Hepatocellular Carcinoma. *Int J Radiat Oncol Biol Phys* (2014) 90:S372–3. doi: 10.1016/j.ijrobp.2014.05.1201
27. Wang H, Cao Y. Spatially Resolved Assessment of Hepatic Function Using 99mtc-IDA SPECT. *Med Phys* (2013) 40:92501. doi: 10.1118/1.4816655
28. Shirai S, Sato M, Noda Y, Kumayama Y, Sonomura T, Kawai N, et al. The Safety Indicator of Radiotherapy for Advanced Hepatoma With Liver Cirrhosis. *J Gastroenterol Hepatol Res* (2013) 2:730–6. doi: 10.6051/j.issn.2224-3992.2013.02.320
29. Shirai S, Sato M, Noda Y, Kishi K, Kawai N, Minamiguchi H, et al. Distribution of Functional Liver Volume in Hepatocellular Carcinoma Patients With Portal Vein Tumor Thrombus in the 1st Branch and Main Trunk Using Single Photon Emission Computed Tomography—Application to Radiation Therapy. *Cancers* (2011) 3:4114–26. doi: 10.3390/cancers3044114
30. Fode MM, Sørensen M, Petersen J, Holt M, Høyer M. EP-2097: Qantification of Liver Function After Stereotactic Body Radiotherapy for Liver Tumors. *Radiother Oncol* (2018) 127:S1152–3. doi: 10.1016/S0167-8140(18)32406-X
31. Price RG, Schaub SK, Nyflot MJ, Chapman TR, Matesan M, Vesselle HJ, et al. Normal Liver Radiation Dose-Response Modeling in Hepatocellular Carcinoma Patients With Longitudinal Sulfur Colloid SPECT/CT Imaging. *Med Phys* (2017) 44:2721–3318. doi: 10.1002/mp.12304
32. De Bari B, Breuneval T, Zeverino M, Godin S, Prior J, Bourhis J, et al. Impact of the Radiation Dose on Hepatic Perfusion Evaluated Using Liver Scintigraphy Mebrofenin. *Strahlenther Onkol* (2016) 192:831–74. doi: 10.1007/s00066-016-1051-3
33. Kim JH, Boucek JA. Correlation of Radiation Dose From 90Y-SIR Treatments of Liver Cancer With Functional SPECT Imaging. *Phys Eng Sci Med* (2020) 43:297–462. doi: 10.1007/s13246-019-00826-6
34. Jumeau R, Ozsahin M, Prior J, Bourhis J, De Bari B. Interest and Feasibility of Integration of 99 mTc-Mebrofenin SPECT Into a Stereotactic Radiotherapy Plan for Liver Cancer. *Strahlenther Onkol* (2015) 191:898–906. doi: 10.1007/s00066-015-0903-6
35. Petersen JBB, Poulsen PR, Worm ES, Hansen AT, Sørensen M, Keiding S, et al. Impact of Intra-Fractional Liver Motions on FDGal-PET Guided Functional Avoidance SBRT Using Scanning Proton Beams. *Radiother Oncol* (2014) 111:S76. doi: 10.1016/S0167-8140(15)30958-0
36. Huang KC, Long D, Yue Y, Tann M, Rhome R, Maxim P, et al. Assessment of the Liver Functions in Different Dose Region After SBRT Using HIDA Spect Scans. *Med Phys* (2019) 46:e209. doi: 10.1002/mp.13589
37. Shirai S, Sato M, Noda Y, Kumayama Y, Shimizu N. Incorporating GSA-SPECT Into CT-Based Dose-Volume Histograms for Advanced Hepatocellular Carcinoma Radiotherapy. *World J Radio* (2014) 6:598. doi: 10.4329/wjr.v6.i8.598
38. Shirai S, Sato M, Noda Y, Kishi K, Ikoma A, Sanda H, et al. SPECT-Based Radiation Therapy and Transcatheter Arterial Chemoembolization for Unresectable Hepatocellular Carcinoma Sized 14 Cm or Greater. *Cancer Clin Oncol* (2012) 1:65–76. doi: 10.5539/cco.v1n1p65
39. Wang H, Feng M, Frey K, Balter J, Haken RT, Lawrence T, et al. Hepatic Function Model Based Upon HIDA SPECT and Dose for Physiological Adaptive RT. *Pract Radiat Oncol* (2013) 3:S2. doi: 10.1016/j.prro.2013.01.010
40. Toya R, Saito T, Shiraishi S, Kai Y, Murakami R, Matsuyama T, et al. Dose-Function Histogram Evaluation Using 99m Tc-GSA SPECT/CT Images for Stereotactic Body Radiation Therapy Planning for Hepatocellular Carcinoma Patients: A Dosimetric Parameter Comparison. *Anticancer Res* (2018) 38:1511. doi: 10.21873/anticanres.12378

41. Furukawa Y, Long DE, Ellsworth SG. Functional Liver-Image Guided Hepatic Therapy (FLIGHT): A Technique to Maximize Hepatic Functional Reserve. *Med Dosim* (2020) 45:117–20. doi: 10.1016/j.meddos.2019.07.007
42. Tsegmed U, Kimura T, Nakashima T, Nakamura Y, Higaki T, Imano N, et al. Functional Image-Guided Stereotactic Body Radiation Therapy Planning for Patients With Hepatocellular Carcinoma. *Med Dosim* (2017) 42:97–103. doi: 10.1016/j.meddos.2017.01.005
43. Bowen SR, Saini J, Chapman TR, Miyaoka RS, Kinahan PE, Sandison GA, et al. Differential Hepatic Avoidance Radiation Therapy: Proof of Concept in Hepatocellular Carcinoma Patients. *Radiother Oncol* (2015) 115:203–10. doi: 10.1016/j.radonc.2015.04.011
44. Long DE, Tann M, Huang KC, Bartlett G, Galle JO, Furukawa Y, et al. Functional Liver Image Guided Hepatic Therapy (FLIGHT) With Hepatobiliary Iminodiacetic Acid (HIDA) Scans. *Pract Radiat Oncol* (2018) 8:429–36. doi: 10.1016/j.prro.2018.04.014
45. Price RG, Apisarnthanarax S, Schaub SK, Nyflot MJ, Chapman TR, Matesan M, et al. Regional Radiation Dose-Response Modeling of Functional Liver in Hepatocellular Carcinoma Patients With Longitudinal Sulfur Colloid SPECT/CT: A Proof of Concept. *Int J Radiat Oncol Biol Phys* (2018) 102:1349–56. doi: 10.1016/j.ijrobp.2018.06.017
46. De Bari B, Breuneval T, Zeverino M, Godin S, Deantonio L, Geldhof C, et al. Hepatobiliary Scintigraphy Allows the Evaluation of Short-Term Functional Toxicity of Liver Stereotactic Body Radiotherapy: Results of a Pilot Study. *PLoS One* (2018) 13:e204013. doi: 10.1371/journal.pone.0204013
47. Bowen SR, Chapman TR, Borgman J, Miyaoka RS, Kinahan PE, Liou IW, et al. Measuring Total Liver Function on Sulfur Colloid SPECT/CT for Improved Risk Stratification and Outcome Prediction of Hepatocellular Carcinoma Patients. *Ejnmmi Res* (2016) 6:57. doi: 10.1186/s13550-016-0212-9
48. Logan JK, Park PC, Wong FC, Erwin WD, Beddar S, Kaseb AO, et al. Outcomes of Patients With Hepatocellular Carcinoma and Advanced Cirrhosis After High-Dose Radiation Therapy Guided by Functional Liver Imaging With Tc99m Sulfur Colloid Liver SPECT-CT. *Int J Radiat Oncol Biol Phys* (2016) 96:E167–8. doi: 10.1016/j.ijrobp.2016.06.1012
49. Simeth J, Baughan N, Dow J, Ten Haken R, Johansson A, Aryal M, et al. Impact of Mis-Match Between Liver Function and Hepatic Perfusion on Functional Avoidance Treatment Planning. *Med Phys* (2018) 45:e120–706. doi: 10.1002/mp.12938
50. Fode MM, Petersen JB, Sørensen M, Holt MI, Keiding S, Høyer M. 2-[18F] Fluoro-2-Deoxy-D-Galactose Positron Emission Tomography Guided Functional Treatment Planning of Stereotactic Body Radiotherapy of Liver Tumours. *Phys Imaging Radiat Oncol* (2017) 1:28–33. doi: 10.1016/j.phro.2017.02.002
51. Kudithipudi V, Day E, Thai N, Kirichenko A. Liver Stereotactic Radiotherapy (SRT) With Functional Treatment Planning for Patients With Intermediate Stage Hepatocellular Carcinoma (HCC). *J Radiat Oncol* (2017) 6:371–7. doi: 10.1007/s13566-017-0325-4
52. Hasan S, Kudithipudi V, Thai NV, Kirichenko AV. Stereotactic Body Radiation Therapy (SBRT) With Functional Treatment Planning for Hepatocellular Carcinoma (HCC) in Patients With Early-Stage Cirrhosis. *Int J Radiat Oncol Biol Phys* (2016) 96:E182. doi: 10.1016/j.ijrobp.2016.06.1047
53. Shirai S, Kumayama Y, Sato M, Noda Y, Chiba T, Kawaguchi M. Cutoff Values for Dose-Liver Function Parameters to Prevent Radiation-Induced Liver Disease in Advanced Hepatoma. *J Gastroenterol Hepatol* (2015) 4:1425–33. doi: 10.6051/j.issn.2224-3992.2015.04.502
54. Nakamura Y, Kimura T, Higaki T, Honda Y, Komoto D, Yamagami T, et al. Clinical Utility of Gadoxetate Disodium-Enhanced Hepatic MRI for Stereotactic Body Radiotherapy of Hepatocellular Carcinoma. *Jpn J Radiol* (2015) 33:627–35. doi: 10.1007/s11604-015-0465-7
55. Lin H. Study of Active Breathing Control in Intensity Modulated Radiotherapy for Primary Liver Cancer-Based on Liver Function Reservation Mode. *【D】 University Jinan* (2019).
56. de Graaf W, Bennink RJ, Veteläinen R, van Gulik TM. Nuclear Imaging Techniques for the Assessment of Hepatic Function in Liver Surgery and Transplantation. *J Nucl Med* (2010) 51:742–52. doi: 10.2967/jnumed.109.069435
57. Bateman TM. Advantages and Disadvantages of PET and SPECT in a Busy Clinical Practice. *J Nucl Cardiol* (2012) 19 Suppl 1:S3–11. doi: 10.1007/s12350-011-9490-9
58. Bak-Fredslund KP, Lykke Eriksen P, Munk OL, Villadsen GE, Keiding S, Sørensen M. Metabolic Liver Function in Humans Measured by 2-(18)F-Fluoro-2-Deoxy-D-Galactose PET/CT-Reproducibility and Clinical Potential. *Ejnmmi Res* (2017) 7:71. doi: 10.1186/s13550-017-0320-1
59. Geisel D, Lüdemann L, Hamm B, Denecke T. Imaging-Based Liver Function Tests–Past, Present and Future. *RöFo* (2015) 187:863–71. doi: 10.1055/s-0035-1553306
60. Yang M, Zhang Y, Zhao W, Cheng W, Wang H, Guo S. Evaluation of Liver Function Using Liver Parenchyma, Spleen and Portal Vein Signal Intensities During the Hepatobiliary Phase in Gd-EOB-D TPA-Enhanced MRI. *BMC Med Imaging* (2020) 20:119. doi: 10.1186/s12880-020-00519-7
61. Fukumitsu N, Nitta K, Terunuma T, Okumura T, Numajiri H, Oshiro Y, et al. Registration Error of the Liver CT Using Deformable Image Registration of MIM Maestro and Velocity AI. *BMC Med Imaging* (2017) 17:30. doi: 10.1186/s12880-017-0202-z
62. Dickhaus H, Floca R, Eisenmann U, Metzner R, Wirtz CR. A Flexible Registration Framework for Multimodal Image Data. *Conf Proc IEEE Eng Med Biol Soc* (2004) 2004:1755–8. doi: 10.1109/IEMBS.2004.1403526

Conflict of Interest: The authors declare that the research was conducted in the absence of any commercial or financial relationships that could be construed as a potential conflict of interest.

frontiers | Frontiers in Oncology

ORIGINAL RESEARCH
published: 29 June 2022
doi: 10.3389/fonc.2022.898771

Real-Time 2D MR Cine From Beam Eye's View With Tumor-Volume Projection to Ensure Beam-to-Tumor Conformality for MR-Guided Radiotherapy of Lung Cancer

Xingyu Nie[1,2] *and Guang Li*[1]*

[1] Department of Medical Physics, Memorial Sloan Kettering Cancer Center, New York, NY, United States, [2] Department of Radiology, University of Kentucky, Lexington, KY, United States

OPEN ACCESS

Edited by:
Yingli Yang,
UCLA Health System, United States

Reviewed by:
Chunhao Wang,
Duke University Medical Center, United States
James Chow,
University of Toronto, Canada

***Correspondence:**
Guang Li
lig2@mskcc.org

Specialty section:
This article was submitted to Radiation Oncology, a section of the journal Frontiers in Oncology

Received: 17 March 2022
Accepted: 20 May 2022
Published: 29 June 2022

Citation:
Nie X and Li G (2022) Real-Time 2D MR Cine From Beam Eye's View With Tumor-Volume Projection to Ensure Beam-to-Tumor Conformality for MR-Guided Radiotherapy of Lung Cancer. Front. Oncol. 12:898771. doi: 10.3389/fonc.2022.898771

Purpose: To minimize computation latency using a predictive strategy to retrieve and project tumor volume onto 2D MR beam eye's view (BEV) cine from time-resolved four-dimensional magnetic resonance imaging (TR-4DMRI) libraries (inhalation/exhalation) for personalized MR-guided intensity-modulated radiotherapy (IMRT) or volumetric-modulated arc therapy (VMAT).

Methods: Two time-series forecasting algorithms, autoregressive (AR) modeling and deep-learning-based long short-term memory (LSTM), were applied to predict the diaphragm position in the next 2D BEV cine to identify a motion-matched and hysteresis-accounted image to retrieve the tumor volume from the inhalation/exhalation TR-4DMRI libraries. Three 40-s TR-4DMRI (2 Hz, 3 × 80 images) per patient of eight lung cancer patients were used to create patient-specific inhalation/exhalation 4DMRI libraries, extract diaphragmatic waveforms, and interpolate them to f = 4 and 8 Hz to match 2D cine frame rates. Along a (40•f)-timepoint waveform, 30•f training timepoints were moved forward to produce 3×(10•f-1) predictions. The accuracy of position prediction was assessed against the waveform ground truth. The accuracy of tumor volume projections was evaluated using the center-of-mass difference (ΔCOM) and Dice similarity index against the TR-4DMRI ground truth for both IMRT (six beam angles, 30° interval) and VMAT (240/480 beam angles, 1.5°/0.75° interval, at 4/8 Hz, respectively).

Results: The accuracy of the first-timepoint prediction is 0.36 ± 0.10 mm (AR) and 0.62 ± 0.21 mm (LSTM) at 4 Hz and 0.06 ± 0.02 mm (AR) and 0.18 ± 0.06 mm (LSTM) at 8 Hz. A 10%–20% random error in prediction-library matching increases the overall uncertainty slightly. For both IMRT and VMAT, the accuracy of projected tumor volume contours on 2D BEV cine is ΔCOM = 0.39 ± 0.13 mm and DICE = 0.97 ± 0.02 at 4 Hz and ΔCOM = 0.10 ± 0.04 mm and DICE = 1.00 ± 0.00 at 8Hz.

Conclusion: This study demonstrates the feasibility of accurately predicting respiratory motion during 2D BEV cine imaging, identifying a motion-matched and hysteresis-accounted tumor volume, and projecting tumor volume contour on 2D BEV cine for real-time assessment of beam-to-tumor conformality, promising for optimal personalized MR-guided radiotherapy.

Keywords: MR-BEV-cine-guided radiotherapy, beam-to-tumor conformality, real-time motion prediction, latency, Motion management

INTRODUCTION

One of the major advantages of magnetic resonance imaging integrated linear accelerator (MR-Linac) is to provide MR-guided radiotherapy (MRgRT), including real-time tumor motion management, making respiratory gating accurate and tumor tracking possible, especially for hypo-fractional stereotactic body radiotherapy (SBRT) (1–3). As MRgRT provides patient-specific imaging in real-time during treatment, adapting to inter-fractional and intra-fractional patient anatomic variations, it offers the best-personalized radiotherapy. Clinically, improved treatment outcomes have been reported showing the benefit of sparing critical organs at risk (OARs) so that the tumor lethal dose can be prescribed and delivered to a mobile target, including lung, liver, and pancreatic cancer (3, 4). Compared with conventional image-guided radiotherapy (IGRT), MRgRT offers many advantages, including real-time imaging with high soft-tissue contrast without ionization radiation. So far, the intensity-modulated radiotherapy (IMRT) technique is available in the MR-Linac and the volumetrically modulated arc therapy (VMAT) technique should be possible in the future.

Currently, dynamic 2D cine imaging in the sagittal and coronal views can be employed for MR-guided IMRT to monitor respiratory-induced tumor motion in real time covering the major motions in the superior–inferior (SI) and anterior–posterior (AP) directions. Although the two cine views infer a 3D tumor motion, they are partial and indirect views of a volumetric tumor related to the radiation beam. Moreover, potential through-plane tumor motion may interfere with motion interpretation. The more effective, optimal view for assessing the beam-to-tumor conformality should be the beam eye's view (BEV), which is how the radiation beam sees the mobile tumor and only needs one cine scan (5–7). Previously, a 2D BEV cine technique with tumor volume projection has been reported feasible for better MRgRT (8). For IMRT treatment, adequate accuracy and performance have been achieved to identify and project a volumetric tumor onto the BEV by 2D–3D matching between the 2D tumor image on the BEV cine images and a time-resolved (TR) 4DMRI library containing volumetric images from multiple breathing cycles (9–12). For MR-guided VMAT, which may be available in the future, real-time communication and computation are required for 2D cine imaging with a rotating BEV and projecting tumor volume with minimal latency.

To overcome system latency, predictive strategies have been applied to provide a just-in-time prediction of tumor motion in the next 30–1,000 ms, using conventional Linac for tumor tracking, including adjusting the radiation beam, a multi-leaf collimator (MLC), or couch position to keep up with a tumor motion (13–15). Various predictive methods have been evaluated, including time-series-based (16), model-based (17), regression-based (18), and machine-learning-based (19, 20) prediction methods. Short-term motion prediction is an effective and efficient approach to overcome the system latency and reduce the frequency of x-ray imaging.

Additionally, respiratory motion hysteresis is a commonly occurring phenomenon in patients, resulting in variations in tumor motion trajectory, orientation, and shape between inhalation and exhalation (21, 22). Therefore, even at the same tumor displacement in the superior–inferior (SI) direction, the tumor shape, orientation, and anterior–posterior (AP) and left–right (RL) positions may vary due to the motion hysteresis (15, 21–24). Therefore, without differentiating the inhalation and exhalation processes, it may add uncertainties in retrieving the motion-matched tumor volume for BEV projection.

In this simulation study, we aimed to minimize the latency in matching a tumor volume by predicting the respiratory motion to identify and project tumor volume in parallel with the next 2D BEV cine acquisition. In addition, to minimize the motion hysteresis effect, two TR-4DMRI image libraries of exhalation and inhalation were created by grouping volumetric images based on their moving directions. Two predictive algorithms, a conventional autoregression (AR) modeling and a deep-learning-based long short-term memory (LSTM) neural network, were applied and evaluated with the known waveforms. The accuracy of tumor volume projection on the 2D BEV cine images was evaluated against the ground truth embedded in the TR-4DMRI datasets. This improved 2D BEV cine technique was evaluated for both MR-guided IMRT and VMAT treatments.

METHODS

In this study, a predictive strategy was proposed and evaluated to identify and project tumor volume onto 2D BEV cine images in real time with minimized system latency and included respiratory motion hysteresis. The workflow of the strategy is shown in **Figure 1**.

Three Time-Resolved 4DMRI Image Datasets, Waveform Extraction, and Interpolation

Eight lung cancer patients were recruited to participate in an IRB-approved protocol study using TR-4DMRI for respirator-induced tumor motion simulation and assessment in a 3T MRI scanner (Ingenia, Philips Healthcare, Amsterdam, Netherlands).

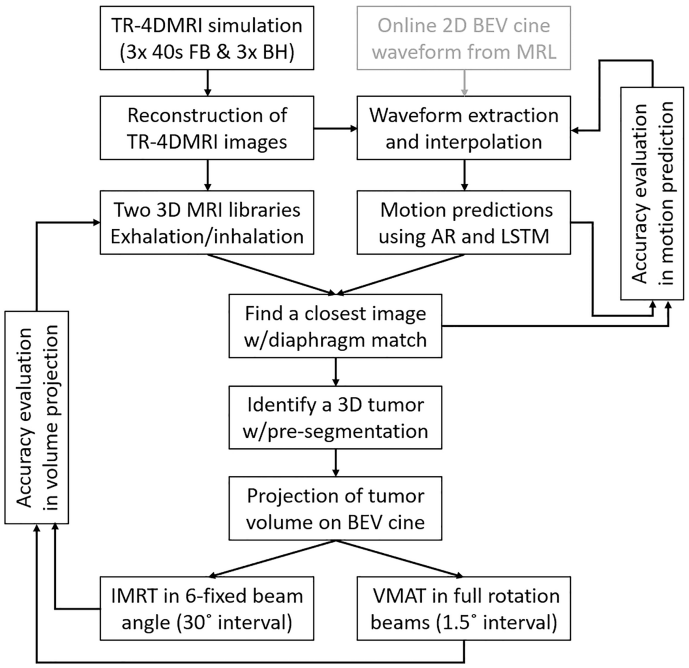

FIGURE 1 | The workflow of the predictive strategy to predict, identify, and project tumor volume onto 2D BEV cine, followed by the verification of projected tumor volume using the center of mass and Dice similarity index against the ground truth for MR-guided IMRT and VMAT. In future clinical applications, the cine waveform can be utilized as well (gray box).

Eight patients were scanned at simulation with 3D cine in free breathing (FB) for 40 (s) at $f = 2$ *Hz* three times within one imaging session. A T1-weighted, multi-shot, turbo field echo pulse sequence was used with SENSE acceleration (6.0) and partial Fourier approximation (0.8), so a total of 3×80 volumetric 3D cine images with a voxel size of $5 \times 5 \times 5$ mm^3 were acquired. Using the same scan protocol with less acceleration (3.75), three 3D cines ($2 \times 2 \times 2$ mm^3) in breath hold (BH) at an arbitrary stage were acquired within 20 s. The TR-4DMRI images were reconstructed based on the super-resolution approach that has been developed *via* deformable image registration between the low-resolution FB and high-resolution BH images. Detailed 4DMRI scanning and reconstruction methods and conditions can be found in the previous publications (9–11).

The diaphragmatic motion waveforms were extracted from TR-4DMRI using an in-house program in MATLAB (MathWorks, MA). A navigator box ($3 \times 3 \times 6$ cm^3) drawn on the right diaphragmatic dome was used to calculate the average voxel intensity at the same SI positions, and the point with the largest gradient was determined as the diaphragm position. Over the 80 images from a 40-s scan, diaphragmatic motion trajectory in a scan series was used as a motion waveform in the superior–inferior (SI) direction. Each of the three waveforms at the frequency of $f = 2$ *Hz* was interpolated using the b-spline function to $f = 4$ *Hz* and $f = 8$ *Hz* to match the possible scanning rates of clinical 2D cine frame rate, containing a total of 40•f timepoints.

Just-in-Time Prediction to Overcome System Latency in the 2D BEV Cine Strategy

Two time-series forecasting algorithms were applied to predict diaphragm motion based on the motion waveforms: (1) a classical autoregressive (AR) modeling algorithm implemented in the MATLAB Econometric Toolbox™ that uses past values as inputs to a regression algorithm to predict future values and (2) a deep-learning long short-term memory (LSTM) recurrent neural network algorithm in the MATLAB Deep Learning Toolbox™ that processes input data by looping over the time steps and updating the network state containing information over previous time steps. Various parameters were tested for the best prediction accuracy and performance in the two predictive algorithms, and the optimal settings include using 30-s training data, 10 AR polynomial degrees, and 20 hidden layers in the neural network using the Adam (Adaptive Moment Estimation) optimizer with the maximum of 150 epochs.

In each of the interpolated 40-s waveforms, a 30-s waveform section with 30•f timepoints was applied as training data to predict the diaphragm position at the next time point in 125 ms at $f = 8$ Hz and 250 ms at $f = 4$ Hz. After a prediction, the training dataset was moved one timepoint forward by adding one new timepoint and removing one old timepoint. The remaining 10-s waveform served as the ground truth to assess the prediction accuracy of n = 10•f-1 predictions per motion waveform. For each patient, a total of $3 \times (10 \bullet f\text{-}1)$ predictions were made and

evaluated to assess both patient-specific and population-based accuracy of motion prediction.

Accounting Tumor Motion Hysteresis by Identifying Tumor With Predicted Motion Direction

The 3 × 80 TR-4DMRI images per patient were categorized as in the inhalation and exhalation processes depending on the diaphragm moving direction from the previous timepoint. Therefore, two TR-4DMRI image libraries of inhalation and exhalation were built with roughly 120 images each. The estimated displacement interval on the diaphragm was 30 mm/120 = 0.25 mm, and the exact interval may vary, depending on the motion range, speed, and number of images. Note that the motion interval can be reduced, as more 40-s TR-4DMRI series could be acquired and added from simulation.

When the next diaphragm position is predicted, the moving direction was first used to select the TR-4DMRI library (inhalation or exhalation), and the predicted amplitude was then applied to identify a matched diaphragm, and therefore the corresponding tumor volume in the library. As exact diaphragm matching may not be found in a library, a small uncertainty should be added on top of the prediction uncertainty for the diaphragm position displacement (ΔD), namely,

$$\Delta D^{matched} = \Delta D^{prediction} + \Delta D^{matching} \quad (1)$$

Once a volumetric image was identified with a matched diaphragm from a library, either for inhalation or for exhalation, the tumor volume projection was evaluated as the difference in the center of mass (ΔCOM) and the DICE similarity index, compared with the image ground truth embedded in the simulation dataset for accuracy assessment.

Accuracy of Tumor Volume Projection on 2D BEV Cine for MR-Guided IMRT and VMAT

For IMRT treatment, six fixed beam angles (0°–150°) with 30° intervals were used to assess the ΔCOM and DICE of the projected tumor volumes between the predicted and ground truth as a function of time during treatment delivery. Mimicking a 6-beam IMRT plan, all TR-4DMRI images in the patient-specific libraries were segmented for tumor volume using an automated MATLAB program on all cuts parallel to the BEV with a 2-mm interval and ready to be projected to the 2D BEV images. The union of all projected contours was used as the final tumor volume projection.

For VMAT treatment, the full rotation was divided into 240 sections with 1.5° intervals in 4-Hz simulation and used to assess the ΔCOM and DICE between the tumor volume projections from the predicted and ground truth. In the 8-Hz simulation, 480 sections per gantry rotation with 0.75° intervals were used. The results were analyzed as a function of gantry angle, assuming that the gantry rotates at a constant speed. It should be noted that clinically the gantry position is known within the MR-integrated Linac system and the beam angle will be updated. In the VMAT cases, much more beam angles were prepared with pre-segmented tumor volume ready to be used.

For both IMRT and VMAT cases, the results of tumor volume projection resulting from the predictions at 125 and 250 ms were evaluated using the ΔCOM and Dice index based on 8- and 4-Hz interpolated waveforms, respectively. The two-tailed Student's t test was used for all comparison, and a p-value of less than 0.05 was considered statistically significant different.

RESULTS

Prediction Accuracy of the AR Modeling and LSTM Deep-Learning Network

Figure 2 illustrates the prediction and matching errors based on the 4- and 8-Hz waveforms. Only the first time point will be used as the diaphragm position in the next 2D BEV cine image for accuracy evaluation, while prediction errors for the first 10 time points are provided, which tend to level off around 1,000 ms at both frequencies. The prediction accuracy is higher at 8 Hz than at 4 Hz, primarily due to more training points being used. Furthermore, the AR method predicts more accurately (0.4 mm) and takes less time (0.4 s) than the LSTM prediction (0.6 mm, 1.5 s) at 4 Hz under the current computing conditions, as shown in **Table 1**. The same trend is observed using the 8-Hz waveform, as shown in **Table 2**.

Tumor Motion Hysteresis and Compensation Using Exhalation and Inhalation Libraries

The motion of the diaphragm spends slightly more time (more images) in exhalation than inhalation phases, as shown in **Table 1**. **Figures 3**, **4** show a couple of examples of motion hysteresis of the tumors in the coronal view (BEV = 0°) and are compensated for by identifying the matched tumor volume using the appropriate inhalation or exhalation TR-4DMRI library.

Verification of 2D BEV Cine With Tumor Volume Projections for IMRT and VMAT Treatments

Table 3 shows the average and standard deviation of COM difference (ΔCOM) and Dice similarity of projected tumor volume between the identified and ground truth for IMRT with six fixed beam angles and for VMAT with rotating beam angles (1.5° interval at 4 Hz and 0.75° interval at 8 Hz). **Figure 5** shows the Dice similarity index in VMAT as a function of beam angle for predictions using the 4- and 8-Hz waveform data.

DISCUSSION

Based on the previous 2D BEV cine approach for MR-guided IMRT (8), we have demonstrated the following three improvements of the approach in this simulation study: (1) the computation latency has been minimized by applying the

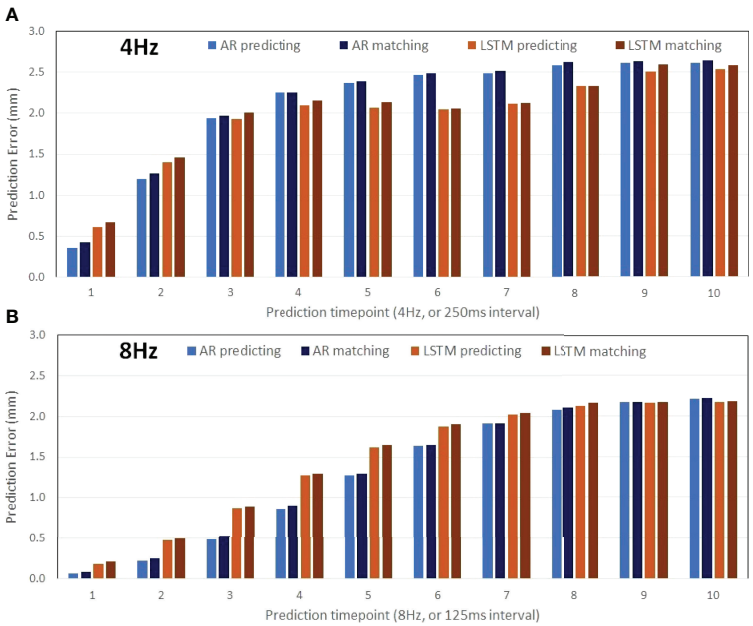

FIGURE 2 | Prediction accuracy of the AR (autoregressive) modeling and the LSTM (long short-term memory) neural network as a function of the time points ahead of training datasets (the 30s of the waveform) using motion waveforms at 4 Hz (**A**: 10 predicted timepoints in 2,500 ms) and at 8 Hz (**B**: 10 predicted timepoints in 1,250 ms). The mean differences increase slightly due to the matching errors.

prediction method in parallel with the 2D cine scan to identify a motion-matched tumor volume without searching from scratch, (2) respiratory-induced tumor motion hysteresis has been explicitely compensated for using the predicted motion to find a match in either inhalation or exhalation libraries depending on the motion direction, and (3) the feasibility of the 2D BEV cine approach to MR-guided VMAT has been tested. In the following, the advantages and limitations of the new 2D BEV cine approach will be discussed in depth.

Minimizing Computation Latency Using Just-in-Time Tumor Motion Prediction

The so-called just-in-time tumor motion prediction has been studied to combat the system latency in respiratory-gated or tumor-tracking radiotherapy, as it can predict several tens or hundreds of milliseconds (ms) ahead of time, allowing the system to start to act before an event occurs. In this study, the predictive strategy is applied to remove the computation latency in the 2D–3D library matching (8) for tumor volume projection.

TABLE 1 | Prediction accuracy with matching uncertainties based on 4Hz motion waveforms.

Patient	Diaphragm motion (mm)	4DMRI libraries		AR accuracy (mm)[b]					LSTM accuracy (mm)[b]				
		Inhale phases	Exhale phases	Prediction			Matched		Prediction			Matched	
				AVG[a]	STD	t (s)	AVG[a]	STD	AVG[a]	STD	t (s)	AVG[a]	STD
1	15.8	89	122	0.24	0.20	0.44	0.30	0.20	0.42	0.28	1.47	0.47	0.32
2	12.9	97	118	0.26	0.20	0.44	0.31	0.17	0.59	0.55	1.46	0.62	0.58
3	20.7	108	110	0.44	0.36	0.44	0.47	0.36	0.88	0.70	1.50	0.93	0.70
4	14.4	108	111	0.45	0.32	0.44	0.48	0.35	0.61	0.39	1.49	0.64	0.38
5	9.6	101	117	0.25	0.19	0.44	0.31	0.18	0.24	0.21	1.45	0.27	0.21
6	15.8	114	102	0.33	0.28	0.44	0.47	0.49	0.64	0.61	1.47	0.65	0.63
7	11.6	95	122	0.42	0.24	0.44	0.42	0.26	0.75	0.48	1.45	0.78	0.51
8	29.1	92	125	0.47	0.49	0.44	0.63	0.49	0.81	1.34	1.45	0.97	1.24
AVG	16.2	100.5	115.9	0.36	0.29	0.44	0.42	0.31	0.62	0.57	1.47	0.67	0.57
STD	6.2	8.8	7.7	0.10	0.10	0.00	0.11	0.13	0.21	0.35	0.02	0.23	0.32

The AR (autoregression) and LSTM (long short-term memory) prediction accuracy and performance, diaphragm motion, two TR-4DMRI libraries in the inhalation and exhalation, and the library matching errors are provided. The AR method provides more accurate prediction results using less time than that of the LSTM method.

[a]*p-value <0.02 for both prediction and matched accuracy between AR and LSTM.*

[b]*No significant difference between prediction and matched accuracy using either AR or LSTM.*

TABLE 2 | Prediction accuracy with matching uncertainties based on 8-Hz motion waveforms.

Patient	Tumor motion and volume				AR accuracy (mm)[b]					LSTM accuracy (mm)[b]				
	SI (mm)	AP (mm)	LR (mm)	Vol (cc)	Prediction			Matched		Prediction			Matched	
					AVG[a]	STD	t (s)	AVG[a]	STD	AVG[a]	STD	t (s)	AVG[a]	STD
1	3.6	6.7	2.1	5.2	0.03	0.03	0.52	0.05	0.06	0.14	0.12	1.87	0.19	0.13
2	9.1	8.0	5.2	16.2	0.05	0.04	0.51	0.06	0.05	0.20	0.17	1.85	0.22	0.16
3	6.6	5.5	8.9	8.8	0.08	0.06	0.50	0.10	0.07	0.15	0.12	1.93	0.19	0.13
4	3.7	4.5	4.1	25.1	0.06	0.05	0.51	0.07	0.06	0.17	0.13	1.89	0.20	0.14
5	3.5	2.1	2.1	3.5	0.04	0.04	0.51	0.06	0.04	0.11	0.09	1.90	0.13	0.10
6	6.0	8.9	9.9	10.0	0.10	0.09	0.50	0.14	0.11	0.17	0.14	1.93	0.20	0.14
7	8.1	8.4	6.5	64.1	0.05	0.04	0.50	0.07	0.05	0.15	0.12	1.92	0.16	0.11
8	5.2	2.7	5.3	1.2	0.06	0.07	0.44	0.09	0.11	0.30	0.45	1.89	0.37	0.51
AVG	5.7	5.9	5.5	16.8	0.06	0.05	0.50	0.08	0.07	0.18	0.17	1.90	0.21	0.18
STD	2.1	2.6	2.9	20.6	0.02	0.02	0.03	0.03	0.03	0.06	0.11	0.03	0.07	0.14

The AR (autoregression) and LSTM (long short-term memory) prediction accuracy and performance, tumor motion, location, and volume, and the library matching errors are provided. The AR method provides more accurate prediction results using less time than that of the LSTM method.

[a]*p-value <0.001 in both prediction and matched accuracy between AR and LSTM.*

[b]*No significant difference between prediction and matched accuracy using either AR or LSTM.*

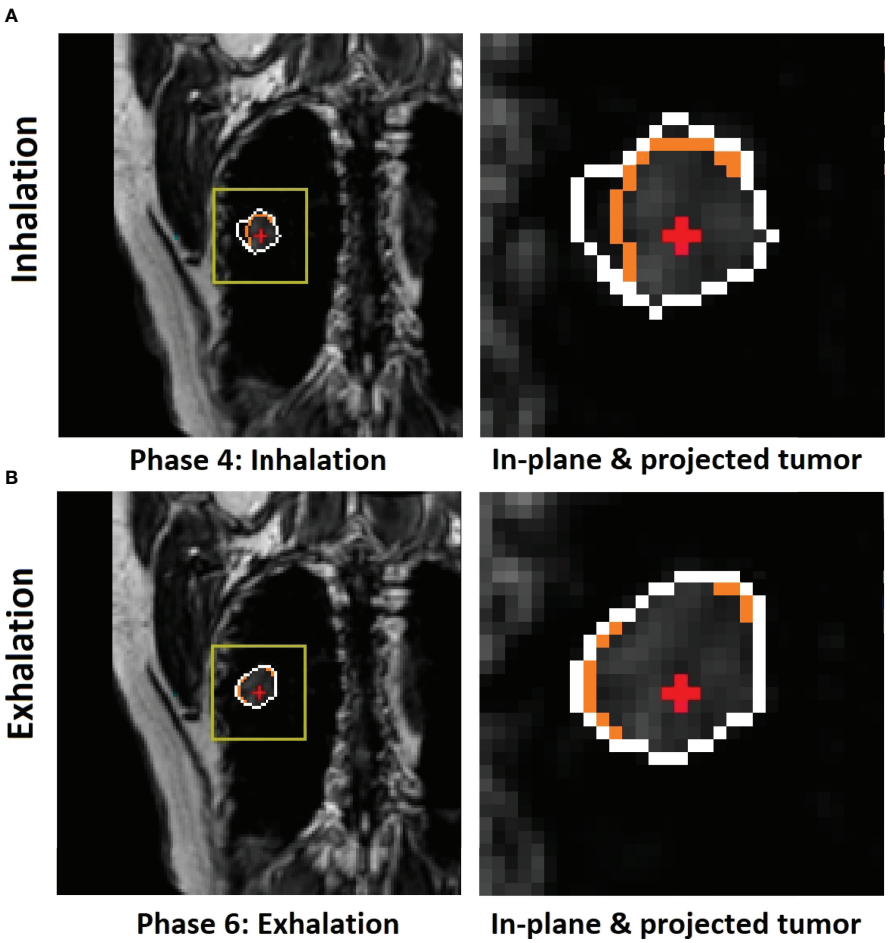

FIGURE 3 | Illustration of motion hysteresis of a posterior peripheral tumor (patient 2, with 20 breathing cycles in 40 s) during mid-inhalation **(A)** and mid-exhalation **(B)** with a similar diaphragm displacement at the zero-gantry angle (BEV = 0°). The isocenter (red cross) position is shown inside the in-plane tumor BEV contour (orange) and the projected volumetric tumor contour (white). Both the in-plane and projected tumor contour shapes and the centers of mass (COMs) are different between inhalation and exhalation. By selectively using either the inhalation or exhalation TR-4DMRI library based on the motion direction, the respiratory hysteresis effect is compensated.

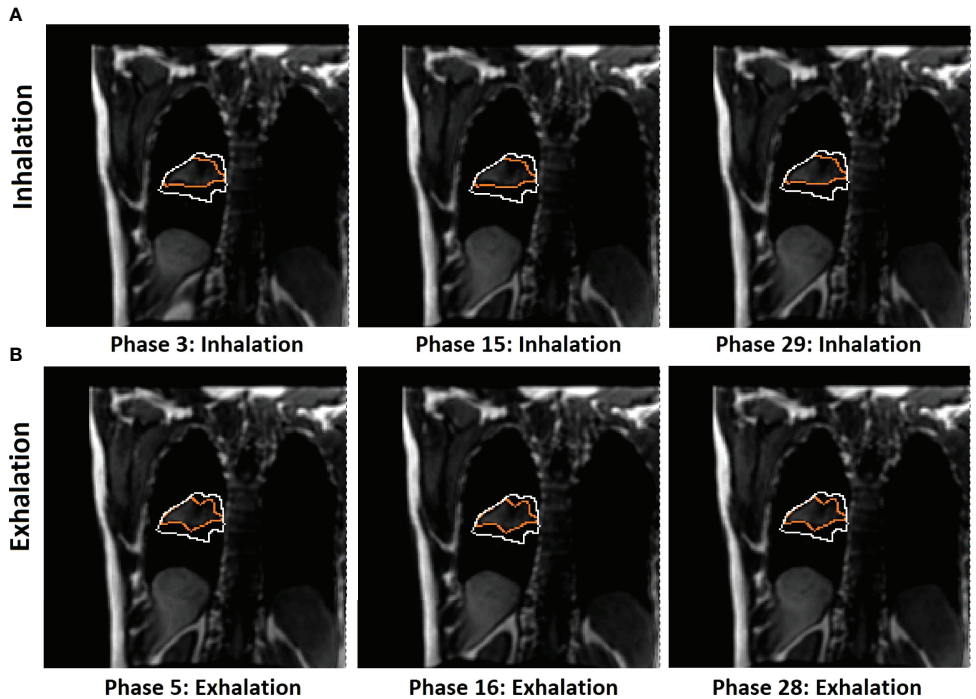

FIGURE 4 | Illustration of 2D BEV (beam angle = 0°) difference of in-plane tumor contours (orange) between mid-inhalation **(A)** and mid-exhalation **(B)** (patient 7, with 17 breathing cycles in 40 s), while projected tumor volume contours (white) are similar in the multi-cycle TR-4DMRI images for this patient. The diaphragm positions are similar in all cases. Due to respiratory hysteresis, including the AP motion, the in-plane tumor contours (orange) are distinctively different between inhalation and exhalation. In contrast, tumor volume projections may not be affected by a through-plane (AP) motion, presenting a stable projected tumor contour. This predictive strategy distinguishes hysteresis-caused tumor volume differences *via* selectively using either the inhalation or exhalation TR-4DMRI library based on the respiratory direction, while the previous method distinguishes them *via* searching for a match with the highest Dice similarity index (8).

TABLE 3 | The accuracy of the center of mass (ΔCOM) and shape (Dice similarity index) of the projected tumor volume onto the 2D BEV cine images.

Patient	4-Hz motion waveforms*						8-Hz motion waveforms*					
	IMRT			VMAT			IMRT			VMAT		
	ΔCOM[a] (mm)	2D[b] Dice	3D[c]Dice	ΔCOM[a] (mm)	2D[b] Dice	3D[c]Dice	ΔCOM[a] (mm)	2D[b] Dice	3D[c]Dice	ΔCOM[a] (mm)	2D[b] Dice	3D[c]Dice
1	0.25	0.98	0.99	0.25	0.98	0.99	0.06	1.00	1.00	0.06	1.00	1.00
2	0.31	0.97	0.98	0.31	0.97	0.98	0.07	1.00	1.00	0.07	1.00	1.00
3	0.64	0.88	0.93	0.64	0.88	0.93	0.17	0.98	0.98	0.17	0.98	0.99
4	0.47	0.94	0.96	0.47	0.94	0.96	0.11	0.99	0.99	0.11	0.99	1.00
5	0.25	0.98	0.99	0.25	0.98	0.99	0.06	0.99	0.99	0.06	0.99	1.00
6	0.42	0.96	0.97	0.42	0.95	0.97	0.12	0.99	0.99	0.12	0.99	1.00
7	0.40	0.97	0.98	0.40	0.97	0.98	0.07	1.00	1.00	0.07	1.00	1.00
8	0.40	0.93	0.95	0.40	0.93	0.95	0.10	0.99	0.99	0.10	0.99	0.99
AVG	0.39	0.95	0.97	0.39	0.95	0.97	0.10	0.99	1.00	0.10	0.99	1.00
STD	0.13	0.03	0.02	0.13	0.03	0.02	0.04	0.01	0.00	0.04	0.01	0.00

At both frequencies of the waveforms for both IMRT and VMAT, a sub-mm accuracy in COM and a greater than 0.95 Dice on average are achieved using the predictive strategy. Additionally, as the prediction accuracy is higher at 8 Hz than at 4 Hz, the accuracy of tumor volume projection is also higher, suggesting the benefit of scanning 2D BEV cine at the highest possible frequency.

[a]*p-value <0.0001 for ΔCOM comparison between 4- and 8-Hz motion waveform.*

[b]*2D Dice refers to the 2D tumor contour on the 2D BEV cine image. p-value < 0.005 for 2D Dice comparison between 4- and 8-Hz motion waveform.*

[c]*3D Dice refers to the tumor volume projection on the 2D BEV cine image. p-value <0.01 for 3D Dice comparison between 4- and 8-Hz motion waveform.*

**No significant difference between ΔCOM, 2D Dice and 3D Dice in both frequencies of motion waveform.*

As the prediction can be started in parallel with the next BEV 2D cine acquisition, the predicted tumor position in the next cine frame should be available and ready to project tumor volume contour onto the 2D BEV cine image. Therefore, the computation latency can be reduced or eliminated if the prediction can be completed within 125 or 250 ms for 8- or 4-Hz cine acquisition, respectively.

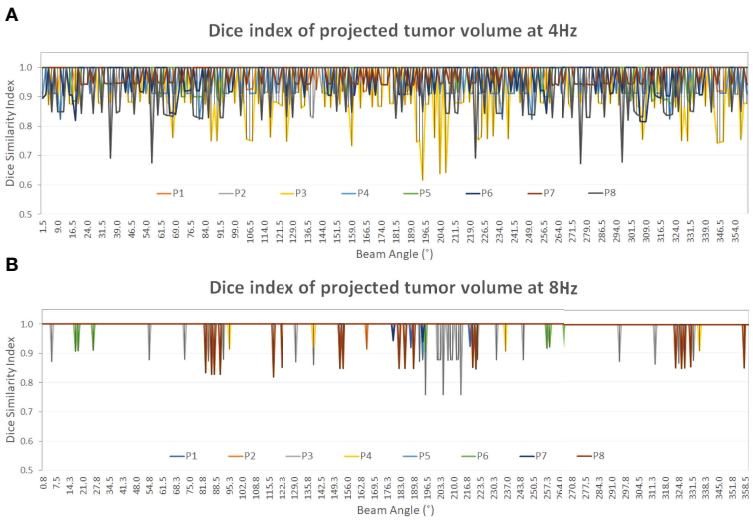

FIGURE 5 | The Dice similarity index of the projected tumor contours on the 2D BEV cine images between the predicted and the ground truth of the tumor volume as a function of beam angle (0°–360°). A constant gantry rotation is assumed for the two plots (Dice value display: 0.4–1.0). At both frequencies, the Dice index of patient 3 (yellow) shows the most variations among the eight patients. From 4 Hz **(A)** to 8 Hz **(B)** the average Dice index increases from 0.97 ± 0.02 to 1.00 ± 0.00 (**Table 3**) as the prediction accuracy increases, as shown in **Tables 1**, **2**.

Interestingly, the prediction accuracy and speed of the AR modeling method outperform the deep-learning-based LSTM neural network method, in both accuracy and performance. As the learning process is progressively reoccurring along with the moving training dataset, the LSTM has to relearn every time in the current algorithm. Therefore, the AR results will be used as the focus of the discussion. As shown in **Tables 1**, **2**, the current AR computation times for prediction are 400 and 500 ms for 4- and 8-Hz training datasets, respectively. The computation time must be reduced to within 125–250 ms to remove the computation latency, and performance enhancement is achievable by optimizing the prediction code, using a more powerful computer, and/or employing parallel computing techniques, including the graphics processing unit (GPU) technique.

On average, the prediction accuracy is higher for the time point that is closer to the training dataset, as illustrated by the predictions of the next 125 ms (8 Hz) and 250 ms (4 Hz), as shown in **Tables 1**, **2**. The higher the 2D cine frame rate, the higher the accuracy of prediction would be, and therefore the more accurate the tumor volume projection. Therefore, it is recommended to apply the highest cine frame rate, as long as the cine image quality is sufficient for tumor visualization. In this study, as the b-spline interpolation was applied to the waveform extracted from TR-4DMRI (2Hz), the waveforms are "smoother" than the actual, which contains random noise. However, even if a 2% random error was added to the interpolated motion waveform, the prediction error should still be at the sub-mm level. A random library matching error was present due to the limited motion interval in the TR-4DMRI library, and on average, the prediction results remain roughly the same (**Figure 2**).

Compensating for the Tumor Motion Hysteresis by Separating Inhalation and Exhalation

It is well known that respiratory-induced tumor motion is direction-dependent, meaning the path for inhalation is different from that of exhalation, namely, motion hysteresis (21, 24). Therefore, when identifying an image with a matching diaphragm or tumor displacement in the SI direction, the motion direction should be considered, in addition to amplitude. In this study, we split the TR-4DMRI library into inhalation and exhalation libraries and applied motion direction first to select the correct library and then found a match with the motion amplitude. Therefore, the hysteresis effect will be accounted for.

Using the current three-series TR-4DMRI, the number of images seems sufficient to have a small-enough motion interval in both inhalation and exhalation libraries, as the uncertainty from slight mismatching does not add too much error on average (**Figure 2**). However, for individual prediction, the finer interval should be helpful to identify a precise diaphragm or tumor position. The library sizes can be easily increased by acquiring more 40-s TR-4DMRI series as additional acquisitions. The 40-s limit is due to the MR scanner memory capacity. Therefore, the number of MR images in the exhalation and inhalation libraries can be increased substantially within a couple of minutes of TR-4DMIR acquisition.

The motion hysteresis has some variation, meaning the inhalation and exhalation path may not be very reproducible, as part of breathing irregularities. Therefore, there is an uncertainty in identifying a tumor volume from the libraries, either through previous 2D–3D library matching (8) or through current inhalation/exhalation library assignment.

Advantages and Limitations of Using BEV 2D Cine for MRgRT Treatments

It is a commonly accepted concept in image-guided radiotherapy that BEV imaging is the most useful guidance because it directly verifies if the radiation beam is targeting a mobile tumor and if beam-to-tumor conformality is acceptable by comparing the projected tumor volume in the planning BEV image and the verification BEV image. In a conventional Linac, an MV electronic portal imaging device (EPID) is used to take the BEV portal image, while in an MR-integrated Linac, a 2D BEV cine image can be acquired by changing the MR imaging orientation to be perpendicular to the radiation beam. Aside from other differences, the 2D BEV cine image provides a slice image, while the EPID produces a radiographic projection image. Therefore, the through-plane tumor motion will affect the MR cine image, and projecting the tumor volume onto the BEV cine becomes necessary. To retrieve tumor volumetric information, we proposed to identify the matched tumor volume in TR-4DMRI libraries *via* either previous 2D–3D library matching (8) or the predictive strategy to identify the motion-matched and hysteresis-compensated tumor volume for volume projection onto the 2D BEV cine image. Although both approaches work, the current approach has the advantage of no computational latency.

In this study, verification of the predicted tumor volume projection against the ground truth illustrates the accuracy of the improved 2D BEV cine strategy. A sub-mm accuracy in prediction and tumor COM has been achieved, while the contour shape similarity of the projected tumor volume is as high as >0.95 against the ground truth. Therefore, the 2D BEV cine with projected tumor volume is sufficiently accurate and reliable and can be viewed in real time as soon as the 2D BEV cine is acquired without computational latency. The current predictive code needs to be optimized on its performance to reduce the computation time from 400 ms to within 250 ms for 4 Hz, including using parallel computing techniques, such as GPU technology.

In this predictive strategy, a high correlation between the diaphragm and tumor motions was assumed, which is often true for a lung or liver tumor that is located near the diaphragm (25–27). If a tumor is away from the diaphragm, its motion amplitude should be only a fraction of that of the diaphragm. Therefore, the tumor volume can be found with an acceptable tolerance when the diaphragm position has a precise match. As the diaphragm is a large object, uncertainties in its position determination are present (28). The sub-mm COM accuracy results have validated the assumption and method of segmenting the diaphragm used in this study. Clinically, if a tumor volume is sufficiently large, the tumor motion trajectory waveform can be directly measured using the same image processing tool on TR-4DMRI images. Clinically, the tumor trajectory from the 2D BEV cine can be also used as the motion of the day (**Figure 1**). Therefore, the error from the imperfect diaphragm–tumor correlation is eliminated, and more accurate identification and projection of tumor volume can be achieved.

Breathing irregularities have been observed and investigated during radiotherapy treatment in comparison with the motion assessment at the simulation (29, 30). Therefore, the TR-4DMRI library may need more images under some "abnormal" breathing conditions, including slightly deeper breathing. Therefore, the TR-4DMRI library represents more possible variations, ensuring the finding of a motion-matched and hysteresis-compensated tumor volume for projection onto the 2D BEV cine image.

Currently, the 2D BEV cine approach with projected tumor volume has only been tested for motion monitoring of peripheral lung cancer; it remains a challenge for centrally located lung tumor, liver, and pancreatic cancer, for which the image contrast between tumor and surrounding normal tissue may not be as clear, making the automatic tumor delineation difficult, even for MR imaging with high soft-tissue contrast. Therefore, further investigation is needed to assess the feasibility of other disease sites.

CONCLUSION

This study has demonstrated an improved 2D BEV cine approach for MR-guided IMRT with minimal computation latency, ability to compensating for respiratory hysteresis, and the feasibility for MR-guided VMAT. The predictive method can achieve sub-mm accuracy to determine the diaphragm position, tumor position, and tumor projection for the next frame of the 2D BEV cine image. The AR algorithm outperforms the LSTM algorithm in the next-frame motion prediction at both 4- and 8-Hz 2D BEV cine frame rates. The potential respiratory hysteresis effect on tumor shape between inhalation and exhalation is accounted for by checking motion direction and using corresponding TR-4DMRI libraries. This approach allows real-time assessment of beam-to-tumor conformality for respiratory gating or tracking during IMRT or VMAT treatments. With further clinical testing, this 2D BEV cine approach has strong potential to serve as optimal personalized imaging guidance in current MR-guided IMRT or future VMAT treatments.

DATA AVAILABILITY STATEMENT

The raw data supporting the conclusions of this article can be made available by the authors upon request without undue reservation.

ETHICS STATEMENT

The studies involving human participants were reviewed and approved by the MSK Institutional Review Board (IRB). The patients/participants provided their written informed consent to participate in this study.

AUTHOR CONTRIBUTIONS

Both authors have made substantial contributions to this work. XN conducted most of the coding and computation. GL proposed the idea, participated in the data acquisition and analysis, and wrote the paper. All authors contributed to the article and approved the submitted version.

ACKNOWLEDGMENTS

This research is in part supported by the MSK Cancer Center Support Grant/Core Grant (P30 CA008748). We are grateful to Dr. Andreas Rimner for patient consenting, MR therapists for patient scanning, and all patients who participated in the IRB-approved protocol study.

REFERENCES

1. Schrenk O, Spindeldreier CK, Burigo LN, Hoerner-Rieber J, Pfaffenberger A. Effects of Magnetic Field Orientation and Strength on the Treatment Planning of Nonsmall Cell Lung Cancer. *Med Phys* (2017) 44(12):6621–31. doi: 10.1002/mp.12631
2. Chin S, Eccles CL, McWilliam A, Chuter R, Walker E, Whitehurst P, et al. Magnetic Resonance-Guided Radiation Therapy: A Review. *J Med Imaging Radiat Oncol* (2020) 64(1):163–77. doi: 10.1111/1754-9485.12968
3. Corradini S, Alongi F, Andratschke N, Belka C, Boldrini L, Cellini F, et al. MR-Guidance in Clinical Reality: Current Treatment Challenges and Future Perspectives. *Radiat Oncol* (2019) 14(1):92. doi: 10.1186/s13014-019-1308-y
4. Das IJ, McGee KP, Tyagi N, Wang H. Role and Future of MRI in Radiation Oncology. *Br J Radiology* (2019) 92(1094):20180505. doi: 10.1259/bjr.20180505
5. Mao W, Hsu A, Riaz N, Lee L, Wiersma R, Luxton G, et al. Image-Guided Radiotherapy in Near Real Time With Intensity-Modulated Radiotherapy Megavoltage Treatment Beam Imaging. *Int J Radiat Oncol Biol Phys* (2009) 75 (2):603–10. doi: 10.1016/j.ijrobp.2009.04.068
6. Li G, Cohen P, Xie H, Low D, Li D, Rimner A. A Novel Four-Dimensional Radiotherapy Planning Strategy From a Tumor-Tracking Beam's Eye View. *Phys Med Biol* (2012) 57(22):7579–98. doi: 10.1088/0031-9155/57/22/7579
7. Inoue M, Shiomi H, Iwata H, Taguchi J, Okawa K, Kikuchi C, et al. Development of System Using Beam's Eye View Images to Measure Respiratory Motion Tracking Errors in Image-Guided Robotic Radiosurgery System. *J Appl Clin Med Phys* (2015) 16(1):5049. doi: 10.1120/jacmp.v16i1.5049
8. Nie X, Rimner A, Li G. Feasibility of MR-Guided Radiotherapy Using Beam-Eye-View 2D-Cine With Tumor-Volume Projection. *Phys Med Biol* (2021) 66 (4):045020. doi: 10.1088/1361-6560/abd66a
9. Li G, Wei J, Kadbi M, Moody J, Sun A, Zhang S, et al. Novel Super-Resolution Approach to Time-Resolved Volumetric 4-Dimensional Magnetic Resonance Imaging With High Spatiotemporal Resolution for Multi-Breathing Cycle Motion Assessment. *Int J Radiat Oncol Biol Phys* (2017) 98(2):454–62. doi: 10.1016/j.ijrobp.2017.02.016
10. Li G, Sun A, Nie X, Moody J, Huang K, Zhang S, et al. Introduction of a Pseudo Demons Force to Enhance Deformation Range for Robust Reconstruction of Super-Resolution Time-Resolved 4DMRI. *Med Phys* (2018) 45(11):5197–207. doi: 10.1002/mp.13179
11. Nie X, Huang K, Deasy J, Rimner A, Li G. Enhanced Super-Resolution Reconstruction of T1w Time-Resolved 4DMRI in Low-Contrast Tissue Using 2-Step Hybrid Deformable Image Registration. *J Appl Clin Med Phys* (2020) 21 (10):25–39. doi: 10.1002/acm2.12988
12. Nie X, Saleh Z, Kadbi M, Zakian K, Deasy J, Rimner A, et al. A Super-Resolution Framework for the Reconstruction of T2-Weighted (T2w) Time-Resolved (TR) 4DMRI Using T1w TR-4DMRI as the Guidance. *Med Phys* (2020) 47(7):3091–102. doi: 10.1002/mp.14136
13. Ruan D, Fessler JA, Balter JM. Real-Time Prediction of Respiratory Motion Based on Local Regression Methods. *Phys Med Biol* (2007) 52(23):7137–52. doi: 10.1088/0031-9155/52/23/024
14. Kalet A, Sandison G, Wu H, Schmitz R. A State-Based Probabilistic Model for Tumor Respiratory Motion Prediction. *Phys Med Biol* (2010) 55(24):7615–31. doi: 10.1088/0031-9155/55/24/015
15. Toftegaard J, Keall PJ, O'Brien R, Ruan D, Ernst F, Homma N, et al. Potential Improvements of Lung and Prostate MLC Tracking Investigated by Treatment Simulations. *Med Phys* (2018) 45(5):2218–29. doi: 10.1002/mp.12868
16. Tolakanahalli RP, Tewatia DK, Tome WA. Time Series Prediction of Lung Cancer Patients' Breathing Pattern Based on Nonlinear Dynamics. *Phys Med* (2015) 31(3):257–65. doi: 10.1016/j.ejmp.2015.01.018
17. Baumgartner CF, Kolbitsch C, McClelland JR, Rueckert D, King AP. Autoadaptive Motion Modelling for MR-Based Respiratory Motion Estimation. *Med Image Anal* (2017) 35:83–100. doi: 10.1016/j.media.2016.06.005
18. Wang G, Li Z, Li G, Dai G, Xiao Q, Bai L, et al. Real-Time Liver Tracking Algorithm Based on LSTM and SVR Networks for Use in Surface-Guided Radiation Therapy. *Radiat Oncol* (2021) 16(1):13. doi: 10.1186/s13014-020-01729-7
19. Bukovsky I, Homma N, Ichiji K, Cejnek M, Slama M, Benes PM, et al. A Fast Neural Network Approach to Predict Lung Tumor Motion During Respiration for Radiation Therapy Applications. *BioMed Res Int* (2015) 2015:489679. doi: 10.1155/2015/489679
20. Chang P, Dang J, Dai J, Sun W. Real-Time Respiratory Tumor Motion Prediction Based on a Temporal Convolutional Neural Network: Prediction Model Development Study. *J Med Internet Res* (2021) 23(8):e27235. doi: 10.2196/27235
21. Seppenwoolde Y, Shirato H, Kitamura K, Shimizu S, van Herk M, Lebesque JV, et al. Precise and Real-Time Measurement of 3D Tumor Motion in Lung Due to Breathing and Heartbeat, Measured During Radiotherapy. *Int J Radiat Oncol Biol Phys* (2002) 53(4):822–34. doi: 10.1016/S0360-3016(02)02803-1
22. Keall PJ, Mageras GS, Balter JM, Emery RS, Forster KM, Jiang SB, et al. The Management of Respiratory Motion in Radiation Oncology Report of AAPM Task Group 76. *Med Phys* (2006) 33(10):3874–900. doi: 10.1118/1.2349696
23. Paganelli C, Lee D, Greer PB, Baroni G, Riboldi M, Keall P. Quantification of Lung Tumor Rotation With Automated Landmark Extraction Using Orthogonal Cine MRI Images. *Phys Med Biol* (2015) 60(18):7165–78. doi: 10.1088/0031-9155/60/18/7165
24. Poels K, Dhont J, Verellen D, Blanck O, Ernst F, Vandemeulebroucke J, et al. A Comparison of Two Clinical Correlation Models Used for Real-Time Tumor Tracking of Semi-Periodic Motion: A Focus on Geometrical Accuracy in Lung and Liver Cancer Patients. *Radiother Oncol* (2015) 115 (3):419–24. doi: 10.1016/j.radonc.2015.05.004
25. Wilms M, Werner R, Ehrhardt J, Schmidt-Richberg A, Schlemmer HP, Handels H. Multivariate Regression Approaches for Surrogate-Based Diffeomorphic Estimation of Respiratory Motion in Radiation Therapy. *Phys Med Biol* (2014) 59(5):1147–64. doi: 10.1088/0031-9155/59/5/1147
26. Yang J, Cai J, Wang H, Chang Z, Czito BG, Bashir MR, et al. Is Diaphragm Motion a Good Surrogate for Liver Tumor Motion? *Int J Radiat Oncol Biol Phys* (2014) 90(4):952–8. doi: 10.1016/j.ijrobp.2014.07.028
27. Jupitz SA, Shepard AJ, Hill PM, Bednarz BP. Investigation of Tumor and Vessel Motion Correlation in the Liver. *J Appl Clin Med Phys* (2020) 21 (8):183–90. doi: 10.1002/acm2.12943
28. Hindley N, Keall P, Booth J, Shieh CC. Real-Time Direct Diaphragm Tracking Using kV Imaging on a Standard Linear Accelerator. *Med Phys* (2019) 46 (10):4481–9. doi: 10.1002/mp.13738
29. Dhont J, Vandemeulebroucke J, Burghelea M, Poels K, Depuydt T, Van DenBegin R, et al. The Long- and Short-Term Variability of Breathing Induced Tumor Motion in Lung and Liver Over the Course of a Radiotherapy Treatment. *Radiother Oncol* (2018) 126(2):339–46. doi: 10.1016/j.radonc.2017.09.001
30. Park S, Farah R, Shea SM, Tryggestad E, Hales R, Lee J. Simultaneous Tumor and Surrogate Motion Tracking With Dynamic MRI for Radiation

Therapy Planning. *Phys Med Biol* (2018) 63(2):025015. doi: 10.1088/1361-6560/aaa20b

Conflict of Interest: The authors declare that the research was conducted in the absence of any commercial or financial relationships that could be construed as a potential conflict of interest.

Publisher's Note: All claims expressed in this article are solely those of the authors and do not necessarily represent those of their affiliated organizations, or those of the publisher, the editors and the reviewers. Any product that may be evaluated in this article, or claim that may be made by its manufacturer, is not guaranteed or endorsed by the publisher.

frontiers | Frontiers in Oncology

ORIGINAL RESEARCH
published: 01 July 2022
doi: 10.3389/fonc.2022.914507

Three-Dimensional Arterial Spin Labeling-Guided Sub-Volume Segmentation of Radiotherapy in Adult Non-Enhancing Low-Grade Gliomas

Zihong Zhu[1,2], *Guanzhong Gong*[2], *Lizhen Wang*[2], *Ya Su*[2], *Jie Lu*[2] *and Yong Yin*[1,2*]

[1] *Department of Oncology, Affiliated Hospital of Southwest Medical University, Luzhou, China,* [2] *Department of Radiation Oncology Physics and Technology, Shandong Cancer Hospital and Institute, Shandong First Medical University and Shandong Academy of Medical Sciences, Jinan, China*

OPEN ACCESS

Edited by:
Yingli Yang,
UCLA Health System, United States

Reviewed by:
Jing Yuan,
Hong Kong Sanatorium and Hospital, Hong Kong SAR, China
Adnan Bibic,
Johns Hopkins University, United States

***Correspondence:**
Yong Yin
yinyongsd@126.com

Specialty section:
This article was submitted to Radiation Oncology, a section of the journal Frontiers in Oncology

Received: *06 April 2022*
Accepted: *30 May 2022*
Published: *01 July 2022*

Citation:
Zhu Z, Gong G, Wang L, Su Y, Lu J and Yin Y (2022) Three-Dimensional Arterial Spin Labeling-Guided Sub-Volume Segmentation of Radiotherapy in Adult Non-Enhancing Low-Grade Gliomas. Front. Oncol. 12:914507. doi: 10.3389/fonc.2022.914507

Objective: The present study aimed to evaluate the feasibility of sub-volume segmentation for radiotherapy planning of adult non-enhancing low-grade gliomas (NE-LGGs) guided by three-dimensional arterial spin labeling (3D-ASL). The differences in high- and low-perfusion areas of NE-LGGs were analyzed using multi-sequence magnetic resonance imaging (MRI) radiomics.

Methods: Fifteen adult patients with NE-LGGs were included in the study. MR images, including T1-weighted imaging (T1WI), T2 Propeller, T2 fluid-attenuated inversion recovery (T2 Flair), 3D-ASL, and contrast-enhanced T1WI (CE-T1WI), were obtained. The gross tumor volume (GTV) was delineated according to the hyperintensity on T2 Flair. The GTV was divided into high- and low-perfusion areas, namely GTV-ASL and GTV-SUB, respectively, based on the differences in cerebral blood flow (CBF) value. The volumes and CBF values of high- and low-perfusion areas were measured and compared. The least absolute shrinkage and selection operator (LASSO) regression was used to select the optimal features of all MR maps. Receiver operating characteristic (ROC) curve analysis was used to evaluate the diagnostic accuracy of the absolute CBF_{mean} ($aCBF_{mean}$), relative CBF_{mean} ($rCBF_{mean}$, normalized by the CBF value of the normal gray matter), and screened features in differentiating high- and low-perfusion areas.

Results: Among the enrolled patients, three (20%) patients with NE-LGGs showed focal intra- and post-radiotherapy contrast enhancement within a prior high-perfusion area of 3D-ASL. The volume ratio of the GTV-ASL to the GTV was (37.08% ± 17.88)% (46.26 ± 44.51 vs. 167.46 ± 209.64 cm^3, P = 0.000). The CBF_{mean} in the high-perfusion area was approximately two times of that in the edema area or normal gray matter (66.98 ± 18.03 vs. 35.19 ± 7.75 or 33.92 ± 8.48 ml/100g/min, P = 0.000). Thirteen features were screened, seven of which were extracted from 3D-ASL. The area undercurve (AUC) values of $aCBF_{mean}$, $rCBF_{mean}$, and firstorder_10Percentile from 3D-

ASL were more than 0.9, of which firstorder_10Percentile was the highest. Their cut-off values were 44.16 ml/100 g/min, 1.49 and 31, respectively.

Conclusion: The difference in blood perfusion in the GTV can be quantified and analyzed based on 3D-ASL images for NE-LGGs, which could guide the sub-volume segmentation of the GTV. 3D-ASL should become a routine method for NE-LGGs during simulation and radiotherapy.

Keywords: low-grade gliomas, non-enhancing, sub-volume segmentation, three-dimensional arterial spin labeling, radiomics

1 INTRODUCTION

Low-grade gliomas account for approximately 15% of all gliomas, which are the most common primary brain tumors in adults (1, 2). Non-enhancing LGGs (NE-LGGs) are a special type of LGGs. These NE-LGGs were not enhanced on conventional enhanced computed tomography (CT)/magnetic resonance imaging (MRI). Their blood vessel wall composition is similar to that of brain-healthy tissue, with a complete blood-brain barrier. Macromolecules used for tumor enhancement cannot pass through the blood-brain barrier to enhance these lesions. Therefore, the lesions show low density on enhanced CT and T1 hypointensity and T2 hyperintensity on enhanced MRI [the manifestation of edema (3, 4)]. Eichberg et al. (5) showed that approximately 20% of gliomas were not enhanced, of which more than 70% were LGGs. LGGs enhanced as commonly as they lacked enhancement (6).

Radiotherapy is an effective treatment for NE-LGGs. At present, the abnormal hyperintensity (edema area) on T2 fluid-attenuated inversion recovery (T2 Flair) is usually used as the standard for delineating the tumor target volume, which often makes the gross tumor volume (GTV) too large. The tumor boundary of NE-LGGs is difficult to identify in conventional imaging, and the blood flow and metabolism of the tumor are significantly different from those of the brain tissue in the edema area in biology (7). Quantifying this difference through functional imaging can clarify the distribution of tumor cell enrichment areas, which could guide the delineation of target volume during radiotherapy. Commonly functional imaging requires intravenous administration of a contrast agent and is therefore somewhat limited.

One method of obtaining perfusion contrast without the need for an external contrast agent is three-dimensional arterial spin labeling (3D-ASL), which generates an image by magnetically labeling water protons of arterial blood as an endogenous tracer. It is not influenced by the destruction of the blood–brain barrier and can reflect microscopic changes such as tissue blood perfusion and micro-vessel density (8, 9). ASL is attractive as not only is a contrast agent application not required, but cerebral blood flow (CBF) can also be quantified in absolute values [ml/min/100 g brain tissue (10)]. Some studies have shown that CBF obtained by ASL perfusion imaging has a significant positive correlation with micro-vessel density (ρ = 0.567) and the expression of vascular endothelial growth factor (r = 0.604) and a significant negative correlation with survival (r = -0.714). Multivariate regression analysis showed that CBF was an independent risk factor for overall survival [OS; HR = 1.028, 95% CI: 1.005–1.051, P = 0.010 (11, 12)]. ASL has been used to guide stereotactic biopsy and operation for glioma. Jin et al. (13) showed that compared with conventional MRI, combined magnetic resonance spectroscopy (MRS) and ASL improved the accuracy of target selection for the stereotactic biopsy of intracranial tumors, especially in three cases, each of low-enhancing and non-enhancing gliomas. Lindner et al. (14) concluded that intraoperative arterial spin-labeling was a feasible, reproducible, and reliable tool to map CBF in brain tumors and seemed to give beneficial information compared to conventional intraoperative MRI in partial resection.

The quality of ASL-derived perfusion maps has reached a level that makes the method useful for many clinical and research applications. A consensus white paper regarding recommended implementation of arterial spin-labeled perfusion MRI for clinical applications has been established, in which pseudo-continuous labeling and a segmented 3D readout were recommended (15). 3D-ASL perfusion imaging can effectively differentiate intracranial tumors from non-neoplastic lesions (16). It has been widely used in diagnosing, grading, and the efficacy evaluation of gliomas (17, 18). However, few reports are on its application in guiding the delineation of radiotherapy targets for NE-LGGs. Thus, we segmented the sub-volume based on the perfusion difference of the GTV in 3D-ASL for

Abbreviations: LGGs, low-grade gliomas; NE-LGGs, non-enhancing low-grade gliomas; CT, computed tomography; MRI, magnetic resonance imaging; T2 Flair, T2 fluid-attenuated inversion recovery; GTV, gross tumor volume; 3D-ASL, threedimensional arterial spin labeling; CBF, cerebral blood flow; OS, overall survival; MRS, magnetic resonance spectroscopy; PACS, Picture Archiving and Communication Systems; WHO CNS5, the fifth edition of the WHO Classification of Tumors of the Central Nervous System; IDH, isocitrate dehydrogenase; NOS, not otherwise specified; T1WI, T1-weighted imaging; CET1WI, contrast-enhanced T1WI; PLD, post labeling delay; NEX, number of excitation; TR, repetition time; TE: echo time; FOV, field of view; GTV-ASL, the high-perfusion area based on 3D-ASL; GTV-SUB, the low-perfusion area based on 3D-ASL; ROIs, the regions of interest; aCBF, absolute CBF value; rCBF, relative CBF value; MNI, Montreal Neurological Institute; GLCM, gray level cooccurrence matrix; GLDM, gray level dependence matrix; GLRLM, gray level run length matrix; GLSZM, gray level size zone matrix; NGTDM, neighborhood gray tone difference matrix;LASSO, the least absolute shrinkage and selection operator; ROC, receiver operating characteristic; AUC: area under curve;DSC, dynamic susceptibility contrast; SPECT, single-photon emission tomography; PET, positron-emission tomography; 18F-FET, 18F-fluoroethyl tyrosine; TBF, tumorblood flow.

radiotherapy planning of NE-LGGs. Radiomics is an emerging technique that can provide more detailed quantification in multi-sequence MR studies. It is also defined as the conversion of images to higher-dimensional data and the subsequent mining of that data. We also analyzed the characteristic differences of high- and low-perfusion areas of NE-LGGs using multi-sequence MRI radiomics and obtained the steady characteristics that could distinguish high- and low-perfusion areas of NE-LGGs. It provides a reference for the clinical definition of radiotherapy target for patients with NE-LGGs and lays a theoretical basis for precision radiotherapy.

2 MATERIALS AND METHODS

2.1 Patients

This retrospective study was approved by the Institutional Review Board of Shandong Cancer Hospital and informed consent forms were obtained from all patients prior to enrollment. Fifteen adult patients with pathologically confirmed glioma from Shandong Cancer Hospital were analyzed between December 2018 and May 2021. Patients showed nonenhancement on diagnostic brain MRI that strongly suggested a diagnosis of World Health Organization (WHO) grade I or II glioma. Radiological studies performed on the patients were accessed by two Neuroradiologists from Picture Archiving and Communication Systems (PACS). WHO grading was reviewed by three neuropathologists according to the fifth edition of the WHO Classification of Tumors of the Central Nervous System [WHO CNS5 (19)]. Patient characteristics are presented in **Table 1**. All enrolled patients received radical radiotherapy with 45–60 Gy in 1.8–2.0 Gy fractions. All but three patients received concurrent temozolomide chemotherapy.

TABLE 1 | Clinical characteristics of all patients.

Characteristics	Number of patients (%)
Age (mean ± SD, year; range)	49 ± 14 (31–74)
Gender	
Female	5 (33%)
Male	10 (67%)
Tumor location	
Unilateral	7 (47%)
Midline[a] (H3 K27-altered status)	5 (33%)
Altered	0 (0%)
Non-altered	5 (33%)
Bilateral (widely diffuse distribution)	3 (20%)
Type of histopathology	
Astrocytoma	15 (100%)
WHO classification	
Grade 2	15 (100%)
IDH mutation status	
Mutant	1 (7%)
Wild type	10 (67%)
NOS	4 (26%)
Median follow-up time[b], Median (range)	12 months (1–29 months)

[a]Midline location includes brainstem, thalamus, cerebellum. [b]The follow-up method was done according to RANO criteria (20). SD, standard deviation. NOS, not otherwise specified. IDH, isocitrate dehydrogenase.

2.2 MRI Protocol

2.2.1 Before Radiotherapy

MRI was performed on a 3.0-T superconducting MR scanner (Discovery 750W, GE Healthcare, USA) equipped with an 8-channel head coil. The head of a patient was fixed with a thermoplastic film. A series of MRI sequences, including T1-weighted imaging (T1WI), T2 Propeller, T2 Flair, 3D-ASL, and contrast-enhanced T1WI (CE-T1WI), were performed for each patient with a slice thickness of 3 mm and no interslice gap width. The common parameters of these sequences are shown in **Table 2**. For CE-T1WI, gadopentetate dimeglumine was power-injected at doses standardized according to the patient's body weight (0.2 ml/kg) at 2 ml/s, and the scan was started at 3–5 min after injection.

2.2.2 3D-ASL Data Acquisition and Post-Processing

Set the labeling plane on the neck in advance and use pseudo-continuous labeling, image acquisition with single-shot gradient-echoecho planar imaging (EPI), labeling duration = 1,500 ms, post-labeling delay (PLD) time = 2,025 ms, the number of excitation (NEX) = 3. The scan time was approximately 4.5–5 min. The parameter values of repetition time (TR), echo time (TE), field of view (FOV), matrix, and flip angle are shown in **Table 2**. Control/label and calibration images were acquired. For measurement of the magnetization of arterial blood and also for segmentation purposes, an M0 calibration image was acquired separately with the same geometry and the same imaging parameters as the ASL without labeling. Background suppression technology was used in the process of image acquisition to reduce physiological noise and motion artifacts. The quantitative CBF maps were generated automatically using GE FuncTool 4.7 software after scanning based on the following equation (21):

$$\mathrm{CBF} = \frac{6000 \cdot \lambda \cdot (\mathrm{SI_{control}} - \mathrm{SI_{label}}) \cdot e^{\frac{\mathrm{PLD}}{T_{1,\mathrm{blood}}}}}{2 \cdot \alpha \cdot T_{1,\mathrm{blood}} \cdot \mathrm{SI_{PD}} \cdot \left(1 - e^{-\frac{\tau}{T_{1,\mathrm{blood}}}}\right)} [\mathrm{ml}/100\ \mathrm{g}/\mathrm{min}]$$

Where λ is the brain/blood partition coefficient in ml/g, $SI_{control}$ and SI_{label} are the time-averaged signal intensities in the control and label images respectively, $T_{1,blood}$ is the longitudinal relaxation time of blood in seconds, α is the labeling efficiency, SI_{PD} is the signal intensity of a proton density-weighted image, τ is the label duration, and PLD is the post-labeling delay. The following parameters were used in this study: $\lambda = 0.9$, PLD = 2,025 ms, $T_{1,blood}$ = 1,650 ms, $\alpha = 0.85$, and τ = 1,500 ms. The SI_{PD} was calculated using echo planar imaging M0 images. A factor of 6,000 converts the units from ml/g/s to ml/100 g/min, which is standard in the physiological literature.

2.2.3 During Radiotherapy

At the 10th–15th radiotherapy, the patient again underwent MR scanning. MRI sequences, machine, and parameters were the same as before radiotherapy.

TABLE 2 | The common parameters of MRI sequences.

Parameters	T1WI	T2 Propeller	T2 FLAIR	CE-T1WI	3D-ASL
TR (ms)	8.5	13,500	11,000	8.5	5,160
TE (ms)	3.2	114	120	3.2	11.5
FOV (cm)	25.6 × 25.6	26 × 26	26 × 26	25.6 × 25.6	25.6 × 25.6
Matrix	256 × 256	416 × 416	320 × 320	256 × 256	512 × 512
Flip angle (°)	12	120	160	12	110

T1WI, T1-weighted imaging; T2 FLAIR, T2 fluid-attenuated inversion recovery; 3D-ASL, three-dimensional arterial spin labeling; CE-T1WI, contrast-enhanced T1WI; TR, repetition time; TE, echo time; FOV, field of view.

2.3 The Definition and Delineation of the Target Volume

Two senior radiologists used MIM Maestro software (version 6.8.8, USA) to delineate the target volume, which was then reviewed by a third senior radiologist. Axial T2 Flair sequences were used to contour the hyperintense signal abnormality as the GTV. The GTV-ASL was defined as a high-perfusion area under the guidance of a CBF map derived from 3D-ASL sequence that was free of cysts, necrosis, calcifications, hemorrhage, and large vessels. The GTV-SUB was the low-perfusion area of GTV, which was obtained by subtracting the GTV-ASL from the GTV. In addition, the boundary of target volume was also determined in conjunction with other conventional sequences such as T1WI, T2 Propeller, and CE-T1WI. Finally, the GTV-ASL and GTV-SUB were copied to the corresponding sequences (T1WI, T2 Propeller, T2 Flair, 3D-ASL, and CE-T1WI) to prepare for later feature extraction.

2.4 CBF Values Measurement

T2 Flair and 3D-ASL images were fused using rigid registration in a workstation with commercially available software (GE Healthcare, ADW 4.7, USA). According to the pseudo-color perfusion of 3D-ASL images, the regions of interest (ROIs) were set at the slice with the highest perfusion signal while avoiding areas of cysts, necrosis, calcifications, hemorrhage, and large vessels. The area of high perfusion was defined as ROI-T. Four ROIs were selected in the edema area around the high-perfusion area and defined as ROI-E. The ROI of brain tissue (ROI-N) was selected from the contralateral mirror gray matter of the lesion (the unilateral cerebral hemisphere) or normal gray matter of the leftinsulalobe (midline or widely diffuse distribution). The ROIs area of the peritumoral edema area and normal gray matter were 100–150 mm^2. The absolute CBF values (aCBF), including maximum CBF values (CBF_{max}), minimum CBF values (CBF_{min}) and average CBF values (CBF_{mean}) of the high-perfusion areas and CBF_{mean} of the edema areas and normal gray matter, were measured, respectively. The CBF values of the high-perfusion area and edema areanormalized by that of normal gray matter (namely relative CBF values, rCBF) were also calculated to correct for age-dependent and patient-dependent variations of cerebral perfusion.

2.5 MR Images Data Pre-Processing

The pre-processing procedure was undertaken before features extraction, including co-registration, denoising, field bias correction, and resampling. All maps were firstly co-registered to T1WI anatomic images. Then, T1WI images were normalized to the Montreal Neurological Institute (MNI) space, which generated a transformed matrix from the native space to the MNI space. Each image was then spatially smoothed with a 6-mm full-width at a half-maximum Gaussian kernel to decrease spatial noise. In order to compensate for non-uniform intensity caused by field inhomogeneity, N4ITK MRI bias field correction was applied to each imaging study. Isotropic resampling to a voxel size of $1 \times 1 \times 1$ mm^3 was performed. All pre-processing was done using MATLAB 2020b software (MathWorks Inc., Natick, MA, USA, http://www.mathworks.com/products/matlab/).

2.6 Features Extraction

All images were transmitted into 3D slicer software (version 4.8.1, http://www.slicer.org,USA). The radiomics features of the GTV-ASL and GTV-SUB mapping areas from five different MR sequences (T1WI, T2 Propeller, T2 Flair, 3D-ASL, and CE-T1WI) were extracted, including morphological features (n = 14), first-order features (n = 18), gray level co-occurrence matrix (GLCM, n = 24), gray level dependence matrix (GLDM, n = 14), gray level run length matrix (GLRLM, n = 16), gray level size zone matrix (GLSZM, n = 16), and neighborhood gray-tone difference matrix (NGTDM, n = 5). A total of 535 features were obtained.

2.7 Features Selection

Feature selection was conducted using python (version 3.8.8, https://www.python.org). Before the features selection process, all the features were normalized to the range of [0, 1] for standardization so that features of different orders of magnitude could be reasonably compared. The variance threshold method was performed to pre-process the features, which first calculated the variance of each feature and then removed features with a variance lower than 0.8 (22). The least absolute shrinkage and selection operator (LASSO) regression was used to select the optimal features. In order to avoid over-fitting, the parameters of the LASSO regression were tuned to select the key features from the high-dimensional feature space using five-fold cross-validation.

The LASSO regression is a shrinkage method that can actively select from a large and potentially multicollinear set of variables in the regression, resulting in a more relevant and interpretable set of predictors (23). LASSO performs *via* a continuous shrinking operation, minimizing regression coefficients in order to reduce the likelihood of overfitting; however, the technique is computed so as to shrink the sum of the absolute

value of regression coefficients, forcing and producing coefficients that are exactly 0; thus, selecting for the nonzero variables to remain. The complexity of LASSO is controlled by λ. The larger λ is, the greater the penalty will be for the linear model with more variables and, finally, a model with fewer variables.

2.8 Statistical Analysis

SPSS (version 25.0, IBM, NY, USA) was used for statistical analysis. Paired t-test or Wilcoxon test was used to compare the target volumes and the CBF values, depending on the distribution defined by the Shapiro–Wilk normality test. Receiver operating characteristic (ROC) curve analysis was performed by using MedCalc Statistical Software version 20.010 (MedCalc Software Ltd, Ostend, Belgium; https://www.medcalc.org; 2021), which evaluated the diagnostic accuracy of the $aCBF_{mean}$, $rCBF_{mean}$ and screened features in distinguishing high- and low-perfusion areas. Data was presented as mean ± standard deviation. All statistical tests were two-tailed, and a P value of <0.05 was considered to be significant. The flow chart of this study is shown in **Figure 1**.

3 RESULTS

3.1 The Comparison of Target Volumes

The volumes of the GTV and GTV-ASL were 167.46 ± 209.64 cm^3 and 46.26 ± 44.51 cm^3, respectively. The volume ratio of the GTV-ASL to the GTV was (37.08% ± 17.88)% (Z = –3.408, P = 0.001, Wilcoxon test). The high-perfusion area of 3D-ASL did not exceed the abnormal hyperintense area (edema area) of T2 Flair for all patients.

3.2 CBF Values

3.2.1 Before Radiotherapy

The aCBF and rCBF values of sub-volumes before radiotherapy in all patients are shown in **Table 3**. The $aCBF_{mean}$ in the high-perfusion area was approximately two times of that in the edema area (t = 7.934, P = 0.000) or normal gray matter (t = 8.368, P = 0.000), but the CBF_{mean} values were comparable between the edema area and normal gray matter (t = 0.495, P = 0.625).

3.2.2 Comparison of CBF Values Before and During Radiotherapy

Six out of 18 patients underwent MR scanning again at the 15th–20th session of radiotherapy. Compared with those before radiotherapy, the CBF_{max}, CBF_{min}, and CBF_{mean} of the high-perfusion area and the CBF_{mean} of the edema area increased by (12.47 ± 46.35)%, (6.55 ± 28.52)%, (11.46 ± 22.13)%, and (6.44 ± 29.65)%, respectively, and the CBF_{mean} in normal gray matter decreased by (5.07 ± 11.76)%. But there was no significant difference in all changes (P > 0.05). **Table 4** shows the details of CBF values.

3.3 Features Selection

A total of 298 features were retained after screening by the variance threshold method, including 63 features in T1WI, 61 features in CE-T1WI, 56 features in 3D-ASL and 59 features in

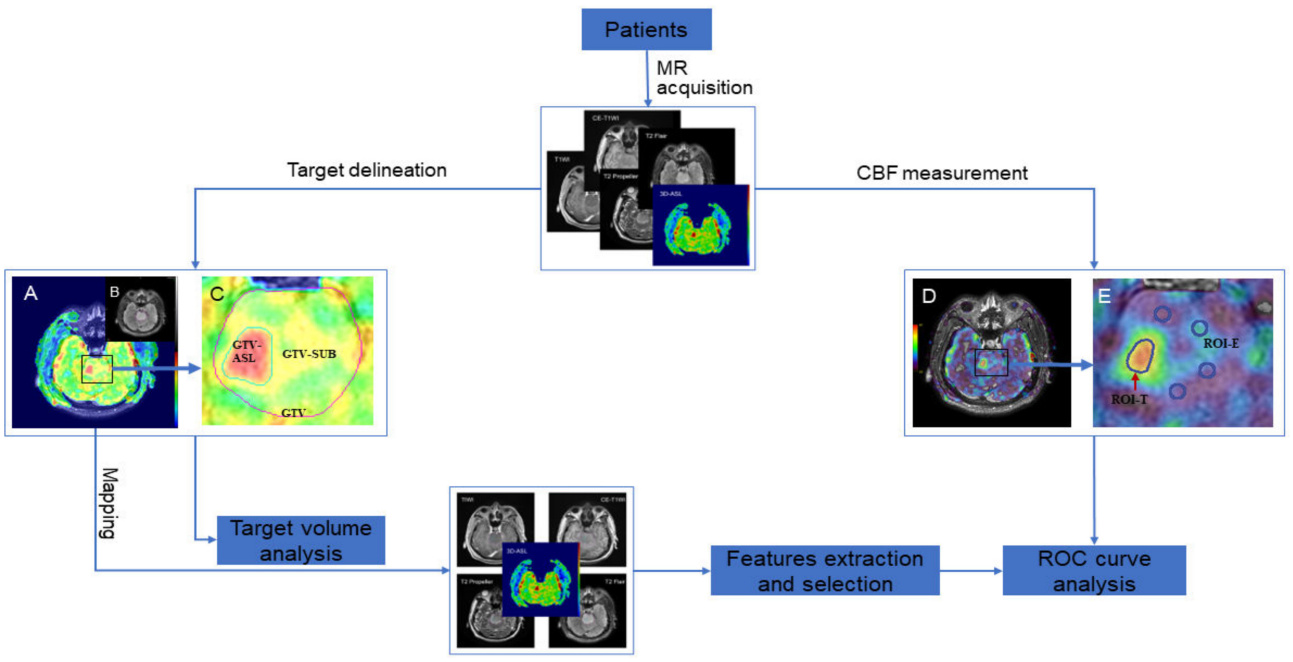

FIGURE 1 | Flow chart of this study. **(A, D)**, fusion images of T2 Flair and 3D-ASL; **(B)** T2 Flair image; **(C, E)**, local magnification of **(A, D)**, respectively.

each of T2 Propeller and T2 Flair, respectively. Based on the LASSO regression, 13 steady features were screened out of the 298 features to differentiate high-and low-perfusion areas. The minimum criteria for five-fold cross-validation were applied during λ selection. The misclassification error was generated versus λ, as shown in **Figure 2**. As λ was equal to 0.04484, which was defined as the optimal λ value with a minimal misclassification error, only 13 features, potentially the most contributing to differentiating high-and low-perfusion areas, remained in the model. Further, 7 out of 13 features were derived from 3D-ASL, as shown in **Figure 3**.

3.4 ROC Curve Analysis

The area under curve (AUC) values of the $aCBF_{mean}$ and $rCBF_{mean}$ were 0.954 and 0.934, respectively. The cut-off values of $aCBF_{mean}$ and $rCBF_{mean}$ were 44.16 ml/100 g/min and 1.49, which yielded 92.86% sensitivity and 92.86% specificity. The AUC value of firstorder_10Percentile from 3D-ASL was 0.990, which was the highest among the 13 remaining features and higher than that of the $aCBF_{mean}$ and $rCBF_{mean}$. The feature with a cut-off of 31 yielded 92.86% sensitivity and 100% specificity. The ROC curve is shown in **Figure 4**.

3.5 Spatial Distribution Between Post-Treatment Focal Contrast Enhancement and Prior High-Perfusion Area

In this study, 3 out of 15 patients (20%) with high-perfusion in 3D-ASL prior to radiotherapy showed new gadolinium contrast enhancement on MRI assessment during radiotherapy or at 3 months post-radiotherapy (**Figures 5**, **6**).

4 DISCUSSION

Most LGGs inevitably develop into high-grade malignant gliomas, and even with effective treatment, the survival rate of patients with LGGs remains poor (24, 25). Tom et al. (26) showed that the incidence of malignant transformation of LGGs was 17%, and the median OS time after malignant transformation was only 2.4 years. As a special type of LGGs, NE-LGGs show no enhancement on CT and MR. If the edema area is used as the main standard for GTV delineation, there will be great blindness. The research of Jakola et al. (27) showed that the blood–brain barrier was destroyed after the malignant transformation of NE-LGGs, and the enhanced area was much smaller than the edema area. Moreover, Tatekawa et al. showed that Flair hyperintense volume for IDH wild-type gliomas showed no significant association with OS (28). If the edema area is defined as the GTV of NE-LGGs, which can ensure the radiation dose coverage of tumor, the radiation damage risk to the surrounding healthy tissues will be increased due to the large.

Dynamic susceptibility contrast (DSC)-MRI, CT perfusion imaging, single-photon emission tomography (SPECT), and H2 [15O] positron-emission tomography (PET) measure perfusion by dynamic imaging of the passage of a contrast agent. The physical basis of ASL offers its greatest advantage over traditional contrast bolus techniques: it is non-invasive. ASL does not require a gadolinium-based tracer, eliminating the risk of nephrogenic systemic fibrosis in patients with renal dysfunction (29). ASL is also favorable for pediatric populations as it avoids the technical difficulties and ethical problems of contrast agents and radiation exposure with CT and nuclear medicine techniques (30). In addition, ASL MRI has been extensively validated against other methods that use exogenous contrast agents, such as 15O-PET, and ASL implementations are now commercially available on all major MRI platforms, with demonstrated reproducibility in multi-center studies (31–34). Thus, we conducted a sub-volume segmentation for the GTV of NE-LGGs based on the CBF perfusion difference derived from 3D-ASL.

Our study found that the lesions of all patients showed no enhancement on CE-T1WI, while hyperintensity on T2 Flair and high local perfusion on 3D-ASL were observed. The local high-perfusion area was within the edema area. The analyses of target volumes revealed that the volume of the GTV-ASL (high-perfusion area) was significantly smaller than the GTV. Wyss et al. (35) studied the spatial heterogeneity between the uptake of ^{18}F-fluoroethyl tyrosine (18F-FET) and CBF. The results showed that the volumes of increased CBF and ^{18}F-FET uptake spatially coincided and were correlated (*rho* = 0.944), and the increase in CBF was more confined to the tumor center. This was similar to the spatial relationship between abnormal hyperintensity on T2 Flair (edema area) and high local perfusion on 3D-ASL for NE-LGGs in this study. Hayes et al. (36) studied the effect of ^{18}F-FET PET on the radiotherapy plan of patients with suspected unenhanced glioblastoma. The results showed that the biological tumor volume of ^{18}F-FET was greater than the GTV of conventional MRI, which may reduce the risk of tumor omission. The high cost of amino acids for PET limits its wide application in clinical settings, and exogenous tracers are used in PET, which may increase the risk of allergy and renal injury. However, 3D-ASL can make up for these deficiencies.

TABLE 3 | The CBF values of sub-volume before radiotherapy (ml/100 g/min).

	High-perfusion area			Edema area	Normal gray matter
	CBF_{max}	CBF_{min}	CBF_{mean}	CBF_{mean}	CBF_{mean}
Absolute values	89.25 ± 39.50	42.33 ± 11.79	66.98 ± 18.03	35.19 ± 7.75	33.92 ± 8.48
Relative values	2.61 ± 0.64	1.34 ± 0.53	2.03 ± 0.53	1.08 ± 0.32	–

CBF_{max}/CBF_{min}/CBF_{mean} represent the maximum, minimum, and average value of cerebral blood flow (CBF), respectively. Relative values are the CBF values of high-perfusion and edema area normalized by that of normal gray matter.

TABLE 4 | CBF values before and during radiotherapy (ml/100 g/min).

	High-perfusion area			Edema area	Normal gray matter
	CBF_{max}	CBF_{min}	CBF_{mean}	CBF_{mean}	CBF_{mean}
Before radiotherapy	77.17 ± 17.45	45.83 ± 9.47	66.09 ± 13.45	38.05 ± 7.81	40.44 ± 12.28
During radiotherapy	86.00 ± 35.79	50.67 ± 11.64	69.31 ± 16.96	40.23 ± 12.57	38.14 ± 12.60
Test statistic	-0.647	-1.336*	-0.314	-0.492	1.077
P values	0.546	0.239	0.753	0.644	0.331

CBF_{max}/CBF_{min}/CBF_{mean} represent the maximum, minimum, and average values of cerebral blood flow (CBF), respectively. The asterisk (*) represents the test statistic of Wilcoxon test and the others are t-test values.

Local control failure is the main reason for the treatment failure of LGGs. In traditional radiotherapy, most LGGs relapse at the site of the primary tumor after radiotherapy (37, 38). This may be related to insufficient radiation dose or excessive dose to the surrounding healthy tissues due to a very large target area, which limits the radiation dose of the central tumor. Most of the tumors in this study were located in the midline (thalamus, brainstem, or cerebellum) or bilateral (widely diffuse distribution), accounting for approximately 53%, but the volume of the local high-perfusion area was significantly smaller than that of the edema area. The reduction of the target volume can avoid the damage of high-dose radiotherapy to the surrounding healthy tissues, especially for patients whose tumors are located in important functional areas such as the midline or whose lesions are diffusely distributed, which will provide a basis for us to further improve the targeted dose for the sub-volume of high perfusion.

In the present study, the CBF_{mean} values were comparable between the peritumoral edema area and normal gray matter. 3D-ASL can differentiate between invasive and non-invasive peritumoral edema; hence, the infiltration area of tumor for NE-LGGs shows high local perfusion, while the edema area around the high-perfusion area is the non-invasive area of angiogenic edema or gliosis, and its CBF value is equivalent to that of surrounding healthy tissue (39). The present study found that the CBF_{mean} of the GTV-ASL was approximately twice that of the GTV-SUB or normal gray matter. Khashbat et al. (40) measured the tumor blood flow (TBF) of 6 non-enhancing low-grade astrocytomas. The results showed that the ratio of TBFmean to CBF_{mean} of brain-healthy tissue was 0.88 ± 0.41, but the region of interest was delineated based on T2WI, and the TBF was measured after mapping to ASL. In fact, the TBF included the CBF of the tumor and the edema area. Our study, however, divided the GTV into high- and low-perfusion areas based on the perfusion difference in 3D-ASL, and measured the CBF values of sub-volume. Furthermore, the number of cases we enrolled was significantly more than that in their study.

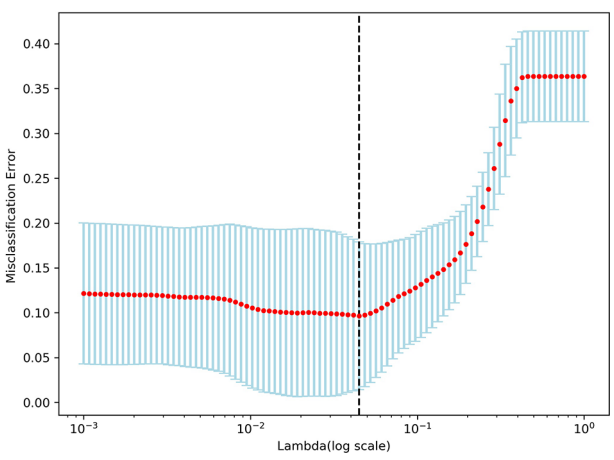

FIGURE 2 | Tuning parameter (λ) selection in the LASSO regression.

This study compared the changes in CBF before and after radiotherapy. The results showed that compared with that before radiotherapy, the CBF values of tumor and edema area increased, while that of normal gray matter decreased after radiotherapy. Calmon et al. (41) studied the changes in CBF values for 43 children with diffuse intrinsic pontine gliomas before radiotherapy, after radiotherapy, treatment progress, and at the last follow-up. The results showed that the ASL-CBF value of all patients after radiotherapy was significantly higher than that before radiotherapy ($P < 0.001$). Petr et al. (42) showed that the perfusion of brain-healthy tissue decreased by -9.8% ± 20.9% ($P = 0.032$) after radiotherapy. Our results are consistent with the trend of CBF noted in these studies.

It is difficult for conventional MRI to identify the nonenhanced tumor or the micro-invasive lesion around the enhanced tumor, but the microscopic differences between the tumor and the peritumoral edema area can be found by imaging radiomics. Yan et al. (43) reported that multimodal MRI radiomics could show different characteristics in the potential progression area of preoperative MRI of glioblastoma. We found that there were significant features in the high- and low-perfusion areas of NE-LGGs after analyzing the features of multi-sequence MRI. The ROC curve analysis was also used in this study, which found that the diagnostic accuracy of the $aCBF_{mean}$, $rCBF_{mean}$ and firstorder_10Percentile from 3D-ASL in differentiating the high- and low-perfusion areas were more than 0.9, of which firstorder_10Percentile was the highest. Therefore, the combination of radiomics features may be helpful in distinguishing the non-enhanced tumors and peritumoral edema of NE-LGGs. And the optimal cut-off values of $aCBF_{mean}$ and $rCBF_{mean}$weredetermined as 44.16 ml/100 g/min and 1.49, respectively, which lay the foundation for

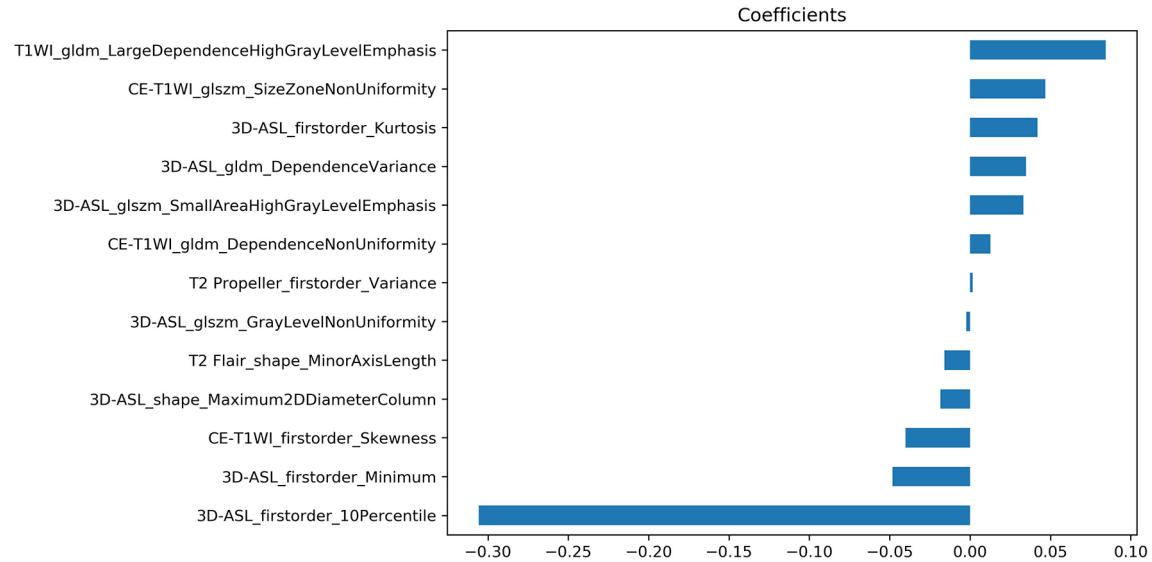

FIGURE 3 | The coefficients of screened features using the LASSO regression.

further research on the threshold determination of sub-volume based on 3D-ASL in the future.

In this study, one patient showed no enhancement in CE-T1WI before radiotherapy, but the new enhancement appeared after 20 sessions of radiotherapy (the irradiation dose was 40 Gy). Cao et al. (44) showed that in the non-enhanced tumor region, contrast uptake increased significantly after the receipt of approximately 10 Gy of irradiation ($P < 0.01$), and reached the maximum after the receipt of approximately 30 Gy of irradiation, while the healthy brain showed only nonsignificant changes during and after irradiation. The blood-tumor barrier was more sensitive to radiation; this finding was similar to the results of the present study. Moreover, three patients with NE-LGGs showed the new gadolinium contrast enhancement after radiotherapy in this study, which was consistent with the high-perfusion area of 3D-ASL before radiotherapy, especially in one patient who showed tumor progression. This finding suggests that 3D-ASL is helpful in

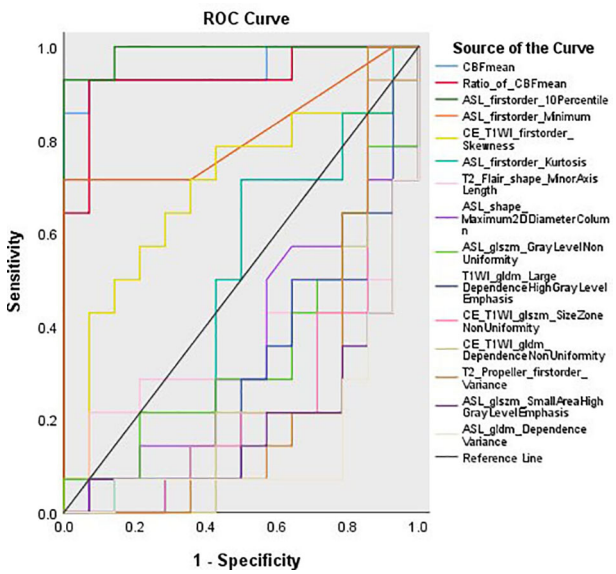

FIGURE 4 | Receiver operating characteristic (ROC) curves.

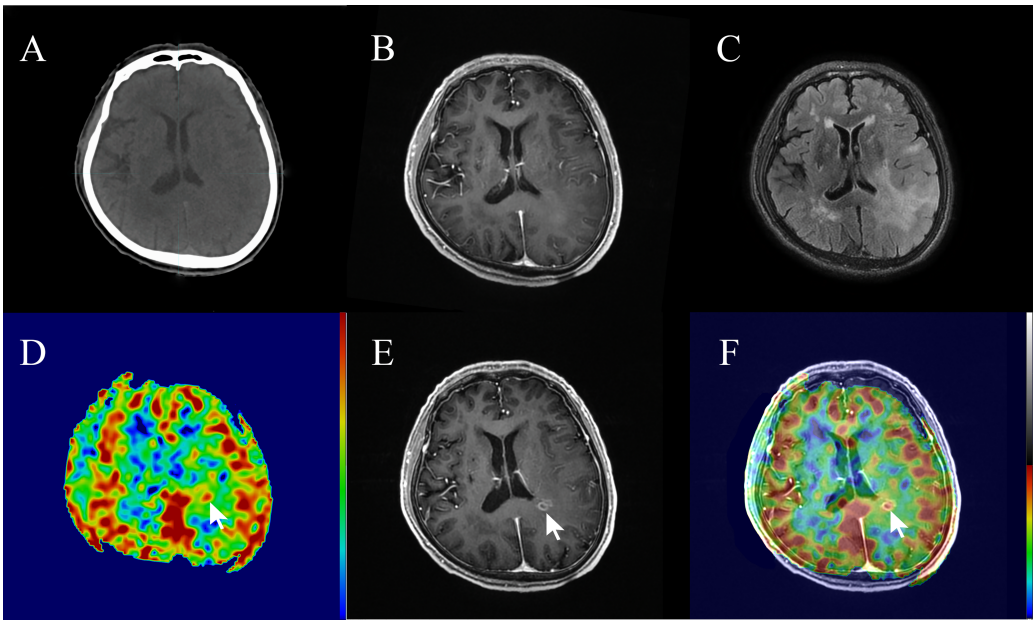

FIGURE 5 | A 74-year-old patient with non-enhancing low-grade glioma (WHO grade II astrocytoma) showed focal contrast enhancement within a prior non-enhanced and high-perfusion area at 20 sessions of radiotherapy (40 Gy). **(A)** Planning plain-CT image. **(B)** Contrast-enhanced T1-weighted imaging (CE-T1WI) before radiotherapy. **(C)** T2 fluid-attenuated inversion recovery (T2 Flair) image before radiotherapy. **(D)** Three-dimensional arterial spin labeling (3D-ASL) image before radiotherapy. **(E)** CE-T1WI at 20 sessions of radiotherapy. **(F)** Fusion image of **(D, E)**.

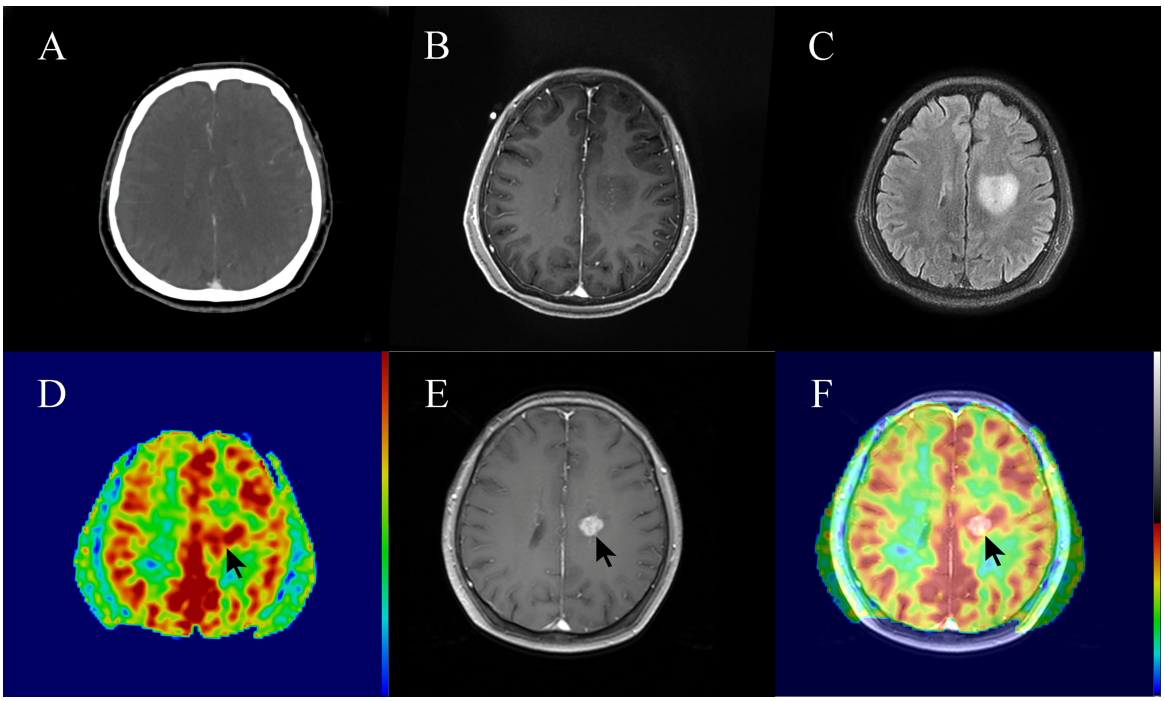

FIGURE 6 | A 62-year-old patient with non-enhancing low-grade glioma (WHO grade II astrocytoma) showed focal post-radiotherapy contrast enhancement within a prior non-enhanced and high-perfusion area at 3 months following radiotherapy. The patient had clinical symptoms such as weakness of the right lower limb, considering the tumor progression. **(A)** Planning contrast-enhanced CT (CE-CT) image. **(B)** Contrast-enhanced T1-weighted imaging (CE-T1WI) before radiotherapy. **(C)** T2 fluid-attenuated inversion recovery (T2 Flair) image before radiotherapy. **(D)** three-dimensional arterial spin labeling (3D-ASL) image before radiotherapy. **(E)** CE-T1WI at 3 months following radiotherapy. **(F)** Fusion image of **(D, E)**.

identifying the infiltration areas of non-enhanced tumors for NE-LGGs.

Our study has some limitations. CBF was initially measured using the general kinetic model, an adaptation of the ASL model described by BUXTON et al. (21). The imperfection of the quantification model and the uncertainty and potential errors of 3D-ASL measured CBF due to the prolonged transit delay between the tagging region and the imaging slice, influenced sub-volume segmentation. Furthermore, GTV and GTV-ASL segmentation was linked to inter-and intra-observer experience and condition.Finally, the sample size was not large enough, and the data had a large degree of dispersion. The next step is to increase the number of cases and apply 3D-ASL to radiotherapy planning to further evaluate the value of this technique in radiotherapy

5 CONCLUSION

The difference in blood perfusion in the GTV can be quantified and analyzed based on 3D-ASL images for NE-LGGs, which guided the sub-volume segmentation of the GTV. The differences between high-and low-perfusion areas in GTV can be identified by multi-sequence MR radiomics features. 3D-ASL should be used as a routine method for NE-LGGs during simulation and radiotherapy, especially if the contrast agent cannot be injected or when contrast enhancement is uncertain.

DATA AVAILABILITY STATEMENT

The original contributions presented in the study are included in the article/supplementary material. Further inquiries can be directed to the corresponding author.

ETHICS STATEMENT

The studies involving human participants were reviewed and approved by Institutional Review Board of Shandong Cancer Hospital. The patients/participants provided their written informed consent to participate in this study.

AUTHOR CONTRIBUTIONS

GG conceived and designed the study. LW and YS collected data. ZZ performed the experiments, made a statistical analysis, and wrote the paper. YY and JL reviewed and edited the manuscript. All authors contributed to the article and approved the submitted version.

FUNDING

This work was supported by the Start-up fund of Shandong Cancer Hospital (YYPY2020-016), and the Key Research and Development Program of Shandong Major Science & Technology Innovation Project (2021SFGC0501).

REFERENCES

1. Ostrom QT, Patil N, Cioffi G, Waite K, Kruchko C, Barnholtz-Sloan JS. CBTRUS Statistical Report: Primary Brain and Other Central Nervous System Tumors Diagnosed in the United States in 2013–2017. *Neuro Oncol* (2020) 22 (12 Suppl 2):iv1–iv96. doi: 10.1093/neuonc/noaa200
2. Nunna RS, Khalid S, Ryoo JS, Sethi A, Byrne RW, Mehta AI. Radiotherapy in Adult Low-Grade Glioma: Nationwide Trends in Treatment and Outcomes. *Clin Transl Oncol* (2021) 23(3):628–37. doi: 10.1007/s12094–020–02458–9
3. Afra D, Osztie E. Histologically Confirmed Changes on CT of Reoperated Low-Grade Astrocytomas. *Neuroradiology* (1997) 39(11):804–10. doi: 10.1007/s002340050509
4. Upadhyay N, Waldman AD. Conventional MRI Evaluation of Gliomas. *Br J Radiol* (2011) 84(Spec Iss 2):S107–11. doi: 10.1259/bjr/65711810
5. Eichberg DG, Di L, Morell AA, Shah AH, Semonche AM, Chin CN, et al. Incidence of High-Grade Gliomas Presenting as Radiographically non-Enhancing Lesions: Experience in 111 Surgically Treated non-Enhancing Gliomas With Tissue Diagnosis. *J Neurooncol* (2020) 147(3):671–9. doi: 10.1007/s11060-020–03474-z
6. Scott JN, Brasher PM, Sevick RJ, Rewcastle NB, Forsyth PA. How Often are Nonenhancing Supratentorial Gliomas Malignant? A Population Study. *Neurology* (2002) 59(6):947–9. doi: 10.1212/wnl.59.6.947
7. Galldiks N, Niyazi M, Grosu AL, Kocher M, Langen KJ, Law I, et al. Contribution of PET Imaging to Radiotherapy Planning and Monitoring in Glioma Patients-a Report of the PET/RANO Group. *Neuro Oncol* (2021) 23 (6):881–93. doi: 10.1093/neuonc/noab013
8. Grade M, Hernandez Tamames JA, Pizzini FB, Achten E, Golay X, Smits MA. Neuroradiologist's Guide to Arterial Spin Labeling MRI in Clinical Practice. *Neuroradiology* (2015) 57(12):1181–202. doi: 10.1007/s00234–015–1571-z
9. Telischak NA, Detre JA, Zaharchuk G. Arterial Spin Labeling MRI: Clinical Applications in the Brain. *J Magn Reson Imaging* (2015) 41(5):1165–80. doi: 10.1002/jmri.24751
10. Wong EC. An Introduction to ASL Labeling Techniques. *J Magn Reson Imaging* (2014) 40(1):1–10. doi: 10.1002/jmri.24565
11. Ningning D, Haopeng P, Xuefei D, Wenna C, Yan R, Jingsong W, et al. Perfusion Imaging of Brain Gliomas Using Arterial Spin Labeling: Correlation With Histopathological Vascular Density in MRI-Guided Biopsies. *Neuroradiology* (2017) 59(1):51–9. doi: 10.1007/s00234–016–1756–0
12. Pang H, Dang X, Ren Y, Zhuang D, Qiu T, Chen H, et al. 3d-ASL Perfusion Correlates With VEGF Expression and Overall Survival in Glioma Patients: Comparison of Quantitative Perfusion and Pathology on Accurate Spatial Location-Matched Basis. *J Magn Reson Imaging* (2019) 50(1):209–20. doi: 10.1002/jmri.26562
13. Jin T, Ren Y, Zhang H, Xie Q, Yao Z, Feng X. Application of MRS-And ASL-Guided Navigation for Biopsy of Intracranial Tumors. *Acta Radiol* (2019) 60 (3):374–81. doi: 10.1177/0284185118780906
14. Lindner T, Ahmeti H, Lübbing I, Helle M, Jansen O, Synowitz M, et al. Intraoperative Resection Control Using Arterial Spin Labeling-Proof of Concept, Reproducibility of Data and Initial Results. *NeuroImage Clin* (2017) 15:136–42. doi: 10.1016/j.nicl.2017.04.021
15. Alsop DC, Detre JA, Golay X, Günther M, Hendrikse J, Hernandez-Garcia L, et al. Recommended Implementation of Arterial Spin-Labeled Perfusion MRI for Clinical Applications: A Consensus of the ISMRM Perfusion Study Group and the European Consortium for ASL in Dementia. *Magn Reson Med* (2015) 73(1):102–16. doi: 10.1002/mrm.25197
16. Soni N, Srindharan K, Kumar S, Mishra P, Bathla G, Kalita J, et al. Arterial Spin Labeling Perfusion: Prospective MR Imaging in Differentiating Neoplastic From non-Neoplastic Intra-Axial Brain Lesions. *Neuroradiol J* (2018) 31(6):544–53. doi: 10.1177/1971400918783058
17. Falk Delgado A, De Luca F, van Westen D, Falk Delgado A. Arterial Spin Labeling MR Imaging for Differentiation Between High-and Low-Grade Glioma-a Meta-Analysis. *Neuro Oncol* (2018) 20(11):1450–61. doi: 10.1093/neuonc/noy095

18. Xu Q, Liu Q, Ge H, Ge X, Wu J, Qu J, et al. Tumor Recurrence Versus Treatment Effects in Glioma: A Comparative Study of Three-Dimensional Pseudo-Continuous Arterial Spin Labeling and Dynamic Susceptibility Contrast Imaging. *Med (Baltim)* (2017) 96(50):e9332. doi: 10.1097/MD.0000000000009332
19. Louis DN, Perry A, Wesseling P, Brat DJ, Cree IA, Figarella-Branger D, et al. The 2021 WHO Classification of Tumors of the Central Nervous System: A Summary. *Neuro Oncol* (2021) 23(8):1231–51. doi: 10.1093/neuonc/noab106
20. Chukwueke UN, Wen PY. Use of the Response Assessment in Neuro-Oncology (RANO) Criteria in Clinical Trials and Clinical Practice. *CNS Oncol* (2019) 8(1):CNS28. doi: 10.2217/cns-2018–0007
21. Buxton RB, Frank LR, Wong EC, Siewert B, Warach S, Edelman RR. A General Kinetic Model for Quantitative Perfusion Imaging With Arterial Spin Labeling. *Magnetic Reson Med: Off J Soc Magnetic Reson Med/Socie Magnetic Reson Med* (1998) 40(3):383–96. doi: 10.1002/mrm.1910400308
22. Wu W, Ye J, Wang Q, Luo J, Xu S. Ct-Based Radiomics Signature for the Preoperative Discrimination Between Head and Neck Squamous Cell Carcinoma Grades. *Front Oncol* (2019) 9:821. doi: 10.3389/fonc.2019.00821
23. Tibshirani R. Regression Shrinkage and Selection *via* the Lasso. *J R Stat Soc Ser B Methodol* (1996) 58(1):267–88. doi: 10.1111/j.2517-6161.1996.tb02080.x
24. Jooma R, Waqas M, Khan I. Diffuse Low-Grade Glioma-Changing Concepts in Diagnosis and Management: A Review. *Asian J Neurosurg* (2019) 14 (2):356–63. doi: 10.4103/ajns.AJNS_24_18
25. Obara T, Blonski M, Brzenczek C, Mézières S, Gaudeau Y, Pouget C, et al. Adult Diffuse Low-Grade Gliomas: 35-Year Experience at the Nancy France Neurooncology Unit. *Front Oncol* (2020) 10:574679. doi: 10.3389/fonc.2020.574679
26. Tom MC, Park DYJ, Yang K, Leyrer CM, Wei W, Jia X, et al. Malignant Transformation of Molecularly Classified Adult Low-Grade Glioma. *Int J Radiat OncolBiol Phys* (2019) 105(5):1106–12. doi: 10.1016/j.ijrobp.2019.08.025
27. Jakola AS, Bouget D, Reinertsen I, Skjulsvik AJ, Sagberg LM, Bø HK, et al. Spatial Distribution of Malignant Transformation in Patients With Low-Grade Glioma. *J Neurooncol* (2020) 146(2):373–80. doi: 10.1007/s11060–020-03391–1
28. Tatekawa H, Uetani H, Hagiwara A, Bahri S, Raymond C, Lai A, et al. Worse Prognosis for IDH Wild-Type Diffuse Gliomas With Larger Residual Biological Tumor Burden. *Ann Nucl Med* (2021) 35(9):1022–9. doi: 10.1007/s12149–021-01637–0
29. Sadowski EA, Bennett LK, Chan MR, Wentland AL, Garrett AL, Garrett RW, et al. Nephrogenic Systemic Fibrosis: Risk Factors and Incidence Estimation. *Radiology* (2007) 243(1):148–57. doi: 10.1148/radiol.2431062144
30. Wang J, Licht DJ, Jahng GH, Liu CS, Rubin JT, Haselgrove J, et al. Pediatric Perfusion Imaging Using Pulsed Arterial Spin Labeling. *J Magn Reson Imaging* (2003) 18(4):404–13. doi: 10.1002/jmri.10372
31. Bokkers RP, Bremmer JP, van Berckel BN, Lammertsma AA, Hendrikse J, Pluim JP, et al. Arterial Spin Labeling Perfusion MRI at Multiple Delay Times: A Correlative Study With H (2)(15)O Positron Emission Tomography in Patients With Symptomatic Carotid Artery Occlusion. *J Cereb Blood Flow Metabolism: Off J Int Soc Cereb Blood Flow Metab* (2010) 30(1):222–9. doi: 10.1038/jcbfm.2009.204
32. Xu G, Rowley HA, Wu G, Alsop DC, Shankaranarayanan A, Dowling M, et al. Reliability and Precision of Pseudo-Continuous Arterial Spin Labeling Perfusion MRI on 3.0 T and Comparison With 15O-Water PET in Elderly Subjects at Risk for Alzheimer's Disease. *NMR Biomed* (2010) 23(3):286–93. doi: 10.1002/nbm.1462
33. Gevers S, van Osch MJ, Bokkers RP, Kies DA, Teeuwisse WM, Majoie CB, et al. Intra-And Multi-Center Reproducibility of Pulsed, Continuous and Pseudo-Continuous Arterial Spin Labeling Methods for Measuring Cerebral Perfusion. *J Cereb Blood Flow Metabolism: Off J Int Soc Cereb Blood Flow Metab* (2011) 31(8):1706–15. doi: 10.1038/jcbfm.2011.10
34. Petersen ET, Mouridsen K, Golay X. The QUASAR Reproducibility Study, Part II: Results From a Multi-Center Arterial Spin Labeling Test-Retest Study. *NeuroImage* (2010) 49(1):104–13. doi: 10.1016/j.neuroimage.2009.07.068
35. Wyss MT, Hofer S, Hefti M, Bärtschi E, Uhlmann C, Treyer V, et al. Spatial Heterogeneity of Low-Grade Gliomas at the Capillary Level: A PET Study on Tumor Blood Flow and Amino Acid Uptake. *J Nucl Med* (2007) 7:1047–52. doi: 10.2967/jnumed.106.038489
36. Hayes AR, Jayamanne D, Hsiao E, Schembri GP, Bailey DL, Roach PJ, et al. Utilizing 18F-Fluoroethyltyrosine (FET) Positron Emission Tomography (PET) to Define Suspected Nonenhancing Tumor for Radiation Therapy Planning of Glioblastoma. *Pract Radiat Oncol* (2018) 8(4):230–8. doi: 10.1016/j.prro.2018.01.006
37. Jaspers JPM, Méndez Romero A, Wiggenraad R, Compter I, Eekers DBP, Nout RA, et al. Pattern of Failure in IDH Mutated, Low Grade Glioma After Radiotherapy-Implications for Margin Reduction. *Radiother Oncol* (2021) 156:43–8. doi: 10.1016/j.radonc.2020.11.019
38. Kamran SC, Dworkin M, Niemierko A, Bussiere M, Oh KS, Loeffler JS, et al. Patterns of Failure Among Patients With Low-Grade Glioma Treated With Proton Radiation Therapy. *Pract Radiat Oncol* (2019) 9(4):e356–61. doi: 10.1016/j.prro.2019.02.002
39. Sunwoo L, Yun TJ, You SH, Yoo RE, Kang KM, Choi SH, et al. Differentiation of Glioblastoma From Brain Metastasis: Qualitative and Quantitative Analysis Using Arterial Spin Labeling MR Imaging. *PloS One* (2016) 11(11):e0166662. doi: 10.1371/journal.pone.0166662
40. Khashbat D, Harada M, Abe T, Ganbold M, Iwamoto S, Uyama N, et al. Diagnostic Performance of Arterial Spin Labeling for Grading Nonenhancing Astrocytic Tumors. *Magn Reson Med Sci* (2018) 17(4):277–82. doi: 10.2463/mrms.mp.2017–0065
41. Calmon R, Puget S, Varlet P, Dangouloff-Ros V, Blauwblomme T, Beccaria K, et al. Cerebral Blood Flow Changes After Radiation Therapy Identifies Pseudoprogression in Diffuse Intrinsic Pontine Gliomas. *Neuro Oncol* (2018) 20(7):994–1002. doi: 10.1093/neuonc/nox227
42. Petr J, Platzek I, Seidlitz A, Mutsaerts HJ, Hofheinz F, Schramm G, et al. Early and Late Effects of Radiochemotherapy on Cerebral Blood Flow in Glioblastoma Patients Measured With non-Invasive Perfusion MRI. *Radiother Oncol* (2016) 118(1):24–8. doi: 10.1016/j.radonc.2015.12.017
43. Yan JL, Li C, van der Hoorn A, Boonzaier NR, Matys T, Price SJ. A Neural Network Approach to Identify the Peritumoral Invasive Areas in Glioblastoma Patients by Using MR Radiomics. *Sci Rep* (2020) 10(1):9748. doi: 10.1038/s41598–020–66691–6
44. Cao Y, Tsien CI, Shen Z, Tatro DS, Ten Haken R, Kessler ML, et al. Use of Magnetic Resonance Imaging to Assess Blood-Brain/Blood-Glioma Barrier Opening During Conformal Radiotherapy. *J Clin Oncol* (2005) 23(18):4127–36. doi: 10.1200/JCO.2005.07.144

Conflict of Interest: All authors declare that the research was conducted in the absence of any commercial or financial relationships that could be construed as a potential conflict of interest.

frontiers | Frontiers in Oncology

ORIGINAL RESEARCH
published: 06 July 2022
doi: 10.3389/fonc.2022.876861

Dynamic Characteristics and Predictive Capability of Tumor Voxel Dose–Response Assessed Using ^{18}F-FDG PET/CT Imaging Feedback

Shupeng Chen[1], *An Qin*[1] *and Di Yan*[1,2]*

[1] Radiation Oncology, William Beaumont Hospital, Royal Oak, MI, United States, [2] Radiation Oncology, Huaxi Hospital/School of Medicine, Chengdu, China

Purpose: Tumor voxel dose–response matrix (DRM) can be quantified using feedback from serial FDG-PET/CT imaging acquired during radiotherapy. This study investigated the dynamic characteristics and the predictive capability of DRM.

Methods: FDG-PET/CT images were acquired before and weekly during standard chemoradiotherapy with the treatment dose 2 Gy × 35 from 31 head and neck cancer patients. For each patient, deformable image registration was performed between the pretreatment/baseline PET/CT image and each weekly PET/CT image. Tumor voxel DRM was derived using linear regression on the logarithm of the weekly standard uptake value (SUV) ratios for each tumor voxel, such as SUV measured at a dose level normalized to the baseline SUV_0. The dynamic characteristics were evaluated by comparing the DRM_i estimated using a single feedback image acquired at the *i*th treatment week (i = 1, 2, 3, or 4) to the DRM estimated using the last feedback image for each patient. The predictive capability of the DRM estimated using 1 or 2 feedback images was evaluated using the receiver operating characteristic test with respect to the treatment outcome of tumor local–regional control or failure.

Results: The mean ± SD of tumor voxel SUV measured at the pretreatment and the 1st, 2nd, 3rd, 4th, and last treatment weeks was 6.76 ± 3.69, 5.72 ± 3.43, 3.85 ± 2.22, 3.27 ± 2.25, 2.5 ± 1.79, and 2.23 ± 1.27, respectively. The deviations between the DRM_i estimated using the single feedback image obtained at the *i*th week and the last feedback image were 0.86 ± 4.87, –0.06 ± 0.3, –0.09 ± 0.17, and –0.09 ± 0.12 for DRM_1, DRM_2, DRM_3, and DRM_4, respectively. The predictive capability of DRM_3 and DRM_4 was significant ($p < 0.001$). The area under the curve (AUC) was increased with the increase in treatment dose level. The DRMs constructed using the single feedback image achieved an AUC of 0.86~1. The AUC was slightly improved to 0.94~1 for the DRMs estimated using 2 feedback images.

Edited by:
Yingli Yang,
UCLA Health System, United States

Reviewed by:
Yuenan Wang,
Peking University, China
Jorge Oldan,
University of North Carolina at Chapel Hill, United States

****Correspondence:***
Di Yan
dyanmay31@gmail.com

Specialty section:
This article was submitted to Radiation Oncology, a section of the journal Frontiers in Oncology

Received: *15 February 2022*
Accepted: *01 June 2022*
Published: *06 July 2022*

Citation:
Chen S, Qin A and Yan D (2022) Dynamic Characteristics and Predictive Capability of Tumor Voxel Dose–Response Assessed Using ^{18}F-FDG PET/CT Imaging Feedback. Front. Oncol. 12:876861. doi: 10.3389/fonc.2022.876861

Conclusion: Tumor voxel metabolic activity measured using FDG-PET/CT fluctuated noticeably during the first 2 treatment weeks and obtained a stabilized reduction rate thereafter. Tumor voxel DRM constructed using a single FDG-PET/CT feedback image after the 2nd treatment week (>20 Gy) has a good predictive capability. The predictive capability improved continuously using a later feedback image and marginally improved when two feedback images were applied.

Keywords: FDG-PET/CT imaging feedback, tumor voxel dose–response DRM, dynamic characteristics and predictive capability, adaptive dose painting, adaptive radiotherapy

INTRODUCTION

Mounting evidence has revealed that genetic and phenotypic variations exist between tumors and within each of the individual tumors (1–3). These variations result in considerable inter-tumoral and intra-tumoral heterogeneities of dose–response to radiotherapy, significantly impacting patient clinical outcomes (4–8). Therefore, targeting individual tumor heterogeneity of dose–response using a spatially non-uniform treatment dose distribution has been suggested and clinically feasible to personalize radiotherapy treatment and improve patient therapeutic ratio (9–14).

Tumor treatment response to radiation is influenced by many biological factors and changes in the tumor microenvironment (15). Most of these factors are unknown before treatment and modified dynamically during the treatment course. Tumor radiosensitivity has been estimated before treatment using *in vitro* clonogenic assay (16–18) or a linear regression model derived from the specific gene expressions (19–21). However, these methods can only measure the tumor intrinsic cellular radiosensitivity and could not be utilized to assess intra-tumoral treatment dose–response modified by tumor cell repopulation (22–24), reoxygenation (25–28), reactivation of immune response (29, 30), etc. There have been different methods to assess intra-tumoral treatment dose–response at the tumor voxel level using biological imaging feedback, i.e., acquiring PET or MR images during the treatment course (8, 14, 31–37).

Treatment feedback images have the potential to explore dynamic features of cellular activities in tumors during the treatment course, which could guide us to select the most efficient and reliable time points to quantify and estimate treatment dose–response for clinical therapeutic decisions. Most importantly, quantified intra-tumoral dose–response will guide the design of heterogeneity treatment doses to maximize the therapeutic ratio (14). In this study, serial weekly fluoro-2-deoxyglucose (FDG)-PET/CT feedback images were used to evaluate the dynamic characteristics of tumor voxel treatment response with respect to different treatment dose levels. The predictive capability of tumor voxel treatment dose–response was studied to determine the time points and minimal numbers of imaging feedback.

METHODS AND MATERIALS

Patient Image Data and Preprocessing

The investigated patients were enrolled in an investigator-initiated clinical trial entitled "a prospective, non-randomized trial evaluating the utility of adaptive radiotherapy in the management of locally advanced head and neck squamous cell carcinomas (HNSCC) patients." The trial was approved (IRB 2012-100) by the Hospital Review Board. In the protocol, pretreatment and weekly FDG-PET/CT imaging was planned for each patient. However, due to different clinical reasons, a number of protocol patients missed their weekly imaging partially. Thirty-one patients who had pretreatment PET/CT images and at least 3 weekly treatment PET/CT images obtained during the first 4 treatment weeks were selected for the present study. Four of 31 patients had experienced biopsy-proven local failure. The median (range) follow-up time is 23 (7~52) months. The details of the tumor characteristics are listed in **Table 1**.

PET/CT scans were performed on the patients 90 min after injection with 4 MBq/kg of FDG acquired in the treatment position with an immobilization mask in place using a time-of-flight Gemini TF Big Bore PET/CT scanner (Philips Medical Systems, Cleveland, OH, USA). PET images were reconstructed using the blob-ordered subsets–time-of-flight reconstruction algorithm with a voxel size of 4 × 4 × 4 mm (3). All treatments were prescribed to deliver a 2-Gy daily dose to the gross tumor volume (GTV) for 35 fractions using intensity-modulated radiation therapy or volumetric modulated arc therapy followed by the online cone-beam CT imaging-guided target position localization. Standard uptake value (SUV) of each PET voxel was calculated by normalizing the average activity concentration to the injected FDG dose per unit body weight with decay correction (38). Tumors manifested on the pretreatment PET/CT images were contoured based on a fixed SUV threshold (=2.5) and modified, if necessary, to exclude air cavities and bony structures. For a tumor that could not be delineated entirely using the cutoff SUV value due to tissue (most likely tongue) inflammation adjacent to the tumors, it was manually adjusted to the clinically used GTV boundary.

Image Registration and Evaluation

The mean ± SD of tumor volume reduction of the 31 patients was 20% ± 18.1% at the 4th treatment week. Therefore, deformable image registration (DIR) was used to account for the tumor shrinkage in the analysis of the tumor voxel dose–response. For each patient, all weekly PET/CT feedback images were registered to the pretreatment PET/CT image using a hybrid biomechanical based DIR method (39), which includes 2 steps: 1) determine tumor boundary following an image intensity-based DIR method

TABLE 1 | Tumor characteristic.

Median age (year)	63 (46–83)
Gender	
Male/female	26 (83.9%)/5 (16.1%)
Primary site	
Base of tongue	15 (48.4%)
Tonsil	8 (25.8%)
Supraglottic	4 (12.9%)
Unknown	2 (6.5%)
Aryepiglottic fold	1 (3.2%)
Nasopharynx	1 (3.2%)
Clinical stage	
II	2 (6.5%)
III	5 (16.1%)
IV	2 (6.5%)
IVA	21 (67.7%)
IVB	1 (3.2%)
Clinical T stage	
1	2 (6.5%)
2	17 (54.8%)
3	6 (19.4%)
4	2 (6.5%)
X	4 (12.9%)
Clinical N stage	
0	1 (3.2%)
1	4 (12.9%)
2a	2 (6.5%)
2b	15 (48.4%)
2c	7 (22.6%)
Unknown	1 (3.2%)
HPV status	
Negative/positive/unknown	6 (19.4%)/23 (74.2%)/2 (6.5%)
Smoking	
Non-smoker	10 (32.2%)
Light smoker (<10 pack-year)	7 (22.6%)
Heavy smoker (>10 pack-year)	14 (45.2%)

HPV, human papillomavirus.

(ADMIRE, v1.12, Elekta Inc.) and 2) regulate the intra-tumoral mesh distribution based on finite element method.

The core of the intensity-based DIR algorithm is a local-correlation-coefficient-based dense non-linear registration algorithm with a regularization term defined as the L2 norm of the first-order spatial derivative of the displacement vector field (DVF). Previous studies have demonstrated that the intensity-based DIR achieved high accuracy for most organ boundary registration of head and neck cancer patients with the Dice similarity coefficient (DSC) ≥0.85 between the contours generated by the registration and by manual delineation (40). However, the voxel-wise displacement accuracy of image intensity-based DIR could be limited within a tumor due to the lack of distinctive image features on CT images. Therefore, the finite element method was used to correct the potential irregular displacements in tumors based on the soft-tissue mechanical characteristic. Our earlier bio-tissue phantom study has demonstrated that the uncertainty of the biomechanical-based registration, most likely, was within 4 mm (or a PET voxel size) in tumors (41). The effect of the registration uncertainty on tumor voxel dose–response assessment has been studied (42).

In this study, the tumor contours generated using the DIR on the feedback images obtained at the 2nd and 4th treatment weeks were compared to the ones manually delineated by experienced physicians. The DSC and the mean surface distance were used to evaluate the tumor boundary registration. The physical plausibility of the DVFs was evaluated using the Jacobian determinant. The Jacobian value describes the local volume change of a tumor voxel after deformation. A Jacobian value = 0.9 indicates 10% volume contraction for the tumor voxel. In comparison, 1.1 indicates a 10% volume expansion.

Tumor Voxel Dose–Response Matrix

Tumor voxel dose–response matrix (DRM) has been quantified using tumor voxel SUV ratio manifested on the pretreatment baseline and FDG-PET/CT treatment feedback images following the DIR (14). Briefly, the logarithm of tumor voxel SUV change ratio obtained during radiotherapy was modeled using a linear random process, as follows:

$$\ln \frac{SUV(v,d)}{SUV_0(v)} = A(v)\cdot d + \xi \tag{1}$$

where the $SUV_0(v)$ and $SUV(v, d)$ are the pretreatment baseline SUV and the SUV after receiving a treatment dose d for a tumor voxel v, respectively. $A(v)$ represents the average slope of the logarithm SUV change ratio during treatment up to the treatment dose d or the systematic component of the random process, and ξ is the random component representing the discrepancy between the linear model and the actual measurement at each dose level. Considering the facts of temporal variations of tumor dose–response caused by tumor reoxygenation and growth during the treatment course, slope A could most likely be modified by the treatment dose. However, due to the limited number of feedback images available, it has been modeled simply using the average slope. Tumor voxel DRM was quantified numerically to match the standard tumor cellular radiosensitivity index, SF_2, to the survival fraction in 2 Gy (14), as follows:

$$DRM(v) = exp\left[\frac{2}{k}\cdot A(v)\right] \tag{2}$$

where k is the calibration factor and equals 0.063 determined based on the average SF_2 obtained from *in vitro* cellular assay of human head and neck tumors (43). DRM value represents tumor cell survival/growth in a tumor voxel during treatment; 0 < DRM < 1 implies that cell killing in the tumor voxel is larger than growth; otherwise, ≥1.

Dose–Response Matrix Estimation

Different numbers of PET feedback images can be used to estimate the average slope A; thus, the DRM is based on **Eqs. 1** and **2**. Given a serial of SUVs of a tumor voxel v measured at different treatment dose levels, the average slope A can be determined using a least-squares method, as follows:

$$Min\sum_{i=1}^{N}\left[A(v)\cdot d_i - ln\frac{SUV(v,d_i)}{SUV_0(v)}\right]^2 \tag{3}$$

where the $SUV(v, d_i)$ is the SUV on the ith feedback image obtained at least 12 h after receiving a treatment dose d_i, and N is

the total number of feedback images being used. One can derive $A(v)$ to be the "weighted average" of the logarithm SUV change ratios (details of derivation are in the **Supplementary Material**), as follows:

$$A(v) = \left[\sum_{i=1}^{N} d_i \cdot ln\frac{SUV(v,d_i)}{SUV_0(v)}\right] / \sum_{i=1}^{N} d_i^2 \quad (4)$$

The later measurement has a larger weight. In principle, the more PET feedback images are used, the more reliable the estimation should be. However, a large number of feedback images would be clinically impractical at the present time due to the extensive cost, patient inconvenience, and extra workload. In addition, an early estimation will be helpful and provide more room for treatment adaptation. Therefore, DRM estimated using 1 or 2 feedback images obtained in the early treatment should be a reasonable choice for clinical implementations and was evaluated in this study.

Dose–Response Matrix Evaluation

Dynamic characteristics of tumor voxel dose–response were evaluated using a single PET feedback image acquired at different dose levels during the treatment course. For each patient, tumor voxel DRM_i was constructed using the feedback image acquired at the *i*th treatment week, $i = 1, 2, 3$, or 4. In this study, the weekly feedback images were acquired within the (mean ± SD) dose range of (7.4 ± 1.8), (17.9 ± 1.8), (26.6 ± 3.9), and (39.1 ± 3.6) Gy. The DRM_i was compared with the DRM_L constructed using the feedback image acquired in the last treatment week or within the dose range of (58 ± 9.1) Gy. DRM_L was used as a reference to evaluate the convergence feature of tumor voxel dose–response during treatment.

The predictive capability of DRM constructed using either 1 or 2 feedback images acquired during the first 4 treatment weeks was evaluated using the receiver operating characteristic (ROC) test with respect to the treatment outcome of local tumor control or failure. As described in a previous study (14), tumor voxel control or failure is highly dependent on two factors, tumor voxel baseline SUV_0 (tumor cell burden in the voxel) and DRM (tumor cell dose–response in the voxel). Therefore, a 2-dimensional cutoff curve or boundary function on the tumor voxel (SUV_0, DRM) domain can be used to test the sensitivity and specificity of tumor voxel control or failure. For each estimated DRM, a boundary function, $BF = a \cdot SUV_0^b(v) + c$, was created on the tumor voxel (SUV_0, DRM) domain to evaluate the sensitivity and specificity of tumor voxel control or failure. The constants a, b, and c in the BF were determined by maximizing the area under the curve (AUC) for all tumor voxels. Tumor voxels above BF were those voxels that are most likely to cause tumor local recurrences. **Figure 1** shows a local control tumor and a local failure tumor with a BF superimposed on the (SUV_0, DRM) domain. Given a treatment dose of 35 × 2 Gy, the true positive (TP) is defined such that a tumor will be locally controlled if the number of tumor voxels outside of the BF < n. The true negative (TN) is defined such that a tumor will be locally failure if the number of tumor voxels outside of the BF ≥ n. The false positive (FP) and the false negative (FN) are defined accordingly. The 95% CI of AUC was determined using the Delong method (44). The statistical significance of the AUC was determined using Mann–Whitney U-statistic (45), where the null hypothesis of AUC = 0.5. Due to the multiple tests performed in the study, the type I error rate would increase. Therefore, the conventional p-value of 0.05 for significance was adjusted to 0.002 based on the Bonferroni method (46). The sensitivity and specificity were determined by maximizing Youden's index (47) (i.e., sensitivity + specificity − 1). Due to the imbalance of the patient dataset, F1 score = 2TP/(2TP + FP + FN) was also included in the evaluation. The predictive capability of tumor voxel DRM was compared with that of the conventional image features including maximum SUV (SUV_{max}), metabolic tumor volume (MTV), and total lesion glycolysis (TLG) obtained from the pretreatment PET image and the weekly PET feedback images. The MTV was defined as the volume of the tumor voxels with SUV > 2.5. The TLG was defined as the MTV times the mean of SUV for a tumor.

RESULTS

Figure 2 shows the tumor voxel SUV measured during the pretreatment and different treatment weeks during radiotherapy. The SUV declined noticeably from 6.76 ± 3.69 measured at pretreatment to 3.85 ± 2.22 measured at the 2nd treatment week. After that, the SUV continuously declined and became stabilized with a mean ± SD of 3.27 ± 2.25, 2.5 ± 1.79, and 2.23 ± 1.27 for the 3rd, 4th, and last treatment weeks, respectively.

The mean ± SD of the DSC between the contours generated by the DIR and the one manually delineated by the physicians was 0.84 ± 0.06 on the week 2 feedback image and was 0.79 ± 0.08 on the week 4 feedback image. The mean surface distances were (1.66 ± 0.54) mm and (1.85 ± 0.63) mm for the week 2 and the week 4 feedback images. No negative Jacobian value was observed for all tumor voxels. **Figure 3** shows the mean ± SD of the Jacobian values for individual patients. The Jacobian value was calculated from the DVFs obtained from the DIR performed between the pretreatment image and the week 2 and week 4 feedback images.

A strong linear relationship between the logarithm tumor voxel SUV change ratio measured within the first 4 treatment weeks at the different treatment dose levels was identified. The mean ± SD of Pearson's correlation coefficient was 0.91 ± 0.15 for all the 20,757 tumor voxels. As a comparison, the correlation coefficient between the tumor voxel SUV change ratio and treatment dose was lower (p-value <0.001, two-sample t-test) with the coefficient being 0.89 ± 0.18 for all tumor voxels. **Figure 4** shows the measured logarithm SUV change ratios *versus* treatment dose and the linear model (red line) from **Eq. 1** for those tumor voxels with the average dose–response DRM being 0.2, 0.4, 0.6, and 0.8, where the average DRM was determined using the first 4 weekly feedback images.

Figure 5 shows the relationship between tumor voxel DRM and tumor voxel SUV change ratio measured at different dose levels derived based on **Eqs. 1** and **2**. The slope of the curve

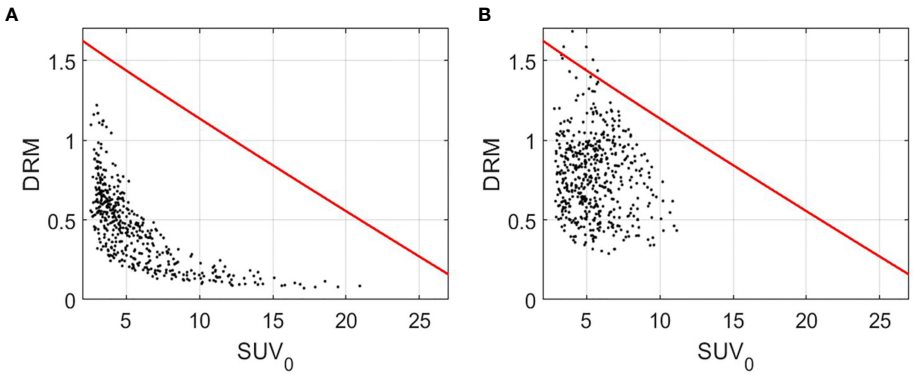

FIGURE 1 | Tumor voxel (SUV_0, DRM) for a local control tumor **(A)** and a local failure tumor **(B)** with the boundary function, $BF = -0.07 \cdot SUV_0^{0.95}(v) + 1.76$ (red curve). DRM and BF were constructed using the PET feedback image acquired during the 3rd treatment week. DRM, dose–response matrix.

decreased with the increase of the dose level. It implies that a DRM estimated at early treatment will be more sensitive to the errors in SUV measurement. Therefore, later DRM estimation will be more reliable.

Figures 6A–C shows the cumulative histograms of DRMs for all tumors, control tumors, and failure tumors, respectively. The distributions of DRM_i for both control and failure groups converge gradually to DRM_L. Both control and failure groups have a certain number of resistant tumor voxels (e.g., DRM > 0.8), and their number gradually reduced during treatment due to reoxygenation. However, the percentage of the reduction for the failures remains smaller compared to the controls. For the controls, the percentage of tumor voxels with DRM > 0.8, V (DRM > 0.8), was 30.5%, 16%, 9.5%, and 3.6% for DRM_1, DRM_2, DRM_3, and DRM_4, respectively. For the failure patients, the corresponding V(DRM > 0.8) was 55.8%, 13.4%, 13.4%, and 7.7%. **Figures 6C–E** show the histogram of the deviation of the DRM, i.e., $DRM_i - DRM_L$ (i = 1, 2, 3, and 4), for different tumor groups. For the control patients, the mean ± SD of DRM deviation was 1.22 ± 3.67, −0.01 ± 0.34, −0.04 ± 0.17, and −0.01 ± 0.08 for the DRM_1, DRM_2, DRM_3, and DRM_4, respectively. For the failure patients, the corresponding DRM deviation was 0.71 ± 4.99, −0.08 ± 0.28, −0.12 ± 0.17, and −0.14 ± 0.12, indicating the systemic underestimation of tumor voxel resistance.

Figure 7 shows the mean ± SD of the deviation between the DRM_L and each of the DRMs estimated using a single feedback image for the tumor voxels within each level of DRM_L. **Figure 7A** shows that the DRM_2 has larger deviations as compared to the DRM_3 and DRM_4 for tumor voxels with respect to different levels of DRM_L in absolute value for all tumor voxels. In contrast, **Figure 7B** shows the relative deviations (%) decrease with the increase of the DRM_L level.

Figures 8A, B show the pretreatment (SUV_0) and ith treatment week (SUV_i) for a local failure tumor. **Figure 8C** shows the 6-month posttreatment (post-Tx) FDG-PET/CT image. The locally high metabolic activity region (arrow) detected the recurrence position. **Figure 8D** shows the tumor voxel DRM estimated using a single weekly feedback image. The highly resistant areas (DRM > 1) on the DRMs, predicted using different weekly PET feedback images, appeared to be consistently close to the recurrence location.

Table 2 shows the ROC test results for the DRMs estimated using different PET feedback images. For those DRMs estimated using a single feedback image, the predictive capability quantified

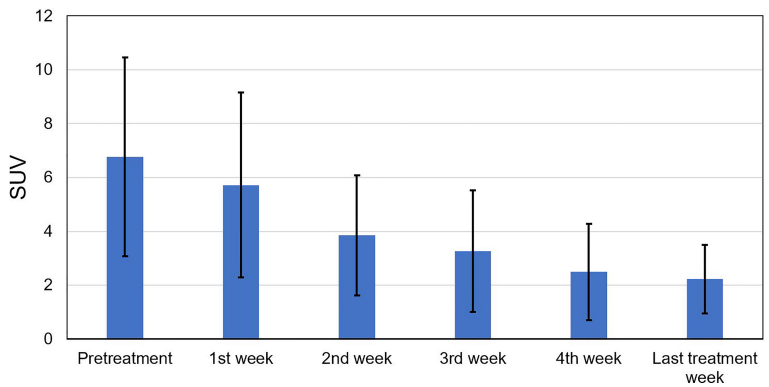

FIGURE 2 | Standard uptake value (SUV) measured at the pretreatment, the 1st to 4th treatment weeks, and the last treatment week for all tumor voxels.

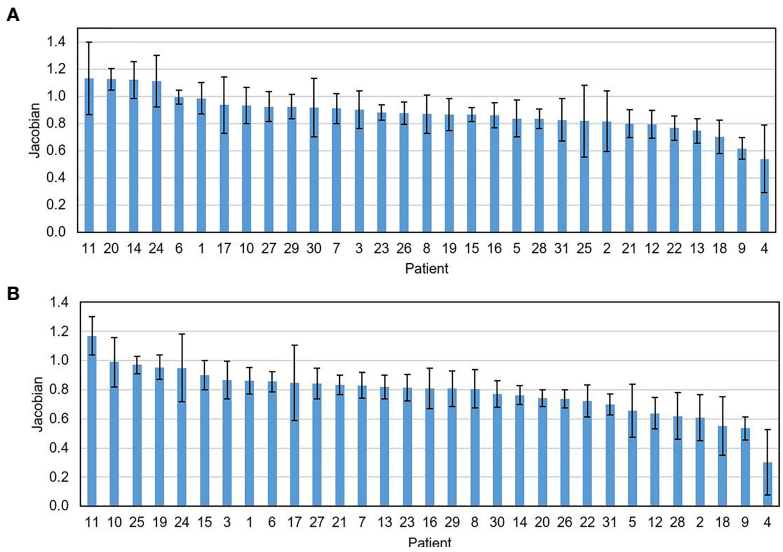

FIGURE 3 | The mean ± SD of the Jacobian value for individual patients calculated on the feedback images obtained at the 2nd **(A)** and the 4th treatment weeks **(B)**.

by AUC was improved from 0.78 for DRM_1 to 1.00 for DRM_4. In contrast, the predictive capability of the DRMs estimated using 2 feedback images remains high, with AUC ≥ 0.95. The predictive capability of the FDG avidity or SUV_{max} remained relatively low. The AUCs for the maximum SUV were 0.61~0.77. Both MTV and TLG achieved a moderate predictive capability with the AUC being 0.74~0.81 and 0.77~0.93, respectively. There is no clear time trend for the predictive capability of SUV_{max}, MTV,

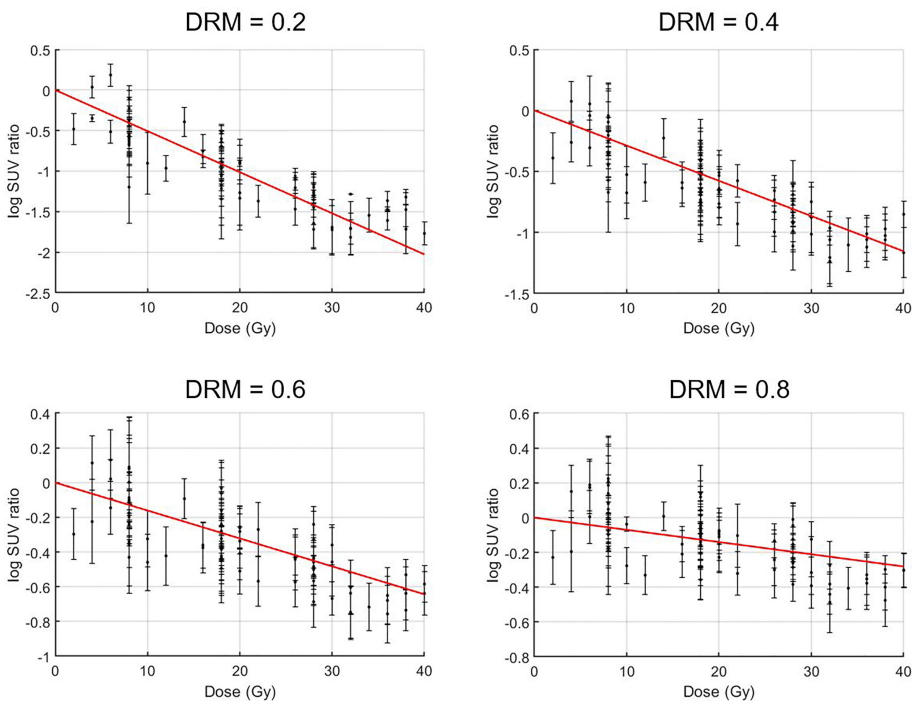

FIGURE 4 | Treatment dose *versus* logarithm standard uptake value (SUV) change ratio for tumor voxels with their average dose–response DRM being 0.2, 0.4, 0.6, and 0.8. Tumor voxel SUV change ratio = $SUV(d)/SUV_0$, i.e., tumor voxel SUV measured at a given dose level d normalized to its baseline SUV_0.

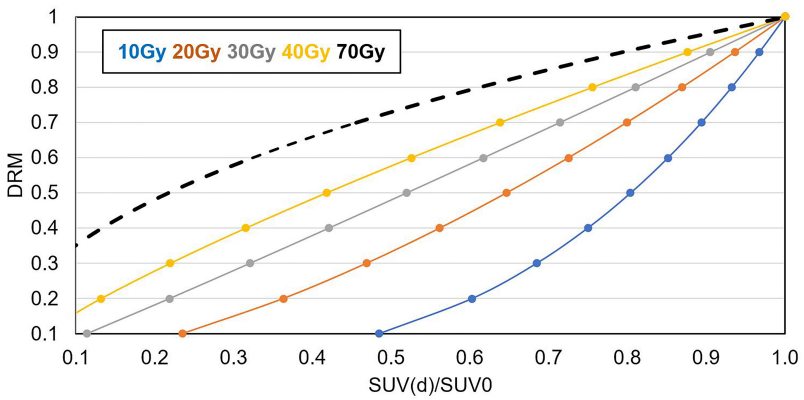

FIGURE 5 | Relationship between SUV(d)/SUV_0 and DRM for d = 10, 20, 30, 40, and 70 Gy.

and TLG. **Tables 3–5** summarize the details of the ROC analysis for the SUV_{max}, MTV, and TLG measured at the pretreatment and different treatment weeks.

DISCUSSION

By utilizing tumor voxel SUV change ratio determined using serial FDG-PET/CT imaging feedback, tumor voxel dose–response can be predicted and combined with the pretreatment SUV to guide treatment dose adaptation (14). The previous study (8) has demonstrated that tumor voxel DRM assessed for head and neck squamous cell carcinoma (HNSCC) had very large intra- and inter-tumoral variations. The variation had similar numerical distribution to the variations of cellular intrinsic radiosensitivity index or *in vitro* SF_2. In addition, the DRM index was found to strongly correlate with the expression of cancer stem cell biomarker CD44 for HNSCC patients (48). Tumor voxel DRM is a dynamic index that is constantly modified by the delivered radiation dose during treatment. Thus, DRMs, estimated using imaging feedback acquired at different treatment dose levels, could have different values

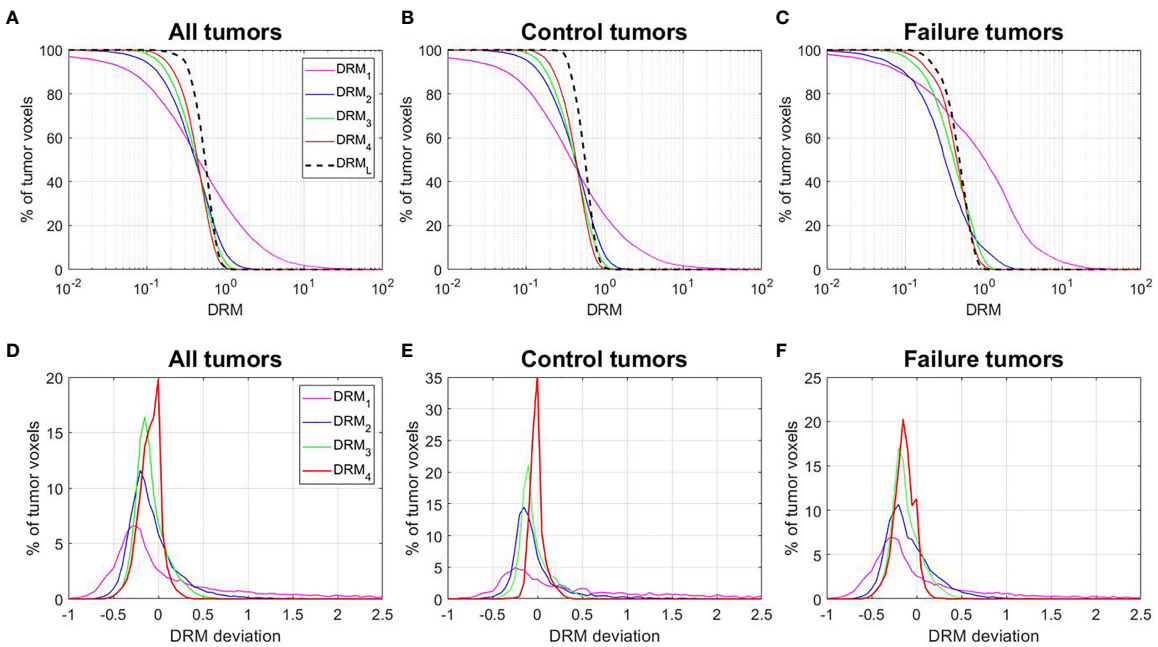

FIGURE 6 | **(A–C)** Cumulative histograms of the dose–response matrix (DRM) for all tumors, control tumors, and failure tumors. **(D–F)** Histograms of the DRM deviations = DRM_i – DRM_L. DRM_i = DRM estimated using the feedback image acquired at the *i*th treatment week; DRM_L = DRM estimated using the last treatment week feedback image.

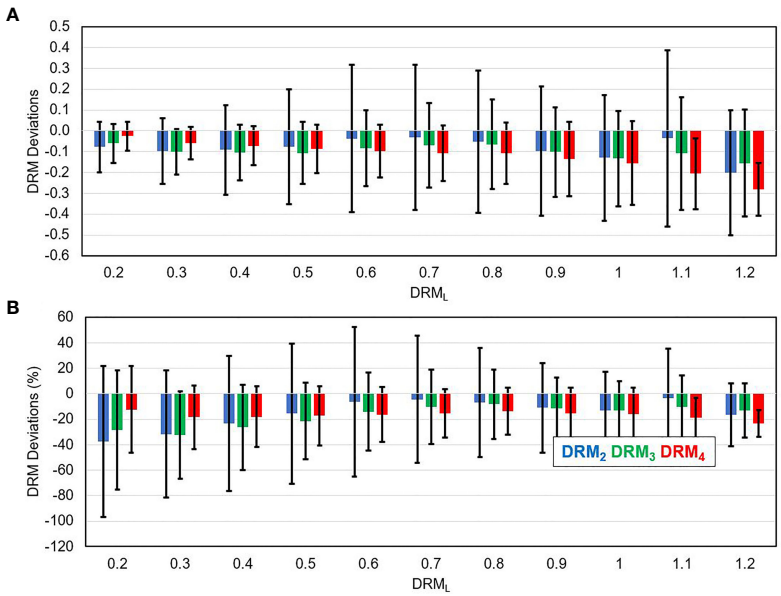

FIGURE 7 | The deviation between the DRM estimated using single weekly PET feedback image (DRM_2, DRM_3, and DRM_4) and the DRM_L estimated using the last feedback image for tumor voxels with different DRM_L values in absolute term **(A)** and relative term **(B)**.

reflecting the dynamic characteristic of radiation-induced tumor voxel dose–response. The current study demonstrated that the tumor voxel DRM became relatively stabilized after the 2nd treatment week (**Figure 2**) or the dose > 20 Gy (for 2 Gy per fraction treatment regimen). However, the stability was dependent on the DRM levels. For those of more resistant tumor voxels, i.e., DRM > 0.8, a larger variation could occur in the later treatment (**Figure 7**). Tumor voxel DRM estimated using either 1 or 2 feedback images acquired within the dose range of 30~40 Gy can predict tumor voxel dose–response and be used for treatment adaptation.

Tumor voxel DRM estimated using a single feedback image is most favorable in clinical practice. The estimated DRM was sensitive to the timing of the PET image feedback. The predictive

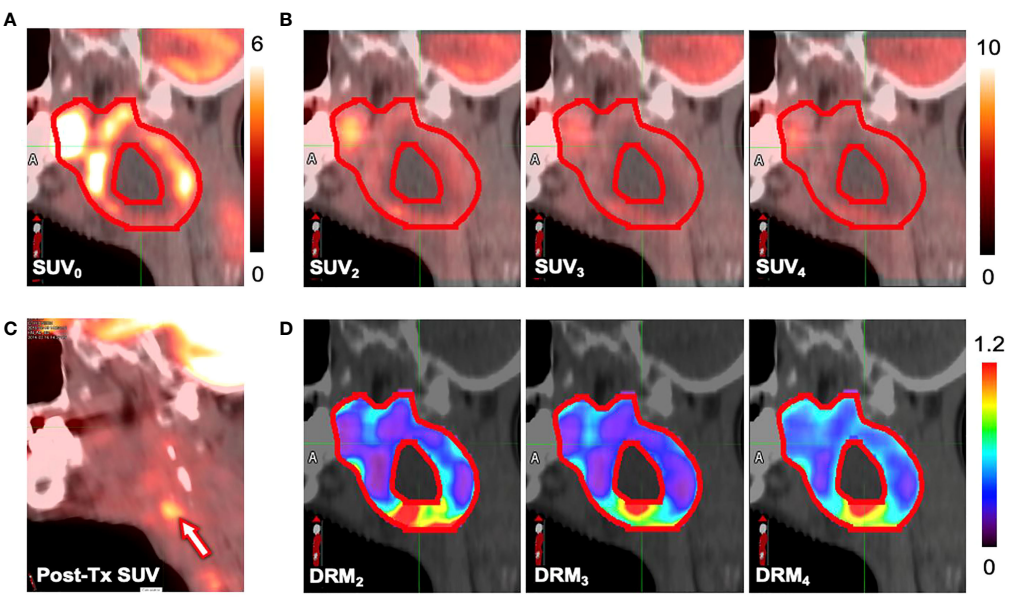

FIGURE 8 | Standard uptake values (SUVs) measured at **(A)** the pretreatment (SUV_0), **(B)** the *i*th treatment week (SUV_i), and **(C)** the 6-month posttreatment. **(D)** The dose–response matrix (DRM) estimated using single feedback image for a patient (primary site: tonsil, stage IV, HPV–) who experienced local recurrence.

TABLE 2 | ROC results for the tumor voxel dose–response matrix (DRM).

	Sensitivity	Specificity	F1 score	AUC [95 CI]	p
DRM_1	0.78	1.00	0.88	0.86[0.67, 1.00]	0.027
DRM_2	0.89	1.00	0.94	0.93[0.82, 1.00]	0.008
DRM_3	0.87	1.00	0.93	0.95[0.87, 1.00]	<0.001
DRM_4	1.00	1.00	1.00	1.00[1.00, 1.00]	<0.001
DRM_{12}	0.91	1.00	0.95	0.94[0.85, 1.00]	0.021
DRM_{13}	0.94	1.00	0.97	0.96[0.88, 1.00]	0.006
DRM_{14}	1.00	1.00	1.00	1.00[1.00, 1.00]	0.016
DRM_{23}	0.91	1.00	0.95	0.94[0.84, 1.00]	0.002
DRM_{24}	1.00	1.00	1.00	1.00[1.00, 1.00]	0.003
DRM_{34}	1.00	1.00	1.00	1.00[1.00, 1.00]	0.002

DRM_i = DRM estimated using the feedback image acquired at ith treatment week.
ROC, receiver operating characteristic; AUC, area under the curve; DRM, dose–response matrix.

TABLE 3 | ROC results for the maximum SUV (SUV_{max}).

SUV_{max} measured at	Sensitivity	Specificity	F1 score	AUC [95 CI]	p
Pretreatment	0.89	0.75	0.92	0.77 [0.38, 1.00]	0.047
1st week	0.91	0.67	0.93	0.72 [0.26, 1.00]	0.121
2nd week	0.52	1.00	0.68	0.72 [0.47, 0.97]	0.127
3rd week	0.32	1.00	0.48	0.61 [0.30, 0.93]	0.250
4th week	0.83	0.67	0.88	0.74 [0.37, 1.00]	0.111

ROC, receiver operating characteristic.

TABLE 4 | ROC results for the metabolic tumor volume (MTV).

MTV measured at	Sensitivity	Specificity	F1 score	AUC [95 CI]	p
Pretreatment	0.59	1.00	0.74	0.81 [0.60, 1.00]	0.024
1st week	0.61	1.00	0.76	0.75 [0.51, 1.00]	0.091
2nd week	0.70	0.70	0.83	0.80 [0.58, 1.00]	0.050
3rd week	0.57	0.82	0.88	0.74 [0.43, 1.00]	0.073
4th week	0.61	1.00	0.76	0.81 [0.56, 1.00]	0.050

ROC, receiver operating characteristic.

TABLE 5 | ROC results for the total lesion glycolysis (TLG).

TLG measured at	Sensitivity	Specificity	F1 score	AUC [95 CI]	p
Pretreatment	0.89	0.75	0.92	0.86 [0.64, 1.00]	0.009
1st week	0.61	1.00	0.76	0.77 [0.50, 1.00]	0.078
2nd week	0.70	1.00	0.83	0.80 [0.60, 1.00]	0.050
3rd week	0.64	1.00	0.78	0.82 [0.61, 1.00]	0.024
4th week	0.78	1.00	0.88	0.93 [0.77, 1.00]	0.008

ROC, receiver operating characteristic.

capability of the DRM improved as the treatment dose level increased (**Table 2**). The feedback image acquired in the 1st treatment week or within the dose range of (7.4 ± 1.8) Gy had minimal predictive capability. The disadvantage of using a very early FDG-PET feedback imaging in tumor response assessment has been studied. A study reported that using the feedback image acquired at the 1st treatment week cannot predict histomorphological tumor response (49). Another study reported that there was an initial increase of FDG uptake in tumors after 6 Gy of radiation dose (50). These very early (dose ¾ 10 Gy) metabolic changes could be caused by the inflammatory and immune response in tumors, which obscures the changes in tumor glucose metabolism induced by therapeutic effects (50). The feedback image acquired at the 2nd treatment week had an improved predictive capability and reduced systematic deviation with respect to the DRM_L constructed in the latest treatment week. However, DRM estimated using the 2nd feedback image still has a larger deviation from the DRM_L compared to the one obtained at the 3rd or 4th treatment week (**Figure 7**). The single feedback image obtained within the 3rd or 4th treatment week was comparable with respect to the DRM_L (**Figure 6**). However, each of them has different advantages and disadvantages. Feedback image acquired within the 3rd treatment week will provide an early prediction and, thus, more room for clinical treatment adaptation. However, an earlier DRM estimation is more

sensitive to the uncertainty in the DRM construction (**Figure 5**). Using **Eqs. 1** and **2**, one can derive the relationship between the uncertainty of tumor voxel SUV and DRM, as follows:

$$\frac{\delta DRM(v)}{DRM(v)} = \frac{2}{k \cdot d} \times \frac{\delta SUV(v,d)}{SUV(v,d)} \quad (5)$$

Thus, the uncertainty in DRM construction caused by the SUV uncertainty is inversely proportional to the treatment dose *d*. As an example, 5% of SUV variation will cause about 7.9% of DRM variation predicted at a dose of 20 Gy, compared to 5.3% at a dose of 30 Gy. Therefore, the time point of single imaging feedback acquired after the 2nd treatment week or >20 Gy faces a tradeoff between the early clinical decision on treatment adaptation and predictive reliability. One clinical option is to select the single feedback time point based on the minimal treatment dose required in a clinical dose painting protocol.

The predictive capability of tumor voxel DRM on treatment outcome of local–regional tumor failure or control was slightly improved when using 2 PET feedback images in the DRM estimation (**Table 2**). Meanwhile, the predictive capability was less sensitive to the timing of feedback imaging. Therefore, if the clinical workload is not a major concern, using 2 feedback images acquired between the end of the 2nd and 4th treatment weeks should be favorable to be used as guidance for target dose adaptation.

Various markers have been developed to predict tumor response to radiation for HNSCC patients. A gene expression profiling created from biopsies was proved to be of high predictive value on treatment outcomes (51, 52). Specific expression patterns of microRNA have been shown to predict therapeutic response in HNSCC patients (53, 54). In addition, as shown in this study and others (55–57), the SUV_{max}, MTV, and TLG obtained from a single FDG-PET image also had good predictive value on the treatment outcome. These markers are all useful in predicting treatment outcomes. However, the purpose of the study is not to demonstrate that the DRM can provide a better or equal prediction of treatment outcome than the other markers. The predictive capability quantified in the study was for evaluating the time point of image feedback for DRM construction. In fact, we used both the pretreatment SUV and DRM obtained from image feedback together to assess treatment outcome (14). Using both the pretreatment tumor voxel SUV, as a surrogate of tumor cell density in tumor voxel, and the tumor voxel DRM, as the radiosensitivity, to assess treatment outcome quantitatively also provides the spatial distribution of tumor voxel dose-efficacy. This important 3D information in tumors will be used to optimize dose distribution design for individual patients in adaptive treatment.

The major weakness of the study was that the patient cohort, especially the failure patient number, is relatively small. Therefore, the predictive capability of the patient outcome should be further validated by a larger patient cohort. To achieve a target power of 0.95, a future clinical trial will need at least 49 patients assuming the null hypothesis to be AUC = 0.5. Here, the target power was defined as the desired probability of rejecting a false null hypothesis. The patient number was estimated using a previously published method (58). Another weakness was the limited number of PET/CT feedback images for each patient used in the study. Due to different clinical reasons and because a number of patients missed 2 to 3 weekly feedback images required in the protocol, the dynamic characteristics of DRM could not be reliably explored.

CONCLUSIONS

Tumor voxel metabolic activity measured using FDG-PET/CT feedback images fluctuated noticeably during the first 2 treatment weeks and then became stabilized thereafter. Single FDG-PET/CT imaging acquired after the 2nd treatment week or the treatment dose >20 Gy is recommended to predict tumor voxel dose–response matrix in the current clinical practice. The time point of image feedback can be selected based on clinical application; later time points should be more reliable.

DATA AVAILABILITY STATEMENT

The data that supports these findings are available on request from the corresponding author.

ETHICS STATEMENT

The studies involving human participants were reviewed and approved by Beaumont Health Institutional Review Board. The patients/participants provided their written informed consent to participate in this study.

AUTHOR CONTRIBUTIONS

SC performed the data acquisition and analysis and wrote the manuscript. AQ developed the deformable image registration code and evaluated the image registration. DY designed the study, supervised the research project, and revised the manuscript. All authors listed have made a substantial, direct, and intellectual contribution to the work and approved it for publication.

FUNDING

SC has been supported by Beaumont Health in this study.

ACKNOWLEDGMENTS

The authors want to acknowledge Dr Hong Ye from Beaumont Health, Royal Oak, for her assistance with statistical analysis.

SUPPLEMENTARY MATERIAL

The Supplementary Material for this article can be found online at: https://www.frontiersin.org/articles/10.3389/fonc.2022.876861/full#supplementary-material

REFERENCES

1. Heppner GH. Tumor Heterogeneity. *Cancer Res* (1984) 44(6):2259–65.
2. Bedard PL, Hansen AR, Ratain MJ, Siu LL. Tumour Heterogeneity in the Clinic. *Nature* (2013) 501(7467):355–64. doi: 10.1038/nature12627
3. Meacham CE, Morrison SJ. Tumour Heterogeneity and Cancer Cell Plasticity. *Nature* (2013) 501(7467):328–37. doi: 10.1038/nature12624
4. Zagars GK, Schultheiss TE, Peters LJ. Inter-Tumor Heterogeneity and Radiation Dose-Control Curves. *Radiother Oncol* (1987) 8(4):353–61. doi: 10.1016/S0167-8140(87)80186-X
5. Suit H, Skates S, Taghian A, Okunieff P, Efird JT. Clinical Implications of Heterogeneity of Tumor Response to Radiation Therapy. *Radiother Oncol* (1992) 25(4):251–60. doi: 10.1016/0167-8140(92)90244-O
6. West CM, Davidson SE, Roberts SA, Hunter RD. Intrinsic Radiosensitivity and Prediction of Patient Response to Radiotherapy for Carcinoma of the Cervix. *Br J Cancer* (1993) 68(4):819–23. doi: 10.1038/bjc.1993.434
7. West CML. Intrinsic Radiosensitivity as a Predictor of Patient Response to Radiotherapy. *Br J Radiol* (1995) 68(812):827–37. doi: 10.1259/0007-1285-68-812-827
8. Yan D, Chen S, Krauss DJ, Deraniyagala R, Ye H, Wilson G. Inter / Intra-Tumoral Dose Response Variations Assessed Using FDG-PET / CT Feedback Images : Impact on Tumor Control and Treatment Dose Prescription. *Radiother Oncol* (2021) 154:235–242. doi: 10.1016/j.radonc.2020.09.052
9. Brahme A, Argren AK. Optimal Dose Distribution for Eradication of Heterogeneous Tumors. *Acta Oncol* (1987) 26(5):377–85. doi: 10.3109/02841868709104364
10. Ling CC, Humm J, Larson S, et al. Towards Multidimensional Radiotherapy (MD-CRT): Biological Imaging and Biological Conformality. *Int J Radiat Oncol Biol Phys* (2000) 47(3):551–560. doi: 10.1016/S0360-3016(00)00467-3
11. Bentzen SM. Theragnostic Imaging for Radiation Oncology: Dose-Painting by Numbers. *Lancet Oncol* (2005) 6(2):112–7. doi: 10.1016/S1470-2045(05)01737-7
12. Bentzen SM, Gregoire V. Molecular Imaging-Based Dose Painting: A Novel Paradigm for Radiation Therapy Prescription. *Semin Radiat Oncol* (2011) 21(2):101–10. doi: 10.1016/j.semradonc.2010.10.001
13. Duprez F, De Neve W, De Gersem W, Coghe M, Madani I. Adaptive Dose Painting by Numbers for Head-and-Neck Cancer. *Int J Radiat Oncol Biol Phys* (2011) 80(4):1045–55. doi: 10.1016/j.ijrobp.2010.03.028
14. Yan D, Chen S, Krauss DJ, Chen PY, Chinnaiyan P, Wilson GD. Tumor Voxel Dose-Response Matrix and Dose Prescription Function Derived Using 18 F-FDG PET/CT Images for Adaptive Dose Painting by Number. *Int J Radiat Oncol Biol Phys* (2019) 104(1):207–18. doi: 10.1016/j.ijrobp.2019.01.077
15. Portella L, Scala S. Ionizing Radiation Effects on the Tumor Microenvironment. *Semin. Oncol* (2019) 46(3):254–60. doi: 10.1053/j.seminoncol.2019.07.003
16. Fertil B, Malaise EP. Inherent Cellular Radiosensitivity as a Basic Concept for Human Tumor Radiotherapy. *Int J Radiat Oncol Biol Phys* (1981) 7(5):621–9. doi: 10.1016/0360-3016(81)90377-1
17. Fertil B, Malaise EP. Intrinsic Radiosensitivity of Human Cell Lines is Correlated With Radioresponsiveness of Human Tumors: Analysis of 101 Published Survival Curves. *Int J Radiat Oncol Biol Phys* (1985) 11(9):1699–707. doi: 10.1016/0360-3016(85)90223-8
18. West CML, Davidson SE, Burt PA, Hunter RD. The Intrinsic Radiosensitivity of Cervical Carcinoma: Correlation With Clinical Data. *Int J Radiat Oncol Biol Phys* (1995) 31(4):841–6. doi: 10.1016/0360-3016(94)00508-7
19. Eschrich SA, Pramana J, Zhang H, Zhao H, Boulware D, Lee JH, et al. A Gene Expression Model of Intrinsic Tumor Radiosensitivity: Prediction of Response and Prognosis After Chemoradiation. *Int J Radiat Oncol Biol Phys* (2009) 75(2):489–496. doi: 10.1016/j.ijrobp.2009.06.014
20. Torres-Roca JF. A Molecular Assay of Tumor Radiosensitivity: A Roadmap Towards Biology-Based Personalized Radiation Therapy. *J Pers Med* (2012) 9(5):547–57. doi: 10.2217/pme.12.55
21. Scott JG, Berglund A, Schell MJ, Mihaylov I, Fulp WJ, Yue B, et al. A Genome-Based Model for Adjusting Radiotherapy Dose (GARD): A Retrospective, Cohort-Based Study. *Lancet Oncol* (2016) 2045(16):1–10. doi: 10.1016/S
22. Withers HR, Taylor JMG, Maciejewski B. The Hazard of Accelerated Tumor Clonogen Repopulation During Radiotherapy. *Acta Oncol* (1988) 27(2):131–46. doi: 10.3109/02841868809090333
23. Roberts SA, Hendry JH. The Delay Before Onset of Accelerated Tumour Cell Repopulation During Radiotherapy: A Direct Maximum-Likelihood Analysis of a Collection of Worldwide Tumour-Control Data. *Radiother Oncol* (1993) 29(1):69–74. doi: 10.1016/0167-8140(93)90175-8
24. Kim JJ, Tannock IF. Repopulation of Cancer Cells During Therapy: An Important Cause of Treatment Failure. *Nat Rev Cancer* (2005) 5(7):516–25. doi: 10.1038/nrc1650
25. Kallman RF. The Phenomenon of Reoxygenation and its Implications for Fractionated Radiotherapy. *Radiology* (1972) 105(1):135–42. doi: 10.1148/105.1.135
26. Eschmann SM, Paulsen F, Bedeshem C, Machulla HJ, Hehr T, Bamberg M, et al. Hypoxia-Imaging With 18F-Misonidazole and PET: Changes of Kinetics During Radiotherapy of Head-and-Neck Cancer. *Radiother Oncol* (2007) 83(3):406–410. doi: 10.1016/j.radonc.2007.05.014
27. Wiedenmann NE, Bucher S, Hentschel M, Mix M, Vach W, Bittner MI, et al. Serial [18F]-Fluoromisonidazole PET During Radiochemotherapy for Locally Advanced Head and Neck Cancer and its Correlation With Outcome. *Radiother Oncol* (2015) 117(1):113–117. doi: 10.1016/j.radonc.2015.09.015
28. Supiot S, Rousseau C, Dore M, Chèze-Le-Rest C, Kandel-Aznar C, Potiron V, et al. Reoxygenation During Radiotherapy in Intermediate-Risk Prostate Cancer. *Radiother Oncol* (2019) 133:16–19. doi: 10.1016/j.radonc.2018.12.022
29. Boustani J, Grapin M, Laurent PA, Apetoh L, Mirjolet C. The 6th R of Radiobiology: Reactivation of Anti-Tumor Immune Response. *Cancers (Basel)* (2019) 11(6):1–16. doi: 10.3390/cancers11060860
30. Lippitz BE, Harris RA. A Translational Concept of Immuno-Radiobiology. *Radiother Oncol* (2019) 140:116–24. doi: 10.1016/j.radonc.2019.06.001
31. Petit SF, Aerts HJWL, van Loon JGM, Offermann C, Houben R, Winkens B, et al. Metabolic Control Probability in Tumour Subvolumes or How to Guide Tumour Dose Redistribution in non-Small Cell Lung Cancer (NSCLC): An Exploratory Clinical Study. *Radiother Oncol* (2009) 91(3):393–398. doi: 10.1016/j.radonc.2009.02.020
32. Bowen SR, Hippe DS, Art Chaovalitwongse W, Duan C, Thammasorn P, Liu X, et al. Voxel Forecast for Precision Oncology: Predicting Spatially Variant and Multiscale Cancer Therapy Response on Longitudinal Quantitative Molecular Imaging. *Clin Cancer Res* (2019) 25(16):5027–37. doi: 10.1158/1078-0432.CCR-18-3908
33. Galbán CJ, Mukherji SK, Chenevert TL, Meyer CR, Hamstra DA, Bland PH, et al. A Feasibility Study of Parametric Response Map Analysis of Diffusion-Weighted Magnetic Resonance Imaging Scans of Head and Neck Cancer Patients for Providing Early Detection of Therapeutic Efficacy. *Transl Oncol* (2009) 2(3):184–90. doi: 10.1593/tlo.09175
34. Servagi-Vernat S, Differding S, Sterpin E, Hanin F-X, Labar D, Bol A, et al. Hypoxia-Guided Adaptive Radiation Dose Escalation in Head and Neck Carcinoma: A Planning Study. *Acta Oncol* (2015) 54:1008–16. doi: 10.3109/0284186X.2014.990109
35. Di Perri D, Lee JA, Bol A, Hanin FX, Janssens G, Labar D, et al. Correlation Analysis of [18F]Fluorodeoxyglucose and [18F]Fluoroazomycin Arabinoside Uptake Distributions in Lung Tumours During Radiation Therapy. *Acta Oncol* (2017) 56(9):1181–8. doi: 10.1080/0284186X.2017.1329594
36. Gouw ZAR, La Fontaine MD, Vogel WV, van de Kamer JB, Sonke JJ, Al-Mamgani A. Single-Center Prospective Trial Investigating the Feasibility of Serial FDG-PET Guided Adaptive Radiation Therapy for Head and Neck Cancer. *Int J Radiat Oncol Biol Phys* (2020) 4(108) 960–8. doi: 10.1016/j.ijrobp.2020.04.030
37. Lin C, Bradshaw T, Perk T, Harmon S, Eickhoff J, Jallow N, et al. Repeatability of Quantitative 18f-NaF PET: A Multicenter Study. *J Nucl Med* (2016) 57(12):1872–1879. doi: 10.2967/jnumed.116.177295
38. Boellaard R. Standards for PET Image Acquisition and Quantitative Data Analysis. *J Nucl Med* (2008) 50(Suppl 1):11S–20S. doi: 10.2967/jnumed.108.057182
39. Qin A, Liang J, Han X, O'Connell N, Yan D. Technical Note: The Impact of Deformable Image Registration Methods on Dose Warping. *Med Phys* (2018) 45(3):1287–94. doi: 10.1002/mp.12741
40. Liu Q, Qin A, Liang J, Yan D. Evaluation of Atlas-Based Auto-Segmentation and Deformable Propagation of Organs-at-Risk for Head-and-Neck Adaptive Radiotherapy. *Recent Patent Top Imaging* (2016) 5:79–87. doi: 10.2174/2451827105999160415123925

41. Qin A, Snyder M, Liang J, Chen S, Yan D. Achievable Accuracy of DIR for Tumor/Organ With Large Progressive Shrinkage During the Radiation Treatment: A Bio-Tissue Phantom Study. *Int J Radiat Oncol Biol Phys* (2021) 111(3):S17. doi: 10.1016/j.ijrobp.2021.07.069
42. Chen S, Yan D, Qin A, Maniawski P, Krauss DJ, Wilson GD. Effect of Uncertainties in Quantitative 18F-FDG PET/CT Imaging Feedback for Intratumoral Dose-Response Assessment and Dose Painting by Number. *Med Phys* (2020) 47(11):5681–92. doi: 10.1002/mp.14482
43. Björk-Eriksson T, West CM, Karlsson E, Slevin NJ, Davidson SE, James RD, et al. The *In Vitro* Radiosensitivity of Human Head and Neck Cancers. *Br J Cancer* (1998) 77(12):2371–5. doi: 10.1038/bjc.1998.394
44. Delong ER, Carolina N. Comparing the Areas Under Two or More Correlated Receiver Operating Characteristic Curves: A Nonparametric Approach. *Biometrics* (1988) 44(3):837–45. doi: 10.2307/2531595
45. Mason SJ, Graham NE. Areas Beneath the Relative Operating Characteristics (ROC) and Relative Operating Levels (ROL) Curves: Statistical Significance and Interpretation. *Q J R Meteorol Soc* (2002) 128(584 PART B):2145–66. doi: 10.1256/003590002320603584
46. Jafari M, Ansari-Pour N. Why, When and How to Adjust Your P Values? *Cell J* (2019) 20(4):604–7. doi: 10.22074/cellj.2019.5992
47. Youden WJ. Index for Rating Diagnostic Tests. *Cancer* (1950) 3(1):32–5. doi: 10.1002/1097-0142(1950)3:1<32::AID-CNCR2820030106>3.0.CO;2-3
48. Yan A, Hanna A, Wilson TG, Deraniyagala R, Krauss DJ, Grzywacz VP, et al. Correlation Between Tumor Voxel Dose Response Matrix and Tumor Biomarker Profile in Patients With Head and Neck Squamous Cell Carcinoma. *Radiother Oncol* (2021) 164:196–201. doi: 10.1016/j.radonc.2021.09.027
49. Gillham CM, Lucey JA, Keogan M, Duffy GJ, Malik V, Raouf AA, et al. 18FDG Uptake During Induction Chemoradiation for Oesophageal Cancer Fails to Predict Histomorphological Tumour Response. *Br J Cancer* (2006) 95 (9):1174–9. doi: 10.1038/sj.bjc.6603412
50. Hautzel H, Müller-Gärtner HW. Early Changes in Fluorine-18-FDG Uptake During Radiotherapy. *J Nucl Med* (1997) 38(9):1384–6.
51. Pramana J, Van den Brekel MWM, van Velthuysen MLF, Wessels LFA, Nuyten DS, Hofland I, et al. Gene Expression Profiling to Predict Outcome After Chemoradiation in Head and Neck Cancer. *Int J Radiat Oncol Biol Phys* (2007) 69(5):1544–52. doi: 10.1016/j.ijrobp.2007.08.032
52. de Jong MC, Pramana J, Knegjens JL, Balm AJM, van denBrekel MWM, Hauptmann M, et al. HPV and High-Risk Gene Expression Profiles Predict Response to Chemoradiotherapy in Head and Neck Cancer, Independent of Clinical Factors. *Radiother Oncol* (2010) 95(3):365–70. doi: 10.1016/j.radonc.2010.02.001
53. Ahmad P, Sana J, Slavik M, Slampa P, Smilek P, Slaby O. MicroRNAs Involvement in Radioresistance of Head and Neck Cancer, Dis. *Markers* (2017) 1–8. doi: 10.1155/2017/8245345
54. Ahmad P, Sana J, Slavik M, Gurin D, Radova L, Gablo NA, et al. MicroRNA-15b-5p Predicts Locoregional Relapse in Head and Neck Carcinoma Patients Treated With Intensity-Modulated Radiotherapy. *Cancer Genomics Proteomics* (2019) 16(2):139–46. doi: 10.21873/cgp.20119
55. Lim R, Eaton A, Lee NY, Setton J, Ohri N, Rao S, et al. 18f-FDG PET/CT Metabolic Tumor Volume and Total Lesion Glycolysis Predict Outcome in Oropharyngeal Squamous Cell Carcinoma. *J Nucl Med* (2012) 53(10):1506–13. doi: 10.2967/jnumed.111.101402
56. Van De Wiele C, Kruse V, Smeets P, Sathekge M, Maes A. Predictive and Prognostic Value of Metabolic Tumour Volume and Total Lesion Glycolysis in Solid Tumours. *Eur J Nucl Med Mol Imaging* (2013) 40(2):290–301. doi: 10.1007/s00259-012-2280-z
57. Pak K, Cheon GJ, Nam H-Y, Kim S-J, Kang KW, Chung J-K, et al. Prognostic Value of Metabolic Tumor Volume and Total Lesion Glycolysis in Head and Neck Cancer: A Systematic Review and Meta-Analysis. *J Nucl Med* (2014) 55 (6):884–90. doi: 10.2967/jnumed.113.133801
58. Obuchowski NA, McClish DK. Sample Size Determination for Diagnostic Accuracy Studies Involving Binormal ROC Curve Indices. *Stat Med* (1997) 16 (13):1529–42. doi: 10.1002/(SICI)1097-0258(19970715)16:13<1529::AID-SIM565>3.0.CO;2-H

Conflict of Interest: The authors declare that the research was conducted in the absence of any commercial or financial relationships that could be construed as a potential conflict of interest.

frontiers | Frontiers in Oncology

ORIGINAL RESEARCH
published: 22 July 2022
doi: 10.3389/fonc.2022.907181

Evaluation of Hybrid VMAT Advantages and Robustness Considering Setup Errors Using Surface Guided Dose Accumulation for Internal Lymph Mammary Nodes Irradiation of Postmastectomy Radiotherapy

Zhe Zhang[1], Daming Li[1], Feng Peng[1], Zhibo Tan[1], Pengfei Yang[1], Zhaoming Peng[1], Xin Li[1,2], Xinyue Qi[3], Weixiao Sun[3], Yajie Liu[1,2] and Yuenan Wang[1,3]**

[1] Department of Radiation Oncology, Peking University Shenzhen Hospital, Shenzhen, China, [2] Hong Kong University of Science and Technology Medical Center, Shenzhen-Peking University, Shenzhen, China, [3] Department of Statistics and Data Science, Southern University of Science and Technology, Shenzhen, China

OPEN ACCESS

Edited by:
Tonghe Wang,
Emory University, United States

Reviewed by:
Mengying Shi,
University of Massachusetts Lowell, United States
James Chow,
University of Toronto, Canada

***Correspondence:**
Yajie Liu
Anthea1966@163.com
Yuenan Wang
yuenan.wang@gmail.com

Specialty section:
This article was submitted to Radiation Oncology, a section of the journal Frontiers in Oncology

Received: 29 March 2022
Accepted: 20 June 2022
Published: 22 July 2022

Citation:
Zhang Z, Li D, Peng F, Tan Z, Yang P, Peng Z, Li X, Qi X, Sun W, Liu Y and Wang Y (2022) Evaluation of Hybrid VMAT Advantages and Robustness Considering Setup Errors Using Surface Guided Dose Accumulation for Internal Lymph Mammary Nodes Irradiation of Postmastectomy Radiotherapy. Front. Oncol. 12:907181. doi: 10.3389/fonc.2022.907181

Objectives: Setup error is a key factor affecting postmastectomy radiotherapy (PMRT) and irradiation of the internal mammary lymph nodes is the most investigated aspect for PMRT patients. In this study, we evaluated the robustness, radiobiological, and dosimetric benefits of the hybrid volumetric modulated arc therapy (H-VMAT) planning technique based on the setup error in dose accumulation using a surface-guided system for radiation therapy.

Methods: We retrospectively selected 32 patients treated by a radiation oncologist and evaluated the clinical target volume (CTV), including internal lymph node irradiation (IMNIs), and considered the planning target volume (PTV) margin to be 5 mm. Three different planning techniques were evaluated: tangential-VMAT (T-VMAT), intensity-modulated radiation therapy (IMRT), and H-VMAT. The interfraction and intrafraction setup errors were analyzed in each field and the accumulated dose was evaluated as the patients underwent daily surface-guided monitoring. These parameters were included while evaluating CTV coverage, the dose required for the left anterior descending artery (LAD) and the left ventricle (LV), the normal tissue complication probability (NTCP) for the heart and lungs, and the second cancer complication probability (SCCP) for contralateral breast (CB).

Results: When the setup error was accounted for dose accumulation, T-VMAT (95.51%) and H-VMAT (95.48%) had a higher CTV coverage than IMRT (91.25%). In the NTCP for the heart, H-VMAT (0.04%) was higher than T-VMAT (0.01%) and lower than IMRT (0.2%). However, the SCCP (1.05%) of CB using H-VMAT was lower than that using T-VMAT (2%)

as well as delivery efficiency. And T-VMAT (3.72) and IMRT (10.5).had higher plan complexity than H-VMAT (3.71).

Conclusions: In this study, based on the dose accumulation of setup error for patients with left-sided PMRT with IMNI, we found that the H-VMAT technique was superior for achieving an optimum balance between target coverage, OAR dose, complication probability, plan robustness, and complexity.

Keywords: SGRT, H-VMAT, PMRT, IMNIs, biological models, setup error

INTRODUCTION

Radiation therapy is an integral part of the comprehensive treatment of breast cancer and has significantly improved the overall survival rate of breast cancer (1–6). But for left-sided breast cancer including internal lymph mammary nodes irradiation (IMNIs), the protection of the organs at risk (OARs) has always been the focus of discussion. An increase in cardiac, especially for the left anterior descending artery (LAD), significantly increases the incidence of ischemic heart disease (1–3). In a study, Darby found that for every 1Gy increase in the mean heart dose, the risk of coronary heart disease increases by 7.4% (1). For women receiving breast radiation therapy, the radiation pneumonitis (RP) of the ipsilateral lung is higher than that of the contralateral lung (4, 5). Fogliata (6) found that for young breast cancer patients, the radiation dose used for treating the contralateral breast (CB) might lead to long-term risks, and the incidence of secondary tumors is also affected by the dose received by the CB. Various techniques, including tangential-VMAT (T-VMAT), intensity-modulated radiation therapy (IMRT), and Hybrid-VMAT (H-VMAT) can reduce the dose of surrounding OARs in modern radiotherapy (7–9).

To determine the dose distribution of the target volume and the OARs during treatment, the setup error needs to be considered (10). Some of the methods used for evaluating the setup errors are based on the value obtained by performing CBCT (11), but these methods may not pay much attention to the interfraction setup error. In this study, we performed surface guided monitoring to obtain the intrafraction and interfraction setup error for analysis (12, 13), and then dose accumulation is performed to obtain a dose distribution for evaluating the robustness of all planning techniques. In some studies, dosimetry for left-sided breast cancer PMRT patients was compared to different planning techniques under dose distributions using setup uncertainty (12, 13), focusing on the evaluation of IMN included left-sided breast cancer based on biological models.

Furthermore, some studies have found that the parameters of these biological models can predict the effects of normal tissues (14–16). Compared to the parameters based on dosimetry, the parameters based on biological models are more directly related to complications and treatment endpoint events (17). This study also retrospectively compared three planning techniques associated with radiobiological effects, including the normal tissue complication probability (NTCP) and the second cancer complication probability (SCCP), considering setup error dose accumulation.

METHOD

Patient Selection

We selected 32 PMRT patients in the radiation therapy department at Peking University Shenzhen Hospital fromApril 2020 to September 2021 [**Table 1**]. The inclusion criteria were as follows: (1) Female patients over 18 years of age with left breast cancer who underwent PMRT; (2) Invasive diagnosis of cancer was confirmed by pathology; (3) Surgical margins were negative; (4) Who received chemotherapy and following pre-radiotherapy standards and guidelines.

Treatment Planning Design

Free-breathing CT scan was performed from the level of the mandible to the lower abdomen on the SOMATOM Definition AS CT Scanner (Siemens Medical Solutions, Erlangen, Germany) with a slice thickness of 3 mm. The patients were immobilized on a customized vacuum bag in the supine position with arms

TABLE 1 | Patient characteristics.

Characteristic	Value
Age (years)	Median 49.5
	Range 30-65
Histologic grading (n)	Grade 2 14
	Grade 3 18
Tumor size (cm)	Median 3.25
	Range 1.5-10
ER/PR status (n)	Negative 13
	Positive 19
Her-2 status (n)	Negative 18
	Positive 14

Abbreviations: LBC, left-sided breast cancer; PMRT, postmastectomy radiotherapy; IMNI, internal lymph mammary nodes irradiation; L, ipsilateral lung; CB, contralateral breast; PTV, planning target volume; IMRT, Intensity-modulated radiotherapy; T-VMAT, Tangential volumetric modulated arc therapy; H-VMAT, Hybrid VMAT; MUs, monitor units; CT, computed tomography; DVH, dose-volume histogram; SGRT, surface gated radiotherapy DIBH, deep inspiration breath hold; TD-TIME, Total delivery time; LAD, left anterior descending artery; LV, left ventricle; NTCP, normal tissue complication probability; SCCP, second cancer complication probability; CBCT, Cone-beam computed tomography.

placed above the head. The clinical target volume (CTV) and OARs for each patient were contoured by one radiation oncologist following the RTOG-1304 (18) guidelines and the RTOG Breast Cancer Atlas (18). CTV included the chest wall (CW), internal lymph mammary nodes (IMNs), and the axillary and supraclavicular lymph nodes. A 5 mm margin was added to the CTV to define as PTV, and the part that intersects the lung and heart was subtracted from the chest wall, but the 5 mm external expansion of IMNs was maintained (19). It is necessary to treat PMRT patients 10 times without bolus and 15 times with bolus in the treatment. However, in this study, only 25 times with bolus plan were evaluated. In the plan design, the PTV is expanded to the skin by 5 mm as an optimized condition for opening the MLC as much as possible. This was done following the procedure described in a study (20) to match the dose outside the skin boundary and reduce the impact of breathing motion on the skin dose.

The Eclipse software (TPS, Eclipse, version 15.6, Varian Medical Systems, Palo Alto, CA, USA) was used. In all plans, the prescribed dose was 50Gy/25 fractions with 6MV photons. The dose volume constraints on the TPS opitimization interface for planning target volume and OARs followed the same objective template [**Table 2**].

The Tangential VMAT plan was designed as four partial arcs, where the upper and lower fields were connected from lymph node to chest wall. Arc 1 and Arc 2 are usually set to 295° to 20° and reversed, and Arc 3 and Arc 4 are set to 40° to 150° and reversed shown as **Figure 1A**. The IMRT plan contains 10 fields, of which three covered lymph nodes (20°, 40° and 160°), six covered chest wall PTV (290°, 315°, 340° and 90°, 120°, 150°) and one covered conjunction part (150°). The collimator irradiated the PTV at different angles while avoiding the lungs and the heart, and the dose outside the skin was compensated by brushing the fluence. To effectively protect the OARs, fixed jaw technology is used in all fields of vision [**Figure 1B**]. In addition, the hybrid VMAT in **Figure 1C** and **Figure 2** includes five fields, two tangential fields covering PTV-CW and IMNs at 70% dose, and two separate partial arcs covering approximately 30% of PTV-CW from 295° to 20° and 40° to 150°, an arc from 150° to 295° covered the PTV axillary and supraclavicular lymph nodes.

TABLE 2 | The dose-volume constraints on TPS optimization interface for planning target volume and organs at risk.

PTV/OAR	Dose–volume constraints
PTV	D95%>5000 cGy
Heart	V20<15%
	D mean<800 cGy
LAD	D mean<3000 cGy
LV	D mean<1000 cGy
Ipsilateral Lung	V5<60%
	V20<25%
	V30<15%
	D mean<1400 cGy
Lungs	V5<60%
	V20<20%
	V30<10%
	D mean<800 cGy
Contralateral Lung	V5<60%
	D mean<600 cGy
Contralateral Breast	D0.1cc<2000 cGy
	D mean<500 cGy

Evaluating Setup Errors and Dose Accumulations

The retrospective study was performed with the Catalyst™ system (C-rad Positioning AB, Uppsala, Sweden). Data and surface images were collected every 50 mS for recording during the 25 fraction treatments in every PMRT patients, and the tolerance was set as 5 mm.

To obtain the Interfraction setup error for optical body surface monitoring, we performed surface acquisition at the first treatment after CBCT was performed as the reference, and then we collected surface data before the patients underwent IGRT. The non-rigid registration algorithm in the analysis tools in Catalyst™ was used to calculate any isocenter shift by matching the reference images and the images before IGRT. The region of interest (ROI) was set as the left-sided chest wall of the patients, which allowed the isocenter shifts to approximate the Interfraction setup error extraction for each treatment (12).

Every patient was treated using a specific treatment technique, and thus, it was impossible to obtain the three intrafraction setup errors in one patient. Hence, we selected 10 patients per technique (T-VMAT, H-VMAT, and IMRT) to

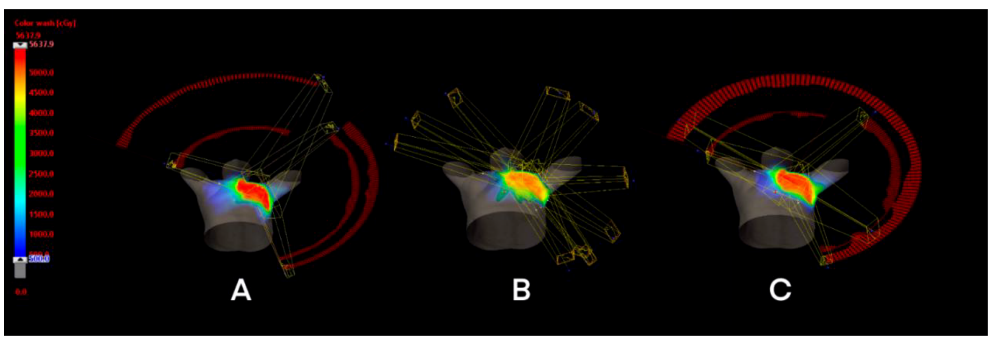

FIGURE 1 | Treatment planning design for three techniques: **(A)** T-VMAT; **(B)** IMRT; **(C)** H-VMAT.

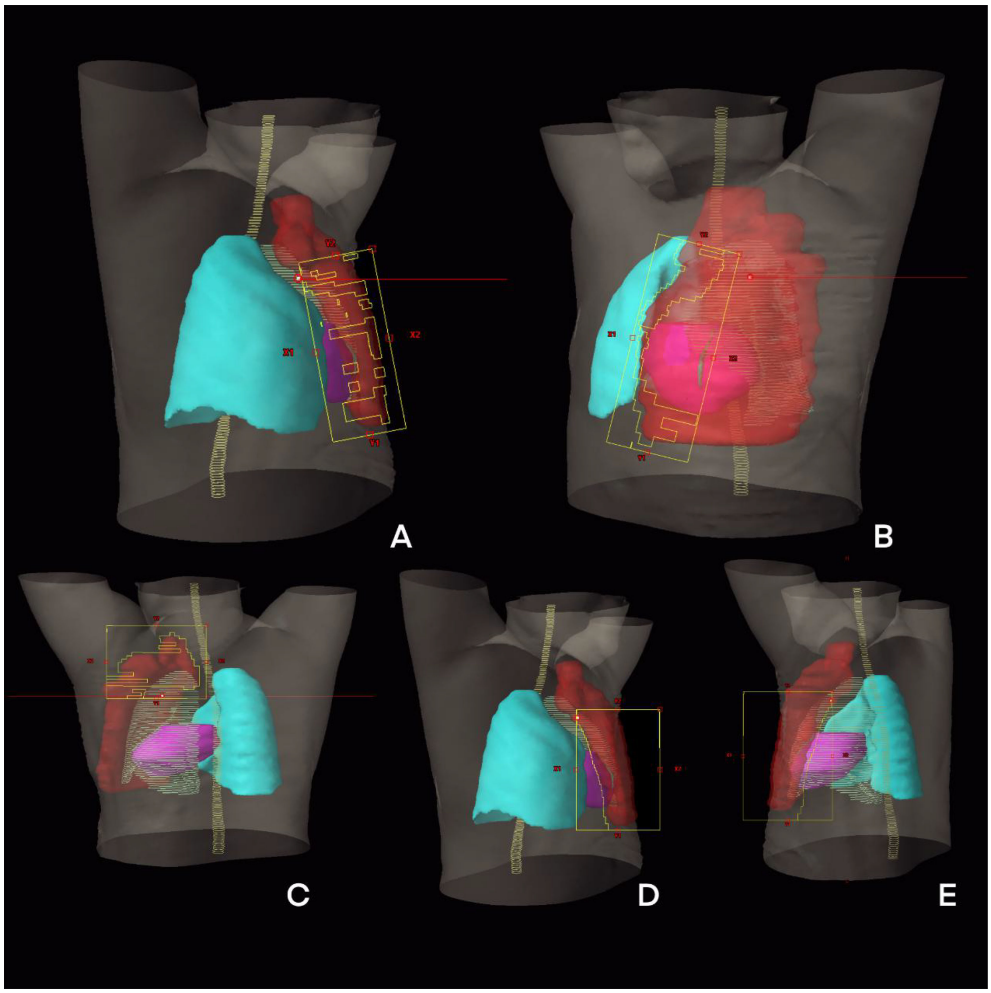

FIGURE 2 | The beam eye view of treatment planning design of H-VMAT technique: **(A)** An arc from 295° to 20°; **(B)** An arc from 40° to 150°; **(C)** Tangential field one; **(D)** Tangential field two; **(E)** An arc from 150° to 295°.

estimate each intrafraction setup error during treatment. To derive the intrafraction setup error of the patients, we first retrieved data for each patient's fraction, including isocenter shifts in the four degrees during the beam-on time, from Catalyst. The data of the 25 fractions for each patient was extracted and divided into five setup error sets, with each set representing the mean value of five fractions. Therefore, set 1 demonstrated the average setup error during the beam-on time from the first fraction to the fifth fraction. Furthermore, each field during the treatment had a slightly different setup error. We subdivided the intrafraction setup error for each field and combined the interfraction setup error; finally, the average setup error per set was calculated.

The setup error of each field in each set was obtained and imported into the Eclipse software to convert each field into an isocenter group. The setup error was entered in four degrees (longitudinal, transversal, vertical, and rotation) and re-calculated five times per technique for each patient. For example, in the H-VMAT plan, we initially used five fields. Next, we used five different isocenter groups for calculations in each set as plan 1 and the sum of five plans was evaluated for one patient using the H-VMAT technique. In total, 480 re-calculations were performed on five sets using each of the three techniques for the 32 patients. The re-calculations for each patient were followed by dose accumulation, and the resulting dose parameter and DVH are shown in **Figure 3**.

Plan Evaluation

The dose parameters were read using the clinical protocol template on eclipse 15.5. The main dosimetry indicators include the coverage of CTV, the dose parameters of each OARs and the radiobiological indicators included lung and heart NTCP and CB SCCP. DVH was imported into MATLAB-based internal programs (MathWorks, Natick, MA) to calculate NTCP and SCCP values (14, 21). The pulmonary endpoint event was RP ≥ grade 2, which was calculated using the EUD-based NTCP model given by

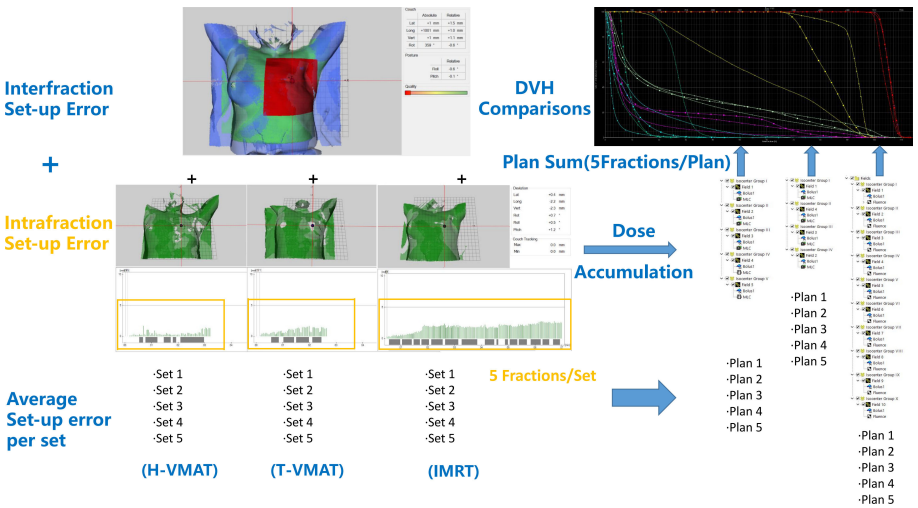

FIGURE 3 | The workflow used to generate the SGRT-based setup errors and dose accumulation is shown. First, non-rigid algorithm was used for interfraction setup error analysis. Then we subdivided the intrafraction setup error of each field and each technique divided 25 fractions into 5 sets (5 fractions per set). Furthermore, sum up the average setup error for each set. Finally, the setup errors imported to TPS and converted each field into an isocenter group, then accumulated and compared dose. In the DVH comparisons figure, —shown as T-VMAT, —shown as H-VMAT, —shown as IMRT.

$$EUD = \left(\sum V_i \cdot D_i^a\right)^{\frac{1}{a}} \quad (1)$$

Here, a is a unitless model parameter that is specific to the normal structure or tumor of interest, and V_i is unitless and represents the i'th partial volume receiving dose D_i in Gy.

$$NTCP = \frac{1}{1 + \left(\frac{TD_{50}}{EUD}\right)^{4\gamma 50}} \quad (2)$$

The TD50 is the tolerance dose for a 50% complication rate at a specific time interval when the whole organ of interest is homogeneously irradiated (22), and the γ_{50} is a unitless model parameter that is specific to the normal structure or tumor of interest and describes the slope of the dose response curve The NTCP for lung calculation has the following parameters: TD_{50} = 24.5 Gy, a = 1, and γ_{50} = 2 (21, 22).

The NTCP of heart used the NTCP-Poisson LQ function to calculate uses cardiac mortality as the end point (23). The dose-response curve for the complete organ volume is given by

$$P(D) = 2^{-\exp\{e\gamma(1-D/D_{50})\}} \quad (3)$$

Here, the dose for 50% response is denoted by D_{50} and the maximum relative slope of the dose-response curve is given by γ. In this model the organization of the functional subunit (FSU) is described in terms of a number of parallel strings in which each string consists of serially organized FSU. The relative seriality is given by the ratio of the number of serial subunits to all subunits and is described by the parameter *s*. For a heterogeneous dose distribution, the complication probability is determined by the equation

$$P = \left\{1 - \prod_{i=1}^{n}\left[1 - P(D_i)^s\right]^{\Delta vi}\right\}^{1/s} \quad (4)$$

Here, *n* is the number of subvolumes in the dose calculation volume (DVH), and $\Delta v_i = v_i/V$, where v_i is the volume of each subvolume in the DVH and *V* is the volume of the organ. The parameters used in the model are D_{50} = 52.3 Gy, γ = 1.28, and s = 1 (20, 21).

Calculating the second cancer complication probability (SCCP) of the contralateral breast takes the secondary incidence of tumor as the endpoint event. The equation can be represented as

$$SCCP_{org} = In_{org} \cdot \sum_i \left(V_i \cdot D_i \cdot e^{-\alpha D_i}\right) \quad (5)$$

Here, α is the cell radio sensitivity (Gy^{-1}) and In_{org} is the absolute cancer incidence rate in percent per gray for the specific organ. The parameters used for the calculation of the SCCP and Schneider model are α = 0.085 and In_{org} = 0.78%/Gy (22, 24).

To compare delivery efficiency and difficulty, the number of monitoring unit (MU), modulation factor and total delivery time were also quantitatively analyzed. The modulation factor is the total number of MU divided by the prescribed dose per fraction as follow. All data are expressed as the mean ± standard deviation. Wilcoxon signed-rank tests were performed in SPSS (25^{th} edition, Chicago, Illinois, USA) to determine significant differences ($p < 0.05$) between treatment planning techniques.

$$MF\left(\frac{MU}{cGy}\right) = \frac{Total\ \ Plan\ \ Monitor\ \ Unit(MU)}{Prescribed\ \ Dose(cGy)} \quad (6)$$

RESULTS

Dose Analysis

T-VMAT covered the largest percentage of CTV among the three methods (98.6%), and the differences between T-VMAT and the other two techniques were statistically significant ($P \leq 0.001$); coverage was the lowest for the IMRT technique. After introducing the positioning error, the coverage rate of T-VMAT was still the highest (95.51%), but H-VMAT reached 95.48%. The difference between T-VMAT and H-VMAT was not significant ($P = 0.428$).

The mean heart dose (MHD) in T-VMAT was 5.34 Gy, which was the lowest dose among the three planning methods. In all pairwise comparisons showed significant differences ($P \leq 0.001$). After dose accumulation, the MHD increased by different degrees, but T-VMAT had the lowest MHD, which was significantly different from IMRT and H-VMAT ($P \leq 0.001$). The T-VMAT technique also had the lowest value for the mean dose of LV (5.76 Gy), but the difference in the values between H-VMAT and T-VMAT was not significant ($P = 0.092$). After re-calculation, the doses of all three groups increased, but the difference in the dose values between H-VMAT and T-VMAT was not significant ($P = 0.871$), while the p-values of the other two groups were significantly different ($P \leq 0.05$). T-VMAT also had the lowest mean dose of LAD (28.9 Gy), and the difference between H-VMAT and T-VMAT was not statistically significant ($P = 0.138$). After adding the setup error, the mean dose of LAD for the three groups showed significant differences in pairwise comparisons ($P \leq 0.05$).

Irrespective of whether the dose of the IL was V5, V20, V30, or the mean dose, IMRT was higher than the other two techniques. There was no significant difference in Dmean and V20, except for those of IMRT vs. H-VMAT. The other dose parameters showed significant differences in the pairwise comparisons ($P \leq 0.05$). After introducing the positioning error, no statistical difference was found for the mean dose. For the whole lung, the highest V5 of the T-VMAT technique was 47.18%, the highest V20 of IMRT was 13.77%, and the highest Dmean of H-VMAT was 8.37 Gy. The results showed that only the five sets of data of IMRT compared to those of the other two techniques were significantly different ($P \leq 0.05$), and there was no significant difference in the parameters between T-VMAT and H-VMAT. After re-calculation, the V5 and mean dose of the T-VMAT technique were the highest among the three techniques. V20 was the highest for the H-VMAT technique, but there was no significant difference when comparing V20 of IMRT with that of the other two groups ($P = 0.247$ with H-VMAT and $P = 0.112$ with T-VMAT).

For CB, all parameters of T-VMAT were significantly higher than those of IMRT and H-VMAT, and Dmean was 5.76 Gy. T-VMAT was significantly different from IMRT ($P = 0.024$), but T-VMAT was not significantly different from H-VMAT ($P = 0.059$). The average dose of T-VMAT after adding the setup error was 6.99 Gy. There was no significant difference between IMRT and H-VMAT ($P = 0.334$); however, the other two groups showed significant differences ($P \leq 0.05$). The dose distribution and dosimetry data are shown in **Figures 4** and **5**, respectively.

Biological Model Analysis

First, the NTCP-Poisson LQ was used to analyze mortality as the endpoint event of the cardiac biological model. The T-VMAT technique had the lowest NTCP before and after adding the setup error (0.0003% and 0.01%), and the highest NTCP was found after implementing the IMRT technique (0.21% and 0.2%). The pairwise comparison showed significant differences ($P \leq 0.001$). The lung endpoint event was analyzed by the LKB model as radiation pneumonia ≥ level 2. The T-VMAT technique had an advantage. The NTCP values before and after adding the setup error were 0.01% and 0.024%, respectively, which were the lowest values among the three techniques. IMRT had the highest values (0.2% and 0.35%), and pairwise comparisons showed significant differences ($P \leq 0.001$). For the SCCP of CB, the secondary incidence of tumors was the endpoint event. T-VMAT had

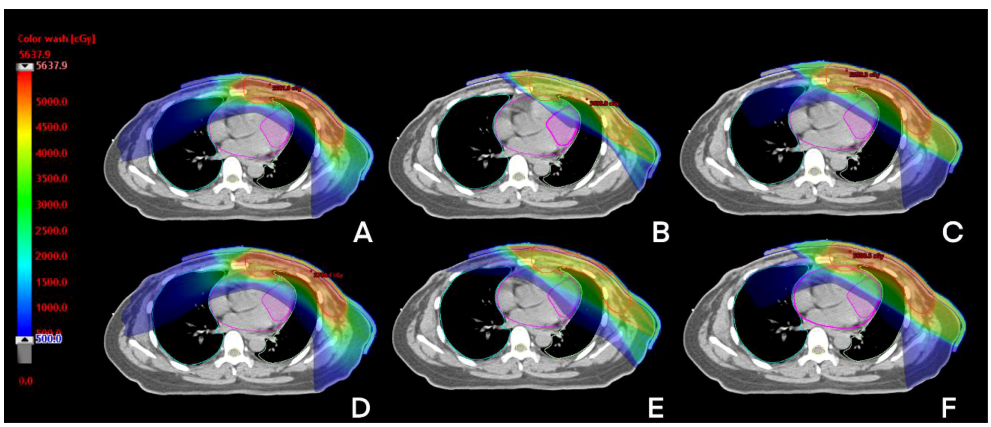

FIGURE 4 | The dose distribution of three techniques before and after setup error re-calculation. A, B, C before setup error [T-VMAT **(A)**, IMRT **(B)**, H-VMAT **(C)**], **(D–F)** after setup error [T-VMAT **(D)**, IMRT **(E)**, H-VMAT**(F)**].

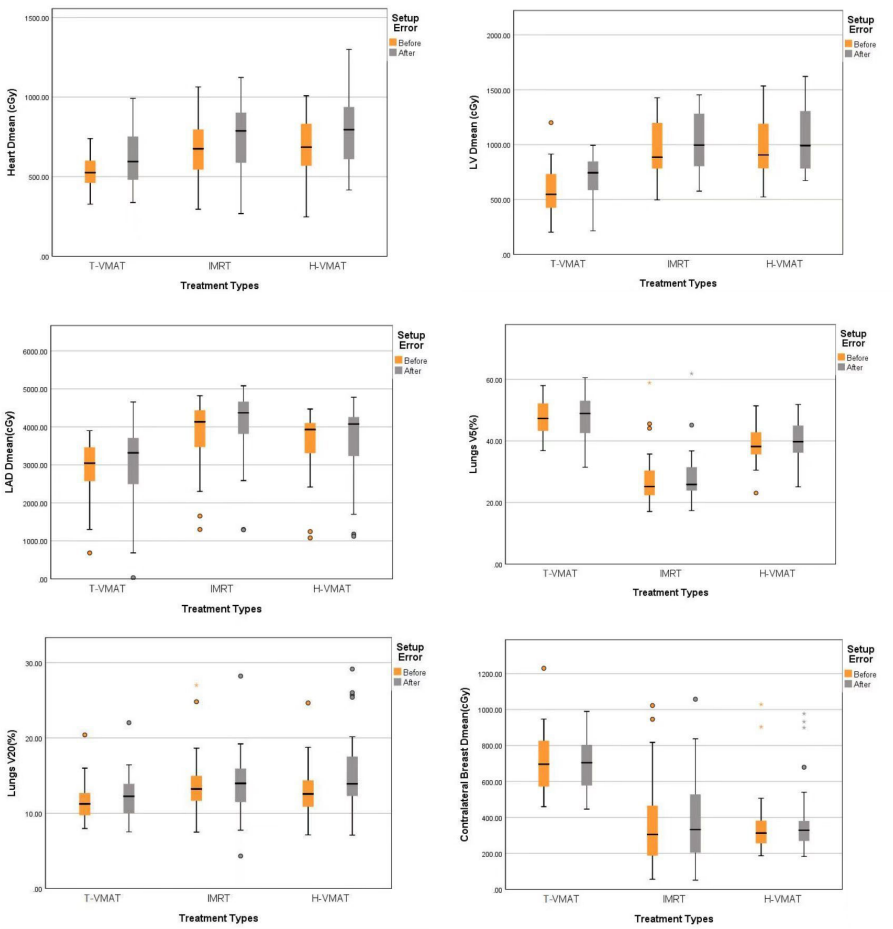

FIGURE 5 | Box-whisker plot of dosimetry parameters with error bars:Heart Dmean, Left ventricle Dmean, Left anterior Dmean, Lungs V5, Lungs V20, Contralateral breast Dmean. Each figures show the dose changes of each OARs before and after the recalculation of setup error. Gray bars represent the accumulated dose after the consideration of setup error, and yellow bars represent the dose not considered of setup error. The points in the graph represent outliers, the black horizontal lines in the figures represent the average of each parameter.

significantly higher secondary incidences of CB than IMRT and H-VMAT, which were 2%, 1.05%, and 1.05%, respectively. After introducing the positioning error, the SCCP was still the highest for T-VMAT (2.01%). For H-VMAT and T-VMAT, the SCCP before and after adding the setting error was not significantly different ($P \leq 0.059$ and $P \leq 0.185$), but the comparison between IMRT and T-VMAT showed a significant difference ($P \leq 0.024$). The biological model analysis was performed to determine significant differences and compare the advantages and disadvantages of various planning methods, as shown in [**Figure 6**]. All dosimetric parameters, biological indices, and the delivery efficiency are shown in **Table 3** and the p-values are shown in **Table 4**.

Delivery Parameters and Plan Complexity

Regarding the delivery parameters (25), IMRT had the highest treatment MUs (2,098) and total delivery time (365.7 s). The values were considerably higher than those of T-VMAT (746.25 and 168 s) and H-VMAT (the 742.34 and 169.5 s). The results of the analysis of plan complexity using modulation factor (26, 27) showed that T-VMAT and H-VMAT also had significantly lesser values than those of IMRT, which were 3.73, 3.71, and 10.5, respectively. IMRT and the other two treatment techniques showed significant differences in the delivery time, MUs, and treatment difficulty ($P \leq 0.001$).

DISCUSSION

For more accurate planning, the quality of the plan needs to be better, and the robustness and complexity of the plan need to be analyzed quantitatively. In 2020, a study (25) suggested that the dose distribution was not similar to the dose delivered to the patient due to uncertainties in dose calculation and treatment delivery, including variations in patient setup and anatomy. C-RAD systems can quantify setup errors in PMRT for breast

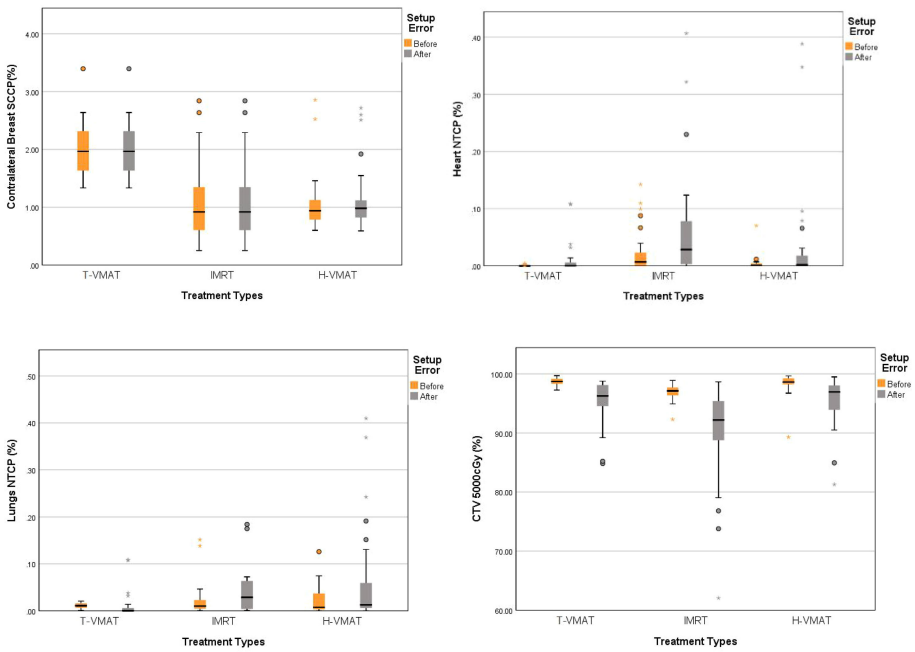

FIGURE 6 | Box-whisker plot of mean radiobiological parameters with error bar: CTV coverage, Contralateral breast SCCP, Heart NTCP, Lungs NTCP with error bars. Each figures show the parameters changes of each organs before and after the recalculation of setup error. Gray bars represent the accumulated dose after the consideration of setup error, and yellow bars represent the dose not considered of setup error. The points in the graph represent outliers, the black horizontal lines in the figures represent the average of each parameter.

TABLE 3 | Summary of the dosimetric parameters, radiobiological indices, and delivery parameters.

Structures	Metric	Conventional			After Setup Error		
		VMAT	IMRT	H-VMAT	VMAT	IMRT	H-VMAT
CTV	D5000cGy(%)	98.67 ± 0.6	96.97 ± 1.28	98.31 ± 1.75	95.51 ± 3.49	91.25 ± 7.83	95.48 ± 4.03
	V105(%)	53.86 ± 9.9	42.93 ± 1.28	49.5 ± 14.3	43.67 ± 12.62	37.31 ± 9.83	41.32 ± 15.09
	D2cc (cGy)	5423.28 ± 36.34	5482.17 ± 58.8	5421.8 ± 77.75	5425.52 ± 66.3	5504.42 ± 98.1	5462.63 ± 1215.7
Heart	V20(%)	5.34 ± 2.56	11.02 ± 4.25	12.39 ± 5.5	7.86 ± 4.25	12.97 ± 5.01	14.12 ± 6.16
	V30(%)	2.13 ± 1.44	7.15 ± 3.27	8.63 ± 4.21	3.75 ± 2.8	8.84 ± 4.09	10.03 ± 5.02
	D mean (cGy)	534.8 ± 108.3	672.58 ± 178.2	679.4 ± 175.63	626.3 ± 174.9	759.38 ± 226.1	763.22 ± 219.3
	NTCP (%)	.0003 ± .0008	.21 ± 0.06	.004 ± 0.012	.01 ± 0.02	.2 ± 1.04	.04 ± 0.09
LAD	Dmean (cGy)	2890.48 ± 769.4	3847.1 ± 883.9	3606.4 ± 792.4	3021.1 ± 1081.9	4000 ± 926.01	3666.84 ± 942.8
LV	Dmean (cGy)	576 ± 215.8	961.5 ± 246.1	980.97 ± 282.6	717.73 ± 166.2	1031.5 ± 261.2	1050 ± 288.02
Ipsilateral Lung	V5(%)	51.2 ± 3.8	52.95 ± 10.27	50.49 ± 6.11	52.47 ± 4.63	54.07 ± 10.3	52.7 ± 5.12
	V20(%)	22.2 ± 2.39	29.6 ± 4.7	28.81 ± 5.8	24.21 ± 3.58	32.2 ± 5.31	31.08 ± 5.50
	V30(%)	13.66 ± 1.7	21.75 ± 3.2	22.84 ± 5.28	16.67 ± 5.6	24.6 ± 3.73	25.08 ± 5.53
	Dmean (cGy)	1192.03 ± 91	1490.8 ± 171.5	1399.9 ± 212.1	1280.82 ± 149.3	1591.3 ± 206.1	1511.25 ± 213.04
Lungs	V5(%)	47.18 ± 5.73	27.52 ± 8.5	38.86 ± 5.488	48.10 ± 6.57	21.55 ± 10.1	40.05 ± 5.89
	V20(%)	11.4 ± 2.37	13.77 ± 3.95	13.03 ± 3.21	12.25 ± 3.04	14.01 ± 4.06	15.43 ± 5.01
	Dmean (cGy)	833.09 ± 98.12	761.12 ± 217.1	837.1 ± 124.06	892.49 ± 128.71	765.79 ± 208.2	881.68 ± 150.44
	NTCP (%)	.01 ± 0.005	.2 ± 0.904	.05 ± 0.18	.024 ± 0.054	.35 ± 1.0	.214 ± 22.35
Contralateral Lung	V5(%)	43.37 ± 11.75	6.64 ± 6.7	28.5 ± 8.3	45.4 ± 9.94	7.64 ± 7.48	30.17 ± 8.49
	V20(%)	2.77 ± 1.66	0.17 ± 0.4	0.18 ± 0.29	3.02 ± 1.77	0.21 ± 0.49	0.44 ± 1.14
	Dmean (cGy)	576.70 ± 112.6	161.07 ± 84.2	374.65 ± 78.22	592.6 ± 120.03	173.05 ± 91.31	394.88 ± 87.97
Contralateral Breast	V5(%)	74.14 ± 20.74	26.5 ± 21.6	11.62 ± 17.18	73.82 ± 20.44	28.33 ± 23.05	13.88 ± 22.46
	Dmean (cGy)	711.75 ± 160.14	357.6 ± 242.3	354.03 ± 1.05	699.54 ± 132.01	381.83 ± 242.9	381.77 ± 203.85
	SCCP (%)	2 ± 0.429	1.05 ± 0.65	1.049 ± 0.47	2.01 ± 0.43	1.06 ± 0.64	1.12 ± 0.55
MUs		746.25 ± 81.6	2098 ± 258.4	742.34 ± 69.6	–	–	–
TD Time(s)		168.62 ± 13.8	365.7 ± 29.8	169.5 ± 15.9	–	–	–
MF		3.73 ± 0.41	10.5 ± 1.29	3.71 ± 0.34	–	–	–

TABLE 4 | P values for three techniques comparison using Wilcoxon signed-rank test.

Structures	Metric	Conventional P Value			After Setup Error P Value		
		VMAT VS IMRT	IMRT VS H-VMAT	VMAT VS H-VMAT	VMAT VS IMRT	IMRT VS H-VMAT	VMAT VS H-VMAT
CTV	D5000cGy(%)	≤.001**	≤.086	≤.001**	≤.001**	≤.001**	≤.428
	V105(%)	≤.611	≤.012*	≤.044*	≤.171	≤.019*	≤.324
	D2cc (cGy)	≤.009*	≤.012*	≤.001**	≤.029*	≤.001**	≤.001**
Heart	V20(%)	≤.006*	≤.152	≤.001**	≤.370	≤.256	≤.044*
	V30(%)	≤.001**	≤.166	≤.001**	≤.038*	≤.264	≤.002*
	D mean (cGy)	≤.007*	≤.936	≤.009*	≤.158	≤.867	≤.213
	NTCP (%)	≤.001**	≤.001**	≤.001**	≤.001**	≤.001**	≤.001**
LAD	Dmean (cGy)	≤.001**	≤.344	≤.138	≤.013*	≤.043*	≤.044*
LV	Dmean (cGy)	≤.001**	≤.445	≤. 092	≤.039*	≤.003*	≤. 871
Ipsilateral Lung	V5(%)	≤.001**	≤.005*	≤.011*	≤.001**	≤.001**	≤.582
	V20(%)	≤.001**	≤.287	≤.001**	≤.032*	≤.841	≤.019*
	V30(%)	≤.001**	≤.006*	≤.001**	≤.028*	≤.033*	≤.949
	Dmean (cGy)	≤.001**	≤.244	≤.001**	≤.077	≤.858	≤.052
Lungs	V5(%)	≤.032*	≤.017*	≤.809	≤.001**	≤.001**	≤.543
	V20(%)	≤.006*	≤.251	≤.100	≤.112	≤.247	≤.007*
	Dmean (cGy)	≤.001**	≤.003*	≤.197	≤.009*	≤.076	≤.390
	NTCP (%)	≤.001**	≤.001**	≤.001**	≤.001**	≤.001**	≤.001**
Contralateral Lung	V5(%)	≤.002*	≤.241	≤.006*	≤.119	≤.487	≤.383
	V20(%)	≤.001**	≤.045*	≤.001**	≤.001**	≤.001**	≤.017*
	Dmean (cGy)	≤.110	≤.685	≤.046*	≤.133	≤.836	≤.088
Contralateral Breast	V5(%)	≤.817	≤.205	≤.046*	≤.508	≤.836	≤.605
	Dmean (cGy)	≤.024*	≤.081	≤.059	≤.001**	≤.334	≤.018*
	SCCP (%)	≤.024*	≤.081	≤.059	≤.024*	≤.340	≤.185
MUs		≤.001**	≤.001**	≤.379	–	–	–
TD Time(s)		≤.001**	≤.001**	≤.873	–	–	–
MF		≤.001**	≤.001**	≤.388	–	–	–

**The P-value is lower than 0.05.*

*** The P-value is lower than 0.001.*

cancer treatment. In our traditional radiation therapy, CBCT was a key method for assessing the positioning error (11, 26). It enabled us to visualize important anatomical details in the patient's body. Additionally, many recent studies have shown that optical body surface monitoring can also assess the patient's setup error, especially in breast cancer patients (28, 29). Theoretically, the target volume is closer to the chest wall for PMRT patients than the patients undergoing breast-conserving therapy, which makes the effect of SGRT more robust and accurate. The dose accumulation obtained by SGRT can extract real-time isocenter shifts, which has great advantages for analyzing intrafraction errors (30). Therefore, in this study, the registered body surface image after performing CBCT was used as the reference. The optical body surface image obtained before treatment and the optical body surface data recorded during the treatment were used to analyze the intra-fraction error. The superposition of the two setup errors was used for dose accumulation to obtain the real-world dose distribution. The non-rigid registration algorithm was selected for image registration. Because each part of ROI was given a corresponding weight according to the distance from the isocenter, a slightly larger or smaller ROI had negligible effects on the results. The rigid algorithm superimposed the changes of skin folds and other changes in the ROI to the final result regardless of the severity, and thus, we used non-rigid registration more in clinical analysis.

The radiobiological response model was used to compare the advantages and disadvantages of the different techniques (7, 8, 31). In general, no technique was better than the other two techniques in all standards, in our dose analysis, after accounting for the setup error. Although the dose advantage of the T-VMAT technique for the lungs and heart was prominent, the dose for CB in T-VMAT was significantly higher than the dose in IMRT and H-VMAT. Stovall et al. described the effect of dose on CB of breast cancer patients. They found that younger patients were more likely to have a long-term risk of breast cancer (32). Macduff et al. evaluated patients below 45 years who were carrying certain rare ATM variants, and they should be more aware of the risk of SCCP of CB cancer (33). This led us to analyze the secondary incidence of breast cancer using the T-VMAT technique, and the SCCP of CB was significantly higher than that in the other two techniques. In the analysis of biological models, the lung and heart complication rates of IMRT were the highest, while the clinical target area coverage was the least. This indicated that, based on setting errors, the impact received was the greatest, which made IMRT the least favored technique in this study. The situation concerning H-VMAT was different. After dose accumulation, the NTCP of the heart and lungs for H-VMAT was significantly lower than that for IMRT and slightly higher than that for T-VMAT. Thus, the dosimetry parameters and the probability of complications met the clinical conditions and standards. Moreover, H-VMAT had a small impact on setup

errors and covered a higher proportion of CTV after introducing the positioning errors. This might immensely help to control the local rate after breast cancer surgery. Thus, H-VMAT can be used clinically in PMRT patients with internal mammary lymph nodes to achieve target dose coverage; additionally, the OAR dose and NTCP were found to be relatively well-balanced.

Among the limitations of the study, the intrafraction error of the optical body surface images for each treatment field in SGRT was not precise. Every patient was treated using a specific treatment technique, it was impossible to obtain the three intrafraction setup errors in one patient. Thus, we selected 10 patients per technique to estimate each intrafraction setup error during treatment. To ensure greater accuracy, we only extracted patient data from fields with the same angles. The interfraction error of each time and the intrafraction error of each field were only approximated to the actual error. CBCT-based image registration is the most recognized method because anatomical structures can be seen, and tumor changes within the target volume are always visible. In this study, PMRT was used to treat patients who had no tumor tissue in the planning target, and the tumor location was close to the optical body surface, and thus, the impact could be minimized. Implementing adaptive radiotherapy (ART) might solve this problem (11). Additionally, the rotation of the patient in two directions (Pitch and Roll) were not accounted for. We wanted to simulate the scenarios introduced by the isocenter to set uncertainty, improve the accuracy of dosimetry, determine the robustness and complexity of the plan, and calculate the bioequivalent dose based on dosimetry. For the whole process, an overall analysis from plan design and implementation to prognosis was conducted. Moreover, the deep inspiration breath-hold (DIBH) technology can significantly reduce the radiation dose that the heart and lungs are exposed to during breast cancer radiotherapy (34, 35). However, the treatment involving free breathing is still the conventional procedure for treating PMRT patients at our center. Hence, the DIBH technique was not used in this study. Future studies can combine various techniques with the DIBH technique for PMRT (15, 36).

CONCLUSION

H-VMAT technique can provide an appropriate balance of target coverage, OAR dose, complication probability, planning of robustness, and delivery efficiency relative to IMRT and VMAT techniques in PMRT patients with internal mammary lymph nodes. We propose a method using SGRT to evaluate the impact of different planning modalities on setup error, which reflected the robustness of the plan in the plan design. In the future, the robustness and complexity of the plan need to be quantified, and the long-term clinical outcomes have to be evaluated to assess its reliability.

DATA AVAILABILITY STATEMENT

The raw data supporting the conclusions of this article will be made available by the authors, without undue reservation.

AUTHOR CONTRIBUTIONS

ZZ conceived idea and wrote the manuscript. PY, ZP, and XL helped with programming and DL analyzed data, XQ and WS helped with statistical analysis. FP and ZT helped with editing the manuscript. YL and YW checked results and critically revised the manuscript. All authors contributed to the article and approved the submitted version.

REFERENCES

1. Darby SC, Ewertz M, McGale P, Bennet AM, Blom-Goldman U, Brønnum D, et al. Risk of Ischemic Heart Disease in Women After Radiotherapy for Breast Cancer. *New Engl J Med* (2013) 368(11):987–98. doi: 10.1056/nejmoa1209825
2. Quirk S, Grendarova P, Phan T, Conroy L, Burke B, Long K, et al. A Retrospective Multi-Institutional Analysis to Define Dosimetric Recommendations for the Left Anterior Descending Artery for Left-Sided Breast Cancer Patients Treated With Radiotherapy. *RadiotheR Oncol* (2020). doi: 10.1016/j.radonc.2020.04.022
3. Nilsson G, Holmberg L, Garmo H, Duvernoy O, Sjögren I, Lagerqvist B, et al. Distribution of Coronary Artery Stenosis After Radiation for Breast Cancer. *J Clin Oncol* (2012) 30:380–6. doi: 10.1200/JCO.2011.34.5900
4. Choi J, Kim YB, Shin KH, Ahn SJ, Lee HS, Park W, et al. Radiation Pneumonitis in Association With Internal Mammary Node Irradiation in Breast Cancer Patients: An Ancillary Result From the KROG 08-06 Study. *J Breast Canc* (2016) 19(3):275–82. doi: 10.4048/jbc.2016.19.3.275
5. Gagliardi G, Bjohle J, Lax I, Ottolenghi A, Eriksson F, Liedberg A, et al. Radiation Pneumonitis After Breast Cancer Irradiation: Analysis of the Complication Probability Using the Relative Seriality Model. *Int J Radiat Oncol Biol Phys* (2000) 46:373–81. doi: 10.1016/S0360-3016(99)00420-4
6. Fogliata A, De Rose F, Franceschini D, Stravato A, Seppälä J, Scorsetti M, et al. Critical Appraisal of the Risk of Secondary Cancer Induction From Breast Radiation Therapy With Volumetric Modulated Arc Therapy Relative to 3D Conformal Therapy. *Int J Radiat Oncol Biol Phys* (2018) 100(3):785–93. doi: 10.1016/j.ijrobp.2017.10.040
7. Edvardsson A, Nilsson MP, Amptoulach S, Ceberg S. Comparison of Doses and NTCP to Risk Organs With Enhanced Inspiration Gating and Free Breathing for Left-Sided Breast Cancer Radiotherapy Using the AAA Algorithm. *Radiat Oncol* (2015) 10(1):1–8. doi: 10.1186/s13014-015-0375-y
8. Liu YC, Chang HM, Lin HH, Lu CC, Lai LH. Dosimetric Comparison of Intensity-Modulated Radiotherapy, Volumetric Modulated Arc Therapy and Hybrid Three-Dimensional Conformal Radiotherapy/Intensity-Modulated Radiotherapy Techniques for Right Breast Cancer. *J Clin Med* (2020) 9 (12):3884. doi: 10.3390/jcm9123884
9. Zhang W, Li R, You D, Su Y, Dong W, Ma Z. Dosimetry and Feasibility Studies of Volumetric Modulated Arc Therapy With Deep Inspiration Breath-Hold Using Optical Surface Management System for Left-Sided Breast Cancer Patients. *Front Oncol* (2020) 10:1711. doi: 10.3389/fonc.2020.01711
10. Ding Z, Xiang X, Zeng Q, Ma J, Dai Z, Kang K, et al. Evaluation of Plan Robustness on the Dosimetry of Volumetric Arc Radiotherapy (VMAT) With

Set - Up Uncertainty in Nasopharyngeal Carcinoma (NPC) Radiotherapy. *Radiat Oncol* (2022), 1–10. doi: 10.1186/s13014-021-01970-8
11. Tamihardja J, Cirsi S, Kessler P, Razinskas G, Exner F, Richter A, et al. Cone Beam CT - Based Dose Accumulation and Analysis of Delivered Dose to the Dominant Intraprostatic Lesion in Primary Radiotherapy of Prostate Cancer. *Radiat Oncol* (2021), 1–9. doi: 10.1186/s13014-021-01933-z
12. Kügele M, Edvardsson A, Berg L, Alkner S, Andersson Ljus C, Ceberg S. Dosimetric Effects of Intrafractional Isocenter Variation During Deep Inspiration Breath-Hold for Breast Cancer Patients Using Surface-Guided Radiotherapy. *J Appl Clin Med Phys* (2018) 19(1):25–38. doi: 10.1002/acm2.12214
13. Liao X, Wu F, Wu J, Peng Q, Yao X, Kang S, et al. Impact of Positioning Errors in the Dosimetry of VMAT Left-Sided Post Mastectomy Irradiation. *Radiat Oncol* (2020) 15(1):1–7. doi: 10.1186/s13014-020-01556-w
14. Seppenwoolde Y, Lebesque JV, de Jaeger K, Belderbos JS, Boersma LJ, Schilstra C, et al. Comparing Different NTCP Models That Predict the Incidence of Radiation Pneumonitis. Normal Tissue Complication Probability. *Int J Radiat Oncol Biol Phys* (2003) 55:724–35. doi: 10.1016/S0360-3016(02)03986-X
15. Mahmoudzadeh H, Lee J, Chan, et al. Robust Optimization Methods for Cardiac Sparing in Tangential Breast IMRT. *Med Phys* (2015) 42(5):2212–22. doi: 10.1118/1.4916092
16. Kwa SL, Theuws JC, Wagenaar A, Damen EM, Boersma LJ, Baas P, et al. Evaluation of Two Dose Volume Histogram Reduction Models for the Prediction of Radiation Pneumonitis. *Radiother Oncol* (1998) 48:61–9. doi: 10.1016/S0167-8140(98)00020-6
17. Wiant D, Wentworth S, Liu H, Sintay B. How Important Is a Reproducible Breath Hold for Deep Inspiration Breath Hold Breast Radiation Therapy? *Radiat Oncol Biol* (2015) 93(4):901–7. doi: 10.1016/j.ijrobp.2015.06.010
18. Mamounas EP, White JR, Bandos H, Bandos H. NSABP B-51/RTOG 1304: Randomized Phase III Clinical Trial Evaluating the Role of Postmastectomy Chest Wall and Regional Nodal XRT (CWRNRT) and Post-Lumpectomy RNRT in Patients (Pts) With Documented Positive Axillary (Ax) Nodes Before Neoadjuvant Chemotherapy (NC) Who Convert to Pathologically Negative Ax Nodes After NC. *J Clin Oncol* 32(15_suppl). TPS1141; 2014 – TPS1141. doi: 10.1200/jco.2014.32.15_suppl.tps1141
19. Van Herk M. Errors and Margins in Radiotherapy. *Semin Radiat Oncol* (2004) 14(1):52–64. doi: 10.1053/j.semradonc.2003.10.003
20. Giorgia N, Antonella F, Alessandro C, Eugenio V, Luca C. Planning Strategies in Volumetric Modulated Arc Therapy for Breast. (2011) 38:4025–31. doi: 10.1118/1.3598442
21. Gay HA, Niemierko A. A Free Program for Calculating EUD-Based NTCP and TCP in External Beam Radiotherapy. *Physica Med* (2007) 23(3–4):115–25. doi: 10.1016/j.ejmp.2007.07.001
22. Burman C, Kutcher GJ, Emami B, Goitein M. Fitting of Normal Tissue Tolerance Data to an Analytic Function. *Int J Radiat Oncol Biol Phys* (1991) 21 (1):123–35. doi: 10.1016/0360-3016(91)90172-Z
23. Gagliardi G, Lax I, Ottolenghi A, Rutqvist LE. Long-Term Cardiac Mortality After Radiotherapy of Breast Cancer–Application of the Relative Seriality Model. *Br J Radiol* (1996) 69(825):839–46. doi: 10.1259/0007-1285-69-825-839
24. Schneider U, Kaser-hotz B. A Simple Dose-Response Relationship for Modeling Secondary Cancer Incidence After Radiotherapy. *Z Med Phys* (2005) 15(1):31–7. doi: 10.1078/0939-3889-00242
25. Hernandez V, Rønn C, Widesott L, Bäck A, Canters R, Fusella M, et al. What is Plan Quality in Radiotherapy? The Importance of Evaluating Dose Metrics, Complexity, and Robustness of Treatment Plans. *RadiotheR Oncol* (2020) 153:26–33. doi: 10.1016/j.radonc.2020.09.038
26. Rankine LJ, Wang Z, Kelsey CR, Ms EB, Driehuys B, Marks LB, et al. Hyperpolarized 129Xe Magnetic Resonance Imaging for Functional Avoidance Treatment Planning in Thoracic Radiation Therapy: A Comparison of Ventilation- and Gas-Exchange-Guided Treatment Plans. *Int J Radiat Oncol Biol Physics.* (2021) 111(4):1044–57. doi: 10.1016/j.ijrobp.2021.07.002
27. Cui G, Housley DJ, Chen F, Mehta VK, Shepard DM. Delivery Efficiency of an Elekta Linac Under Gated Operation. *J Appl Clin Med Phys* (2014) 15(5):2–11. doi: 10.1120/jacmp.v15i5.4713
28. Macfarlane MJ, Jiang K, Mundis M, Nichols E, Gopal A, Chen S, et al. Comparison of the Dosimetric Accuracy of Proton Breast Treatment Plans Delivered With SGRT and CBCT Setups. (2021) 22(9):153–8. doi: 10.1002/acm2.13357
29. Sarudis S, Karlsson A, Bäck A. Surface Guided Frameless Positioning for Lung Stereotactic Body Radiation Therapy. (2021) 22(9):215–26. doi: 10.1002/acm2.13370
30. Jacobse JN, Duane FK, Boekel NB, Schaapveld M, Hauptmann M, Hooning MJ, et al. Radiation Dose-Response for Risk of Myocardial Infarction in Breast Cancer Survivors. *Radiat Oncol Biol* (2019) 103(3):595–604. doi: 10.1016/j.ijrobp.2018.10.025
31. Ma J, Li J, Xie J, Chen J, Zhu C, Cai G, et al. Post Mastectomy Linac IMRT Irradiation of Chest Wall and Regional Nodes: Dosimetry Data and Acute Toxicities. *Radiat Oncol* (2013) 8(1):81. doi: 10.1186/1748-717X-8-81
32. Stovall M, Smith SA, Langholz BM, et al. Women's Environmental, Cancer, and Radiation Epidemiology Study Collaborative Group. Dose to the Contralateral Breast From Radiotherapy and Risk of Second Primary Breast Cancer in the WECARE Study. *Int J Radiat Oncol Biol* 72(4):1021–30. doi: 10.1016/j.ijrobp.2008.02.040
33. McDuff SGR, Bellon JR, Shannon KM, Gadd MA, Dunn S, Rosenstein BS , et al. ATM Variants in Breast Cancer: Implications for Breast Radiotherapy Treatment Recommendations. *Int J Radiat Oncol Biol Phys* (2021). doi: 10.1016/j.ijrobp.2021.01.045. S0360-3016(21)00119-X.
34. Zhang J, Huang L, Wu F, Wang G, Wu L, Huang B, et al. Tailoring PTV Expansion to Improve the Dosimetry of Post Modified Radical Mastectomy Intensity-Modulated Radiotherapy for Left-Sided Breast Cancer Patients by Using 4D CT Combined With Cone Beam CT. *J Appl Clin Med Phys* (2021) 22 (5):139–46. doi: 10.1002/acm2.13244
35. Poeta S, Jourani Y, De Caluwé A, Van den Begin R, Van Gestel D, Reynaert N, et al. Split-VMAT Technique to Control the Deep Inspiration Breath Hold Time for Breast Cancer Radiotherapy. *Radiat Oncol* (2021) 16(1):77. doi: 10.1186/s13014-021-01800-x
36. Bahig H, de Guise J, Vu T, Blais D, Chartrand-Lefebvre C, Nguyen NT, et al. In a Heartbeat: An Assessment of Dynamic Dose Variation to Cardiac Structures Using Dual Source Computed Tomography. *Int J Radiat Oncol Biol Phys* (2018) 102(4):950–9. doi: 10.1016/j.ijrobp.2018.01.049

Conflict of Interest: The authors declare that the research was conducted in the absence of any commercial or financial relationships that could be construed as a potential conflict of interest.

frontiers | Frontiers in Oncology

TYPE Original Research
PUBLISHED 09 August 2022
DOI 10.3389/fonc.2022.916840

OPEN ACCESS

EDITED BY
Yingli Yang,
UCLA Health System, United States

REVIEWED BY
Marta Zerunian,
Sapienza University of Rome, Italy
Ri Na Yoo,
The Catholic University of Korea,
South Korea

*CORRESPONDENCE
Songbing He
captain_hsb@163.com

†These authors contributed equally to this work

SPECIALTY SECTION
This article was submitted to Radiation Oncology, a section of the journal Frontiers in Oncology

RECEIVED 10 April 2022
ACCEPTED 19 July 2022
PUBLISHED 09 August 2022

CITATION
Shi X, Zhao M, Shi B, Chen G, Yao H, Chen J, Wan D, Gu W and He S (2022) Pretreatment blood biomarkers combined with magnetic resonance imaging predict responses to neoadjuvant chemoradiotherapy in locally advanced rectal cancer. *Front. Oncol.* 12:916840. doi: 10.3389/fonc.2022.916840

Pretreatment blood biomarkers combined with magnetic resonance imaging predict responses to neoadjuvant chemoradiotherapy in locally advanced rectal cancer

Xinyu Shi[1†], Min Zhao[2†], Bo Shi[1], Guoliang Chen[1], Huihui Yao[1], Junjie Chen[1], Daiwei Wan[1], Wen Gu[1] and Songbing He[1*]

[1]Department of General Surgery, The First Affiliated Hospital of Soochow University, Suzhou, China, [2]Department of Nuclear Medicine, The First Affiliated Hospital of Soochow University, Suzhou, China

Aim: To investigate the value of pretreatment blood biomarkers combined with magnetic resonance imaging (MRI) in predicting the efficacy of neoadjuvant chemoradiotherapy (NCRT) in patients with locally advanced rectal cancer (LARC).

Methods: This study involved patients with LARC who received NCRT and subsequently underwent total mesenteric excision from June 2015 to June 2021 at the First Affiliated Hospital of Soochow University. Patients with incomplete courses of neoadjuvant therapy, comorbidities with other malignancies or diseases that affect the study outcome, and those who underwent unplanned surgery were ultimately excluded. Laboratory data such as albumin, CEA, various blood cell levels, and MRI related data such as tumor regression grade assessed by magnetic resonance imaging (mrTRG) were collected from the included patients one week prior to NCRT. MrTRG is a common clinical imaging metric used to assess the degree of tumor regression in rectal cancer, primarily based on morphological assessment of residual tumor. Furthermore, pretreatment blood biomarkers such as neutrophil to lymphocyte ratio (NLR), lymphocyte to monocyte ratio (LMR), albumin to fibrinogen ratio (AFR), and prealbumin to fibrinogen ratio (PFR) were assessed. The independent variables for pathologic complete response (pCR) to NCRT were determined by univariate and multivariate logistic regression analyses. Receiver operating characteristic (ROC) curve analysis was used to examine the performance of MRI with or without pretreatment blood biomarkers in predicting pCR using DeLong's method. A nomogram was created and confirmed internally.

Results: Fifty-nine individuals with LARC satisfied the inclusion criteria, among which 23 showed pCR after NCRT. Logistic regression analysis demonstrated that pretreatment CEA (≤ 3 μg/L, OR = 0.151, P = 0.039), NLR (OR = 4.205, P =

0.027), LMR (OR = 0.447, P = 0.034), and PFR (OR = 0.940, P = 0.013) were independent predictors of pCR to NCRT. The AUCs of mrTRG alone and mrTRG plus the above four pretreatment blood biomarkers were 0.721 (P =0.0003) and 0.913 (P <0.0001), respectively. The constructed nomogram showed a C-index of 0.914.

Conclusion: Pretreatment blood biomarkers combined with MRI can help clinical efforts by better predicting the efficacy of NCRT in patients with locally advanced rectal cancer.

KEYWORDS

locally advanced rectal cancer, neoadjuvant chemoradiotherapy, pathological complete response, blood biomarkers, magnetic resonance imaging, prognosis

Introduction

According to the global cancer statistics in 2020, colorectal cancer (CRC) is the second deadliest malignant tumor worldwide (1). Rectal cancer accounts for approximately 30% of colorectal cancer cases, and the proportion is increasing annually. In addition, most patients with rectal cancer are already locally advanced at the time of diagnosis and have a poor prognosis.

Since studies have reported the superiority of preoperative chemoradiotherapy over postoperative chemoradiotherapy, the conventional treatment modality of locally advanced rectal cancer (LARC) is neoadjuvant chemoradiotherapy (NCRT) followed by total mesenteric excision (TME) (2, 3). In recent years, the total neoadjuvant therapy (TNT) modality and the watch-and-wait (W&W) strategy have received increasing attention (4–7).

However, a significant variation in individual responses to NCRT has been noted during clinical treatment. Approximately 50%-60% of rectal cancer patients show staged shrinkage after NCRT, whereas about 10%-30% show pathologic complete response (pCR) (5). However, approximately one-third of patients show poor sensitivity to chemoradiotherapy, and NCRT efficacy is strongly linked to the prognosis of these patients (8). Therefore, the early prediction of NCRT efficacy is particularly important in the diagnosis and treatment of locally advanced rectal cancer.

Based on the principles of pathological tumor regression grading (pTRG), Patel et al. proposed magnetic resonance imaging for assessing tumor regression grade (mrTRG) in 2011 (9). However, this traditional morphological qualitative assessment based on T2-weighted imaging may fail to predict treatment response when assessing residual tumors (10). Since conventional MRI provides only morphological information, it is difficult to distinguish treatment-induced fibrosis, necrosis, and tumor residuals (11). In contrast, functional MRI such as diffusion-weighted imaging (DWI) can provide information at the molecular level of the tumor (12). DWI indirectly reflects the biology of human tissues by assessing the diffusive motion of water molecules and providing a quantitative index of the apparent diffusion coefficient (ADC). Recent studies have used DWI techniques to assess the efficacy of neoadjuvant therapy in patients with rectal cancer (13, 14). The efficacy of ADC values in predicting the efficacy of neoadjuvant therapy for rectal cancer remains controversial. The reasons for this may be related to factors such as the use of different methods to outline the region of interest (ROI) and different b-values. Therefore, until a uniform standard is reached in clinical as well as scientific research, assessment based on a single imaging image is inevitably a bit subjective.

Several economically feasible blood markers have been explored in recent clinical studies to predict tumor regression response after NCRT, such as neutrophil to lymphocyte ratio (NLR), prognostic nutritional index (PNI), and carcinoembryonic antigen (CEA) (15–23). Some foreign scholars explored whether the combined use of magnetic resonance imaging (MRI) parameters with CEA levels could better predict the efficacy of NCRT than MRI parameters alone. It was found that the combination of mrTRG and CEA improved the AUC value from 0.680 to 0.728 compared to mrTRG alone (24). However, although the performance of MRI parameters in combination with CEA for predicting pTRG improved, it was still unsatisfactory. Therefore, it was natural to question whether more satisfactory results could be obtained using additional and more valuable blood biomarkers in combination with MRI.

Thus, in this study, we aimed to investigate whether combining multiple blood biomarkers with T2WI-based mrTRG could significantly improve the power of MRI in predicting the efficacy of neoadjuvant chemoradiotherapy in

patients with LARC. We also established a new model of MRI parameters and multiple blood markers. We have reason to believe that this is the first study to combine multiple blood biomarkers with MRI to predict the efficacy of neoadjuvant chemoradiotherapy in rectal cancer. This study will provide new ideas and methods for the selection of treatment strategies for neoadjuvant chemoradiotherapy in patients with rectal cancer.

Materials and methods

Patients

This retrospective study initially screened LARC patients who underwent NCRT and subsequent surgery at the First Affiliated Hospital of Soochow University from June 2015 to June 2021. The follow-up period was from the clinical diagnosis of rectal cancer to 2 weeks after TME surgery, encompassing the entire neoadjuvant treatment. The inclusion criteria were as follows: (1) rectal cancer with positive clinical stage T3-T4 or positive lymph nodes as determined by preoperative MRI, without distant metastases; (2) adenocarcinoma of the rectum less than 10 cm from the anal verge as confirmed by pathology of the colonoscopic biopsy specimen; (3) no previous chemotherapy or pelvic radiotherapy experience; (4) complete clinical process information, including laboratory test results within 7 days before the start of NCRT and tumor pathological characteristics; (5) complete imaging information, including rectal MRI images 4 weeks before NCRT and 6-8 weeks after NCRT; and (6) complete resection without positive tumor margins. The standards for exclusion were as follows: (1) incomplete completion of preoperative chemoradiotherapy treatment; (2) evidence of acute and chronic infections, autoimmune diseases, and hematological disorders; (3) palliative surgery or partial resection or emergency surgery; and (4) synchronous malignancies or medical history of other malignancies. This study was approved by the ethics committee of the First Affiliated Hospital of Soochow University.

Treatment

In this study, all patients received neoadjuvant chemoradiotherapy. Patients received preoperative radiation in the pelvic region in 25 fractions at a dose of 45 Gy, and the original tumor was irradiated with an additional 5.4 Gy in three doses, making the maximum dosage 50.4 Gy (25). Capecitabine was administered at a dose of 825 mg/m^2 twice daily from Monday to Friday throughout the radiotherapy period. In the interval after radiotherapy and before surgery, patients received 2 to 3 cycles of neoadjuvant chemotherapy in one of two regimens, the CapeOX (43 cases, 72.9%) and the FOLFOX (16 cases, 27.1%). All patients underwent surgery according to the principle of TME at 4 to 8 weeks after NCRT. Patients were considered for adjuvant chemotherapy 3–4 weeks following surgery.

Pathological assessment of the response to NCRT

Pathological response to NCRT was evaluated by two independent pathologists according to the four-tier American Joint Committee on Cancer (AJCC) seventh edition tumor regression grade (TRG) classification. The pathological TRGs (pTRGs) system was defined as follows: pTRG0, no remaining viable cancer cells; pTRG1, single cells or rare residual cancer cells; pTRG2, residual cancer with a desmoplastic response; and pTRG3, minimal evidence of tumor response (26). The pCR was defined as pTRG 0 and the other grades were defined as non-pCR.

MRI assessment of the response to NCRT

All patients underwent rectal MRI 4 weeks before and 6-8 weeks after NCRT. The assessment of rectal cancer MRI parameters was performed by two radiologists with more than 3 years of experience in rectal cancer MRI staging. T-stage, N-stage, the distance from the anal verge to the lower edge of the tumor, and the status of the circumferential resection margin (mrCRM) were assessed by rectal MRI 4 weeks prior to NCRT. If the distance between the tumor and the mesorectal fascia on MRI was greater than or equal to 1 mm, the case was considered definitive mrCRM (9). The assessment of mrTRG was based on rectal MRI 6-8 weeks after NCRT: grade 1, mucosal or mucosal inferior 1 to 2 mm scar or marked normalization of the rectal wall; grade 2, dense fibrosis with no obvious residual tumor; grade 3, more than 50% of fibrosis or mucus and visible residual tumor signal; grade 4, minimal fibrosis/mucinous degeneration, mostly tumor; and grade 5, same as a primary tumor or tumor progression (10). Like pTRGs, mrTRGs were classified into good response and poor response, with mrTRG 1 or 2 and mrTRG 3, 4, or 5 indicating good and poor response, respectively.

Data collection and definitions

All patients underwent routine blood tests, liver and kidney function tests, coagulation tests, and serum CEA tests. All blood specimens were tested in our laboratory one week before the start of NCRT. The pretreatment blood biomarkers were calculated as follows:

NLR = neutrophil count /lymphocyte count;

PLR = platelet count /lymphocyte count;

$$\text{LMR} = \text{lymphocyte count} / \text{monocyte count};$$

$$\text{SII} = \text{platelet count} \times \text{neutrophil count} / \text{lymphocyte count};$$

$$\text{PNI} = 10 \times \text{serum albumin}(\text{g/dL}) + 0.005 \times \text{total lymphocyte count}(\text{per mm3});$$

$$\text{AFR} = \text{Serum albumin} / \text{fibrinogen};$$

$$\text{PFR} = \text{Serum prealbumin} / \text{fibrinogen}$$

In previous studies different cut-off values have been used for these biomarkers. For example, for NLR, Braun LH et al. adopted a cut-off value of 4.06, and neoadjuvant therapy tended to work well in patients with rectal cancer with pre-treatment NLR below 4.06 (15). However, some studies have also used 2.0 and 3.05 as cut-off values for NLR (22, 23). And there are also some scholars who did not convert these biomarkers into dichotomous variables (20, 21). Therefore, our study used continuous variables for all biomarkers.

Statistical analyses

The Statistical Package for the Social Sciences, version 20.0, was used to conduct statistical analyses (IBM SPSS Inc., Chicago, USA). Continuous variables were analyzed using the Student's t-test for normally distributed variables or the Mann-Whitney U test for skewed distributed variables. Categorical variables were assessed using the Chi-square test or Fisher's exact test (if the expected frequencies were <5). A univariate and multivariate logistic regression model was utilized to determine predictive factors for pCR to NCRT. DeLong's technique was used to compare the areas under the curves (AUC) based on receiver operating characteristic (ROC) curves analysis of mrTRG alone versus the combination of mrTRG and pretreatment blood biomarkers for the prediction of pCR. A predictive nomogram was developed using R version 4.1.3 (R-Project, Institute of Statistics and Mathematics, Vienna, Austria) based on the findings of multivariate logistic regression analysis. The nomogram's performance was evaluated using internal validation and AUC. Furthermore, the Harrell's concordance index (C-index) was calculated to evaluate the discriminating capability of the nomogram. A two-sided $P < 0.05$ was considered statistically significant.

Results

Patient characteristics

From June 2015 to June 2021, we initially enrolled 100 LARC patients to receive neoadjuvant therapy, with 59 patients ultimately completing the study (see Figure 1). Patients who have not completed their course of chemoradiotherapy (n = 13), those who received concomitant targeted agents during NCRT

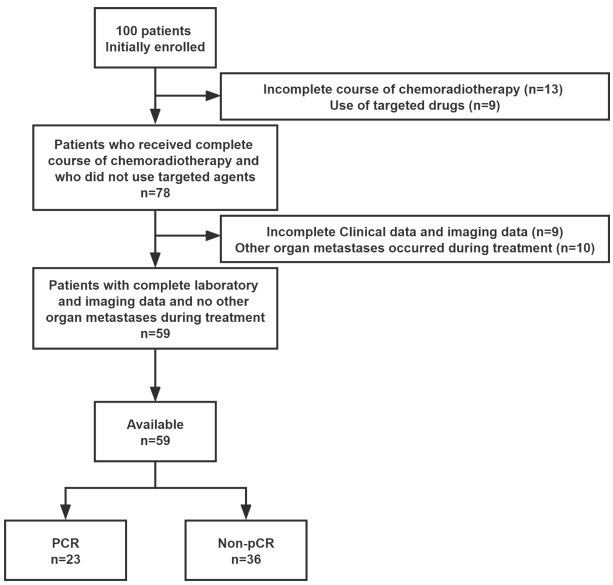

FIGURE 1
Filtering process of patient data from the initial inclusion of patients.

(n = 9), those with incomplete laboratory records or imaging data (n = 9), and those with metastases to other organs (n = 10), were excluded from the study. Ultimately, 59 patients who satisfied all criteria were included in the study. All patients included underwent rectal MRI for clinical staging and assessment of treatment outcome before and after neoadjuvant chemoradiotherapy. For all 59 patients, the pTRGs according to each mrTRG are displayed in Table 1. Patient characteristics are summarized in Table 2. Among the 59 patients, pCR (pTRG 0) was observed in 23 (29.0%) patients, pTRG 1 in 16 (27.1%), pTRG 2 in 8 (13.6%) and pTRG 3 in 12 (20.3%). The median pretreatment biomarkers levels of serum albumin, prealbumin, hemoglobin, NLR, PLR, LMR, SII, PNI, AFR, and PFR were 41.1 g/L (range,33.1-49.2), 222.6 mg/L (range,149.9-345.5), 136 g/L (range,73-147), 2.65 (range,1.46-4.55), 133.85 (range,50.23-562.50), 3.59 (range,2.03-9.00), 552.3 (range,241.66-1644.78), 41.11 (range,33.11-49.21), 18.19 (range,14.13-22.17), and 95.95 (range, 60.69-157.05), respectively. The number of patients with CEA >3μg/L was 41(69.5%).

Predictors of pCR to NCRT

The relationships between patient demographics, tumor features, pretreatment biomarkers and MRI parameters, and pCR are shown in Table 2. Clinical biomarkers such as gender, age, BMI, the distance from the anal verge to the lower edge of the tumor, T stage, N stage, and mrCRM, and pretreatment blood biomarkers such as serum albumin, serum prealbumin, hemoglobin, PLR, SII, and PNI were not associated with pCR to NCRT (all P > 0.05).

According to the univariate analysis, mrTRG (1-2 vs. < 3-5, OR = 0.129, 95% CI 0.038-0.432, P = 0.001), pretreatment CEA level (≤ 3.0 vs. > 3.0, OR = 0.183, 95% CI 0.055-0.608, P = 0.006), pretreatment NLR (OR = 2.648, 95% CI 1.202-5.834, P = 0.016), pretreatment LMR (OR = 0.581, 95% CI 0.396-0.851, P < 0.001), pretreatment AFR (OR = 0.674, 95% CI 0.456-0.997, P = 0.048), and pretreatment PFR (OR = 0.969, 95% CI 0.941-0.998, P = 0.036) were significantly associated with pCR to NCRT (Table 3). Multivariate Logistic regression analysis demonstrated that mrTRG (1-2 vs. < 3-5, OR = 0.074, 95% CI 0.011-0.499, P = 0.007), pretreatment CEA level (≤ 3.0 vs. > 3.0, OR = 0.151, 95% CI 0.025-0.913, P = 0.039), pretreatment NLR (OR = 4.205, 95% CI 1.175-15.052, P = 0.027), pretreatment LMR (OR = 0.447, 95% CI 0.212-0.939, P < 0.034), and pretreatment PFR (OR = 0.940, 95% CI 0.896-0.987, P = 0.013) were independent predictors of pCR to NCRT (Table 3).

Overall, the pCR group had higher LMR and PFR, but lower NLR and CEA levels.

Pretreatment biomarkers improve the predictive performance of MRI

Figure 2 shows the ROCs for mrTRG alone (Figure 2A) and mrTRG plus pretreatment blood biomarkers for predicting pCR (Figures 2B-D). The AUCs for mrTRG plus biomarkers for predicting pCR were significantly larger than that for mrTRG alone (Table 4).

Nomogram for pCR to NCRT

Based on the significant predictors in the logistic regression analysis, a nomogram for the prediction of pCR to NCRT in LARC patients was developed, as shown in Figure 3A. The predicted probability of pCR for NCRT could be easily obtained by adding up the scores of each variable and then drawing a straight line. The patients with higher total scores tended to achieve a higher probability of pCR to NCRT. The internally validated calibration curves revealed good agreement between the predicted and actual probability of pCR to NCRT (Figure 3B). The nomogram performance was verified internally, and it exhibited a C-index of 0.914 (95% CI 0.838-0.988) and AUC of 0.913, as illustrated in Figure 3C.

Discussion

The results of this study revealed that 23 (39.0%) of 59 LARC patients who received NCRT achieved pCR. CEA, NLR, LMR,

TABLE 1 pTRG according to mrTRG.

mrTRG	pTRG				Total
	0	1	2	3	
mrTRG 1	7 (77.8)	2 (22.2)	0	0	9 (15.3)
mrTRG 2	7 (63.6)	3 (27.3)	1 (9.1)	0	11 (18.6)
mrTRG 3	6 (26.1)	8 (34.8)	4 (17.4)	5 (21.7)	23 (39.0)
mrTRG 4	3 (21.4)	2 (14.3)	3 (21.4)	6 (42.9)	14 (23.7)
mrTRG 5	0	1 (50.0)	0	1 (50.0)	2 (3.4)
Total	23 (39.0)	16 (27.1)	8 (13.6)	12 (20.3)	59 (100.0)

Values are expressed as number (%). pTRG, pathologic tumor regression grade; mrTRG, tumor regression grade assessed by magnetic resonance imaging.

TABLE 2 Patient characteristics and response to NCRT.

Variables	Number (%) (n = 59)	PCR (n = 23)	Non-pCR (n = 36)	*P*
Gender				
Male	44 (74.6%)	15	29	0.156
Female	15 (25.4%)	8	7	
Age				
≥ 60	30 (50.8%)	12	18	0.542
< 60	29 (49.2%)	11	18	
BMI				
≥ 24	27 (45.8%)	8	19	0.139
< 24	32 (54.2%)	15	17	
Distance from the anal verge (cm)				
≥ 5	30 (50.8%)	9	21	0.121
< 5	29 (49.2%)	14	15	
Clinical T stage				
T 1-2	5 (8.5%)	1	4	0.346
T 3-4	54 (91.5%)	22	32	
Clinical N stage				
N 0-1	25 (42.4%)	11	14	0.341
N 2	34 (57.6%)	12	22	
mrCRM				
(+)	24 (40.7%)	6	18	0.059
(–)	35 (59.3%)	17	18	
mrTRG				
1-2 (Good)	20 (33.9%)	14	6	**0.001**
3-5 (Poor)	39 (66.1%)	9	30	
Pretreatment biomarkers levels [median (range)]				
Serum albumin (g/L)	41.1 (33.1-49.2)	41.2 (33.1-49.2)	40.95 (34.9-47.4)	0.196
Serum prealbumin (mg/L)	222.6 (149.9-345.5)	251.5 (165.5-345.5)	215.9 (149.9-332.0)	0.058
Hemoglobin (g/L)	136 (73-147)	134 (73-155)	136 (94-174)	0.217
NLR	2.65 (1.46-4.55)	2.17 (1.46-4.01)	2.74 (1.46-4.55)	**0.011**
PLR	133.85 (50.23-562.50)	155.19 (50.23-562.50)	131.27 (77.1-348.57)	0.232
LMR	3.59 (2.03-9.00)	4.76 (2.16-9.00)	3.38 (2.03-8.61)	**0.005**
SII	552.3 (241.66-1644.78)	488.43 (284.75-1625.63)	598.47 (241.66-1644.78)	0.511
PNI	41.11 (33.11-49.21)	41.21 (33.11-49.21)	40.96 (34.91-47.41)	0.196
AFR	18.19 (14.13-22.17)	18.77 (14.84-22.17)	17.61 (14.13-20.04)	**0.041**
PFR	95.95 (60.69-157.05)	106.08 (75.23-157.05)	92.04 (60.69-144.98)	**0.028**
CEA				
> 3	41 (69.5%)	11	30	**0.007**
≤ 3	18 (30.5%)	12	6	

NCRT, neoadjuvant chemoradiotherapy; pCR, pathologic complete response; BMI, body mass index; MrCRM, mesorectal circumferential resection margin status; MrTRG, tumor regression grade assessed by magnetic resonance imaging; NLR, neutrophil to lymphocyte ratio; PLR, platelet to lymphocyte ratio; LMR, lymphocyte to monocyte ratio; SII, systemic immune-inflammation index; PNI, prognostic nutritional index; AFR, albumin to fibrinogen ratio; PFR, prealbumin to fibrinogen ratio; CEA, carcinoembryonic antigen. Bold values indicate that P-value is significant.

and PFR were significant predictors of pCR, superior to markers such as PLR, SII, and PNI. High values of pretreatment LMR and PFR and low values of NLR and CEA were positively correlated with pCR. High pre-NCRT AFR was positively correlated with pCR in univariate logistic regression analysis, but not in multivariate logistic regression analysis. This discrepancy may be due to the high correlation between PFR and AFR in multivariate regression analysis. In the ROC curves analysis, the AUCs of individual biomarkers (NLR, LMR, PFR, and CEA) in combination with mrTRG were 0.774, 0.778, 0.831, and 0.798, respectively, which were all higher than that of mrTRG alone (AUC of 0.721). Furthermore, expectedly, the AUC of mrTRG in combination with all four biomarkers (NLR, LMR, PFR, and CEA) was the highest (0.913).

Scholars are increasingly recognizing a possible cross-link between systemic inflammatory responses and nutritional risk,

TABLE 3 Univariate and Multivariate Logistic regression analysis for response to NCRT.

Variables	Univariate analysis		Multivariate analysis	
	OR (95% CI)	*P*	OR (95% CI)	*P*
mrTRG				
1-2 vs. 3-5	0.129 (0.038-0.432)	0.001	0.074 (0.011-0.499)	**0.007**
Pretreatment CEA (μg/L)				
≤ 3.0 vs. > 3.0	0.183 (0.055-0.608)	0.006	0.151 (0.025-0.913)	**0.039**
Pretreatment biomarkers				
NLR	2.648 (1.202-5.834)	0.016	4.205 (1.175-15.052)	**0.027**
LMR	0.581 (0.396-0.851)	0.005	0.447 (0.212-0.939)	**0.034**
AFR	0.674 (0.456-0.997)	0.048	0.730 (0.379-1.403)	0.345
PFR	0.969 (0.941-0.998)	0.036	0.940 (0.896-0.987)	**0.013**

NCRT, neoadjuvant chemoradiotherapy; mrTRG, tumor regression grade assessed by magnetic resonance imaging; CEA, carcinoembryonic antigen; NLR, neutrophil to lymphocyte ratio; LMR, lymphocyte to monocyte ratio; AFR, albumin to fibrinogen ratio; PFR, prealbumin to fibrinogen ratio. CI, confidence interval.
Bold values mean that P-value is significant.

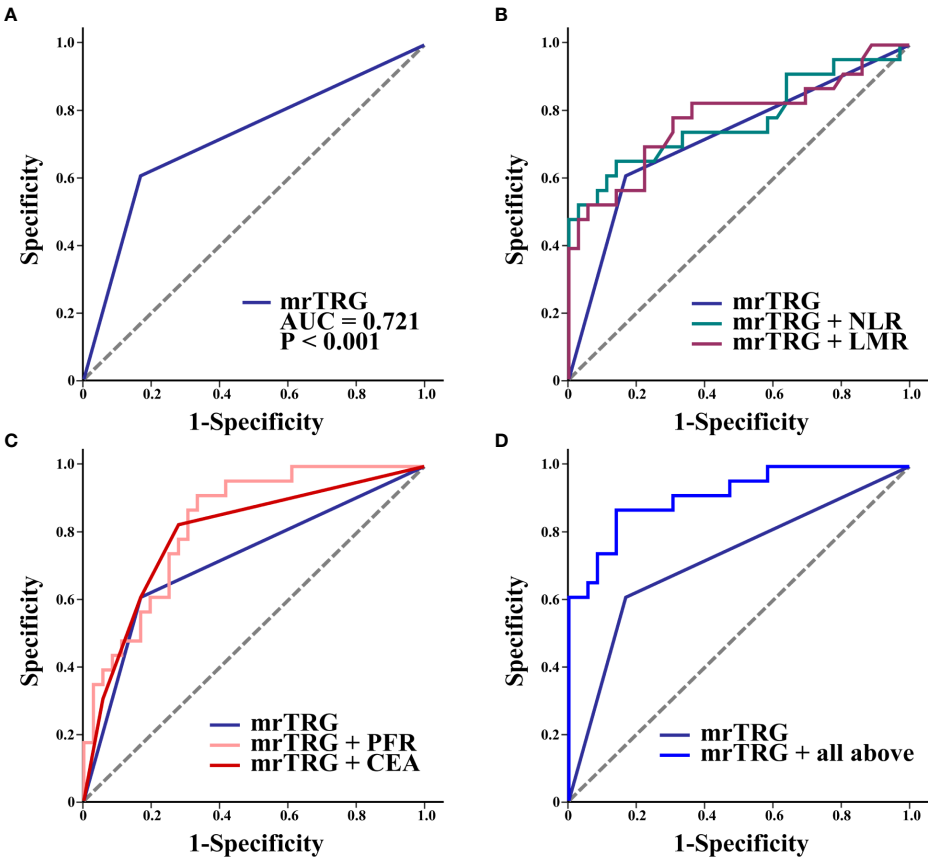

FIGURE 2
ROC curves of mrTRG (1-2 vs. 3-5) alone **(A)** and mrTRG plus pretreatment biomarkers (NLR, LMR, PFR, CEA and all above four biomarkers) **(B–D)** for the prediction of pCR.

TABLE 4 AUC values of each roc curve.

Parameters	pCR	
	AUC (95% CI)	P[a)]
mrTRG	0.721 (0.589-0.830)	0.0003
mrTRG + NLR	0.774 (0.647-0.873)	0.0001
mrTRG + LMR	0.778 (0.651-0.876)	<0.0001
mrTRG + PFR	0.831 (0.711-0.916)	<0.0001
mrTRG + CEA	0.798 (0.674-0.892)	<0.0001
mrTRG + all above four biomarkers	0.913 (0.810-0.971)	<0.0001

pCR, pathologic complete response; mrTRG, tumor regression grade assessed by magnetic resonance imaging; CEA, carcinoembryonic antigen; NLR, neutrophil to lymphocyte ratio; LMR, lymphocyte to monocyte ratio; AFR, albumin to fibrinogen ratio; PFR, prealbumin to fibrinogen ratio. CI, confidence interval.
[a]P are for the comparison of each AUC and that of mrTRG based on DeLong's method.

as well as tumor-associated immune responses. Various inflammatory cells and inflammatory mediators are important components of the tumor microenvironment. For example, lymphocytes can induce cytotoxicity leading to tumor cell death and inhibit tumor cell proliferation and migration (27, 28). Sustained local and systemic inflammatory responses can be involved in the development, progression and prognosis of many malignancies through various mechanisms such as inhibition of DNA damage and apoptosis by inflammatory cytokines (29, 30). Malignancies can in turn lead to severe nutritional imbalances and even cachexia, directly activating proteolysis and lipolysis in target organs through a variety of pathways, such as pro-inflammatory factors with catabolic effects that can act as mediators of cachexia (31). This catabolism occurs mainly in skeletal muscle, adipose tissue, and myocardium, and its consequences include increased chemotherapy toxicity, complication rates of surgery, and increased mortality (32). In contrast, the cytotoxic effect of chemoradiotherapy causes necrosis of tumor cells and alters the local and systemic inflammatory response, thus increasing the recognition of tumor antigens by the body's immune system (33). Therefore, early assessment of the sensitivity of patients with malignant tumors to radiotherapy is essential.

In imaging, conventional rectal MRI is a classic tool for clinical assessment of rectal cancer staging and the effectiveness of neoadjuvant therapy. The application of apparent diffusion coefficient (ADC) values from diffusion-weighted imaging (DWI) to predict the tumor regression response after NCRT in rectal cancer has been studied (34–36). Some studies have investigated the performance of maximum standardized uptake values (SUVs) of 18F-FDG PET or its dynamics before and after NCRT in predicting pCR in rectal cancer patients (37, 38). However, many tools and parameters are currently not up to a uniform standard.

In recent years, some inflammatory biomarkers and nutritional biomarkers can directly or indirectly respond to the inflammatory response and nutritional status of the body and have been found to be independent prognostic factors in patients with rectal cancer treated with NCRT (39–43). Most of the previous studies have focused on one or a few biomarkers, exploring their relationship with the efficacy of neoadjuvant chemotherapy in rectal cancer (44–48). However, it is clear that no single biomarker is currently powerful enough to achieve accurate prediction independently, and new models combining blood biomarkers and imaging parameters can achieve better outcomes. In this study, valuable blood biomarkers were filtered and combined with mrTRG to take advantage of the unique advantages of the different parameters as much as possible. A common feature of previous studies is the conversion of the obtained biomarkers from continuous variables to dichotomous variables, thus grouping patients in a simple way. However, it generates the problem of using different cut-off values in different studies. We did not perform simple dichotomization of the raw data in this study. It not only avoids the problem of various cut-off values due to sample differences, but also retains the advantage of continuous variables.

Our study has a few limitations. First, since this is a retrospective study with limited sample size, the possibility of selection bias during data collection cannot be excluded. Second, the blood biomarkers analyzed in this study are non-specific and may be influenced by various physiological or pathological factors. Hence, their values can vary over time. Nevertheless, our study focused only on the predictive role of these blood biomarkers prior to NCRT. Moreover, to analyze the efficacy of NCRT in treating rectal cancer, the final results should be tracked to determine long-term patient outcomes. In this study, the biomarkers' long-term prognostic ability was not investigated. Thus, further large sample-sized studies are needed to determine these effects.

Conclusion

This study extensively screened a variety of valuable pre-neoadjuvant blood biomarkers, such as CEA, NLR, LMR, and PFR, that could serve as predictors of pathologic complete regression and help improve the performance of MRI in predicting the efficacy of neoadjuvant therapy in patients with locally advanced rectal cancer. Combining pretreatment blood

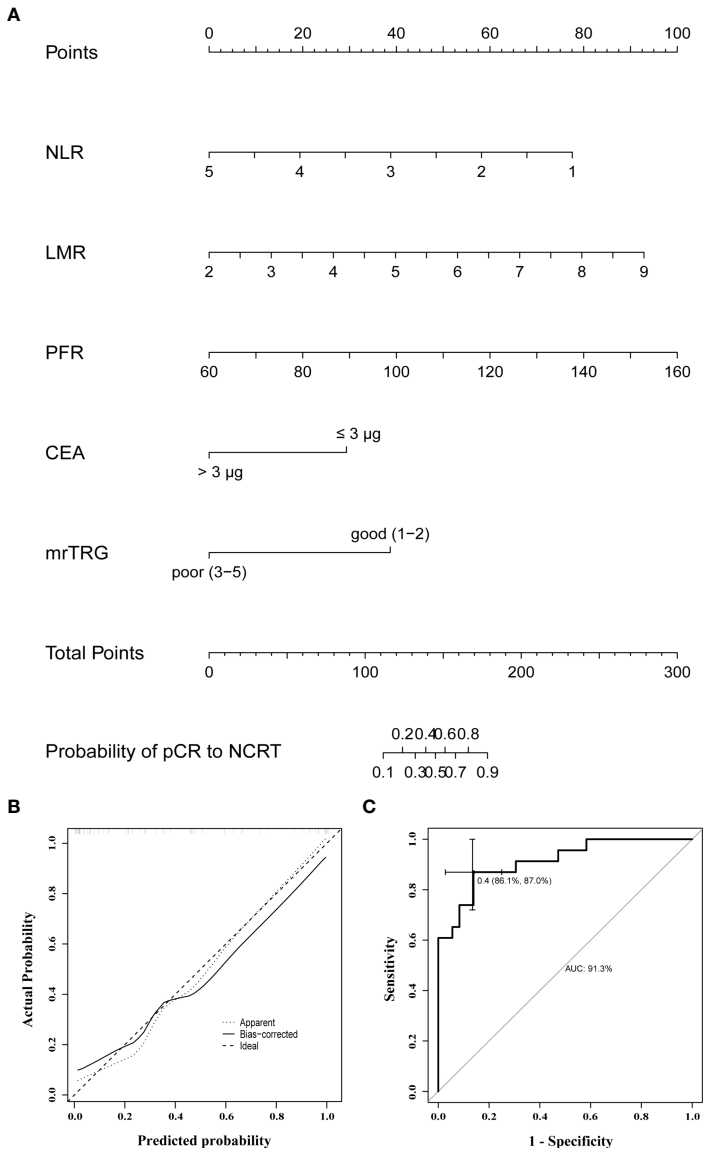

FIGURE 3
(A) A nomogram for predicting the probability of pCR to NCRT in LARC patients; **(B)** curves with internal validation for the nomogram; **(C)** ROC analysis of the nomogram. NCRT, neoadjuvant chemoradiotherapy; pCR, pathologic complete response; mrTRG, tumor regression grade assessed by magnetic resonance imaging; NLR, neutrophil to lymphocyte ratio; LMR, lymphocyte to monocyte ratio; PFR, prealbumin to fibrinogen ratio; CEA, carcinoembryonic antigen.

biomarkers with MRI metrics to create a clinical prediction model can effectively predict the efficacy of neoadjuvant therapy and thus help determine the optimal individual treatment regimen for LARC patients.

Data availability statement

The original contributions presented in the study are included in the article/supplementary material. Further inquiries can be directed to the corresponding author.

Ethics statement

The present retrospective study was approved by the Ethics Committee of the First Affiliated Hospital of Soochow University (Suzhou, China; approval no. 2022099), with a waiver of informed consent. Written informed consent for participation was not required for this study in accordance with the national legislation and the institutional requirements.

Author contributions

SH: design and guidance, study supervision, and critical revision of the manuscript. XS: statistical analysis of the data, interpretation of the significance of the outcome, and manuscript drafting. MZ: software application, and production of partial charts. BS, GC, HY, JC, DW and WG: data acquisition. All authors have made contributions to this article and agree with the final version of the article.

Funding

This work was supported by National Science Foundation (NSF) of Jiangsu Province of China grants (BK20191172), Project of Gusu Medical Key Talent of Suzhou City of China (GSWS2020005), and Project of New Pharmaceutics and Medical Apparatuses of Suzhou City of China (SLJ2021007).

Acknowledgments

The author's thank all staff working in the department of general surgery in the First Affiliated Hospital of Soochow University, Soochow, China.

Conflict of interest

The authors declare that the research was conducted in the absence of any commercial or financial relationships that could be construed as a potential conflict of interest.

Publisher's note

References

1. Sung H, Ferlay J, Siegel RL, Laversanne M, Soerjomataram I, Jemal A, et al. Global cancer statistics 2020: GLOBOCAN estimates of incidence and mortality worldwide for 36 cancers in 185 countries. *CA Cancer J Clin* (2021) 71(3):209–49. doi: 10.3322/caac.21660

2. Sauer R, Becker H, Hohenberger W, Rödel C, Wittekind C, Fietkau R, et al. Preoperative versus postoperative chemoradiotherapy for rectal cancer. *N Engl J Med* (2004) 351(17):1731–40. doi: 10.1056/NEJMoa040694

3. Song JH, Jeong JU, Lee JH, Kim SH, Cho HM, Um JW, et al. Preoperative chemoradiotherapy versus postoperative chemoradiotherapy for stage II-III resectable rectal cancer: A meta-analysis of randomized controlled trials. *Radiat Oncol J* (2017) 35(3):198–207. doi: 10.3857/roj.2017.00059

4. Fokas E, Allgäuer M, Polat B, Klautke G, Grabenbauer GG, Fietkau R, et al. Randomized phase II trial of chemoradiotherapy plus induction or consolidation chemotherapy as total neoadjuvant therapy for locally advanced rectal cancer: CAO/ARO/AIO-12. *J Clin Oncol* (2019) 37(34):3212–22. doi: 10.1200/JCO.19.00308

5. van der Valk MJM, Hilling DE, Bastiaannet E, Meershoek-Klein Kranenbarg E, Beets GL, Figueiredo NL, et al. Long-term outcomes of clinical complete responders after neoadjuvant treatment for rectal cancer in the international watch & wait database (IWWD): An international multicentre registry study. *Lancet* (2018) 391(10139):2537–45. doi: 10.1016/S0140-6736(18)31078-X

6. Renehan AG, Malcomson L, Emsley R, Gollins S, Maw A, Myint AS, et al. Watch-and-wait approach versus surgical resection after chemoradiotherapy for patients with rectal cancer (the OnCoRe project): A propensity-score matched cohort analysis. *Lancet Oncol* (2016) 17(2):174–83. doi: 10.1016/S1470-2045(15)00467-2

7. Dossa F, Chesney TR, Acuna SA, Baxter NN. A watch-and-wait approach for locally advanced rectal cancer after a clinical complete response following neoadjuvant chemoradiation: A systematic review and meta-analysis. *Lancet Gastroenterol Hepatol* (2017) 2(7):501–13. doi: 10.1016/S2468-1253(17)30074-2

8. Park IJ, You YN, Agarwal A, Skibber JM, Rodriguez-Bigas MA, Eng C, et al. Neoadjuvant treatment response as an early response indicator for patients with rectal cancer. *J Clin Oncol* (2012) 30(15):1770–6. doi: 10.1200/JCO.2011.39.7901

9. Patel UB, Taylor F, Blomqvist L, George C, Evans H, Tekkis P, et al. Magnetic resonance imaging-detected tumor response for locally advanced rectal cancer predicts survival outcomes: MERCURY experience. *J Clin Oncol* (2011) 29(28):3753–60. doi: 10.1200/JCO.2011.34.9068

10. van der Paardt MP, Zagers MB, Beets-Tan RG, Stoker J, Bipat S. Patients who undergo preoperative chemoradiotherapy for locally advanced rectal cancer restaged by using diagnostic MR imaging: A systematic review and meta-analysis. *Radiology* (2013) 269(1):101–12. doi: 10.1148/radiol.13122833

11. Leach MO, Brindle KM, Evelhoch JL, Griffiths JR, Horsman MR, Jackson A, et al. The assessment of antiangiogenic and antivascular therapies in early-stage clinical trials using magnetic resonance imaging: issues and recommendations. *Br J Cancer* (2005) 92(9):1599–610. doi: 10.1038/sj.bjc.6602550

12. Pham TT, Liney GP, Wong K, Barton MB. Functional MRI for quantitative treatment response prediction in locally advanced rectal cancer. *Br J Radiol* (2017) 90(1072):20151078. doi: 10.1259/bjr.20151078

13. Tang Z, Zhang XY, Liu Z, Li XT, Shi YJ, Wang S, et al. Quantitative analysis of diffusion weighted imaging to predict pathological good response to neoadjuvant chemoradiation for locally advanced rectal cancer. *Radiother Oncol* (2019) 132:100–8. doi: 10.1016/j.radonc.2018.11.007

14. Delli Pizzi A, Caposiena D, Mastrodicasa D, Trebeschi S, Lambregts D, Rosa C, et al. Tumor detectability and conspicuity comparison of standard b1000 and ultrahigh b2000 diffusion-weighted imaging in rectal cancer. *Abdom Radiol (NY)* (2019) 44(11):3595–605. doi: 10.1007/s00261-019-02177-y

15. Braun LH, Baumann D, Zwirner K, Eipper E, Hauth F, Peter A, et al. Neutrophil-to-Lymphocyte ratio in rectal cancer-novel biomarker of tumor immunogenicity during radiotherapy or confounding variable? *Int J Mol Sci* (2019) 20(10):2448. doi: 10.3390/ijms20102448

16. Zhang Y, Liu X, Xu M, Chen K, Li S, Guan G. Prognostic value of pretreatment systemic inflammatory markers in patients with locally advanced rectal cancer following neoadjuvant chemoradiotherapy. *Sci Rep* (2020) 10(1):8017. doi: 10.1038/s41598-020-64684-z

17. Deng YX, Lin JZ, Peng JH, Zhao YJ, Sui QQ, Wu XJ, et al. Lymphocyte-to-monocyte ratio before chemoradiotherapy represents a prognostic predictor for locally advanced rectal cancer. *Onco Targets Ther* (2017) 10:5575–83. doi: 10.2147/OTT.S146697

18. Dolan RD, Alwahid M, McSorley ST, Park JH, Stevenson RP, Roxburgh CS, et al. A comparison of the prognostic value of composite ratios and cumulative scores in patients with operable rectal cancer. *Sci Rep* (2020) 10(1):17965. doi: 10.1038/s41598-020-73909-0

19. Wang YY, Liu ZZ, Xu D, Liu M, Wang K, Xing BC. Fibrinogen-albumin ratio index (FARI): A more promising inflammation-based prognostic marker for patients undergoing hepatectomy for colorectal liver metastases. *Ann Surg Oncol* (2019) 26(11):3682–92. doi: 10.1245/s10434-019-07586-3

20. Wang Y, Chen L, Zhang B, Song W, Zhou G, Xie L, et al. Pretreatment inflammatory-nutritional biomarkers predict responses to neoadjuvant

chemoradiotherapy and survival in locally advanced rectal cancer. *Front Oncol* (2021) 11:639909. doi: 10.3389/fonc.2021.639909

21. Li A, He K, Guo D, Liu C, Wang D, Mu X, et al. Pretreatment blood biomarkers predict pathologic responses to neo-CRT in patients with locally advanced rectal cancer. *Future Oncol* (2019) 15(28):3233–42. doi: 10.2217/fon-2019-0389

22. Sun Y, Huang Z, Chi P. An inflammation index-based prediction of treatment response to neoadjuvant chemoradiotherapy for rectal mucinous adenocarcinoma. *Int J Clin Oncol* (2020) 25(7):1299–307. doi: 10.1007/s10147-020-01670-5

23. Kim TG, Park W, Kim H, Choi DH, Park HC, Kim SH, et al. Baseline neutrophil-lymphocyte ratio and platelet-lymphocyte ratio in rectal cancer patients following neoadjuvant chemoradiotherapy. *Tumori* (2019) 105(5):434–40. doi: 10.1177/0300891618792476

24. Yoo GS, Park HC, Yu JI, Choi DH, Cho WK, Park YS, et al. Carcinoembryonic antigen improves the performance of magnetic resonance imaging in the prediction of pathologic response after neoadjuvant chemoradiation for patients with rectal cancer. *Cancer Res Treat* (2020) 52 (2):446–54. doi: 10.4143/crt.2019.261

25. Roels S, Duthoy W, Haustermans K, Penninckx F, Vandecaveye V, Boterberg T, et al. Definition and delineation of the clinical target volume for rectal cancer. *Int J Radiat Oncol Biol Phys* (2006) 65(4):1129–42. doi: 10.1016/j.ijrobp.2006.02.050

26. Schrag D, Weiser MR, Goodman KA, Gonen M, Cercek A, Reidy DL, et al. Neoadjuvant FOLFOX-bev, without radiation, for locally advanced rectal cancer. *J Clin Oncol* (2010) 28(Suppl):15S. doi: 10.1200/jco.2010.28.15_suppl.3511

27. Kim HJ, Choi GS, Park JS, Park S, Kawai K, Watanabe T. Clinical significance of thrombocytosis before preoperative chemoradiotherapy in rectal cancer: Predicting pathologic tumor response and oncologic outcome. *Ann Surg Oncol* (2015) 22(2):513–9. doi: 10.1245/s10434-014-3988-8

28. Ferrone C, Dranoff G. Dual roles for immunity in gastrointestinal cancers. *J Clin Oncol* (2010) 28(26):4045–51. doi: 10.1200/JCO.2010.27.9992

29. Mantovani A, Allavena P, Sica A, Balkwill F. Cancer-related inflammation. *Nature* (2008) 454(7203):436–44. doi: 10.1038/nature07205

30. Mishra A, Liu S, Sams GH, Curphey DP, Santhanam R, Rush LJ, et al. Aberrant overexpression of IL-15 initiates large granular lymphocyte leukemia through chromosomal instability and DNA hypermethylation. *Cancer Cell* (2012) 22(5):645–55. doi: 10.1016/j.ccr.2012.09.009

31. Baracos VE, Martin L, Korc M, Guttridge DC, Fearon KCH. Cancer-associated cachexia. *Nat Rev Dis Primers* (2018) 4:17105. doi: 10.1038/nrdp.2017.105

32. Kazemi-Bajestani SM, Mazurak VC, Baracos V. Computed tomography-defined muscle and fat wasting are associated with cancer clinical outcomes. *Semin Cell Dev Biol* (2016) 54:2–10. doi: 10.1016/j.semcdb.2015.09.001

33. Ko EC, Formenti SC. Radiotherapy and checkpoint inhibitors: A winning new combination? *Ther Adv Med Oncol* (2018) 10:1758835918768240. doi: 10.1177/1758835918768240

34. Bulens P, Couwenberg A, Haustermans K, Debucquoy A, Vandecaveye V, Philippens M, et al. Development and validation of an MRI-based model to predict response to chemoradiotherapy for rectal cancer. *Radiother Oncol* (2018) 126 (3):437–42. doi: 10.1016/j.radonc.2018.01.008

35. Barbaro B, Vitale R, Valentini V, Illuminati S, Vecchio FM, Rizzo G, et al. Diffusion-weighted magnetic resonance imaging in monitoring rectal cancer response to neoadjuvant chemoradiotherapy. *Int J Radiat Oncol Biol Phys* (2012) 83(2):594–9. doi: 10.1016/j.ijrobp.2011.07.017

36. Lambrecht M, Vandecaveye V, De Keyzer F, Roels S, Penninckx F, Van Cutsem E, et al. Value of diffusion-weighted magnetic resonance imaging for prediction and early assessment of response to neoadjuvant radiochemotherapy in rectal cancer: Preliminary results. *Int J Radiat Oncol Biol Phys* (2012) 82(2):863–70. doi: 10.1016/j.ijrobp.2010.12.063

37. Murcia Duréndez MJ, Frutos Esteban L, Luján J, Frutos MD, Valero G, Navarro Fernández JL, et al. The value of 18F-FDG PET/CT for assessing the response to neoadjuvant therapy in locally advanced rectal cancer. *Eur J Nucl Med Mol Imaging* (2013) 40(1):91–7. doi: 10.1007/s00259-012-2257-y

38. Leccisotti L, Gambacorta MA, de Waure C, Stefanelli A, Barbaro B, Vecchio FM, et al. The predictive value of 18F-FDG PET/CT for assessing pathological response and survival in locally advanced rectal cancer after neoadjuvant radiochemotherapy. *Eur J Nucl Med Mol Imaging* (2015) 42(5):657–66. doi: 10.1007/s00259-014-2820-9

39. Yang J, Xu H, Guo X, Zhang J, Ye X, Yang Y, et al. Pretreatment inflammatory indexes as prognostic predictors for survival in colorectal cancer patients receiving neoadjuvant chemoradiotherapy. *Sci Rep* (2018) 8(1):3044. doi: 10.1038/s41598-018-21093-7

40. Jung SW, Park IJ, Oh SH, Yeom SS, Lee JL, Yoon YS, et al. Association of immunologic markers from complete blood counts with the response to preoperative chemoradiotherapy and prognosis in locally advanced rectal cancer. *Oncotarget* (2017) 8(35):59757–65. doi: 10.18632/oncotarget.15760

41. An L, Yin W-T, Sun D-W. Albumin-to-alkaline phosphatase ratio as a promising indicator of prognosis in human cancers: Is it possible? *BMC Cancer* (2021) 21(1):247. doi: 10.1186/s12885-021-07921-6

42. Ishikawa D, Nishi M, Takasu C, Kashihara H, Tokunaga T, Higashijima J, et al. The role of neutrophil-to-lymphocyte ratio on the effect of CRT for patients with rectal cancer. *In Vivo* (2020) 34(2):863–8. doi: 10.21873/*in vivo*.11850

43. Li H, Wang H, Shao S, Gu Y, Yao J, Huang J. Pretreatment albumin-to-Fibrinogen ratio independently predicts chemotherapy response and prognosis in patients with locally advanced rectal cancer undergoing total mesorectal excision after neoadjuvant chemoradiotherapy. *Onco Targets Ther* (2020) 13:13121–30. doi: 10.2147/OTT.S288265

44. Okugawa Y, Toiyama Y, Oki S, Ide S, Yamamoto A, Ichikawa T, et al. Feasibility of assessing prognostic nutrition index in patients with rectal cancer who receive preoperative chemoradiotherapy. *JPEN J Parenter Enteral Nutr* (2018) 42(6):998–1007. doi: 10.1002/jpen.1041

45. Xiao WW, Zhang LN, You KY, Huang R, Yu X, Ding PR, et al. A low lymphocyte-to-Monocyte ratio predicts unfavorable prognosis in pathological T3N0 rectal cancer patients following total mesorectal excision. *J Canc* (2015) 6 (7):616–22. doi: 10.7150/jca.11727

46. Nozoe T, Kohno M, Iguchi T, Mori E, Maeda T, Matsukuma A, et al. The prognostic nutritional index can be a prognostic indicator in colorectal carcinoma. *Surg Today* (2012) 42(6):532–5. doi: 10.1007/s00595-011-0061-0

47. Dayde D, Tanaka I, Jain R, Tai MC, Taguchi A. Predictive and prognostic molecular biomarkers for response to neoadjuvant chemoradiation in rectal cancer. *Int J Mol Sci* (2017) 18(3):573. doi: 10.3390/ijms18030573

48. Tokunaga R, Sakamoto Y, Nakagawa S, Izumi D, Kosumi K, Taki K, et al. Comparison of systemic inflammatory and nutritional scores in colorectal cancer patients who underwent potentially curative resection. *Int J Clin Oncol* (2017) 22 (4):740–8. doi: 10.1007/s10147-017-1102-5

frontiers | Frontiers in Oncology

ORIGINAL RESEARCH
published: 10 August 2022
doi: 10.3389/fonc.2022.881439

Dosimetric Evaluation of Commercially Available Flat vs. Self-Produced 3D-Conformal Silicone Boluses for the Head and Neck Region

Stephan Pollmann, André Toussaint, Michael Flentje, Sonja Wegener and Victor Lewitzki*

University Hospital Würzburg, Würzburg, Germany

Background: Boluses are routinely used in radiotherapy to modify surface doses. Nevertheless, considerable dose discrepancies may occur in some cases due to fit inaccuracy of commercially available standard flat boluses. Moreover, due to the simple geometric design of conventional boluses, also surrounding healthy skin areas may be unintentionally covered, resulting in the unwanted dose buildup. With the fused deposition modeling (FDM) technique, there is a simple and possibly cost-effective way to solve these problems in routine clinical practice. This paper presents a procedure of self-manufacturing bespoke patient-specific silicone boluses and the evaluation of buildup and fit accuracy in comparison to standard rectangular commercially available silicone boluses.

Methods: 3D-conformal silicone boluses were custom-built to cover the surgical scar region of 25 patients who received adjuvant radiotherapy of head and neck cancer at the University Hospital Würzburg. During a standard CT-based planning procedure, a 5-mm-thick 3D bolus contour was generated to cover the radiopaque marked surgical scar with an additional safety margin. From these digital contours, molds were 3D printed and poured with silicone. Dose measurements for both types of boluses were performed with radiochromic films (EBT3) at three points per patient—at least one aimed to be in the high-dose area (scar) and one in the lower-dose area (spared healthy skin). Surface–bolus distance, which ideally should not be present, was determined from cone-beam CT performed for positioning control. The dosimetric influence of surface–bolus distance was also determined on slab phantom for different field sizes. The trial was performed with hardware that may be routinely available in every radiotherapy department, with the exception of the 3D printer. The required number of patients was determined based on the results of preparatory measurements with the help of the statistical consultancy of the University of Würzburg. The number of measuring points represents the total number of patients.

Results: In the high-dose area of the scar, there was a significantly better intended dose buildup of 2.45% (95%CI 0.0014–0.0477, p = 0.038, N = 30) in favor of a 3D-conformal bolus. Median distances between the body surface and bolus differed significantly between 3D-conformal and commercially available boluses (3.5 vs. 7.9 mm, p = 0.001).

OPEN ACCESS

Edited by:
Yingli Yang,
UCLA Health System, United States

Reviewed by:
Hyejoo Kang,
Loyola University Chicago, United States
Gozde Yazici,
Hacettepe University, Turkey

****Correspondence:***
Stephan Pollmann
stephan.pollmann@stud-mail.uni-wuerzburg.de

Specialty section:
This article was submitted to Radiation Oncology, a section of the journal Frontiers in Oncology

Received: *22 February 2022*
Accepted: *21 June 2022*
Published: *10 August 2022*

Citation:
Pollmann S, Toussaint A, Flentje M, Wegener S and Lewitzki V (2022) Dosimetric Evaluation of Commercially Available Flat vs. Self-Produced 3D-Conformal Silicone Boluses for the Head and Neck Region. Front. Oncol. 12:881439. doi: 10.3389/fonc.2022.881439

The surface dose at the slab phantom did not differ between commercially available and 3D-conformal boluses. Increasing the surface–bolus distance from 5 to 10 mm decreased the surface dose by approximately 2% and 11% in the 6 × 6- and 3 × 3-cm^2 fields, respectively. In comparison to the commercially available bolus, an unintended dose buildup in the healthy skin areas was reduced by 25.9% (95%CI 19.5–32.3, $p < 0.01$, N = 37) using the 3D-conformal bolus limited to the region surrounding the surgical scar.

Conclusions: Using 3D-conformal boluses allows a comparison to the commercially available boluses' dose buildup in the covered areas. Smaller field size is prone to a larger surface–bolus distance effect. Higher conformity of 3D-conformal boluses reduces this effect. This may be especially relevant for volumetric modulated arc therapy (VMAT) and intensity-modulated radiotherapy (IMRT) techniques with a huge number of smaller fields. High conformity of 3D-conformal boluses reduces an unintended dose buildup in healthy skin. The limiting factor in the conformity of 3D-conformal boluses in our setting was the immobilization mask, which was produced primarily for the 3D boluses. The mask itself limited tight contact of subsequently produced 3D-conformal boluses to the mask-covered body areas. In this respect, bolus adjustment before mask fabrication will be done in the future setting.

Keywords: flat silicone bolus, individual silicone bolus, 3D conformal silicone bolus, 3D printer, head and neck cancer, fused deposition modeling (FDM), surface dose measurement, volumetric modulated arc therapy (VMAT)

INTRODUCTION

In radiotherapy, the 3D printing fused deposition modeling (FDM) technique introduced by Crump (1) has been used in a variety of ways including the creation of individualized phantoms, brachytherapy applicators, or intraoral stents (2–4). The fabrication of individualized boluses *via* 3D printing represents another application of this technique.

Bolus material can effectively modify the radiation dose to the skin and mucosal surfaces (5–7). Liquid-impregnated gauzes, wax, gel, and silicone overlays are conventionally used for this purpose. In this context, a transition between bolus and skin that is as seamless as possible is crucial for the predictability of dose distribution, as even small gaps can lead to significant superficial dose reductions and dose inhomogeneity (8–12).

A literature review by Pugh et al. showed that the improved surface conformity of 3D-printed boluses could prove beneficial for volumetric modulated arc therapy (VMAT), as the presence of air gaps can result in a 10% reduction in surface dose for small field sizes and oblique incident beams (13).

Gaps under commercially available boluses are commonly observed in the head and neck region, as irregularities on the surface can lead to wrinkling or poor bolus formability. Furthermore, since VMAT with numerous small fields prone to the dose effects of increased surface–bolus distance plays a prominent role in the treatment of head and neck tumors, bolus conformity may be of importance. A simultaneous reduction of the bolus cover on healthy skin enabled by the bolus individualization may reduce side effects.

Individual boluses produced *via* 3D printing are typically made of solid plastics and have been tested in numerous dosimetric analyses (13–18). A major drawback of this design is the low flexibility and thus patient comfort. The use of new 3D printing techniques such as FDM may offer the possibility to produce cost-effective, individual, and flexible boluses for routine clinical use (19–24). Therefore, in this study, we combined FDM with a silicone casting process so that we were able to get flexible 3D-compliant boluses and implement the attachment into routine clinical workflow.

Previous studies of 3D-conformal flexible boluses did not pay attention to the dose effects outside the covered area. The merits of 3D-conformal boluses in terms of accuracy of superficial dose application have so far been demonstrated in the context of simulations and phantom measurements (8–12). This adds to the clinical advantage of adjusting the bolus configuration to the individual patient situation. A detailed investigation of economic and clinical aspects however was not planned yet.

While a comparable production process of a flexible bolus was already described (18), existing studies are limited to the evaluation by means of a static anthropomorphic phantom and recalculation using the therapy planning system (TPS) (16, 25). Further, to our knowledge, there are no reports of an evaluation of the fit accuracy for patients and the dosimetric characteristics using *in vivo* dosimetry.

The aim of this study was to investigate dose coverage of superficial target volumes (surgical scars) with the simultaneous investigation of dose reduction in surrounding healthy skin by *in*

Abbreviations: CBCT, cone-beam CT; DICOM, digital imaging and communications in medicine; FDM, fused deposition modeling; HUs, Hounsfield units; IMRT, intensity-modulated radiotherapy; MU, monitor units; STL, standard triangulation language; TPS, therapy planning system; VMAT, volumetric modulated arc therapy.

vivo dosimetry with 3D-conformal and commercially available silicone boluses. A standardized workflow for bolus production was also introduced. Radiochromic films were used to evaluate dose buildup and to quantify the influence of gaps between bolus and skin. The conformity of the 3D-printed boluses was investigated by measuring the distance between bolus and skin in the TPS.

MATERIALS AND METHODS

Equivalence of Materials

To test the equivalence of materials from conventional and individual boluses with respect to dose buildup, six measurements each were performed using MOSFET-live dosimetry on the slab phantom. For this purpose, a commercially available bolus and a flat-cast self-produced bolus were used, each with a layer thickness of 0.5 cm and an area of 30 cm × 30 cm. Irradiation was performed with the fixed number of 100 monitor units (MUs) at a focus-slab phantom distance of 100 cm in standing field technique with a nominal field size of 10 × 10 cm^2 on a Siemens linear accelerator (model Siemens Primus Mevatron M, 6 MV).

Influence of Bolus–Surface Distance and Field Size on Dose Reduction

To estimate the influence of surface–bolus distance and field size on the dose reduction, EBT3-film measurements were performed on the surface of a slab phantom. For this purpose, a conventional bolus with a size of 30 × 30 cm^2 was placed parallel to the slab phantom surface at different heights (0, 5, 10, and 20 mm) and irradiated at different field sizes (1 × 1, 2 × 2, 3 × 3, 4 × 4, and 6 × 6 cm^2). 3D-printed spacers with very thin support structures of varying heights were used at a distance of 4 cm from the central beam axis for suspension of the boluses. The irradiation was performed in the static field technique with a Siemens linear accelerator (Siemens Primus Mevatron M, 6 MV) with 200 MUs. The experimental setup is shown in **Figure 1**.

Preparation of the Individual Bolus

First, molds for flabs with edge lengths of 10 × 10 × 0.5 cm were printed, and the dimensions of the casting product were checked for quality assurance.

The planning CTs of 25 patients receiving adjuvant radiotherapy of the head and neck were exported to the TPS

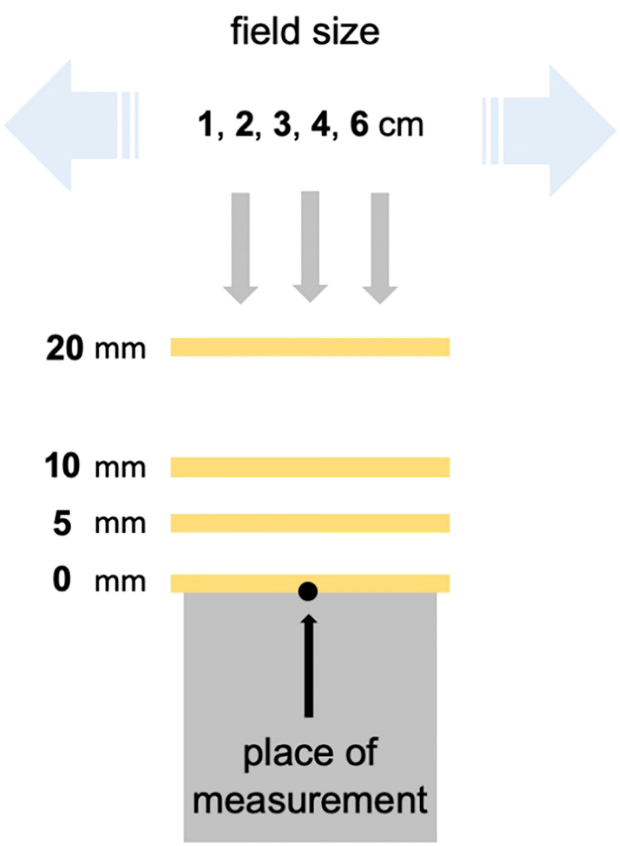

FIGURE 1 | Experimental setup to estimate the influence of distance and field size on dose reduction.

Pinnacle®. An appropriate treatment plan was then determined by the treating radiation oncologist. A virtual 5-mm-thick bolus contour (brown contour, **Figure 2A**) with a virtual density of 1 g cm^{-3} was generated by TPS. The fiducial marking of the target volume (surgical scar) was located and manually drawn along its course for each CT slice (purple contour, **Figure 2A**). The contour indicating the course of the scar was subsequently radially expanded by 2.4 cm to ensure reliable scar coverage (blue contour, **Figure 2A**). With a radius of 2.4 cm around the marker and a CT layer thickness of 3 mm, an even number of layers in the orthogonal direction was obtained. The intersection of the brown and blue volumes was defined as the individual bolus contour (green contour, **Figure 2A**). From this template, a silicone bolus was produced and is shown in **Figure 2B** for comparison. **Figure 2C** shows a commercially available bolus.

The 3D-conformal bolus contour was exported as a digital imaging and communications in medicine (DICOM) file and converted to standard triangulation language (STL) format using slicing software (3D-Slicer, Version 4.10.2, Slicer Community). This step enabled further processing in 3D printing software (Meshmixer, Version 3.5, Autodesk Inc.). To reduce the time of 3D printing and improve the conformity of the bolus, the surface of the contour was smoothed (**Figure 3**).

The processed and optimized contour was converted into a corresponding casting mold using "Ultimaker Cura" (Version 4.4.1). An automated Cura print profile (**Table 1**) was defined for this application.

Two differently colored crosslinking silicones (Wagnersil 9N, Wagner Dental GmbH & Co. KG) with a density of 1.05 g cm^{-3} and silicone oil (density of 0.97 g cm^{-3}) were selected to fill the casting mold. The two silicone components were prepared in a 1:1 ratio. The overall mixing ratio of silicone to silicone oil was 70%:30% v/v due to its ideal softening effect. The mixture was stirred slowly with a glass rod until homogeneous coloration was observed for maximum crosslinking. Afterward, the mixture was filled into the mold, which was printed out of polylactide (PLA NX1, 1.75 mm, white, Extrudr, FD3D GmbH). Air bubbles could be avoided in previous experiments by stirring and filling the silicone slowly. After complete filling of the mold, a minimum time of 30 min was given for the crosslinking reaction before the covering mold was removed (**Figure 4**).

Dosimetric Investigation of Individual Boluses in Clinical Practice

Three consecutive measurements were made using the commercially available bolus at first and then three more were made subsequently using the 3D-conformal bolus. Both kinds of bolus were placed outside the immobilization mask. Therefore, radiochromic films (8 mm × 10 mm) were placed at three positions located inside the irradiation field. At least one of these was located in the expected high-dose area, directly on the visible surgical scar and preferably in the concave area. Another measurement was taken in the area of healthy skin, which was spared by the individual bolus. The localization of the third position varied depending on the feasibility of these two modalities. These positions were marked with metal pellets; on another day, a cone-beam CT (CBCT) was regularly scheduled. Irradiation of patient plans was performed with an Elekta Versa HD linear accelerator at 6 MV. The single

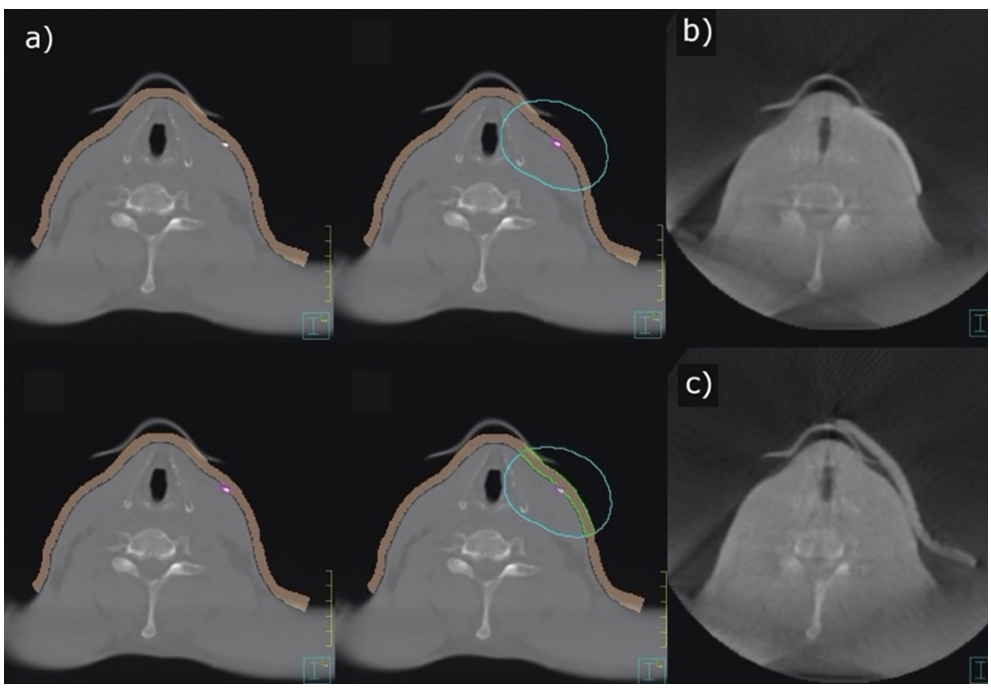

FIGURE 2 | Contouring of an individual bolus **(A)**, 3D-conformal bolus **(B)**, and commercially available bolus **(C)**.

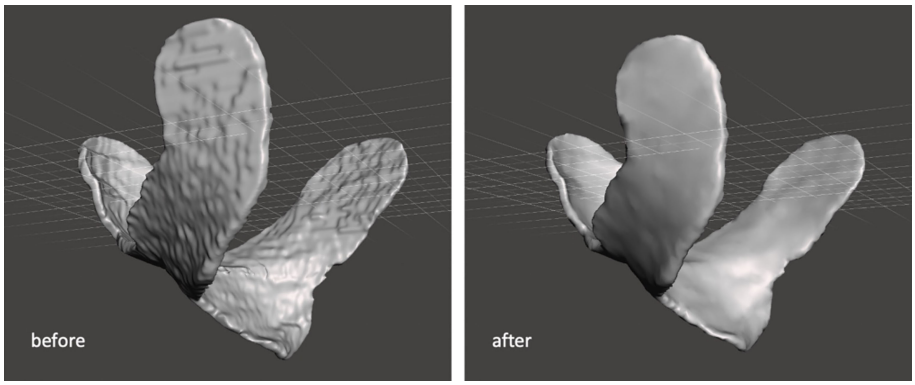

FIGURE 3 | Smoothing the contour of 3D-conformal bolus.

TABLE 1 | Setting of the automated Cura print profile.

Parameter	Setting
Layer height	0.2 mm
Wall thickness	0.8 mm
Wall line count	2
Top/bottom thickness	0.8 mm
Top/bottom layers	4
Infill density	5%
Infill pattern	Gyroid
Printing temperature	205°C
Build plate temperature	60°C
Enable retraction	Yes
Print speed	70 mm/s
Z hop when retracted	Yes
Enable print cooling	Yes
Fan speed	100%
Build plate adhesion type	Brim
Mold mode	On
Minimal mold width	0.8 mm
Mold roof height	0.8 mm
Mold angle	60°
Supports	Outside only

prescribed dose varied from 1.8 to 2.0 to 2.2 Gy (D95) with a simultaneous integrated boost (SIB) according to the risk profile of the corresponding treatment volume.

The films were read out 1 week after the measurement as stated in the manufacturer's instructions. One CBCT with the commercially available bolus, one CBCT with the 3D-conformal bolus, and the CBCT with the marker were imported into the TPS. The Pinnacle Windowing Protocol "Head" (window, 326; level, 900; L+W, 1226 RAW) was chosen, and the distances between the skin and both boluses were measured at the positions indicated by the markers. All materials and programs are listed in **Table 2**.

RESULTS

Equivalence of Materials

Doses at the surface of the slab phantom only changed insignificantly under conventional and cast boluses (under conventional bolus, mean = 101.5 cGy, SD = 1.8 cGy; under individual bolus, mean = 103.3 cGy, SD = 1.8 cGy). Both materials could therefore be considered comparable for dose buildup.

Influence of Field Size and Bolus–Surface Distance on Dose

The measured values given in **Table 3** as a percentage dose are shown graphically in **Figure 5**. It can be shown that dose reduction due to bolus elevation increases with decreasing field size. While an increase of the surface–bolus distance from 0 to 5 mm still led to a dose reduction of 28.7% for a field size of 1 cm^2, the dose was reduced by only 4.3% for a field size of 2 cm^2. Likewise, an increase of the air gap from 0 to 10 mm resulted in a greater relative dose reduction than a further increase from 10 to 20 mm in all cases.

Dosimetric Evaluation of Individual Boluses

Across all patients, there were 75 different locations that could be measured. Of these, at a total of 30 different positions, a surface dose could be determined in the scar region under conventional and individual boluses (**Figure 6**). These shown doses are the mean of three single fractions measured by film dosimetry with SDs indicated. The quotient of the surface doses under conventional and individual boluses reveals relative dose increase or decrease. A dependent t-test shows a significant dose difference of +2.45% in the scar region under individual boluses (95%CI 0.0014–0.0477, $p < 0.05$, $N = 30$) in comparison to standard ones.

A total of 37 different positions could be determined at which it was possible to avoid covering healthy skin (sparing) by applying individual boluses (**Figure 7**). The stated doses are the mean value from three single doses as well. A dependent t-test shows a significant dose reduction of 25.9% on skin spared by the omitted bolus coverage (95%CI 19.5–32.3, $p < 0.01$, $N = 37$).

At a total of 8 measurement points, neither of the first two criteria was applied, as the measuring point was located under both the individual and conventional boluses but not directly on a scar due to other inadequate attachment options. These points had to be removed from the evaluation.

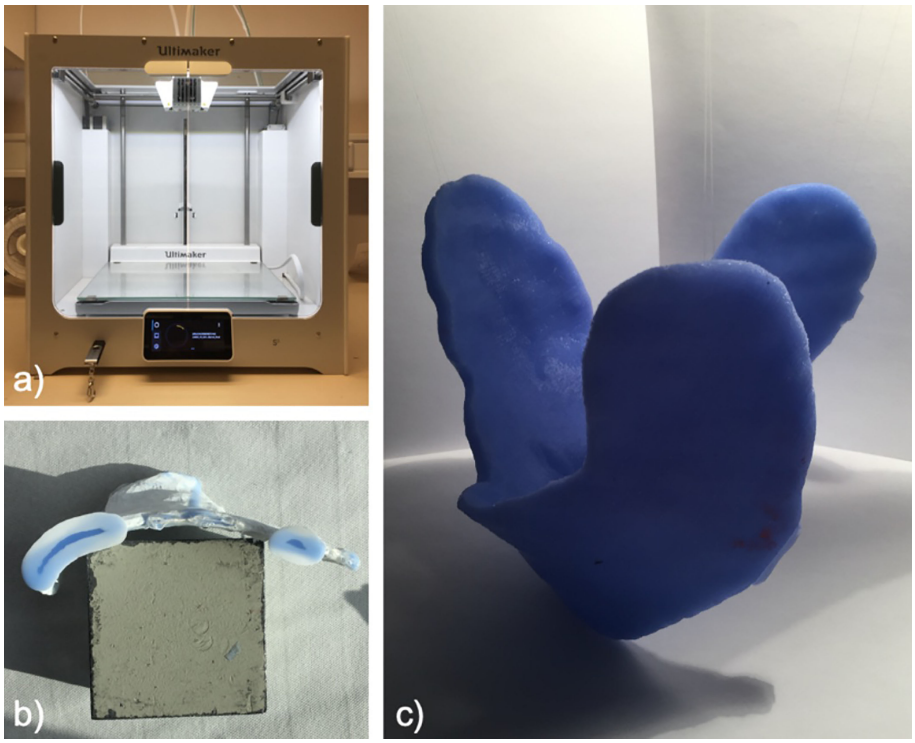

FIGURE 4 | Preparation of the mold with 3D printer **(A)**, mold **(B)**, and individual bolus **(C)**.

Surface–bolus distances could be measured at 36 different measurement sites under conventional boluses, while 37 measurement points could be determined under individual boluses.

The two populations were compared using a Wilcoxon test on connected samples. The median spacing (50th percentile) under individual and conventional boluses differed significantly (3.5 vs. 7.9 mm, $p = 0.001$). Thus, individual bolus adjustment resulted in a significant distance reduction (Δ surface–bolus distance). The results are shown in **Figure 8**. Points 11 and 42 represent statistical outliers.

DISCUSSION

The production of a flexible individual silicone bolus following the suggested procedure was feasible. All boluses endured the mechanical stress during the whole course of the treatment. Measurements on the slab phantom confirmed the dosimetric equivalence of the silicone bolus.

The majority of dose measurements on the scar region are consistent with the expected dose range between the D95 prescription levels of 180 cGy for the lower dose target volume and 220 cGy for the higher dose target volume. Details depend on the location of the individual measurement points in relation to the target volumes and dose distributions. A small but statistically significant increase of the measured dose on the scar region for individual bolus was demonstrated. At the same time, a statistically relevant decrease of the air gap size by 4.4 mm was found. In general, as shown in the slab phantom measurements, the surface dose decreases with increasing gap size. Therefore, the observations seem consistent.

The measured increase in dose buildup may be partly due to the better fit, but irregularities in the bolus thickness may also be a cause. The individual bolus provided approximately 5 ± 0.5 mm of buildup material due to material and thickness accuracy. Therefore, we would expect dose variations of up to 3%, and the measured dose increase of 2.45% is in this range.

In areas of large surface slope gradients (e.g., mandible and neck), the determination of the surface–bolus distance at the point of measurement is challenging. Surface–bolus distances represent an average of measurements from three adjacent CT slices. Further, all stated distance measurements in the transverse plane are performed perpendicular to the patient's surface. The gap size can differ slightly from the projection of the orthogonal beam direction typically encountered using the VMAT technique. In addition, a field size dependence of the dose reduction at different air gap sizes was observed in the slab phantom.

Omission of unintended skin coverage by bolus resulted in a statistically significant dose reduction of 25.9%. Thus, the resulting dose distributions using individual bolus provided adequate buildup in the scar region and improved sparing of healthy skin.

TABLE 2 | Materials and programs.

Materials and programs	Name of product	Manufacturer
3D printer	Ultimaker S5	Ultimaker B.V., Utrecht, Netherlands
3D printing software	Ultimaker Cura, Version 4.4.1	http://ultimaker.com (Open Source)
Commercially available bolus	Superflab, No. 8117-0.5	Mick Radio-Nuclear Instruments, Inc. An Eckert & Ziegler BEBIG Company, Mount Vernon, USA
Film dosimetry	Gafchromic™ EBT3 Dose range, 0.1 cGy to 10 Gy	Ashland Advanced Materials, Bridgewater, USA
Film dosimetry software	Film QA Pro 2015, Version 5.0.5603.15737	Ashland™ Inc., Covington, USA
Linear accelerator	Siemens Primus Mevatron M 6 MV, Elekta Versa HD™	ELEKTA Instrument AB, Kungstensgatan 18, 113 57 Stockholm, Sweden
Modeling software	Meshmixer, Version 3.5	Autodesk Inc. www.meshmixer.com (Open Source)
MOSFET	MOSFET 20	Thomson & Nielsen Electronics Ltd., Ottawa, Kanada
PLA coil	PLA NX1, 2.85 mm, white	Extrudr, FD3D GmbH, Lauterach, Austria
Slab phantom	RW3 Slab Phantom	PTW-Freiburg, Freiburg im Breisgau, Germany
Therapy planning system	Pinnacle$^{3®}$, Version 16.2	Philips Medical Systems, Hamburg, Germany
Scanner	EPSON® Expression 11000XL	Seiko Epson Corporation, Suwa, Nagano, Japan
Silicone component 1	Wagnersil 9N Premium Dubliersilikon 1:1 Additionsvernetzender RTV-2K Silikonkautschuk	Wagner Dental GmbH & Co. KG, Hückelhoven, Germany
Silicone component 2	Wagnersil 9N Premium Dubliersilikon 1:1 Additionsvernetzender RTV-2K Silikonkautschuk	Wagner Dental GmbH & Co. KG, Hückelhoven, Germany
Slicing software	3D-Slicer, Version 4.10.2	Slicer Community www.slicer.org (Open Source)
Silicone oil	Wagnersil S200 Hochreines, farbloses, geruchloses Silikonöl	Wagner Dental GmbH & Co. KG, Hückelhoven, Germany

The PLA coil in table 1 has a thickness of 2.85 mm.

TABLE 3 | Relative dose according to field size and surface bolus distance in mm.

Field size [cm × cm]	Absolute and Relative dose at distance 0 mm [cGy/%]	Relative dose at distance 5 mm [%]	Relative dose at distance 10 mm [%]	Relative dose at distance 20 mm [%]
1 × 1	168.8/100	71.3	47.5	34.9
2 × 2	177.2/100	95.7	77.9	61.6
3 × 3	194.5/100	95.6	85.8	75.3
4 × 4	195.6/100	98.5	93.0	87.5
6 × 6	201.3/100	99.8	97.6	97.0

3D printers are becoming more widespread and affordable for most radiotherapy departments. The cost of such a printer and the personal engagement during the production process of individual bolus must be weighted against the cost of commercial bolus and expected therapy outcome using individual versus commercial bolus. Since unwanted dose discrepancies due to bolus cavities increase with smaller field size, a 3D-conformal adaptation of boluses seemed particularly interesting for VMAT of the head and neck region in which a high number of small field apertures are common.

The use of individual bolus has some limitations in clinical practice. A gapless bolus application is impeded in some areas by the thermoplastic masks used for immobilization, which causes some cavities themselves. Additionally, even for an initially perfectly fitting bolus, further gaps may arise during the course of the treatment by treatment-induced changes in the irradiated target volume, such as a decrease in swelling in the head and neck region or changes in position during mask fitting. Due to the first problem, we plan to use a 3D surface scanner to manufacture an individual bolus to be fitted under the thermoplastic mask.

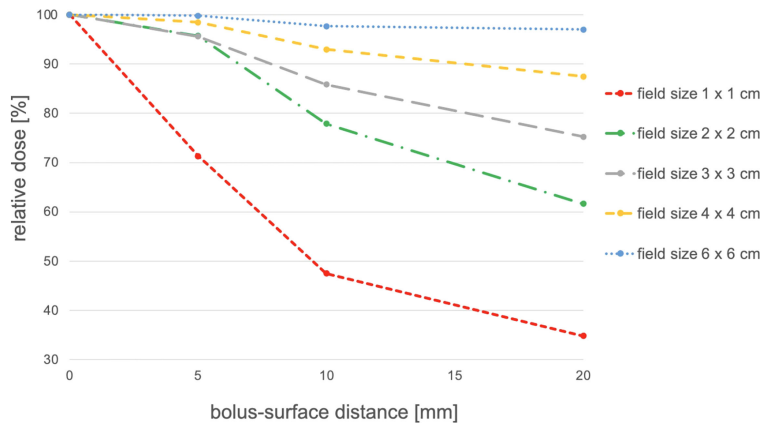

FIGURE 5 | Influence of bolus–surface distance and field size on dose reduction.

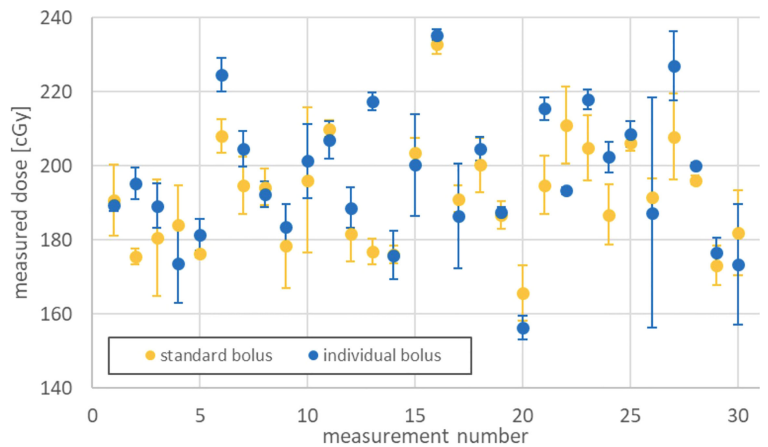

FIGURE 6 | Surface dose under standard and individual boluses.

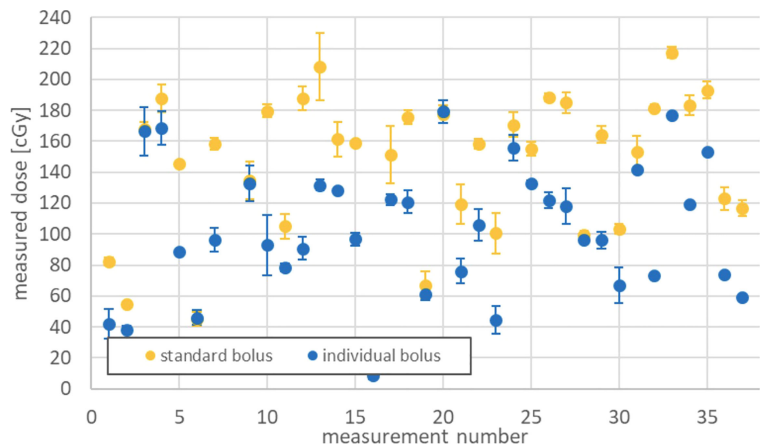

FIGURE 7 | Dose sparing on healthy skin by applying individual boluses.

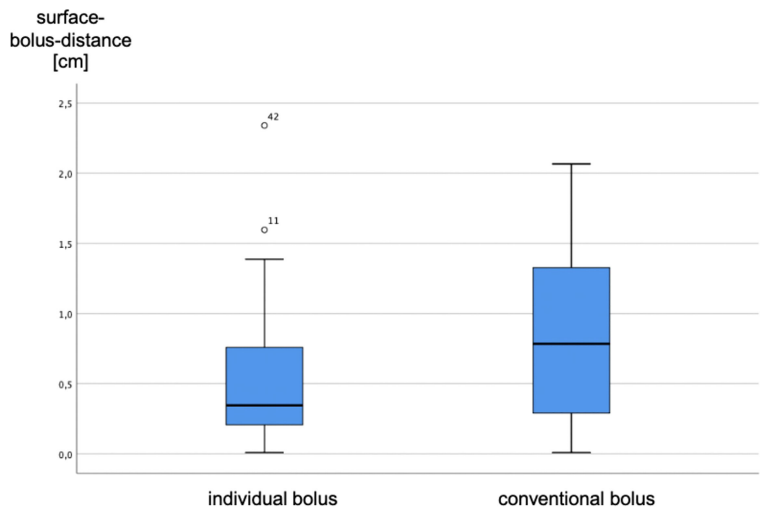

FIGURE 8 | Surface–bolus distances under conventional and individual boluses.

This allows full integration of individual bolus into the immobilization mask. The dose buildup effect caused by the masks, which was absent at measurement points outside the mask fixation, may bias the conclusion of a purely bolus-related dose buildup.

CONCLUSION

Individual boluses *via* FDM in conjunction with silicone casting are possible and practicable. The individual steps required were optimized with regard to the virtual generation of the bolus contour from the TPS, the production of a mold using 3D modeling software, and the mixing ratios of the silicone casting components. The boluses did tolerate the mechanical stresses over the entire treatment period.

Measurements comparing individual and conventional bolus variants showed a slight but significant increase in surface dose in the critical scar region in favor of individual ones. The custom manufacturing process significantly reduced unwanted dose exposure to healthy skin with a dose decrease of 25.9%. Likewise, a better fitting of the customized bolus was evident with a significant reduction in the surface–bolus distance (3.5 vs. 7.9 mm).

DATA AVAILABILITY STATEMENT

The original contributions presented in the study are included in the article/**Supplementary Material**. Further inquiries can be directed to the corresponding author.

ETHICS STATEMENT

The studies involving human participants were reviewed and approved by the Ethics Committee of the University Hospital Würzburg (Director: Prof. Dr. Roland Jahns). The patients/participants provided their written informed consent toparticipate in this study.

AUTHOR CONTRIBUTIONS

SP, VL, MF, AT, and SW designed the study. SP, SW, and VL were involved in the data collection and analysis. All authors critically reviewed and gave final approval of the manuscript.

FUNDING

This publication was supported by the Open Access Publication Fund of the University of Würzburg.

ACKNOWLEDGMENTS

This publication was supported by the Department of Radiotherapy of the University Hospital Würzburg. The authors wish to thank Dr. Mark Gainey, University Hospital Freiburg, for proofreading the manuscript.

SUPPLEMENTARY MATERIAL

The Supplementary Material for this article can be found online at: https://www.frontiersin.org/articles/10.3389/fonc.2022.881439/full#supplementary-material

REFERENCES

1. Hull CW. *Apparatus for Production of Three-Dimensional Objects by Stereolithography*. U.S: The U.S. Patent and Trademark Office (1986).
2. Zavan R, McGeachy P, Madamesila J, Villarreal-Barajas J-E, Khan R. Verification of Acuros XB Dose Algorithm Using 3D Printed Low-Density Phantoms for Clinical Photon Beams. *J Appl Clin Med Phys* (2018) 19(3):32–43. doi: 10.1002/acm2.12299
3. Woods K, Ayan AS, Woollard J, Gupta N. Quality Assurance for a Six Degrees-of-Freedom Table Using a 3D Printed Phantom. *J Appl Clin Med Phys* (2018) 19(1):115–24. doi: 10.1002/acm2.12227
4. Zhao Y, Moran K, Yewondwossen M, Allan J, Clarke S, Rajaraman M, et al. Clinical Applications of 3-Dimensional Printing in Radiation Therapy. *Med Dosim* (2017) 42(2):150–5. doi: 10.1016/j.meddos.2017.03.001
5. Kudchadker RJ, Antolak JA, Morrison WH, Wong PF, Hogstrom KR. Utilization of Custom Electron Bolus in Head and Neck Radiotherapy. *J Appl Clin Med Phys* (2003) 4(4):321–33. doi: 10.1120/jacmp.v4i4.2503
6. Martin TW, Boss MK, LaRue SM, Leary D. 3D-Printed Bolus Improves Dose Distribution for Veterinary Patients Treated With Photon Beam Radiation Therapy. *Can Vet J* (2020) 61(6):638–44.
7. Fujimoto K, Shiinoki T, Yuasa Y, Hanazawa H, Shibuya K. Efficacy of Patient-Specific Bolus Created Using Three-Dimensional Printing Technique in Photon Radiotherapy. *Phys Med* (2017) 38:1–9. doi: 10.1016/j.ejmp.2017.04.023
8. Boman E, Ojala J, Rossi M, Kapanen M. Monte Carlo Investigation on the Effect of Air Gap Under Bolus in Post-Mastectomy Radiotherapy. *Phys Med* (2018) 55:82–7. doi: 10.1016/j.ejmp.2018.10.023
9. Kong M, Holloway L. An Investigation of Central Axis Depth Dose Distribution Perturbation Due to an Air Gap Between Patient and Bolus for Electron Beams. *Australas Phys Eng Sci Med* (2007) 30(2):111–9. doi: 10.1007/BF03178415
10. Sharma SC, Johnson MW. Surface Dose Perturbation Due to Air Gap Between Patient and Bolus for Electron Beams. *Med Phys* (1993) 20(2):377–8. doi: 10.1118/1.597079
11. Behrens CF. : Dose Build-Up Behind Air Cavities for Co-60, 4, 6 and 8 MV. Measurements and Monte Carlo Simulations. *Phys Med Biol* (2006) 51 (22):5937–50. doi: 10.1088/0031-9155/51/22/015
12. Li XA, Yu C, Holmes T. A Systematic Evaluation of Air Cavity Dose Perturbation in Megavoltage X-Ray Beams. *Med Phys* (2000) 27(5):1011–7. doi: 10.1118/1.598966
13. Pugh R, Lloyd K, Collins M, Duxbury A. The Use of 3D Printing Within Radiation Therapy to Improve Bolus Conformity: A Literature Review. *J Radiother Pract* (2017) 16(03):319–25. doi: 10.1017/S1460396917000115
14. Ricotti R, Vavassori A, Spoto R, Ciardo D, Pansini F, Bazani A, et al. Dosimetric Properties of 3D-Printed Flat Bolus for External Radiotherapy. *Phys Med* (2016) 32:e1–e70. doi: 10.1016/j.ejmp.2016.01.198
15. Su S, Moran K, Robar JL. Design and Production of 3D Printed Bolus for Electron Radiation Therapy. *J Appl Clin Med Phys* (2014) 15(4):194–211. doi: 10.1120/jacmp.v15i4.4831
16. Chatchumnan N, Kingkaew S, Aumnate C, Sanghangthum T. Development and Dosimetric Verification of 3D Customized Bolus in Head and Neck Radiotherapy. *J Radiat Res* (2022) 63(3):428–34. doi: 10.1093/jrr/rrac013
17. McCallum S, Maresse S, Fearns P. Evaluating 3D-Printed Bolus Compared to Conventional Bolus Types Used in External Beam Radiation Therapy. *Curr Med Imaging* (2021) 17(7):820–31. doi: 10.2174/1573405617666210202114336
18. Kong Y, Yan T, Sun Y, Qian J, Zhou G, Cai S, et al. A Dosimetric Study on the Use of 3D-Printed Customized Boluses in Photon Therapy: A Hydrogel and Silica Gel Study. *J Appl Clin Med Phys* (2019) 20(1):348–55. doi: 10.1002/acm2.12489
19. Biltekin F, Yazici G, Ozyigit G. Characterization of 3D-Printed Bolus Produced at Different Printing Parameters. *Med Dosim* (2021) 46(2):157–63. doi: 10.1016/j.meddos.2020.10.005
20. Munoz L, Rijken J, Hunter M, Nyathi T. Investigation of Elastomeric Materials for Bolus Using Stereolithography Printing Technology in Radiotherapy. *BioMed Phys Eng Express* (2020) 6(4):045014. doi: 10.1088/2057-1976/ab9425
21. Dai G, Xu X, Wu X, Lei X, Wei X, Li Z, et al. Application of 3D-Print Silica Bolus for Nasal NK/T-Cell Lymphoma Radiation Therapy. *J Radiat Res* (2020) 61(6):920–8. doi: 10.1093/jrr/rraa084
22. Park JW, Oh SA, Yea JW, Kang MK. Fabrication of Malleable Three-Dimensional-Printed Customized Bolus Using Three-Dimensional Scanner. *PLoS One* (2017) 12(5):e0177562. doi: 10.1371/journal.pone.0177562
23. Park SY, Choi CH, Park JM, Chun M, Han JH, Kim JI. A Patient-Specific Polylactic Acid Bolus Made by a 3D Printer for Breast Cancer Radiation Therapy. *PLoS One* (2016) 11(12):e0168063. doi: 10.1371/journal.pone.0168063
24. Canters RA, Lips IM, Wendling M, Kusters M, van Zeeland M, Gerritsen RM, et al. Clinical Implementation of 3D Printing in the Construction of Patient Specific Bolus for Electron Beam Radiotherapy for non-Melanoma Skin Cancer. *Radiother Oncol* (2016) 121(1):148–53. doi: 10.1016/j.radonc.2016.07.011
25. Wang KM, Rickards AJ, Bingham T, Tward JD, Price RG. Technical Note: Evaluation of a Silicone-Based Custom Bolus for Radiation Therapy of a Superficial Pelvic Tumor. *J Appl Clin Med Phys* (2022) 23(4):e13538. doi: 10.1002/acm2.13538

Conflict of Interest: The authors declare that the research was conducted in the absence of any commercial or financial relationships that could be construed as a potential conflict of interest.

frontiers | Frontiers in Oncology

TYPE Original Research
PUBLISHED 29 September 2022
DOI 10.3389/fonc.2022.897700

OPEN ACCESS

EDITED BY
An Liu,
City of Hope National Medical Center, United States

REVIEWED BY
Athanasios G. Zafeirakis,
Army Share Fund Hospital (NIMTS), Greece
Felix Dietlein,
Boston Children's Hospital and Harvard Medical School, United States

*CORRESPONDENCE
Jing Cai
jing.cai@polyu.edu.hk

SPECIALTY SECTION
This article was submitted to Radiation Oncology, a section of the journal Frontiers in Oncology

RECEIVED 16 March 2022
ACCEPTED 12 September 2022
PUBLISHED 29 September 2022

CITATION
Lau YC, Chen S, Ho CL and Cai J (2022) Reliability of gradient-based segmentation for measuring metabolic parameters influenced by uptake time on 18F-PSMA-1007 PET/CT for prostate cancer.
Front. Oncol. 12:897700.
doi: 10.3389/fonc.2022.897700

Reliability of gradient-based segmentation for measuring metabolic parameters influenced by uptake time on 18F-PSMA-1007 PET/CT for prostate cancer

Yu Ching Lau[1,2], Sirong Chen[2], Chi Lai Ho[2] and Jing Cai[1]*

[1]Department of Health Technology and Informatics, The Hong Kong Polytechnic University, Hong Kong, Hong Kong SAR, China, [2]Department of Nuclear Medicine and Positron Emission Tomography, Hong Kong Sanatorium and Hospital, Hong Kong, Hong Kong SAR, China

Purpose: To determine an optimal setting for functional contouring and quantification of prostate cancer lesions with minimal variation by evaluating metabolic parameters on 18F-PSMA-1007 PET/CT measured by threshold-based and gradient-based methods under the influence of varying uptake time.

Methods and materials: Dual time point PET/CT was chosen to mimic varying uptake time in clinical setting. Positive lesions of patients who presented with newly diagnosed disease or biochemical recurrence after total prostatectomy were reviewed retrospectively. Gradient-based and threshold-based tools at 40%, 50% and 60% of lesion SUVmax (MIM 6.9) were used to create contours on PET. Contouring was considered completed if the target lesion, with its hottest voxel, was delineated from background tissues and nearby lesions under criteria specific to their operations. The changes in functional tumour volume (FTV) and metabolic tumour burden (MTB, defined as the product of SUVmean and FTV) were analysed. Lesion uptake patterns (increase/decrease/stable) were determined by the percentage change in tumour SUVmax at ±10% limit.

Results: A total of 275 lesions (135 intra-prostatic lesions, 65 lymph nodes, 45 bone lesions and 30 soft tissue lesions in pelvic region) in 68 patients were included. Mean uptake time of early and delayed imaging were 94 and 144 minutes respectively. Threshold-based method using 40% to 60% delineated only 85 (31%), 110 (40%) and 137 (50%) of lesions which all were contoured by gradient-based method. Although the overall percentage change using threshold at 50% was the smallest among other threshold levels in FTV measurement, it was still larger than gradient-based method (median: 50% =-7.6% vs gradient=0%). The overall percentage increase in MTB of gradient-based method (median: 6.3%) was compatible with the increase in tumour SUVmax. Only a small proportion of intra-prostatic lesions (<2%), LN (<4%),

bone lesions (0%) and soft tissue lesions (<4%) demonstrated decrease uptake patterns.

Conclusions: With a high completion rate, gradient-based method is reliable for prostate cancer lesion contouring on 18F-PSMA-1007 PET/CT. Under the influence of varying uptake time, it has smaller variation than threshold-based method for measuring volumetric parameters. Therefore, gradient-based method is recommended for tumour delineation and quantification on 18F-PSMA-1007 PET/CT.

KEYWORDS

prostate cancer, PSMA, PET, uptake time, tumour delineation, tumour volume, metabolic tumour burden, tumour

Introduction

The clinical use of prostate specific membrane antigen (PSMA) ligand for PET imaging has revolutionized the diagnostic and therapeutic paradigm of prostate cancer. The usefulness of PSMA PET/computed tomography (CT) in guiding radiotherapy (RT) has been widely reported, especially for the detection of local recurrence and metastasis including lymph nodes (LN) and osseous lesions in which conventional imaging modalities may be less sensitive to depict (1, 2). It is clinically useful for the delineation of intraprostatic lesions without clear margin in primary disease and the localisation of oligometastatic lesions usually having small physical size at early biochemical recurrence after prostatectomy. Image-derived metabolic parameters such as tumour maximum standardized uptake value (SUVmax), functional tumour volume (FTV) and metabolic tumour burden (MTB) were reported to be useful for disease quantification. Contours on PSMA PET/CT was also shown to be of clinical significance in tumour volume delineation which led to changes in treatment plan (3–7).

Lesion contouring is labour-intensive in treatment planning workflow especially when contours are drawn manually. Threshold-based and gradient-based methods are clinically available semi-automatic segmentation on PET images with higher reliability and smaller inter-observer bias (8–10). Although different approaches and settings have been suggested for PSMA PET/CT, they are specific to clinical application and target lesion type which limits their practicality in routine practice (11–16).

PET tracer uptake is a pharmacokinetic process. The rates of tracer uptake in different tissues vary with tracer concentration and cellular microenvironment. Acquiring PET images at different time points gives rise to variations in metabolic parameters. Standardization of PET imaging protocol has been proposed (17, 18). Nevertheless, there is no consensus on the optimal uptake time for 18F-PSMA PET/CT as evident by the wide range of uptake time in previous studies (19–21). This technical factor varies from patient to patient, from scan to scan, even within a single imaging centre. However, there is no study evaluated the variations in metabolic parameters measured by gradient-based and threshold-based methods at different uptake times in clinical 18F-PSMA PET/CT examinations.

Therefore, an efficient and reliable lesion contouring method with smaller level of variation is of interest to clinical practice for this increasingly common and important image guidance. This study aimed to determine an optimal setting for contouring prostate cancer lesions on 18F-PSMA-1007 PET/CT with minimal variation under the influence of uptake time.

Methods and materials

Patient data

In this study, dual time point imaging was selected to mimic the varying uptake time in clinical setting. Clinical 18F-PSMA-1007 PET/CT examinations performed in the Hong Kong Sanatorium and Hospital from November 2019 to May 2021 were reviewed retrospectively under an Internal Review Board (IRB)-approved protocol. To allow direct comparison, only cases scanned using cross calibrated PET/CT scanners of the same model (Siemens Biograph Vision 600) were retrieved from image archive.

To obtain an appropriate representation of lesions requiring functional contouring for metabolic quantification in daily clinical practice, only patients who were [a] newly diagnosed by confirmed biopsy of primary disease and positive MRI findings without any medical treatments, or [b] presented with the first biochemical recurrence after prostatectomy without any post-operative treatments were selected. Considered that 18F-

PSMA-1007 uptake can be non-specific, only positive lesions reported by certified nuclear medicine physician were included.

Scan preparation and image acquisition

Pre-examination fasting was not required. Injected activity of 18F-PSMA-1007 was calculated according to patient's weight (6.5-11.0 mCi). After intravenous injection, patients were requested to take a rest in preparation room for a minimum uptake period of 90 minutes before scanning. Whole-body scans were acquired after urination, spanning from base of skull to upper thigh. Patients performed normal breathing with both arms positioned above head. Non-contrast CT was performed (120 kVp, 90 mAs, pitch 0.8 and rotation time 0.5 second) followed by PET acquisition (static bed, 2 minutes per bed). Regional delayed imaging was performed as per physician's order when clinically indicated. PET images were reconstructed using parameters optimized for small lesion depiction (4 iterations 4 subsets, gaussian filter 5 mm at FWHM, voxel size 1.65 x 1.65 x 1.5 mm, point spread function and time-of-flight options enabled).

Image measurement

Images were loaded to imaging workstation (MIM 6.9, MIM Software INC., US). Both gradient-based and threshold-based tools used for contouring have been described earlier as follows (22). Gradient-based method is a textual analysis detecting the point having the greatest slope of lesion activity profile by calculating its spatial derivative. A starting point is defined near the centre of lesion. Six axes with visualized length are dragged out by user. The spatial gradients along these axes are calculated interactively. These axes are restricted to a large spatial gradient that detected near the edge of the lesion. The ellipsoid volume formed is used as a starting boundary for gradient detection. When mouse button is released, the lesion contour is created at the edge detected using the maximal spatial gradient along each axis. Threshold-based method creates contour in a user defined spherical volume covering the entire target lesion by including those having values larger than the chosen threshold in the form of percentage of lesion SUVmax.

Gradient-based and threshold-based methods using 40%, 50% and 60% of lesion SUVmax were used to create tumour contours on both early and delayed images. Tumour SUVmax, FTV and MTB (defined as the product of mean standardized uptake value (SUVmean) and FTV) were exported for analyses. All lesions were categorized into four groups according to their types: intra-prostatic lesions, LN, bone lesions, and soft tissue lesions in pelvic region. The uptake times of scans (from tracer injection and the start of acquisitions) were recorded.

Data analysis

Contouring was considered completed if [a] the target lesion was delineated from background tissues and nearby lesions without the need of manual adjustment or smoothing, [b] the contour encompassed the hottest voxel of the target lesion, [c] in gradient-based method, none of the axes starting from the lesion centre has extended out of the lesion without detecting and restricted by a large spatial gradient near the edge, and [d] in threshold-based method, the contour was created without being constrained by the user defined spherical volume. Completion rate was determined for each segmentation method as:

$$\text{Completion Rate} = \frac{\text{Number of lesion with completed contouring}}{\text{Total number of lesion}} \times 100\,\%$$

To determine the levels of variation of segmentation methods, percentage changes in FTV and MTB of each completed contour pair were calculated as follows. A segmentation method that gives consistent FTV with percentage change approaching zero, is preferred.

$$\%\ \text{change in FTV} = \frac{\text{FTV}_{\text{delayed}} - \text{FTV}_{\text{early}}}{\text{FTV}_{\text{early}}} \times 100\,\%$$

$$\%\ \text{change in MTB} = \frac{\text{MTB}_{\text{delayed}} - \text{MTB}_{\text{early}}}{\text{MTB}_{\text{early}}} \times 100\,\%$$

Percentage change in tumour SUVmax of each lesion was calculated as:

$$\%\ \text{change in tumour SUVmax} = \frac{\text{SUVmax}_{\text{delayed}} - \text{SUVmax}_{\text{early}}}{\text{SUVmax}_{\text{early}}} \times 100\,\%$$

Lesion uptake pattern was determined by the percentage change in tumour SUVmax. Limits were adopted from a previous study on 68Ga-PSMA PET/CT as follows (23):

a. "increase" for +10% or more, or
b. "decrease" for -10% or more, or
c. "stable" within ±10%.

Statistical analyses were performed using IBM SPSS Statistics (version 26, IBM Corp., US). Tumour SUVmax, FTV and MTB were compared between time points using paired t-tests. Percentage changes in SUVmax of lesions in newly diagnosed

and post-prostatectomy group were compared using independent sample t-test. Two-sided p-value<0.05 was considered statistically significant.

Results

A total of 275 lesions (135 intra-prostatic lesions, 65 LN, 45 bone lesions and 30 soft tissue lesions in pelvic region) in 68 patients (44 newly diagnosed and 24 with prostatectomy done) were included in this study. Same number of lesions was detected on both time points. Mean uptake time of early and delayed imaging were 94 ± 16.8 and 144 ± 14.3 minutes respectively.

Completion rate

Table 1 summarises the completion rates in all lesions and each lesion type. Contouring of all the 275 lesions were completed using gradient-based method. Completion rates were lower using threshold-based method. For each threshold level, the lowest rate was observed for intra-prostatic lesions because of failure to separate target lesions from nearby more intense lesions; the highest rate was seen in bone lesions which were usually having a well-defined margin. In all lesion types, the completion rates dropped with threshold level because of the inclusion of background activity when lesion contrast was insufficient.

FTV

The median percentage changes in FTV of all lesions and within each lesion type were summarised in Table 2. Gradient-based method outperformed threshold-based method at 50% (-7.6%) even though it gave the most consistent measurements among different threshold levels. In per lesion type analysis, gradient-based method generally demonstrated a higher consistency for all lesion types (-2.6% to 0%), without any significant difference detected between time points. On the contrary, FTV measured by threshold-based method were generally smaller on delayed time point, with relatively large decrease for LN and soft tissue lesions.

MTB

MTB using gradient-based method generally demonstrated increases in all lesion types, ranged from 2.1% to 9.8%. Meanwhile, the changes using threshold-based method were diverse, ranged from -3.2% to 5.6% for threshold-40%, -8.1% to 7.4% for threshold-50% and -9.2% to 6.0% for threshold-60%. The increase observed for gradient-based method was compatible with the increase in tumour SUVmax.

Tumour SUVmax

Table 3 summarises the mean tumour SUVmax on early and delayed images. Increase in delayed SUVmax was observed [all p<0.05]. Mean percentage changes in SUVmax for intra-prostatic lesions, LN, bone lesions and soft tissue lesions were 10.2%, 11.1%, 12.0% and 10.0% respectively.

Uptake pattern

Majority of the lesions showed stable or increase pattern on delayed images, except a small proportion of intra-prostatic lesions (<2%), LN (<4%), bone lesions (0%) and soft tissue lesions (<4%) which demonstrated decrease pattern. There was a larger proportion of bone lesions in the post-prostatectomy group showing increase pattern, with a significantly larger mean percentage change in SUVmax than the newly diagnosed group (17.0% vs 9.3%, [p<0.05]).

Efficacy for contouring heterogeneous lesions

Threshold-based method showed inadequacy for delineating heterogeneous lesions. Figure 1 shows an example of gradient-based and threshold-based contours of a prostatic mass (early SUVmax 98). The threshold-based contours failed to include entire active sub-volume of the tumour no matter which threshold level was used, with a substantially smaller FTV and MTB when compared to the gradient-based contours. Figure 2 shows another illustration of gradient-based and threshold-

TABLE 1 Completion rates of gradient-based and threshold-based segmentation methods.

	All lesions	Intra-prostatic lesions	LN	Bone lesions	Soft tissue lesions
Gradient	100%	100%	100%	100%	100%
Threshold-40%	31%	11%	51%	67%	23%
Threshold-50%	40%	19%	63%	76%	33%
Threshold-60%	50%	29%	71%	87%	43%

TABLE 2 Median percentage changes in FTV of gradient-based and threshold-based segmentation methods.

%	All lesions	Intra-prostatic lesions	LN	Bone lesions	Soft tissue lesions
Gradient	0.0	0.0	-2.0	-2.6	0.0
Threshold-40%	-8.8*	-5.9	-16.0*	-7.3*	-17.5
Threshold-50%	-7.6*	-4.4	-17.6*	-5.2	-13.7*
Threshold-60%	-12.0*	-4.5	-18.9*	-6.3	-15.2

(* = significant difference between time points [$p<0.05$]).

based contours of lesions in bilateral prostatic lobes. Tumour in left prostate could not be delineated even though threshold level at 40% was applied to whole prostate. When contoured separately using different threshold levels, the extent of tumorous activity being delineated on right lobe using 40% was significantly lesser than left lobe using 60% and those on gradient-based contours. Gradient-based method demonstrated a higher level of confidence for delineating the entire tumour volume than threshold-based contours.

Discussion

The delineation of tumorous activity is a critical step during the translation of functional information on PET images to radiotherapy platform. The variations in metabolic parameters must be handled when treatment planning and disease monitoring are concerned. Fixing the exact uptake time is usually not feasible in clinical practice due to case scheduling, throughput and patients' conditions. Therefore, addressing the variations from imaging work and measurement methodology can be another practical approach. Our results suggested that gradient-based method is more robust for tumour delineation and quantification on 18F-PSMA-1007 PET/CT. Having similar properties on targeting membrane glycoprotein overexpressed on prostate cancer cell surface with comparable detection sensitivity, common PSMA agents should exhibit similar image characteristics within their optimal uptake periods in which the working principles of the contouring algorithms are based on. Hence, our conclusions should be generalizable to other PSMA agents.

Although CT-based volume has been considered as standard of reference, contouring of prostate cancer lesions on CT images can be difficult and operator-dependent especially for lesions with ill-defined boundary and small size. Functional contouring using semi-automatic segmentation on PET images is an alternative. In our study, gradient-based method created contours for all lesions. Intra-prostatic lesions were the most difficult for threshold-based contouring. The lower completion rate can be attributed to the presence of nearby hot lesions and the lower lesion contrast. Although a higher threshold value can be useful, it results in shrinkage of tumour contour which may be unrealistic for gross tumour volume. In contrast, gradient-based method relies on the rate of change of neighbouring voxel values for edge detection, which is more versatile under challenging conditions. Tumour heterogeneity can be another issue for generating contours. Figure 1 shows an example of another problem in contouring of a heterogeneous intra-prostatic lesion using threshold-based method. The maximum voxel value is much higher than other active sub-volumes within the tumour. Threshold-based method failed to delineate the whole tumour volume using all the threshold values applied. The FTV and MTB were considerably smaller when compared to gradient-based method. Moreover, adjusting threshold level on lesions showing different tracer avidity of the same patient is sometimes necessary when they cannot be contoured using a single level, which subsequently requires manual correction because of a large discrepancy on disease extent in contours as illustrated in Figure 2. Gradient-based method has improved the delineation of heterogeneous tumours in both situations, which echoes with the findings from a recent study (8). Therefore, gradient-based method is more robust than threshold-based method in clinical setting.

SUVmax is known to vary with uptake time. Despite, the degree of variation as observed in this study (Table 3) may be less significant in clinical context when coexisted with inter-patient and intra-patient variability in PSMA biodistribution (24, 25). Notwithstanding, the repeatability of PSMA PET/CT was proven and shown to be similar to 18FDG PET/CT that has been extensively used clinically with confidence (26, 27). The effect of lesion contouring using common segmentation methods on volumetric parameters with such variation in SUVmax and image appearance is the main concern of this study. Gradient-based and threshold-based segmentation methods have been evaluated in various aspects including the accuracy for delineating true tumour volume verified by

TABLE 3 Mean tumour SUVmax ± SD on early and delayed images.

	Early	Delayed
All lesions	8.7 ± 13.1	9.7 ± 14.6
Intra-prostatic lesions	11.3 ± 17.1	12.5 ± 19.0
LN	5.6 ± 5.8	6.2 ± 6.3
Bone lesions	6.8 ± 4.6	7.6 ± 5.2
Soft tissue lesions	6.8 ± 7.7	7.7 ± 12.5

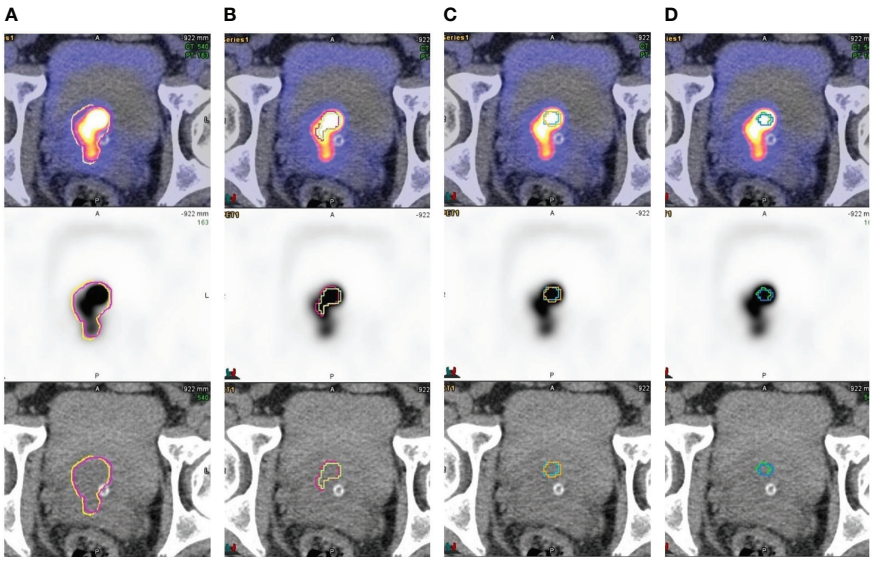

FIGURE 1
Contouring of a heterogenous prostatic mass involving bilateral base-mid gland TZ and R apex **(A)** gradient-based, **(B)** threshold-40%, **(C)** threshold-50% and **(D)** threshold-60%. Early and delayed contours were overlaid on axial plane. Threshold-based method failed to delineate the whole tumour volume using all that threshold values applied. Gradient-based contours delineated the tumorous activity with higher level of confidence.

histopathological evidence, the accuracy of spatial measurement using phantom as well as the inter-operator difference. In fact, a threshold value between 40% and 60% is commonly adopted for PSMA PET/CT threshold-based lesion segmentation in RT planning (14, 28–31). A recent study reported that FTV measured by threshold-based method using 55% had the highest correlation to CT volume among other values for metastatic lymph nodes (16). Although our findings revealed that threshold value at 50% gives relatively stable FTV and MTB measurements, the use of threshold-based method becomes

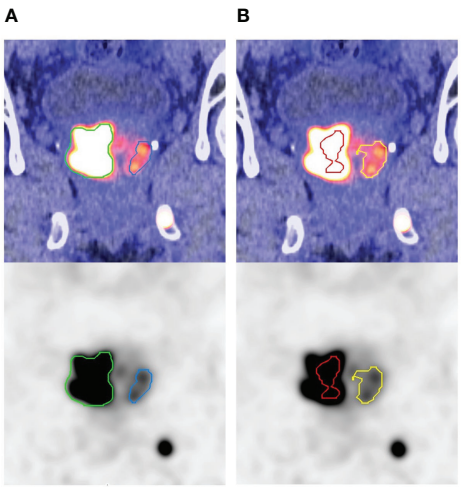

FIGURE 2
Countours on coronal plane of a heterogenous prostatic mass involving bilateral prostatic lobes by **(A)** gradient-based and **(B)** threshold-based methods (right lobe: 40% in red; left lobe: 60% in yellow). Different threshold levels were applied because a single level could not delineate tumours in right and left prostate lobes, which resulted in large discrepancy in disease extent of contours. Gradient-based contours improved the delineation with higher level of confidence.

questionable under the variation in tumour volume that we observed (corresponding to the ~16-19% decrease in FTV of LN for threshold-based using 50-60% in Table 2). In addition, dynamic uptake patterns of oligometastasis on 68Ga-PSMA PET/CT was reported by a previous study showing a larger proportion (21%) of bone lesion with decreased uptake on delayed time point (23). This further suggests the limitation of using threshold-based method on 68Ga-PSMA PSMA PET/CT as it relies on direct computation on SUVmax. Furthermore, the accuracy of gradient-based method for volumetric measurement at high lesion contrast commonly seen on PSMA PET/CT has been validated recently (32). In this regard, gradient-based method is a better option with smaller variation.

Gradient-based algorithm can benefit the current practice in different ways, which relies heavily on manual drawing and threshold-based method. Gradient-based contour is 3-dimensional which has a high degree of operator independence. The uncertainty of margin delineation is relatively low when compared to simple numerical analysis. The reasonable computing time also enables handy and efficient contouring for clinical use. Nevertheless, there are some precautions when operating the tool on images. Firstly, it is difficult to select the same seed in active volume by eyeballing which may affect the analysis of the tumour activity profile and result in slightly different contours for repeating attempts. Secondly, single attempt may not be able to include the entire volume of a heterogeneous lesion, especially when the slope of activity gradient is not constant along its margin. Repeated drawing is necessary to append tumour volume that is missing on the original contour. Since the operation requires a certain level of human input and experience, user training is essential to standardize the practice within a workgroup. It is also important that contouring of low count lesion using gradient-based method is subject to a larger uncertainty because textual analysis is primarily affected by high image noise and low lesion contrast. Nonetheless, its performance is still better than threshold-based method under these challenging conditions.

MTB is an image-based quantification marker of tumour burden in oncology. It is often used for monitoring systemic therapy in prostate cancer. In PET image quantification, increase in SUVmax is usually associated with increase in SUVmean. Recalling the mathematical definition of MTB (the product of SUVmean and FTV), it is plausible that an increased tumour SUVmax together with a stable FTV will result in an increased MTB. Compared to the decrease in MTB of LN and soft tissue lesions using threshold-based method, the increase using gradient-based method can be explained. Therefore, gradient-based method should be more reliable than threshold-based method for the measurement of MTB. It is noteworthy that measurement error propagates by the multiplication of two factors with individual variability. Minimizing variations in these parameters would become more critical for clinical applications using MTB which should be specific and confined by the measurement methodology.

There are limitations in this study. Physiologic motions such as bowel movement and urine accumulation in bladder are inevitable, even if patients are requested to stay on scanner between the acquisitions. During the examinations, patients were repositioned for delayed imaging. The displacement of internal body structures and body positioning may deform soft lesions, causing inherent variation which is not related to uptake time. However, this limitation is also present in real clinical situations between simulation and subsequent treatments. It is also noteworthy that benign lesions could not be completely excluded from our samples without histopathological or longitudinal evidence. In view of this, the inclusion or exclusion of lesions was not purely determined by their tracer avidity. The clinical reporting performed by nuclear medicine physicians often took other clinical factors and concomitant image findings into consideration, such as CT appearance, overall disease extent and patient's clinical history. Nevertheless, the true metabolic nature of lesion should have a relatively small impact on our findings about the consistency of functional contouring methods under the variation of PET imaging.

Conclusion

With a high completion rate, gradient-based method is reliable for prostate cancer lesion contouring on 18F-PSMA-1007 PET/CT. Under the influence of varying uptake time, it has smaller variation than threshold-based method for measuring volumetric parameters. Therefore, gradient-based method is recommended for tumour delineation and quantification on 18F-PSMA-1007 PET/CT.

Data availability statement

The raw data supporting the conclusions of this article will be made available by the authors, without undue reservation.

Ethics statement

The studies involving human participants were reviewed and approved by Institutional Review Board of the Hong Kong Polytechnic University. Written informed consent for participation was not required for this study in accordance with the national legislation and the institutional requirements.

Author contributions

YCL, SC, CLH, and JC contributed to study design, methodology development, results interpretation, and manuscript review. CLH offered administrative and material support for clinical data and imaging data collection. YCL wrote the manuscript. JC supervised the study. All authors contributed to the article and approved the submitted version.

Funding

This research was partly supported by research grants of Project of Strategic Importance Fund (P0035421) from The Hong Kong Polytechnic University.

Conflict of interest

The authors declare that the research was conducted in the absence of any commercial or financial relationships that could be construed as a potential conflict of interest.

Publisher's note

References

1. Schmidt-Hegemann NS, Fendler WP, Buchner A, Stief C, Rogowski P, Niyazi M, et al. Detection level and pattern of positive lesions using psma Pet/Ct for staging prior to radiation therapy. *Radiat Oncol* (2017) 12(1):176. doi: 10.1186/s13014-017-0902-0

2. Zschaeck S, Wust P, Beck M, Wlodarczyk W, Kaul D, Rogasch J, et al. Intermediate-term outcome after psma-pet guided high-dose radiotherapy of recurrent high-risk prostate cancer patients. *Radiat Oncol* (2017) 12(1):140. doi: 10.1186/s13014-017-0877-x

3. Bettermann AS, Zamboglou C, Kiefer S, Jilg CA, Spohn S, Kranz-Rudolph J, et al. [(68)Ga-]Psma-11 Pet/Ct and multiparametric mri for gross tumor volume delineation in a slice by slice analysis with whole mount histopathology as a reference standard - implications for focal radiotherapy planning in primary prostate cancer. *Radiother Oncol* (2019) 141:214–9. doi: 10.1016/j.radonc.2019.07.005

4. Walacides D, Meier A, Knöchelmann AC, Meinecke D, Derlin T, Bengel FM, et al. Comparison of 68ga-psma ligand Pet/Ct versus conventional cross-sectional imaging for target volume delineation for metastasis-directed radiotherapy for metachronous lymph node metastases from prostate cancer. *Strahlenther Onkol* (2019) 195(5):420–9. doi: 10.1007/s00066-018-1417-9

5. Syndikus I, Cruickshank C, Staffurth J, Tree A, Henry A, Naismith O, et al. Pivotalboost: A phase iii randomised controlled trial of prostate and pelvis versus prostate alone radiotherapy with or without prostate boost (Cruk/16/018). *Clin Transl Radiat Oncol* (2020) 25:22–8. doi: 10.1016/j.ctro.2020.08.003

6. Kerkmeijer LGW, Groen VH, Pos FJ, Haustermans K, Monninkhof EM, Smeenk RJ, et al. Focal boost to the intraprostatic tumor in external beam radiotherapy for patients with localized prostate cancer: Results from the flame randomized phase iii trial. *J Clin Oncol* (2021) 39(7):787–96. doi: 10.1200/jco.20.02873

7. Schiller K, Sauter K, Dewes S, Eiber M, Maurer T, Gschwend J, et al. Patterns of failure after radical prostatectomy in prostate cancer - implications for radiation therapy planning after 68ga-Psma-Pet imaging. *Eur J Nucl Med Mol Imaging* (2017) 44(10):1656–62. doi: 10.1007/s00259-017-3746-9

8. Pfaehler E, Burggraaff C, Kramer G, Zijlstra J, Hoekstra OS, Jalving M, et al. Pet segmentation of bulky tumors: Strategies and workflows to improve inter-observer variability. *PloS One* (2020) 15(3):e0230901. doi: 10.1371/journal.pone.0230901

9. Shah B, Srivastava N, Hirsch AE, Mercier G, Subramaniam RM. Intra-reader reliability of fdg pet volumetric tumor parameters: Effects of primary tumor size and segmentation methods. *Ann Nucl Med* (2012) 26(9):707–14. doi: 10.1007/s12149-012-0630-3

10. Sridhar P, Mercier G, Tan J, Truong MT, Daly B, Subramaniam RM. Fdg pet metabolic tumor volume segmentation and pathologic volume of primary human solid tumors. *AJR Am J Roentgenol* (2014) 202(5):1114–9. doi: 10.2214/ajr.13.11456

11. Draulans C, De Roover R, van der Heide UA, Kerkmeijer L, Smeenk RJ, Pos F, et al. Optimal 68ga-psma and 18f-psma pet window levelling for gross tumour volume delineation in primary prostate cancer. *Eur J Nucl Med Mol Imaging* (2020) 48(4):1211-18. doi: 10.1007/s00259-020-05059-4

12. Spohn SKB, Kramer M, Kiefer S, Bronsert P, Sigle A, Schultze-Seemann W, et al. Comparison of manual and semi-automatic [18f]Psma-1007 pet based contouring techniques for intraprostatic tumor delineation in patients with primary prostate cancer and validation with histopathology as standard of reference. *Front Oncol* (2020) 10:600690. doi: 10.3389/fonc.2020.600690

13. Schmuck S, von Klot CA, Henkenberens C, Sohns JM, Christiansen H, Wester HJ, et al. Initial experience with volumetric 68ga-psma I&T Pet/Ct for assessment of whole-body tumor burden as a quantitative imaging biomarker in patients with prostate cancer. *J Nucl Med* (2017) 58(12):1962–8. doi: 10.2967/jnumed.117.193581

14. Seifert R, Herrmann K, Kleesiek J, Schäfers M, Shah V, Xu Z, et al. Semiautomatically quantified tumor volume using 68ga-Psma-11 pet as a biomarker for survival in patients with advanced prostate cancer. *J Nucl Med* (2020) 61(12):1786–92. doi: 10.2967/jnumed.120.242057

15. Vinsensia M, Chyoke PL, Hadaschik B, Holland-Letz T, Moltz J, Kopka K, et al. 68ga-psma Pet/Ct and volumetric morphology of pet-positive lymph nodes stratified by tumor differentiation of prostate cancer. *J Nucl Med* (2017) 58(12):1949–55. doi: 10.2967/jnumed.116.185033

16. Mittlmeier LM, Brendel M, Beyer L, Albert NL, Todica A, Zacherl MJ, et al. Feasibility of different tumor delineation approaches for (18)F-Psma-1007 Pet/Ct imaging in prostate cancer patients. *Front Oncol* (2021) 11:663631. doi: 10.3389/fonc.2021.663631

17. Antunovic L, Rodari M, Rossi P, Chiti A. Standardization and quantification in Pet/Ct imaging: Tracers beyond fdg. *PET Clin* (2014) 9(3):259–66. doi: 10.1016/j.cpet.2014.03.002

18. Wahl RL, Jacene H, Kasamon Y, Lodge MA. From recist to percist: Evolving considerations for pet response criteria in solid tumors. *J Nucl Med* (2009) 50 Suppl 1(Suppl 1):122s–50s. doi: 10.2967/jnumed.108.057307

19. Giesel FL, Hadaschik B, Cardinale J, Radtke J, Vinsensia M, Lehnert W, et al. F-18 labelled psma-1007: Biodistribution, radiation dosimetry and histopathological validation of tumor lesions in prostate cancer patients. *Eur J Nucl Med Mol Imaging* (2017) 44(4):678–88. doi: 10.1007/s00259-016-3573-4

20. Kuten J, Fahoum I, Savin Z, Shamni O, Gitstein G, Hershkovitz D, et al. Head-to-Head comparison of 68ga-Psma-11 with 18f-Psma-1007 Pet/Ct in staging prostate cancer using histopathology and immunohistochemical analysis as a reference standard. *J Nucl Med* (2020) 61(4):527–32. doi: 10.2967/jnumed.119.234187

21. Rahbar K, Afshar-Oromieh A, Seifert R, Wagner S, Schäfers M, Bögemann M, et al. Diagnostic performance of 18f-Psma-1007 Pet/Ct in patients with biochemical recurrent prostate cancer. *Eur J Nucl Med Mol Imaging* (2018) 45(12):2055–61. doi: 10.1007/s00259-018-4089-x

22. Werner-Wasik M, Nelson AD, Choi W, Arai Y, Faulhaber PF, Kang P, et al. What is the best way to contour lung tumors on pet scans? Multiobserver validation

of a gradient-based method using a nsclc digital pet phantom. *Int J Radiat Oncol Biol Phys* (2012) 82(3):1164–71. doi: 10.1016/j.ijrobp.2010.12.055

23. Alberts I, Sachpekidis C, Gourni E, Boxler S, Gross T, Thalmann G, et al. Dynamic patterns of [68ga]-Psma-11 uptake in recurrent prostate cancer lesions. *Eur J Nucl Med Mol Imaging* (2020) 47(1):160–7. doi: 10.1007/s00259-019-04545-8

24. Demirci E, Sahin OE, Ocak M, Akovali B, Nematyazar J, Kabasakal L. Normal distribution pattern and physiological variants of 68ga-Psma-11 Pet/Ct imaging. *Nucl Med Commun* (2016) 37(11):1169–79. doi: 10.1097/mnm.0000000000000566

25. Sahakyan K, Li X, Lodge MA, Werner RA, Bundschuh RA, Bundschuh L, et al. Semiquantitative parameters in psma-targeted pet imaging with [(18)F] Dcfpyl: Intrapatient and interpatient variability of normal organ uptake. *Mol Imaging Biol* (2020) 22(1):181–9. doi: 10.1007/s11307-019-01376-9

26. Jansen BHE, Cysouw MCF, Vis AN, van Moorselaar RJA, Voortman J, Bodar YJL, et al. Repeatability of quantitative (18)F-dcfpyl Pet/Ct measurements in metastatic prostate cancer. *J Nucl Med* (2020) 61(9):1320–5. doi: 10.2967/jnumed.119.236075

27. Seifert R, Sandach P, Kersting D, Fendler WP, Hadaschik B, Herrmann K, et al. Repeatability of (68)Ga-Psma-Hbed-Cc Pet/Ct-derived total molecular tumor volume. *J Nucl Med* (2021) 63(5):746–53. doi: 10.2967/jnumed.121.262528

28. Draulans C, Pos F, Smeenk RJ, Kerkmeijer L, Vogel WV, Nagarajah J, et al. (68)Ga-Psma-11 pet, (18)F-Psma-1007 pet, and mri for gross tumor volume delineation in primary prostate cancer: Intermodality and intertracer variability. *Pract Radiat Oncol* (2021) 11(3):202–11. doi: 10.1016/j.prro.2020.11.006

29. Thomas L, Kantz S, Hung A, Monaco D, Gaertner FC, Essler M, et al. (68) Ga-Psma-Pet/Ct imaging of localized primary prostate cancer patients for intensity modulated radiation therapy treatment planning with integrated boost. *Eur J Nucl Med Mol Imaging* (2018) 45(7):1170–8. doi: 10.1007/s00259-018-3954-y

30. Werner RA, Bundschuh RA, Bundschuh L, Lapa C, Yin Y, Javadi MS, et al. Semiquantitative parameters in psma-targeted pet imaging with [(18)F]Dcfpyl: Impact of tumor burden on normal organ uptake. *Mol Imaging Biol* (2020) 22 (1):190–7. doi: 10.1007/s11307-019-01375-w

31. Zamboglou C, Fassbender TF, Steffan L, Schiller F, Fechter T, Carles M, et al. Validation of different psma-Pet/Ct-Based contouring techniques for intraprostatic tumor definition using histopathology as standard of reference. *Radiother Oncol* (2019) 141:208–13. doi: 10.1016/j.radonc.2019.07.002

32. Fedrigo R, Kadrmas DJ, Edem PE, Fougner L, Klyuzhin IS, Petric MP, et al. Quantitative evaluation of psma pet imaging using a realistic anthropomorphic phantom and shell-less radioactive epoxy lesions. *EJNMMI Phys* (2022) 9(1):2. doi: 10.1186/s40658-021-00429-9

frontiers | Frontiers in Oncology

TYPE Original Research
PUBLISHED 04 October 2022
DOI 10.3389/fonc.2022.918296

OPEN ACCESS

EDITED BY
Jing Cai
Hong Kong Polytechnic University, Hong Kong, SAR China

REVIEWED BY
Mengying Shi,
University of Massachusetts Lowell, United States
You Zhang,
University of Texas Southwestern Medical Center, United States

*CORRESPONDENCE
Yun Ge
geyun@nju.edu.cn
Guoping Shan
shang3118@163.com

SPECIALTY SECTION
This article was submitted to Radiation Oncology, a section of the journal Frontiers in Oncology

RECEIVED 12 April 2022
ACCEPTED 15 September 2022
PUBLISHED 04 October 2022

CITATION
Zhang Y, Zhou H, Chu K, Wu C, Ge Y, Shan G, Zhou J, Cai J, Jin J, Sun W, Chen Y and Huang X (2022) Setup error assessment based on "Sphere-Mask" Optical Positioning System: Results from a multicenter study. *Front. Oncol.* 12:918296. doi: 10.3389/fonc.2022.918296

Setup error assessment based on "Sphere-Mask" Optical Positioning System: Results from a multicenter study

Yan Zhang[1], Han Zhou[1], Kaiyue Chu[2], Chuanfeng Wu[3], Yun Ge[1]*, Guoping Shan[1,4]*, Jundong Zhou[3], Jing Cai[2], Jianhua Jin[2], Weiyu Sun[1], Ying Chen[1] and Xiaolin Huang[1]

[1]School of Electronic Science and Engineering, Nanjing University, Nanjing, China, [2]Department of Radiotherapy, Nantong Tumor Hospital, Nantong, China, [3]Department of Radiotherapy, Suzhou Municipal Hospital, Suzhou, China, [4]Department of Radiation Physics, Zhejiang Cancer Hospital, Hangzhou, China

Background: The setup accuracy plays an extremely important role in the local control of tumors. The purpose of this study is to verify the feasibility of "Sphere-Mask" Optical Positioning System (S-M_OPS) for fast and accurate setup.

Methods: From 2016 to 2021, we used S-M_OPS to supervise 15441 fractions in 1981patients (with the cancer in intracalvarium, nasopharynx, esophagus, lung, liver, abdomen or cervix) undergoing intensity-modulated radiation therapy (IMRT), and recorded the data such as registration time and mask deformation. Then, we used S-M_OPS, laser line and cone beam computed tomography (CBCT) for co-setup in 277 fractions, and recorded laser line-guided setup errors and S-M_OPS-guided setup errors with CBCT-guided setup result as the standard.

Results: S-M_OPS supervision results: The average time for laser line-guided setup was 31.75s. 12.8% of the reference points had an average deviation of more than 2 mm and 5.2% of the reference points had an average deviation of more than 3 mm. Co-setup results: The average time for S-M_OPS-guided setup was 7.47s, and average time for CBCT-guided setup was 228.84s (including time for CBCT scan and manual verification). In the LAT (left/right), VRT (superior/inferior) and LNG (anterior/posterior) directions, laser line-guided setup errors (mean $\pm$SD) were -0.21$\pm$3.13mm, 1.02$\pm$2.76mm and 2.22$\pm$4.26mm respectively; the 95% confidence intervals (95% CIs) of laser line-guided setup errors were -6.35 to 5.93mm, -4.39 to 6.43mm and -6.14 to 10.58mm respectively; S-M_OPS-guided setup errors were 0.12$\pm$1.91mm, 1.02$\pm$1.81mm and -0.10$\pm$2.25mm respectively; the 95% CIs of S-M_OPS-guided setup errors were -3.86 to 3.62mm, -2.53 to 4.57mm and -4.51 to 4.31mm respectively.

Conclusion: S-M_OPS can greatly improve setup accuracy and stability compared with laser line-guided setup. Furthermore, S-M_OPS can provide comparable setup accuracy to CBCT in less setup time.

KEYWORDS

S-M_OPS, CBCT, laser line, setup, radiotherapy

1 Introduction

Radiotherapy is an important treatment for cancer, which can be used alone or in combination with chemotherapy and surgery to improve patient survival or prolong life (1–3). And the accuracy of radiotherapy setup directly determines the effect of fractional treatment (2, 4). Nowadays, the most frequently setup method is using thermoplastic combine markers for the patient positioning in fractions, and re-acquiring images for the positioning verification when necessary (5, 6). Commonly used image acquisition technologies for setup include cone beam computed tomography (CBCT), electronic portal imaging device (EPID), magnetic resonance imaging (MRI), binocular X-ray image guidance (including implanted gold fiducial markers), etc. (5, 7). Among them, CBCT has become the most important imaging tool for the radiotherapy setup in the past several years considering its unique advantages: three-dimensional imaging, sufficient contrast and low radiation dose, etc. (8, 9). Recent studies have shown that acquiring image for positioning verification in each fraction is beneficial to improve positioning accuracy. But these image acquisition technologies not only make patients suffer from additional radiation, but also cause extra time consumption, burdening those countries and regions with insufficient radiotherapy resources (5, 10, 11). Taking China as an example, there were 4.57 million new cancer cases in 2020, accounting for 23% of the global new cancer cases (19.29 million cases) (12, 13). However, the rate of radiotherapy equipment per million population in China was only 1.5 (14), which was lower than the WHO requirement (4 devices per million population) (15). Furthermore, other low- and middle-income countries (LIMICs) have more scant radiotherapy resources (16). Therefore, considering the time consumption and additional radiation dose, the number of unnecessary image-guided setup should be generally minimized (17–19).

In view of the above problems, many new setup methods have been proposed, including Catalyst (20), Sentinel (21), ExacTrac (7, 22–24), etc. Catalyst and Sentinel use structured light to capture 3D surface of the patient, and register the acquired surface to the previous recorded one for setup error detection. ExacTrac is assisted by two orthogonal KV-level X-ray imaging systems. Although above methods adopt new technologies in clinic, the improvement of the speed, accuracy and stability is limited. In addition, for some daily setup methods, represented by the laser line, it is also difficult to achieve high-precision and high-stability tumor positioning.

In this study, in order to assess the setup speed, accuracy and stability of "Sphere-Mask" Optical Positioning System (S-M_OPS), we used S-M_OPS to collect clinical setup data, and used co-setup experiment of S-M_OPS, laser line and CBCT to verify the feasibility of S-M_OPS for fast and accurate setup.

2 Materials and methods

2.1 S-M_OPS

S-M_OPS is an infrared optical positioning system that enables non-invasive precise positioning during setup and real-time tracking during treatment (25). It adopts rigid registration, which has been proven reliable (26). S-M_OPS consists of the infrared binocular camera, thermoplastic mask, positioning spheres, and S-M_OPS treatment planning system (S-M_OPS TPS), which can provide functions such as calculation, registration, monitoring, recording and early warning.

Process of S-M_OPS can be mainly divided into preparation stage, planning stage and treatment stage, as shown in Figure 1:

Preparation stage: The purpose is to record the position of treatment isocenter. The detailed procedures are listed as follows: 1) Through the stickum on the bottom of the spheres, fix an infrared positioning sphere on the front of the gantry arm and on the couch close to the linear accelerator, respectively; 2) Rotate the accelerator and the couch; 3) Track the positioning spheres by infrared binocular camera, and obtain the rotation axes of the accelerator and the couch; 4) Record the intersection of the two axes (or the midpoint of the common perpendicular line of the two axes) as the treatment isocenter. Note: Considering that the relative position between infrared binocular camera and couch is fixed, it is sufficient to register once. However, in order to reduce the influence of mechanical error on the setup accuracy, the isocenter position should be obtained once a day and the registration repeatability error of

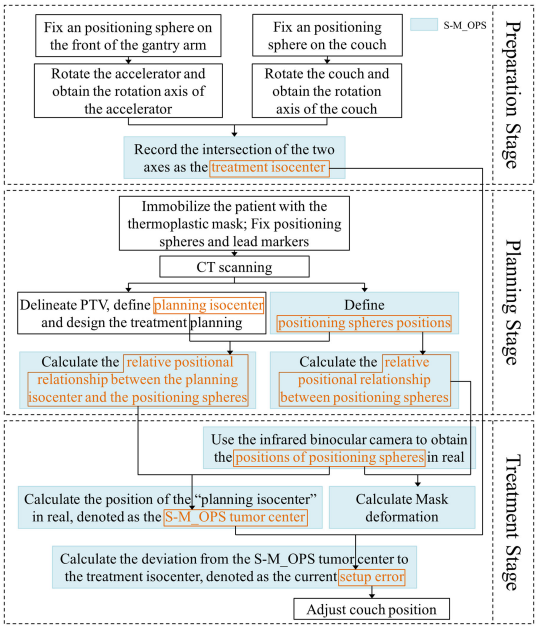

FIGURE 1
The workflow of S-M_OPS.

treatment isocenter should be kept within 0.5mm (If repeatability error is greater than 0.5mm, arrange for the staff to calibrate the accelerator).

Planning stage: The purpose is to acquire the position of planning isocenter, the relative positional relationship between positioning spheres, and relative positional relationship between the planning isocenter and the positioning spheres. The detailed procedures are listed as follows: 1) Immobilize the patient with the thermoplastic mask, and fix the positioning spheres on the thermoplastic mask permanently according to the standard sphere positions (as shown in Figure 2, the positioning spheres are located at the bony markers). 2) Perform the CT scan. 3) The physicist delineates PTV, defines planning isocenter (the intersection of the lead marks) and designs the treatment plan. 4) S-M_OPS TPS loads CT images and recognizes positioning spheres positions in the CT images. 5) S-M_OPS TPS loads the treatment plan and obtains the planning isocenter. 6) S-M_OPS TPS calculates the relative positional relationship between positioning spheres according to the positions of positioning spheres in the CT image. 7) S-M_OPS TPS calculates the relative positional relationship between the planning isocenter and the positioning spheres according to the positions of positioning spheres and the position of the planning isocenter.

Treatment stage: The purpose is to calculate the setup error. The detailed procedures are listed as follows: 1) S-M_OPS uses infrared binocular camera to obtain the positions of positioning spheres in real. 2) According to positions of positioning spheres and the relative positional relationship between the planning isocenter and the positioning spheres (obtained in the planning stage), S-M_OPS TPS calculates the position of the "planning isocenter" in real, denoted as the S-M_OPS tumor center. 3) According to the treatment isocenter obtained in the preparation stage, S-M_OPS TPS calculates the deviation from the S-M_OPS tumor center to the treatment isocenter, denotes as the current setup error. 4) The radiotherapist can move the couch according to the setup error calculated by S-M_OPS TPS. 5) Meanwhile, S-M_OPS TPS can calculate the mask deformation according to the change of the relative positional relationship between positioning spheres.

2.2 Supervision setting and population

We cooperated with 12 hospitals in China (Appendix p1) from 2016 to 2021. Use S-M_OPS to supervise 15441 fractions in 1981 patients (with cancers in intracalvarium, nasopharynx, esophagus, lung, liver, abdomen or cervix) undergoing intensity-modulated radiation therapy (IMRT), and to record the data such as registration time, mask deformation and setup error.

Note: Registration time referred to the time for aligning laser lines to crosshairs on the thermoplastic mask. Mask deformation was defined as the geometric distance L_i ($L_i = \sqrt{(A_i - B_i)^2}$) between the sphere i's position B_i during the treatment stage and the sphere i's position A_i during the planning stage ($i = 1…N$, N was the number of spheres supervised). The setup error referred

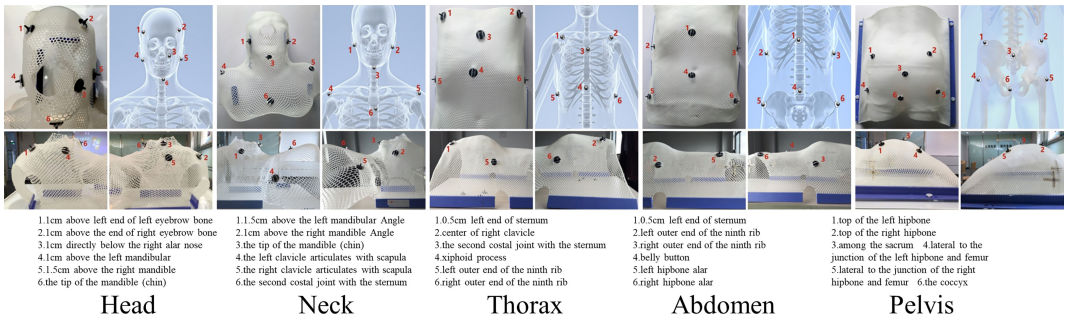

FIGURE 2
Reference positions of the positioning spheres in different parts (Upper left: top view; Upper right: skeletal diagram; Lower left: left view; Lower right: right view).

to the laser line-guided error calculated with CBCT-guided setup result as the standard.

2.3 Co-setup setting and population

We randomly selected 277 from 15441 fractions mentioned above for the co-setup of S-M_OPS, laser line and CBCT. The specific clinical experiment flow is shown in Figure 3. In addition, we performed the preparation stage of S-M_OPS before each fraction, and confirmed the repeatability error was less than 0.5mm.

In this study, we arranged three physicists with more than 5 years of work experience for manual verification of CBCT automatic registration results, and took the average of the manual verification results as final CBCT registration result. As shown in Figure 4, the CBCT tumor center location (denoted as CBCT tumor center) was obtained from CBCT registration, the laser line tumor center location (denoted as laser line tumor center) was obtained from laser line registration and the S-M_OPS tumor center location (denoted as S-M_OPS tumor center) was obtained from S-M_OPS registration. Taking CBCT registration result as reference, we calculated the laser line-guided setup error (denoted as D_{Laser}, as shown in Figure 4)

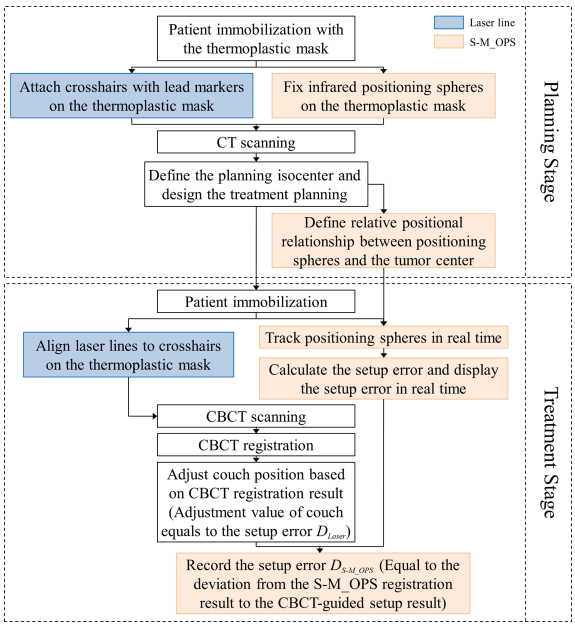

FIGURE 3
The workflow of clinical co-setup experiment.

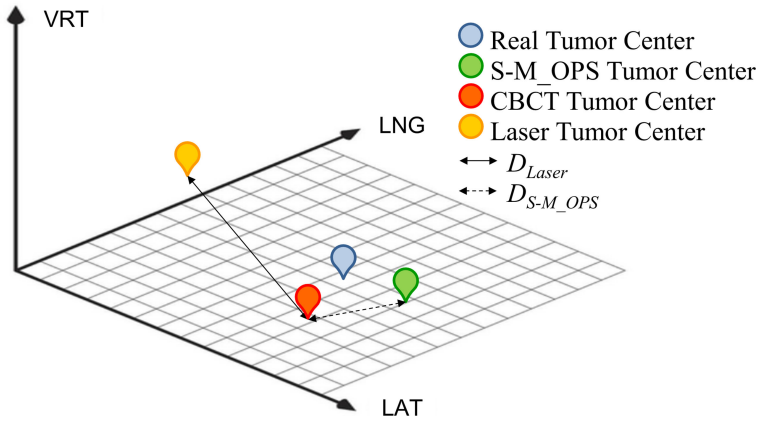

FIGURE 4
Schematic diagram of CBCT tumor center, laser line tumor center, S-M_OPS tumor center, D_{Laser} and $D_{S\text{-}M\_OPS}$.

and the S-M_OPS-guided setup error (denoted as $D_{S\text{-}M\_OPS}$, as shown in Figure 4). D_{Laser} was defined as the deviation from the laser line tumor center to the CBCT tumor center, and $D_{S\text{-}M\_OPS}$ was defined as the deviation from the S-M_OPS tumor center to the CBCT tumor center.

For laser line-guided setup errors and S-M_OPS-guided setup errors, *F*-test was adopted to test for equality of variances. Statistical significance was defined as $p<0.05$.Note: In the co-setup study, patients were scanned with the Brilliance^{TM} Big Bore CT Scanner (PHILIPS, Eindhoven, Netherlands), with 3mm slice thickness for head and 5mm for chest and abdomen. The treatment planning system was Pinnacle treatment planning system (PHILIPS, Eindhoven, Netherlands) and the CBCT was XVI system (Elekta, Stockholm, Sweden).

This study was approved by the hospital ethics committee. All patients involved provided written informed consent before participating into the study.

3 Results

3.1 S-M_OPS supervision results

1981 patients consisted of 1223 males (61.7%) and 758 females (38.3%), with average age of 63.6 years and a median age of 66 years. We finally obtained 4949 valid data of registration time, 15441 valid sets of mask deformation (a total of 78443 valid reference points) and 13827 valid sets of setup errors.

Registration time: The average time was 31.75s, the standard deviation (SD) was 29.42s, and the median was 22s. The specific distribution is shown in Figure 5A.

Mask deformation: The data distribution is shown in Figure 5B: the average deformation was 1.14±1.16mm, and the median was 0.90mm. Among all the reference points, 87.2% were deformed by less than 2mm, and 94.8% were deformed by less than 3mm.

Setup error: Taking the S-M_OPS registration result as the standard, the laser line-guided setup error distributions in different directions were shown in Figures 5C–E. In the LAT, VRT and LNG directions, the 95% CIs of the setup errors were -3.75 to 4.42mm, -3.92 to 4.84mm and -5.50 to 4.51mm respectively, and the setup errors (mean ± SD) were 0.34 ±2.09mm, 0.46±2.24mm and -0.49±2.55mm respectively.

3.2 Co-setup results

3.2.1 D_{Laser} and $D_{S\text{-}M\_OPS}$

The specific distributions of D_{Laser} and $D_{S\text{-}M\_OPS}$ are shown in Figure 6. In LAT (left/right), VRT (superior/inferior), LNG (anterior/posterior) and D ($D=\sqrt{LAT^2+LNG^2+VRT^2}$) directions, the setup errors (mean±SD) of D_{Laser} were -0.21 ±3.13mm, 1.02±2.76mm, 2.22±4.26mm and 5.36±3.58mm respectively, and the 95% confidence intervals (95% CIs) of D_{Laser} were -6.35 to 5.93mm, -4.39 to 6.43mm, -6.14 to 10.58mm and -1.65 to 12.38mm respectively. The setup errors (mean±SD) of $D_{S\text{-}M\_OPS}$ were 0.12±1.91mm, 1.02±1.81mm, -0.10±2.25mm and 2.94±2.09mm respectively, and the 95%CIs of $D_{S\text{-}M\_OPS}$ were -3.86 to 3.62mm, -2.53 to 4.57mm, -4.51 to 4.31mm and -1.15 to 7.04mm respectively. It indicated that S-M_OPS-guided setup accuracy and stability were better than those of laser line-guided in all directions. The results of *F*-test were showed in Table 1. A significant difference favouring S-M_OPS in all direction was observed ($p<0.01$ in all direction).

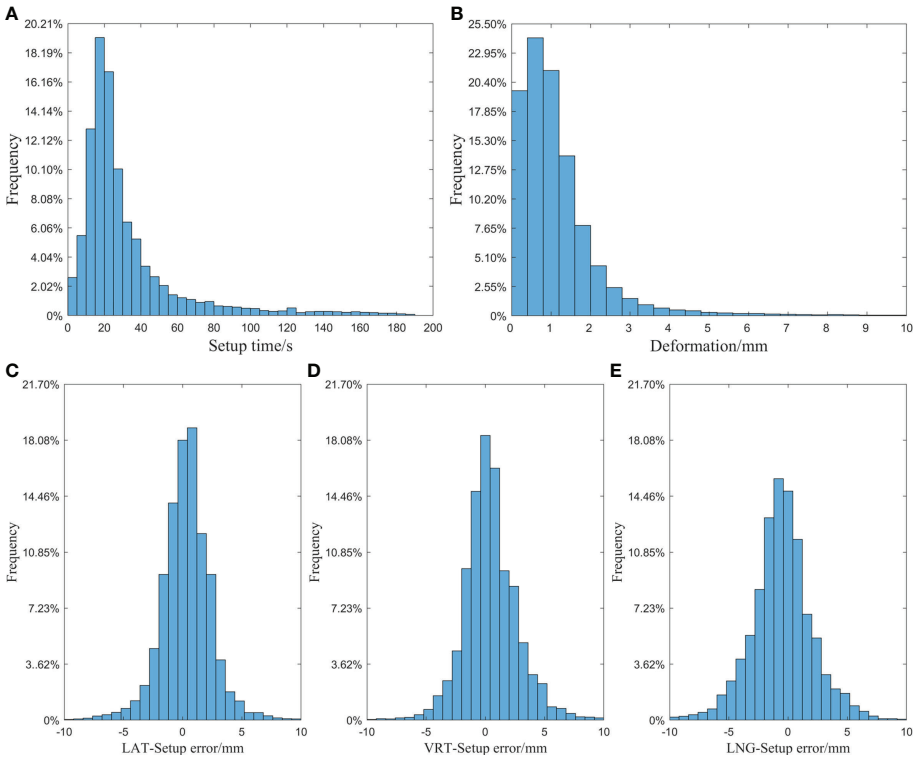

FIGURE 5
(A) Histogram of setup time of laser line; **(B)** Histogram of mask deformation; **(C)** Histogram of setup error in the LAT direction; **(D)** Histogram of setup error in the VRT direction; **(E)** Histogram of setup error in the LNG direction.

3.2.2 D_{Laser} and $D_{S\text{-}M\_OPS}$ of different parts

We subdivided 277 sets of data into cancer in intracalvarium (24 cases), nasopharynx (21 cases), esophagus (80 cases), lung (35 cases), liver (25 cases), abdomen (28 cases) and cervix (64 cases). The mean±SD of D_{Laser} and $D_{S\text{-}M\_OPS}$ of above parts in the LAT, VRT, LNG and D directions are shown in Table 1, and the 95% CIs are shown in Figure 7.

3.3 Clinical setup consistency

In addition to the SD and 95% CI, clinical setup consistency is also a crucial index of the setup stability. The clinical setup consistency can be defined as the proportion of the setup error meets the setup requirements clinically. For different parts, the clinical setup consistency has different requirements. For head, neck and thorax, setup error less than ±3.0 mm can be considered to meet clinical setup requirement, and for abdomen and cervix, setup error shouldn't be greater than ±5.0 mm (27–29). Figure 8 shows the laser line-guided setup consistencies and S-M_OPS-guided setup consistencies in different parts and directions. It showed that S-M_OPS could better meet the clinical setup requirements on various parts in all directions.

4 Discussion

We can evaluate a setup method from multiple perspectives generally, such as setup accuracy, setup stability, setup time and safety. High setup accuracy and setup stability can reduce additional radiation and improve safety. The shorter setup time can not only reduce patients discomfort caused by prolonged immobility, but also greatly improve the utilization efficiency of radiotherapy equipment, which is especially important for countries with insufficient radiotherapy resources. From the supervised results, the mean time for laser line-guided setup was 31.75s. In addition, through our records, the mean time for CBCT-guided setup was 228.84s (including the time for CBCT scan and the time for manual verification of automatic registration results). The mean time for S-M_OPS-guided setup was 7.47s. We find compared with CBCT-guided setup, S-M_OPS-guided setup does not require time for imaging and manual verification, which reduces setup time significantly. What's more, the CBCT-guided registration result or

10.3389/fonc.2022.918296

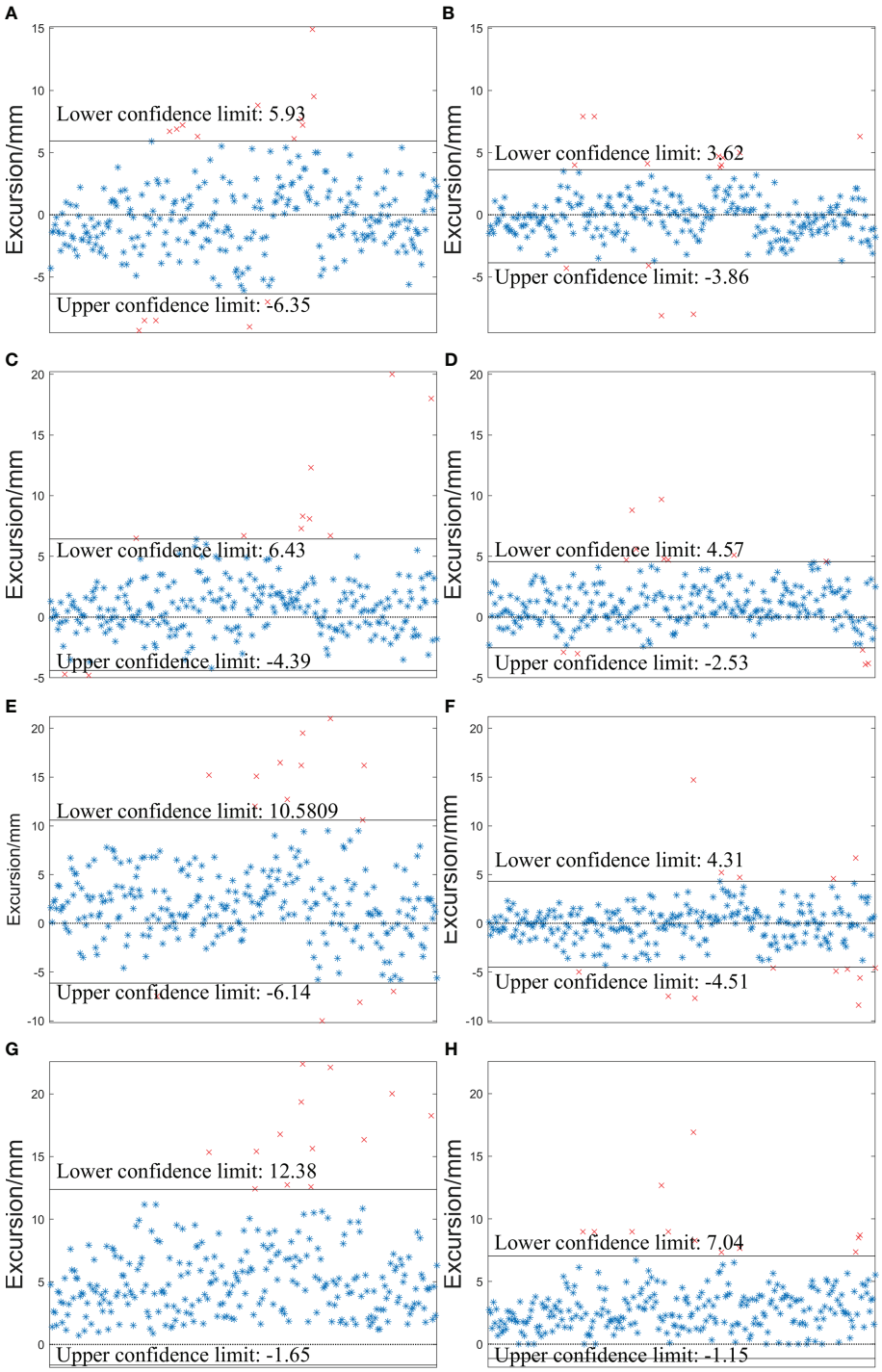

FIGURE 6

Distributions of D_{Laser} and $D_{S\text{-}M\_OPS}$ in the LAT (left/right), VRT (superior/inferior) and LNG (anterior/posterior) and D ($D = \sqrt{LAT^2 + LNG^2 + VRT^2}$) directions. **(A)** D_{Laser} -LAT; **(B)** $D_{S\text{-}M\_OPS}$ -LAT; **(C)** D_{Laser} -VRT; **(D)** $D_{S\text{-}M\_OPS}$ -VRT ; **(E)** D_{Laser} -LNG; **(F)** $D_{S\text{-}M\_OPS}$ -LNG; **(G)** D_{Laser} -D; **(H)** $D_{S\text{-}M\_OPS}$ -D.

TABLE 1 Comparisons among laser line-guided setup errors and S-M_OPS-guided setup errors.

		LAT		VRT		LNG		D	
		Mean ± SD	*p*	Mean ± SD	*p*	Mean ± SD	*p*	Mean ± SD	*p*
All	Laser	-0.21 ± 3.13	$<10^{-15}$	1.02 ± 2.76	$<10^{-11}$	2.22 ± 4.26	$<10^{-24}$	5.36 ± 3.58	$<10^{-17}$
	S-M_OPS	0.12 ± 1.91		1.02 ± 1.81		-0.10 ± 2.25		2.94 ± 2.09	
Intracalvarium	Laser	-1.24 ± 1.52	0.01	-0.22 ± 1.52	0.21	2.00 ± 2.56	$<10^{-4}$	3.67 ± 1.72	$<10^{-3}$
	S-M_OPS	-0.66 ± 0.94		0.32 ± 1.29		-0.03 ± 1.09		1.85 ± 0.84	
Nasopharynx	Laser	-1.20 ± 1.40	0.02	0.13 ± 1.91	0.03	2.09 ± 3.00	$<10^{-6}$	3.92 ± 2.15	$<10^{-2}$
	S-M_OPS	-0.64 ± 0.88		1.25 ± 1.26		-0.06 ± 0.89		1.93 ± 1.15	
Esophagus	Laser	-0.30 ± 3.29	$<10^{-2}$	1.05 ± 2.36	0.29	2.18 ± 3.46	$<10^{-8}$	5.10 ± 2.83	$<10^{-2}$
	S-M_OPS	0.23 ± 2.32		0.95 ± 2.22		-0.54 ± 1.78		3.15 ± 2.17	
Lung	Laser	-1.65 ± 3.83	$<10^{-5}$	1.39 ± 2.21	0.06	2.91 ± 3.34	0.44	5.84 ± 3.02	0.45
	S-M_OPS	-0.40 ± 1.86		1.21 ± 1.68		0.03 ± 3.43		3.15 ± 3.08	
Liver	Laser	2.79 ± 2.10	0.06	2.02 ± 1.91	0.05	6.43 ± 5.15	$<10^{-7}$	7.76 ± 5.22	$<10^{-4}$
	S-M_OPS	1.87 ± 1.51		1.67 ± 1.37		2.04 ± 1.55		3.54 ± 2.09	
Abdomen	Laser	-0.28 ± 2.52	0.12	1.40 ± 3.98	$<10^{-3}$	0.82 ± 3.28	0.43	4.93 ± 3.25	0.02
	S-M_OPS	-0.29 ± 2.01		-0.04 ± 2.01		-0.26 ± 3.17		3.64 ± 2.14	
Cervix	Laser	-0.25 ± 3.16	$<10^{-10}$	0.98 ± 3.49	$<10^{-10}$	1.00 ± 5.38	$<10^{-13}$	5.79 ± 4.37	$<10^{-13}$
	S-M_OPS	-0.73 ± 1.35		1.39 ± 1.45		-0.41 ± 1.94		2.78 ± 1.58	

Values are shown in mean ± SD and *p*-value (*F*-test).

the laser line-guided registration result is physicist-dependent, which can be affected by personal experience. In contrast, S-M_OPS adopts point-optimized registration algorithm. It can provide unique registration result based on mathematical optimization calculations.

In addition to setup time, the mask deformation is also often overlooked by radiotherapists. It is generally caused by patient's wrong posture, inaccurate setup, respiratory movement and body size change. The data (Figure 5B) showed that 12.8% of reference points had an average deviation of more than 2 mm

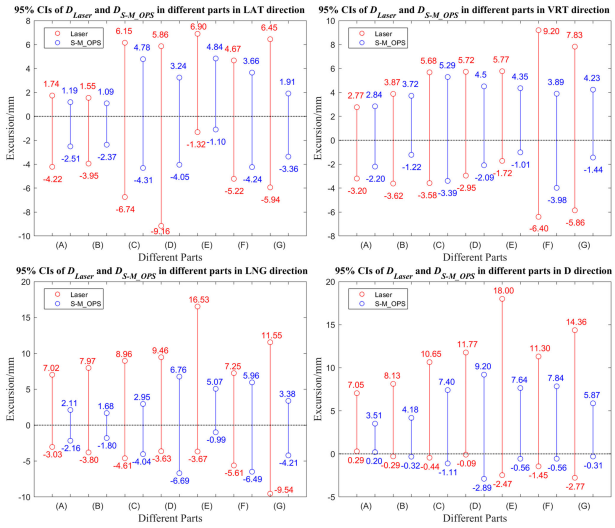

FIGURE 7
95% Confidence intervals of D_{Laser} and $D_{S\text{-}M\_OPS}$ in different parts in the LAT, VRT, LNG and D directions. **(A)** Intracalvarium; **(B)** Nasopharynx; **(C)** Esophagus; **(D)** Lung; **(E)** Liver **(F)** Abdomen; **(G)** Cervix.

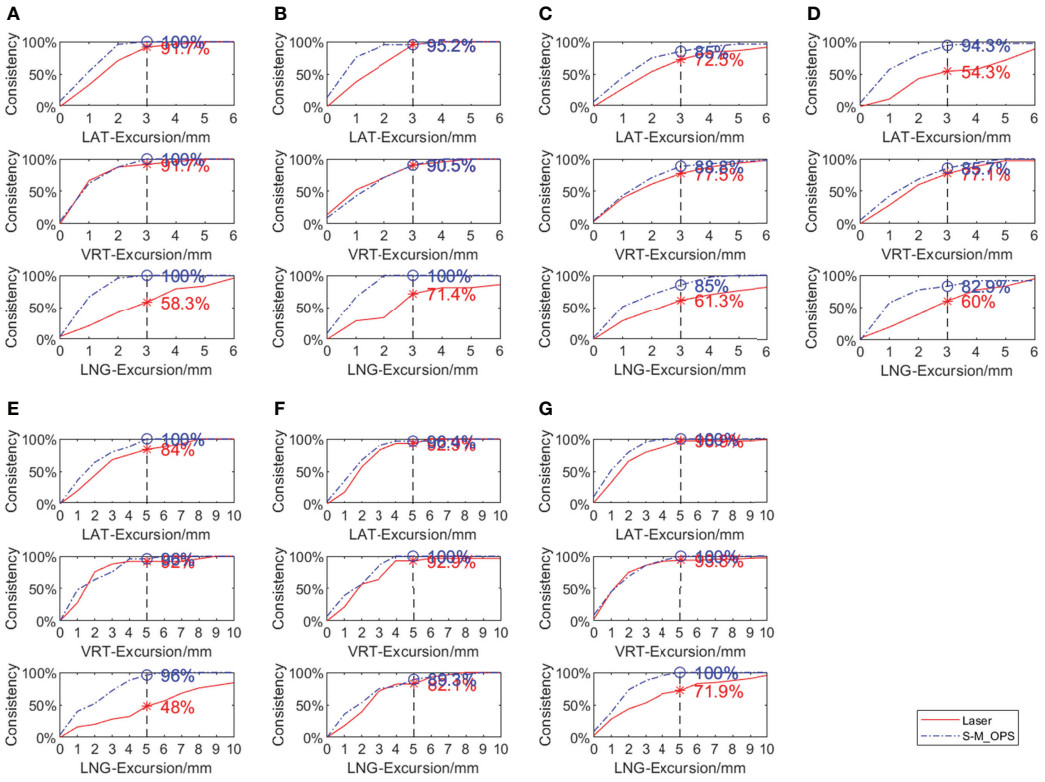

FIGURE 8
Comparison between laser line-guide setup consistency and S-M_OPS-guide setup consistency in different parts in the LAT, VRT, and LNG directions **(A)** Intracalvarium; **(B)** Nasopharynx; **(C)** Esophagus; **(D)** Lung; **(E)** Liver **(F)** Abdomen; **(G)** Cervix.

and 5.2% had an average deviation of more than 3 mm in fractions. Therefore, if the setup error is small but the mask deformation is large, it may result from the patient's wrong posture. So the patient should be re-immobilized. What's more, after a long treatment cycle, there may exist some changes of the patient's body size. Under this circumstance, the thermoplastic mask should be reshaped and the radiotherapy treatment plan should be remade, especially for obese patients.

Throughout the co-setup experiment, in order to reduce the uncertainties caused by mechanical error and human factor, we performed the preparation stage of S-M_OPS first to reduce the uncertainty caused by linear accelerator. In addition, we arranged three experienced physicists for manual verification in order to exclude the influence of human factors. However, we took the mechanical error of laser line and the human factor of laser line-guided registration into consideration, because these uncertainties were unavoidable for laser line-guided setup.

First, according to Table 1, it showed that S-M_OPS provided better setup accuracy than laser line, especially in the LNG direction. This was mainly due to the presence of slice thicknesses of 2 to 5 mm in CT data. In the radiotherapy planning stage, the lead marks were fixed on the thermoplastic mask, and lead marks were imaged by CT. The intersection of lead marks in the CT image was the planning isocenter, and the positions of lead markers on the thermoplastic mask were the positions where laser lines were aligned. Ideally, the intersection of the laser lines should be the location of the planning isocenter for radiotherapy. However, due to the thickness of CT slices, the lead markers appeared in multiple consecutive slices, and the center of the lead marker was not necessarily imaged on a specific layer. So this will lead to a deviation from the selected planning isocenter to the ideal planning isocenter. And it would lead to the deviation from the selected planning center to the intersection of laser lines (ideal planning isocenter), especially in LNG direction. While S-M_OPS uses the positioning spheres with diameter of 11mm, which can be imaged by the CT and show up in at least 2 slices. According to different cross-sections' diameters of the same positioning sphere on consecutive CT slices, S-M_OPS can accurately calculate the position of positioning sphere's center in combination with the geometric relationship. Therefore, there is no necessity to image S-M_OPS positioning sphere center on a specific CT slice, which makes S-M_OPS provide high setup accuracy in the LNG direction. And it can also qualitatively draw the above conclusion from the supervision results of S-

M_OPS (mean, SD and 95% CI of Figures 5C, D, E), which shows laser line-guided setup results and S-M_OPS-guided setup results have the largest difference in the LNG direction.

Second, according to the shorter confidence intervals (Figures 6, 7) and smaller SDs (Table 1), it also concluded that S-M_OPS could provide higher setup stability ($p< 0.01$ in all directions). High setup stability was attributed to the fact that S-M_OPS used multiple reference markers (6 positioning spheres) and selected 3 to 6 markers for registration. These selected marks were most consistent with the relative positional relationship between positioning spheres obtained during the treatment planning stage. So S-M_OPS is more likely to reduce setup errors and provides the higher setup stability.

Compared with the laser line, S-M_OPS significantly improved the clinical setup consistency in all parts. Especially in the areas with many bony structures such as the intracalvarium and pelvis, the setup consistencies of S-M_OPS all reached 100% in LAT, VRT and LNG directions. In addition, our experiments also showed that the S-M_OPS-guided setup consistencies were not prominent when applied in the esophagus and lungs, where S-M_OPS-guided setup consistencies were less than 90% in most directions. It was mainly due to the influence of respiratory movement, and deformation of thermoplastic mask was difficult to reflect the position changes of organs and tissue accurately. However, it might also be caused by the following reason: this study was based on CBCT-guided setup results, and CBCT was not suitable for monitoring intra-fraction motion considering the time spent on scan and reconstruction. Therefore, it remains to be further studied whether the S-M_OPS-guided setup consistency can be calculated based on CBCT-guided setup result in the esophagus and lung.

And finally, compared with the Sentinel, Catalyst and ExacTrac, S-M_OPS-guided setup errors were smaller than those of Sentinel and Catalyst in all parts and directions. And S-M_OPS-guided setup errors were smaller than those of ExacTrac in the vast majority of the setup results (shown in Table 2) (20–22, 30, 31). For Sentinel and Catalyst, the setup accuracy is mainly affected by the following three factors. First, there is not enough light reflected from the surface (20, 21). Second, due to the posture changes in different fractions, the surface is prone to deformation. Third, the surface is symmetrical along the VRT direction, which can affect the positioning accuracy in LNG and VRT direction (32). Different from Sentinel and Catalyst, S-M_OPS enhance the reflective light by coating positioning sphere's surface with reflective material. Second, S-M_OPS used thermoplastic mask to immobilize the patient to maintain a relatively invariant posture. Third, the distribution of positioning spheres is asymmetric. Therefore, S-M_OPS-guided setup accuracy and stability are higher. For ExacTrac, it needs X-ray imaging to assist with setup. However, X-ray imaging not only brings additional radiation, but also takes a lot of time. According to Linthout N's clinical trial report, the average time of ExacTrac-guided setup was 191s (33), which was much greater than time consumption of S-M_OPS-guided setup (7.47s). In addition, in terms of the complexity of the operation, ExacTrac needs X-ray imaging. Sentinel and Catalyst need to adjust parameters (gain and integration time) (20, 21), but S-M_OPS doesn't need additional operation, which bring convenience to radiotherapists.

5 Conclusion

In conclusion, the setup accuracy and stability of S-M_OPS are significantly higher than those of laser line, Sentinel, Catalyst and ExacTrac. What's more, S-M_OPS has the comparable setup accuracy to CBCT and the shorter setup

TABLE 2 Comparisons among S-M_OPS-guided setup errors, Sentinel-guided setup errors, Catalyst-guided setup errors and ExacTrac-guided setup errors.

		Head and neck/mm	Thorax/mm	Pelvis/mm	Overall/mm
LAT	S-M_OPS	0.1 ± 2.1	-0.1 ± 1.9	-0.6 ± 1.6	-0.2 ± 1.9
	Sentinel	0.9 ± 1.8	1.2 ± 3.6	-2.5 ± 4.1	-1.0 ± 3.6
	Catalyst	0.3 ± 2.4	0.7 ± 3.3	1.2 ± 2.5	-0.7 ± 2.8
	ExacTrac	4.1 ± 2.7	0.1 ± 1.8	-0.6 ± 2.7	N/A
VRT	S-M_OPS	1.0 ± 2.1	1.1 ± 1.8	1.0 ± 1.8	1.0 ± 1.9
	Sentinel	-2.7 ± 3.8	0.8 ± 5.1	-4.6 ± 7.3	1.0 ± 6.3
	Catalyst	-3.7 ± 3.4	-0.7 ± 3.8	0.2 ± 3.7	-1.3 ± 4.0
	ExacTrac	1.2 ± 0.5	0.2 ± 2.4	-0.3 ± 2.3	N/A
LNG	S-M_OPS	-0.4 ± 1.7	0.2 ± 3.2	-0.4 ± 2.4	-0.3 ± 2.3
	Sentinel	-0.8 ± 3.6	0.8 ± 4.3	-5.1 ± 7.4	-1.8 ± 5.9
	Catalyst	-0.2 ± 3.4	2.4 ± 3.2	1.8 ± 3.7	1.5 ± 3.6
	ExacTrac	1.1 ± 0.7	-0.6 ± 1.8	1.6 ± 3.5	N/A

Values are shown in mean ± SD with best shown with shading.
NA, not applicable.

time, which is especially suitable for countries with insufficient radiotherapy resources.

Data availability statement

The raw data supporting the conclusions of this article will be made available by the authors, without undue reservation.

Ethics statement

The studies involving human participants were reviewed and approved by Medical Technology Access Management Committee, Medical Department, Nantong Tumor Hospital. The patients/participants provided their written informed consent to participate in this study. Written informed consent was obtained from the individual(s) for the publication of any potentially identifiable images or data included in this article.

Author contributions

YZ and YG contributed to the concept of the study. YZ, HZ, YG, WS, YC and XH reviewed the manuscript. YZ, YG designed the study and did the literature search. YZ, KC, CW, YG, GS, JZ, JC and JJ collected the data. YZ, KC, CW, YG, GS, JZ, JC and JJ contributed to the data analysis and data interpretation. YZ and YG drafted the manuscript. YZ, HZ, YG, YC and XH revised the manuscript. YZ and YG have verified the data and had final decision to submit for publication. All authors contributed to the article and approved the submitted version.

Funding

This study was supported by the Jiangsu Provincial Social Development Key R&D Program (BE2020685), the National Natural Science Foundation of China (81973872), the Natural Science Foundation of Jiangsu Province (BK20191250) and the Nanjing Medical University Science and Technology Development Fund (NMUB2020271).

Conflict of interest

The authors declare that the research was conducted in the absence of any commercial or financial relationships that could be construed as a potential conflict of interest.

Publisher's note

All claims expressed in this article are solely those of the authors and do not necessarily represent those of their affiliated organizations, or those of the publisher, the editors and the reviewers. Any product that may be evaluated in this article, or claim that may be made by its manufacturer, is not guaranteed or endorsed by the publisher.

References

1. Chang JY, Senan S, Paul MA, Mehran RJ, Louie AV, Balter P, et al. Stereotactic ablative radiotherapy versus lobectomy for operable stage I non-Small-Cell lung cancer: A pooled analysis of two randomised trials. *Lancet Oncol* (2015) 16(6):630–7. doi: 10.1016/S1470-2045(15)70168-3

2. Citrin DE. Recent developments in radiotherapy. *New Engl J Med* (2017) 377 (11):1065–75. doi: 10.1056/NEJMra1608986

3. World Health Organization. *Who list of priority medical devices for cancer management*. Geneva, Switzerland: World Health Organization (2017) Available at: https://www.who.int/publications/i/item/9789241565462

4. Hong TS, Tomé WA, Chappell RJ, Chinnaiyan P, Mehta MP, Harari PM. The impact of daily setup variations on head-and-Neck intensity-modulated radiation therapy. *Int J Radiat Oncol Biol Phys* (2005) 61(3):779–88. doi: 10.1016/j.ijrobp.2004.07.696

5. Ding GX, Alaei P, Curran B, Flynn R, Gossman M, Mackie TR, et al. Image guidance doses delivered during radiotherapy: Quantification, management, and reduction: Report of the aapm therapy physics committee task group 180. *Med Phys* (2018) 45(5):e84–99. doi: 10.1002/mp.12824

6. Paluska P, Hanus J, Sefrova J, Rouskova L, Grepl J, Jansa J, et al. Utilization of cone-beam ct for reconstruction of dose distribution delivered in image-guided radiotherapy of prostate carcinoma–bony landmark setup compared to fiducial markers setup. *J Appl Clin Med Phys* (2013) 14(3):99–112. doi: 10.1120/jacmp.v14i3.4203

7. Willoughby T, Lehmann J, Bencomo JA, Jani SK, Santanam L, Sethi A, et al. Quality assurance for nonradiographic radiotherapy localization and positioning systems: Report of task group 147. *Med Phys* (2012) 39(4):1728–47. doi: 10.1118/1.3681967

8. Scarfe WC, Farman AG. What is cone-beam ct and how does it work? *Dental Clinics North America* (2008) 52(4):707–30. doi: 10.1016/j.cden.2008.05.005

9. Bissonnette JP, Balter PA, Dong L, Langen KM, Lovelock DM, Miften M, et al. Quality assurance for image-guided radiation therapy utilizing ct-based technologies: A report of the aapm tg-179. *Med Phys* (2012) 39(4):1946–63. doi: 10.1118/1.3690466

10. Sun H, Lin T, Xie K, Gao L, Sui J, Ni X. Imaging study of pseudo-ct images of superposed ultrasound deformation fields acquired in radiotherapy based on step-by-Step local registration. *Med Biol Eng Comput* (2019) 57(3):643–51. doi: 10.1007/s11517-018-1912-2

11. Webster A, Appelt A, Eminowicz G. Image-guided radiotherapy for pelvic cancers: A review of current evidence and clinical utilisation. *Clin Oncol-Uk* (2020) 32(12):805–16. doi: 10.1016/j.clon.2020.09.010

12. Sung H, Ferlay J, Siegel RL, Laversanne M, Soerjomataram I, Jemal A, et al. Global cancer statistics 2020: Globocan estimates of incidence and mortality worldwide for 36 cancers in 185 countries. *CA Cancer J Clin* (2021) 71(3):209–49. doi: 10.3322/caac.21660

13. Ferlay J, Ervik M, Lam F, Colombet M, Mery L, Piñeros M, et al. *Global cancer observatory: Cancer today*. Lyon: International Agency for Research on Cancer; 2018 (2020).

14. Ye YJ-L Z, Wei J, Ji-Ping L, Kun-Kun Ma, Shi-Gong K, Jin-Yi L, et al. Survey on the basic information of personnel and facilities of radiotherapy in Chinese

mainland in 2019. *China Cancer* (2020) 29:321–6. doi: 10.11735/j.issn.1004-0242.2020.05.A001

15. Huh SJ, Nishimura T, Park W, Nakamura K. Comparison of radiotherapy infrastructure between Korea and Japan. *Jpn J Clin Oncol* (2019) 49(11):1024–8. doi: 10.1093/jjco/hyz124

16. Grover S, Xu MJ, Yeager A, Rosman L, Groen RS, Chackungal S, et al. A systematic review of radiotherapy capacity in low-and middle-income countries. *Front Oncol* (2015) 4:380. doi: 10.3389/fonc.2014.00380

17. Parikh NR, Lee PP, Raman SS, Cao M, Lamb J, Tyran M, et al. Time-driven activity-based costing comparison of ct-guided versus Mr-guided sbrt. *Jco Oncol Pract* (2020) 16(11):e1378–e85. doi: 10.1200/JOP.19.00605

18. Zhao Y, Zhang L, Fu Y, Wang M, Zhang L. Socioeconomic disparities in cancer treatment, service utilization and catastrophic health expenditure in China: A cross-sectional analysis. *Int J Env Res Pub He* (2020) 17(4):1327. doi: 10.3390/ijerph17041327

19. Colceriu-Şimon IM, Băciuţ M, Ştiufiuc RI, Aghiorghiesei A, Ţărmure V, Lenghel M, et al. Clinical indications and radiation doses of cone beam computed tomography in orthodontics. *Med Pharm Rep* (2019) 92(4):346. doi: 10.15386/mpr-1434

20. Stieler F, Wenz F, Shi M, Lohr F. A novel surface imaging system for patient positioning and surveillance during radiotherapy. *Strahlenther Oncol* (2013) 189 (11):938–44. doi: 10.1007/s00066-013-0441-z

21. Stieler F, Wenz F, Scherrer D, Bernhardt M, Lohr F. Clinical evaluation of a commercial surface-imaging system for patient positioning in radiotherapy. *Strahlenther Onkol* (2012) 188(12):1080–4. doi: 10.1007/s00066-012-0244-7

22. Sarkar B, Ganesh T, Munshi A, Manikandan A, Roy S, Krishnankutty S, et al. *Rotational positional error-corrected linear set-up margin calculation technique for lung stereotactic body radiotherapy in a dual imaging environment of 4-d cone beam ct and exactrac stereoscopic imaging*. Italy: La radiologia medica (2021). p. 1–10. doi: 10.1007/s11547-021-01355-7

23. Jin J-Y, Yin F-F, Tenn SE, Medin PM, Solberg TD. Use of the brainlab exactrac X-ray 6d system in image-guided radiotherapy. *Med Dosim* (2008) 33 (2):124–34. doi: 10.1016/j.meddos.2008.02.005

24. Gevaert T, Verellen D, Tournel K, Linthout N, Bral S, Engels B, et al. Setup accuracy of the novalis exactrac 6dof system for frameless radiosurgery. *Int J Radiat Oncol Biol Phys* (2012) 82(5):1627–35. doi: 10.1016/j.ijrobp.2011.01.052

25. Zhang J, Ge Y, Chen Y, Chen X. (2013). A study on the positioning accuracy of patient positioning based on optical positioning system for nasopharyngeal carcinoma: Compared with conventional method, in: *2013 IEEE International Conference on Medical Imaging Physics and Engineering (ICMIPE)*, IEEE Beijing Sect, Shenyang, CHINA 11–3. doi: 10.1109/ICMIPE.2013.6864493

26. Al-Saleh MA, Alsufyani NA, Saltaji H, Jaremko JL, Major PW. Mri and cbct image registration of temporomandibular joint: A systematic review. *J Otolaryngol-Head N* (2016) 45(1):1–7. doi: 10.1186/s40463-016-0144-4

27. Mohandass P, Khanna D, Kumar TM, Thiyagaraj T, Saravanan C, Bhalla NK, et al. Study to compare the effect of different registration methods on patient setup uncertainties in cone-beam computed tomography during volumetric modulated arc therapy for breast cancer patients. *J Med Phys* (2018) 43(4):207. doi: 10.4103/jmp.JMP_67_18

28. Velec M, Waldron JN, O'Sullivan B, Bayley A, Cummings B, Kim JJ, et al. Cone-beam ct assessment of interfraction and intrafraction setup error of two head-and-Neck cancer thermoplastic masks. *Int J Radiat Oncol Biol Phys* (2010) 76 (3):949–55. doi: 10.1016/j.ijrobp.2009.07.004

29. Batumalai V, Holloway L, Delaney GP. A review of setup error in supine breast radiotherapy using cone-beam computed tomography. *Med Dosim* (2016) 41(3):225–9. doi: 10.1016/j.meddos.2016.05.001

30. Clemente S, Chiumento C, Fiorentino A, Simeon V, Cozzolino M, Oliviero C, et al. Is exactrac X-ray system an alternative to cbct for positioning patients with head and neck cancers? *Med Phys* (2013) 40 (11):111725. doi: 10.1118/1.4824056

31. Castro A, Bardella L, Panichella J, Erlich F, Batista D. Su-E-J-49: Pelvic treatment setup differences between skin markers-based and bony references using brainlab exactrac. *Med Phys* (2013) 40(6Part7):160. doi: 10.1118/1.4814261

32. Pallotta S, Simontacchi G, Marrazzo L, Ceroti M, Paiar F, Biti G, et al. Accuracy of a 3d Laser/Camera surface imaging system for setup verification of the pelvic and thoracic regions in radiotherapy treatments. *Med Phys* (2013) 40 (1):011710. doi: 10.1118/1.4769428

33. Linthout N, Verellen D, Tournel K, Reynders T, Duchateau M, Storme G. Assessment of secondary patient motion induced by automated couch movement during on-line 6 dimensional repositioning in prostate cancer treatment. *Radiother Oncol* (2007) 83(2):168–74. doi: 10.1016/j.radonc.2007.04.015

Appendix

Jiangsu Provincial Hospital of Chinese Medicine
Nantong Tumor Hospital
Subei People's Hospital of Jiangsu Province
Suzhou Municipal Hospital
Huai'an Second People's Hospital
YYixing Tumor Hospital
Baoying People's Hospital
Yangzhou First People's Hospital
Zhejiang Cancer Hospital
Xinghua City People's Hospital
The People's Hospital of Yizheng
Jiangsu Corps Hospital of Armed Police Forces

frontiers | Frontiers in Oncology

TYPE Original Research
PUBLISHED 04 October 2022
DOI 10.3389/fonc.2022.921607

OPEN ACCESS

EDITED BY
Yingli Yang,
UCLA Health System, United States

REVIEWED BY
Yulin Song,
Memorial Sloan Kettering Cancer Center, United States
Alireza Amouheidari
Isfahan Milad Hospital, Iran

*CORRESPONDENCE
Linlin Wang
wanglinlinatjn@163.com
Jinming Yu
sdyujinming@126.com

†These authors have contributed equally to this work

SPECIALTY SECTION
This article was submitted to Radiation Oncology, a section of the journal Frontiers in Oncology

RECEIVED 16 April 2022
ACCEPTED 13 September 2022
PUBLISHED 04 October 2022

CITATION
Zhang G, Liu X, Wang L, Zhu J and Yu J (2022) Development and feasibility evaluation of an AR-assisted radiotherapy positioning system. *Front. Oncol.* 12:921607. doi: 10.3389/fonc.2022.921607

Development and feasibility evaluation of an AR-assisted radiotherapy positioning system

Gongsen Zhang[1†], Xinchao Liu[2†], Linlin Wang[1,2*], Jian Zhu[1] and Jinming Yu[1*]

[1]1Department of Radiology, Shandong Cancer Hospital and Institute, Shandong First Medical University and Shandong Academy of Medical Sciences, Jinan, China, [2]Cancer Center, Shandong University, Jinan, China

Purpose: The aim of this study is to develop an augmented reality (AR)–assisted radiotherapy positioning system based on HoloLens 2 and to evaluate the feasibility and accuracy of this method in the clinical environment.

Methods: The obtained simulated computed tomography (CT) images of an "ISO cube", a cube phantom, and an anthropomorphic phantom were reconstructed into three-dimensional models and imported into the HoloLens 2. On the basis of the Vuforia marker attached to the "ISO cube" placed at the isocentric position of the linear accelerator, the correlation between the virtual and real space was established. First, the optimal conditions to minimize the deviation between virtual and real objects were explored under different conditions with a cube phantom. Then, the anthropomorphic phantom–based positioning was tested under the optimal conditions, and the positioning errors were evaluated with cone-beam CT.

Results: Under the normal light intensity, the registration and tracking angles are 0°, the distance is 40 cm, and the deviation reached a minimum of 1.4 ± 0.3 mm. The program would not run without light. The hologram drift caused by the light change, camera occlusion, and head movement were 0.9 ± 0.7 mm, 1.0 ± 0.6 mm, and 1.5 ± 0.9 mm, respectively. The anthropomorphic phantom–based positioning errors were 3.1 ± 1.9 mm, 2.4 ± 2.5 mm, and 4.6 ± 2.8 mm in the X (lateral), Y (vertical), and Z (longitudinal) axes, respectively, and the angle deviation of Rtn was 0.26 ± 0.14°.

Conclusion: The AR-assisted radiotherapy positioning based on HoloLens 2 is a feasible method with certain advantages, such as intuitive visual guidance, radiation-free position verification, and intelligent interaction. Hardware and software upgrades are expected to further improve accuracy and meet clinicalbrendaannmae requirements.

KEYWORDS

radiotherapy positioning, augmented reality, image visualization, HoloLens 2, accuracy

1. Introduction

Radiotherapy is one of the primary treatments for cancers, and more than 50% of patients receive radiation therapy during the course of their illness (1, 2). A critical step of radiotherapy is lying the patient in the correct position on the couch of the linear accelerator for the accuracy of radiation dose delivery. Currently, patient positioning based on treatment room lasers and markers on skin or fixation devices is still routine in most radiotherapy departments. Many techniques were developed to improve the patient positioning accuracy, such as cone beam computed tomography (CBCT) and MRI-Linac. Although these techniques have improved patient positioning, there are some disadvantages: First, it makes radiotherapy more complex and expensive. Second, additional radiation dosages were delivered to the patient, which may cause unexpected consequences. Third, the complicated treatment procedures can increase the therapist's workload, resulting in fatigue, such as fatigue caused by switching attention between printed treatment plans, screens, lasers, and markers. Last but not least, these techniques can only reflect the positioning errors at the time of scanning but cannot provide real-time and non-rigid positioning guidance (3, 4).

Augmented reality (AR) is a promising visualization technology developed on the basis of virtual reality. It allows people to experience a scenario where virtual and real objects coexist (5). In recent years, AR technology has been increasingly used in medicine, such as education and training (6–8) and hologram-guided surgery (9–11). Talbot et al. first utilized the AR technique to guide the positioning of radiotherapy patients (12), which was subsequently explored and improved by Tarutani et al. (13) and Johnson et al. (14). However, there are some limitations for these methods. On the one hand, the assembly based on display devices, cameras, and computing devices increases the complexity of the system, which is not conducive to convenient technical implementation. The user's AR experience is significantly compromised due to the phantom's AR contour being displayed on a two-dimensional screen. On the other hand, the virtual-real patient alignment is based on the operator's human eye judgment, and there is a lack of effective object tracking methods.

Microsoft HoloLens 2 is a portable head-mounted AR device that integrates multiple necessary hardware and multi-functions such as computing, holographic display, and intelligent interaction, which may provide a solution with AR characteristics for patient positioning. In this paper, an AR-assisted patient positioning system based on HoloLens 2 was developed. A three-dimensional (3D) virtual model generated by treatment planning CT was anchored to the treatment position and visualized by the therapist with HoloLens 2. The innovation is that the therapist can adjust the couch under the guidance of this intuitive hologram and virtual coordinate derived from object tracking, until the real model and virtual model were registered. In addition, Vuforia SDK was used for isocenter calibration, virtual and real space coordinate system establishment, and patient tracking (15). The feasibility and accuracy of the system were evaluated in the clinical environment. As far as we know, our system is the first radiotherapy positioning method solely based on a head-mounted AR device, providing 3D object tracking and virtual coordinate indication.

2. Methods and materials

2.1 System overview

The system provides assistance for radiotherapy therapists to perform radiotherapy positioning under an intuitive holographic guidance. In our proposed AR-assisted method, HoloLens 2 was the only required hardware. Moreover, a proprietary SDK, Vuforia, was introduced and worked with the front-facing cameras of HoloLens 2 for automatic registration and real-time tracking, which improved the stability of anchored hologram in physical space to a certain extent and achieved good registration accuracy. In addition to system development and data preparation, we also designed a complete experimental process from optimal conditions exploration to phantom testing in the actual radiotherapy positioning clinical environment, as shown in Figure 1.

2.2 3D reconstruction and visualization of CT simulation image

One "ISO cube" (5 × 5 × 5 cm), one cube phantom (10 × 10 × 10 cm), and an anthropomorphic phantom (ATOM Dosimetry verification phantom) were used in this experiment. Lead markers were attached to the surface of phantoms according to the clinical routine. Vuforia markers were also attached to the "ISO cube" and two phantoms. CT simulation images were obtained with SIEMENS SOMATOM Confidence and uploaded to Varian Eclipse treatment planning system. Slice thickness was 3 mm. The treatment plan was formulated on the basis of the simulation CT. To simplify the experimental procedures, the reference points determined by three tiny lead markers were artificially defined as the isocenter. The DICOM RT images were exported to Python package and 3D Slicer programs to automatically reconstruct 3D models. Then, the 3D models and pre-designed user interface (UI) were imported into the AR scene and deployed to HoloLens 2 for holographic visualization (Figure 2).

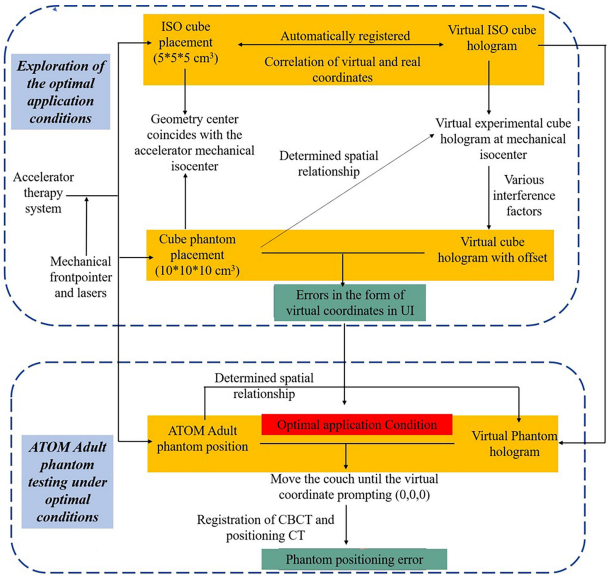

FIGURE 1
The overall experimental for the proposed AR-assisted positioning system.

2.3 Registration between real and virtual space

The lasers have been professionally calibrated before the experiment. An "ISO cube" (5 × 5 × 5 cm) used for daily QA (quality assurance) was used as a "registration cube", and it was placed at an isocentric position so that its geometric center coincided with the mechanical isocenter of the linear accelerator with the aid of room lasers and the mechanical front-pointer (Figure 3). After the therapist put on the HoloLens 2 and initiated the test procedure, the front-facing camera of the HoloLens 2 detected the Vuforia marker attached to the "ISO cube", the virtual cube would automatically be registered to the "ISO cube" (Figure 3). The therapist could perform the voice command "fixed" or the gesture interaction (Figure 3) to anchor the virtual "ISO cube", and the correlation between virtual and real space coordinates was established. At the same time, the holographic phantom would be displayed on the HoloLens 2 automatically.

2.4 Cube phantom and ATOM phantom test

2.4.1 Cube phantom test

Like the procedure for positioning "ISO cube", a cube phantom (10 × 10 × 10 cm) was placed at the isocenter of the linear accelerator. After the HoloLens 2 detected the Vuforia marker attached to the cube phantom, the position coordinates of the Vuforia marker in the established virtual space coordinate system were displayed in the virtual UI interface. Meanwhile, the coordinates of the geometric center of the cube phantom were also calculated on the basis of the known space relationships between it and Vuforia marker and were displayed. The "Offset" in the virtual UI interface reflected the deviation between the virtual and real geometric center (Figure 4). In addition, the spatial deviation was calculated with the following formula, and the results were averaged to determine the overall error:

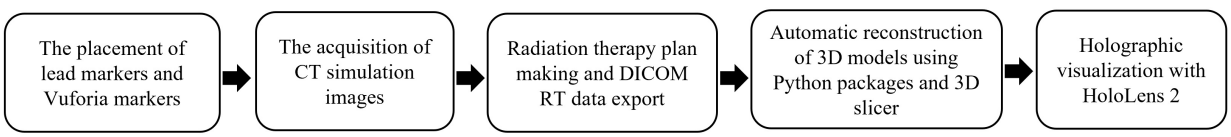

FIGURE 2
The flow from CT simulation image acquisition to holographic model visualization.

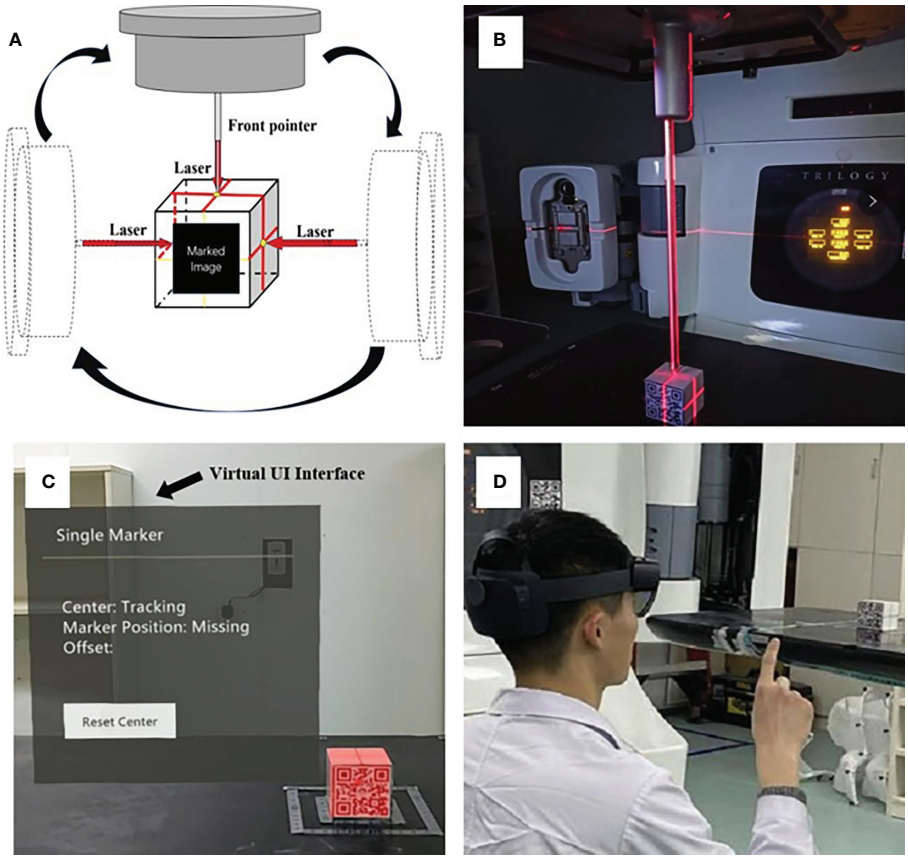

FIGURE 3
The establishment of the correlation between virtual and real space: precise placement of the "ISO cube" in the isocentric position with the aid of lasers and the mechanical front-pointer **(A, B)**; automatic registration of virtual "ISO cube" and real "ISO cube" based on the HoloLens 2's detection of Vuforia marker, and the arrow points to the virtual UI interface **(C)**; the gesture interaction to anchor the correlation between virtual and real space **(D)**.

$$D = \sqrt{X^2 + Y^2 + Z^2} \quad (1)$$

where X, Y, and Z denote the coordinates of the real geometric center in directions of lateral, vertical, and longitudinal, respectively, of the established virtual space coordinates. The factors that can impact the system's accuracy were tested, including different angles, different distances, different room light intensities, and with or without camera occlusion and head movement (Figure 4). Different angles, including registration angles and tracking angles, refer to the angle between the HoloLens 2's front-facing camera and the Vuforia marker on the "ISO cube" or the Vuforia marker on the cube phantom, respectively: 0° refers to the direction perpendicular to the Vuforia marker; 30°, 45°, 60°, and 90° are the included angles between the HoloLens 2's front camera and the vertical direction, respectively, in the horizontal plane. The distances between the front camera of HoloLens 2 and the Vuforia marker are 30, 40, 50, 60, and 70 cm. The light intensity in the treatment room for daily use is divided into normal light intensity (405.0 Lux) and low light intensity (230.0 Lux). For camera occlusion, the therapist artificially covers the front camera of HoloLens 2 for a few seconds when the holographic phantom was displayed on the HoloLens 2. The spatial drift of hologram caused by light changes, camera occlusion, and head movement can be evaluated with the variations of the above formula:

$$D = \sqrt{(X_2 - X_1)^2 + (Y_2 - Y_1)^2 + (Z_2 - Z_1)^2} \quad (2)$$

where X_1, Y_1, and Z_1 and X_2, Y_2, and Z_2, denote the coordinates of the real geometric center before and after light intensity, camera occlusion, and head movement changes, respectively.

2.4.2 Anthropomorphic phantom test

An anthropomorphic phantom was used to test the HoloLens 2–based patient positioning system in the clinical environment (Figure 5). After the registration between real and virtual space was established under the optimal

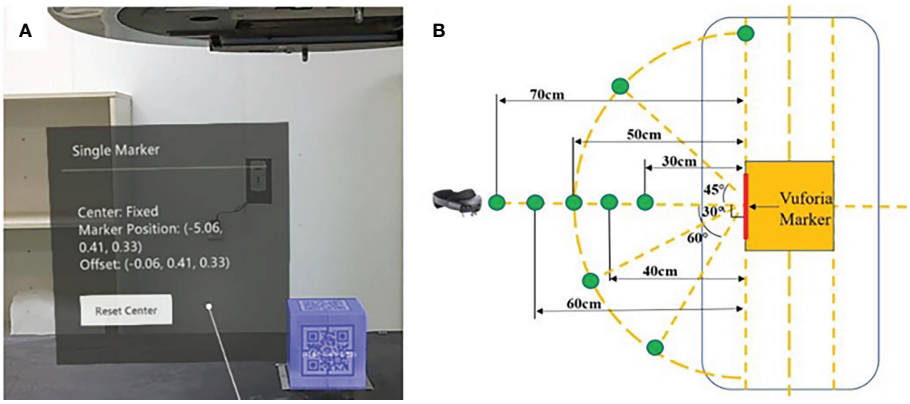

FIGURE 4
Display of offset between virtual and real geometric centers in virtual UI interface **(A)** and the units of coordinate are in centimeters; the schematic diagram of partial exploratory conditions **(B)**.

exploratory conditions and the holographic anthropomorphic phantom (blue model) in the treatment position was displayed, the therapist moved the treatment couch with the rough guidance of holographic phantom and the fine instructions of virtual coordinates until the virtual coordinates prompting 0,0,0. Then, CBCT was performed to evaluate the positioning errors (Figure 6).

2.4.3 Statistical analysis

The experimental data were presented as mean ± SD and were analyzed by paired Student's t-tests. $P<0.05$ was considered to represent a statistically significant difference.

3. Results

3.1 Exploration of optimal conditions

The factors affecting accuracy and stability were confounding, and a method of controlling variates was adopted in the measurement process. The registration angle, tracking angle, and tracking distance affect the recognition and tracking of the Vuforia marker, which has further influence on the coordinate construction and the spatial position accuracy of the holographic model in the AR scenes. For the registration angle and tracking angle, we tested the system performance at 0°, 30°, 45°, and 60°, respectively, with a total of 40 measurements;

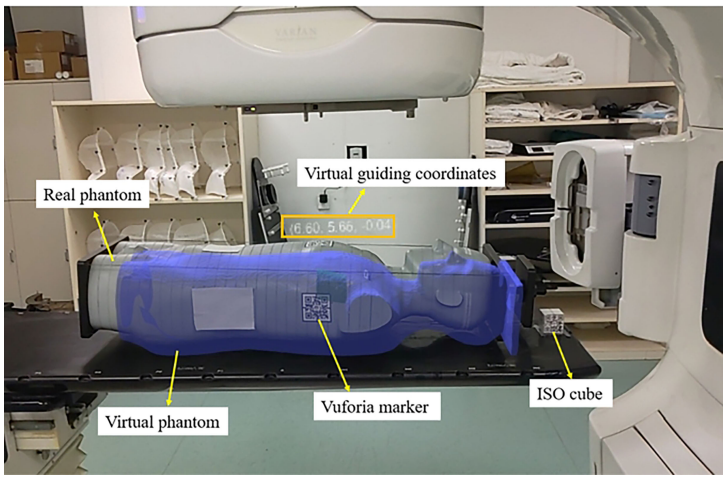

FIGURE 5
The AR scene of the therapist's perspective shows a virtual anthropomorphic phantom in the treatment position.

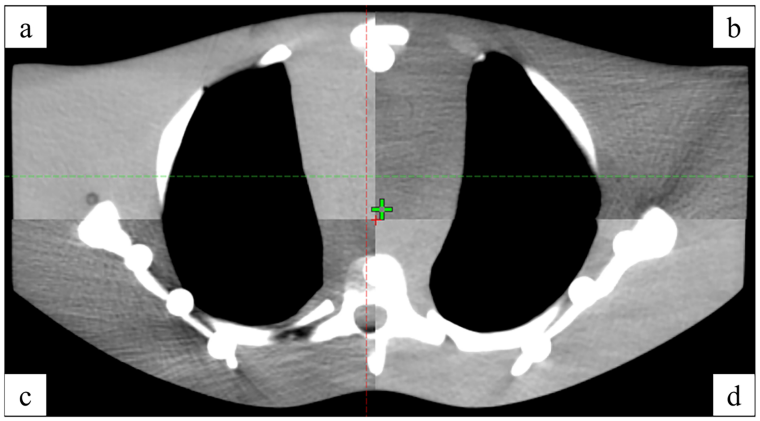

FIGURE 6
The registration between CBCT **(A, D)** and simulated positioning CT **(B, C)**.

for the distance, we tested between 30 and 70 cm with a step of 10 cm, and the total number of tests is 50. In addition, the light intensity, camera occlusion, and head movement may affect the accuracy and stability of signal feedback and detection of the depth sensors. The tests for the above three factors were performed 20 times, respectively. The results are summarized in Tables 1–3. The results of different registration angles were first recorded under the conditions that the tracking angle was consistent with the registration angle, the distance was 50 cm, light intensity was normal, and there was no camera occlusion and head movement. The results showed that there was no significant difference between 0° and 45° (P = 0.84), and significant differences between 0° and other angles (as shown in Table 1). Because 0° was easier to control, it was chosen as one of the optimal conditions. Next, the results of different tracking angles were recorded under the registration angle of 0°, and other conditions were the same as above, demonstrating significant differences between 0° and other angles (as shown in Table 2). Therefore, the tracking angle was consistent with the registration angle, and both were 0°, which can be regarded as one of the best conditions for further exploration. Then, the results of different tracking distances were recorded under the conditions that the registration angle and the tracking angle were 0°, light intensity was normal, the space deviation was minimized to 1.4 ± 0.3 mm at a distance of 40 cm, and there were significant differences between 40 cm and other distances (as shown in Table 3). The results of different light intensity in the treatment room under above optimal conditions were

TABLE 1 Errors at different registration angles.

Angle (degrees)	X (mm)	Y (mm)	Z (mm)	D (mm)	P_1
0	0.8 ± 0.4	0.9 ± .5	1.2± ± 0.7	1.9 ± 0.5	–
30	2.4 ± 0.6	0.7 ± 0.4	0.3 ± 0.2	2.5 ± 0.6	0.04
45	1.6 ± 0.4	0.4 ± 0.3	0.6 ± 0.3	1.8 ± 0.5	0.84
60	2.3 ± 0.6	0.9 ± 0.6	2.6 ± 0.9	3.7 ± 0.9	<0.01

Statistical significance P_1: 0 degree vs. other registration angles.

TABLE 2 Errors at different tracking angles.

Angle (degrees)	X (mm)	Y (mm)	Z (mm)	D (mm)	P_2
0	0.8 ± 0.4	0.9 ± 0.5	1.2 ± 0.7	1.9 ± 0.5	–
30	1.3 ± 1.1	2.0 ± 0.9	1.2 ± 0.9	3.0 ± 1.1	0.01
45	2.0 ± 1.6	2.1 ± 0.7	1.8 ± 1.8	3.9 ± 1.4	<0.01
60	1.9 ± 1.5	2.3 ± 0.8	2.4 ± 1.8	4.3 ± 1.4	<0.01

Statistical significance P_2: 0 degree vs. other tracking angles.

recorded, demonstrating no significant differences between the normal and the low light intensity (P = 0.83). The hologram drift produced by the light changes is 0.7 ± 0.4 mm. However, the program will not work without lights. The hologram drift caused by camera occlusion and head movement were 1.0 ± 0.6 mm and 1.5 ± 0.9 mm, respectively (Table 4). On the basis of the results above, the optimal conditions can be summarized as follows: the registration angle and the tracking angle were consistent at 0°, the distance was 40 cm, light intensity was normal, and there was no camera occlusion and head movement.

3.2 Accuracy results of the anthropomorphic phantom

The positioning errors in the X, Y, and Z directions were 3.1 ± 1.9 mm, 3.0 ± 2.8 mm, and 4.6 ± 2.8 mm, respectively. In addition, the angle deviation of Rtn was 0.26 ± 0.14°.

4. Discussion

In this study, an innovative AR-assisted radiotherapy positioning system was developed with HoloLens 2 as the only core hardware and provided patient tracking and virtual coordinate indication for radiation therapist, instead of relying on the human eye for virtual-real alignment (12–14, 16). Compared with the related works, this improves the convenience (12, 16), accuracy (17), and practicality of AR guidance systems. The feasibility and accuracy of this method were evaluated in the actual clinical environment. Because of the high-precision requirement of radiotherapy positioning, it is necessary to fully explore the positioning method based on the HoloLens 2 and Vuforia SDK, avoiding the factors that increase the offset between the virtual object and real object. Opposite ideas were adopted in the two stages of the experimental process. We adopted fixing the real object and then watching the virtual coordinates to explore optimal conditions based on the cube phantom. On the contrary, in the anthropomorphic phantom positioning stage, the real object was transferred under the guidance of the virtual coordinates to simulate the actual process. The results from the optimal condition exploration stage show that some factors indeed influence the accuracy of the proposed AR-assisted system, such as the distance between HoloLens 2 and Vuforia marker, as well as the registration and tracking angles, which were related to the size and plane attributes of the Vuforia marker used, respectively. In addition, camera occlusion and head movement caused hologram drift, and the randomness of drift may be brought more significant positioning errors to a certain extent.

Furthermore, the change of indoor light intensity for daily use had no significant effect on the results. Our experiments found that the virtual coordinates were prone to fluctuations, so we obtained relatively stable readings. However, the optimal application conditions obtained were not fully and accurately applied to anthropomorphic phantom–based positioning tests, except for the registration step based on the "ISO cube". For one thing, the acquisition of real-time coordinates depended on the real-time tracking of the Vuforia marker attached to the anthropomorphic phantom. However, it was difficult for the therapist to maintain the optimal distance, tracking angle, and stationary head. For another, unlike the cube phantom, although we used a relatively flat chest, the surface still has a specific curvature, which led to the pattern distortion of the Vuforia marker and may impact the recognition and tracking process. We also found that the heavier anthropomorphic phantom caused the bed to settle, unlike the lighter cube phantom. At the same time, the virtual phantom remained in its original

TABLE 3 Errors at different tracking distances.

Distance (cm)	X (mm)	Y (mm)	Z (mm)	D (mm)	P_3
30	0.9 ± 0.5	0.9 ± 0.3	1.1 ± 0.5	1.8 ± 0.3	<0.01
40	0.7 ± 0.3	1.0 ± 0.4	0.6 ± 0.4	1.4 ± 0.3	–
50	0.8 ± 0.4	0.9 ± 0.5	1.2 ± 0.7	1.9 ± 0.5	0.02
60	1.4 ± 1.0	1.4 ± 0.9	1.7 ± 0.9	3.2 ± 1.5	<0.01
70	2.0 ± 1.4	1.7 ± 1.0	1.8 ± 0.7	3.5 ± 1.0	<0.01

Statistical significance P_3: 40 cm vs. other tracking distances.

TABLE 4 The hologram drifts are caused by the light intensity change, camera occlusion, and head movement.

Drift factors	Light intensity change	Camera occlusion	Head movement
Mean (mm)	0.7	1.0	1.5
SD (mm)	0.4	0.6	0.9

position, resulting in an inherent positional deviation between the virtual and real phantom that ultimately affected positioning accuracy. The good thing was that the bed settlement could be roughly corrected according to the general outline of the virtual phantom.

The results of the anthropomorphic phantom showed that, although the accuracy is in millimeter scale, it is still not up to the requirements of clinical use at present. However, considering the advantages that this method does bring. First, the virtual 3D model is directly presented in the treatment position so that the patient positioning process is more intuitive and straightforward. Second, the decrease of CBCT frequency reduces the cost of treatment and non-treatment dose for patients. Third, the valuable information is presented in real time in virtual form, which realizes paperless and screenless and solves the problem of attention shift, and optimizes human ergonomics with the adjustment of virtual UI interface (18) in the process of positioning. Fourth, unlike CBCT, which can only collect position information at a particular moment, AR-assisted positioning can continuously monitor and correct the patient's position. Fifth, in combination with other artificial intelligence technology can realize the automatic identification of patients or fixed appliances to avoid human error. Finally, it helps radiologists remotely guide the patient's radiotherapy positioning and bring high-quality patient education by presenting previously invisible beams, target areas, and organs at risk.

Therefore, it is necessary for us to continue to explore ways to reduce the positioning error in future work. On the one hand, we will consider two or more HoloLens 2 to collaborate, share, and exchange information and realize the complementation of spatial information. On the other hand, considering the limitation caused by the planar Vuforia marker and inspired by the surface-guided radiation therapy technology, we will try to adopt binocular stereo vision or structured light to obtain the overall surface information of the phantom as the basis for 3D holographic image reconstruction. In the future, we look forward to advancing hardware and software to make automatic registration more accurate and the spatial hologram more stable.

5. Conclusion

We developed an AR-assisted positioning system for radiotherapy based on HoloLens 2 and evaluated its feasibility and accuracy. The results showed that the system's accuracy is in millimeters, which roughly meets clinical requirements and still needs to be further improved. However, considering the advantages, including intuitive visual guidance, radiation-free position verification, and intelligent interaction, the proposed AR method has a promising future.

Data availability statement

The raw data supporting the conclusions of this article will be made available by the authors, without undue reservation.

Author contributions

All authors contributed to the study's conception and design. Material preparation, data collection, and analysis were performed by GZ, XL, and LW. All authors read and approved the final manuscript.

Funding

This work was supported by the National Natural Science Foundation of China (grant numbers 8217102892, 81972863, 81627901, and 82030082) and Natural Science Foundation of Shandong Province (grant numbers ZR2019LZL012).

Conflict of interest

The authors declare that the research was conducted in the absence of any commercial or financial relationships that could be construed as a potential conflict of interest.

Publisher's note

References

1. Delaney G, Jacob S, Featherstone C, Barton M. The role of radiotherapy in cancer treatment: estimating optimal utilization from a review of evidence-based clinical guidelines. *Cancer* (2005) 104(6):1129–37. doi: 10.1002/cncr.21324

2. Begg AC, Stewart FA, Vens C. Strategies to improve radiotherapy with targeted drugs. *Nat Rev Cancer* (2011) 11(4):239–53. doi: 10.1038/nrc3007

3. Brock KK, Hawkins M, Eccles C, Moseley JL, Moseley DJ, Jaffray DA, et al. Improving image-guided target localization through deformable registration. *Acta Oncol* (2008) 47(7):1279–85. doi: 10.1080/02841860802256491

4. Guckenberger M, Meyer J, Vordermark D, Baier K, Wilbert J, Flentje M. Magnitude and clinical relevance of translational and rotational patient setup errors: A cone beam CT study. *Int J Radiat Oncol Biol Phys* (2006) 65(3):934–42. doi: 10.1016/j.ijrobp.2006.02.019

5. Cipresso P, Giglioli I, Raya MA, Riva G. The past, present, and future of virtual and augmented reality research: A network and cluster analysis of the literature. *Front Psychol* (2018) 9:2086. doi: 10.3389/fpsyg.2018.02086

6. Gnanasegaram JJ, Leung R, Beyea JA. Evaluating the effectiveness of learning ear anatomy using holographic models. *J Otolaryn Head Neck Surg* (2020) 49(1):63. doi: 10.1186/s40463-020-00458-x

7. Condino S, Turini G, Parchi PD, Viglialoro RM, Piolanti N, Gesi M, et al. How to build a patient-specific hybrid simulator for orthopaedic open surgery: Benefits and limits of mixed-reality using the Microsoft HoloLens. *J Healthc Eng* (2018) 2018:5435097. doi: 10.1155/2018/5435097

8. House PM, Pelzl S, Furrer S, Lanz M, Simova O, Voges B, et al. Use of the mixed reality tool "VSI patient education" for more comprehensible and imaginable patient educations before epilepsy surgery and stereotactic implantation of DBS or stereo-EEG electrodes. *Epilepsy Res* (2020) 159:106247. doi: 10.1016/j.eplepsyres.2019.106247

9. Saito Y, Sugimoto M, Imura S, Morine Y, Ikemoto T, Iwahashi S, et al. Intraoperative 3D hologram support with mixed reality techniques in liver surgery. *Ann Surg* (2020) 271(1):e4–7. doi: 10.1097/SLA.0000000000003552

10. Peh S, Chatterjea A, Pfarr J, Schäfer JP, Weuster M, Klüter T, et al. Accuracy of augmented reality surgical navigation for minimally invasive pedicle screw insertion in the thoracic and lumbar spine with a new tracking device. *Spine J* (2020) 20(4):629–37. doi: 10.1016/j.spinee.2019.12.009

11. Li Y, Chen X, Wang N, Zhang W, Li D, Zhang L, et al. A wearable mixed-reality holographic computer for guiding external ventricular drain insertion at the bedside. *J Neurosurg* (2018), 131(5):1–8. doi: 10.3171/2018.4.JNS18124

12. Talbot J, Meyer J, Watts R, Grasset R. A method for patient set-up guidance in radiotherapy using augmented reality. *Australas Phys Eng Sci Med* (2009) 32 (4):203–11. doi: 10.1007/BF03179240

13. Tarutani K, Takaki H, Igeta M, Fujiwara M, Okamura A, Horio F, et al. Development and accuracy evaluation of augmented reality-based patient positioning system in radiotherapy: A phantom study. *In Vivo* (2021) 35 (4):2081–7. doi: 10.21873/invivo.12477

14. Johnson PB, Jackson A, Saki M, Feldman E, Bradley J. Patient posture correction and alignment using mixed reality visualization and the HoloLens 2. *Med Phys* (2022) 49(1):15–22. doi: 10.1002/mp.15349

15. Frantz T, Jansen B, Duerinck J, Vandemeulebroucke J. Augmenting microsoft's HoloLens with vuforia tracking for neuronavigation. *Healthc Technol Lett* (2018) 5(5):221–5. doi: 10.1049/htl.2018.5079

16. Li C, Lu Z, He M, Sui J, Lin T, Xie K, et al. Augmented reality-guided positioning system for radiotherapy patients. *J Appl Clin Med Phys* (2022) 23(3): e13516. doi: 10.1002/acm2.13516

17. Cosentino F, John NW, Vaarkamp J. RAD-AR: RADiotherapy - augmented reality, in: *2017 International Conference on Cyberworlds (CW)*, Chester, (2017) (UK: *IEEE*). pp. 226–8.

18. Janabi HF, Aydin A, Palaneer S, Macchione N, Al-Jabir A, Khan MS, et al. Effectiveness of the HoloLens mixed-reality headset in minimally invasive surgery: a simulation-based feasibility study. *Surg Endosc* (2020) 34(3):1143–9. doi: 10.1007/s00464-019-06862-3

frontiers | Frontiers in Oncology

TYPE Original Research
PUBLISHED 14 October 2022
DOI 10.3389/fonc.2022.921473

OPEN ACCESS

EDITED BY
Davide Cusumano,
Agostino Gemelli University Polyclinic (IRCCS), Italy

REVIEWED BY
Marta Scorsetti,
Humanitas Research Hospital, Italy
Amedeo Capotosti,
Department of Diagnostic Imaging, Oncological Radiotherapy and Hematology (IRCCS), Italy

*CORRESPONDENCE
Steven N. Seyedin
sseyedin@hs.uci.edu

SPECIALTY SECTION
This article was submitted to Radiation Oncology, a section of the journal Frontiers in Oncology

RECEIVED 15 April 2022
ACCEPTED 23 September 2022
PUBLISHED 14 October 2022

CITATION
Seyedin SN, Bassalow R, Mawlawi OR, Turner LM, Patel RR, Mazin SR, Oderinde OM, Voronenko Y, Wages CA, Olcott PD, Chang JY, Balter PA and Welsh JW (2022) The potential of biology-guided radiation therapy in thoracic cancer: A preliminary treatment planning study. *Front. Oncol.* 12:921473. doi: 10.3389/fonc.2022.921473

The potential of biology-guided radiation therapy in thoracic cancer: A preliminary treatment planning study

Steven N. Seyedin[1]*, Rostem Bassalow[2], Osama R. Mawlawi[3], Lehendrick M. Turner[4], Roshal R. Patel[5], Samuel R. Mazin[6], Oluwaseyi M. Oderinde[6], Yevgen Voronenko[6], Cody A. Wages[4], Peter D. Olcott[6], Joe Y. Chang[4], Peter A. Balter[7] and James W. Welsh[4]

[1]Department of Radiation Oncology, University of California, Irvine-Chao Family Comprehensive Cancer Center, Orange, CA, United States, [2]Northwest Medical Physics Center, Lynnwood, WA, United States, [3]Department of Imaging Physics, The University of Texas MD Anderson Cancer Center, Houston, TX, United States, [4]Department of Radiation Oncology, The University of Texas MD Anderson Cancer Center, Houston, TX, United States, [5]Department of Radiation Oncology, Memorial Sloan Kettering Cancer Center, New York, NY, United States, [6]RefleXion Medical, Hayward, CA, United States, [7]Department of Radiation Physics, The University of Texas MD Anderson Cancer Center, Houston, TX, United States

Purpose: We investigated the feasibility of biology-guided radiotherapy (BgRT), a technique that utilizes real-time positron emission imaging to minimize tumor motion uncertainties, to spare nearby organs at risk.

Methods: Volumetric modulated arc therapy (VMAT), intensity-modulated proton (IMPT) therapy, and BgRT plans were created for a paratracheal node recurrence (case 1; 60 Gy in 10 fractions) and a primary peripheral left upper lobe adenocarcinoma (case 2; 50 Gy in four fractions).

Results: For case 1, BgRT produced lower bronchus V40 values compared to VMAT and IMPT. For case 2, total lung V20 was lower in the BgRT case compared to VMAT and IMPT.

Conclusions: BgRT has the potential to reduce the radiation dose to proximal critical structures but requires further detailed investigation.

KEYWORDS

radiation therapy, stereotactic radiotherapy, thoracic cancer, BgRT, PET guidance

Introduction

In the last years, the role of stereotactic ablative radiation therapy (SABR) has expanded dramatically with clinical trials demonstrating an overall survival benefit of SABR for oligometastatic disease and early-stage lung cancer (1–3). One of the major limitations to expanding SABR to other systemic sites is the anatomic proximity of many tumors to critical structures that are particularly sensitive to radiation effects and severe toxicities associated with respiratory-induced tumor motion during SABR delivery (4). With improvements in image guidance radiotherapy, recent advances in radiation precision to reduce toxicity risk have included MR-guided radiation therapy with an increase in soft tissue visualization as well as real-time adaptive CT imaging (5, 6).

One approach to reducing surrounding normal tissue dose during SABR is to increase the precision of radiation therapy delivery. RefleXion Medical (Hayward, CA) aims to achieve this by utilizing outgoing tumor positron emission tomography (PET) imaging data to deliver a tracked dose to a moving target during the normal breathing cycle, a concept called biology-guided radiotherapy (BgRT). This may reduce the dose to sensitive structures without the need for additional motion management techniques. The first BgRT machine, known as RefleXion X1®, is FDA cleared for intensity-modulated radiotherapy (IMRT) and SABR, while the BgRT component is available for investigational use.

In addition, the role of the biological signature from PET images in characterizing oncological diseases (directed personalized medicine) cannot be overemphasized. Studies have shown that PET images plays a crucial role in generating robust clinical trial data to support response-adapted treatment, predict treatment outcome, and enhance tumor staging (7, 8).

In this study, we investigated the feasibility of the BgRT dose to various tumor-adjacent structures by performing a preliminary dosimetric comparison to two other modern radiation therapy techniques, volumetric modulated arc therapy (VMAT) and intensity-modulated proton therapy (IMPT), for two challenging thoracic tumors.

Methods and materials

About the RefleXion X1 system

RefleXion X1 radiotherapy machine

The RefleXion X1 radiotherapy machine is a linear accelerator (linac) architecture with an integrated PET, an MV detector, and a 16-slice fan beam kVCT subsystem, all mounted on a 60 RPM rotatable slip-ring gantry (Figure 1) (9). The linac component produces a 6-MV (flattening filter free) beam with a nominal dose rate of 850 cGy/min. The X1 has a high-speed binary multi-leaf collimator (MLC) with 64 leaves, each leaf having a 6.25-mm width at the isocenter to achieve a highly conformal treatment delivery. The PET subsystem of the X1 machine is designed to acquire PET emissions, which is useful for creating BgRT plans and guiding the beamlet delivery guidance in real time. It has two symmetrically opposed 90°C arcs of PET detectors with 64 scintillation multi-pixel counter (MPPC) modules on each arc. Animations illustrating the technology and machine design are available at the RefleXion website (10). For treatment delivery on the X1 machine, the system leverages on the couch which operates in 5 degrees of freedom and translates (in the IEC-Y direction) the patient through the therapy plane to deliver the therapeutic beam to the whole tumor length and also mitigate interplay effects.

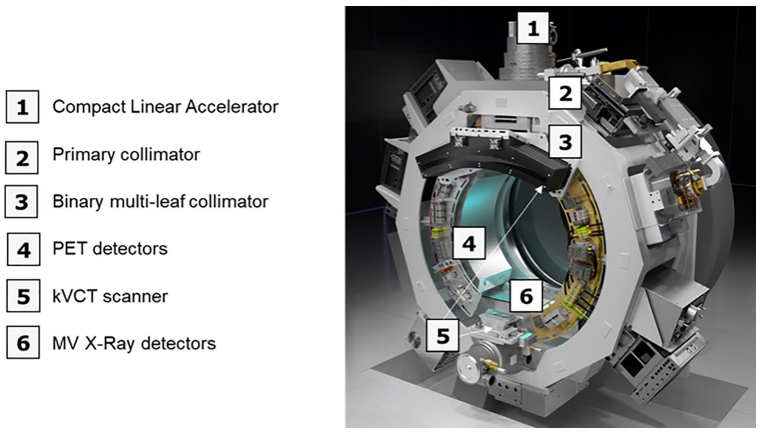

FIGURE 1
An overview of the X1 radiotherapy system showing the major components (without the couch component).

BgRT contouring

In standard treatment planning for respiratory induced tumor, the internal target volume (ITV) is contoured based on the tumor/gross tumor volume (GTV) motion extent provided by the 4DCT images during the simulation CT acquisition.

In contrast, BgRT planning uses a single-phase GTV to create a PTV from applying a biology-guidance margin (BgM) which accounts for intrinsic biologic guidance localization uncertainties to the GTV (Figure 2). A second volume generated is the biology-tracking zone (BTZ) which encompasses the motion extent of the GTV with addition of the BgM. The BTZ is not a treatment volume but the limiting region where the treatment dose would be delivered. It means that the PET signal from outside the BTZ would not be a useful information to guide the therapeutic beamlet delivery in real time. Due to the PET biological signature, a 3-mm BgM was chosen instead to account for biological localization uncertainties in the BgRT workflow and algorithm. In addition, a 4-mm isotropic expansion was included to account for the BTZ dose delivery region extent. These expansions were selected due to the spatial resolution of the RefleXion X1 PET detectors (11). The BgRT planning process consists of first defining the target coverage goals and organ-at-risk (OAR) constraints and subsequently calculating a fluence mapping from a planning PET image to achieve the desired dose objectives using the cost function optimization process.

BgRT treatment planning system

BgRT delivers a radiotherapy plan to the tumor envelope using the annihilated photons emanating from the PET avidity tumor. It allows radiation dose delivery based on the collection and processing of PET data from a radiotracer that is injected into a patient on the day of treatment. In this way, BgRT uniquely utilizes radiotracer uptake as a biological beacon for targeting, tracking, and adjusting dose delivery in real time to account for target motion. Before treatment, patient PET data are collected to evaluate the patient's candidacy for BgRT treatment. For ^{18}F-FDG, the acceptable threshold for activity concentration (AC) and the normalized tumor signal (NTS) are 5 kBq/cc and 2.7, respectively. However, these metrics may change for non-FDG radiotracers.

The BgRT treatment planning system (TPS) is built to use the PET data to optimize the treatment plans. The first step in the treatment planning process is to import the CT simulation and CT-defined RT structures to the BgRT TPS. Then, the physician will define the prescribed dose objectives, and the patient is approved for PET data acquisition procedure on the X1 machine. Post PET data acquisition, the BgRT TPS algorithm will then use the acquired PET data to create a fluence map that will satisfy the prescribed dose objectives. In this study, the PET data used for BgRT planning were acquired on a third-party diagnostic static ring PET system (PET data from the institutional archive) and extrapolated to a rotating dual arc PET system on the X1 machine.

BgRT plan delivery

During BgRT delivery, the machine utilizes rapidly acquired "limited time sampled (LTS)" PET images to guide the beam using the mapping calculated during BgRT planning. The LTS imaging data include 500 ms of data acquisition but are updated every 100 ms in a sliding-window scheme. The average latency is around 400 ms and is compensated by adding a BgRT-related margin at the time of planning. This allows for tracked delivery to the target in real time as it moves within the BTZ. The updated LTS imaging data at the 100-ms interval is used to calculate a partial fluence, which is segmented into machine instruction to deliver the fluence until the whole planned dose is delivered to the PET-avid tumor. BgRT accounts for various treatment- and tumor-motion-related uncertainties, potentially allowing its safe use to treat tumors that are both close to critical structures and mobile (i.e., lung malignancies). A prior iteration of the BgRT algorithm has been published (9, 12).

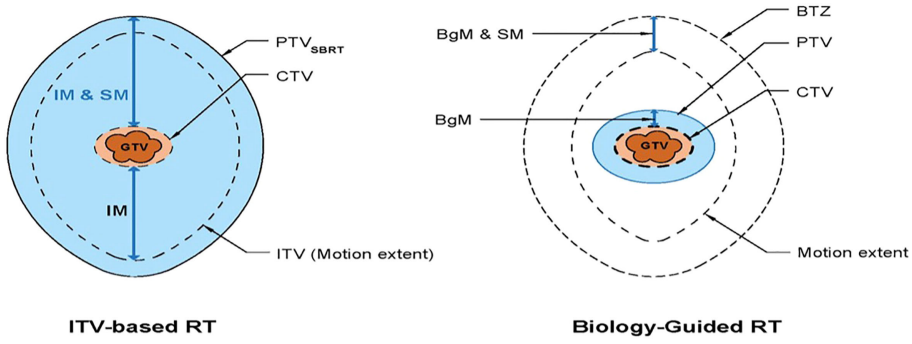

FIGURE 2
Schematic diagram showing the standard RT volumes (left) versus the BgRT volumes (8). IM, internal margin; SM, setup margin; BgM, biology-guided margin; BTZ, biology-tracking zone.

Patients and dose rationale

Because 4D-PET/CT data were required in order to create BgRT plans at the time this study began, we accessed an archive of patients with available ^{18}F-FDG-PET/CT data without iodine contrast collected through approved institutional review board (IRB 2008-0853). From this set, two patients with lung tumors amenable to SABR were selected for dosimetric analysis. All data were appropriately anonymized.

The first patient was a 76-year-old woman who had been treated twice with VMAT (once to 50 Gy in 10 fractions and the second time to 60 Gy in 10 fractions) for a right middle lobe bronchoalveolar carcinoma. Approximately 6 months after the second treatment, a recurrence developed in a right lower paratracheal node. This node was encompassed in the GTV, which was expanded to create the planning target volume (PTV), as described below. Plans for BgRT, VMAT, and IMPT were created with the goal of administering 60 Gy in 10 fractions (BED 96; α/β =10) to at least 95% of the PTV while attempting to minimize the dose to the aorta, bronchus, chest wall, and esophagus. This prescription was considered to be safe for using SABR to treat centrally located tumors and was recently confirmed by initial phase I results of RTOG 0813 data finding 12 Gy per fraction to be the maximal tolerated dose (13). In addition, our institution had published data validating the efficacy of treating central tumors in 10 fractions when unable to meet normal structure constraints for four fraction plans (14). This case was chosen for the difficulty in meeting normal-tissue dose constraints because of the retreatment and the dose overlap within critical structures.

The second treatment-plan comparison was for a 75-year-old woman with a newly diagnosed 2.5 cm × 2.5 cm lung adenocarcinoma in the left upper lobe, with close proximity to the chest wall. BgRT, VMAT, and IMPT plans were created to deliver 50 Gy in four fractions to at least 95% of the PTV while attempting to minimize the chest wall V30 and the dose to the left lung. This dose and fractionation produces a BED of 112.5, and BED ≥100 has been retrospectively found to produce an approximate 90% local control rate at 3 years (15).

Initial 4D positron emission tomography/computerized tomography (PET/CT) data were obtained with a GE Healthcare Discovery PET/CT 690.

Treatment planning parameters for all plans

Because the patients selected from an IRB imaging study, radiation planning was performed from the 4D-CT imaging previously obtained as part of the study described above rather than a standard CT simulation.

VMAT and IMPT plans were created using commercial treatment planning systems. BgRT plans were created using research treatment planning software (v2017, RefleXion Medical, Hayward, CA). The same planning goals and OAR constraints were used for planning across all modalities (BgRT, VMAT, IMPT). All three modalities for both patients were normalized such that PTV D_{95}, the fraction of the prescription dose covering 95% of the PTV volume, was equal to the prescribed dose (D_{rx}) in order to facilitate comparison of critical structure doses for all three modalities. A recent retrospective analysis of early-stage lung cancers treated with SABR noted higher rates of local control when PTV D_{95} BED_{10} was greater than 86 Gy, making PTV D_{95} an ideal normalization metric (16). D_1 (fraction of the prescription dose that covers 1% of the PTV) was calculated for both cases to represent the maximum PTV dose, which was then divided by the prescribed dose to reflect differences in treatment heterogeneity.

For VMAT and IMPT plans, a GTV was contoured on a single phase from the 4DCT scan. No other 4D imaging was used to generate the treatment volume. For case 1, 6-mm isotropic expansions to generate the PTV from the GTV were chosen as mediastinal recurrences demonstrate minimal motion within 7 mm (17). Additionally, due to prior radiation treatment, smaller margins were chosen to minimize treatment volumes and prior dose overlap. For case 2, 8-mm isotropic expansion to generate the PTV from the GTV was utilized as upper respiratory tumor display minimal motion (18).

VMAT planning

Volumetric modulation was achieved by using two dynamic arcs per patient. The arc arrangement for case 1 consisted of a total of 356° geometry starting at 182° and ending at 178°. The arc arrangement for case 2 consisted of a total of 184° geometry starting at 352° and ending at 176°. Collimation per arc was chosen to maximize blocking adjacent structures while providing adequate treatment to targets.

IMPT planning

Scanning-beam IMPT plans were created by using an inverse-planning format and single-field optimization technique, meaning that each beam individually covers the target. Appropriately weighted objectives were used to maximize coverage and conformality while minimizing hot spots. Care was taken regarding beam selection to reduce exposure to normal tissues, particularly critical structures distal to the target.

BgRT planning

The BgRT plan used the same GTV as the VMAT and IMPT plan. However, because the BgRT can deliver a tracked dose of radiation to a moving target, the range of motion of the target does not need to be included in the PTV expansion.

Results

Table 1 summarizes results for the two patients. In terms of doses to critical structures for the first patient, BgRT delivered comparable maximum point doses of 1 cc of the aorta (BgRT 56.4 Gy, VMAT 61.2 Gy, and IMPT 53.9 Gy) and 5 cc of the aorta (47.9 Gy BgRT, 54.2 Gy VMAT, and 40.6 Gy IMPT). BgRT decreased bronchus V40 values (38.7%) compared to 43.7% for VMAT and 41.9% for IMPT, and bronchus D5cc doses (46.5 Gy BgRT) compared to 54.6 Gy VMAT and 51.3 Gy IMPT. BgRT esophageal V40 were lower (4.0%) than VMAT (10.6%) but higher than IMPT (1.7%), while the D5cc values were similar (1.8 Gy) to both VMAT (2.2 Gy) and IMPT (3.7 Gy). Similar degrees of treatment inhomogeneity (D_1/D_{rx}) were present in the BgRT (114.3%) and VMAT (113.1%) plans, but the IMPT plan was higher (121.2%). CT images with isodose lines and the corresponding DVH data are shown in Figures 3, 4.

For the second patient, involving SABR to the chest wall, the BgRT chest wall V30 (1.4%) was less than those of VMAT (3.6%) and IMPT (2.1%). Total lung V20 was also lower in BgRT (7.5%) compared to VMAT (10.8%) and IMPT (9.3%). The D_1/D_{rx} for the BgRT, VMAT, and IMPT plans were 114.9%, 108.6%, and 122.5%, respectively. CT images with isodose lines and the corresponding DVH data are shown in Figures 5, 6.

Discussion

This preliminary treatment planning report investigated the feasibility of using BgRT to deliver a therapeutic beam to adjacent OAR and compare the dosimetric performance to VMAT or IMPT for the treatment of challenging thoracic tumors. Although BgRT uses traditional linac technology with an integrated PET subsystem, it represents an advancement in its consideration of both tumor motion and treatment-related uncertainties.

TABLE 1 Dose–volume statistics for the two clinical cases.

Case 1	BgRT	VMAT	IMPT
D1/Drx, %	114.3	113.1	121.2
Bronchus V40, % (cc)	38.7 (6.0)	43.7 (6.7)	41.9 (6.5)
Bronchus D1cc, Gy	61.2	64.9	64.9
Bronchus D5cc, Gy	46.5	54.6	51.3
Aorta V40, % (cc)	7.6 (10.8)	10.7 (15.2)	3.5 (5.0)
Aorta D1cc, Gy	56.4	61.2	53.9
Aorta D5cc, Gy	47.9	54.2	40.6
Esophagus V40, % (cc)	4.0% (0.6)	10.6 (1.7)	1.7 (0.3)
Esophagus D1cc, Gy	36.9	49.4	29.9
Esophagus D5cc, Gy	1.8	2.2	3.7
Mean lung, Gy	5.9	6.1	4.5
Lung V20, %	3.8	4.5	4.5
Chest wall V30, %	3.7	5.2	2.6
Case 2	**BgRT**	**VMAT**	**IMPT**
D1/Drx, %	115.0	108.7	122.6
Chest wall V30, % (cc)	1.4 (27.8)	3.6 (71.1)	2.1 (40.6)
Mean lung, Gy	4.7	5.7	4.6
Lung V20, %(cc)	7.5 (312.8)	10.8 (449.0)	9.3 (385.1)

Our first case involved a paratracheal lymph node relapse after VMAT for two primary bronchoalveolar carcinomas in the right middle lobe. A retrospective evaluation of the composite dose to the aorta for 35 patients who received radiation as retreatment for NSCLC showed that composite doses of >120 Gy to 1 cc of the aorta correlated with high-grade aortic toxicity (19). The location of the primary (previously treated) lesions near the aorta in our first case (Figure 3) prompted us to evaluate the aorta dose. We found that BgRT and IMPT would produce similar maximum doses to 1 cc of the aorta and thus equivalent 1 cc composite doses. Additionally, a lower bronchus V_{40} (11% lower in the BgRT plan than VMAT and 8% lower than in the IMPT plan) could reduce the risk of radiation-induced bronchial necrosis (20, 21).

In the second case, we investigated radiation exposure to the total lung and chest wall for the treatment of an upper lobe tumor, a situation commonly encountered in the clinic. A previous investigation of SABR for thoracic tumors noted that a chest wall V30 greater than 30 cc was associated with higher rates of chest wall toxicity (22). Of the three treatment techniques examined here, the BgRT plans had lower V30 values (27.8 cc) compared to VMAT and IMPT (71.1 cc and 40.6 cc, respectively). BgRT had the lowest V20 for the total lung (7.5%) compared to IMPT (9.3%) or VMAT (10.8%), which is notable because higher lung V20 values are associated with increased risk of radiation pneumonitis (23). The ability of BgRT to reduce exposure of the chest wall and lung could reduce the risk of acute and chronic radiation-induced toxicity.

The primary goal of this study is to explore the feasibility and potential of BgRT to reduce nearby organ dose. Nevertheless, limitations are present in this dosimetric comparison study. Because we compared treatment plans for only two patients, no statistical comparisons were possible. Minor dose reductions to nearby critical structure obtained by BgRT may not translate to a clinical benefit. BgRT targets metabolically active tissue emitting a positron from ^{18}F tagged to a modified glucose unit; however, elevated glucose metabolism occurs in a variety of conditions other than cancer (24). This could lead to mistreatment of falsely positive PET avid non-malignant conditions if not accounted. Finally, smaller PTV expansion margins for BgRT plans compared to IMPT and VMAT plans produce a smaller PTV volume which reduces the dose to nearby structures. Further experimental work is required to validate the safety of the 3-mm GTV expansion margins used to create the PTV for the BgRT plans. However, the purpose of the study was to explore the dosimetric reduction potential of BgRT due to its ability to track tumor motion and deliver radiation using PET signaling in real time, which prompted the use of smaller margins than conventional IMRT or VMAT planning. Finally, the authors

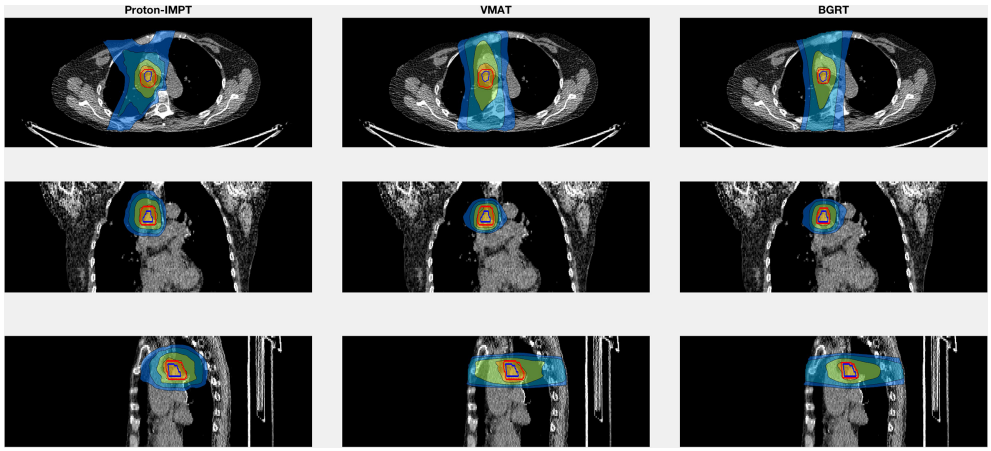

FIGURE 3
Isodose line images for case 1, involving a right lower paratracheal node recurrence after two VMAT regimens for a right middle lobe bronchoalveolar carcinoma. Isodose lines depicted are 10 Gy (blue), 20 Gy (teal), 40 Gy (green), and 60 Gy (yellow). GTV is contoured in blue. PTV displayed in red (6 mm GTV expansion for IMPT and VMAT and 3 mm for BgRT).

acknowledge that although our model attempts to limit the doses to critical structures in the VMAT and IMPT plans, these dose distributions may vary slightly in 4D gated plans, which is currently under investigation.

Because BgRT utilizes positron emissions to target radiation, logistical obstacles remain when integrating the technology into clinical practice. Various steps in the workflow including imaging, dose evaluation, and BgRT delivery require further elucidation. Although radiation-induced inflammation tends to peak at several weeks after treatment, high avidity in surrounding areas that are inflamed after single-fraction high-dose radiation certainly poses an obstacle for use of BgRT (25). Because patients undergoing BgRT would require daily injections of a positron-emitting radioactive tracer, BgRT would ideally be suited for patients who need high-dose hypofractionated SABR treatment. The use of SABR has increased over the past decade especially in the setting of metastatic disease with or without immunotherapy (26–28). BgRT could be applied in the oligometastatic setting, improving the workflow and allowing SABR on a greater

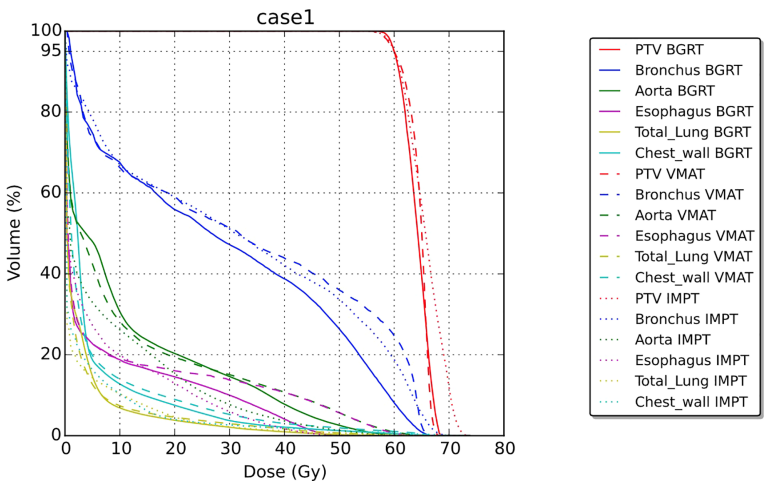

FIGURE 4
Dose–volume histogram for case 1.

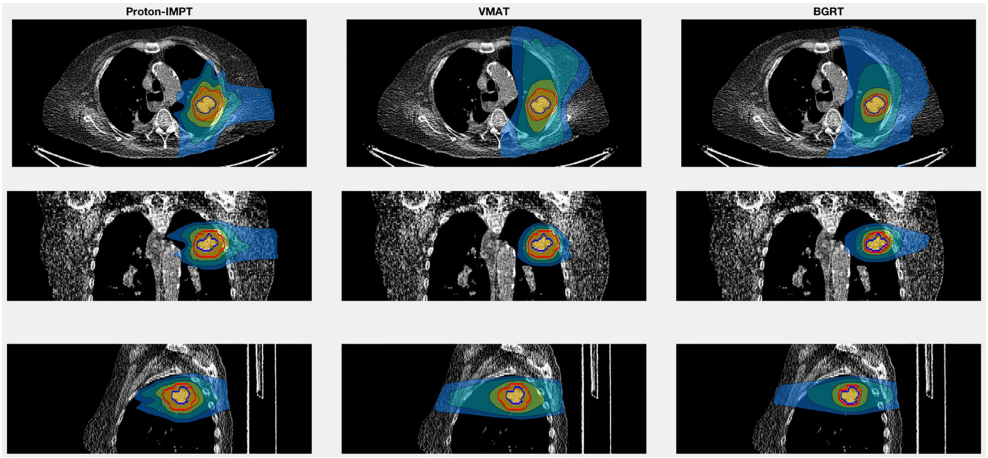

FIGURE 5
Isodose line images for case 2, involving a newly diagnosed adenocarcinoma in the upper lobe of the left lung. Isodose lines depicted are 10 Gy (blue), 20 Gy (teal), 40 Gy (green), and 50 Gy (yellow). GTV is contoured in blue. PTV displayed in red (8 mm GTV expansion for IMPT and VMAT and 3 mm for BgRT).

number of isocenters. Because BgRT may be able to target the GTV in real time, another possible approach to integrating it into clinical practice would be for weekly boosts to IMRT.

In summary, because BgRT can provide real-time radiation treatment independent of tumor motion, it has the potential to be the next logical progression toward increasing precision of radiation treatment. This preliminary investigation demonstrates BgRT's dosimetric feasibility compared to non-gated VMAT and IMPT. However, further investigation effectively comparing BgRT to other photon and proton treatment modalities to learn if BgRT has the potential to reduce the dose to adjacent critical structures to a greater extent is needed. Given the necessity for daily tracer injections, BgRT is currently suited toward hypofractionated radiation. However, as this technology enters into the clinic, novel applications of BgRT into the classical 2-Gy per fraction

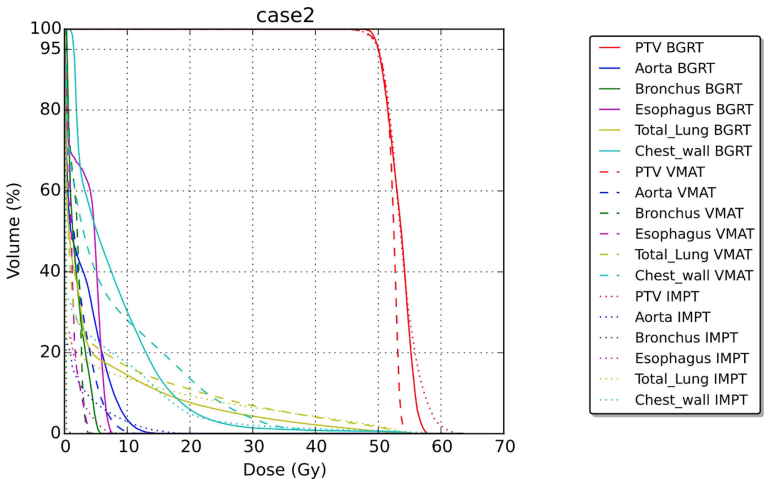

FIGURE 6
Dose–volume histogram for case 2.

course require exploration, potentially as a boost. Going forward, entirely new fractionation schedules could be developed specifically to exploit the benefits of BgRT.

Data availability statement

The data analyzed in this study is subject to the following licenses/restrictions: They are the CT Dicom datasets, which we don't have the privilege to share. Requests to access these datasets should be directed to ooderinde@reflexion.com.

Author contributions

SS, RB, JW, and SM conceptualized the work. PO, OM, LT, and YV supervised the work. SS and RB collected the data, carried out the treatment planning, and analyzed the data. SS, RB, JW, OO, SM, PO, OM, LT, JC, CW, PB, and YV wrote and revised the manuscript. All authors contributed to the article and approved the submitted version.

Conflict of interest

JW is a member of the board of advisors and has equity at RefleXion Medical. SM is the founder and CTO of RefleXion Medical. YV is a software architect, RB is a medical physicist, PO is a PET engineer at RefleXion Medical and OO is a clinical scientist at RefleXion Medical.

The remaining authors declare that the research was conducted in the absence of any commercial or financial relationships that could be construed as a potential conflict of interest.

Publisher's note

References

1. Palma DA, Olson R, Harrow S, Gaede S, Louie AV, Haasbeek C, et al. Stereotactic ablative radiotherapy for the comprehensive treatment of oligometastatic cancers: Long-term results of the SABR-COMET phase II randomized trial. *J Clin Oncol* (2020) 38(25):2830–8. doi: 10.1200/JCO.20.00818

2. Gomez DR, Tang C, Zhang J, Blumenschein GR Jr, Hernandez M, Lee JJ, et al. Local consolidative therapy vs. maintenance therapy or observation for patients with oligometastatic non-Small-Cell lung cancer: Long-term results of a multi-institutional, phase II, randomized study. *J Clin Oncol* (2019) 37(18):1558–65. doi: 101200/JCO1900201

3. Chang JY, Mehran RJ, Feng L, Verma V, Liao Z, Welsh JW, et al. Stereotactic ablative radiotherapy for operable stage I non-small-cell lung cancer (revised STARS): long-term results of a single-arm, prospective trial with prespecified comparison to surgery. *Lancet Oncol* (2021) 22(10):1448–57. doi: 10.1016/S1470-2045(21)00401-0

4. Chi A, Nguyen NP, Komaki R. The potential role of respiratory motion management and image guidance in the reduction of severe toxicities following stereotactic ablative radiation therapy for patients with centrally located early stage non-small cell lung cancer or lung metastases. *Front Oncol* (2014) 4:151. doi: 10.3389/fonc.2014.00151

5. Luterstein E, Cao M, Lamb J, Raldow AC, Low DA, Steinberg ML, et al. Stereotactic MRI-guided adaptive radiation therapy (SMART) for locally advanced pancreatic cancer: A promising approach. *Cureus* (2018) 10(3):e2324. doi: 10.7759/cureus.2324

6. Byrne M, Archibald-Heeren B, Hu Y, Teh A, Beserminji R, Cai E, et al. Varian Ethos online adaptive radiotherapy for prostate cancer: Early results of contouring accuracy, treatment plan quality, and treatment time. *J Appl Clin Med Phys* (2022) 23(1):e13479. doi: 10.1002/acm2.13479

7. Boellaard R, Delgado-Bolton R, Oyen WJ, Giammarile F, Tatsch K, Eschner W, et al. FDG PET/CT: EANM procedure guidelines for tumour imaging: version 2.0. *Eur J Nucl Med Mol Imaging* (2015) 42(2):328–54. doi: 10.1007/s00259-014-2961-x

8. El Naqa I, Grigsby P, Apte A, Kidd E, Donnelly E, Khullar D, et al. Exploring feature-based approaches in PET images for predicting cancer treatment outcomes. *Pattern Recognit* (2009) 42(6):1162–71. doi: 10.1016/j.patcog.2008.08.011

9. Oderinde OM, Shirvani SM, Olcott PD, Kuduvalli G, Mazin S, Larkin D, et al. The technical design and concept of a PET/CT linac for biology-guided radiotherapy. *Clin Transl Radiat Oncol* (2021) 29:106–12. doi: 10.1016/j.ctro.2021.04.003

10. Available at: https://reflexion.com/our-technology/.

11. Hu Z, Ferri V, Iagaru A, Kovalchuk N, Han B, et al. Image-mode performance characterisation of a positron emission tomography subsystem designed for biology-guided radiotherapy (BgRT). *Br J Radiol* (2022).

12. Hrinivich WT, Phillips R, Da Silva AJ, Radwan N, Gorin MA, Rowe SP, et al. Online prostate-specific membrane antigen and positron emission tomography-guided radiation therapy for oligometastatic prostate cancer. *Adv Radiat Oncol* (2020) 5(2):260–8. doi: 10.1016/j.adro.2019.10.006

13. Bezjak A, Paulus R, Gaspar LE, Timmerman RD, Straube WL, Ryan WF, et al. Safety and efficacy of a five-fraction stereotactic body radiotherapy schedule for centrally located non-Small-Cell lung cancer: NRG Oncology/RTOG 0813 trial. *J Clin Oncol* (2019) 37(15):1316–25. doi: 10.1200/JCO.18.00622

14. Chang JY, Li QQ, Xu QY, Allen PK, Rebueno N, Gomez DR, et al. Stereotactic ablative radiation therapy for centrally located early stage or isolated parenchymal recurrences of non-small cell lung cancer: how to fly in a "no fly zone". *Int J Radiat Oncol Biol Phys* (2014) 88(5):1120–8. doi: 10.1016/j.ijrobp.2014.01.022

15. Onishi H, Shirato H, Nagata Y, Hiraoka M, Fujino M, Gomi K, et al. *Hypofractionated stereotactic radiotherapy (HypoFXSRT) for stage I non-small cell lung cancer: updated results of 257 patients in a Japanese multi-institutional study. J Thorac Oncol* (2007) 2(7 Suppl 3):S94–100. doi: 10.1097/JTO.0b013e318074de34

16. Zhao L, Zhou S, Balter P, Shen C, Gomez DR, Welsh JD, et al. Planning target volume D95 and mean dose should be considered for optimal local control for stereotactic ablative radiation therapy. *Int J Radiat Oncol Biol Phys* (2016) 95(4):1226–35. doi: 10.1016/j.ijrobp.2016.01.065

17. Schmidt ML, Hoffmann L, Knap MM, Rasmussen TR, Folkersen BH, Toftegaard J, et al. Cardiac and respiration induced motion of mediastinal lymph node targets in lung cancer patients throughout the radiotherapy treatment course. *Radiother Oncol* (2016) 121(1):52–8. doi: 10.1016/j.radonc.2016.07.015

18. Liu HH, Balter P, Tutt T, Choi B, Zhang J, Wang C, et al. Assessing respiration-induced tumor motion and internal target volume using four-dimensional computed tomography for radiotherapy of lung cancer. *Int J Radiat Oncol Biol Phys* (2007) 68(2):531–40. doi: 10.1016/j.ijrobp.2006.12.066

19. Evans JD, Gomez DR, Amini A, Rebueno N, Allen PK, et al. Aortic dose constraints when reirradiating thoracic tumors. *Radiother Oncol* (2013) 106(3):327–32. doi: 10.1016/j.radonc.2013.02.002

20. Mehta AC, Dweik RA. Necrosis of the bronchus. role of radiation. *Chest* (1995) 108(5):1462–6. doi: 10.1378/chest.108.5.1462

21. Antunes A, Gomes J, Neves S, Oliveira A, Almeida J, JM ES, et al. Necrosis of bronchus in lung cancer. *J Bronchology Interv Pulmonol* (2011) 18(4):348–51. doi: 10.1097/LBR.0b013e318235d805

22. Dunlap NE, Cai J, Biedermann GB, Yang W, Benedict SH, Sheng K, et al. Chest wall volume receiving >30 gy predicts risk of severe pain and/or rib fracture after lung stereotactic body radiotherapy. *Int J Radiat Oncol Biol Phys* (2010) 76 (3):796–801. doi: 10.1016/j.ijrobp.2009.02.027

23. Yamashita H, Takahashi W, Haga A, Nakagawa K. Radiation pneumonitis after stereotactic radiation therapy for lung cancer. *World J Radiol* (2014) 6(9):708–15. doi: 10.4329/wjr.v6.i9.708

24. Barthel H, Schroeter ML, Hoffmann KT, Sabri O. PET/MR in dementia and other neurodegenerative diseases. *Semin Nucl Med* (2015) 45(3):224–33. doi: 10.1053/j.semnuclmed.2014.12.003

25. Ulaner GA, Lyall A. Identifying and distinguishing treatment effects and complications from malignancy at FDG PET/CT. *Radiographics* (2013) 33 (6):1817–34. doi: 10.1148/rg.336125105

26. Lin AJ, Roach M, Bradley J, Robinson C. Combining stereotactic body radiation therapy with immunotherapy: current data and future directions. *Transl Lung Cancer Res* (2019) 8(1):107–15. doi: 1021037/tlcr20180816

27. Palma DA, Olson R, Harrow S, Gaede S, Louie AV, Haasbeek C, et al. Stereotactic ablative radiotherapy versus standard of care palliative treatment in patients with oligometastatic cancers (SABR-COMET): a randomised, phase 2, open-label trial. *Lancet* (2019) 393(10185):2051–8. doi: 10.1016/S0140-6736(18)32487-5

28. Videtic GM, Hu C, Singh AK, Chang JY, Parker W, Olivier KR, et al. A randomized phase 2 study comparing 2 stereotactic body radiation therapy schedules for medically inoperable patients with stage I peripheral non-small cell lung cancer: NRG oncology RTOG 0915 (NCCTG N0927). *Int J Radiat Oncol Biol Phys* (2015) 93(4):757–64. doi: 10.1016/j.ijrobp.2015.07.2260

Frontiers in Oncology

Advances knowledge of carcinogenesis and tumor progression for better treatment and management

The third most-cited oncology journal, which highlights research in carcinogenesis and tumor progression, bridging the gap between basic research and applications to imrpove diagnosis, therapeutics and management strategies.

Discover the latest Research Topics

See more →

Frontiers

Avenue du Tribunal-Fédéral 34
1005 Lausanne, Switzerland
frontiersin.org

Contact us

+41 (0)21 510 17 00
frontiersin.org/about/contact